Studies in Applied Mechanics

46

Damage Mechanics in Engineering Materials

edited by

G.Z. Voyiadjis
J.-W. Ju
J.-L. Chaboche

Elsevier

STUDIES IN APPLIED MECHANICS 46

Damage Mechanics in Engineering Materials

STUDIES IN APPLIED MECHANICS

20. Micromechanics of Granular Materials (Satake and Jenkins, Editors)
21. Plasticity. Theory and Engineering Applications (Kaliszky)
22. Stability in the Dynamics of Metal Cutting (Chiriacescu)
23. Stress Analysis by Boundary Element Methods (Balas, Sládek and Sládek)
24. Advances in the Theory of Plates and Shells (Voyiadjis and Karamanlidis, Editors)
25. Convex Models of Uncertainty in Applied Mechanics (Ben-Haim and Elishakoff)
28. Foundations of Mechanics (Zorski, Editor)
29. Mechanics of Composite Materials - A Unified Micromechanical Approach (Aboudi)
31. Advances in Micromechanics of Granular Materials (Shen, Satake, Mehrabadi, Chang and Campbell, Editors)
32. New Advances in Computational Structural Mechanics (Ladevèze and Zienkiewicz, Editors)
33. Numerical Methods for Problems in Infinite Domains (Givoli)
34. Damage in Composite Materials (Voyiadjis, Editor)
35. Mechanics of Materials and Structures (Voyiadjis, Bank and Jacobs, Editors)
36. Advanced Theories of Hypoid Gears (Wang and Ghosh)
37A. Constitutive Equations for Engineering Materials
Volume 1: Elasticity and Modeling (Chen and Saleeb)
37B. Constitutive Equations for Engineering Materials
Volume 2: Plasticity and Modeling (Chen)
38. Problems of Technological Plasticity (Druyanov and Nepershin)
39. Probabilistic and Convex Modelling of Acoustically Excited Structures (Elishakoff, Lin and Zhu)
40. Stability of Structures by Finite Element Methods (Waszczyszyn, Cichoń and Radwańska)
41. Inelasticity and Micromechanics of Metal Matrix Composites (Voyiadjis and Ju, Editors)
42. Mechanics of Geomaterial Interfaces (Selvadurai and Boulon, Editors)
43. Materials Processing Defects (Ghosh and Predeleanu, Editors)
44. Damage and Interfacial Debonding in Composites (Voyiadjis and Allen, Editors)
45. Advanced Methods in Materials Processing Defects (Predeleanu and Gilormini, Editors)
46. Damage Mechanics in Engineering Materials (Voyiadjis, Ju and Chaboche, Editors)

General Advisory Editor to this Series:
Professor Isaac Elishakoff, Center for Applied Stochastics Research, Department of Mechanical Engineering, Florida Atlantic University, Boca Raton, FL, U.S.A.

STUDIES IN APPLIED MECHANICS 46

Damage Mechanics in Engineering Materials

Edited by

George Z. Voyiadjis

Department of Civil and Environmental Engineering
Louisiana State University
Baton Rouge, LA, USA

Jiann-Wen Woody Ju

Department of Civil Engineering
University of California at Los Angeles
Los Angeles, CA, USA

Jean-Louis Chaboche

ONERA
Resistance des Structures, BP 72
F-92322 Chatillon Cedex, France

1998

ELSEVIER
Amsterdam - Lausanne - New York - Oxford - Shannon - Singapore - Tokyo

ELSEVIER SCIENCE Ltd
The Boulevard, Langford Lane
Kidlington, Oxford OX5 1GB, U.K.

Copyright © 1998 Elsevier Science Ltd

All rights reserved. No part of this publication may be reproduced, stored in a retrieval system or transmitted in any form or by any means, electronic, electrostatic, magnetic tape, mechanical, photocopying, recording or otherwise, without permission in writing from the publishers.

First edition 1998

Library of Congress Cataloging in Publication Data
A catalog record from the Library of Congress has been applied for.

ISBN: 0-080-43322-7

♾ The paper used in this publication meets the requirements of ANSI/NISO Z39.48-1992 (Permanence of Paper)

Printed in The Netherlands.

FOREWORD

This book contains thirty papers that are based on the presentations made in the eleven-session Symposium on "Damage Mechanics in Engineering Materials" on the occasion of the Joint ASME/ASCE/SES Mechanics Conference (McNU97), held in Evanston, Illinois, June 28-July 2, 1997. These sessions were mainly in the constitutive modeling of damage mechanics of engineering materials. These papers represent the most recent work conducted on damage mechanics in engineering materials. They encompass macromechanical/micromechanical constitutive modeling, experimental procedures, and numerical modeling. Inelastic behavior, interfaces, damage, fracture, failure, and computational methods are included.

The book is divided into six parts. Part I is general and deals with the study of damage mechanics. Part II is on the localization and damage. Damage in Brittle Materials is presented in Part III, while Part IV deals with damage in metals and metal matrix composites. The computational aspects of damage models are presented in two papers in Part V. Finally, two papers in Part VI present damage in polymers and elastomers. The papers discuss topics ranging from theoretical treatments to experimental investigation. The papers investigate both micromechanics and continuum aspects of damage in materials.

We express our gratitude to all the authors that contributed to this work. Their time and effort are greatly appreciated.

George Z. Voyiadjis
Baton Rouge, Louisiana

Jiann-Wen Woody Ju
Los Angeles, California

Jean-Louis Chaboche
Paris, France

September 1997

This Page Intentionally Left Blank

TABLE OF CONTENTS

PART II: LOCALIZATION AND DAMAGE

PART III: DAMAGE IN BRITTLE MATERIALS

PART IV: DAMAGE IN METALS AND METAL MATRIX COMPOSITES

This Page Intentionally Left Blank

PART I

DAMAGE MECHANICS

This Page Intentionally Left Blank

Damage Mechanics in Engineering Materials
G.Z. Voyiadjis, J.-W.W. Ju and J.-L. Chaboche (Editors)
1998 Elsevier Science B.V.

Continuum Damage Mechanics of Composites: Towards a Unified Approach

J.L. Chaboche, O. Lesné, T. Pottier
O.N.E.R.A.
29 avenue de la Division Leclerc
92320 Châtillon, France

Abstract

A constitutive framework is developed for the inelastic analysis of composite structures. It is based on a Continuum Damage Mechanics approach, at the mesoscopic level of each ply (for laminates) or at the macroscopic level for more homogeneous sequences. The theory is developed in a hierarchical order, involving the successive modelling of elasticity coupled with damage, elasto-viscoplasticity coupled with damage and viscoelasticity/recovery coupled with damage. A particular attention is focused on the modelling of damage deactivation effects, which stays a key difficulty for cyclic loadings. The capabilities of the models are illustrated on three quite different materials, a SiC/SiC composite, a SiC/Ti composite and a C/PMR15 composite.

1. INTRODUCTION

The inelastic analysis of composite structural elements needs the development of good constitutive equations that incorporate both the inelastic-plastic-viscoplastic behaviour and the effect of the progressive damage growth. For computational efficiency evidences, this had to be done at some continuum level, often called the mesoscale for composite structures.

During the past decade, specific efforts have been done in the constitutive modelling of composite materials. Different classes of theories have been developed with the helps of micromechanics, but at the scale of the continuum, assuming the existence of a Representative Volume Element of material (RVE). In this paper, we concentrate the efforts on the macroscopic modelling tools, directly useful for the structural inelastic analysis, based on the continuum thermodynamics with internal variables and Continuum Damage Mechanics (CDM) concepts.

A rapid survey of the literature does not show a very large number of researchers in this field, and at the macroscopic continuum level, for developing constitutive models for composites, from the theoretical basis to the complete identification and application. We can mention Talreja [1-2], Allen et al. [3], Ladeveze and Allix [4-6], Robinson et al. [7], Kattan and Voyiadjis [8], Perreux and Oytana [9], Chow and Yang [10] and probably some few others. The number of references should obviously increase considerably if we consider modelling efforts based on micromechanics, using self consistent methods, homogenization techniques, cell analysis or any other kind of micro-macro transformation.

The researches made at ONERA around a number of composite systems used in Aeronautics and Aerospace applications have contributed to develop a succession of macroscopic constitutive and damage models that can be organized through a hierarchical modelling structure, as shown in section 2 below. In the present paper, we try to summarize and to discuss these modelling capabilities, showing some exploitations on various materials. In section 2, are recalled the various scales for a composite structure analysis and the proposed hierarchy of models. In section 3, is presented the general framework for this constitutive equations development, including the damage deactivation effects (closure effects), plastic flow and damage evolution rules. Section 4 gives some examples of applications, to Ceramic Matrix Composites (CMC), Metal Matrix Composites (MMC) and Organic Matrix Composites (OMC). In every case, they are long fibre unidirectional or woven composite systems, but the same approach has also been applied to short fibre systems, like in [11].

2. A HIERARCHICAL MODELLING OF COMPOSITE STRUCTURES

First, we should have to indicate the various scales that play role in the inelastic analysis of a composite structure :

- The component or structural level, where the composite part is often in the form of a laminate. In some very macroscopic (elastic) analysis, the laminate itself is considered as a continuum. When considering inelastic and damage processes, this way of modelling has now to be considered as insufficient : using the finite element structural analysis, in the framework of a plate or shell or pseudo 3D discretization, we should have to dissociate the kinematic assumptions (displacement discretization) and the material behaviour discretization that must be treated ply by ply.

- The scale of the elementary ply is the one at which we presently develop macroscopic constitutive equations (it is often called the mesoscopic scale). Fig.1 illustrates the laminate decomposition. The ply has a unidirectional structure for classical OMC laminates and some MMC's laminates but can be also composed of woven fabrics, like in the applications given in section 4 on SiC/SiC or C/PMR15.

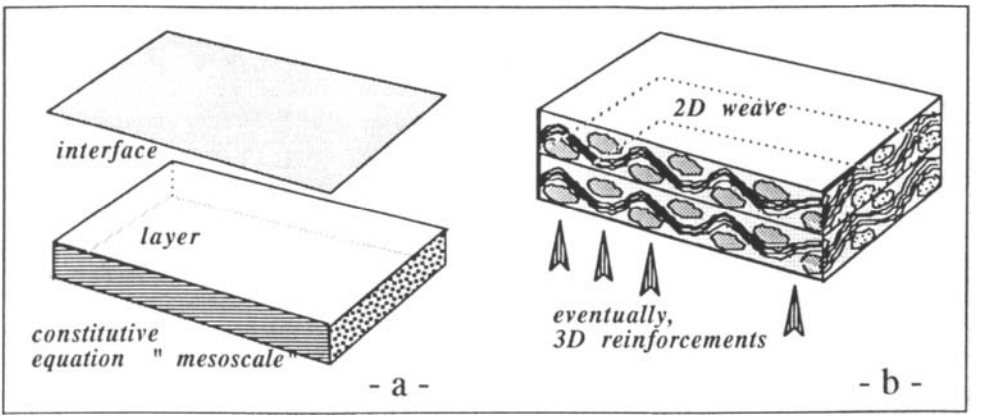

Figure 1. Schematics of (a) mesoscopic analysis in laminates,
(b) plain weave structure with homogeneous stacking sequence.

The ply assemblage (fibre + matrix or yarn + matrix) is then considered as a continuum, even in the presence of damage (transverse cracks for example). At this level, we could also consider special interfacial models to describe the progressive damage and delamination between adjacent plies, as developed by Allix and Ladevèze [12-13] and more recently Lo and Allen [14].

- The microscale, in which we use the constitutive equations of the elementary constituents, matrix, fibres, fibre/matrix interfaces, etc... In some case, the analysis has to be made via a double level micro-macro approach (fibre + matrix to give the yarn behaviour, then yarn + matrix to model the ply behaviour). Difficulties increase when taking into account microcracking, either in the matrix or at the fibre/matrix interface.

- Smaller scale could also be considered when interacting with the composite processing routes ; an example is the various interphases, diffusion zones and the roughness aspects in the region of interface between fibre and matrix. This is far beyond the scope of the present paper.

The constitutive and damage models that are formulated in the next section obey to a hierarchical structure that can be elaborated as follows. Figure 2 illustrates the main features of the corresponding modelling specificities and capabilities on examples that are or have been treated by ONERA co-workers :

a) The basic behaviour corresponds to the elastic damaged material (brittle damage), as illustrated by CMC's, especially SiC-SiC plain weaves composites.

The main non-linearity observed in the tensile response is associated to the damage development (matrix micro-cracking). One of the clear specificities of the tension-compression behaviour is the damage deactivation effect that takes place under unloading/reverse loading conditions, associated to the closure of previously created and opened microcracks. This effect must play role in the frame of the state potential as an elastic reversible process, leading to a bilinear kind of elastic behaviour.

b) In some other CMC's or in C-SiC composites, where the larger thermal expansion mismatch induces larger manufacture residual stresses, the microcrack closure and damage deactivation takes place at a non-zero stress state. As illustrated on Fig. 2, this effect produces irreversible strains that can be associated to the damage development itself, without any additional state variable or additional dissipative processes.

c) In some other cases, for the C/C for example, we need to introduce an evolution of the closure strain. In other words, the irreversible strain (or "plastic" strain) evolves during the damage grows. Then, we have additional state variables and evolution equations. The corresponding irreversible strains can be associated both to the friction effects between fibres, yarns etc... and to the damage driven friction effects on the previously developed micro-cracks.

d) Other plasticity effects are clearly due to the inelastic behaviour of the matrix itself. This is the case for metal matrix composite, for example in the SiC/Ti system that will be studied in this paper, or for organic matrix composites where it is necessary to describe the matrix viscoelastic behaviour under transverse or shear loading conditions. The tension-compression behaviour of the C/PMR15 system in a 45° direction (to the yarn axes) is a clear illustration of this situation. In these systems, we need the combination of the previous modelling capabilities a-b-c to a more or less classical plastic or viscoelastic constitutive equation.

e) The last aspect, not addressed in the present paper, is related to additional hysteretic effects associated to damage/friction interactions at the fibre/matrix interfaces. Quite limited in the SiC/SiC system such effects can be more pronounced in other CMC's. In such cases, the matrix microcracks are often bridged by intact fibres and the dissipative processes take place in the fibre-matrix interface near the crack opening region, producing both fibre matrix decohesion and sliding. The corresponding friction mechanisms, enhanced by the matrix damage (microcracks) development are clearly the cause for increasingly hysteretic effects that take place during the unloading-reloading cycles, hysteresis that have nothing to see with the matrix behaviour (point d).

3. GENERAL FRAMEWORK OF THE CONSTITUTIVE MODELS

3.1. The state potential

We consider the small strain assumption. The constitutive models are based on the continuum thermodynamics with internal variables. We assume the existence of a state potential, from which can be derived all the state equations, that is the ones governing the reversible processes. We consider here the free energy as the thermodynamic state potential, depending on the observable variables ε, the total strain and T, the temperature and on a set of internal state variables :

$$\psi = \psi(\varepsilon, T, \varepsilon_p, \varepsilon_c, \alpha_j, r, \delta_\alpha, \boldsymbol{d}) \qquad (1)$$

ε_p is the plastic strain, usually defined through the unloaded configuration, but will be defined more specifically below, in the framework of the damage deactivation rule. ε_c is the strain state associated to the deactivation (at which the deactivation can take place), α_j, j=1,2, ... are a set of kinematic hardening variables, and r is the isotropic hardening variable.

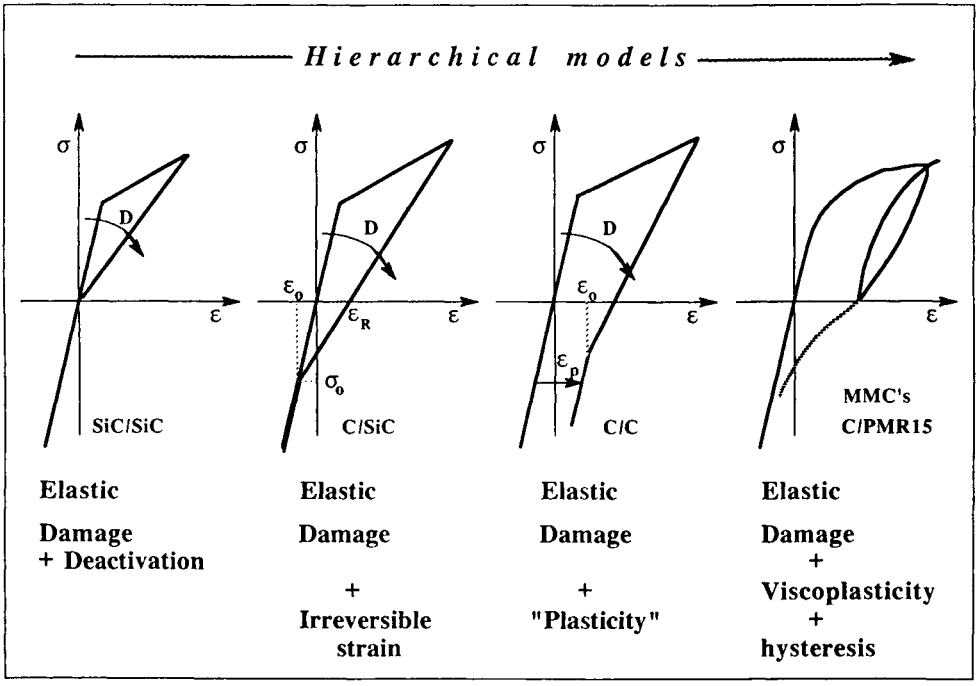

Figure 2. Schematics of the hierarchical modelling framework.

In the present CDM approach, we consider two kinds of damage variables :
- δ_α, α=1,2,3 represent three scalar damage variables associated to the microcrack that develop parallel or perpendicular to the reinforcements (fibres, yarns). The use of scalars is motivated by the fact that these damages have known material directions $\boldsymbol{p}_\alpha$ (where $\boldsymbol{p}_\alpha$ is the vector perpendicular to the corresponding family of microcracks).

Table 1
The state equations of the damaged elastic behaviour for both active and deactivated damage :

state potential :

$$\psi = \frac{1}{2}(\varepsilon - \varepsilon_p - \varepsilon_\theta):\tilde{\mathbf{L}}:(\varepsilon - \varepsilon_p - \varepsilon_\theta) + \frac{1}{2}(\varepsilon - \varepsilon_c):(\mathbf{L}^{eff} - \tilde{\mathbf{L}}):(\varepsilon - \varepsilon_c) + \frac{1}{2}\sum \alpha_i:\tilde{\mathbf{C}}_i:\alpha_i \quad (2)$$

$$\tilde{\mathbf{L}} = \mathbf{L}_o - \sum_\alpha \delta_\alpha [\mathbf{A}_\alpha:\mathbf{K}_\alpha]_s - [\mathbf{D}(d):\mathbf{K}]_s \qquad \bar{\varepsilon} = \varepsilon - \varepsilon_c \quad (3)$$

$$\mathbf{L}^{eff} = \tilde{\mathbf{L}} + \eta\left\{\sum_{\alpha=1}^{3} h(-p_\alpha.\bar{\varepsilon}.p_\alpha)\delta_\alpha \mathbf{P}_\alpha:[\mathbf{A}_\alpha:\mathbf{K}_\alpha]_s:\mathbf{P}_\alpha + \sum_{i=1}^{3} h(-n_i.\bar{\varepsilon}.n_i)\,\mathbf{N}_i:[\mathbf{D}(d):\mathbf{K}]_s:\mathbf{N}_i\right\} \quad (4)$$

$$\tilde{\mathbf{C}}_i = \mathbf{C}_i - \sum_\alpha \delta_\alpha [\mathbf{A}_\alpha:\mathbf{K}_\alpha^p]_s - [\mathbf{D}(d):\mathbf{K}^p]_s \quad (5)$$

$$\mathbf{D}(d) = \gamma[1 \otimes d]_s + \frac{1}{2}(1-\gamma)[1 \underline{\otimes} d + 1 \overline{\otimes} d]_s \quad (6)$$

$$\mathbf{A}_k = p_k \otimes p_k \otimes p_k \otimes p_k + \sum_{i=2}^{3} \alpha_{kj}[(p_k \otimes p_k)\otimes(p_j \otimes p_j)]_s + \sum_{i=2}^{3} \beta_{kj}[(p_k \otimes p_j)_s \otimes (p_k \otimes p_j)_s] \quad (7)$$

$$\mathbf{P}_i = p_i \otimes p_i \otimes p_i \otimes p_i \qquad \mathbf{N}_i = n_i \otimes n_i \otimes n_i \otimes n_i \quad (8)$$

state equations :

$$\sigma = \frac{\partial \psi}{\partial \varepsilon} = \tilde{\mathbf{L}}:(\varepsilon - \varepsilon_p - \varepsilon_\theta) + (\mathbf{L}^{eff} - \tilde{\mathbf{L}}):(\varepsilon - \varepsilon_c) \quad (9)$$

$$\sigma_p = \frac{\partial \psi}{\partial \varepsilon_p} = \tilde{\mathbf{L}}:(\varepsilon - \varepsilon_p - \varepsilon_\theta) = \sigma - (\mathbf{L}^{eff} - \tilde{\mathbf{L}}):(\varepsilon - \varepsilon_c) \quad (10)$$

$$\mathbf{X}_i = \frac{\partial \psi}{\partial \alpha_i} = \tilde{\mathbf{C}}_i:\alpha_i \quad (11)$$

- $\boldsymbol{d}$ is a second order damage tensor that describes microcracks which orientations are given by the direction of the damaging loading (and not by the constituents). Though a fourth rank damage tensor could be more appropriate to describe a general induced anisotropy (Chaboche [15-16], Lubarda and Krajcinovic [17]), we limit ourselves to a second rank damage tensor

The chosen form for the state potential is indicated in Table 1, together with the corresponding state equations. The specific choices made for the damage deactivation and plastic strain definition will be discussed in the next two sub-sections. Let us remark that a dual formulation is still possible, using the Gibbs free enthalpy instead of (1), as was developed by Maire and Lesne [18].

In table 1, we have decomposed the free energy into the elastic part ψ_e, and the inelastic one ψ_p, assuming the uncoupling between the hardening and elastic behaviour. The elastic energy is decomposed into two quadratic terms (eqn (1)) that will be explained below. $\varepsilon_\theta = m\theta = m\,(T-T_0)$ is the thermal expansion.

3.2. Damage effect and damage deactivation rule

The elastic behaviour is described by relation (9) in table 1, where $\mathbf{L}^{eff}$ is defined in two steps. First, $\tilde{\mathbf{L}}$ is the present elastic stiffness tensor for all damages active, i.e. all microcracks open. It is obtained from the damage variables via eqn (2) in which $\mathbf{K}_\alpha$ and $\mathbf{K}$ are given material dependent tensors, related to the initial symmetries. $\mathbf{D}(\boldsymbol{d})$ is a fourth rank damage effect tensor, build up from the second rank damage by eqn (6), and $\delta_k \mathbf{A}_k$ plays the same role for the scalar damages, using (7). Second, we define $\mathbf{L}^{eff}$ from $\tilde{\mathbf{L}}$, taking into account the damage deactivation effects via eqn (4), where h is the Heaviside function and $\mathbf{P}_\alpha$, $\mathbf{N}_i$ are fourth order projection operators (8), $\boldsymbol{n}_i$ (i=1,2,3) being the principal orthonormal system in which is written the deactivation.

This damage deactivation rule was proposed initially by Chaboche [19]. It is chosen in order to eliminate any stress-strain discontinuity when the activation/deactivation takes place, that is when the normal component $\bar{\varepsilon}_i = \mathrm{Tr}(-\mathbf{N}_i : \bar{\varepsilon}_i) = \boldsymbol{n}_i \cdot \bar{\boldsymbol{e}} \cdot \boldsymbol{n}_i$ or $\bar{\varepsilon}_\alpha = \boldsymbol{p}_\alpha \cdot \bar{\varepsilon} \cdot \boldsymbol{p}_\alpha$ change sign. The projection operation with $\mathbf{N}_i$ in (4) selects only the corresponding "diagonal term" L_{ii} in the stiffness matrix. The material parameter η allows description of partial deactivation effects, with $0 \le \eta \le 1$.

The energy ψ_p, the stored energy associated to hardening, could also be decomposed similarly to the elastic energy, showing the active terms with $\tilde{\mathbf{C}}_j$ and the deactivation ones. However, it would increase the complexity and need additional deactivation rules, in terms of α_i, the deactivation taking place

independently of the elastic one. For these reasons, we only consider the active situation, using the damaged hardening modulus $\tilde{\mathbf{C}}_j$ in eqs (1) and (11).

There is no deactivation effect for hardening but a corresponding effect will be discussed in the frame of the yield function determination. The operators $\mathbf{K}_\alpha^p$ and $\mathbf{K}^p$, different in principle of $\mathbf{K}_\alpha$ and $\mathbf{K}$, are material dependent fourth rank tensors.

Table 2
Thermodynamic forces associated with the scalar and tensorial damage variables

damage affinities :

$$y_\alpha = -\frac{\partial \psi}{\partial \delta_\alpha} = \frac{1}{2}(\varepsilon - \varepsilon_p - \varepsilon_\theta) : [\mathbf{A}_\alpha : \mathbf{K}_\alpha]_s : (\varepsilon - \varepsilon_p - \varepsilon_\theta) + \frac{1}{2}\sum_i \alpha_i : [\mathbf{A}_\alpha : \mathbf{K}_\alpha^p]_s : \alpha_i$$
$$- \frac{1}{2}\eta\, h(-Tr(\varepsilon_\alpha^*))\ \varepsilon_\alpha^* : [\mathbf{A}_\alpha : \mathbf{K}_\alpha]_s : \varepsilon_\alpha^* \qquad (12)$$

$$\varepsilon_\alpha^* = \mathbf{P}_\alpha : (\varepsilon - \varepsilon_c) = p_\alpha . \bar{\varepsilon} . p_\alpha \qquad (13)$$

$$\mathbf{y} = -\frac{\partial \psi}{\partial \boldsymbol{d}} = -\frac{\gamma}{4}\left[(\varepsilon - \varepsilon_p - \varepsilon_\theta)\, Tr(\bar{\sigma}) + \bar{\sigma}\, Tr(\varepsilon - \varepsilon_p - \varepsilon_\theta)\right] + \frac{1-\gamma}{2}\left[\bar{\sigma} . (\varepsilon - \varepsilon_p - \varepsilon_\theta)\right]_s$$
$$+ \sum_i \left\{\frac{\gamma}{4}\left[\alpha_i\, Tr(\bar{\mathbf{X}}_i) + \bar{\mathbf{X}}_i\, Tr(\alpha_i)\right] + \frac{1-\gamma}{2}\left[\bar{\mathbf{X}}_i . \alpha_i\right]_s\right\}$$
$$- \eta \sum_i h(-Tr(\varepsilon_i^*))\left[\frac{\gamma}{4}\left[\varepsilon_i^*\, Tr(\bar{\sigma}_i^*) + \bar{\sigma}_i^*\, Tr(\varepsilon_i^*)\right] + \frac{\gamma}{4}(\bar{\sigma}_i^* . \varepsilon_i^*)_s\right] \qquad (14)$$

$$\bar{\sigma} = \mathbf{K} : \bar{\varepsilon} \qquad \varepsilon_i^* = \mathbf{N}_i : (\varepsilon - \varepsilon_c) = n_i . \bar{\varepsilon} . n_i \qquad \bar{\sigma}_i^* = \mathbf{K} : \varepsilon_i^* \qquad (15)$$

Remark : The projection direction p_α is fixed by the initial composite symmetries (constituent directions). However, the choice for the principal deactivation directions n_i is open. The natural way should be to take the principal directions of the damage tensor $\boldsymbol{d}$ (closure of the subjacent "principal micro-cracks"), but that leads to some indeterminations in the initial undamaged conditions for the thermodynamic affinity $\mathbf{y}$ associated to damage. Presently, we prefer to use the principal directions of ε-ε_c.

Remark : In order to reduce the number of material dependent parameters, the fourth rank tensors $\mathbf{K}_\alpha$ and $\mathbf{K}$ can be selected as identical to the initial undamaged stiffness $\mathbf{L}_o$. It leads then to the classical definition of the damage through the stiffness change. We can also select the particular case where the tensors $\mathbf{K}_\alpha^p$ and $\mathbf{K}^p$ are identical to $\mathbf{C}_i$.

Table 3
The damage loading surfaces and corresponding damage rate equations :

Scalar variables :

$$g_\alpha = \langle y_\alpha \rangle - r_\alpha(\delta_1, \delta_2, \delta_3) \leq 0 \qquad (16)$$

Tensorial variable :

$$g = \Phi\left[(\mathbf{y}:\mathbf{Q}:\mathbf{y})^{1/2}\right] - \xi Tr(\boldsymbol{d}) - (1-\xi)Tr(\mathbf{y}.\boldsymbol{d}) \leq 0 \qquad (17)$$

rate equations :

$$\dot{\delta}_\alpha = \dot{\mu}_\alpha \frac{\partial g_\alpha}{\partial y_\alpha} \qquad \dot{\boldsymbol{d}} = \dot{\mu} \frac{\partial g}{\partial \mathbf{y}} \qquad (18)$$

3.3. Damage evolution rules

For the damage evolution equations, we follow the standard procedure and the corresponding normality rules. A dissipation potential is assumed to exist and is assimilated with the damage loading surface (that enclose all the non-damaging states) expressed in the space of the thermodynamic forces y_i and $\mathbf{y}$ associated to the damage state variables δ_i and $\boldsymbol{d}$. These thermodynamic forces are indicated in table 2 and the corresponding damage evolution equations in Table 3.

More specifically, the scalar damages are assumed to obey multiple criteria (dependent or independent), with one independent multiplier $\dot{\mu}_i$ for each damage growth (determined by the corresponding consistency condition $g_i = \dot{g}_i = 0$). For the tensor damage, we necessary have to introduce some scalar invariants. In equation (17), we combine the possibilities for an homothetical evolution ($\xi = 1$) and a quasi-independant evolution ($\xi = 0$), in terms of loading directions.

Let us point out two assumptions made in the present way of damage modelling :

- We use the standard rule in order to match automatically the Second Principle of thermodynamics. However, the dissipation potentials for damage and plasticity are considered independently, with independent multipliers, as proposed by Chow and Wei [19], Hansen and Schreyer [20], Chaboche [21].

- The evolution is considered as rate independent. In the normality rules (18), we have multipliers $\dot{\mu}_\alpha$ and $\dot{\mu}$ that must be determined by the corresponding consistency conditions $\dot{g}_\alpha = 0$, $\dot{g} = 0$.

3.4. Modelling of plastic flow, without damage

For the plastic flow, we use a yield surface in the stress space or more precisely in the "active stress" space σ_p. In fact, σ_p is the thermodynamic affinity associated to ε_p in the thermodynamic potential, and is given by (10) in table 1. The yield surface obeys a Hill's criterion, eqn (19) table 4, where the fourth rank tensor **H** is depending on the material.

In order to meet the thermodynamic requirement (the Second Principle), we assume the existence of a set of dissipative potentials, F_p, F_s, associated to plasticity and thermal recovery processes. This way of generalizing the standard procedure has been discussed recently by Chaboche [21]. The specific choices are given by eqs (19) and (20). The generalized normality assumptions writes as (21) (22) and shows in the kinematic hardening evolution the combination of three terms : the normal (linear) hardening, the dynamic recovery term, proportional to the modulus of the plastic strain rate and the static recovery term.

Table 4
The viscoplastic theory for the undamaged configuration :

yield criterion and dissipation potential :

$$f = \left((\sigma_p - \mathbf{X}):\mathbf{H}:(\sigma_p - \mathbf{X})\right)^{1/2} - R - k = \left\|\sigma_p - \mathbf{X}\right\|_H - R - k \qquad \mathbf{X} = \sum_i \mathbf{X}_i \qquad (19)$$

$$F_p = f + \frac{1}{2}\sum_i \gamma_i \, \mathbf{X}_i:\mathbf{C}_i^{-1}:\mathbf{X}_i \qquad F_s = \frac{1}{2}\sum_i \frac{\gamma_{si}}{m+1}\left(\mathbf{X}_i:\mathbf{C}_i^{-1}:\mathbf{X}_i\right)^{\frac{m+1}{2}} \qquad (20)$$

normality rule :

$$\dot{\varepsilon}_p = \dot{\lambda}\frac{\partial F_p}{\partial \sigma_p} = \dot{\lambda}\frac{\mathbf{H}:(\sigma_p - \mathbf{X})}{\left\|\sigma_p - \mathbf{X}\right\|_H} = \dot{\lambda}\,\mathbf{n} \qquad (21)$$

$$\dot{\alpha}_j = -\dot{\lambda}\frac{\partial F_p}{\partial \mathbf{X}_j} - \frac{\partial F_s}{\partial \mathbf{X}_j} = \dot{\varepsilon}_p - \gamma_j \mathbf{C}_j^{-1}:\mathbf{X}_j\,\dot{\lambda} - \gamma_{sj}\left\|\mathbf{X}_j\right\|^{m-1}\mathbf{C}_j^{-1}:\mathbf{X}_j \qquad (22)$$

plasticity : $\qquad f = \dot{f} = 0 \;\rightarrow\; \dot{\lambda}$

viscoplasticity : $\qquad \dot{\lambda} = \left\langle \frac{f}{K} \right\rangle^n \qquad (23)$

dissipation :

$$\mathcal{D} = \sigma_p:\dot{\varepsilon}_p - \sum_i \mathbf{X}_i:\dot{\alpha}_i - R\,\dot{r} \geq 0 \qquad (24)$$

The plastic multiplier $\dot{\lambda}$ is determined either by the consistency condition $\dot{f} = 0$ in the rate independent case or by a viscoplastic equation (23) in the reverse case (which is assumed here). Let us remark that $\dot{\lambda}$ is the modulus of the plastic strain rate as defined by $\dot{p} = \left\| \dot{\varepsilon}_p \right\|_{H^{-1}} = \left(\dot{\varepsilon}_p : \mathbf{H}^{-1} : \dot{\varepsilon}_p \right)^{1/2} = \dot{\lambda}$.

The isotropic hardening evolution equation, governing the scalar variable r is not addressed in the present paper. It can be postulated of a form similar to the kinematic hardening, incorporating a linear term, a recall term (dynamic recovery) and a static recovery term (Nouailhas [22]).

Table 5
The viscoplasticity theory for the damaged configuration :

yield criterion and dissipation potential :

$$\tilde{\sigma}_p = \mathbf{M}^{eff} : \sigma_p \qquad \tilde{\mathbf{X}}_i = \tilde{\mathbf{M}}_i : \mathbf{X}_i \qquad \tilde{\mathbf{X}} = \sum_i \tilde{\mathbf{X}}_i \tag{25}$$

$$\mathbf{M}^{eff} = \tilde{\mathbf{M}} + \eta_p \left\{ \sum_{\alpha=1}^{3} h(-p_\alpha . \sigma_p . p_\alpha) \delta_\alpha \mathbf{P}_\alpha : \left(\mathbf{I} - \tilde{\mathbf{M}} \right) : \mathbf{P}_\alpha + \sum_{i=1}^{3} h(-n_i . \sigma_p . n_i) \mathbf{N}_i : \left(\mathbf{I} - \tilde{\mathbf{M}} \right) : \mathbf{N}_i \right\} \tag{26}$$

$$f = \left((\tilde{\sigma}_p - \tilde{\mathbf{X}}) : \mathbf{II} : (\tilde{\sigma}_p - \tilde{\mathbf{X}}) \right)^{1/2} - R - k = \left\| \tilde{\sigma}_p - \tilde{\mathbf{X}} \right\|_H - R - k \tag{27}$$

$$F_p = f + \frac{1}{2} \sum_i \gamma_i \, \mathbf{X}_i : \tilde{\mathbf{C}}_i^{-1} : \mathbf{X}_i \qquad F_s = \frac{1}{2} \sum_i \frac{\gamma_{si}}{m+1} \left(\mathbf{X}_i : \tilde{\mathbf{C}}_i^{-1} : \mathbf{X}_i \right)^{\frac{m+1}{2}} \tag{28}$$

normality rule :

$$\dot{\varepsilon}_p = \dot{\lambda} \frac{\partial F_p}{\partial \sigma_p} = \dot{\lambda} \frac{\mathbf{M}^{eff^T} : \mathbf{II} : (\mathbf{M}^{eff} : \sigma_p - \mathbf{X})}{\left\| \sigma_p - \mathbf{X} \right\|_H} \tag{29}$$

$$\dot{\alpha}_j = -\dot{\lambda} \frac{\partial F_p}{\partial \mathbf{X}_j} - \frac{\partial F_s}{\partial \mathbf{X}_j} = \tilde{\mathbf{M}}_i^T : \mathbf{M}^{eff^{-T}} : \dot{\varepsilon}_p - \gamma_j \tilde{\mathbf{C}}_j^{-1} : \mathbf{X}_j \dot{\lambda} - \gamma_{sj} \left\| \mathbf{X}_j \right\|^{m-1} \tilde{\mathbf{C}}_j^{-1} : \mathbf{X}_j \tag{30}$$

3.5. Viscoplastic flow coupled with damage

In the above equation for the viscoplastic flow, we introduce the damage coupling effect through an effective stress concept (table 5).

We assume the same kind of damage effectiveness between elastic and plastic behaviour and use the effective stresses $\tilde{\sigma}_p$ and $\tilde{\mathbf{X}}_i$ in the yield criterion and plastic potential, instead of σ_p and $\mathbf{X}_i$ in the undamaged situation (equation (27)) :

$\tilde{\sigma}_p = \tilde{\mathbf{M}}(d) : \sigma_p$, $\tilde{X}_i = \tilde{\mathbf{M}}_i(d) : X_i$ $\tilde{\mathbf{M}} = \tilde{\mathbf{M}}(d)$ and $\mathbf{M}_i = \tilde{\mathbf{M}}_i(d)$

in eqs (25), (26) are the damage effect fourth rank operators which choice will be discussed below in section 3.6. Due to the standard procedure and normality rule the rate equations for ε_p and α_j follow easily.

In the case where damage deactivation takes place, there are several possibilities for introducing its effects in the plastic/viscoplastic equation. We could have played with an effective Hill's operator $\tilde{\mathbf{H}}$ and its deactivation counterpart $\mathbf{H}^{eff}$, with a deactivation criterion based on the overstress σ_p-X.

In the present theory, we have preferred to define an effective damage effect tensor $\mathbf{M}^{eff}$, eqn (26), in which the damage is deactivated with a rule exactly similar to the one used for elasticity. In eqn (26), the projection operators $\mathbf{P}_i$ and $\mathbf{N}_i$ are the same as before but the deactivation is written in terms of the "normal" value of σ_p (instead of ε-ε_c).

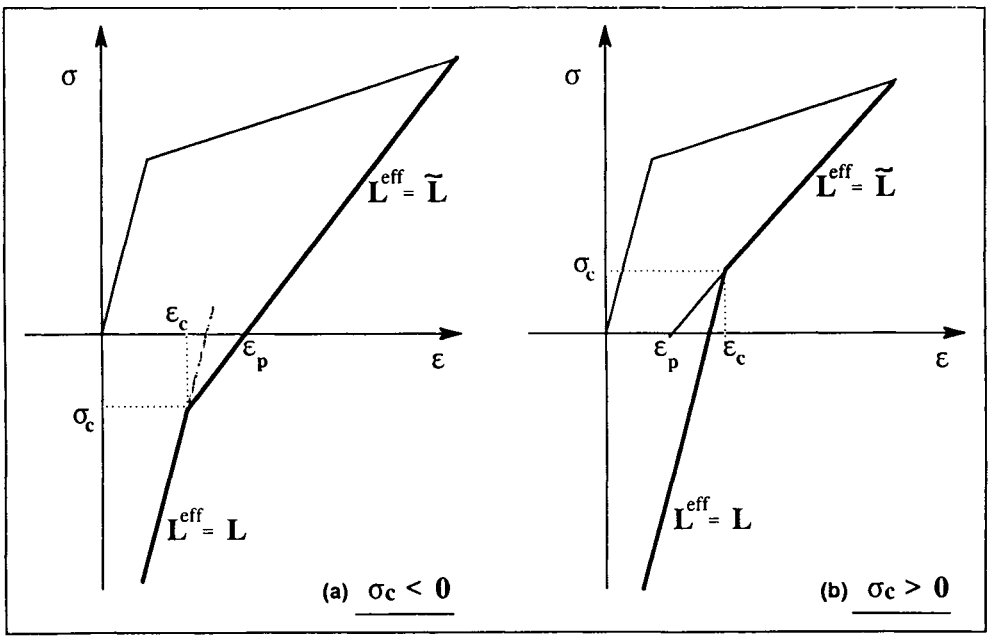

Figure 3. Schematics of the plastic strain definition after a tensile damage :
(a) closure point with a negative tensile stress
(b) closure point with a positive stress.

This is necessary in order to prevent any discontinuity of the stress-strain response but introduces different instants for the deactivation. There is no deactivation effect on the operators $\tilde{\mathbf{M}}_i$ associated with the various back-stresses, but this is sufficient to correctly meet the experimental results. Let us note that, due to the generalized normality, we still check the thermodynamic requirement of a positive dissipation.

3.6. Some remarks

The effective stress definition is based on the description of the elastic behaviour of the damaged material. There are two main assumptions possible :

(i) the energy equivalence principle [23], that assumes the same elastic energy in the effective (undamaged) space,

(ii) the strain equivalence principle [24], that assumes the comparison between damaged and undamaged configurations through the strain response.

Other generalizations have been proposed (Chow [25]) involving the plastic work equivalence, but they are no more tractable in the frame of a state equivalence. The advantage of the energy equivalence is the automatic symmetry of the damaged stiffness and the possibility to completely treat the state problem within the effective undamaged space. This way was intensively used by Voyiadjis and Kattan [8], [26], and more recently by Kruch et al. [27] for the two scale elasto plastic and damage modelling of MMC's. However, we still prefer to use the strain equivalence assumption in the present work, due to his larger flexibility. Contrary to the energy equivalence, any damaged induced anisotropy can be modelled. For instance, the damage effect tensors $\tilde{\mathbf{M}}$ and $\tilde{\mathbf{M}}_i$ can easily be determined from the damaged stiffness, all damages considered as active :

$$\tilde{\mathbf{M}} = \mathbf{L} : \tilde{\mathbf{L}}^{-1} \qquad \tilde{\mathbf{M}}_i = \mathbf{C}_i : \tilde{\mathbf{C}}_i^{-1} .$$

The damage deactivation rule chosen in section 3.2 introduces a specific definition for the plastic strain itself. This question is present in every theory where the deactivation effects introduce a bi-linear (or non linear) elastic behaviour. Assuming a rate independent behaviour (and the small strain hypothesis), examination of eq (9) leads to the following definition :

- *The plastic strain ε_p is defined by the elastic linear unloading, all damages active, eventually linearly extrapolated to the zero stress state.*

This property is obvious from the active damage assumption, considering $\mathbf{L}^{\text{eff}} = \tilde{\mathbf{L}}$ in eqn (9), leading to $\varepsilon = \varepsilon_p$ for $\sigma = 0$. Figure 3 illustrates this definition in the case of tension-compression, after damaging in tension (within the simplification of constant off-diagonal compliance terms, not depending on

damage). Two situations are considered : (a) When the closure strain ε_c leads to a negative closure stress, the most usual case, the plastic strain is defined by the (true) residual strain at zero stress. (b) In the reverse case, the plastic strain definition uses a linear extrapolation to zero stress instead of the true bilinear elastic unloading.

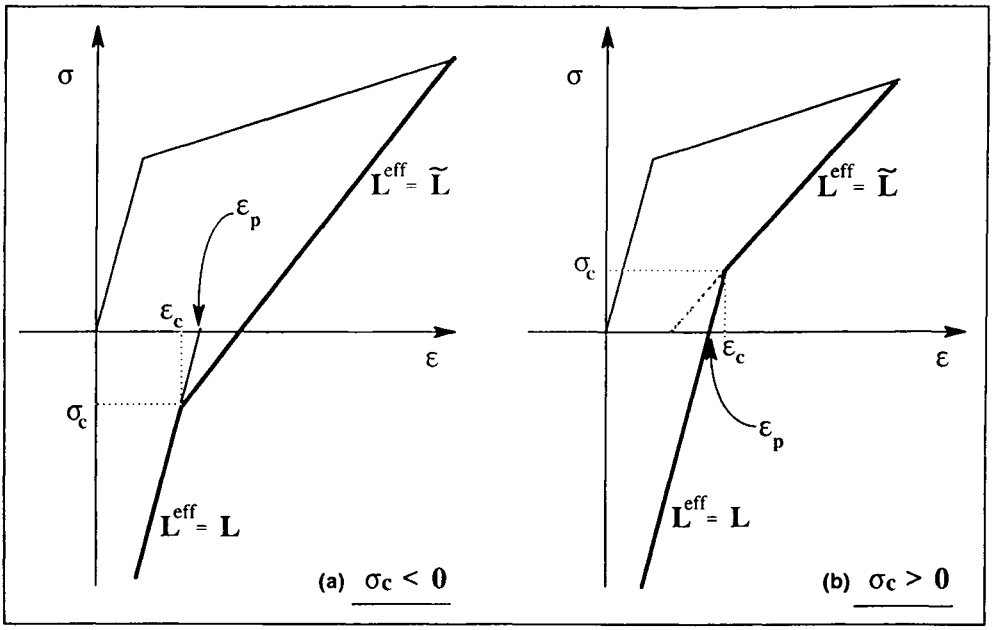

Figure 4. Schematics of the reverse hypothesis for the plastic strain definition closure point with (a) a negative tensile stress, (b) a positive stress.

Let us note that in some other theories (Gérard and Baste [28]) it has been considered a variable definition of ε_p : in case (b), ε_p was defined as in figure 4-b, by extrapolation, at the beginning of the unloading (BC), but by the true residual strain at $\sigma = 0$ when the damage is deactivated (CD). The varying ε_p at the instant of deactivation leads to some theoretical shortcomings.

Another form of deactivation equation could have been proposed, generalizing directly the one used by Chaboche et al. [29] for the elastic-brittle case (CMC's). Instead of (2), the free energy could be postulated :

$$\psi = \frac{1}{2}(\varepsilon - \varepsilon_p) : \mathbf{L} : (\varepsilon - \varepsilon_p) + \frac{1}{2}(\varepsilon - \varepsilon_c) : (\mathbf{L}^{eff} - \mathbf{L}) : (\varepsilon - \varepsilon_c) + \psi_p \tag{32}$$

leading to the stress :

$$\sigma = \mathbf{L} : (\varepsilon - \varepsilon_p) + (\mathbf{L}^{eff} - \mathbf{L}) : (\varepsilon - \varepsilon_c) \tag{33}$$

This complementary choice can describe (in principle) the same kind of deactivation behaviour, with the same bilinear unloading but a different definition of the plastic strain, as illustrated by figure 4 :

- *The plastic strain ε_p is defined by the elastic linear unloading, all damages deactivated (from compressive side) eventually extrapolated to the zero stress state.*

The formulation given in section 3.2 is preferred due to the following main reasons :

- It gives a more natural definition for the plastic strain, through the direct unloading from the loading that has produced both plasticity and damage.

- It leads to a plastic strain that does not differ too much from the residual strain at zero stress. This is especially true for the observed behaviour in SiC/Ti MMC's (see section 4.2), where the closure strain is not varying much but the closure stress (after tension) becomes significantly negative. The assumption (33) leads to much larger differences.

- It allows a consistent description of the dissipation during plastic flow, through the active stress σ_p defined by eqn (10). The above choice (32) introduces much less natural interpretations.

- It describes easily a positive dissipation associated to the evolution of the closure strain ε_c. This aspect is not addressed in the present paper but the assumption that ε_c evolves only for active damage is immediately consistent with thermodynamics, which is not the case with the other formulation.

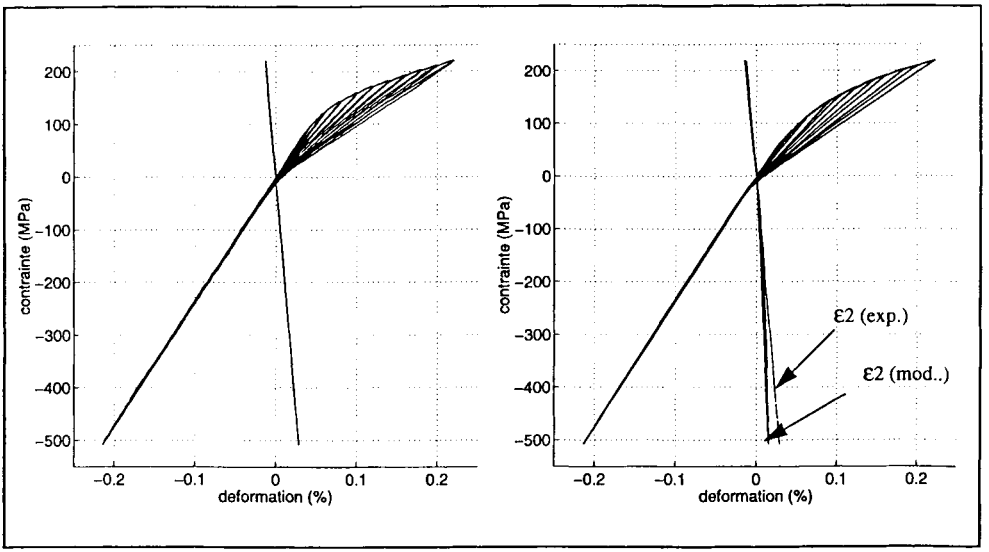

Figure 5. SiC/SiC cyclic tension-compression in the 0° direction :
(a) experiments, (b) modelling.

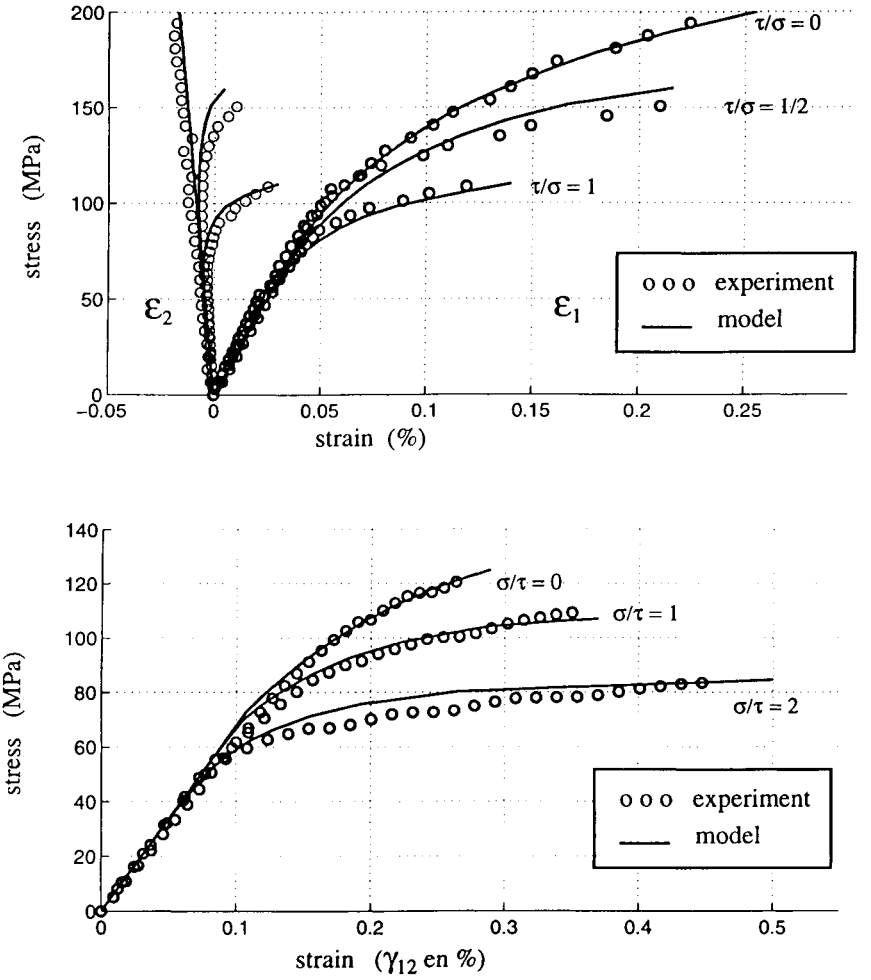

Figure 6. SiC/SiC tension-torsion prediction : (a) monotonic tensile responses, (b) monotonic shear for various stress ratios responses.

4. OVERVIEW OF SOME APPLICATIONS

The constitutive and damage models presented in section 3 have been applied to several kinds of composite systems. Some results are given below for 3 of them :

(i) a ceramic matrix composite,
(ii) an organic matrix woven composite, C/PMR15,
(iii) a SiC/Ti metal matrix unidirectional composite.

4.1. Application to the SiC/SiC composites

The material is constituted of woven layers, with a plain weave structures. Each yarn is composed of a large number of SiC fibres and constitutes by itself a unidirectional composite. The plies are superposed in a continuous stacking sequence, so that we do not need to consider the stratification and the material can be considered as macroscopically homogeneous, as a 3D continuum.

The material is elastic brittle and two kinds of matrix microcracks are developing : the ones parallel to the fibres (transverse cracks), that we describe by scalar damage variables, and the ones that develop more or less perpendicular to the maximum principal stress, that we describe by a second rank damage tensor [18], [29]. We use the damage rules indicated in table 3, especially a rule like (17), that allows to introduce a shape change in the loading surface as damage progresses [18]. Obviously, we neglect any plastic or viscoplastic behaviour.

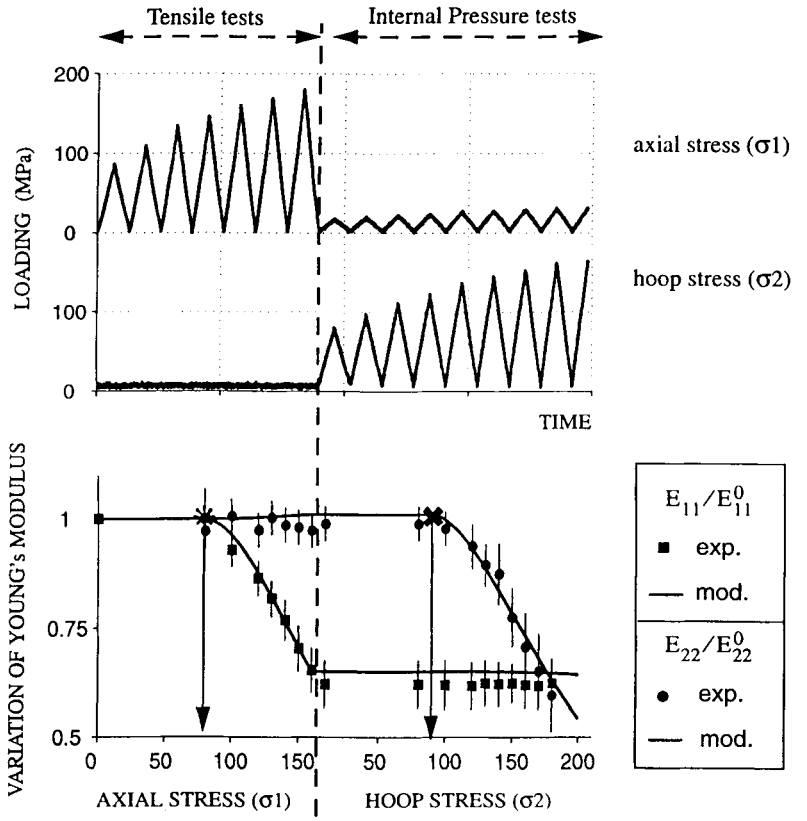

Figure 7. Prediction of Young's modulus change (directions 1 and 2) on SiC/SiC under a sequence incremental tension followed by incremental internal pressure.

Some results are selected in figures 5 to 7 showing successively the model capability for uniaxial and multiaxial loading conditions. In particular, we observe the correct reproduction of the microcrack closure effect for 0° tension-compression loadings, a slightly less good result for the 45° direction. The tension-torsion on tubular specimens is correctly predicted (the experiments were not introduced into the model determination procedure). Moreover, under cyclic shear (torsion), with increasing extrema, the model is able to reproduce further damage at each peak (thanks to the choice of rule like (17). Moreover, a biaxial test under increasing tensile peaks, followed by increasing internal pressure maxima, is correctly predicted both in terms of the stress-strain responses and for the two Young's modulus (as measured by unloadings/low level reloadings). Figure 7 demonstrates the model capability.

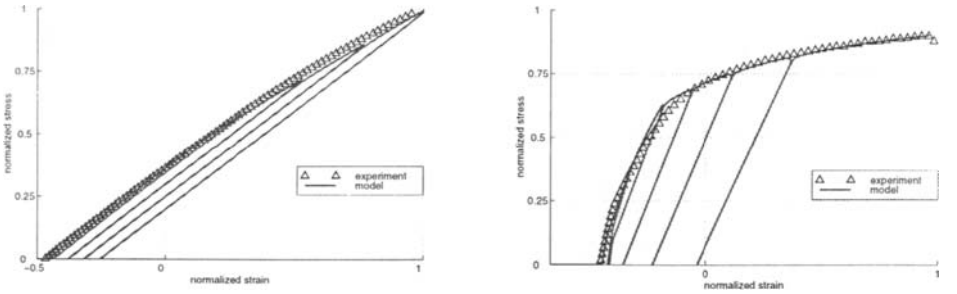

Figure 8. SiC/Ti MMC tensile responses at 450°C : monotonic tests and simulations with unloadings (a) longitudinal, (b) transverse.

4.2. Application to a SiC/Ti metal matrix composite

The material is composed of long SiC fibres (SM11-40*) and a 6242 titanium matrix. It is used in the unidirectional form and tested in the longitudinal and transverse directions at 450 and 550°C. In that case, we considered only one set of scalar damage variables [30] but further studies should also consider the tensorial damage. The elastic-viscoplastic behaviour of the material is described by equations of table V, with two back stresses (one linear hardening, one non linear hardening) but no static recovery effects.

One specificity of the macroscopic model application is that it is built up from a micro-macro analysis based on the constitutive equations of the matrix and fibres [11] [30]. The tensors $\mathbf{L}$ and $\mathbf{C}_i$ are obtained from that analysis and contain the constituent characteristics (behaviour, geometry and arrangements).

The deactivation rule is applied in terms of the Total Strain, as indicated by eqn (4). Presently, we consider that ε_c is the thermal strain ε_θ, determined after

the modelling of the manufacturing process. In further work, we should have a slightly evolving ε_c

Figure 8 shows the correct modelling, both for the longitudinal and transverse directions. In this last case, we observe the damage at the very beginning after the elastic domain (by the Young's modulus decrease), followed by a significant plastic strain and a slower damage evolution. Figures 9 and 10 demonstrate the capability of the model under cyclic loading conditions (with stress reversals). In particular, we observe in figure 10 the damage deactivation around a constant total strain (near 0).

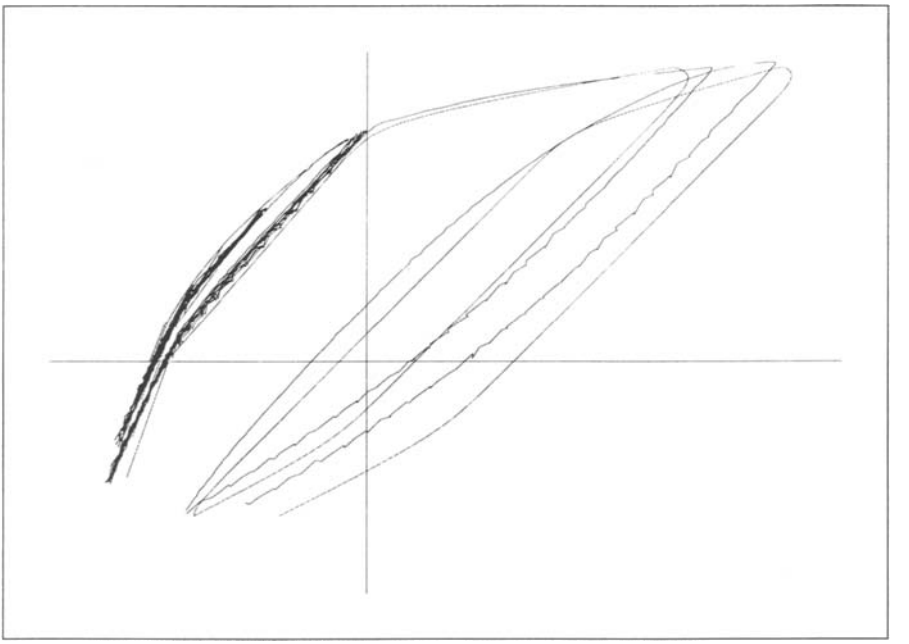

Figure 9. Stress controlled cyclic tests on SiC/Ti
at 550°C and the corresponding simulations.

4.3. Application to a C/PMR15 composite

The material is a woven composite, with the eight hardness satin arrangement. The woven plies are superposed identically so that there is a symmetry between the directions 0° and 90°. The nature of the organic matrix and the stiffness of the eight hardness satin weave introduces extremely different responses for the 0° and 45° uniaxial tension experiments :

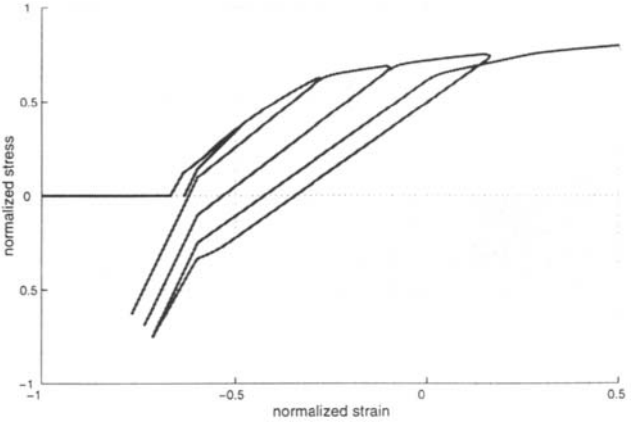

Figure 10. Stress controlled cyclic simulations
with increased compression and damage deactivation.

- For the 0° direction, we have essentially an elastic linear response. The damage is not really observable before the specimen failure. It is only on the transverse strain (Poisson's effect) that we can measure the damage effect.

- In the 45° direction, the response is essentially the one of the matrix, viscoelastic, with large hysteretic cycles. The damage grows only for large stress levels but its direct measurement through stiffness change is difficult due to the viscoelastic hysteretic effects.

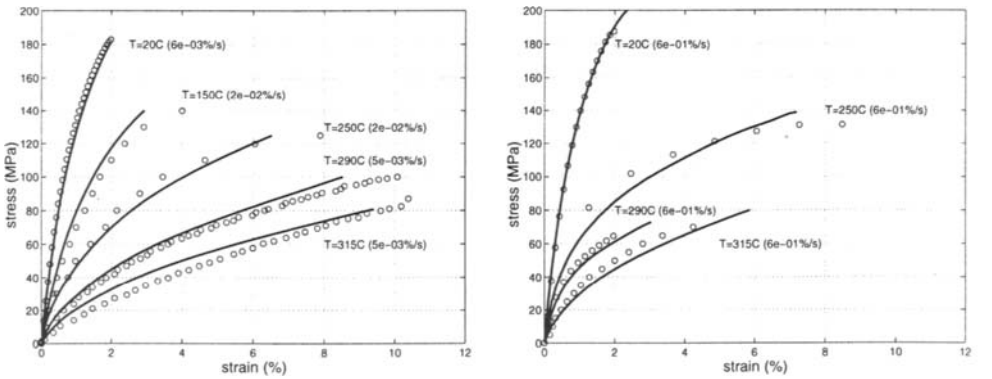

Figure 11. Monotonic tensile curve simulation for C/PMR15 in the ± 45° direction. oooo tests ; - - - - calculations ; (a) low strain rate, (b) high strain rate.

An extensive experimental study has been performed, at various temperatures, including cyclic tension, cyclic tension-compression, creep, creep followed by recovery tests etc... Figures (11) and (12) show only a few results. Modelling was done by using the following choices [31] :

- The viscous behaviour is described by the viscoplastic framework, considering visco-elasticity as a limiting case of viscoplasticity [32] without yield stress (k = R = 0 in eqn (27)).

- The back stress is decomposed into 3 to 5 elementary back stresses in order to be able to simulate the hysteretic effects.

- The static recovery effect in eqn (30) is taken into account, that provides a quasi complete strain recovery after unloading and a sufficient hold at the test temperature.

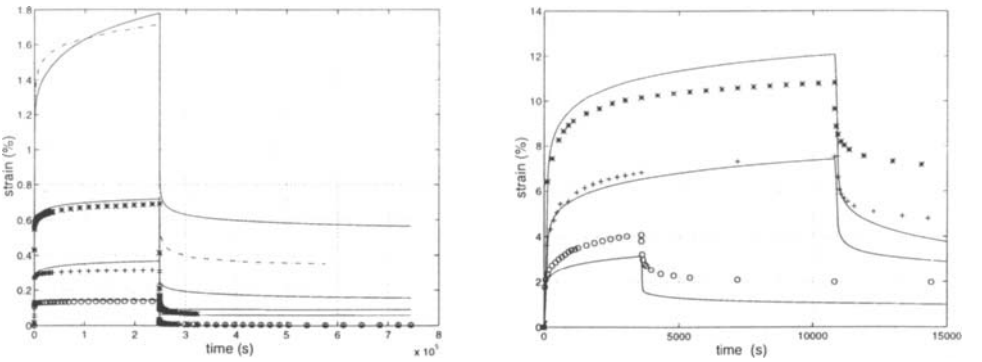

Figure 12. Tensile creep and recovery for C/PMR15 in the ± 45° direction.
* + o tests ; ····· calculations ; (a) at room temperature ; (b) at 315°C.

5. CONCLUSION

A general constitutive framework has been developed that describes various behaviours and various kinds of composites. The hierarchical structure of the models has been illustrated by the application to three very different composite systems, involving the elastic-damaging case, with deactivation (SiC/SiC), the addition of viscoplasticity (SiC/Ti) and the addition of viscoelasticity and static recovery effects (C/PMR15).

The proposed combined constitutive and damage equations are able to take into account both the initial anisotropy of the composite and the damage induced anisotropy, together with the effects of damage deactivation during elastic or viscoplastic reversals.

These directionality effects refer to microstructural aspects : the constituent arrangements and the assumed directions of microcracks. Obviously, this is done through the global approach of CDM so that the local description of microcracks is not introduced in detail. Instead of a completely deductive approach (still to be developed for "predictive applications"), we have mixed micromechanical considerations and the macroscopic phenomenological approach.

The proposed framework is already able to incorporate many of the most significant non-linearities in the composite behaviour. Some further developments and improvements are needed in order :

- to reproduce more completely some damage deactivation effects. Some experiments show that the shear initial stiffness is recovered after damage deactivation, which is not possible within the present deactivation rule.

- to describe the hysteretic effects and associated "inelastic strains" that are not induced by the matrix behaviour but by microslips between fibre, matrix and microcracks, including the interface behaviour.

References

[1] Talreja R., "Transverse cracking and stiffness reduction in composite laminates", J. Comp. Mater., Vol 19, (1985), pp 355-375.

[2] Talreja R., "Continuum modelling of damage in ceramic matrix composites", Mechanics of Materials, Vol 12, (1991), pp 165-180.

[3] Allen D.H., Groves S.E. and Harris C.E., "A thermomechanical constitutive theory for elastic composites with distributed damage", Part I and II, Int. J. Solid Structures, (1987), pp 1301-1338.

[4] Allix O., Ladeveze P., Le Dantec E. and Vittecoq E., "Damage mechanics for composite laminates under complex loading", Yielding Damage and Failure of Anisotropic Solids, EGF5, Mechanical Engineering Publications, London, (1990), pp 551-569.

[5] Ladeveze P., Gasser A. and Allix O., "Damage mechanics modelling for ceramic composites", Journal of Engineering Materials and Technology, Vol 116, (1994).

[6] Ladeveze P., "A damage computational approach for composites: Basic aspects and micromechanical relations", Computational Mechanics, Vol 17, (1995), pp 142-150.

[7] Robinson D.N., Binienda W.K. and Miti-Kavuma M., "Creep and creep rupture of strongly reinforced metallic composites", NASA Contractor Report 185286, University of Akron, (1990).

[8] Kattan P. and Voyiadjis G.Z., "Overall damage and elastoplastic deformation in fibrous metal matrix composites", Int. J. Plast., Vol 9, (1993), pp 931-949.

[9] Perreux D. and Oytana C., "Continuum damage mechanics for microcrackes composites", Comp. Eng., (1993), pp 155-122.

[10] Chow C.L. and Fan Yang, "Three-Dimensional inelastic stress analysis of center notched composite laminates with damage", Int. J. Damage Mechanics, Vol 6, (1997), pp 23-50.

[11] Chaboche J.L., Kruch S. and El Mayas N., "Thermo-elasto-viscoplastic constitutive equations for metal matrix composites", CR Acad. Sci. Paris, t.319, série II, (1994), pp 971-977.

[12] Allix O. and Ladeveze P., "Damage analysis for laminate delamination", Proc. 5th Int. Symp. On Num. Meth. in Engng., Springer, (1989), pp 347-354.

[13] Allix O. and Ladeveze P., "Interlaminar interface modelling for the prediction of laminate delamination", J. Composite Structures, Vol 22, (1992), pp 235-242.

[14] Lo D.C. and Allen D.H., "Modelling of delamination damage evolution in laminated composites subjected to low velocity impact", Int. J. Damage Mechanics, Vol 3, (1994), pp 378-407.

[15] Chaboche J.L., "Anisotropic creep damage in the framework of continuum damage mechanics", Nuclear Engng and design, Vol 79, (1984), pp 309-319.

[16] Chaboche J.L., "Development of CDM for elastic solids sustaining anisotropic and unilateral damage", Int. J. of Damage Mechanics, Vol 2, (1993).

[17] Lubarda V.A. and Krajcinovic D., "Damage tensors and the crack density distribution", Int. J. Solids Structures, Vol 30, (1993), pp 2859-2877.

[18] Maire J.F. and Lesne P.M., "A damage model for Ceramic Matrix Composite", Aerospace Science and Technology, Vol 2, (1997).

[19] Chow C.L. and Wei Y., "A model of continuum damage mechanics for fatigue failure", Int. J. Fract., Vol 50, (1991), pp 301-316.

[20] Hansen N. and Schreyer H.L., "A thermodynamically consistent framework for theories of elastoplasticity coupled with damage", Int. J. Solids Structures, Vol 31, (1994), pp 359-389.

[21] Chaboche J.L., "Unified cyclic viscoplastic constitutive equations: development, capabillities and thermodynamic framework", Unified Constitutive Laws of Plastic Deformation, Krausz and Krausz eds, Academic Press, (1996).

[22] Nouailhas D., "Unified modelling of cyclic viscoplasticity: Application to austenitic stainless steels", Int. J. of Plasticity, Vol 5, (1989), pp 501-520.

[23] Cordebois J.P. and Sidoroff F., "Anisotropie élastique induite par endommagement", Col. Euromech 115, Comportement Mécanique des Solides Anisotropes, Grenoble, 1979, Publi. CNRS, (1982).

[24] Chaboche J.L., "Sur l'utilisation des variables d'état interne pour la description du comportement viscoplastique et de la rupture par endommagement", Symp. Franco-Polonais de Rhéologie et Mécanique, Cracovie, (1977).

[25] Chow C.L. and Lu T.J., "An analytical experimental study of Mixed-Mode ductile fracture under non-proportional loading", Int. J. Damage Mechanics, Vol 1, (1992), pp 191-236.

[26] Voyiadjis G.Z. and Kattan P.I., "Equivalence of the overall and local approaches to damage in metal matrix composites, to appear in Int. J. of Plasticity.

[27] Kruch S., Chaboche J.L. and Pottier T., "Two-scale viscoplastic and damage analysis of a metal matrix composite", in « Damage and interfacial debonding in composites », G.Z. Voyiadjis, D.H. Allen eds, Elsevier, (1996), pp 45-55.

[28] Gérard A. and Baste S., "Comportement non linéaire des composites à matrice céramique en cycle de charge-décharge", CR Acad. Sci. Paris, t.313, série II, (1991), pp 1361-1366.

[29] Chaboche J.L., Lesne P.M. and Maire J.F., "A constitutive and damage model mixing scalar and tensorial damage variables", CR Acad. Sci. Paris, t.322, série IIb, (1996), pp 187-193.

[30] Pottier T., Kruch S. and Chaboche J.L., "Analyse de l'endommagement macroscopique d'un composite à matrice métallique", Proc. JNC10, D. Baptiste, A. Vautrin eds., AMAC, (1996), pp 1361-1371.

[31] Legrand N., Rémy L., Dambrine B. and Molliex L., "Etude micomécanique de la fatigue oligocyclique d'un composite à matrice métallique base titane renforcé par des fibres unidirectionnelles de SiC", Proc. JNC10, D. Baptiste, A. Vautrin eds., AMAC, (1996), pp 1349-1360.

[32] Lesné O. and Lesne P.M., "Modélisation du comportement de composites à matrice organique C/PMR15", Proc. JNC10, D. Baptiste, A. Vautrin eds., AMAC, (1996), pp 947-958.

[33] Chaboche J.L., "Thermodynamic formulation of constitutive equations and application to the viscoplasticity and viscoelasticity of metals and polymers", To appear in Int. J. Solid Structures, (1997).

Acknowledgements

The cooperation with SNECMA and the financial support of both SNECMA and the French Ministry of defence (DRET) are gratefully acknowledged.

Damage Mechanics in Engineering Materials
G.Z. Voyiadjis, J.-W.W. Ju and J.-L. Chaboche (Editors)
© 1998 Elsevier Science B.V. All rights reserved.

Space of Damage Conjugate Force and Damage Potential of Elastic-Plastic-Damage Materials

K. HAYAKAWA[1] and S. MURAKAMI[2]

[1]Department of Mechanical Engineering, Shizuoka University
Johoku, Hamamatsu, Shizuoka, 432, JAPAN

[2]Department of Mechanical Engineering, Nagoya University
Furo-cho, Chikusa-ku, Nagoya, 464-01, JAPAN

Fundamental aspects of damage conjugate force of irreversible thermodynamics for elastic-plastic-damage materials and the appropriate selection of the spaces for the description of the damage surface and damage potential were first discussed. It was elucidated that the Gibbs thermodynamic potential facilitates the description of the experimental damage surface, since the damage conjugate force can be easily related to stress. It was emphasized that the normality law of damage potential must be examined in the space of the damage conjugate force which can be positive under any multiaxial state of stress, because of the positiveness of the damage evolution. Finally, a series of experiments was carried out in order to investigate whether the damage potential in the space of the damage conjugate force can be identical to the damage surface.

1 INTRODUCTION

Continuum damage mechanics (CDM) based on irreversible thermodynamics [1-17] is one of the most systematic approaches for the unified modeling of the coupled phenomena of elastic-plastic deformation and material damage. The existence of the damage potential and the related damage surface is postulated a priori in the usual framework of this approach. Under this postulation the damage evolution equation can be derived by use of the associated flow rule and the normality law [5, 6, 9-11, 13-19]. However, since the irreversible thermodynamics gives only the thermodynamically admissible framework, the identification of the fundamental aspects of these equations should have recourse to a series of experiments.

Though thermodynamical framework gives a damage potential and the corresponding damage surface in damage conjugate force space, experimental verifications of the damage surface were performed in stress space [20-23]. Therefore, in order to facilitate the comparison of the experimental damage surface with the theoretical one, the damage conjugate force should have a simple relation to stress tensor.

Moreover, as regards the experiments mentioned above, they were concerned only with the verification of the existence of the damage surface. Thus, the further experimental investigations are necessary to clarify the validity of the assumption of the associated flow rule

and the normality law of damage evolution, i.e., the existence of the damage potential. In this case the damage conjugate force space should be employed for the verification of the existence of the damage potential.

The present paper is concerned with the thermodynamical modeling of constitutive and damage evolution equations of elastic-plastic-damage materials, in order that the experimental damage surface conducted in the combined stress space [23] can be described properly. Based on the discussion on the space of damage surface and the damage conjugate force, the Gibbs thermodynamic potential is first employed so that the theoretical damage surface in the space of the damage conjugate force may be related to the experimental one in the stress space. The Gibbs thermodynamic potential is assumed to be decomposed into three parts; the complementary energy affected by damage, the potential concerning the plastic deformation and the potential describing a surface energy due to damage [8, 10, 11, 14, 15, 17].

The damage surface is expressed as a function of the damage conjugate force, and postulates the associated flow rule and the normality law from which the damage evolution equation is derived. Then, the resulting equations are applied to the experimental results of the spheroidized graphite cast iron.

Finally, the validity of the associated flow rule and the normality law is discussed in reference to the corresponding results of the experiments.

2 MODELING OF ELASTIC-PLASTIC-DAMAGE MATERIALS

2.1 Space of Damage Conjugate Force by Use of Gibbs Thermodynamic Potential

The present authors have discussed the constitutive and the damage evolution equations of elastic-brittle [16] and elastic-plastic-damage materials [17] by means of the irreversible thermodynamics theory. Since the Helmholtz free energy was employed in these papers, the damage conjugate force was expressed as a function of elastic strain tensor. Thus, the examination of the validity of these proposed theories necessitates the experiments governed by the elastic strain. However, the experiments governed by the elastic strain may be difficult in the case of the elastic-plastic-damage materials, because the elastic strain can not be easily determined due to the change in the elastic properties by the development of damage.

Because of this situation, most experimental studies on the geometry and the properties of the damage surfaces of composites [20], geological materials [21, 22] and elastic-plastic damage polycrystalline metals [23] have been conducted under combined stress space. From the viewpoint of the simplicity in the experimental formulation of the constitutive and damage evolution equations, the damage conjugate force may be preferably related to stress tensor. Of course, we could express the damage conjugate force as a function of stress by use of the relation between the stress and the elastic strain, even though the Helmholtz free energy is employed. However, the resulting expression of damage conjugate force may have very complicated form.

In the present paper, therefore, the constitutive and damage evolution equations will be developed by use of the Gibbs thermodynamic potential.

2.2 Internal Variables

Inelastic deformation of the elastic-plastic-damage materials such as polycrystalline

metals is usually caused by not only the change of the dislocation structure, the deformation and rotation of grains, but also the internal damage due to the nucleation and growth of the microscopic cavities. The state of such damage is often dependent on the direction of the applied stress[4, 8, 9], and hence is anisotropic. Besides the anisotropy of the damage itself, the anisotropy of the elastic and (or) plastic deformation due to the anisotropic damage may be observed in the damaged process of materials. Therefore, In order to describe the behavior of the elastic-plastic-damage materials, we will employ a scalar isotropic hardening variable r, a second rank symmetric damage tensor $\boldsymbol{D}$ [24, 25], and a scalar variable β which prescribes the further development of the damage. The scalar variable β corresponds to the scalar isotropic hardening variable r in the theory of plasticity [16].

2.3 Formulation of Gibbs Thermodynamic Potential

We take elastic-plastic-damage of polycrystalline materials with moderate ductility, and assume that the Gibbs thermodynamic potential Γ consists of the complementary energy Γ^e due to the elastic deformation, the potential related to the plastic deformation Γ^p and that of damage Γ^d. The potential Γ^p may be the distortion energy of lattice related to dislocation structure, while Γ^d may be related to the surface energy due to the cavity nucleation. Though the complementary energy Γ^e will be influenced by damage through the effect of degradation of the elastic property, the influence of damage to other state variables on other potentials may be small. Thus, the Gibbs thermodynamic potential Γ of these materials per unit mass have the following expression [10, 11]:

$$\Gamma(\boldsymbol{\sigma}, r, \boldsymbol{D}, \beta) = \Gamma^e(\boldsymbol{\sigma}, \boldsymbol{D}) + \Gamma^p(r) + \Gamma^d(\beta) \tag{1}$$

If the material is assumed to be isotropic in the initial undamaged state, $\Gamma^e(\boldsymbol{\sigma}, \boldsymbol{D})$ of equation (1) can be expressed as an isotropic scalar function of two symmetric tensors $\boldsymbol{\sigma}$ and $\boldsymbol{D}$. According to the representation theory of non-linear algebra, the most general form of the isotropic scalar function $\Gamma^e(\boldsymbol{\sigma}, \boldsymbol{D})$ can be expressed as the combination of the ten basic invariants of two symmetric tensors $\boldsymbol{\sigma}$ and $\boldsymbol{D}$ [29, 30]. At the initial undamaged state, the elastic behavior of the elastic-plastic materials is assumed to be isotropic and linear, and thus the function $\Gamma^e(\boldsymbol{\sigma}, \boldsymbol{D})$ is quadratic in $\boldsymbol{\sigma}$. On the other hand, since $\Gamma^e(\boldsymbol{\sigma}, \boldsymbol{D})$ will decrease as damage develops, it will be supposed to be linear in $\boldsymbol{D}$ [4, 5].

If we incorporate further the crack closure effects under compressive stress and the related conditions for continuous transition of stress-strain responses from crack opening to closure [32, 33], the elastic-damage complementary energy is given as follows:

$$\begin{aligned}\Gamma^e(\boldsymbol{\sigma}, \boldsymbol{D}) = & -\frac{\nu_0}{2E_0}(\mathrm{tr}\boldsymbol{\sigma})^2 + \frac{1+\nu_0}{2E_0}\mathrm{tr}\boldsymbol{\sigma}^2 \\ & + \vartheta_1 \mathrm{tr}\boldsymbol{D}(\mathrm{tr}\boldsymbol{\sigma})^2 + \vartheta_2 \mathrm{tr}\boldsymbol{D}\mathrm{tr}\bar{\boldsymbol{\sigma}}^2 + \vartheta_3 \mathrm{tr}\boldsymbol{\sigma}\mathrm{tr}(\boldsymbol{\sigma}\boldsymbol{D}) + \vartheta_4 \mathrm{tr}\left(\bar{\boldsymbol{\sigma}}^2\boldsymbol{D}\right)\end{aligned} \tag{2}$$

where symbols E_0 and ν_0 are Young's modulus and Poisson's ratio at the initial undamaged state, while ϑ_1 through ϑ_4 are material constants. The symbol $\bar{\boldsymbol{\sigma}}$ is the modified stress tensor representing closure effects of microcracks [2, 25, 31, 32] and is given in the principal stress coordinate system as follows:

$$\bar{\sigma}_I = \langle \sigma_I \rangle - \zeta \langle -\sigma_I \rangle \equiv \xi(\sigma_I)\sigma_I \qquad (I = 1,2,3, \text{ no sum.}) \tag{3a}$$

$$\xi(\sigma_I) = H(\sigma_I) + \zeta H(-\sigma_I) \tag{3b}$$

where $\langle\ \rangle$ is Macauley bracket, $H(\ )$ is Heaviside step function, and σ_I (I = 1, 2, 3) are the principal values of $\boldsymbol{\sigma}$. The capital index I indicates the principal stress coordinate. Furthermore, the symbol ζ $(0 \le \zeta \le 1)$ is a material constant describing the extent of crack closure effect, i.e., $\zeta = 1$ implies complete closure while $\zeta = 0$ implies vanishing effects.

As for the other terms in equation (1), $\Gamma^p(r)$ represents the effects of the isotropic hardening of plastic deformation, while $\Gamma^d(\beta)$ is introduced by assuming the linear relation between internal variable β and its conjugate force B. Thus, we have

$$\Gamma^p(r) = R_\infty \left[r + \frac{1}{b}\exp(-br) \right] \tag{4}$$

$$\Gamma^d(\beta) = \frac{1}{2} K_d \beta^2 \tag{5}$$

where R_∞, b and K_d are material constants.

2.4 Elastic-Damage Constitutive Equation and Thermodynamic Conjugate Forces

According to the conventional procedure of the thermodynamic formulation, the elastic constitutive equation of the damaged material can be obtained by the use of equation (4) and equation (10), and leads to

$$\boldsymbol{\varepsilon}^e = \frac{\partial \Gamma^e}{\partial \boldsymbol{\sigma}} = -\frac{\nu_0}{E_0}(\mathrm{tr}\boldsymbol{\sigma})\boldsymbol{I} + \frac{1+\nu_0}{E_0}\boldsymbol{\sigma} + 2\vartheta_1(\mathrm{tr}\boldsymbol{D}\mathrm{tr}\boldsymbol{\sigma})\boldsymbol{I} + 2\vartheta_2(\mathrm{tr}\boldsymbol{D})\bar{\boldsymbol{\sigma}} : \frac{\partial \bar{\boldsymbol{\sigma}}}{\partial \boldsymbol{\sigma}} + \vartheta_3\left[\mathrm{tr}(\boldsymbol{\sigma}\boldsymbol{D})\boldsymbol{I} + (\mathrm{tr}\boldsymbol{\sigma})\boldsymbol{D}\right] + \vartheta_4(\bar{\boldsymbol{\sigma}}\boldsymbol{D} + \boldsymbol{D}\bar{\boldsymbol{\sigma}}) : \frac{\partial \bar{\boldsymbol{\sigma}}}{\partial \boldsymbol{\sigma}} \tag{6}$$

It should be noted that the stress-strain relation of equation (6) should have a continuous transition from the crack opening to closure [32, 33]. However, the condition for the continuous transition of equation (6) can not be examined in general case, but can be confirmed in the particular case of plane stress written in the corresponding principal coordinate system.

The conjugate forces corresponding to internal state variables $\boldsymbol{D}$, r and β, on the other hand, can be derived by the use of equations (2), (4) and (5):

$$\boldsymbol{Y} \equiv \frac{\partial \Gamma^e}{\partial \boldsymbol{D}} = \left[\vartheta_1(\mathrm{tr}\boldsymbol{\sigma})^2 + \vartheta_2 \mathrm{tr}\bar{\boldsymbol{\sigma}}^2\right]\boldsymbol{I} + \vartheta_3(\mathrm{tr}\boldsymbol{\sigma})\boldsymbol{\sigma} + \vartheta_4\bar{\boldsymbol{\sigma}}^2 \tag{7}$$

$$R \equiv \frac{\partial \Gamma^p}{\partial r} = R_\infty\left[1 - \exp(-br)\right] \tag{8}$$

$$B \equiv \frac{\partial \Gamma^d}{\partial \beta} = K_d \beta \tag{9}$$

Since the Gibbs thermodynamic potential has been employed, the damage conjugate force $\boldsymbol{Y}$ of equation (7) can be expressed as a function of stress tensor.

2.5 Dissipation Potential

The dissipation of the plastic deformation in polycrystalline materials is mainly produced by dislocation motion under the applied stress, while the dissipation of damage is governed by the release of internal energy due to the development of microscopic cavities. Thus, we represent these dissipation mechanisms by two different potential functions, i.e., plastic potential F^p and damage potential F^d. Then, the total dissipation potential can be given as the sum of these two parts of dissipation:

$$F(\boldsymbol{\sigma}, \boldsymbol{Y}, R, B; \boldsymbol{D}, r, \beta) = F^p(\boldsymbol{\sigma}, R; \boldsymbol{D}) + F^d(\boldsymbol{Y}, B; \boldsymbol{D}, r) \tag{10}$$

where the quantity preceding the semicolon (;) in the expression of the potential F denotes the variables while those after (;) are the parameters.

Since damage will lead to the reduction of load carrying area and induce the stress concentration around defects, it may bring about the reduction of yield surface. In view of this effect, the damage tensor $\boldsymbol{D}$ has been included in F^p of equation (10) as a parameter. The experimental results on the damage surface show that the geometry of the surfaces does not always remains similar, but may depend on the current damage state [23]. Furthermore, the development of damage is also dependent on a plastic deformation. Thus, the tensor $\boldsymbol{D}$ together with the internal state variable of isotropic hardening r are incorporated into the damage potential F^d as a parameter in order to have more precise description of the damage development.

2.5.1 Plastic Dissipation Potential

Let us assume the associate flow rule; i.e., the yield surface is identical to the plastic dissipation potential $F^p(\boldsymbol{\sigma}, R; \boldsymbol{D})$. By restricting the present discussion to relatively simple loading histories, the following isotropic hardening yield surface can be assumed by extending the von Mises yield condition to the damaged materials [10, 11]:

$$F^p(\boldsymbol{\sigma}, R; \boldsymbol{D}) = \sigma_{eq} - (\sigma_Y + R) = 0 \tag{11}$$

$$\sigma_{eq} = \sqrt{\frac{3}{2}\boldsymbol{\sigma}' : \boldsymbol{M}(\boldsymbol{D}) : \boldsymbol{\sigma}'} \tag{12}$$

where $\boldsymbol{\sigma}'$ is the deviatoric stress tensor, while $\boldsymbol{M}(\boldsymbol{D})$ is a fourth rank symmetric tensor with damage tensor $\boldsymbol{D}$ as an argument.

The yield function of equation (11) furnishes the constitutive equation for plastic strain rate $\dot{\varepsilon}_{ij}^p$ and the rate of isotropic hardening variable $\dot{r}$ as follows:

$$\dot{\varepsilon}_{ij}^{p} = \dot{\Lambda}^{p} \frac{\partial F^{p}}{\partial \sigma'_{ij}} = \frac{3}{2} \dot{\Lambda}^{p} \frac{M_{ijkl}\sigma'_{kl}}{\sigma_{eq}} \tag{13}$$

$$\dot{r} = \dot{\Lambda}^{p} \frac{\partial F^{p}}{\partial(-R)} = \dot{\Lambda}^{p} \tag{14}$$

where the parameter $\dot{\Lambda}^{p}$ is an unknown multiplier determined from the consistency condition $\dot{F}^{p} = 0$, and will be given later in Section 2.6.

The loading / unloading conditions of equation (13) are defined by the condition that the following Kuhn-Tucker relations should be always satisfied [27, 35]:

$$\dot{\Lambda}^{p} \geq 0, \quad F^{p} \leq 0, \quad \dot{\Lambda}^{p} F^{p} = 0 \tag{15}$$

The function $\boldsymbol{M}(\boldsymbol{D})$ in equation (12) should be specified so that it may properly describe the increased effects of stress due to damage. By postulating moderate effects of $\boldsymbol{D}$ on the plastic deformation, $\boldsymbol{M}(\boldsymbol{D})$ is expressed by the following linear function of $\boldsymbol{D}$:

$$\left[M(\boldsymbol{D})\right]_{ijkl} = \frac{1}{2}\left(\delta_{ik}\delta_{jl} + \delta_{il}\delta_{jk}\right) + \frac{1}{2}c^{p}\left(\delta_{ik}D_{jl} + D_{ik}\delta_{jl} + \delta_{il}D_{jk} + D_{il}\delta_{jk}\right) \tag{16}$$

where c^{p} is a material constant.

2.5.2 Damage Dissipation Potential

As was observed in the previous experiments on damage surface in stress space by the present authors[23], there exists a damage surface which prescribes the limitation of damage development, and the loading / unloading and neutral loading condition holds with respect to the surface. From theoretical point of view, on the other hand, the existence of the damage dissipation potential F^{d} will be proved if the damage evolution depends only on the damage conjugate force and the current material state [18], and damage evolution can be expressed by the normality rule of F^{d}.

In the present paper, we will assume the associate flow rule as in the case of the plasticity. Furthermore, the function F^{d} will be expressed as a function of the damage conjugate force $\boldsymbol{Y}$ in order to satisfy the thermodynamic requirement.

According to the experimental results [23], the geometry of the damage surface depends not only on the hydrostatic stress, but also on plastic deformation and the current state of damage.

Thus, based on the above discussion, the damage surface will be assumed so that the surface may describe the experimental one [23] as follows:

$$F^{d}(\boldsymbol{Y}, B; \boldsymbol{D}, r) = Y_{eq} + c^{r} r \,\mathrm{tr}\boldsymbol{D}\mathrm{tr}\boldsymbol{Y} - \left(B_{0} + B\right) = 0 \tag{17}$$

$$Y_{eq} = \sqrt{\frac{1}{2}\boldsymbol{Y} : \boldsymbol{L}(\boldsymbol{D}) : \boldsymbol{Y}} \tag{18}$$

where $\boldsymbol{L}(\boldsymbol{D})$ is a fourth rank tensor function of the damage tensor $\boldsymbol{D}$ describing the damage-induced change of the damage surface. The symbol B_0 in equation (17) is a material constant to specify the size of the initial damage surface.

As regards the tensor $\boldsymbol{L}(\boldsymbol{D})$, it should be determined so that equation (17) may describe the corresponding experimental results. In the present paper, since the material damage in the elastic-plastic material employed is not so significant, the tensor $\boldsymbol{L}(\boldsymbol{D})$ can be given by a linear function of damage tensor $\boldsymbol{D}$ and furnishes as follows:

$$\left[\boldsymbol{L}(\boldsymbol{D})\right]_{ijkl} = \frac{1}{2}\left(\delta_{ik}\delta_{jl} + \delta_{il}\delta_{jk}\right) + \frac{1}{2}c^d\left(\delta_{ik}D_{jl} + D_{ik}\delta_{jl} + \delta_{il}D_{jk} + D_{il}\delta_{jk}\right) \tag{19}$$

The evolution equations of damage $\boldsymbol{D}$ and β are given as follows:

$$\dot{\boldsymbol{D}} = \dot{\Lambda}^d \frac{\partial F^d}{\partial \boldsymbol{Y}} = \dot{\Lambda}^d \left[\frac{\boldsymbol{L} : \boldsymbol{Y}}{2Y_{eq}} + c^r r(\mathrm{tr}\boldsymbol{D})\boldsymbol{I} \right] \tag{20}$$

$$\dot{\beta} = \dot{\Lambda}^d \frac{\partial F^d}{\partial(-B)} = \dot{\Lambda}^d \tag{21}$$

where $\dot{\Lambda}^d$ can be derived from the consistency condition $\dot{F}^d = 0$, and will be given in Section 2.6. Similarly to the plasticity case, the loading / unloading conditions for the damage evolution are specified by the following Kuhn-Tucker relations [27, 35]:

$$\dot{\Lambda}^d \geq 0, \quad F^d \leq 0, \quad \dot{\Lambda}^d F^d = 0 \tag{22}$$

2.6 Calculation of Multipliers

When damage and plasticity occur simultaneously, the multipliers $\dot{\Lambda}^p$ and $\dot{\Lambda}^d$ must be obtained by solving simultaneously the consistency condition for the plastic yield surface and the damage surface as follows [35]:

$$\dot{\Lambda}^p = \frac{\dfrac{\partial F^p}{\partial \boldsymbol{\sigma}} : \dot{\boldsymbol{\sigma}}}{\dfrac{dR}{dr}} + \frac{\left(\dfrac{\partial F^p}{\partial \boldsymbol{D}} : \dfrac{\partial F^d}{\partial \boldsymbol{Y}}\right)\left(\dfrac{\partial F^d}{\partial \boldsymbol{Y}} : \dot{\boldsymbol{Y}}\right)}{\left(\dfrac{dR}{dr}\right)\left(\dfrac{dB}{d\beta} - \dfrac{\partial F^d}{\partial \boldsymbol{D}} : \dfrac{\partial F^d}{\partial \boldsymbol{Y}}\right)} \tag{23}$$

$$\dot{\Lambda}^d = \frac{\dfrac{\partial F^d}{\partial \boldsymbol{Y}} : \dot{\boldsymbol{Y}}}{\dfrac{dB}{d\beta} - \dfrac{\partial F^d}{\partial \boldsymbol{D}} : \dfrac{\partial F^d}{\partial \boldsymbol{Y}}} \tag{24}$$

3. COMPARISON WITH THE EXPERIMENTS ON TUBULAR SPECIMENS OF SPHEROIDIZED GRAPHITE CAST IRON

3.1 Specimen of Spheroidized Graphite Cast Iron

Tubular specimens of spheroidized graphite cast iron FCD400 (JIS) were employed in the present experiments. The wall thickness of the specimen is 1 mm, and may be sufficiently thick to ensure the continuum assumption because the average diameter of spheroidized graphite particles is about $30\,\mu$m. The fracture mechanism of the spheroidized graphite cast iron has been found mainly to be the decohesion at the interfaces between the graphite particles and the ferrite matrix, in addition to the ductile failure of ferrite matrix induced by the development of microcracks and plastic deformation.

3.2 Uniaxial Tension Tests

The material constants in equations (1)-(24) are identified so that the test results under uniaxial tension shown in Figs. 1, 2 and 3 together with the initial damage surface of Fig. 8 may be described by these equations. The material constants thus determined are as follows:

$$
\begin{aligned}
&E_0 = 169\,\mathrm{GPa},\ \nu_0 = 0.285,\ \zeta = 0.89,\\
&\vartheta_1 = -3.95\times10^{-7}\,\mathrm{MPa}^{-1},\ \vartheta_2 = 4.00\times10^{-6}\,\mathrm{MPa}^{-1},\\
&\vartheta_3 = -4.00\times10^{-7}\,\mathrm{MPa}^{-1},\ \vartheta_4 = 2.50\times10^{-6}\,\mathrm{MPa}^{-1},\\
&b = 15,\ R_0 = 293.0\,\mathrm{MPa},\ R_\infty = 250.0\,\mathrm{MPa},\ c^p = 1.0,\\
&K_d = 1.3,\ B_0 = 0.273,\ c^d = -15.0,\ c^r = 50.0
\end{aligned}
\tag{25}
$$

Fig. 1 shows the comparison between the experimental uniaxial stress-strain relation and the corresponding prediction by equations (6), (13), (14), (20) and (21). It can be seen that the experimental result can be precisely described by the present theory.

Figs. 2 and 3, on the other hand, show the comparison of Young's modulus E_1 and Poisson's ratio ν_{12} which is the ration of transverse strain induced by the axial tension to the

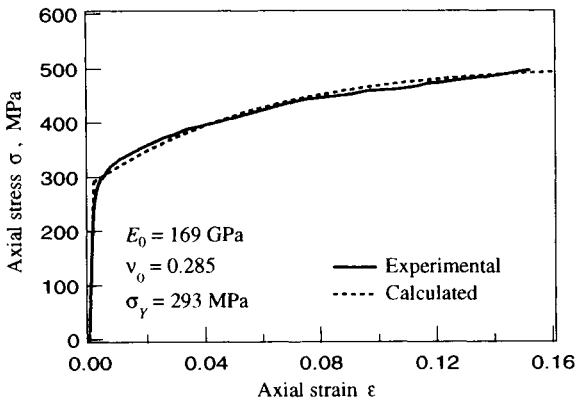

Fig. 1 Experimental and calculated stress-strain curves under uniaxial tension.

axial strain. Young's modulus E_1 and Poisson's ratio ν_{12} under uniaxial tension tests were measured in the unloading processes which were carried out at every 1.5% increment of strain on the corresponding stress-strain curve [23].

In Fig. 2, the decrease in the experimental results of E_1 is observed due to internal damage, and E_1 attains to about 90% of its initial value at failure. This feature can be described well by the calculated result.

Fig. 3, on the other hand, shows that the present theory with damage anisotropy can describe the observed decrease of Poisson's ratio ν_{12} precisely. Moreover, Poisson's ratio ν_{12} attains to 92% of its initial value. As observed in equation (25), the material constants ϑ_1 and ϑ_3 must have negative values in order to describe the larger decrease in Young's modulus than that in Poisson's ratio. Though the damage-induced change

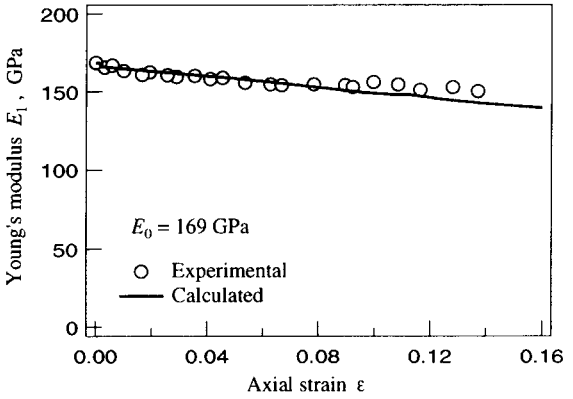

Fig.2 Results of Young's modulus under uniaxial tension.

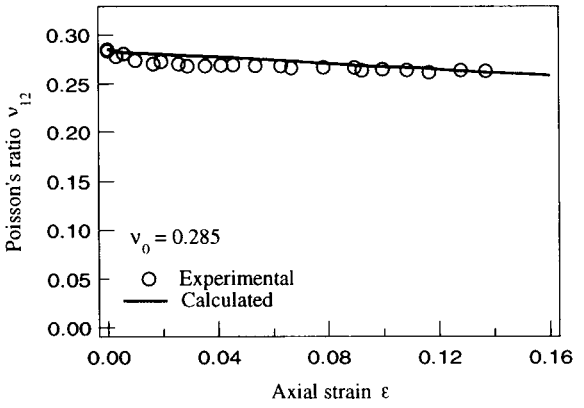

Fig.3 Results of Poisson's ratio under uniaxial tension.

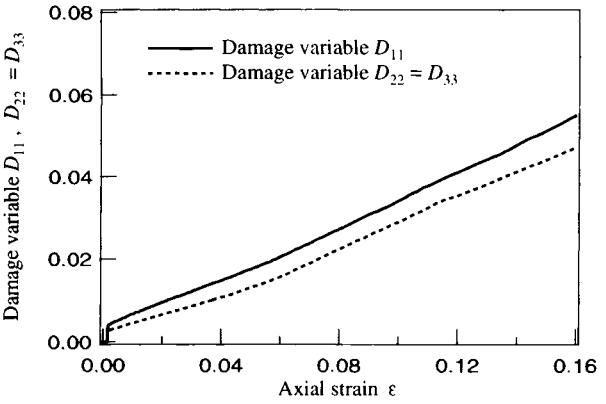

Fig.4 Predicted results of damage variable under uniaxial tension.

of Poisson's ratio can not be described by the isotropic damage theory [36], the present theory of anisotropic damage can describe the observed decrease of Poisson's ratio precisely.

Finally, the damage evolution curves predicted by equation (20) together with the material constants of equation (25) are entered in Fig.4. A solid line in this figure shows the damage component D_{11} of the axial direction x_1. Moreover, broken line shows D_{22} and D_{33} of the direction perpendicular to x_1. As observed in Fig.4, the anisotropy of the damage is not so significant, and this is attributable to the fact that the spheroidized graphite cast iron employed in this experiments is rather ductile, and the anisotropy in the cavity formation in this materials is rather small.

3.3 Torsional Tests

Fig.5 shows the comparison between the experimental results of shear stress-shear strain curve and the corresponding prediction by the same equations in the case of uniaxial tension. The material constants (25) which had been determined by the preceding uniaxial loading tests were again employed. Since the shear yield stress is $\tau_Y = 168$ MPa, i.e., approximately $1/\sqrt{3}$ of the tensile yield stress σ_Y (= 293MPa), the initial yield of the present material obeys the von Mises criterion of equation (11). Fig.5 also assures the close agreement of the present theory with the experiment.

Evolution of the damage components are shown in Fig.6. In this figure, the principal values $\hat{D}_{11}$, $\hat{D}_{22}$ and $\hat{D}_{33}$ are entered, since the directions of the principal stress may play the most important role to the clack opening or closure. As observed in this figure, the damage component $\hat{D}_{11}$ in the principal direction $\hat{x}_1$ is larger than the component $\hat{D}_{22}$, which may be accounted for by the difference in the damage development in two directions $\hat{x}_1$ and $\hat{x}_2$. This results is due to the introduction of the modified stress $\overline{\boldsymbol{\sigma}}$ of equation (3) into the Gibbs thermodynamic potential $\Gamma^e(\boldsymbol{\sigma}, \boldsymbol{D})$ of equation (2).

From physical point of view, the damage is caused mainly by the microscopic defects produced by the tensile principal stress, while the compressive principal stress leads to less material damage than the tensile one because of the crack closure effect. Therefore, the actual

material behavior can be properly described by the present formulation.

Furthermore, the damage variable $\hat{D}_{33}$ of the principal direction $\hat{x}_3$ does not differ much from $\hat{D}_{11}$ and $\hat{D}_{22}$. This result shows that the damage development of this material under torsional loading also has rather insignificant anisotropy even though there exist certain unilateral nature. Physically, this results is explained by the fact that the damage of this material mainly occurs by the decohesion of almost the whole boundary of the spheroidized graphite and the ferrite matrix.

Fig.7 gives a comparison between the observed and the predicted shear modulus G_{12}. The shear modulus G_{12} decreases according to the damage growth, and leads to about 93% of its initial value at fracture.

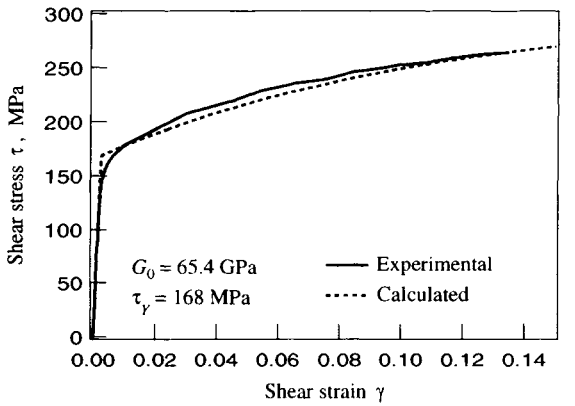

Fig.5 Experimental and predicted shear stress-shear strain.

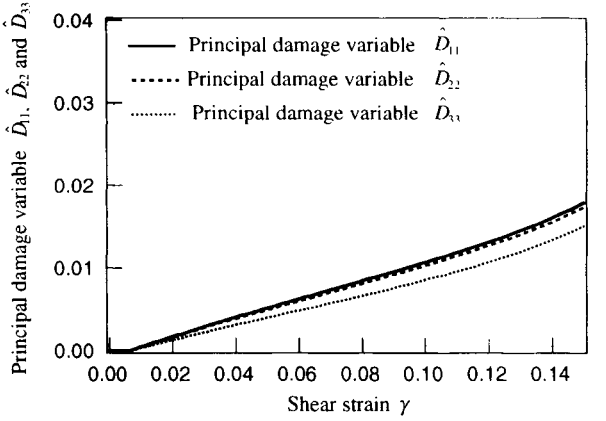

Fig.6 Predicted result of damage variable under torsion.

3.4 Comparison of the damage surface

Fig.8 shows the initial, subsequent and final damage surfaces obtained by the experiments and the prediction of the theoretical damage surface (17), respectively. The symbols ○, □ and △ correspond to the initial, subsequent and final damage surface by experiments, respectively, while a solid, broken and dotted line represent the predicted results of the theoretical damage surface of equation (17). The prediction of the damage surfaces is performed as follows: the value of the axial stress and the shear stress are obtained so that they can satisfy equation (17), in which the value of $B_0 + B$ has been prescribed at the uniaxial stress state corresponding to the initial, subsequent and final states.

As regards the initial damage surface, the experimental results can be described by the proposed damage surface of equation (17), which has a first quadrant of an ellipse in the space

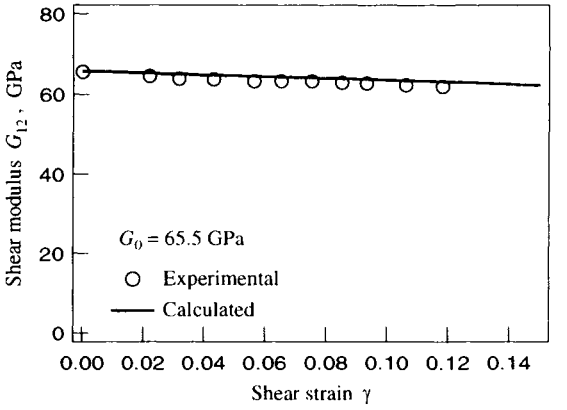

Fig.7 Experimental and predicted results of shear modulus under torsion.

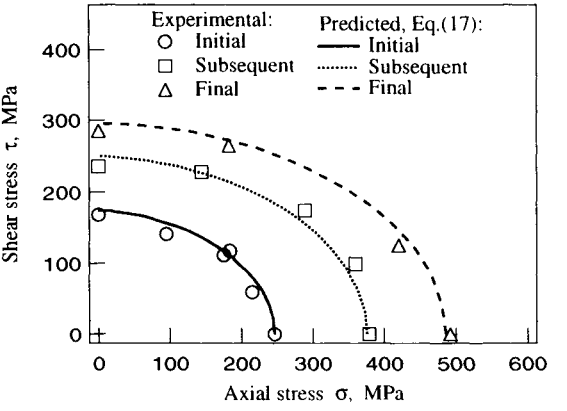

Fig.8 Damage surfaces under combined stress space

of axial tensile and shear stress. The ellipse of the initial damage surface has the aspect ratio of $\sigma/\tau = 1.46$, which is in contrast to the ellipse ($\sigma/\tau = \sqrt{3}$) of the initial yield surface of von Mises type. From this difference, it is found that the influence of hydrostatic stress can not be neglected for damage development due to microcrack nucleation and growth. In the present theory, this effect has been represented by the term of $\mathrm{tr}\boldsymbol{\sigma}$ in the damage conjugate force $\boldsymbol{Y}$ of equation (7), which in turn results from the expression of Γ^e of equation (2).

On the other hand, the aspect ratio of the subsequent damage surface is $\sigma/\tau = 1.62$, which is closer to the aspect ratio of von Mises type than that of the initial damage surface. This is because the increasing plastic deformation of the ferrite matrix will govern gradually the damage process, and final damage surface, whose aspect σ/τ is approximately $\sqrt{3}$, might have been governed by the ductile damage.

The proposed damage surface and the damage evolution equation derived by the consistency condition and the normality rule of equation (17) can describe the geometry of each damage surface. This implies the validity of the introduction of the effect of the current state of the material damage, the hydrostatic stress and the plastic deformation into the damage surface of equation (17).

4 EXPERIMENTAL VALIDATION OF DAMAGE POTENTIAL

Though the discussion of the preceding section revealed that there exists the damage surface in stress space and that the condition of loading / unloading and neutral loading is sufficiently satisfied [23], the validity of the normality law of the damage surface remains unconfirmed. Thus, further experimental investigations are necessary to validate the existence of a damage potential surface. For this investigations a series of experiments are performed to verify the validation of the assumption of the normality law in the present paper.

Let us first note that the normality law of the damage evolution should be discussed not in stress space but in the space of damage conjugate force. This is due to the fact that, though the stress space can give reversed directions under some loading conditions, the damage evolution can be always positive unless there are healing effects. On the other hand, the damage conjugate force is always positive in the space of axial-torsional stress. Therefore, the normality law must be examined in the space of damage conjugate force. It should be noted that the material constants ϑ_1 through ϑ_4 must be determined so that the damage behavior of the specific material may be described properly. We must select such material constants that the damage conjugate force equation (16) are negative if the healing effect of damage will occurs under the corresponding stress states (for instance, $\vartheta_1 = \vartheta_2 = \vartheta_4 = 0$, $\vartheta_3 > 0$ under stress state $\sigma_{11} < 0$, $\mathrm{tr}\boldsymbol{\sigma} > 0$).

4.1 Procedure of Experiment

First, we will employ the tubular specimens which we used before in the experimental verification of the damage surface [23]. Each specimen is subjected to loading along the three different proportional loading paths A: O-A_0-A_1-A_2, B: O-B_0-B_1-B_2 and C: O-C_0-C_1-C_2 as shown in Fig. 12. In this figure, A_0, B_0 and C_0 are the stress states on the initial damage surface, while A_1, B_1 and C_1 are on the subsequent damage surface[23]. Furthermore, A_2, B_2 and C_2 are the stress states before the final fracture. Then, at the stress states A_1, B_1, C_1, A_2, B_2 and C_2, Young's modulus E_1, Poisson's ratio ν_{12} and Shear modulus G_{12} were determined with

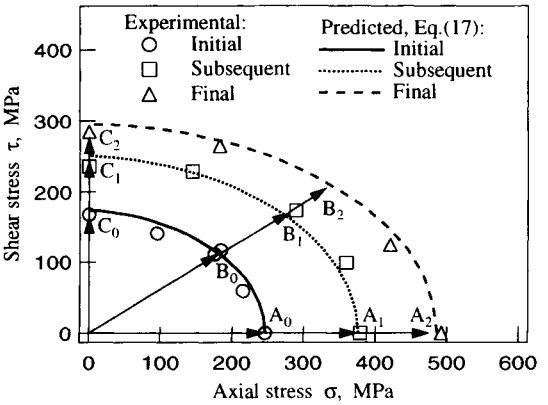

Fig.9 Stress paths for verification of normality law of damage surface

confident coefficient of 99%.

The components D_{11}, D_{22} and D_{33} of the damage tensor $\boldsymbol{D}$ on the each stress state were calculated by the equations of Young's modulus E_1, Poisson's ratio ν_{12} and the shear modulus G_{12} with material constants (25) obtained from equation (6) as follows:

$$E_1 = \frac{E_0}{1+2E_0\left\{(\vartheta_1+\vartheta_2)\mathrm{tr}\boldsymbol{D}+(\vartheta_3+\vartheta_4)D_{11}\right\}} \tag{26}$$

$$\nu_{12} = \frac{\nu_0-\left\{2\vartheta_1\mathrm{tr}\boldsymbol{D}+\vartheta_3(D_{11}+D_{22})\right\}}{1+2E_0\left\{(\vartheta_1+\vartheta_2)\mathrm{tr}\boldsymbol{D}+(\vartheta_3+\vartheta_4)D_{11}\right\}} \tag{27}$$

$$G_{12} = \frac{E_0}{2(1+\nu_0)+2E_0\left\{\vartheta_2(1+\zeta^2)\mathrm{tr}\boldsymbol{D}+\vartheta_4(1+\zeta^2)D_{11}\right\}} \tag{28}$$

where the damage component D_{12} has been excluded in equation (28), since the component D_{12} has very small value in comparison with the other components D_{11}, D_{22} and D_{33}.

By solving these equations as simultaneous equations of the three unknowns of D_{11}, D_{22} and D_{33}, the experimental values of the damage variable can be obtained. However, the simultaneous equations by use of E_1, ν_{12} and G_{12} obtained by experiments do not always furnish physically admissible set of the values of D_{11}, D_{22} and D_{33}. Therefore, in the present paper, the values of D_{11}, D_{22} and D_{33} are determined so that E_1, ν_{12} and G_{12} calculated by equations (26)~(28) with the material constants (25) may exist in the confidence interval for experimental values of E_1, ν_{12} and G_{12} with confidence coefficient of 99%.

4.2 Comparison between experiment and theory

Figs. 10(a) and (b) show the relation between the damage variable D_{11}-D_{22} and D_{11}-

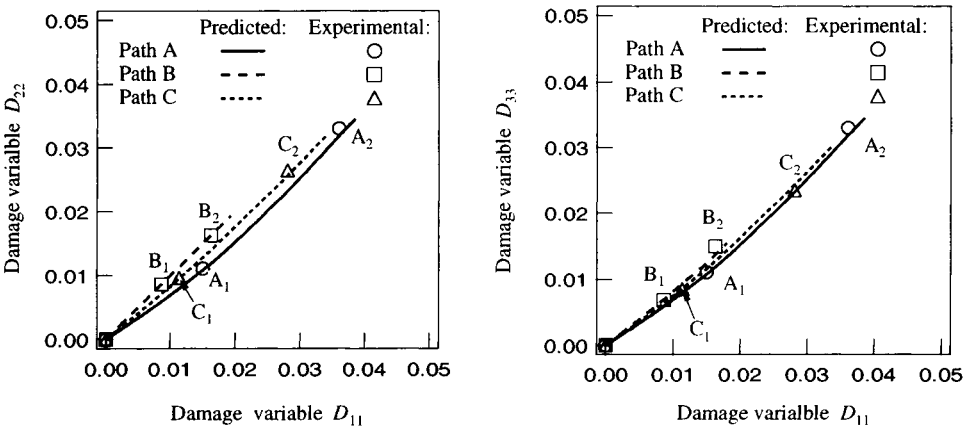

(a) Damage variable D_{11} -D_{22} relation (b) Damage variable D_{11} - D_{33} relation

Fig.10 Damage development along the corresponding loading path A, B and C.

D_{33}. Three lines and symbols show the predicted and experimental results for the corresponding paths A, B and C. The experimental results on each path show a good agreement with the theoretical one. Furthermore, as observed in Figs. 13(a) and (b), the development of damage along each path tends to isotropic, namely the slope of the tangent of each line leads to $\pi/4$. This feature of insignificant anisotropy may be accounted for by the damage development observed in Fig.7.

Figs. 11 (a) and (b) show the initial and the subsequent damage surfaces and the direction of damage evolution obtained by the experiments in the space of the damage conjugate force, projected on Y_{11}-Y_{22} and Y_{11}-Y_{33} plane. The directions of damage growth on the stress point A_0, B_0, C_0, A_1, B_1 and C_1 were obtained from Figs.10(a) and (b).

As observed in the initial and the subsequent damage surface covered by experiments, the range that the damage conjugate force can vary is very narrow. Therefore, the proposed damage evolution equations (20) which is derived by assuming the normality law of the damage surface can be nearly isotropic. The directions of the stress states A_0, B_0 and C_0 on the initial damage surface, and the directions of the stress states A_1, B_1 and C_1 on the subsequent damage surface can be found to satisfy the normality law because each direction is almost perpendicular to the initial and the subsequent damage surface described by equation (17).

From these results, it follows that the proposed damage surface of equation (17) is found to be identical to the damage potential, and that the assumption of the damage potential and the corresponding normality law in deriving the damage evolution equation is certified.

5. CONCLUSIONS

Constitutive and the damage evolution equations of the elastic-plastic-damage materials were developed based on irreversible thermodynamics, and their validity was discussed by performing a series of experiments under combined state of stress. The conclusions obtained

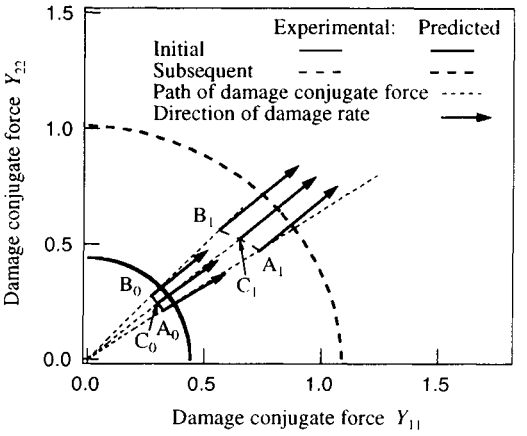

(a) Projection to Y_{11} - Y_{22} plane

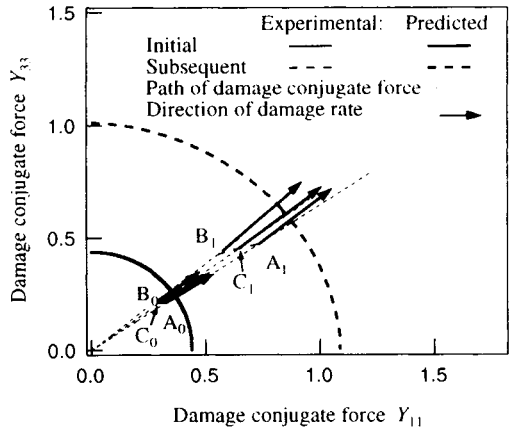

(b) Projection to Y_{11} - Y_{33} plane

Fig.11 Directions of damage development in the space of damage conjugate force

from the present work are summarized as follows:

1) It was found that the employment of the Gibbs thermodynamical potential was appropriate to relate the damage experiments in stress space to the present theory.
2) The resulting constitutive and damage evolution equations could describe the anisotropic change in the elastic properties of the spheroidized graphite cast iron due to damage with good agreements.
3) The proposed damage surface was verified to describe the experimental initial and the subsequent damage surface expressed in stress space properly. This is because that the

effects of the hydrostatic stress, plastic deformation and the current damage state in the proposed damage surface are effectively introduced.

4) The direction of the experimental damage rate vectors is confirmed to coincide with the outward normal of the initial and subsequent damage surface in the space of the damage conjugate force. This validates the existence of the damage potential and the normality law on damage evolution, which are the common postulation in deriving the damage equation by use of damage mechanics based on irreversible thermodynamics.

REFERENCES

1. Chaboche, J. L. 1980. "Sur l'utilisation des variables d'etat interne pour la descrption du comportement viscoplastiquee et de la rupture par endomagement", in *Problemes Lineaires de Mecanique*, PWN, Warsaw: 139-159.
2. Lemaitre, J. and J. L. Chaboche, 1990. *Mechanics of Solid Materials*: Cambridge University Press.
3. Lemaitre, J. 1992. *A Course on Damage Mechanics*: Springer - Verlag.
4. Krajcinovic, D. and G. U. Fonseka. 1981. "The continuous damage mechanics of brittle materials, Parts I and II", *J. Appl. Mech., Trans. ASME*, 48: 809-824.
5. Krajcinovic, D. 1983. "Constitutive theory of damaging materials", *J. Appl. Mech., Trans ASME.*, 50: 355-360.
6. Krajcinovic, D. and S. Selvaraj, 1984. "Creep Rapture of Metals - An Analytical Model", *J. Engng. Mat. Technol., Trans. ASME.*, 106: 405-409
7. Cordebois, J. P. and F. Sidoroff. 1982. "Damage induced elastic anisotropy", in *Mechanical Behavior of Anisotropic Solids*, J. P. Boehler, ed.: Matinus Nijhoff, The Hague: 761-774.
8. Cordebois, J.P. and F. Sidoroff. 1982. "Endommagement Anistrope en Elasticite et Plasticite", *J. Mec. Theor. Appl., Numero Special*: 45-60
9. Lemaitre. J. 1985. "A continuous damage mechanics model for ductile fracture", *J. Engng. Mat. Tech., Trans. ASME.*, 107: 83-89.
10. Chow, C. L. and J. Wang. 1987. "An anisotropic theory of continuum damage mechanics for ductile fracture", *Engng. Fact. Mech.*, 27: 547-558.
11. Chow, C.L. and J. Wang. 1988. "A finite element analysis of continuum damage mechanics for ductile fracture", *Int. J. of Fracture*, 38: 83-102.
12. Chaboche, J. L. 1988. "Continuum Damage Mechanics: Part I - General Theory", *J. Appl. Mech., Trans. ASME.*, 55: 59-64
13. Kattan. P.1. and G. Z. Voyiadjis, 1990. "A coupled theory of damage mechanics and finite strain elasto-plasticity I. Damage and elastic deformations", *Int. J. Engng. Sci.*, 28: 421-435.
14. Voyiadjis, G. Z. and P.1. Kattan, 1990. "A coupled theory of damage mechanics and finite strain elasto-plasticity II. Damage and finite strain plasticity ", *Int. J. Engng. Sci.*, 28: 505-524.
15. Yazdani, S. 1993. "On a class of continuum damage mechanics theories ", *Int. J. Damage Mech.*, 2: 162-176.
16. Murakami, S. and K. Kamiya, 1997. "Constitutive and Damage evolution Equations of Elastic-Plastic-Brittle Materials Based on Irreversible Thermodynamics ", *Int. J. Mech. Sci.*, 39: 473-486.

17. Hayakawa, K., S. Murakami and Y. Liu, "Irreversible thermodynamics theory for elastic-plastic-damage materials", *Euro. J. Mech., A/Solids*, (Submitted).
18. Rice, J. R. 1975. "Continuum mechanics and thermodynamics of plasticity in relation to microscale deformation mechanics ", in Constitutive Equations in Plasticity, A. S . Argon, ed., The MIT Press, Cambridge: 23-79.
19. Maugin, G. A. 1992. The Thermomechanics of Plasticity and Fracture. Cambridge University Press .
20. Curtis, P. T., M. G. Bader and J. E. Bailey, 1978. "The stiffness and strength of a polyamide thermoplastic reinforced with glass and carbon fiber", *J. Mat. Sci.*, 13: 377-390.
21. Holcomb, D. J. 1984. "Discrete memory in rock: a review", *J. Rheology*, 28: 725-757.
22. Holcomb, D. J. and L. S. Costin. 1986. "Detecting damage surface in brittle materials using acoustic emissions", *J. Appl. Mech., Trans. ASME.*, 53: 536-544.
23. Murakami, S., K. Hayakawa and Y. Liu, "Damage Evolution and Damage Surface of Elastic-Plastic-Damage Materials Under Multiaxial Loading", *Int. J. Damage Mech.* (Submitted) .
24. Murakami, S. and N. Ohno, 1980, "A continuum theory of creep and creep damage", in *Creep of Structures, 3rd IUTAM Symposium on Creep in Structures*, A. R. S. Ponter, D. R. Hayhurst, Eds., Springer, Berlin, 422-444.
25. Murakami, S. 1988. "Mechanical modeling of material damage", *J. Appl. Mech., Trans. ASME.*, 55: 280-286.
26. Lu, T. J. and C. L. Chow, 1990. "On Constitutive Equations of Inelastic Solids with Anisotropic Damage", *Theoretical and Applied Fracture Mechanics*, 14: 187-218.
27. Ju, J. W., 1989, "On energy based coupled elstoplastic damage theories: constitutive modeling and computational aspect, *Int. J. Solids Struct.*, 27: 803-833.
28. Malvern, L. E. 1969. *Introduction to the Mechanics of a Continuous Medium*: Prentice-Hall.
29. Truesdell, C and W. Noll, 1965. "The Non-Linear Field Theories of Mechanics", in *Encyclopedia of Physics*, Flugge, S . ed, Volume III / 3: Springer-Verlag.
30. Leigh, D. C., 1968, *Nonlinear Continuum Mechanics*: McGraw-Hill Book Company, New York.
31. Ladeveze, P. and J. Lemaitre, 1984, "Damage Effective Stress in Quasi-Unilateral Material Conditions", *IUTAM Congress, Lyngby, Denmark.*
32. Chaboche, J. L., 1992, "Damage induced anisotropy: on the difficulties associated with the active / passive unilateral condition", *Int. J. Damage Mech.*, 1: 148-171.
33. Chaboche, J. L., 1993, "Development of continuum damage mechanics for elastic solids sustaining anisotropic and unilateral damage", Int. *J. Damage Mech.*, 2, 311 -329 .
34. Ramtani, S., 1990. "Contribution à la Modélisation du Comportement Multiaxial du Béton Endommagé avec Description du Caractère Unilatéral", Thèse, Univ. Paris VI.
35. Hansen, N. R. and H. L. Schreyer, 1994, "A thermodynamically consistent framework for theories of elastoplasticity coupled with damage", *Int. J. Solids Struct.*, 31: 359-389.
36. Ju, J. W. 1990. "Isotropic and anisotropic damage variable in continuum damage mechanics", *J. Engng. Mech., Trans. ASCE.*, 116: 2764-2770.
37. Lubarda, V. A. and D. Krajcinovic. 1995. "Constitutive structure of rate theory of damage in brittle elastic solids ", *Appl. Math. Comput.*, 67: 81 - 101.

Damage Mechanics in Engineering Materials
G.Z. Voyiadjis, J.-W.W. Ju and J.-L. Chaboche (Editors)
© 1998 Elsevier Science B.V. All rights reserved.

Kinematics of Large Elastoplastic Damage Deformation

G.Z. Voyiadjis and T. Park

Department of Civil and Environmental Engineering, Louisiana State University, Baton Rouge, LA 70803 U.S.A.

ABSTRACT

In this paper the kinematics of damage for finite strain, elasto-plastic deformation is introduced using the fourth-order damage effect tensor through the concept of the effective stress within the framework of continuum damage mechanics. In the absence of the kinematic description of damage deformation leads one to adopt one of the following two different hypotheses for the small deformation problems. One uses either the hypothesis of strain equivalence or the hyphothesis of energy equivalence in order to characterize the damage of the material. The proposed approach in this work provides a general description of kinematics of damage applicable to finite strains. This is accomplished by directly considering the kinematics of the deformation field and furthermore it is not confined to small strains as in the case of the strain equivalence or the strain energy equivalence approaches. In this work, the damage is described kinematically in both the elastic domain and plastic domain using the fourth order damage effect tensor which is a function of the second-order damage tensor. The damage effect tensor is explicitly characterized in terms of a kinematic measure of damage through a second-order damage tensor. Two kinds of second-order damage tensor representations are used in this work with respect to two reference configurations. The finite elasto-plastic deformation behavior with damage is also viewed here within the framework of thermodynamics with internal state variables. Using the consistent thermodynamic formulation one introduces seperately the strain due to damage and the associated dissipation energy due to this strain.

1 Theoretical Preliminaries

A continuous body in an initial undeformed configuration that consists of the material volume Ω° is denoted by C°, while the elasto-plastic damage deformed configuration

at time t after the body is subjected to a set of external agencies is denoted by C^t. The corresponding material volume at time, t is denoted by Ω^t. Upon elastic unloading from the configuration C^t an intermediate stress free configuration is denoted by C^{dp}. In the framework of continuum damage mechanics a number of fictitious configurations, based on the effective stress concept, are assumed that are obtained by fictitiously removing all the damage that the body has undergone. Thus the fictitious configuration of the body denoted by $\bar{C}^t$ is obtained from C^t by fictitiously removing all the damage that the body has undergone at C^t. Also the fictitious configuration denoted by $\tilde{C}^p$ is assumed which is obtained from C^{dp} by fictitiously removing all the damage that the body has undergone at C^{dp}. While the configuration $\bar{C}^p$ is the intermediate configuration upon unloading from the configuration $\bar{C}^t$. The initial undeformed body may have a pre-existing damage state. The initial fictitious effective configuration denoted by $\bar{C}^\circ$ is defined by removing the initial damage from the initial undeformed configuration of the body. In the case of no initial damage existing in the undeformed body, the initial fictitious effective configuration is identical to the initial undeformed configuration. Cartesian tensors are used in this work and the tensorial index notation is employed in all equations. The tensors used in the text are denoted by boldface letters. However, superscripts in the notation do not indicate tensorial index but merely stand for corresponding deformation configurations such as "e" for elastic, "p" for plastic, and "d" for damage etc. The barred and tilded notations refer to the fictitious effective configurations.

2 Description of Damage State

The damage state can be described using an even order tensor (Leckie [5], Onat [11] and Betten [1]). Ju [4] pointed out that even for isotropic damage one should employ a damage tensor(not a scalar damage variable) to characterize the state of damage in materials. However, the damage generally is anisotropic due to the external agency condition or the material nature itself. Although the fourth-order damage tensor can be used directly as a linear transformation tensor to define the effective stress tensor, it is not easy to characterize physically the fourth-order damage tensor compared to the second-order damage tensor. In this work, the damage is considered as a symmetric second-order tensor. However, damage tensor for the finite elasto-plastic deformation can be defined in two reference systems [9]. The first one is the damage tensor denoted by $\boldsymbol{\phi}$ representing the damage state with respect to the current damaged configuration, C^t. Another one is denoted by $\boldsymbol{\varphi}$ and is representing the damage state with respect to the elastically unloaded damage configuration, C^{dp}. Both are given by Murakami [8] as follows

$$\phi_{ij} = \sum_{k=1}^{3} \hat{\phi}_k \hat{n}_i^k \hat{n}_j^k \quad (no\ sum\ in\ k) \tag{1}$$

and

$$\varphi_{ij} = \sum_{k=1}^{3} \hat{\varphi}_k \hat{m}_i^k \hat{m}_j^k \quad (no\ sum\ in\ k) \tag{2}$$

where $\hat{\boldsymbol{n}}^k$ and $\hat{\boldsymbol{m}}^k$ are eigenvectors corresponding to the eigenvalues, $\hat{\phi}_k$ and $\hat{\varphi}_k$, of the damage tensors, $\boldsymbol{\phi}$ and $\boldsymbol{\varphi}$, respectively.

3 Fourth-Order Anisotropic Damage Effect Tensor

In a general state of deformation and damage, the effective stress tensor $\bar{\boldsymbol{\sigma}}$ is related to the Cauchy stress tensor $\boldsymbol{\sigma}$ by the following linear transformation (Murakani and Ohno [10])

$$\bar{\sigma}_{ij} = M_{ikjl}\sigma_{kl} \tag{3}$$

where $\boldsymbol{M}$ is a fourth-order linear transformation operator called the damage effect tensor. Depending on the form used for $\boldsymbol{M}$, it is very clear from equation (3) that the effective stress tensor $\bar{\boldsymbol{\sigma}}$ is generally nonsymmetric. Using a non-symmetric effective stress tensor as given by equation (3) to formulate a constitutive model will result in the introduction of the Cosserat and a micropolar continua. However, the use of such complicated mechanics can be easily avoided if the proper fourth-order linear transformation tensor is formulated in order to symmetrize the effective stress tensor. Such a linear transformation tensor called the damage effect tensor is obtained in the literature [6, 13] using symmetrization methods. One of the symmetrization methods given by Cordebois and Sidoroff [2] and Lee *et al.* [6] is expressed as follows

$$\bar{\sigma}_{ij} = (\delta_{ik} - \phi_{ik})^{-1/2}\sigma_{kl}(\delta_{jl} - \phi_{jl})^{-1/2} \tag{4}$$

The fourth-order damage effect tensors corresponding to equations (4) is defined such that

$$M_{ikjl} = (\delta_{ik} - \phi_{ik})^{-1/2}(\delta_{jl} - \phi_{jl})^{-1/2} \tag{5}$$

4 The Kinematics of Damage for Elasto-Plastic Behavior with Finite Strains

4.1 A Multiplicative Decomposition

A schematic drawing representing the kinematics of elasto-plastic damage deformation is shown in Figure 1. C° is the initial undeformed configuration of the body which may have an initial damage in the material.

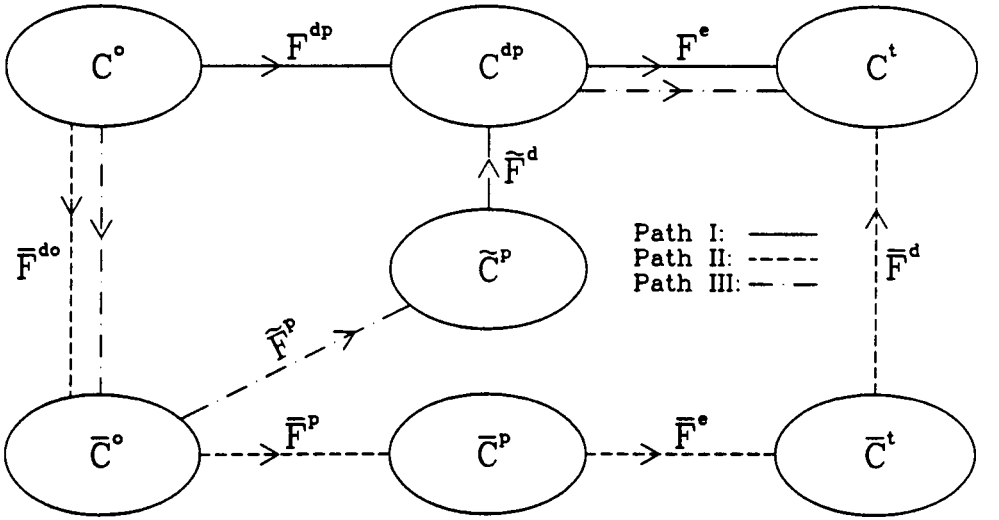

Figure 1: Schematic representation of elasto-plastic damage deformation configuration

C^t represents the current elasto-plastically deformed and damaged configuration of the body. The configuration $\bar{C}^\circ$ represents the initial configuration of the body that is obtained by fictitiously removing the initial damage from the C° configuration. If the initial configuration is undamaged consequently there is no difference between configurations C° and $\bar{C}^\circ$. Configuration $\bar{C}^t$ is obtained by fictitiously removing the damage from configuration C^t. Configuration C^{dp} is an intermediate configuration upon elastic unloading. In the most general case of large deformation processes, damage may be involved due to void and microcrack development because of external agencies. Although damage in the microlevel is a material discontinuity, damage can be considered as an irreversible deformation process in the framework of Continuum Damage Mechanics. Furthermore, one assumes that upon unloading from the elasto-palstic damage state, the elastic part of the deformation can be completely recovered while no additional plastic deformation and damage takes place. Thus upon unloading the elasto-plastic damage deformed body from the current configuration C^t will elastically unload to an intermediate stress free

configuration denoted by C^{dp} as shown in Fig 1. Although the damage process is an irreversible deformation thermodynamically, however, deformation due to damage itself can be partially or completely recovered upon unloading due to closure of micro-cracks or contraction of micro-voids. Nevertheless, recovery of damage deformation does not mean the healing of damage. No naterials are brittle or ductile. The deformation gradient tensor and the Green deformation tensor of the elasto-plastic damage deformation can be obtained through Path I, Path II or Path III as shown in Figure 1. Considering Path I the deformation gradient referred to the undeformed configuration, C° is denoted by $\boldsymbol{F}$ and is polarly decomposed into the elastic deformation gradient denoted by $\boldsymbol{F}^{e}$ and the damage-plastic deformation gradient denoted by $\boldsymbol{F}^{dp}$ such that

$$F_{ij} = F^{e}_{ik} F^{dp}_{kj} \tag{6}$$

The elastic deformation gradient is given by

$$F^{e}_{ij} = \frac{\partial x_i}{\partial x^{dp}_j} \tag{7}$$

The corresponding damage-plastic deformation gradient is given by

$$F^{dp}_{ij} = \frac{\partial x^{dp}_i}{\partial X_j} \tag{8}$$

The Right Cauchy Green deformation tensor, $\boldsymbol{C}$, is given by

$$C_{ij} = F^{dp}_{nk} F^{e}_{ki} F^{e}_{nm} F^{dp}_{mj} \tag{9}$$

The finite deformation damage models by Ju [3] and Zbib [17] emphasize that "added flexibility" due to the existence of microcracks or microvoids is already embedded in the deformation gradient implicity. Murakami [9] presented the kinematics of damage deformation using the second-order damage tensor. However, the lack of an explicit formulation for the kinematics of finite deformation with damage leads to the failure in obtaining an explicit derivation of the kinematics that directly consider the damage deformation. Although most finite strain elasto-plastic deformation processes involve damage such as micro-voids, nucleations and micro-crack development due to external agencies, however, only the elastic and plastic deformation processes are cosidered kinematically due to the complexity in the involvement of damage deformation. In this work, the kinematics of damage will be explicitely characterized based on continuum damage mechanics. The elastic deformation gradient corresponds to elastic stretching and rigid body rotations due to both internal and external constraints. The plastic deformation gradient is arising from purely irreversible processes due to dislocations in the material. Damage may be initiated and evolves in both the elastic and plastic deformation processes. Particularly,

damage in the elastic deformation state is termed elastic damage which is the case for most brittle materials while damage in the plastic deformation state is termed plastic damage which is mainly for ductile materials. Additional deformation due to damage consists of damage itself with additional deformation due to elastic and plastic deformation. This causes loss of elastic and plastic stiffness. In this work, kinematics of damage deformation is completely described for both damage and the coupling of damage with elasto-plastic deformation. The total Lagrangian strain tensor is expressed as follows

$$\begin{aligned} \mathcal{E}_{ij} &= \frac{1}{2}(F^{dp}_{ki}F^{dp}_{kj} - \delta_{ij}) + \frac{1}{2}F^{dp}_{mi}(F^{e}_{km}F^{e}_{kn} - \delta_{mn})F^{dp}_{nj} \\ &= \mathcal{E}^{dp}_{ij} + F^{dp}_{mi}\epsilon^{e}_{mn}F^{dp}_{nj} \\ &= \mathcal{E}^{dp}_{ij} + \mathcal{E}^{e}_{ij} \end{aligned} \tag{10}$$

where $\boldsymbol{\mathcal{E}}^{dp}$ and $\boldsymbol{\mathcal{E}}^{e}$ are the Lagrangian damage-plastic strain tensor and the Lagrangian elastic strain tensor measured with respect to the reference configuration C°, respectively. While $\boldsymbol{\varepsilon}^{e}$ is the Lagrangian elastic strain tensor measured with respect to the intermediate configuration C^{dp}. Similiarly, the Eulerian strains corresponding to deformation gradients $\boldsymbol{F}^{e}$ and $\boldsymbol{F}^{dp}$ are given by

$$e^{dp}_{ij} = \frac{1}{2}(\delta_{ij} - F^{dp^{-1}}_{ki}F^{dp^{-1}}_{kj}) \tag{11}$$

$$\epsilon^{e}_{ij} = \frac{1}{2}(\delta_{ij} - F^{e^{-1}}_{ki}F^{e^{-1}}_{kj}) \tag{12}$$

The total Eulerian strain tensor can be expressed as follows

$$\begin{aligned} \epsilon_{ij} &= \epsilon^{e}_{ij} + F^{e^{-1}}_{ki}e^{dp}_{km}F^{e^{-1}}_{mj} \\ &= \epsilon^{e}_{ij} + \epsilon^{dp}_{ij} \end{aligned} \tag{13}$$

The strain $\boldsymbol{e}^{dp}$ is refered to the intermediate configuration C^{dp}, while the strains $\boldsymbol{\epsilon}$, $\boldsymbol{\epsilon}^{e}$, and $\boldsymbol{\epsilon}^{dp}$ are defined relative to the current configuration as a reference. The relationship between the Lagrangian and Eulerian strains is obtained directly in the form

$$\mathcal{E}_{ij} = F_{ki}\epsilon_{kl}F_{lj} \tag{14}$$

The kinematics of finite strain elasto-plastic deformation including damage is completely described in Path I. In order to describe the kinematics of damage and plastic deformation, the deformation gradient given by equation (6) may be further decomposed into

$$F_{ij} = F^{e}_{ik}F^{d}_{km}F^{p}_{mj} \tag{15}$$

However, it is very difficult to characterize physically only the kinematics of deformation due to damage inspite of its obvious physical phenomena. The damage, however, may be defined through the effective stress concept. Similarly the kinematics of damage can be described using the effective kinematic configuration. Considering Path II the deformation gradient can be alternatively expressed as follows

$$F_{ij} = \bar{F}^d_{ik}\bar{F}^e_{km}\bar{F}^p_{mn}\bar{F}^{d\circ}_{nj} \tag{16}$$

where $\bar{\boldsymbol{F}}^d$ is the fictitious damage deformation gradient from configuration $\bar{C}^t$ to C^t and is given by

$$\bar{F}^d_{ij} = \frac{\partial x_i}{\partial \bar{x}_j} \tag{17}$$

The elastic deformation gradient in the effective configuration is given by

$$\bar{F}^e_{ij} = \frac{\partial \bar{x}_i}{\partial \bar{x}^p_j} \tag{18}$$

The corresponding plastic deformation gradient in the effective configuration is given by

$$\bar{F}^p_{ij} = \frac{\partial \bar{x}^p_i}{\partial \bar{X}_j} \tag{19}$$

while the fictitious initial damage deformation gradient from configuration $\bar{C}^\circ$ to C° is given by

$$F^{d\circ}_{ij} = \frac{\partial \bar{X}_i}{\partial X_j} \tag{20}$$

Similar to Path I, the Right Cauchy Green deformation tensor, $\boldsymbol{C}$, is given by

$$C_{ij} = \bar{F}^{d\circ}_{mk}\bar{F}^p_{kp}\bar{F}^e_{pq}\bar{F}^d_{qi}\bar{F}^d_{mn}\bar{F}^e_{nr}\bar{F}^p_{rs}\bar{F}^{d\circ}_{sj} \tag{21}$$

The Lagrangian damage strain tensor measured with respect to the fictious configuration $\bar{C}^t$ is given by

$$\bar{\varepsilon}^d_{ij} = \frac{1}{2}(\bar{F}^d_{ki}\bar{F}^d_{kj} - \delta_{ij}) \tag{22}$$

and the corresponding Lagrangian effective elastic strain tensor measured with respect to the fictious configuration $\bar{C}^p$ is given by

$$\bar{\varepsilon}^e_{ij} = \frac{1}{2}(\bar{F}^e_{ki}\bar{F}^e_{kj} - \delta_{ij}) \tag{23}$$

The Lagrangian effective plastic strain tensor measured with respect to the fictious undamaged initial configuration $\bar{C}^{\circ}$ is given by

$$\bar{\varepsilon}^{p}_{ij} = \frac{1}{2}(\bar{F}^{p}_{ki}\bar{F}^{p}_{kj} - \delta_{ij}) \tag{24}$$

The total Lagrangian strain tensor is therefore expressed as follows

$$\begin{aligned}\bar{\mathcal{E}}_{ij} = {} & \frac{1}{2}(\bar{F}^{do}_{ki}\bar{F}^{do}_{kj} - \delta_{ij}) + \frac{1}{2}\bar{F}^{do}_{mi}(\bar{F}^{p}_{km}\bar{F}^{p}_{kn} - \delta_{mn})\bar{F}^{do}_{nj} + \frac{1}{2}\bar{F}^{do}_{ni}\bar{F}^{p}_{rn}(\bar{F}^{e}_{qr}\bar{F}^{e}_{qs} - \delta_{rs})\bar{F}^{p}_{sm}\bar{F}^{do}_{mj} \\ & + \frac{1}{2}\bar{F}^{do}_{wi}\bar{F}^{p}_{nw}\bar{F}^{e}_{rn}(\bar{F}^{d}_{qr}\bar{F}^{d}_{qs} - \delta_{rs})\bar{F}^{e}_{sm}\bar{F}^{p}_{mk}\bar{F}^{do}_{kj}\end{aligned} \tag{25}$$

The Lagrangian initial damage strain tensor measured with respect to the reference configuration C° is denoted by

$$\bar{\mathcal{E}}^{do}_{ij} = \frac{1}{2}(\bar{F}^{do}_{ki}\bar{F}^{do}_{kj} - \delta_{ij}) \tag{26}$$

The Lagrangian plastic strain tensor measured with respect to the reference configuration C° is denoted by

$$\bar{\mathcal{E}}^{p}_{ij} = \bar{F}^{do}_{ki}\bar{\varepsilon}^{p}_{km}\bar{F}^{do}_{mj} \tag{27}$$

One now defines the Lagrangian elastic strain tensor measured with respect to the reference configuration C° as follows

$$\bar{\mathcal{E}}^{e}_{ij} = \bar{F}^{do}_{ni}\bar{F}^{p}_{nk}\bar{\varepsilon}^{e}_{km}\bar{F}^{p}_{mr}\bar{F}^{do}_{rj} \tag{28}$$

and the corresponding Lagrangian damage strain tensor measured with respect to the reference configuration C° is given by

$$\bar{\mathcal{E}}^{d}_{ij} = \bar{F}^{do}_{wi}\bar{F}^{p}_{wn}\bar{F}^{e}_{nk}\bar{\varepsilon}^{d}_{km}\bar{F}^{e}_{mr}\bar{F}^{p}_{rs}\bar{F}^{do}_{sj} \tag{29}$$

The total Lagrangian strain is now given as follows through the additive decomposition of the corresponding strains

$$\mathcal{E}_{ij} = \bar{\mathcal{E}}^{do}_{ij} + \bar{\mathcal{E}}^{p}_{ij} + \bar{\mathcal{E}}^{e}_{ij} + \bar{\mathcal{E}}^{d}_{ij} \tag{30}$$

Finaly Path III gives the deformation gradient as follows

$$F_{ij} = F^{e}_{il}\tilde{F}^{d}_{lm}\tilde{F}^{p}_{mn}\bar{F}^{do}_{nj} \tag{31}$$

where $\tilde{\boldsymbol{F}}^d$ is the fictious damage deformation gradient from configuration $\tilde{C}^p$ to C^{dp} and is given by

$$\tilde{F}^d_{ij} = \frac{\partial x_i^{dp}}{\partial \tilde{x}_j^p} \tag{32}$$

and the corresponding plastic deformation gradient in the effective configuration is given by

$$\tilde{F}^p_{ij} = \frac{\partial \tilde{x}_i^p}{\partial \bar{X}_j} \tag{33}$$

Similar to Path II, the Right Cauchy Green deformation tensor $\boldsymbol{C}$ is given by

$$C_{ij} = \bar{F}^{do}_{mk}\tilde{F}^p_{kp}\tilde{F}^d_{pq}F^e_{qi}F^e_{mn}\tilde{F}^d_{nr}\tilde{F}^p_{rs}\bar{F}^{do}_{sj} \tag{34}$$

The Lagrangian damage strain tensor measured with respect to the fictitious intermediate configuration $\tilde{C}^p$ is given by

$$\tilde{e}^d_{ij} = \frac{1}{2}(\tilde{F}^d_{ki}\tilde{F}^d_{kj} - \delta_{ij}) \tag{35}$$

The total Lagrangian strain tensor is expressed as follows

$$\begin{aligned}\bar{\mathcal{E}}_{ij} = {} & \frac{1}{2}(\bar{F}^{do}_{ki}\bar{F}^{do}_{kj} - \delta_{ij}) + \frac{1}{2}\bar{F}^{do}_{mi}(\tilde{F}^p_{km}\tilde{F}^p_{kn} - \delta_{mn})\bar{F}^{do}_{nj} + \frac{1}{2}\bar{F}^{do}_{ni}\tilde{F}^p_{rn}(\tilde{F}^d_{qr}\tilde{F}^d_{qs} - \delta_{rs})\bar{F}^p_{sm}\bar{F}^{do}_{mj} \\ & + \frac{1}{2}\bar{F}^{do}_{wi}\tilde{F}^p_{nw}\tilde{F}^d_{rn}(F^e_{qr}F^e_{qs} - \delta_{rs})\tilde{F}^d_{sm}\tilde{F}^p_{mk}\bar{F}^{do}_{kj}\end{aligned} \tag{36}$$

The Lagrangian damage strain tensor measured with respect to the reference configuration C° is denoted by

$$\tilde{\mathcal{E}}^d_{ij} = \bar{F}^{do}_{ki}\tilde{F}^p_{mk}\tilde{e}^d_{mn}\tilde{F}^p_{nq}\bar{F}^{do}_{qj} \tag{37}$$

The Lagrangian elastic strain tensor measured with respect to the reference configuration C° is denoted by

$$\mathcal{E}^e_{ij} = \bar{F}^{do}_{li}\tilde{F}^p_{kl}\tilde{F}^d_{mk}e^e_{mn}\tilde{F}^d_{nq}\tilde{F}^p_{qr}\bar{F}^{do}_{rj} \tag{38}$$

The corresponding total Lagrangian strain is now given by

$$\mathcal{E}_{ij} = \bar{\mathcal{E}}^{do}_{ij} + \tilde{\mathcal{E}}^p_{ij} + \tilde{\mathcal{E}}^d_{ij} + \mathcal{E}^e_{ij} \tag{39}$$

The total Lagrangian strain tensors obtained by considering the three paths are given by equations (10), (30) and (39). From the equivalency of these total strains, one obtains

the explicit presentations of the kinematics of damage as follows. With the assumption of the equivalence between the elastic strain tensors given by equations (10) and (39), the damage-plastic deformation gradient given by (8) and the Lagrangian damage plastic strain tensor can be expressed as follows

$$F_{ij}^{dp} = \bar{F}_{ik}^{do}\tilde{F}_{kl}^{p}\tilde{F}_{lj}^{d} \tag{40}$$

and

$$\mathcal{E}_{ij}^{dp} = \bar{\mathcal{E}}_{ij}^{do} + \tilde{\mathcal{E}}_{ij}^{p} + \tilde{\mathcal{E}}_{ij}^{d} \tag{41}$$

Furthermore one obtains the following expression from equations (30) and (39) as follows

$$\bar{\mathcal{E}}_{ij}^{e} + \bar{\mathcal{E}}_{ij}^{d} = \tilde{\mathcal{E}}_{ij}^{d} + \mathcal{E}_{ij}^{e} \tag{42}$$

which concludes that $\tilde{C}^p$ and $\bar{C}^p$ are the same. Substituting equations (29), (37) and (38) into equation (42), one obtains the effective Lagrangian elastic strain tensor as follows

$$\bar{\mathcal{E}}_{ij}^{e} = \bar{F}_{ki}^{do}\bar{F}_{mk}^{p}[\tilde{\epsilon}_{mn}^{d} - \bar{F}_{qm}^{e}\tilde{\epsilon}_{qr}^{d}\bar{F}_{rn}^{e} + \tilde{F}_{qm}^{d}\epsilon_{qr}^{e}\tilde{F}_{rn}^{d}]\bar{F}_{ns}^{p}\bar{F}_{sj}^{do} \tag{43}$$

Using equations (28) and (43) one can now express $\bar{\boldsymbol{\epsilon}}$ as follows

$$\bar{\epsilon}_{ij}^{e} = \tilde{\epsilon}_{ij}^{d} - \bar{F}_{mi}^{e}\tilde{\epsilon}_{mn}^{d}\bar{F}_{nj}^{e} + \tilde{F}_{mi}^{d}\epsilon_{mn}^{e}\tilde{F}_{nj}^{d} \tag{44}$$

This expression gives a general relation of the effective elastic strain for finite strains of elasto-plasic damage deformation. For the special case when one assumes that

$$\tilde{\epsilon}_{ij}^{d} - \bar{F}_{mi}^{e}\tilde{\epsilon}_{mn}^{d}\bar{F}_{nj}^{e} = 0 \tag{45}$$

equation (44) can be reduced to the following expression

$$\bar{\epsilon}_{ij}^{e} = \tilde{F}_{ki}^{d}\epsilon_{kl}^{e}\tilde{F}_{lj}^{d} \tag{46}$$

This relation is similar to that obtained without the consideration of the kinematics of damage and only utilizing the hypothesis of elastic energy equivalence. However, equation (46) for the case of finite strains is given by relation (44) which cannot be obtained through the hypothesis of elastic energy equivalence. Equation (45) maybe valid only for some special cases of the small strain theory.

4.2 Fictitious Damage Deformation Gradients

The two fictitious deformation gradients given by equations (17) and (32) may be used to define the damage tensor in order to describe the damage behavior of solids.

Since the fictitious effective deformed cofiguration denoted by $\bar{C}^t$ is obtained by removing the damages from the real deformed configuration denoted by C^t, therefore the differential volume of the fictitious effective deformed volumes denoted by $d\bar{\Omega}^t$ is obtained as follows [12]

$$\begin{aligned} d\bar{\Omega}^t &= d\Omega^t - d\Omega^d \\ &= \sqrt{(1-\hat{\phi}_1)(1-\hat{\phi}_2)(1-\hat{\phi}_3)}\, d\Omega^t \end{aligned} \tag{47}$$

or

$$d\Omega^t = \bar{J}^d d\bar{\Omega}^t \tag{48}$$

where Ω^t is the volume of damage in the configuration C^t and $\bar{J}^d$ is termed the Jacobian of the damage deformation which is the determinant of the fictitious damage deformation gradient. Thus the Jacobian of the damage deformation can be written as follows

$$\begin{aligned} \bar{J}^d &= |\bar{F}^d_{ij}| \\ &= \frac{1}{\sqrt{(1-\hat{\phi}_1)(1-\hat{\phi}_2)(1-\hat{\phi}_3)}} \end{aligned} \tag{49}$$

The determinant of the matrix $[\,a\,]$ in equation (??) is given by

$$\begin{aligned} |\,[\,a\,]\,| &= |\,[\,b\,]^T|\;|\,[\,\hat{a}\,]\,|\;|\,[\,b\,]\,| \\ &= |\,[\,\hat{a}\,]\,| \\ &= \frac{1}{\sqrt{(1-\hat{\phi}_1)(1-\hat{\phi}_2)(1-\hat{\phi}_3)}} \end{aligned} \tag{50}$$

Thus one assumes the following relation without loss of generality

$$\bar{F}^d_{ij} = [\delta_{ij} - \phi_{ij}]^{-\frac{1}{2}} \tag{51}$$

Although the identity is established between $\bar{J}^d$ and $|a|$, however, this is not sufficient to demonstrate the validity of equation (51). This relation is assumed here based on the physics of the geometrically symmetrized effective stress concept [12]. Similiarly, the fictitious damage deformation gradient $\tilde{\boldsymbol{F}}^d$ can be written as follows

$$\tilde{F}^d_{ij} = [\delta_{ij} - \varphi_{ij}]^{-\frac{1}{2}} \tag{52}$$

Finally, assuming that $\bar{\boldsymbol{x}} = \tilde{\boldsymbol{x}}$ based on equation (42) the relations between $\tilde{\boldsymbol{F}}^d$ and $\bar{\boldsymbol{F}}^d$, and $\boldsymbol{\varphi}$ and $\boldsymbol{\phi}$ are given by

$$\tilde{F}^d_{ij} = F^e_{ki}\bar{F}^d_{kl}F^{e^{-1}}_{lj} \tag{53}$$

and

$$\varphi_{ij} = F^e_{ki}\phi_{kl}F^{e^{-1}}_{lj} \tag{54}$$

5 Irreversible Thermodynamics

The finite elasto-plastic deformation behavior with damage can be viewed within the framework of thermodynamics with internal state variables. The Helmholtz free energy per unit mass in an isothermal deformation process at the current state of the deformation and material damage is assumed as follows:

$$\Psi = \psi + \Upsilon \tag{55}$$

where ψ is the strain energy which is a purely reversible stored energy, while Υ is the energy associated with specific microstructural changes produced by damage and plastic yielding. Conceptionally, the energy Υ is assumed to be an irreversible energy. In generall, an explicit presentation of the energy Υ and its rate $\dot{\Upsilon}$ is limited by the complexities of the internal microstructural changes, however, only two internal variables which are associated with damage and plastic hardening, respectively are considered in this work. For the sake of a schematic description of the above stated concepts, the uniaxial stress-strain curves shown in Figure 2 are used. In Figure 2, $\bar{E}$ is the initial undamaged Young's modulus, E is the damaged Young's modulus, $\mathcal{S}$ is the second Piola Kirchhoff stress, and $\mathcal{E}$ is the Lagrangian strain. Eventhough these notations are for the case of uniaxial state, they can be used in indicial tensor notation in the equations below without loss of generality. Refering to the solid curve in Figure 2, the total Lagrangian strain tensor $\boldsymbol{\mathcal{E}}$ is given by

$$\mathcal{E}_{ij} = \mathcal{E}^p_{ij} + \mathcal{E}^e_{ij} + \mathcal{E}^d_{ij} \tag{56}$$

where $\boldsymbol{\mathcal{E}}^p$ is the plastic strain tensor, $\boldsymbol{\mathcal{E}}^e$ is the elastic strain tensor, and $\boldsymbol{\mathcal{E}}^d$ is the additional strain tensor due to damage. Comparing equations (10) and (56) one notes that

$$\mathcal{E}^{dp}_{ij} = \mathcal{E}^p_{ij} + \mathcal{E}^d_{ij} \tag{57}$$

Furthermore the additional strain tensor due to damage can be decomposed as follows

$$\mathcal{E}^d_{ij} = \mathcal{E}^{d'}_{ij} + \mathcal{E}^{d''}_{ij} \tag{58}$$

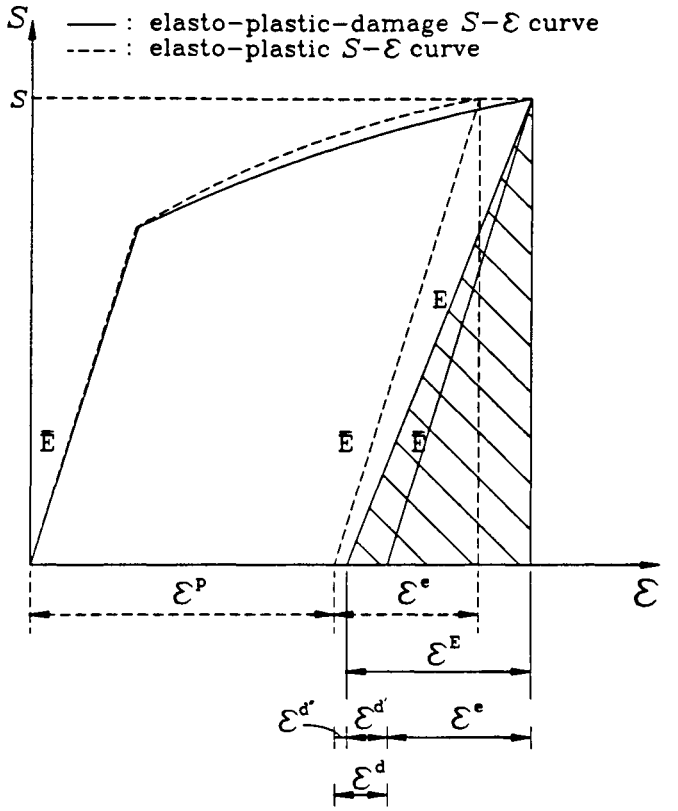

Figure 2: Schematic representation of elasto-plastic damage strain increments in the case of a uniaxial stress-strain curve

Furthermore the additional strain tensor due to damage can be decomposed as follows

$$\mathcal{E}_{ij}^{d} = \mathcal{E}_{ij}^{d'} + \mathcal{E}_{ij}^{d''} \tag{58}$$

where $\boldsymbol{\mathcal{E}}^{d''}$ is the irrecoverable damage strain tensor due to lack of closure of the micro-cracks and microvoids during unloading, while $\boldsymbol{\mathcal{E}}^{d'}$ is the elastic damage strain due to reduction of the elastic stiffness tensor. tensor,$\mathcal{E}^{E}$ due to unloading can be obtained by

$$\mathcal{E}_{ij}^{E} = \mathcal{E}_{ij}^{e} + \mathcal{E}_{ij}^{d'} \tag{59}$$

The srain energy ψ which is shown as the shaded triangular area in Figure 2 is assumed as follows

$$\psi = \frac{1}{2\rho}\mathcal{E}^E_{ij}E_{ijkl}\mathcal{E}^E_{kl} \tag{60}$$

where ρ is the specific density. Furthermore this strain energy can be decomposed into the elastic strain energy ψ^e and the damage strain energy ψ^d as follows

$$\psi = \psi^e + \psi^d \tag{61}$$

The elastic strain energy, ψ^e is given by

$$\psi^e = \frac{1}{2\rho}\mathcal{E}^e_{ij}\bar{E}_{ijkl}\mathcal{E}^e_{kl} \tag{62}$$

and the corresponding damage strain energy ψ^d is given by

$$\psi^d = \frac{1}{2\rho}\mathcal{E}^E_{ij}E_{ijkl}\mathcal{E}^E_{kl} - \frac{1}{2\rho}\mathcal{E}^e_{ij}\bar{E}_{ijkl}\mathcal{E}^e_{kl} \tag{63}$$

where $\bar{\boldsymbol{E}}$ and $\boldsymbol{E}$ are the initial undamaged elastic stiffness and the damaged elastic stiffness, respectively. These stiffnesses are defined such that

$$\bar{E}_{ijkl} = \frac{\partial^2\Psi}{\partial\mathcal{E}^e_{ij}\partial\mathcal{E}^e_{kl}} \tag{64}$$

and

$$E_{ijkl} = \frac{\partial^2\Psi}{\partial\mathcal{E}^E_{ij}\partial\mathcal{E}^E_{kl}} \tag{65}$$

The damaged elastic stifness in the case of finite deformation is given by Park and Voyiadjis [12] as follows

$$E_{ijrs} = N_{ikjl}\bar{E}_{klpq}N_{prqs} \tag{66}$$

where

$$\begin{aligned} N_{ikjl} &= M^{-1}_{ikjl} \\ &= a^{-1}_{ik}a^{-1}_{jl} \end{aligned} \tag{67}$$

The elastic damage stiffness given by equation (66) is symmetric. This is in line with the classic sense of continnum mechanics which is violated by using the hypothesis of strain

equivalence. Using the similar relation between the Lagrangian and the Eulerian strain tensors given by equation (14), the corresponding strain energy given by equation(60) can be written as follows

$$\begin{aligned} \psi &= \frac{1}{2\rho}\epsilon^E_{mn}F_{mi}F_{nj}E_{ijkl}F_{rk}F_{sl}\epsilon^E_{rs} \\ &= \frac{1}{2\rho}\epsilon^E_{mn}\Lambda_{mnrs}\epsilon^E_{rs} \end{aligned} \tag{68}$$

where $\boldsymbol{\epsilon}^E$ is the Eulerian strain corresponding to the Lagrangian strain shown in equation (59), and $\boldsymbol{\Lambda}$ is termed the Eulerian elastic stiffness which is given by

$$\Lambda_{mnrs} = F_{mi}F_{nj}E_{ijkl}F_{rk}F_{sl} \tag{69}$$

The second Piola-Kirchhoff stress tensor, $\boldsymbol{\mathcal{S}}$ is defined as follows

$$\begin{aligned} \mathcal{S}_{ij} &= \rho\frac{\partial\psi}{\partial\mathcal{E}^E_{ij}} \\ &= \rho\frac{\partial\psi^e}{\partial\mathcal{E}^e_{ij}} \end{aligned} \tag{70}$$

The second Piola-Kirchhoff stress tensor, $\boldsymbol{\mathcal{S}}$ is related to the Cauchy stress tensor, $\boldsymbol{\sigma}$ by the following relation

$$\mathcal{S}_{ij} = JF^{-1}_{ik}\sigma_{km}F_{jm} \tag{71}$$

The Kirchhoff stress tensor $\boldsymbol{\mathcal{T}}$ is related to the Cauchy stress tensor by

$$\mathcal{T}_{ij} = J\sigma_{ij} \tag{72}$$

The rate of the Helmholtz free energy is then given as follows

$$\dot{\Psi} = \dot{\psi} + \dot{\Upsilon} \tag{73}$$

If the deformation process is assumed to be isothermal with negligible temperature non-uniformoties, the rate of the Helmholtz free energy can be written using the first law of thermodynamics (balance of energy) as follows.

$$\dot{\Psi} = \mathcal{T}_{ij}\mathcal{D}_{ij} - T\eta \tag{74}$$

where T is the temperature and η is the irreversible entropy production rate. The product $T\eta$ represents the energy dissipation rate associated with both the damage and plastic deformation processes. The energy of the dissipation rate is given as follows

$$T\eta = \mathcal{S}_{ij}\dot{\mathcal{E}}^{d''}_{ij} + \mathcal{S}_{ij}\dot{\mathcal{E}}^{p}_{ij} - \dot{\Upsilon} \tag{75}$$

The first two terms on the right-hand side of equation (75) represent a macroscopically non-recoverable rate of work expanded on damage and plastic processes, respectively. Furthermore the rate of the additional strain tensor due to damage is given by

$$\dot{\mathcal{E}}^{d}_{ij} = \dot{\mathcal{E}}^{d''}_{ij} + \dot{\mathcal{E}}^{d'}_{ij} \tag{76}$$

If we assume that a fraction of the additional strain tensor can be recoverd during unloading, then the elastic damage tensor due to the reduction of the elastic stiffness is given by

$$\dot{\mathcal{E}}^{d'}_{ij} = c\,\dot{\mathcal{E}}^{d}_{kj} \tag{77}$$

where c is a fraction which ranges from 0 to 1. Then the permenant damage strain due to lack of closure of micro-cracks and micro-cavities is given by

$$\dot{\mathcal{E}}^{d''}_{ij} = (1-c)\dot{\mathcal{E}}^{d}_{kj} \tag{78}$$

Thus the energy of the dissipation rate given by equation (74) can be written as follows

$$\begin{aligned} T\eta &= (1-c)\mathcal{S}_{ij}\dot{\mathcal{E}}^{d}_{ij} + \mathcal{S}_{ij}\dot{\mathcal{E}}^{p}_{ij} - \dot{\Upsilon} \\ &= (1-c)\mathcal{T}_{ij}\mathcal{D}^{d}_{ij} + \mathcal{T}_{ij}\mathcal{D}^{p}_{ij} - \dot{\Upsilon} \end{aligned} \tag{79}$$

The rate of energy associated with a specific microstructural change due to both the damage and the plastic processes can be decomposed as follows

$$\dot{\Upsilon} = \dot{\Upsilon}^{d} + \dot{\Upsilon}^{p} \tag{80}$$

where one defines that

$$\rho\dot{\Upsilon}^{d} = \mathcal{Y}_{ij}\dot{\phi}_{ij} \tag{81}$$

and

$$\rho\dot{\Upsilon}^{p} = \mathcal{A}_{ij}\dot{\alpha}_{ij} \tag{82}$$

where $\boldsymbol{\mathcal{Y}}$ and $\boldsymbol{\mathcal{A}}$ are the general forces conjugated by damage and plastic yielding, respectively. They are defined as follows

$$\begin{aligned} \mathcal{Y}_{ij} &= \rho\frac{\partial\Psi}{\partial\phi_{ij}} \\ &= \rho\frac{\partial\psi^{ed}}{\partial\phi_{ij}} + \rho\frac{\partial\Upsilon}{\partial\phi_{ij}} \end{aligned} \tag{83}$$

$$\mathcal{A}_{ij} = \rho\frac{\partial\Psi}{\partial\alpha_{ij}} \tag{84}$$

In view of equation (79) one notes that it is equivalent to the work by Lubarda and Krajcinovic [7] when $(1-c) = \frac{1}{2}$.

6 Constitutive Equation for Finite Elasto-Plastic Deformation with Damage Behavior

The kinematics and the thermodynamics discussed in the previous sections provide the basis for a finite deformation damage elasto-plasticity. In this section the basic structure of the constitutive equations are reviewed based on the generalized Hooke's law, originally obtained for small elastic strains such that the second Piola-Kirchoff stress tensor $\boldsymbol{S}$ is the gradient of free energy Ψ with respect to the Lagrangian elastic strain tensor $\boldsymbol{\mathcal{E}}^E$ given by equation (70). Referring to Figure 2 one obtains the following relation when generalized to the three dimensional state of stress and strain

$$\begin{aligned} \mathcal{S}_{ij} &= \bar{E}_{ijkl}(\mathcal{E}_{kl} - \mathcal{E}^p_{kl} - \mathcal{E}^d_{kl}) && (148a) \\ &= \bar{E}_{ijkl}\mathcal{E}^e_{kl} && (148b) \\ &= E_{ijkl}(\mathcal{E}^e_{kl} + \mathcal{E}^{d'}_{kl}) && (148c) \\ &= E_{ijkl}(\mathcal{E}_{kl} - \mathcal{E}^{d''}_{kl} - \mathcal{E}^p_{kl}) && (148d) \end{aligned} \tag{85}$$

From the incremental analysis one obtains the following rate form of the constitutive equation by differentiating equation (148a)

$$\dot{\mathcal{S}}_{ij} = \bar{E}_{ijkl}(\dot{\mathcal{E}}_{kl} - \dot{\mathcal{E}}^p_{kl} - \dot{\mathcal{E}}^d_{kl}) \tag{86}$$

Consiquently the constitutive equation of the elasto-pastic damage behavior can be written as follows

$$\dot{\mathcal{S}}_{ij} = E^{DP}_{ikjl}\dot{\mathcal{E}}_{kl} \tag{87}$$

where $\boldsymbol{E}^{DP}$ is the damage elasto-plastic stifness and is expressed as follows

$$E^{DP}_{ijkl} = \bar{E}_{ikjl} - E^p_{ikjl} - E^d_{ikjl} \tag{88}$$

where $\boldsymbol{E}^p$ is the plastic stiffness and $\boldsymbol{E}^d$ is the damage stiffness. Both $\boldsymbol{E}^p$ and $\boldsymbol{E}^d$ are the reduction in stiffness due to the plastic and damage deteriorations, respectively. The plastic stiffness and the damage stiffness can be obtaind by using the flow rule and damage evolution law, respectively. By assuming that the reference state coincides with the current configuration, the second Piola-Kirchoff stress rate, $\dot{\boldsymbol{S}}$ can be replaced by the corotational rate of the Cauchy stress tensor $\boldsymbol{\sigma}$ and the rate of Lagrangian strain tensor $\dot{\boldsymbol{\mathcal{E}}}$ by the deformation rate $\boldsymbol{\mathcal{D}}$ as follows

$$\sigma_{ij} = E^{DP}_{ijkl}\mathcal{D}_{kl} \tag{89}$$

The corotational rate of the Cauchy stress tensor, $\boldsymbol{\sigma}$ is related to the rate of the rate of the Cauchy stress tensor, $\dot{\boldsymbol{\sigma}}$ as follows

$$\sigma_{ij} = \dot{\sigma}_{ij} - \mathcal{W}^*_{ik}\sigma_{kj} + \sigma_{ik}\mathcal{W}^*_{kj} \tag{90}$$

where

$$W^* = W - W^p - W^d \tag{91}$$

The details of the complete constitutive models using the proposed kinematics and the evolution laws of damage will be stated in the forthcoming paper.

7 CONCLUSION

The fourth-order anisotropic damage effect tensor, $\boldsymbol{M}$, using the kinematic measure for damage expressed through the second-order damage tensor $\boldsymbol{\phi}$, is reviewed here in reference to the symmetrization of the effective stress tensor. This introduces a distinct kinematic measure of damage which is complimentary to the deformation kinematic measure of strain. A thermodynamically consistent evolution equation for the damage tensor, $\boldsymbol{\phi}$ together with a generalized thermodynamic force conjugate to the damage tensor was presented in the paper by Voyiadjis and Park [14, 15]. Voyiadjis and Venson [16] quantified the physical values of the eigenvalues, $\hat{\phi}_k$ $(k = 1, 2, 3)$, and the second-order damage tensor, $\boldsymbol{\phi}$, for the unidirectional fibrous composite by measuring the crack densities with the assumption that one of the eigen-directions of the damage tensor coincides with the fiber direction.

The fourth-order anisotropic damage effect tensor used here is obtained through the geometrical symmetrization of the effective stress [2]. This tensor is used here for the kinematic description of damage. The explicit representation of the fourth-order damage effect tensor is obtained with reference to the principal damage direction coordinate system.

The damage elasto-plastic deformation for finite strain is also described here using the kinematics of damage. In this work the multiplicative decomposition of the deformation gradient and the additive decomposition of the Lagrangian strain tensor are used in order to describe the kinematics of damage. Both formulations are used to deduce seperately the strain due to damage and the coupled elasto-plastic, elastic-damage and plastic-damage strains.

The thermodynamic formulation introduces seperately the strain due to damage and the associated dissipation energy due to this strain as shown by equations(63). In the previous work by Voyiadjis and Park [14] this term was ignored due to the lack of the formulation of the kinematics of strain due to damage. A new free energy is presented in this work for finite elasto-plastic deformation with damage. Using this free energy the generalized thermodynamic force associated with the second-order damage tensor can be

derived. Using the consistent thermodynamic formulation one introduces seperately the strain due to damage and the associated dissipation energy due to this strain.

Both constitutive relations between the rate of the second Piola-Kirchhoff stress tensor and the Lagrangian strain rate, and between the corotational rate of the Cauchy stress and the deformation rate are established for the elasto-plastic model with damage. The resulting tangential elasto-plastic damage stiffness is obtained in the form of an additive decomposition of the respective elastic, plastic and damage stiffnesses.

ACKNOWLEDGMENT

The research described in this paper was sponsored by the Air Force Office of Scientific Research under Grants F49620-93-1-0097DEf and F49620-92-J-0463.

References

[1] J. Betten. Applications of Tensor Functions to the Formulation of Constitutive Equations Involving Damage and Initial Anisotropy. *Engineering Fracture Mechanics*, 25(5/6):573–584, 1986.

[2] J. P. Cordebois and F. Sidoroff. Damage Induced Elastic Anisotropy. In J. P. Boehler, editor, *Mechanical Behavior of Anisotropic Solids, Colloque Euromech 115, Villard-de-Lans, June 19-22*, pages 761–774. Martinus Nijhoff Publishers, 1979.

[3] J. W. Ju. Energy-Based Coupled Elastoplasic Damage Models at Finite Strains. *Journal of Engineering Mechanics*, 115(11):2507–2525, 1989.

[4] J. W. Ju. Isotropic and Anisotropic Damage Variables in Continuum Damage Mechanics. *Journal of Engineering Mechanics*, 116(12):2764–2770, 1990.

[5] F. A. Leckie. Tensorial Nature of Damage Measuring Internal Variables. *International Journal of Solids and Structures*, 30(1):19–36, 1993.

[6] H. Lee, G. Li, and S. Lee. The Influence of Anisotropic Damage on the Elastic Behavior of Materials. In *International Seminar on Local Approach of Fracture, Moret-sur-Loing, France*, pages 79–90, june 1986.

[7] V.A. Lubarda and D. Krajcinovic. Some Fundamental Issues in Rate Theory of Damage-Elastoplasticity. *International Journal of Plasticity*, 11(7):763–797, 1995.

[8] S. Murakami. Notion of Continuum Damage Mechanics and its Application to Anisotropic Creep Damage Theory. *Journal of Engineering Materials and Technology*, 105:99–105, 1983.

[9] S. Murakami. Mechanical Modelling of Material Damage. *Journal of Applied Mechanics*, 55:280–286, june 1988.

[10] S. Murakami and N. Ohno. A Continuum Theory of Creep and Creep Damage. In A. R. S. Ponter and D. R. Hayhurst, editors, *Creep in Structures, IUTAM 3rd Symposium, Leicester,UK, Septmber 8-12*, pages 422–443. Springer Verlag, 1980.

[11] E. T. Onat. Representation of Mechanical Behavior in the Presence of Internal Damage. *Engineering fracture Mechanics*, 25(5/6):605–614, 1986.

[12] T. Park and G. Z. Voyiadjis. Kinematic Description of Damage. *Journal of Applied Mechanics*. accepted for publication.

[13] F. Sidoroff. Description of Anisotropic Damage Application to Elasticity. In Jean-Paul Boehler, editor, *Mechanical Behavior of Anisotropic Solids / N°295 Comportement Mécanique Des Solides Anisotropes*. Martinus Nijhoff Publishers, 1979. Proceedings of the Euromech Colloquim 115, N°295 Villard-de-Lans, June 19-22, 1979, France.

[14] G. Z. Voyiadjis and T. Park. Anisotropic Damage of Fiber Reinforced MMC Using An Overall Damage Analysis. *Journal of Engineering Mechanics*, 121(11):1209–1217, 1995.

[15] G. Z. Voyiadjis and T. Park. Local and Interfacial Damage Analysis of Metal Matrix Composites. *International Journal of Engineering Science*, 33(11):1595–1621, 1995.

[16] G. Z. Voyiadjis and A. R. Venson. Experimental Damage Investigation of a SiC-Ti Aluminide Metal Matrix Composite. *International Journal of Damage Mechanics*, 4(4):338–361, October 1995.

[17] H. M. Zbib. On the Mechanics of Large Inelastic Deformations: Kinematics and Constitutive Modeling. *ACTA Mechanica*, 96:119–138, 1993.

Damage Mechanics in Engineering Materials
G.Z. Voyiadjis, J.-W.W. Ju and J.-L. Chaboche (Editors)
© 1998 Elsevier Science B.V. All rights reserved.

Scale and Boundary Conditions Effects in Elasticity and Damage Mechanics of Random Composites

K. Alzebdeh[a], I. Jasiuk[b], and M. Ostoja-Starzewski[c]

[a]Electromotor Division, General Motors Corp., 55th Street, La Grange, IL 60525-8051, U.S.A.

[b]The George W. Woodruff School of Mechanical Engineering, Georgia Institute of Technology, Altanta, GA 30332-0405, U.S.A.

[c]Institute of Paper Science and Technology, 500 10th Street, N.W., Atlanta, GA 30318, U.S.A.

1. INTRODUCTION

Spatial randomness, as opposed to periodic geometries, may have a significant effect on damage formation in composite materials. This issue was studied extensively over the last few years [1, 2, 3, 4], and in this paper we report new results on effects of scale and boundary conditions in the determination of meso-scale continuum-type models for elasticity and fracture. These models are formulated on scales larger than the single inclusion, yet smaller than the conventional continuum limit. The latter corresponds to the classical concept of a Representative Volume Element (RVE) which presupposes the presence of a statistical representation of the microstructure with all the typical microheterogeneities, and thus calls for relatively large volumes. Indeed, according to Hill [5], an RVE should be such that the relations between volume average stress and strain should be the same regardless of whether kinematic or stress boundary conditions have been used.

In our previous papers [2, 3, 4], we have developed a classification of damage states and patterns as well as a characterization of their statistical scatter as a function of the spatial resolution scale. This involves two parameters - stiffness ratio and strain-to-failure ratio of both phases - which define a damage plane onto which various aspects of systems's response are being mapped, thereby resulting in so-called damage maps. However, a comprehensive study of damage micromechanics requires an understanding of the influence of type of loading applied through the specimen boundaries on its effective response. Motivated by the earlier results on elasticity of undamaged random materials [6, 7], in this paper we investigate this aspect in the context of the out-of-plane elastic and elastic-brittle response of matrix-inclusion composites with randomly distributed inclusions. That is, we define several types of boundary conditions and study a range of different responses that may result. The analysis is based on a representation of the composite by a very fine two-dimensional spring network, whereby damage evolution is simulated by sequentially removing/breaking bonds in accordance with the local state of stress/strain concentrations.

2. TYPES OF BOUNDARY CONDITIONS AND CONSEQUENCES FOR ELASTIC MODULI

The heterogeneity of many composite materials - i.e., their piecewise continuous nature - is a primary motivation for introducing an effective continuum approximation. The latter is typically set up on macroscales, that is, scales which are mathematically infinite compared to the dimension of a single inclusion (grain). While this is sufficient in many situations where interest is only in the fields of stress, strain and displacement which vary slowly relative to the microscale, there is a number of cases where a resolution at intermediate, so-called meso-scales is necessary. The concept of a *meso-scale* $\delta = L/d$ is defined in the Fig. 1a) below with the help of a *window* of size L relative to the inclusion diameter d.

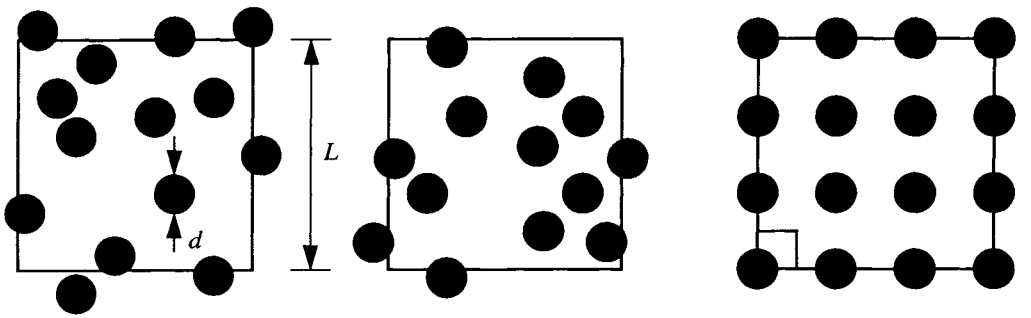

Figure 1. Two windows of the same scale δ, showing (a) a disordered microstructure, (b) a disordered microstructure with periodicity L; (c) shows a periodic unit cell.

This window concept [6, 7] allows the formulation of effective constitutive relations on a given scale δ, and immediately raises the question of the choice of boundary conditions which should thereby be involved. As we have showed in our preceding papers [6, 7], essential [8] (also called displacement, or Dirichlet)

$$u(\underset{\sim}{x}) = \bar{\varepsilon} \cdot \underset{\sim}{x} \qquad \forall \underset{\sim}{x} \in \partial B_u \tag{1}$$

and natural [8] (also called traction, or Neumann)

$$t(\underset{\sim}{x}) = \bar{\sigma} \cdot \underset{\sim}{x} \qquad \forall \underset{\sim}{x} \in \partial B_t \tag{2}$$

conditions play a fundamental role here. Here, $\bar{\varepsilon}$ is a prescribed volume (area) average strain, and $\bar{\sigma}$ is a prescribed volume (area) average stress. Adoption of these boundary conditions leads to a *hierarchy of scale-dependent bounds* on the macroscopic effective tensor $\boldsymbol{C}^{eff}$, that is [9]

$$\boldsymbol{C}^R \equiv (\boldsymbol{S}^R)^{-1} \equiv \langle \boldsymbol{S}_1^n \rangle^{-1} \leq \langle \boldsymbol{S}_\delta^n \rangle^{-1} \leq \langle \boldsymbol{S}_\delta^n \rangle^{-1} \leq \boldsymbol{C}^{eff} \leq \langle \boldsymbol{C}_\delta^e \rangle \leq \langle \boldsymbol{C}_{\delta'}^e \rangle \leq \langle \boldsymbol{C}_1^e \rangle \equiv \boldsymbol{C}^V \qquad \forall \delta' < \delta \tag{3}$$

In the above, $\boldsymbol{C}_\delta^e$ and $\boldsymbol{S}_\delta^n$ stand for effective stiffness and compliance tensors on the scale δ, which were obtained under essential and natural conditions, respectively. It was shown in [10] that a material's response under any uniform boundary conditions of mixed type, at any scale δ, is bounded by (3).

Another viewpoint on this issue is provided by a consideration of finite scale periodicity in the microstructure. Thus, if L represents a periodic length scale, we are led to Fig. 1b). With a periodic microstructure there comes naturally a periodic boundary condition

$$\begin{aligned} u(\underset{\sim}{x} + \underset{\sim}{L}) &= u(\underset{\sim}{x}) + \bar{\underset{\sim}{\varepsilon}} \cdot \underset{\sim}{x} \\ t(\underset{\sim}{x} + \underset{\sim}{L}) &= -t(\underset{\sim}{x}) \end{aligned} \qquad \forall \underset{\sim}{x} \in \partial B^p \tag{4}$$

where $\bar{\underset{\sim}{\varepsilon}}$ is a prescribed constant strain. The advantage of this approach lies in (i) the removal of a boundary effect, and (ii) prediction of responses closer to $\boldsymbol{C}^{eff}$ than those resulting from (1) and (2) at any fixed δ. The second advantage implies a faster approach to homogenization than that resulting from either (1) or (2). It is important to note that the periodic unit cell of Fig. 1c) is a special case of Fig. 1b); it represents a classical concept employed in a large portion of recent and ongoing work in micromechanics of elasticity, plasticity and damage.

A specimen's response on the mesoscale (δ finite) is, in general, anisotropic. We therefore employ the radius R

$$R \equiv C_{12,\,max} = \sqrt{(C_{11} - C_{22})^2/4 + C_{12}^2} \tag{5}$$

of the corresponding Mohr's circle to quantify a given elasticity tensor, while the trace $tr\boldsymbol{C}_\delta \equiv C_{ii}/2$ is used to describe this tensor's fundamental magnitude.

In Fig. 2a) we show the hierarchy (3) in terms of the trace of the effective stiffness tensors for a matrix-inclusion composite with locally isotropic constituents having inclusions that are 10 times softer. This is the case of a 35% volume fraction of inclusions, with the stiffness of inclusions being $C^{(i)} = 0.1$, and that of the matrix being $C^{(m)} = 1$. In Fig. 2b) we display the radii R of the corresponding Mohr's circle for three boundary conditions 'dd,' 'tt' and 'dt' listed below. As expected, very large windows need to be taken in order to homogenize the material; this situation gets worse as contrast increases [7]. Thus, a question arises as to a possibility of finding some other boundary conditions that might more rapidly lead to the response $\boldsymbol{C}^{eff}$ at much smaller scales than say $\delta = 48$ in Fig. 2b). In fact, usual laboratory testing procedures typically employ mixed boundary conditions, where the displacement is being applied in, say, y-direction, while surface tractions are zero in the x-direction.

The above considerations lead us to several different conditions shown in Fig. 3. In particular, we have here:

a) displacement (dd)
b) traction (tt)
c) mixed: displacement-traction (dt)
d) displacement-periodic (dp)
e) traction-periodic (tp).

a)

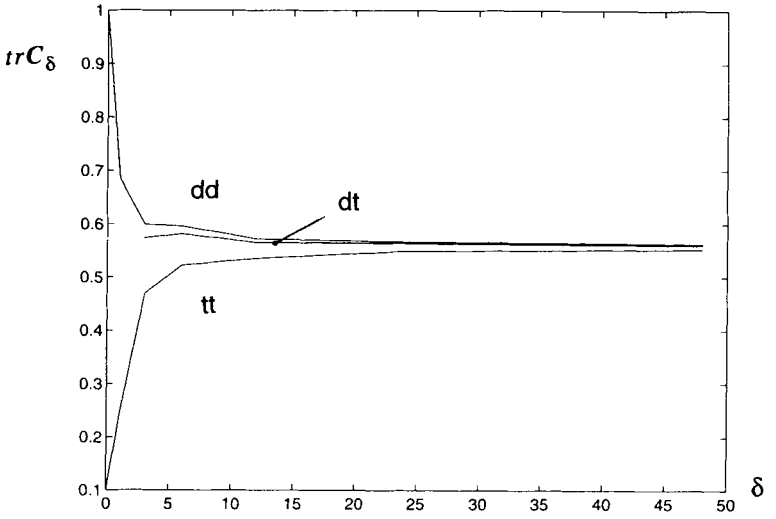

b)

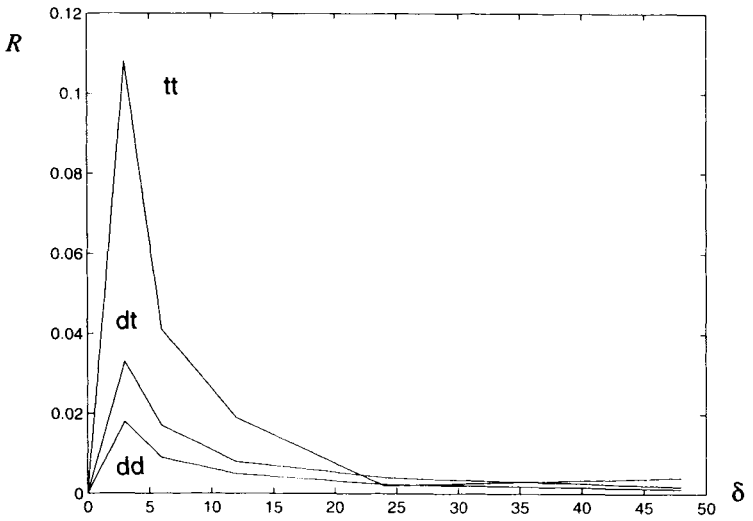

Figure 2a) A hierarchy of scale dependent bounds, normalized by $C^{(m)} = 1$, of stiffnesses of the disk-matrix composite of Fig. 1a) at the stiffness contrast $C^{(i)}/C^{(m)} = 0.1$; b) Radii of the corresponding Mohr's circles as function of δ.

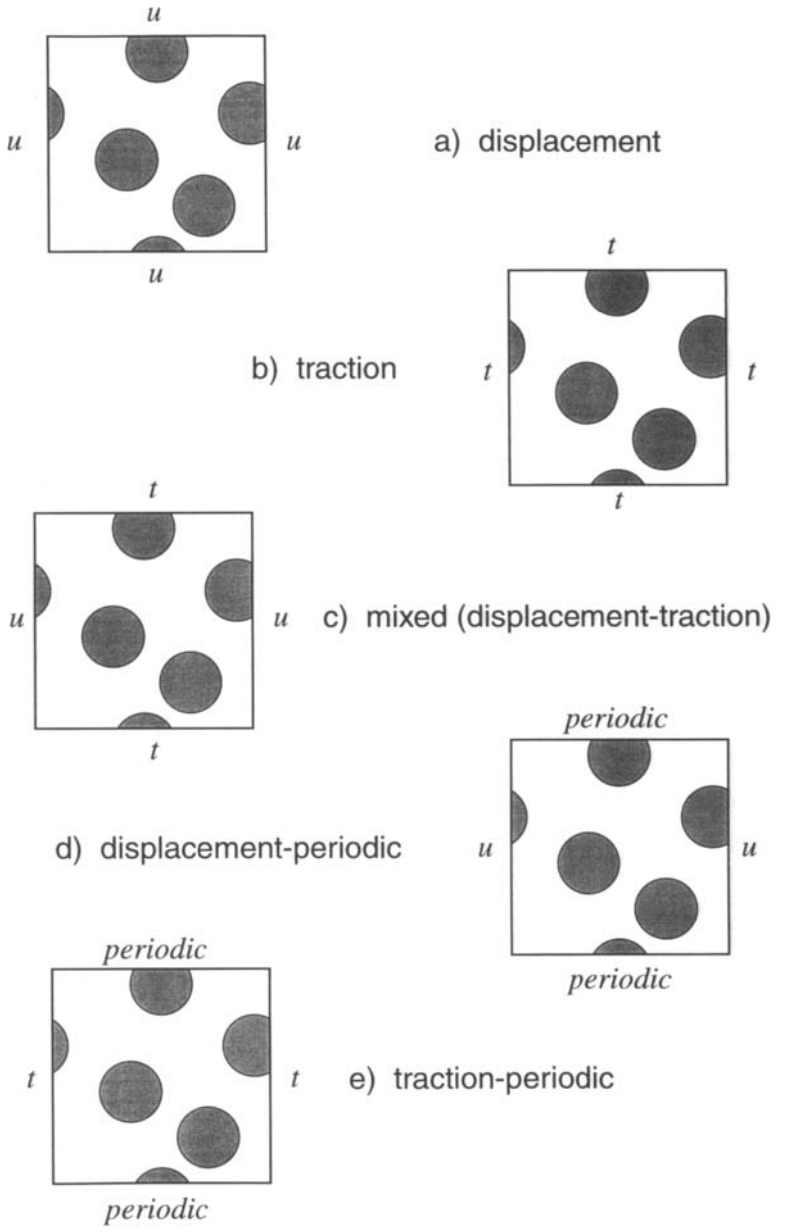

Figure 3. Five types of boundary conditions: (a) displacement, (b) traction, c) mixed (displacement-traction), d) displacement-periodic, e) traction-periodic.

In Figs. 4, 5, and 6 we present the histograms and probability fits to trC_δ and R as functions of the window size δ for the cases of displacement, traction, and mixed boundary condition for a matrix-inclusion composite at the stiffness contrast 0.1; of course, in the case of traction conditions we calculate the compliance and show $\langle trS_\delta \rangle^{-1}$ in columns 'tp' and 'tt' of Table 1. In particular, in each of these Figures, we have five rows, each of which corresponds to $\delta = 3$, 6, 12, 24, and 48. As discussed in detail in our papers [4, 7], the most convenient and best justified probability distribution for composite materials is the *beta distribution*. It is given by

$$f(x;a_1, a_2, \delta_1, \delta_2) = \frac{\left(\frac{x-\delta_1}{\delta_2-\delta_1}\right)^{a_1-1}\left(1-\frac{x-\delta_1}{\delta_2-\delta_1}\right)^{a_2-1}}{(\delta_2-\delta_1)B(a_1, a_2)} \tag{6}$$

where a_1, a_2, δ_1, and δ_2 are adjustable parameters, and $B(a_1, a_2) = \Gamma(x)\Gamma(y)/(\Gamma(x, y))$ is the beta function.

It is easily observed that both invariants decrease toward zero as the window size increases, with the traces being relatively symmetric and all the radii being very non-symmetric. Whereas this last observation is consistent with the fact that the radius must be a positive valued random variable, more insight into the matter can be gleaned from the Table 3 below.

The Figures 4 - 6 are augmented by Tables 1 - 4 which, for five different boundary conditions and five different δ's, give the following:

Table 1: averages of traces,

Table 2: coefficients of variation (COV) of traces,

Table 3: averages of radii,

Table 4: coefficients of variation (COV) of radii,

All these data are listed in five rows - again corresponding to five window scales reported in the above figures. In fact, we also provide here the data obtained from the displacement-periodic ('dp') and traction-periodic ('tp') conditions, while the displacement, displacement-traction, and traction conditions are denoted by 'dd', 'dt,' and 'tt'. The latter were obtained for microstructures lacking any periodicity (Fig. 1a), while the former did, of course, require a periodicity, such as shown in Fig. 1b). However, the common characteristic of all the simulated cases was the same volume fraction of 35%.

It can now be gleaned from Table 1 that 'dd' and 'tt' bound the other three sets of results, with 'dt' being stiffer than 'dp', and this one being stiffer than 'tp'. While Tables 2 and 3 depict the heuristically expected trends, an entirely new observation follows from Table 4: the COV of the radius R of either $\langle \boldsymbol{C}_\delta^e \rangle$ or $\langle \boldsymbol{S}_\delta^n \rangle$, for all the boundary conditions studied here, is approximately constant. The variations that are observed may probably be attributed to a limited number of realizations $\boldsymbol{B}(\omega)$ of the random composite $\boldsymbol{B}$ that were run in the Monte Carlo sense. In all of the above we used 300 $\boldsymbol{B}(\omega)$'s at $\delta = 3$, 200 at $\delta = 6$, 100 at $\delta = 12$, 50 at $\delta = 24$, and 20 at $\delta = 48$.

Table 1: average trace

	dd	dp	dt	tp	tt
$\delta = 3$	0.598	0.567	0.574	0.476	0.469
$\delta = 6$	0.596	0.056	0.581	0.512	0.523
$\delta = 12$	0.572	0.561	0.565	0.534	0.535
$\delta = 24$	0.568	0.559	0.564	0.546	0.549
$\delta = 48$	0.562	0.558	0.560	0.552	0.553

Table 2: COV of trace

	dd	dp	dt	tp	tt
$\delta = 3$	0.096	0.014	0.102	0.054	0.109
$\delta = 6$	0.035	0.005	0.038	0.021	0.041
$\delta = 12$	0.016	0.003	0.017	0.008	0.017
$\delta = 24$	0.005	0.001	0.006	0.003	0.006
$\delta = 48$	0.002	0.0008	0.002	0.001	0.002

Table 3: average of *R*

	dd	dp	dt	tp	tt
$\delta = 3$	0.018	0.017	0.033	0.144	0.108
$\delta = 6$	0.009	0.011	0.017	0.058	0.041
$\delta = 12$	0.0049	0.005	0.008	0.024	0.019
$\delta = 24$	0.0023	0.003	0.004	0.012	0.002
$\delta = 48$	0.0012	0.0013	0.0018	0.006	0.004

Table 4: COV of *R*

	dd	dp	dt	tp	tt
$\delta = 3$	0.566	0.636	0.464	0.530	0.546
$\delta = 6$	0.576	0.485	0.416	0.517	0.536
$\delta = 12$	0.490	0.498	0.415	0.529	0.541
$\delta = 24$	0.6075	0.511	0.423	0.422	0.593
$\delta = 48$	0.652	0.613	0.611	0.423	0.627

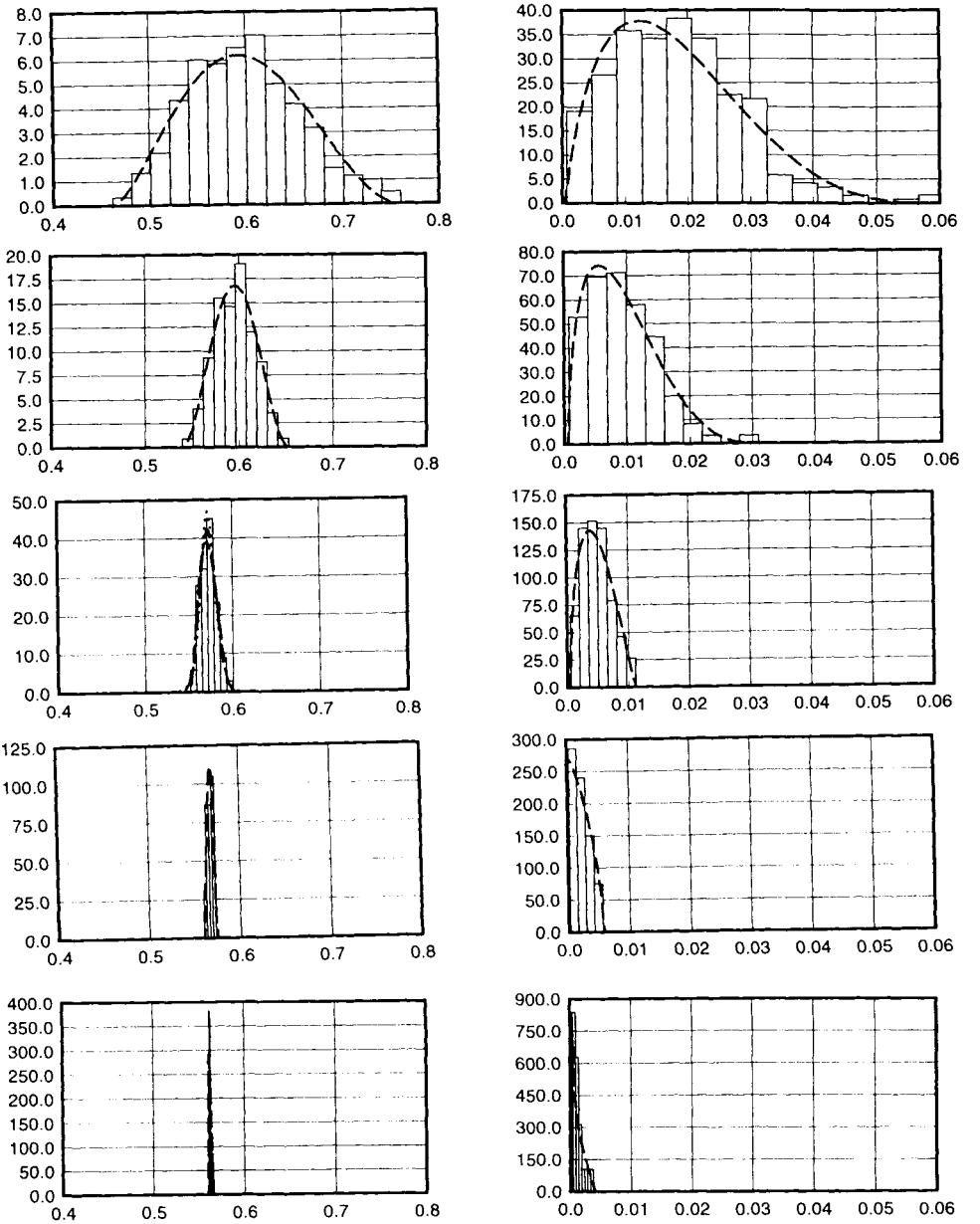

Figure 4. The histograms and probability fits to trC_δ (left column) and R (right column) as functions of the window size $\delta = 3$, 6, 12, 24, and 48 under displacement boundary condition of a matrix-inclusion composite at contrast 0.1

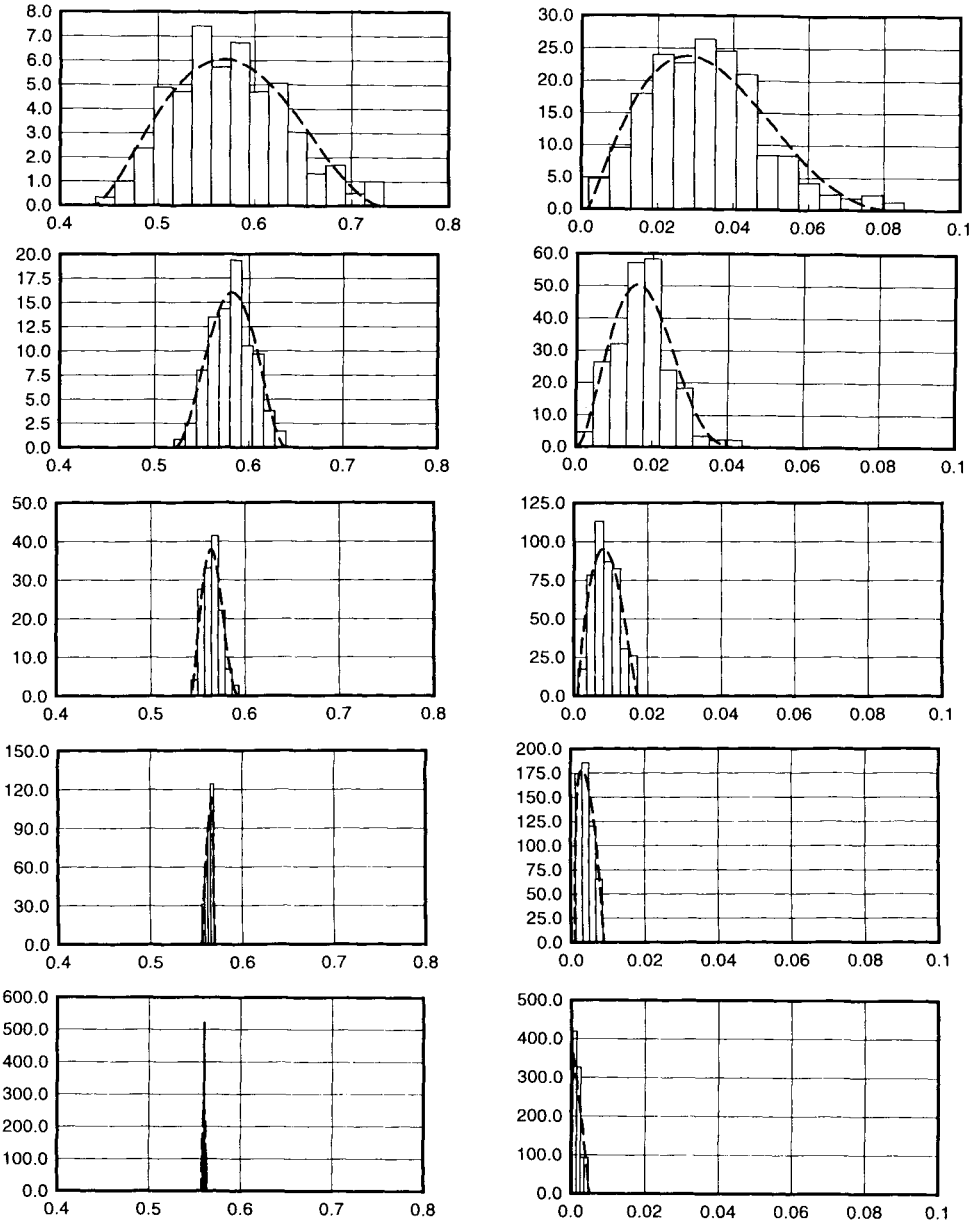

Figure 5. The histograms and probability fits to trC_δ (left column) and R (right column) as functions of the window size δ = 3, 6, 12, 24, and 48 under mixed (displacement-traction) boundary condition of a matrix-inclusion composite at contrast 0.1

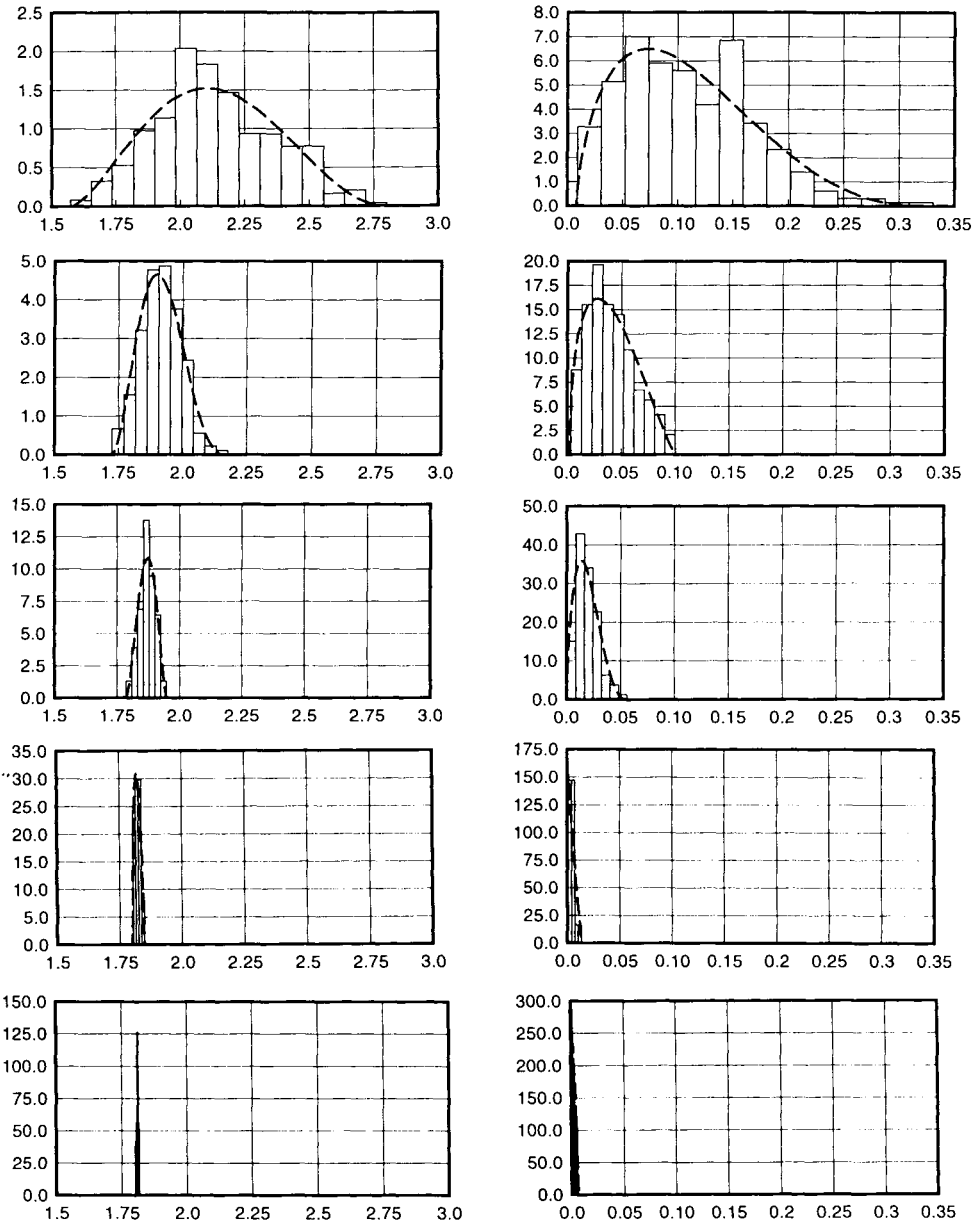

Figure 6. The histograms and probability fits to trS_δ (left column) and R (right column) as functions of the window size δ = 3, 6, 12, 24, and 48 under traction boundary condition of a matrix-inclusion composite at contrast 0.1

3. SCALE EFFECTS FOR SEVERAL BOUNDARY CONDITIONS

3.1 The spring network method

Our tool in the investigation of all these responses is a numerical simulation method based on a very fine two-dimensional spring network representation of the composite [11], whereby damage evolution is simulated by sequentially removing/breaking bonds in accordance with the local state of stress/strain concentrations. This spring network method has, in fact, been used in establishing the results of the previous section, i.e., just in the elastic range. In the following, we first describe the salient features of this approach, and then turn to a study of the damage responses.

The continuum composite (the transverse plane of a fiber-matrix composite) is discretized using a square spring network. Thus, the stiffness tensor of a unit cell of this spring network, modeling an isotropic continuum, is given as

$$C_{11} = C_{22} = \frac{k}{2} \qquad C_{12} = C_{21} = 0 \tag{7}$$

where k is half the bond spring constant. In case of calculation of effective stiffnesses of undamaged materials at stiffness contrast $C^{(i)}/C^{(m)} = 0.1$ we choose the inclusion diameter, d, to be ten times the lattice spacing.

This resolution, however, is not high enough to simulate damage evolution due to the problem of mesh dependence. Thus, we introduce a refined version of a square lattice model through the addition of diagonal bonds - a tetratriangular lattice; see [12] for an in-plane elasticity formulation. This is, in effect, a non-local spring network model since the diagonal bonds connect second, rather than first, nearest neighbors. Twenty spacings per inclusion for this diagonal bond model have been found to practically remove the mesh dependence. We therefore carry out the comparisons of a square lattice and a square lattice with diagonal bonds at this resolution of twenty spacings - this is discussed further in Section 2.2 below.

The coordinates of inclusions' centers are generated through a Poisson point process; they are rounded off so as to place the disk centers on the nodes of the spring network. In order to avoid the problem of arbitrarily narrow necks between the inclusions, we force the disks centers to be at least two lattice spacings apart. Next, the spring constants of matrix and inclusion bonds ($k^{(m)}$ and $k^{(i)}$) are assigned according as they fall in a given phase, while any bond straddling the circular matrix-inclusion boundaries has its spring constant $k^{(b)}$ assigned according to a series spring system weighted by the partial lengths ($l^{(m)}$ and $l^{(i)}$) of the bonds that belong to the respective matrix and inclusion domains, that is

$$k^b = \left(\frac{l^{(m)}}{lk^{(m)}} + \frac{l^{(i)}}{lk^{(i)}} \right)^{-1} \qquad l = |\underline{l}^b| = l^m + l^i \tag{8}$$

A solution for the displacement field $u(\underline{x})$ over the window domain is accomplished by employing a conjugate gradient method [13] with respect to the total energy (sum of energies stored in all the spring bonds), while subject to chosen boundary conditions. The total potential

energy E stored in the network provides a basis for determination of the equivalent, effective medium, according to the relation

$$E = \frac{V_\delta}{2} \bar{\varepsilon} \cdot C_\delta(\omega) \cdot \bar{\varepsilon} \tag{9}$$

In (9) V_δ is the volume of $\mathbf{B}_\delta(\omega)$.

The spring networks allow a possibility of simulating fracture events, such as a simultaneous growth of many cracks, through the removal of spring bonds according to their exceeding local failure criteria, while taking full account of the resulting stress redistribution throughout the lattice. In our two-phase composite two basic failure criteria are needed: failure of matrix bonds and failure of inclusion bonds; these are expressed in terms of the matrix (inclusion) bond strain relative to the critical matrix (inclusion) strain

$$\varepsilon^{(m)} \geq \varepsilon_{cr}^{(m)} \qquad \text{and} \qquad \varepsilon^{(i)} \geq \varepsilon_{cr}^{(i)} \tag{10}$$

Additionally, we postulate a failure criterion of any bond straddling the circular matrix-inclusion boundaries: the critical strain is weighted by the partial lengths ($l^{(m)}$ and $l^{(i)}$) of the bond that belong to the respective matrix and inclusion domains, that is

$$\varepsilon_{cr}^{b} = \frac{l\varepsilon_{cr}^{(m)}}{l^{(m)}} + \frac{l\varepsilon_{cr}^{(i)}}{l^{(i)}} \qquad l = \left|\underset{\sim}{l}^{b}\right| = l^{(m)} + l^{(i)} \tag{11}$$

3.2 Effects of boundary conditions on damage mechanics of random composites

It is well known that the sensitivity of fracture and damage phenomena to material disorder is generally higher than that of effective elastic responses. In this section we report our ongoing research on the dependence of the effective meso-scale damage responses to various types of boundaries conditions. Two aspects are here of primary interest: the character of damage patterns and the effective stress-strain curves. For a composite of stiffness contrast $C^{(i)}/C^{(m)} = 10$ and strain-to-failure contrast $\varepsilon_{cr}^{(i)}/\varepsilon_{cr}^{(m)} = 10$, the following boundary conditions are investigated:

on a square lattice:
- displacement
- traction
- mixed (displacement-traction)
- displacement-periodic
- traction-periodic
- periodic-periodic

and on a square lattice with diagonal bonds:
- displacement.

First of all, we note that, for the chosen case of material parameters, cracks form outside the

inclusions, although fracture is concentrated in their vicinity due to the stress and strain concentrations there. It is observed from Fig. 7 that the damage patterns strongly depend on the choice of the boundary conditions. Additionally, as shown in Fig. 8, the effective stress-strain curves are very sensitive to this choice too. Clearly, the displacement conditions add stiffness and, in a sense, structural integrity to the material, but, as they change to mixed (displacement-traction) or entirely traction conditions, the material becomes much weaker. This is also explained by the fact that the load controlled fracture is unstable.

In accordance with this observation, the effective responses of two displacement controlled tests, compared in Fig. 7 g) and h), are several times stiffer and stronger than the other ones involving tractions. Furthermore, the test corresponding to a square lattice without the diagonal bonds turns out to be stiffer and stronger (vide Fig. 8 b) than the one with such bonds. It is gratifying, however, that their damage patterns differ very little - compare Figs. 7a) and 7g). Thus, we may conclude that, the damage (i.e., crack) patterns of elastic-brittle composites with stiffer and stronger inclusions in anti-plane loading - but not their effective stress-strain curves - can be adequately simulated by square lattices without resort to tetratriangular ones. This and other related issues require further investigation in other regions of the parameter plane.

ACKNOWLEDGMENTS

This research was supported by the NSF under grants No. MSS 9202772 and MSS 9402285, as well as the Research for Excellence Fund from the State of Michigan.

REFERENCES

1. M. Ostoja-Starzewski, P.Y. Sheng and I. Jasiuk, ASME J. Engng. Mat. Tech., Vol. 116, 384-391 (1994).
2. M. Ostoja-Starzewski and J.D. Lee, Intl. J. Fracture, Vol. 75, R51-R57 (1996).
3. M. Ostoja-Starzewski, P.Y. Sheng and I. Jasiuk, Engng. Fracture Mech., in press (1997).
4. K. Alzebdeh, A. Al-Ostaz, I. Jasiuk and M. Ostoja-Starzewski, Intl. J. Solids Struct, in press, 1997.
5. R . Hill, J. Mech. Phys. Solids, Vol. 11, 357-372 (1963).
6. M. Ostoja-Starzewski, Appl. Mech. Rev., Vol. 47(1, Part 2), S221-S230 (1994).
7. M. Ostoja-Starzewski, Intl. J. Solids Struct., in press (1997).
8. G.A. Strang, Introduction to Applied Mathematics, Wellesley-Cambridge Press (1986).
9. C. Huet, J. Mech. Phys. Solids, Vol. 38, 813-841 (1990).
10. S. Hazanov and C. Huet, J. Mech. Phys. Solids, Vol. 41, 1995-2011 (1994).
11. M. Ostoja-Starzewski, P.Y. Sheng and K. Alzebdeh, Comput. Mater. Sci., Vol. 7 (1&2), 82-93, (1996).
12. L. Monette and M.P. Anderson, Modelling Simul. Mater. Sci. and Eng., Vol. 2, 53-56 (1994).
13. W.H. Press, W.T. Vetterling, S.A. Teukolsky, and B.P. Flannery, Numerical Recipes, Cambridge University Press (1990).

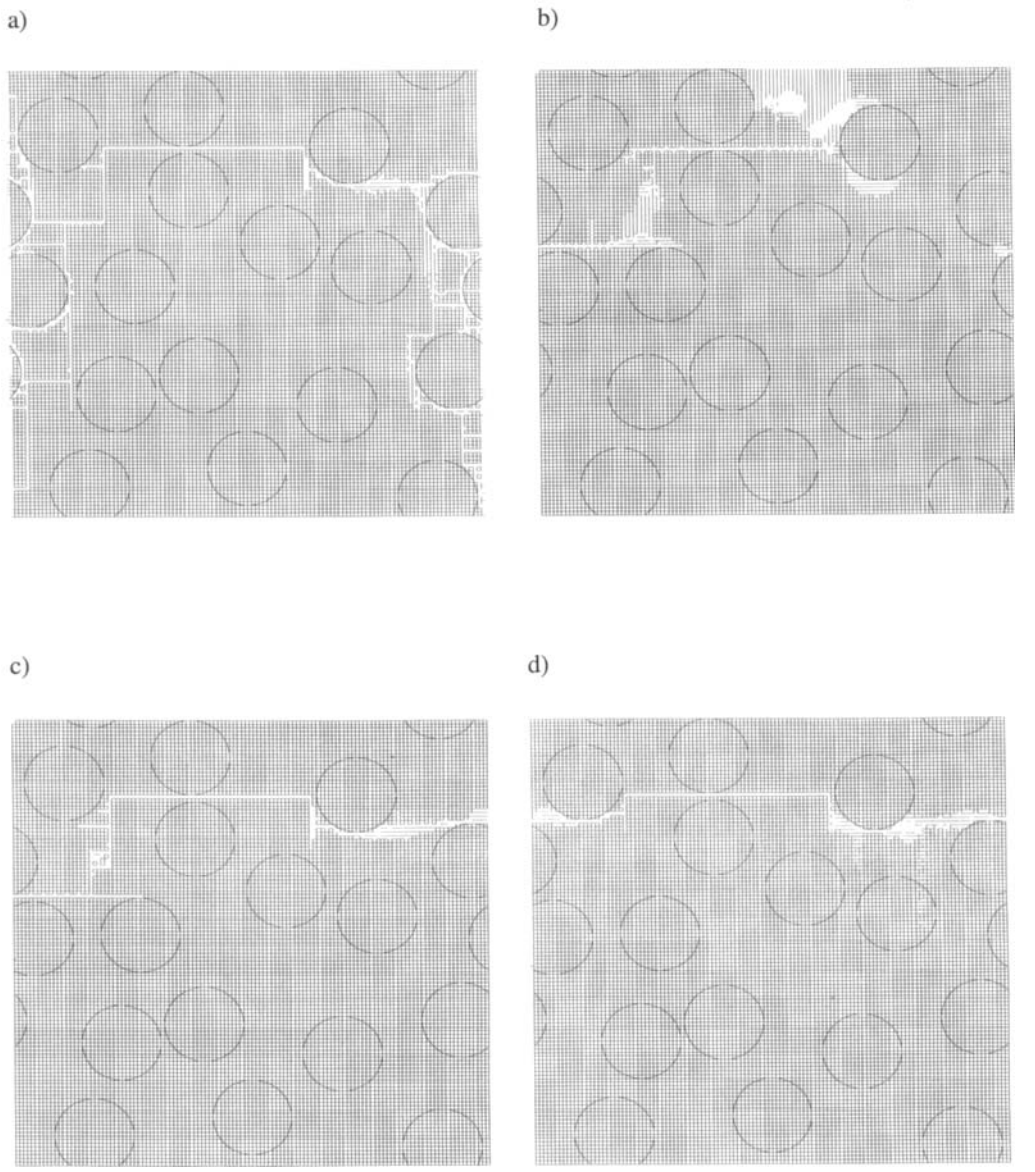

Figure 7. Crack patterns under (a) displacement, (b) traction, (c) mixed (essential-traction), and (d) displacement-periodic boundary conditions on a square lattice.

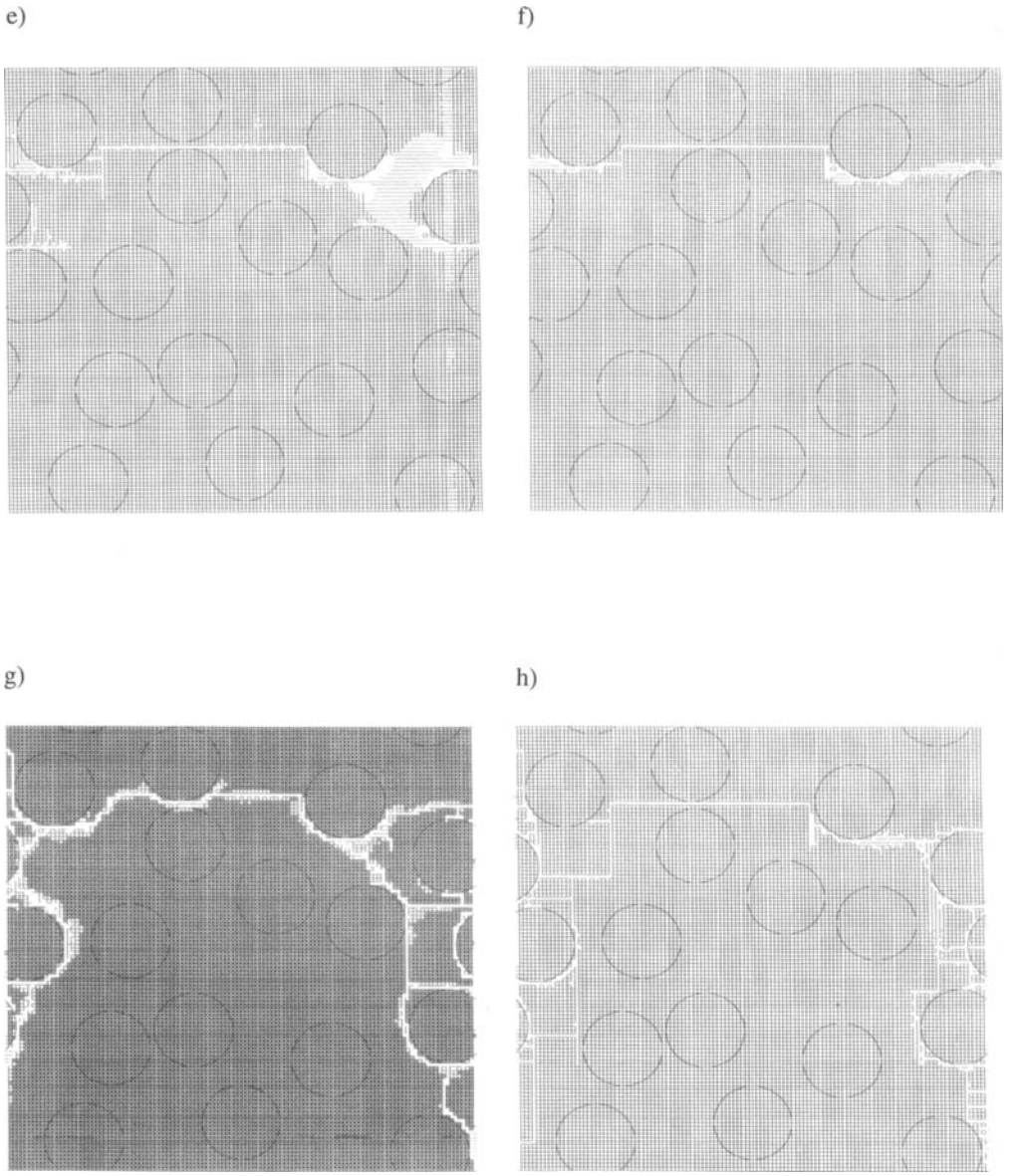

Figure 7-cntd. Crack patterns under (e) traction-periodic, (f) periodic-periodic conditions on a square lattice, and (g) displacement conditions on a lattice with diagonal bonds. For a comparison, (a) is repeated next to (g) as (h)

a)

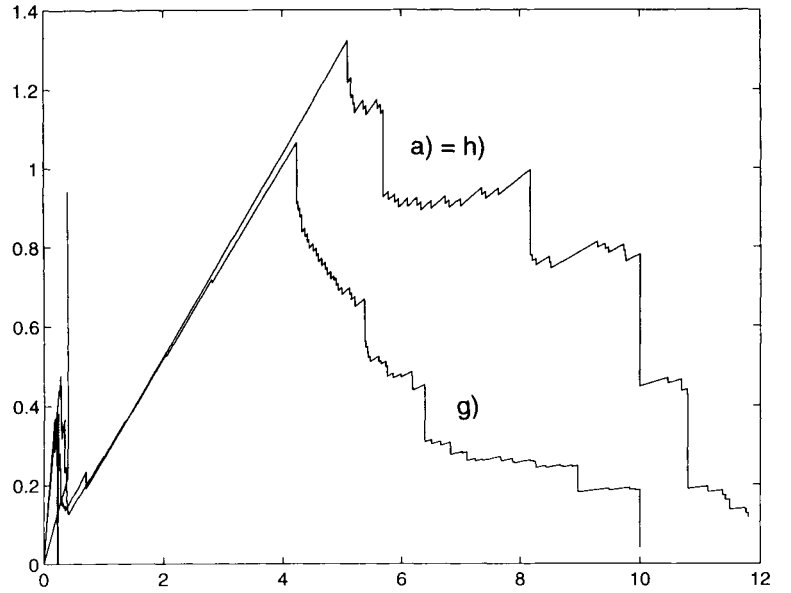

b)

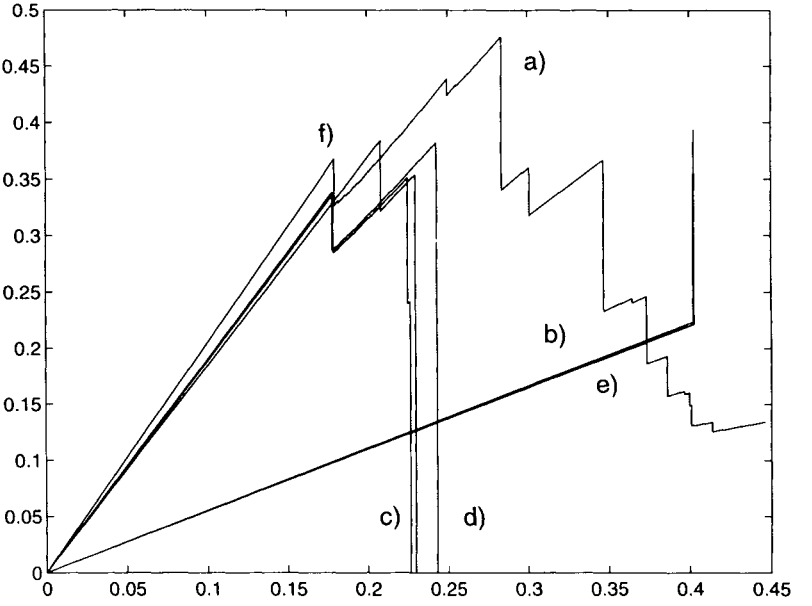

Figure 8. Effective stress-strain curves for all the cases of Fig. 7. The lower figure shows a blowup of cases other than kinematic boundary conditions.

Damage Mechanics in Engineering Materials
G.Z. Voyiadjis, J.-W.W. Ju and J.-L. Chaboche (Editors)
© 1998 Elsevier Science B.V. All rights reserved.

The Effect of Fiber Bridging on Self-Similar Crack Growth: A Penny-shaped Crack Evolvement in a Unidirectional, Fibrous Composite

Kai X. Hu, Chao-pin Yeh and Karl W. Wyatt
Applied Simulation and Modeling Research
Motorola, Inc.
1303 E Algonquin Road, Annex 2
Schaumburg, IL 60196

Abstract

As a result of matrix cracking in fiber reinforced composites, fracture planforms assume a wide variation of profiles due to the fact that fiber bridging strongly affects the behavior of local crack fronts. This observation raises the question on the legitimacy of commonly used penny-shaped crack solutions when applied to fiber reinforced composites. Accordingly, investigation of the effects of fracture front profiles on mechanical responses is the thrust of this paper. We start with the solution of a penny-shaped crack in a unidirectional, fiber reinforced composite, which demonstrates necessarity of considering wavy fracture fronts in fiber reinforced composites. A theoretical framework for fiber reinforced composites with irregular fracture fronts due to matrix cracking is then established via a micromechanics model. The difference between small crack-size matrix cracking and large crack-size matrix cracking is investigated in detail. It is shown that the bridging effect is insignificant when matrix crack size is small and solution of effective property are obtained using Mori-Tanaka's method by treating cracks and reinforcing fibers as distinct, but interacting phases. When the crack size becomes large, the bridging effects has to be taken into consideration. With bridging tractions obtained in consistency with the micromechanics solution, and corresponding crack energy backed out, the effective properties are obtained through a modification of standard Mori-Tanaka's treatment of multi-phase composites. Analytical solutions show that the generalization of a crack density of a penny-shaped planform is insufficient in describing the effective responses of fiber-reinforced composites with matrix cracking. Approximate solutions that account for the effects of the irregularity of crack planforms are given in closed forms for several cases, including rectangle, polygon, rhombus, cross and the wavy fracture front.

1. Introduction

Matrix cracking has been observed as one of the major failure modes in a fiber reinforced ceramic composite material. The failure normally starts from a uniform crack initiation and as they continue to grow under field use conditions, those cracks finally interact and coalesce to form a localized failure zone. One technique of monitoring the structure integrity made of these composites is to record the material repsonses in a non-destructive manner. For such applications and many others, the overall properties of a microcracked composite is critical for the purpose of correlating recorded data to structural integrity. Although there is an extensive body of literature devoted to addressing cracking induced material behavior changes in composite materials (e.g., Taya and Chou, 1981, Zhao et al., 1989, Divert 1986, 1990, Huang et al., 1994a and Hu and Huang1993 for micromechanics treatments, and Kachanov 1985, 1987 and 1993, Hu and Chandra, 1993, Hu et al 1993a, b, Hu et al. 1994 and Chandra et al. 1995 for numerical treatments), lit-

tle has been done in terms of addressing the effects of fiber bridging on the overall composite behavior. Fiber bridging brought about complexity to a ceramic composite material in two aspects. First, composite behavior changes significantly during its load-carrying life span. When a fresh composite structure starts initiating small cracks, there is no bridging taking place since the crack size in this duration is normally smaller than fibers'. As the cracks continue to grow, the bridging extent expands to resist the crack growth. This process transfers to different stages of a structural life profile, which has to be known to interpret non-destructive data. Second, the crack growth in a fiber bridging environment is very complex and the planform of a crack, or the profile of fracture fronts is being strongly affected by local bridging fibers. Therefore, self-similar crack growth is to hardly be maintained.

This paper presents a theoretical treatment of effective mechanical repsonses of fiber reinforced ceramic composites suffering from matrix cracking with a motivation of including the effects of fiber bridging and the effects of irregular fracture fronts as a result of continued crack growth under a fiber bridging environment. In Section 2, a penny-shaped crack with fiber bridging is considered and the solution reveals a wavy variation of stress intensity factor and energy release rate along the fracture front, which will subsequently grow into a wavy fracture planform. Section 3 focuses on the solution of effective properties when the size of irregular planform cracks is small whereby bridging is insignificant. Section 4 investigated the effective properties of fiber reinforced ceramic composites under a bridging environment. Simplification of the results under approximate conditions is presented in Section 5, where the effects of irregular fracture fronts are investigated. A brief summary of the results are presented in Section 6.

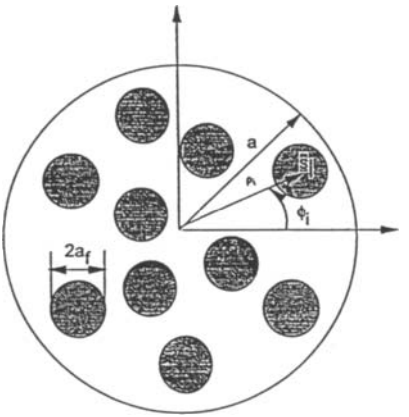

Figure 1. Typical distribution of fibers inside a penny-shaped crack.

2. Growth Of Penny-shaped Cracks In Fiber Reinforced Composites

To illustrate the necessarity of irregular fracture fronts in composite materials, a uni-directional, fiber reinforced composite, subject to matrix cracking is considered. Assuming that a remote stress in fiber direction creates the matrix cracking initially in the form of a penny-shaped crack perpendicular to the fiber direction. The focus here is on the solution of local stress intensity factors along the fracture front of the penny-shaped crack subject to the remote stress. The details of fiber distribution inside the penny-shaped crack are to be considered since the bridging trac-

tions exist over only those areas where a fiber exists. Representative fiber patches inside a penny-shaped crack are shown in Figure 1, and bridging tractions are imposed over these fiber patches. The bridging tractions over each patch area are as yet unknown and may vary with the position inside each fiber patch. We assume that a linear bridging law exists such that the bridging traction, s, can be related to the crack opening displacement, u, through the following relationship:

$$u = K\sigma \qquad (1)$$

where K is the proportionality constant. The crack opening displacement under the remote stress, σ_{33}^0, and bridging tractions can be written as (Fabrikant 1989, Gao and Rice 1987)

$$w(\rho,\phi) = 4H\sigma_{33}^0\left(a^2-\rho^2\right)^{1/2} - \frac{2}{\pi}H\sum_{i=1}^{N}\iint_{S_i}\frac{\sigma_i(\rho_0,\phi_0)}{R}tan^{-1}\left(\frac{\eta}{R}\right)\rho_0 d\rho_0 d\phi_0 \qquad (2)$$

where $s_i(r_0, f_0)$ represents the as yet unknown bridging traction distribution over the ith fiber patch, S_i is the area of the ith fiber patch with radius a, the integration is carried out over all N patches inside the penny-shaped crack in order to account for the total crack opening contribution from all the bridging fiber patches, and

$$R = \left[\rho^2+\rho_0^2-2\rho\rho_0\cos(\phi-\phi_0)\right]^{1/2}, \qquad (3)$$

$$\eta = \frac{\left[\left(a^2-\rho^2\right)\left(a^2-\rho_0^2\right)\right]^{1/2}}{a} \qquad (4)$$

$$H = \frac{1-\nu^2}{\pi E} \qquad (5)$$

Imposing the bridging law over all the fiber patches, we have the following normalized governing equation:

$$4\left[\left(\frac{a}{a_f}\right)^2-\left(\frac{\rho}{a_f}\right)^2\right]^{1/2} - \frac{2}{\pi}\sum_{i=1}^{N}\iint_{S_i}\frac{\sigma_i(\rho_0,\phi_0)}{\sigma_{33}^{mx}}tan^{-1}\frac{\eta}{R}\frac{\rho_0 d\rho_0 d\phi_0}{Ra_f} = \xi\sigma_j(\rho,\phi) \qquad (\rho,\phi)\in S_j, j=1,\ldots,N \qquad (6)$$

where x is a dimensionless configuration constant,

$$\xi = \frac{K}{Ha_f} \qquad (7)$$

The bridging strength increases as the value of x decreases; x varies over a wide range, depending on the particular bridging configuration. To solve for the unknown bridging tractions, $\sigma_i(\rho_0,\phi_0)$, we assume that

$$\sigma_i(\rho_0,\phi_0) = \sum_{n=0}^{M}\sum_{m=0}^{M} r^m\left(a_{mn}\cos n\theta + b_{mn}\sin n\theta\right) \qquad (8)$$

where (r, q) are the local polar coordinates associated with the ith fiber, a_{mn} and b_{mn} are the unknown coefficients, and M is the number of terms, which is truncated for the purpose of numerical efficiency. Equation (6) can then be solved by satisfying the integral equation at a sufficient number of collocation points. It is noted, however, that the integration becomes singular due to R -> 0 when $S_i = S_j$. The integration singularity can be removed by transforming the coordinates (ρ_0, ϕ_0) to (ρ'_0, ϕ'_0) as follows:

$$\rho_0\cos\phi_0 = \rho'_0\cos\phi'_0 + \rho\cos\phi \qquad (9a)$$

$$\rho_0\sin\phi_0 = \rho'_0\sin\phi'_0 + \rho\sin\phi \qquad (9b)$$

In the numerical implementation, the collocation points should be evenly distributed over each fiber in order to secure a spatially smooth, convergent solution. Our numerical calculations show that very accurate bridging transactions with relative errors of less 5% can be obtained with truncation terms of M = 6 for fiber densities up to 40%.

The normalized stress intensity factor (SIF) can be obtained in terms of bridging tractions following an approach by Cherepanov (1979):

$$\frac{K(\phi)}{K_0} = 1 - \frac{1}{2\pi a}\sum_{i=1}^{N}\iint_{S_i}\frac{\sigma_i(\rho_0,\phi_0)}{\sigma_{33}^0}\frac{\left(a^2-\rho_0^2\right)^{1/2}\rho_0 d\rho_0 d\phi_0}{a^2-\rho_0^2-2a\rho_0\cos(\phi-\phi_0)} \qquad (10)$$

where $K_0 = 2\sigma_{33}^0\sqrt{\pi a}/\pi$ is the stress intensity factor due to remote loading σ_{33}^0, without the presence of fiber bridging. The energy release rate can be readily evaluated from the SIF (Tada et al. 1985),

$$G(\phi) = \frac{1-\nu_m^2}{E_m}[K(\phi)]^2. \qquad (11)$$

Simplification of the solution for the fiber-bridged crack system can be achieved if the bridging force variation inside each fiber is insignificant such that

$$\sigma_i(\rho_0,\phi_0) = \sigma_i = \text{constant} \qquad (12)$$

and the governing equation becomes

$$4\left[\left(\frac{a}{a_f}\right)^2-\left(\frac{\rho}{a_f}\right)^2\right]^{1/2} - \frac{2}{\pi}\sum_{i=1}^{N}\frac{\sigma_i}{\sigma_{33}^0}\iint_{S_i}\tan^{-1}\left(\frac{\eta}{R}\right)\frac{\rho_0 d\rho_0 d\phi_0}{Ra_f} = \xi\sigma_j$$

$$(\rho,\phi)\in S_j,\ j = 1,\ldots,N \qquad (13)$$

If the area S_i of each fiber is also very small compared to that of the penny-shaped crack, or $a/a_f \gg 1$ (a_f is the characteristic fiber radius), the equation can be approximately satisfied by collocating (r, f) at only one particular point inside each fiber. If the choice of that collocation points is made at the centers, (ρ_j,ϕ_j), of each fiber, along with the approximation of integrals, we obtain

$$4\left[\left(\frac{a}{a_f}\right)^2-\left(\frac{\rho_j}{a}\right)^2\right]^{1/2} - \sum_{i=1}^{N} I_{ij}\frac{\sigma_i}{\sigma_{33}^0} = \xi\sigma_j \qquad j = 1,\ldots,N \qquad (14)$$

where

$$I_{ij} = 2\frac{a_f}{R_{ij}}\tan^{-1}\frac{\eta_{ij}}{R_{ij}} \qquad \text{for } i\neq j \qquad (15)$$

and

$$R_{ij} = \left[\rho_j^2+\rho_i^2-2\rho_i\rho_j\cos(\phi_j-\phi_i)\right]^{1/2} \qquad \text{for } i\neq j \qquad (16)$$

$$\eta_{ij} = \frac{\left[\left(a^2-\rho_j^2\right)\left(a^2-\rho_i^2\right)\right]^{1/2}}{a} \qquad (17)$$

and

$$I_{ij} = \frac{2}{\pi}\iint_{S_i}\tan^{-1}\left(\frac{\eta}{R}\right)\frac{\rho_0 d\rho_0 d\phi_0}{Ra} \qquad \text{for } i = j \qquad (18)$$

where a coordinate transformation similar to that given in Equations (9a, b) is required to eliminate the singularity, ensuring the accurate evaluation of I_{ij} for i = j. From Equation (14) or its parent form, Equation (6), we can identify the following three major factors that affect a bridged-crack system: (1) the dimensionless configuration constant, as characterized by K/Ha in the case of a linear bridge; (2) the fiber distribution patterns as represented by ρ_i/a and f_i; and (3) the ratio of crack to fiber radius.

The simplification presented here reduces the solution matrix to a minimum size, allowing closed-form solutions for certain fiber distribution patterns. For example, we consider a penny-shaped crack bridged by six symmetric fibers. In this case, all the fibers have equal bridging transactions of s_i/s_0 (= s_2/s_0,..., s_6/s_0). Equation (14) becomes

$$4\left[\left(\frac{a}{a_f}\right)^2-\left(\frac{\rho_1}{a}\right)^2\right]^{1/2}-\left(\sum_{i=1}^{6} I_{i1}\right)\frac{\sigma_1}{\sigma_0} = \xi\frac{\sigma_1}{\sigma_0} \qquad (19)$$

The bridging traction can be given in the closed form as

$$\frac{\sigma_1}{\sigma_0} = \frac{4\left[\left(\frac{a}{a_f}\right)^2-\left(\frac{\rho_1}{a_f}\right)^2\right]^{1/2}}{\xi+\sum_{i=1}^{6} I_{i1}} \qquad (20)$$

It is emphasized here that the simplified solution presented in this section is valid when the fiber radius is small compared to the penny-shaped crack's size. Our numerical results for a number of fiber distribution patterns show that the simplified solution can yield results with an error of less than 15% for fiber volume fractions as much as 50%. Therefore, use of the simplified solution can be justified for the most commonly used fiber-reinforced composite systems.

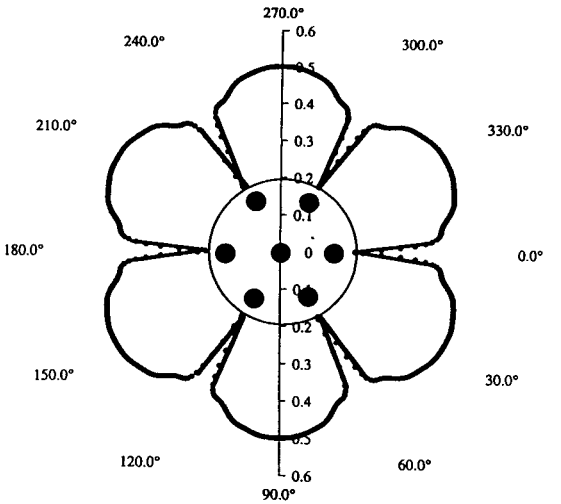

Figure 2. SIF variations along the front of a penny-shaped crack.

The effect of fiber distribution on the spatial variation of fracture front behavior now can be brought out. The fiber distribution may vary drastically inside a penny-shaped crack, reflecting the complexity of processing and the statistical nature of the location of crack nucleation. In order to examine the effect of fiber distribution patterns on the fracture front behavior, a typical offsetting arrangements with seven fibers inside the penny-shaped crack (average fiber spacing, $\bar{a}/a$ = 0.9), are considered and the solution can be obtained in the closed form in a fashion similar to the case of six fibers. It is noted that there the variations of SIFs follows a wavy form along the fracture front (Figure 2) where the wave peaks at locations away from bridging fibers and bottoms at locations close to bridging fibers. In concluding this section, fiber bridging is strongly affecting

the local behavior and by a crack growth theory, a planform of a penny-shaped crack can not be maintained. This phenomenon necessitates the investigation of overall mechanical properties of composite materials with matrix cracking featuring irregular fracture fronts.

3. Elastic Properties For Fiber Reinforced Composites With Small Matrix Cracks Of Irregular Fracture Fronts

A fiber-reinforced composite containing planar matrix cracks of small-size, $S/S_f << 1$, is investigated first (where S is the area of a typical matrix crack and S_f the area of a typical fiber cross section). In this case, the effect of fiber bridging on overall mechanical property is insignificant. Therefore, the solution for a fiber-reinforced composite containing small-sized matrix cracks can be obtained by treating the composite as a material with two phases of inclusions, one being the reinforcing fibers and the other being cracks. A micromechanics approach, using Mori-Tanaka's average technique, will be adapted in the present study. The micromechanics analysis, when employed for solution of effective properties, involves two ingredients: a proper stress-strain definition and a geometric model accounting for phase interactions. The stress-strain relationship for overall composite responses can be addressed by a direct approach (Benveniste 1987) or by an energy equivalence approach (Budiansky 1965, Huang et al. 1993). When used for hybrid composites with coexisting reinforcements and cracks, the energy approach has been proven to be advantageous since crack energy can be evaluated through the concept of an energy release rate (Budiansky and O'Connell 1976, Huang et al. 1993). In the following, an energy balance framework will be utilized and adapted to the Mori-Tanaka average technique in order to obtain the solution for effective composite properties.

Consider a large block of composite material comprised of reinforcing fibers in the x_3 direction and a system of small-sized parallel matrix cracks in the direction perpendicular to the fibers. The fibers are assumed to be cylindrical and are randomly distributed in the x_1-x_2 plane. The cracks of irregular fracture fronts are assumed to be randomly distributed in planes perpendicular to the fiber direction. The elastic modulus and Poisson's ratio of the matrix are E_m and n_m, and those of the fibers are E_f and n_f. Due to the aligned distribution of fibers and cracks, the composite shows an orthotropic behavior and can be characterized by the following general stress-strain relation:

$$\sigma_{ij} = C_{ijkl}\varepsilon_{kl} \quad \text{or} \quad \varepsilon_{ij} = C^{-1}_{ijkl}\sigma_{kl} \qquad (21\text{-}22)$$

where C_{ijkl} is the elastic moduli tensor of the composite material. In order to determine C_{jikl} or its inverse (tensor of elastic constants), apply a uniform stress, $\sigma_{ij} = \sigma^0_{ij}$, to the surface of the block of composite material. The strain energy of the composite material is, from the homogenization, given as

$$U = \frac{1}{2}C^{-1}_{ijkl}\sigma^0_{ij}\sigma^0_{kl}V \qquad (23)$$

where V is the total volume of the composite material. On the other hand, one can view the strain energy from each individual phase. For a composite system with inclusions and cracks, the strain energy can be given as (Huang et al. 1993)

$$U = \frac{1}{2}\left\{\frac{1+\nu_m}{E_m}\sigma^0_{ii}\sigma^0_{jj} - \frac{\nu_m}{E_m}\sigma^0_{ii}\sigma^0_{jj}\right.$$

$$+c_f\left[\left(1-\frac{1+\nu_m}{1+\nu_f}\frac{E_f}{E_m}\right)\sigma_{ij}^0-\varepsilon_{ij}^f+\frac{\nu_m-\nu_f}{(1-2\nu_f)(1+\nu_f)}\frac{E_f}{E_m}\sigma_{ii}^0\varepsilon_{jj}^f\right]\Bigg\}V$$

$$+\sum_{i=1}^{N}\int\!\!\int_{S_i}\sigma_{ij}^0 n_i u_j dS \qquad (24)$$

where $\varepsilon_{ij}^f = 1/V_f\int_{V_f}\varepsilon_{ij}\,dV$ is the average fiber strain, the last term is the total crack energy under the specified loading condition, S_i is the area of a particular crack in the composite block, and N is the number of cracks in that block. The last term in Equation (24) represents the total crack energy in the block. By energy equivalence, we have, from Eqs. (23) and (24),

$$C_{ijkl}^{-1}\sigma_{ij}^0\sigma_{kl}^0 = \frac{1+\nu_m}{E_m}\sigma_{ij}^0\sigma_{ij}^0 - \frac{\nu_m}{E_m}\sigma_{ii}^0\sigma_{jj}^0$$

$$+c_f\left[\left(1+\frac{1+\nu_m}{1+\nu_f}\right)\sigma_{ij}^0-\varepsilon_{ij}^f+\frac{\nu_m-\nu_f}{(1-2\nu_f)(1+\nu_f)}\frac{E_f}{E_m}\sigma_{ii}^0\varepsilon_{jj}^f\right]$$

$$+\frac{1}{V}\sum_{i=1}^{N}\int\!\!\int_{S_i}\sigma_{ij}^0 n_i u_j dS \qquad (25)$$

where S is the area of a crack surface; for the small crack size considered here, $S/S_f << 1$. n_i is the normal of the crack surface and u_i is the crack opening displacements in the composite material (with microcracks), subject tractions derived from σ_{ij}^0 on crack surface.

Equation (25) is an exact representation of the energy equivalence between two views of the cracked composite: one regards the composite as an effective, homogeneous medium, and the other considers the details of the individual phases -- the matrix, fibers, and cracks. The major difficulty in obtaining the effective responses of microcracked composite materials lies in accurate evaluation of average fiber stress and crack opening displacements. This is especially so for crack energy when fracture fronts become irregular and when fiber bridging is taking place for each individual crack. In order to overcome this difficulty in determining the effective property of the microcracked composites, or C_{ijkl}, a scheme for obtaining average fiber strain, as well as the crack energy represented by the last term in Equations (24) and (25), has to be developed to approximately account for interactions among the matrix, fibers, and cracks. It is this scheme for evaluating the average fiber strain and crack energy that introduces a variety of approximations associated with a micromechanics model. Two schemes, the Mori-Tanaka method (e.g., Taya and Chou 1981; Weng 1984, 1990; Benveniste 1987) and the inclusion-matrix-composite model, also referred to as the generalized self-consistent method (e.g., Christensen and Lo 1979; Benveniste 1986; Siboni and Benveniste 1991; Huang et al. 1994a, c), have gained a wide range of acceptance. These two schemes are competing in some applications and complementary in others [see Christensen (1990), Wang and Weng (1992), and Huang et al. (1994b) for detailed discussions on their comparisons]. In what follows, we use the Mori-Tanaka method to evaluate the average fiber strain and crack energy. It is noted here that the Mori-Tanaka method is relatively simple in terms of providing closed-form solutions, it is unambiguous in terms of accommodating multiphase inclusions (as is certainly the case for the microcracked composite under consideration), and it has the typical features of a micromechanics model. These features will be modified as they becomes insufficient as the extent of fiber bridging increases (see Section 4).

In order to implement the Mori-Tanaka method, we apply a remote stress, $\sigma_{33} = \sigma_0$ ($\sigma_{ij}^0 = 0$,

otherwise). The aligned ellipsoidal inclusions are used so that a solution for the long, cylindrical fibers can be derived by taking the limit of the aligned ellipsoidal axis to infinity. The average stresses of the matrix material in the composite system will be developed due to the remote stress $\sigma_{33} = \sigma_0$. The state of the average matrix stress is not necessarily coaxial with the remote stress; it is, however, axisymmetric and can be expressed as $\left(\sigma_{11}^{mx}, \sigma_{22}^{mx}, \sigma_{33}^{mx}\right)$. The average fiber stress can be characterized, by reasoning, as $\left(\sigma_{11}^{fb}, \sigma_{22}^{fb}, \sigma_{33}^{fb}\right)$. One can show that the average stress in cracks, in a limit sense, is zero (Benveniste 1987, Zhao et al. 1989). The stress equilibrium then requires

$$(1-c_f)\begin{pmatrix} \sigma_{11}^{mx} \\ \sigma_{33}^{mx} \end{pmatrix} + c_f \begin{pmatrix} \sigma_{11}^{fb} \\ \sigma_{33}^{fb} \end{pmatrix} = \begin{pmatrix} 0 \\ \sigma_0 \end{pmatrix} \tag{26}$$

The key assumption of Mori-Tanaka's method used to contain the average fiber stress and crack energy was described in Chandra et al (1996). The average fiber stress and crack energy release can be obtained by embedding a single typical fiber and a single crack in an infinitely extended matrix material subject to the average matrix stress state $\left(\sigma_{11}^{mx}, \sigma_{22}^{mx}, \sigma_{33}^{mx}\right)$. The average fiber stresses $\left(\sigma_{11}^{fb}, \sigma_{22}^{fb}, \sigma_{33}^{fb}\right)$ can be related to $\left(\sigma_{11}^{mx}, \sigma_{22}^{mx}, \sigma_{33}^{mx}\right)$ through the solution of the single-fiber system. After inverting the readily derivable single-fiber solution given by Mura (1982), we have

$$\begin{pmatrix} \sigma_{11}^{mx} \\ \sigma_{33}^{mx} \end{pmatrix} = \begin{bmatrix} m_{11}, m_{13} \\ m_{31}, m_{33} \end{bmatrix} \begin{pmatrix} \sigma_{11}^{fb} \\ \sigma_{33}^{fb} \end{pmatrix} \tag{27}$$

where

$$m_{11} = \frac{1}{2}\{1 - \nu_m + \beta[1 - (1+2\nu_m)\nu_i]\} \tag{28a}$$

$$m_{13} = \frac{1}{2}\beta(\nu_m - \nu_i) \tag{28b}$$

$$m_{31} = \frac{\nu_m}{1-\nu_m} + \beta[\nu_m - (2+\nu_m)\nu_i] \tag{28c}$$

$$m_{33} = \beta(1 - \nu_m \nu_i) \tag{28d}$$

$$\beta = \frac{E_m}{E_1\left(1-\nu_m^2\right)} \tag{28e}$$

Substituting Eq. (27) into Eq. (26), we have

$$\begin{pmatrix} c_f + (1-c_f)m_{11} & (1-c_f)m_{13} \\ (1-c_f)m_{31} & c_f + (1-c_f)m_{33} \end{pmatrix} \begin{pmatrix} \sigma_{aa}^{fb} \\ \sigma_{33}^{fb} \end{pmatrix} = \begin{pmatrix} 0 \\ \sigma_0 \end{pmatrix} \tag{29}$$

The solution of Eq. (29) leads to

$$\frac{\sigma_{11}^{fb}}{\sigma_0} = -\frac{c_m}{2\gamma}(\nu_m - \nu_i)\beta \tag{30}$$

$$\frac{\sigma_{33}^{fb}}{\sigma_0} = \frac{1}{\gamma}\left\{ c_f + \frac{c_m}{2}\left[\frac{1}{1-\nu_m} + \beta(1 - \nu_i - 2\nu_m\nu_i)\right]\right. \tag{31}$$

$$\frac{\sigma_{11}^{mx}}{\sigma_0} = \frac{\sigma_{22}^{mx}}{\sigma_0} = \frac{\gamma}{2\gamma}(\nu_m - \nu_i)\beta \tag{32}$$

$$\frac{\sigma_{33}^{mx}}{\sigma_0} = \frac{1}{c_m}\left(1 - \frac{c_f^2}{\gamma}\right) - \frac{c_f}{\gamma}\left[\frac{1}{1-\nu_m} + \beta(1 - \nu_i - 2\nu_m\nu_i)\right] \tag{33}$$

where

$$\gamma = \frac{c_m^2}{2}\beta(v_m - v_i)\left[\frac{v_m}{1-v_m} + \beta(v_m - 2v_i - v_m v_i)\right] + [c_f + c_m\beta(1 - v_m v_i)]$$
$$x\left\{c_f + \frac{c_m}{2}\left[\frac{1}{1-v_m} + \beta(1 - v_i - 2v_m v_i)\right]\right\} \qquad (34)$$

Now turn to evaluation of a single representative crack energy, W,

$$W = \iint_S w\sigma_{22}^{mx} dS = \frac{1-v_m^2}{E_m}\left(\sigma_{33}^{mx}\right)^2 \sqrt{A}\iint_S w_0 dS = \frac{16\left(1-v^2\right)}{3E_m}\left(\frac{\sigma_0}{\varsigma}\right)^2 A^{\frac{3}{2}}\bar{w}_0 \qquad (35)$$

Where w is the opening displacement of a single crack in an infinitely extended matrix material subject to the average matrix stress, σ_{33}^{mx}, and after normalization against the square root of crack area, A, $w_0 = \frac{E_m w}{3(1-v^2)\sigma_{22}^{mx}\sqrt{A}}$, is the dimensionless crack opening displacement, ς is a dimensionless material constant equal to the inverse of the right hand side of Equation (33) and finally $\bar{w}_0$ .is the dimensionless crack displacement averaged over the crack surface area.

With the solution of the average fiber stresses (or strains) and the crack energy in hand, the governing equation (Eq. 25) for the determination of effective moduli can be implemented, giving

$$\frac{1}{E_3} = \frac{1}{E_m} + c_f\left\{\frac{1}{2}\left(\frac{1}{G_f} - \frac{1}{G}\right)\frac{\sigma_{33}^{fb}}{\sigma^0} + \left(\frac{v_m}{E_m} - \frac{v_f}{E_f}\right)\frac{\sigma_{11}^{fb} + \sigma_{22}^{fb} + \sigma_{33}^{fb}}{\sigma^0}\right\}$$
$$+\frac{1-v_m^2}{E_m}\frac{16}{3\varsigma^2}\frac{N}{V}A^{\frac{3}{2}}\bar{w}_0 \qquad (36)$$

While Eq. (36), along with Eqs. (31)-(55), provides a complete solution for the longitudinal modulus E_3, further simplification is possible. The final result is found to be

$$\frac{E_3}{E_m} = \left\{\left[c_m + c_f\left(\frac{E_f}{E_m} + \frac{4c_f c_m (v_f - v_m)^2}{E_m\left(c_f/K_m + c_m/K_f + 1/G_m\right)}\right)\right]^{-1}\right.$$
$$\left.+\left(1-v^2{}_m\right)\frac{16}{3\varsigma^2}\frac{N}{V}A^{\frac{3}{2}}\bar{w}_0\right\}^{-1} \qquad (37)$$

where G_m and K_m are the shear and in-plane bulk moduli of the matrix material and K_f are the in-plane bulk moduli of the fibers.

Following a similar spirit, the other components of the stiffness tensor, for example, the shear modulus in z-x plane, can be obtained by modifying Equations (26-37) with replacement of corresponding remote stress and Eshelby solution. Since our focus is on the the modulus most severely weakened by cracks, we only present the the solution to E_3.

It should be noted that the asymmetric stiffness tensor may be resulted in when Mori-Tanaka's method is utilized for a composite with a multi-phase inclusions of anisotropic properties and non-spherical or non-cylinderical shapes (Benveniste et al. 1991 and Ferrari 1991). Here we have followed the Mori-Tanaka Method derived by Huang et al. (1995), where a mathematical treatment toovercome asymmetric stiffness tensor was given.

4. Elastic Properties For Fiber Reinforced Composites With Large-Size Matrix Cracks Of Irregular Fracture Fronts

When large-size cracks develop, the fibers will bridge across the cracks and, as described

before, the geometric intersections of fibers and cracks will create a feature that is distinct from that of small-size matrix cracks. First, the bridging fibers falling inside a crack will exert a distribution of closing tractions over the area of a crack where a fiber exists. Second, the fibers inside a crack are not entirely immersed in the surrounding matrix material. Those fibers falling inside a crack will remain surrounded by the matrix material, with the exception that a free exposition of the fiber surface occurs along the crack opening. One important assumption of the present study is that the effect of the fiber exposition is neglected. This assumption can be well justified under a small deformation conditions where crack opening always remains small. Therefore, we can still consider the fibers as being entirely surrounded by matrix material. When crack opening displacements are small in comparison to fiber length, as they are for most fiber-reinforced composite systems, the effect of fiber expositions is marginal. In order to account for the effect of fiber bridging on crack opening displacements, and eventually on the effective moduli, the energy equivalence equation should be modified. The Mori-Tanaka scheme is modified such that a typical crack surface is imposed with a distribution of closing tractions (or bridging forces). Although the average matrix stresses can still be evaluated following the procedures detailed in Section 3, the crack energy release rate will also depend on the average matrix stress and the bridging tractions.

If one cuts the fibers along a crack plane, a pair of opposite tractions appears on the cut fiber sections. It is noted that these tractions are the bridging forces. Keep in mind that the bridging tractions can be approximated as the average fiber axial stress. We further distributed these bridging tractions over the area of planform crack. The uniform bridging tractions obtained are

$$\frac{\sigma_b}{\sigma_0} = c_f \sigma_{33}^{fb} = \frac{1}{\gamma}\left\{c^2 + \frac{c_f c_m}{2}\left[\frac{1}{1-\nu_m} + \beta\,(1-\nu_i-\nu_f\nu_i)\right]\right\} \tag{38}$$

The crack energy is then found to be

$$W = \frac{1-\nu_m^2}{E_m}\left(\sigma_{33}^{mx} - c_f\sigma_{33}^{bf}\right)^2 \sqrt{A}\iint_S w_0 dS + \frac{16\left(1-\nu_m^2\right)}{3E_m}\left(\frac{1}{\varsigma}-\frac{1}{\xi}\right)^2 \sigma_0^2 A^{\frac{3}{2}} \bar{w}_0 \tag{39}$$

where ς is the inverse of right hand side in Equation (38). The effective longitudinal modulus can be obtained in a similar manner:

$$\frac{E_3}{E_m} = \left\{\left[c_m + c_f\left(\frac{E_f}{E_m} + \frac{4c_f c_m(\nu_f-\nu_m)^2}{E_m\left(c_f/K_m + c_m/K_m + 1/G_m\right)}\right)\right]^{-1} + \frac{16\left(1-\nu^2{}_m\right)}{3}\left(\frac{1}{\varsigma}-\frac{1}{\xi}\right)^2 \frac{N}{V} A^{\frac{3}{2}} \bar{w}_0\right\}^{-1} \tag{40}$$

The solutions given in Eqs. (39) and (40) are modifications of the standard micromechanics solutions given in Eqs. (36) and (37). This modification provides one possible avenue, based entirely on a micromechanics model, to account for the effect of fiber bridging. The main theme in deriving the solution is to distribute, over cracks, the bridging tractions that are self-consistent with the average fiber stresses obtained by a micromechanics analysis.

It should be noted that the modified micromechanics solution provides a self-consistent approach to accommodating the bridging effect within a micromechanics framework. The model, however, does not consist of any physical input for the development of bridging. This issue can be addressed in a transition model that calls for solution for cracks with bridging from discrete fibers, where a full bridging solution with a bridging law governing relevant mechanisms can be

obtained (Hu, et al 1995). Also, our analysis shows that the modified micromechanics solution has applicability to most SiC-reinforced ceramics within a commonly used fiber volume fraction range of up to 40%. There are cases (with combinations of constituent properties and high volume fraction) that may produce negative values of $\left(\sigma_{33}^{mx} - c_f \sigma_{33}^{fb}\right)$ or $\left(\sigma_{13}^{mx} - c_f \sigma_{13}^{fb}\right)$. This implies that cracks are not opened based on the micromechanics solution. A simple approach to account for this is to discard the crack influence term in Eqs. (39) and (40) when cracks are not open. Other approaches include the consideration of fiber stress variations in the axial direction.

5. Crack Density and Approximate Solutions For Irregular Fracture Fronts

Crack density has been introduced for penny-shaped cracks of average radius a by Bristow (1960)

$$\rho = \frac{Na^3}{V} \qquad (41)$$

and it has been generalized for cracks with irregular planform, for example, by Budiansky and O'Connell (1976)

$$\rho = \frac{2NA^2}{\pi V P} \qquad (42)$$

Remarkably, the definition for penny-shaped cracks stems directly from that fact that the crack opening displacements when averaged over the crack planform area becomes a constant. For irregular crack planforms, there is no warrant that the displacements averaged over the crack area will become independent of other geometric constants, which define the planform of the irregular crack fronts. One can always evaluate the crack opening displacements in an infinitely extended matrix material with only a single crack and then obtain effective properties by using Equations (37) and (40), thus, avoiding any error that arises from a generalization formula such as Equation (42).

The effective properties of a microcracked solid expressed directly in terms of the geometric variations of crack planforms other than a lumped parameter are desirable. Although closed forms of such solutions are highly unlikely, the crack energy solutions of Fabrikant (1989) under the condition of truncating a polynomial solution up to 4th terms can be utilized to obtain closed-form approximations. That simplification gives

$$\frac{E_3}{E_m} = \left\{\left[c_m + c_f\left(\frac{E_f}{E_m} + \frac{4c_f c_m (v_f - v_m)^2}{E_m\left(c_f/K_m + c_m/K_f + 1/G_m\right)}\right)\right]^{-1} + \frac{16\left(1-\nu_m^2\right)}{3}\frac{\rho}{\varsigma^2}\right\}^{-1} \qquad (43)$$

Where ρ is the crack density and reduces to the definition given in Equation (41) for penny-shaped cracks.

The dependence of ρ on the irregularity of several crack planforms is given as follows.

(1) For a rectangle of width a and length b, $\varepsilon = \frac{a}{b} \le 1$

$$\rho = \frac{NA^{3/2}}{V}\frac{\sqrt{\varepsilon}}{12\sqrt{1+\varepsilon^2}} \qquad (44)$$

(2) For or a n-sided polygon of equal length,

$$\rho = \frac{NA^{3/2}}{V}\frac{\sqrt{\cot\left(\frac{\pi}{n}\right)}}{n^{3/2}\sin\left(\frac{\pi}{n}\right)} \qquad (45)$$

(3) For rhombus of semi-axis, a and b, $\varepsilon = \frac{a}{b} \leq 1$

$$\rho = \frac{NA^{3/2}}{V} \frac{\sqrt{2\varepsilon}}{12(1+\varepsilon)} \qquad (46)$$

(4) For a centrically intersected cross of two rectangles of width a and b, $\varepsilon = \frac{a}{b} \leq 1$

$$\rho = \frac{NA^{3/2}}{V} \frac{\sqrt{2\varepsilon}}{12\sqrt{1-\varepsilon}\,[\sqrt{2(1+\varepsilon^2)} - 1]} \qquad (47)$$

6. Conclusions and Discussion

The effective moduli of a fiber-reinforced composite with matrix cracking have been investigated in this paper. Our analysis reveals that a penny-shaped crack can not be maintained in a penny-shaped planform if fiber bridging is in effect. From the crack driving force solution derived, it is shown that the continued growth of a penny-shaped crack will produce a wavy fracture fronts. As a result, fiber reinforced ceramic composites with fiber bridging will always assume irregular planforms. To account for the effect of fiber bridging on effective moduli, the Mori-Tanaka's method is utilized with a modification of crack energy under unknown bridging tractions, which in turn are obtained during the process of micromechanics solution. One can always obtain the effective properties by carrying out numerical solutions for the really simplified micromechanics model, that is, a single crack of irregular planform being embedded in an infinitely extended matrix material subjecting a stress state of the magnitude of average matrix material. It is shown that there is no warrant that a lumped crack density will be sufficient in describing the effective properties of fiber reinforced ceramic composites. The approximate closed-form solutions are obtained with a modification of crack density that incorporates the effects of irregularity of fracture fronts on the effective properties.

In fiber reinforced ceramic composites, fiber bridging controls the local toughness behavior, and consequently governs crack growth behavior. Fracture fronts evolves around a certain crack growth law during the structural life span. The evolution of fracture planform is a critical issue that has to be understood before a micromechanics model, combined with no-destructive measurements can be applied to predict the structural integrity. For non-penny shaped cracks, as we described in Equations (44-46), if the mathematical treatment by Huang et al. (1995) is used, it may eliminate the asymmetry. But without getting the details worked out, the effect of asymmetry may well affect the accuracy of those formula given in Equations (44-46).Work on this and on crack planform evolution will constitute a part of our future investigation.

Acknowledgments

This work has been supported under an ARPA Contract (No. MDA972-93-2-0017), entitled "Optimized Module And Area Array I/O Thin Film CMOS Technologies In Support Of Cryo Electronic And High Temperature Superconducting Applications" during 1994-1995 and continued recently under an ARPA contract (No. F33615-97-2-1026), entitled "Electronic Systems Manufacturing: Low Cost Mixed Mode Modules Computer Aided Mechanical Design & Analysis Infrastructure Development," for 1996-1998. The authors gratefully acknowledge Frank Patten, Bob Parker, Dan Radack and Stu Wolf of ARPA, and Luis Concha and Bill Russell of Wright Laboratory, Wright-Paterson AFB for their helpful discussions and suggestions.

References

Benveniste, Y., 1986, "On the Effective Thermal Conductivity of Multi-Phase Composites," ZAMP, Vol. 37, 696-713.

Benveniste, Y., 1987, "A New Approach to the Application of Mori-Tanaka's Theory in Composite Materials," Mech. Mat., Vol 6, pp. 147-157.

Benveniste, Y., 1992, "Uniform Fields and Universal Relations in Piezoelectric Composites," J. Mech. Phys. Solids, Vol. 40, pp. 1295-1312.

Benveniste, Y., 1993, "Exact Results in the Micromechanics of Fibrous Piezoelectric Composites Exhibiting Pyroelectricity," Proc. R. Soc. Lond. A, Vol. 441, pp. 59-81.

Benveniste, Y., Dvorak, G. J., and Chen, T., 1991, "On diagonal Symmetry of the Approximate Effective Stiffness Tensor of Heterogeneous Media," J. Mech. Phys. Solids, Vol. 39, pp. 927-946

Budiansky, B., 1965, "On the Elastic Moduli of Some Heterogeneous Material," J. Mech. Phys. Solids, Vol. 13, pp. 223-227.

Budiansky, B. and O'Connell, R.J., 1976, "Elastic Moduli of a Cracked Solid," Int. J. Solids Struc., Vol. 12, pp. 81-97.

Chandra, A., Huang, Y., Wei, X., and Hu, K.X., 1995, "A Hybrid Micro-Macro BEM Formulation for Micro-Crack Clusters in Elastic Components," Int. J. Num. Meth. Eng., Vol. 38, pp 1215-1236.

Cherepanov, G.P., 1979, Mechanics of Brittle Fracture, McGraw-Hill, New York.

Christensen, R.M., 1990, "A Critical Evaluation for a Class of Micro-Mechanics Models," J. Mech. Phys. Solids, Vol. 38, pp. 379-404.

Christensen, R.M. and Lo, K.H., 1979, "Solutions for Effective Shear Properties in Three Phase Sphere and Cylinder Models," J. Mech. Phys. Solids, Vol. 27, pp. 315-330.

Christensen, R., Schantz, H., and Shapiro, J., 1992, "On the Range of Validity of the Mori-Tanaka Method," J. Mech. Phys. Solids, Vol. 40, pp. 69-73.

Dvorak, G.J., 1986, "Thermal Expansion of Elastic-Plastic Composite Materials," J. App. Mech., Vol. 53, pp. 737-743.

Dvorak, G.J., 1990, "On Uniform Fields in Heterogeneous Media," Proc. R. Soc. Lond. A, Vol. 431, pp. 89-110.

Fabrikant, V.I., 1989, Application of Potential Theory in Mechanics--A Selection of New Results, Kluwer Academic Publishers, Dordrecht, The Netherlands.

Ferrari, M., 1991, "Asymmetry and the High Concentration Limit of the Mori-Tanaka Effective Medium Theory," Mechanics of Materials, Vol. 11, pp. 251-156.

Gao, H. and Rice, J.R., 1987, "Somewhat Circular Tensile Cracks," Int. J. Fracture, Vol. 33, pp. 155-174.

Hu, K. X. and Chandra, A., 1993, "Interactions among general systems of cracks and anti-cracks: an integral equation approach," ASME J. Appl. Mech., 60, pp. 920-928.

Hu, K. X. and Huang, Y., 1993, "A microcracked solid reinforced by rigid-line fibers," Composites Sci. Tech., 49, pp. 145-151.

Hu, K. X., Chandra, A. and Huang Y., 1993a, "Multiple void-crack Interaction," Int. J. Solids Struc., 30, pp. 1473-1489.

Hu, K. X., Chandra, A. and Huang, Y., 1993b, "Fundamental solutions for dilute inclusions embedded in microcracked solids," Mech. Materials, Vol. 16, pp. 281-294.

Hu, K. X., Chandra, A., and Huang, Y., 1994, "On Interacting Bridged-Crack Systems," Int. J.

Solids and Struc., Vol. 31, pp. 599-611.

Huang, Y., Hu, K.X., and Chandra, A., 1993, "The Effective Elastic Moduli of Microcracked Composite Materials," Int. J. Solids and Struc., Vol. 30, pp. 1907-1918.

Huang, Y., Hu, K.X., and Chandra, A., 1994a, "A Generalized Self-Consistent Mechanics Method for Microcracked Solids," J. Mech. Phys. Solids, Vol. 42, pp. 1273-1291.

Huang, Y., Hu, K.X., and Chandra, A., 1994b, "Several Variations of the Generalized Self-Consistent Method for Hybrid Composites," Composites Sci. and Tech., Vol. 52, pp. 19-27.

Huang, Y., Hu, K.X., Wei, X. and Chandra, A., 1994c, "A Generalized Self-Consistent Mechanics Method for Composite Materials with Multiphase Inclusions," J. Mech. Phys. Solids, Vol. 42, pp. 491-504.

Huang, Y., Hwang, K. C., Hu, K.X., and Chandra, A., 1995, "A unified Energy Approach to a Class of Mechanics Models for Composite Materials," Acta Mechanica Sinica, Vol. 11, pp. 59-75.

Kachanov, M., 1985, "A Simple Technique Of Stress Analysis In Elastic Solids with Many Cracks " Int. J. Fracture, Vol. 28, pp. R11-R19.

Kachanov, M., 1987, "Elastic Solids with Many Cracks: A Simple Method of Analysis," Int. J. Solids Structures, Vol. 23, pp. 23-43

Kachanov, M., 1993, "Elastic Solids with Many Cracks and Related Problems," Advanced in Applied Mechanics (J.W. Hutchinson and T.Y. Wu, eds.), Vol. 30, pp. 259-445, Academic Press, San Diego.

Mura, T., 1982, Micromechanics of Defects in Solids, 2nd Edition, Martinus Nijhoff Publishers, The Hague, The Netherlands.

Norris, A.N., 1985, "A Differential Scheme for the Effective Moduli of Composites," Mech. Mat., Vol. 4, pp. 1-16.

Siboni, G. and Benveniste, Y., 1991, "A Micromechanics Model for the Effective Thermomechanical Behavior of Multiphase Composite Media," Mech. Mat., Vol. 11, pp. 107-122.

Tada, H., Paris, P.C., and Irwin, G.R., 1985, The Stress Analysis of Cracks Handbook, Paris Productions, Inc., St. Louis, Missouri.

Taya, M. and Chou, T.-W., 1981, "On Two Kinds of Ellipsoidal Inhomogeneities in an Infinite Elastic Body: An Application to a Hybrid Composite," Int. J. Solids Struc., Vol. 17, pp. 553-563.

Wang, Y.M. and Weng, G.J., 1992, "The Influence of Inclusion Shape on the Overall Viscoelastic Behavior of Composites," ASME J. Appl. Mech., Vol. 59, pp. 510-518.

Weng, G.J., 1984, "Some Elastic Properties of Reinforced Solids, with Special Reference to Isotropic Containing Spherical Inclusions," Int. J. Eng. Sci., Vol. 22, pp. 845-856.

Weng, G.J., 1990, "The Theoretical Connection Between Mori-Tanaka's Theory and the Hashin-Shtrikman-Walpole Bounds," Int. J. Eng. Sci., Vol. 28, pp. 1111-1120.

Zhao, Y.H., Tandon, G.P., and Weng, G.J., 1989, "Elastic Moduli of a Class of Porous Materials," Acta Mechanica, Vol. 76, pp. 105-130.

Damage Mechanics in Engineering Materials
G.Z. Voyiadjis, J.-W.W. Ju and J.-L. Chaboche (Editors)
© 1998 Elsevier Science B.V. All rights reserved.

Crack-tip singularity in damaged materials

Yan Liu and Sumio Murakami

Department of Mechanical Engineering, Nagoya University
Furo-cho, Chikusa-ku, Nagoya 464-01, Japan

The effects of the preceding damage field on the stress singularity of a growing mode III crack are investigated from the view point of *Continuum Damage Mechanics* (CDM). By postulating a circular damage field at the crack-tip represented by a power law function r^m of radius r, analytical solutions of asymptotic stress and strain fields were first obtained. It was found that the asymptotic stress field depends on the power law exponent m of the given damage distribution, and the well known elastic singularity disappears when the damage exponent m becomes larger than 3/4. However, the strain field was ascertained to be always singular regardless of the exponent m. Then, for more general damage distributions, numerical analyses by means of the finite element method were performed, and the effects of the geometry of three local damage fields on the stress distribution around the crack-tip were elucidated. It was shown that, though the damage field behind the crack-tip gives significant influence on the stress field in front of a growing crack, the analytical solution for the circular damage field gives essentially similar stress singularity as that for more general damage distribution. The results give important insights into some fundamental aspects of the local approach to fracture based on CDM.

1. INTRODUCTION

Stress and train singularity at a crack-tip plays an essential role in fracture mechanics (Broek, 1974), since it governs the stability and the rate of crack growth. Thus the crack-tip stress fields in an intact (undamaged) material have been investigated extensively; the asymptotic solutions of the stress fields have been obtained not only for linear elastic material (Irwin, 1957), but also for power-law hardening plastic material (Hutchinson, 1968; Rice and Rosengren, 1968)

However, crack growth in elastic-plastic and creep materials is usually brought about by the nucleation, growth and coalescence of microscopic cavities in the front of the crack-tip. In such fracture process, the crack-tip stress field and the stress singularity will

be influenced not only by the nonlinearity of stress-strain relation, but also by the considerable reduction of stiffness due to the material damage.

As a result of this importance, the effects of the material damage on the crack-tip stress fields have been investigated from *Continuum Damage Mechanics* (CDM) point of view in some recent papers (Wang and Chow, 1992; Zhang and Gross, 1993; Zhang, Hwang and Hao, 1993; Astafjev and Grigorova, 1995). Wang and Chow (1992), for example, analyzed the mode I stress field in a damaged power-law elastic-plastic material, and elucidated that the original HRR singularity is not largely influenced by the inclusion of damage. In their analysis, they postulated that the damage develops from an intact material and the damaged state is specified by the current field variables. Zhang and Gross (1993), on the other hand, performed a similar analysis for the asymptotic stress field of mode III crack in a power-law strain-hardening material damaged by uniformly distributed microcracks oriented in directions different from that of the main crack. This analysis shows that the stress fields in the damaged material have the same structure as that of the HRR field in an undamaged material. The asymptotic solution for mode III crack in a damaged elastic material was discussed also by Zhang, Hwang and Hao (1993) by postulating that the damage field is governed by the current strain field. Their results showed two possible damage distributions; a uniform distribution and a power-law one that takes zero at crack-tip. However, in actual crack growth problems, the damage distribution in front of the crack-tip is not uniform, but is dependent on the history of the field variables.

The damage field in front of a crack-tip is not uniform in general, and the damage field brought about by a growing crack depends on the history of the field variables governing the damage. Thus the results of the analyses based on the such damage fields cannot give sufficient information on the effects of the preceding damage on the crack behavior. In this respect, Astafjev and Grigorova (1995) derived an asymptotic stress field for a history-dependent creep damage evolution. However, their solution required an unrealistic condition that a complete damage zone exists in the 1/4 plane behind the crack-tip.

The present paper aims to elucidate the effects of the preceding damage on the stress and strain singularity at a crack-tip of a growing crack. In order to present the damage states in front of a growing crack from the viewpoint of CDM, a idealized circular damage distribution that takes a critical damage value at the crack-tip, represented by a power law function r^m of radius r, is employed first. The elastic asymptotic field of a mode III crack is obtained, and the effects of the preceding damage distribution on the stress and strain singularity are discussed. Then, in order to elaborate the analysis, finite element calculation was performed for more general damage distributions, and the resulting stress singularity is compared with the corresponding analytical solution.

Besides the stability and the rate of crack growth, the singularity of crack-tip field is influential also in the problem of mesh-dependence in the local approach of fracture based on CDM and Finite Element Method (FEM). Thus the results of the present analyses will provide important insight not only into the effects of the preceding damage on crack growth behavior, but also into the mesh-dependent problem of the local approach.

2. FIELD EQUATION AND ITS ANALYTICAL SOLUTION

2.1 Material damage and stiffness reduction

When a material is subjected to internal damage due to microscopic defects or cavities, the change in the elastic moduli will occur together with the reduction in the yield stress, tensile strength and fracture ductility of the material. According to the continuum damage theory, if the anisotropy of the damage is not salient, the internal damage can be presented by a scalar damage variable D $(0 \le D \le D_{cr})$, where D_{cr} is the critical damage value for fracture. In this case, reduction of the shear modulus μ of the material can be expressed as follows (Kachanov, 1986; Lemaitre and Chaboche, 1990):

$$\mu = \mu_0(1 - D/D_{cr}) \tag{1}$$

where μ_0 is the shear modulus of the undamaged material.

For a crack under anti-plane shear load (mode III) shown in Figure 1, we will employ two coordinate systems O-xyz and O-$r\theta z$ with the origin at the crack-tip. In the case of a growing crack, the damage variable in Eq. (1) should take its critical value $D = D_{cr}$ at $r =$ 0 (crack-tip), and decrease to $D = 0$ in the undamaged zone. In order to facilitate an ana-

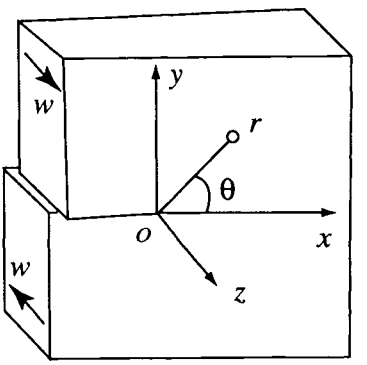

Figure 1. An anti-plane shear (mode III) crack

lytical solution, we will first suppose an idealized circular damage distribution around the crack-tip, and represent the damage variable D as follows:

$$D = D(r) \tag{2}$$

For the convenience of the following analysis, we introduce a new function to denote the reduction of shear modulus μ due to damage, i.e,

$$g(r) = \mu(r)/\mu_0 = 1 - D(r)/D_{cr} \tag{3}$$

Since $0 \le D(r) \le D_{cr}$ and $D(0) = D_{cr}$, we have the following restriction to the function $g(r)$:

$$0 \le g(r) \le 1, \quad g(0) = 0 \tag{4}$$

2.2 Basic equations and its solutions

For a mode III crack shown in Figure 1, the only non-zero displacement component is

$$w = w(r,\theta) \tag{5}$$

Thus, we have two corresponding non-zero components of shear strain and stress as follows:

$$\varepsilon_{rz} = \varepsilon_{zr} = \frac{1}{2}\frac{\partial w}{\partial r}, \quad \varepsilon_{\theta z} = \varepsilon_{z\theta} = \frac{1}{2}\frac{1}{r}\frac{\partial w}{\partial \theta} \tag{6}$$

$$\sigma_{rz} = \sigma_{zr} = \mu(r)\frac{\partial w}{\partial r}, \quad \sigma_{\theta z} = \sigma_{z\theta} = \mu(r)\frac{1}{r}\frac{\partial w}{\partial \theta} \tag{7}$$

By neglecting the body force, the equation of equilibrium of the problem leads to

$$\frac{\partial \sigma_{rz}}{\partial r} + \frac{\sigma_{rz}}{r} + \frac{1}{r}\frac{\partial \sigma_{\theta z}}{\partial \theta} = 0 \tag{8}$$

Substituting Eqs. (3) and (5)-(7) into Eq. (8), we obtain the following basic equation for the displacement w in the polar coordinate system

$$\frac{\partial^2 w(r,\theta)}{\partial r^2} + [1 + \alpha(r)]\frac{1}{r}\frac{\partial w(r,\theta)}{\partial r} + \frac{1}{r^2}\frac{\partial^2 w(r,\theta)}{\partial \theta^2} = 0 \tag{9}$$

where

$$\alpha(r) = r \cdot g'(r) / g(r) \tag{10}$$

In the special case of $D(r) = 0$, $g(r)$ is reduced to a constant and Eq. (9) recovers the conventional equation for non-damaged elastic medium.

We seek solution of Eq. (7) in the form of

$$w(r,\theta) = \hat{L} \cdot r^s \tilde{w}(\theta) \tag{11}$$

where $\hat{L}$ and s are unknown constants, and $\tilde{w}(\theta)$ is an unknown function of θ. Since the displacement w at the crack-tip ($r = 0$) is zero, the constant s in the above equation should be positive, i.e.

$$s > 0 \tag{12}$$

Substitution of Eq. (11) into Eq. (9) leads to the following ordinary differential equation for $\tilde{w}(\theta)$:

$$\tilde{w}''(\theta) + [s^2 + s\alpha(r)]\tilde{w}(\theta) = 0 \tag{13}$$

The general solution of Eq. (13) is

$$\tilde{w}(\theta) = B \cdot \cos[\theta\sqrt{s[s+\alpha(r)]}) + C \cdot \sin[\theta\sqrt{s[s+\alpha(r)]}) \tag{14}$$

where B and C are constants. Because of the asymmetry of the anti-plane shear deformation of $\tilde{w}(\theta)$, we have

$$B = 0 \tag{15}$$

Substituting Eqs. (14) and (15) into (9), we have the general solution of Eq. (9) as follows:

$$w(r,\theta) = L \cdot r^s \sin[\theta\sqrt{s[s+\alpha(r)]}] \tag{16}$$

where $L = C \cdot \hat{L}$. Shear stress components $\sigma_{\theta z}$ and σ_{rz} are now obtained from Eq. (16) and Eq. (7) as follows:

$$\sigma_{rz} = L \cdot \mu(r) r^{s-1} \{s \cdot \sin[\theta\sqrt{s[s+\alpha(r)]}] + \cos[\theta\sqrt{s[s+\alpha(r)]}] \frac{s\theta}{2\sqrt{s[s+\alpha(r)]}} [\alpha(r) - \alpha(r)^2 + \beta(r)]\} \tag{17}$$

$$\sigma_{\theta z} = L \cdot \mu(r) r^{s-1} \sqrt{s[s+\alpha(r)]} \cos[\theta\sqrt{s[s+\alpha(r)]}] \tag{18}$$

where the function $\beta(r)$ is defined as

$$\beta(r) = r^2 \cdot g''(r)/g(r) \tag{19}$$

Finally Stress free boundary conditions on the crack surfaces require that

$$\sigma_{\theta\theta}(\pm\pi) = 0 \tag{20}$$

In view of Eq. (18), this implies

$$\cos(\pi\sqrt{s[s+\alpha(r)]}) = 0 \tag{21}$$

or

$$\sqrt{s[s+\alpha(r)]} = \frac{k}{2}, \quad k = 1,3,5... \tag{22}$$

By solving Eq. (21), we have

$$s = \frac{\sqrt{\alpha(r)^2 + k^2} - \alpha(r)}{2}, \quad k = 1,3,5... \tag{23}$$

where another root of s from Eq. (21) has been excluded because of the condition (11).

2.3 Power law damage distribution

In view of Eq. (23), in order that the exponent s may be a constant as assumed in Eq. (11), the damage (or the shear modulus) distribution function $g(r)$ should satisfy the following relation:

$$\alpha(r) = \frac{r \cdot g'(r)}{g(r)} = m \ (= const.) \tag{24}$$

where m is a constant. Solving the differential equation (24) with the condition $(4)_2$, we obtain the following power law function for the damage distribution:

$$g(r) = (r/r_0)^m \tag{25}$$

where r_0 is a constant, and represents a characteristic size of the damage zone. While $r < r_0$ gives $D > 0$ and $\mu < \mu_0$, we have $D = 0$ and $\mu = \mu_0$ when $r = r_0$. According to the Eq. $(4)_1$, we have the following restriction to the function $g(r)$:

$$r_0 \geq r \geq 0, \quad m > 0 \tag{26}$$

According to Eq. (24), the existence of a power law type solution of Eq. (9) requires that the damage distribution function $g(r)$ should be a power law type. However, it is worth emphasizing that the power law distribution of damage, Eq. (25), can be an asymptotic representation to an arbitrary damage distribution g(r) which tends to zero $o(r^m)$ (with $m > 0$) for $r \to 0$.

In the following analysis, the power-law type distribution of damage (25) will be employed to investigate the effects of damage field on the crack-tip stress field. Figure 2 shows the power-law damage distribution for different values of exponent m.

2.4 General solutions of deformation and stress

A general solution of the problem can be obtained for a power law damage distribution (25). By use of Eqs. (24) and (25) we can now rewrite Eq. (23) as

$$s = \frac{\sqrt{m^2 + k^2} - m}{2}, \quad k = 1,3,5... \tag{27}$$

Then, by use of Eq. (25), Eq. (19) leads to

$$\beta(r) = m(m-1) \tag{28}$$

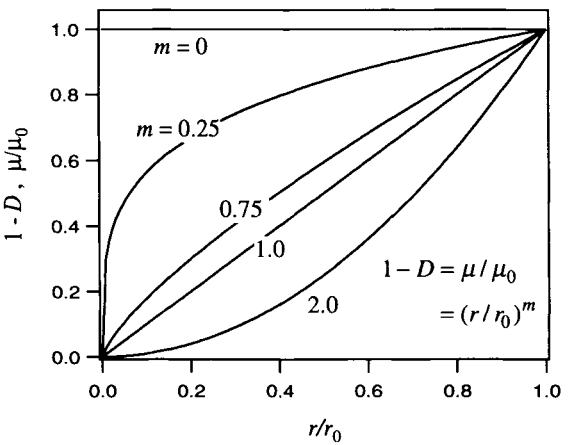

Figure 2. Distribution of damage and variation of shear modulus in front of a crack-tip

Substituting Eqs. (24), (27) and (28) into Eqs. (16)-(18), and summing up every terms for $k = 1, 3, 5,...$, we obtain the following general solutions for deformation and stress:

$$w(r,\theta) = \sum_{j=1}^{M} L^{(2j-1)} \cdot r^{(\sqrt{m^2+(2j-1)^2}-m)/2} \sin[(2j-1)\theta/2] \tag{29}$$

$$\sigma_{rz} = \frac{\mu(r)}{2} \sum_{j=1}^{M} \{L^{(2j-1)} \cdot r^{(\sqrt{m^2+(2j-1)^2}-m-2)/2} (\sqrt{m^2+(2j-1)^2}-m)\sin[(2j-1)\theta/2]\} \tag{30}$$

$$\sigma_{\theta z} = \frac{\mu(r)}{2} \sum_{j=1}^{M} \{L^{(2j-1)} \cdot r^{(\sqrt{m^2+(2j-1)^2}-m-2)/2} (2j-1)\cos[(2j-1)\theta/2]\} \tag{31}$$

where $L^{(2j-1)}$ (j=1,2,3...) are unknown constants which should be determined from the remote boundary conditions.

2.5 Asymptotic fields of stress and strain

In order to elucidate the effects of damage distribution on the singular stress field, we are more interested in the asymptotic solution for $r \to 0$. Since the power law damage function employed in the present analysis can be considered as an asymptotic representation to arbitrary damage distribution, the asymptotic solutions of Eqs. (29)-(31) give more general insight into the crack behavior in damaged materials.

When $r \to 0$, the dominant terms of the general solutions (29)-(31) are those with minimum exponent j of r. Thus we obtain the asymptotic solutions of the deformation and stress fields as follows:

$$w^{(a)}(r,\theta) = \sqrt{\frac{2}{\pi}} \frac{P_{III} r_0^m}{\mu_0} \cdot r^{(\sqrt{m^2+1}-m)/2} \cdot \sin\frac{\theta}{2} \tag{32}$$

$$\sigma_{xz}^{(a)}(r,\theta) = \frac{P_{III}}{\sqrt{2\pi}} \cdot r^{(\sqrt{m^2+1}+m-2)/2} \cdot \tilde{\sigma}_{xz}(\theta,m) \tag{33}$$

$$\sigma_{yz}^{(a)}(r,\theta) = \frac{P_{III}}{\sqrt{2\pi}} \cdot r^{(\sqrt{m^2+1}+m-2)/2} \cdot \tilde{\sigma}_{yz}(\theta,m) \tag{34}$$

where P_{III}, $\tilde{\sigma}_{xz}(\theta,m)$ and $\tilde{\sigma}_{yz}(\theta,m)$ are parameter and functions representing the magnitude and the circumferential distribution of the asymptotic fields, and are given by

$$P_{III} = \sqrt{\frac{\pi}{2}} \frac{L^{(1)}\mu_0}{r_0^m} \tag{35}$$

$$\tilde{\sigma}_{xz}(\theta,m) = -[1-(\sqrt{m^2+1}-m-1)\cos\theta]\sin\frac{\theta}{2} \tag{36}$$

$$\tilde{\sigma}_{yz}(\theta,m) = [\sqrt{m^2+1}-m-(\sqrt{m^2+1}-m-1)\cos\theta]\cos\frac{\theta}{2} \tag{37}$$

In Eqs. (32)-(34), the superscript "(a)" denotes the asymptotic solution.

Figures 3 and 4 show, respectively, the radial and the circumferential distribution of the stress fields (33)-(34) for several different values of m. In particular, it will be observed from Figure 3 that the stress singularity will disappear if the exponent m becomes larger than 0.75. Because of its importance, the effect of damage distribution on stress singularity will be discussed in some details in the next Section.

Substituting Eq. (32) into Eq. (6), we obtain also the asymptotic strain fields as follows:

$$\varepsilon_{rz}^{(a)}(r,\theta) = \sqrt{\frac{2}{\pi}}\frac{P_{III}r_0^m}{\mu_0}r^{-(m+2-\sqrt{m^2+1})/2}\cdot(\sqrt{m^2+1}-m)\sin\frac{\theta}{2} \tag{38}$$

$$\varepsilon_{\theta z}^{(a)}(r,\theta) = \sqrt{\frac{2}{\pi}}\frac{P_{III}r_0^m}{\mu_0}r^{-(m+2-\sqrt{m^2+1})/2}\cdot\cos\frac{\theta}{2} \tag{39}$$

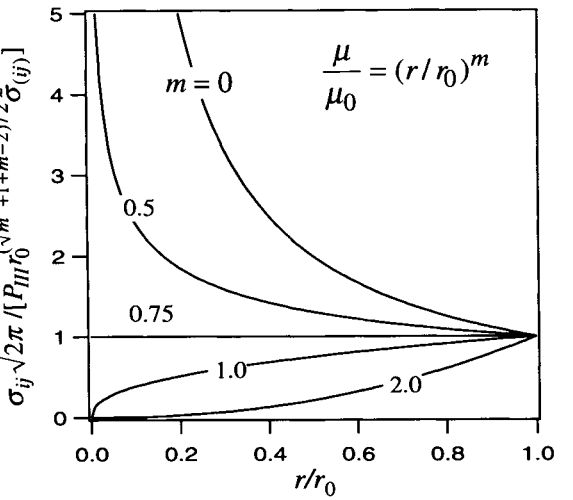

Figure 3. Radial distribution of asymptotic stress field in front of a crack-tip in elastic-damage material

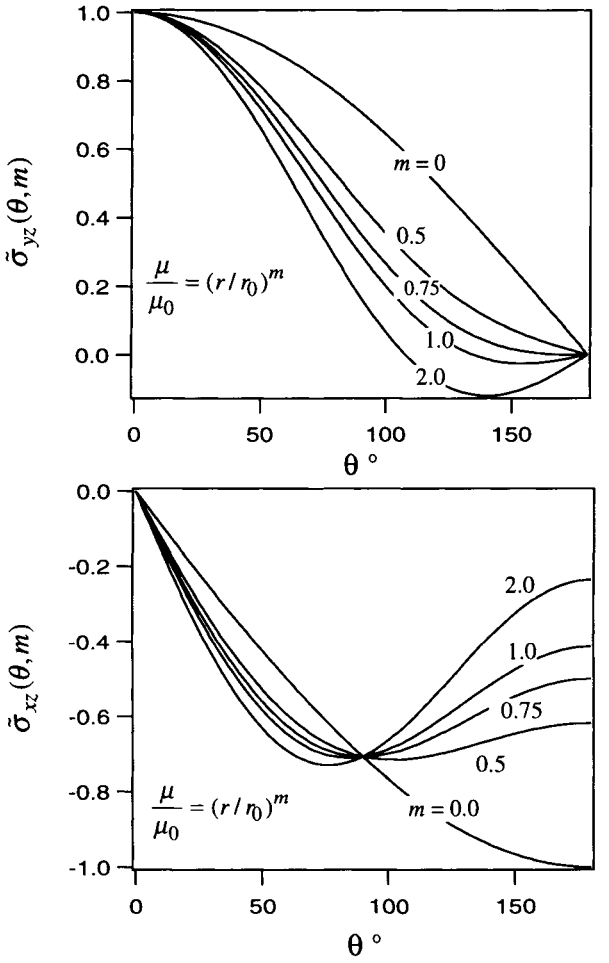

Figure 4. Circumferential distribution of asymptotic stress field in front of a crack-tip in elastic damage material

Obviously, when $m = 0$, the above solutions will recover to the well known elastic strain fields with -1/2 singularity. However, for any positive value of the damage exponent m, the strain exponent $-(m + 2 - \sqrt{m^2 + 1})/2$ is always negative, which implies that the crack-tip strains are always singular in the present solutions. This is not surprising because the damage distribution assumed in the present analysis takes a critical damage value at the crack-tip. Such a crack-tip of critical damage implies a growing crack, or a separation

process of the material element at the crack-tip, and thus we have infinite (singular) strains at the crack-tip.

3. EFFECTS OF DAMAGE DISTRIBUTION ON STRESS SINGULARITY

It was observed from Figure 3 that the radial distribution of asymptotic stress fields are influenced significantly by the exponent m of the damage distribution; in particular, the well known stress singularity in a cracked elastic material will disappear in a damaged material for $m \geq 3/4$. This influence of the exponent m on the crack-tip stress singularity will be discussed in more detail.

3.1 Case $m = 0$

Substitution of $m = 0$ into Eqs. (32)-(34) gives conventional elastic crack-tip field that has a well-known singularity of -1/2; i.e.

$$w^{(a)}(r,\theta) = \frac{K_{III}}{\mu_0}\sqrt{\frac{2r}{\pi}} \cdot \sin\frac{\theta}{2} \tag{40}$$

$$\sigma_{xz}(r,\theta) = -\frac{K_{III}}{\sqrt{2\pi r}} \cdot \sin\frac{\theta}{2} \tag{41}$$

$$\sigma_{yz}(r,\theta) = \frac{K_{III}}{\sqrt{2\pi r}} \cdot \cos\frac{\theta}{2} \tag{42}$$

where stress intensity factor K_{III} is given by

$$K_{III} = \underset{r\to 0}{Lim}[\sqrt{2\pi r}(\sigma_{yz})\big|_{\theta=0}] = \sqrt{\frac{\pi}{2}}L^{(1)}\mu_0 = P_{III}\big|_{m=0} \tag{43}$$

Obviously, Eqs. (3) and (24) show that an undamaged elastic medium $D = 0$ leads to $m = 0$. Moreover, the condition $m = 0$ implies also a transient damage state in which a crack-tip is not completely damaged, or $D < D_{cr}$ at the crack-tip. The damage distribution in this transient damage state is illustrated in Figure 5, and can be represented by a relation

$$g(r) = \xi[1 + \eta(r)] \tag{44}$$

where ξ $(0 < \xi < 1)$ is a parameter, and $\eta(r)$ is an arbitrary function for which $\eta(0) = 0$ and $\eta'(0)$, $\eta''(0)$ exist.

Substituting Eq. (42) into Eqs. (24) and (19), and taking a limit of $r \to 0$, we have

$$m = 0, \quad \beta = 0 \tag{45}$$

This shows that, Eqs. (40)-(42) are also the asymptotic solutions for a crack with a partly damaged crack-tip shown in Figure 5. Then, the correspondent stress intensity factor leads to

$$K_{III} = \sqrt{\frac{\pi}{2}} \xi L^{(1)} \mu_0 \tag{46}$$

which is subjected to the influences of damage through ξ and $L^{(1)}$ and is smaller than the value given by Eq. (43). As an important example of this partly damaged crack-tip, we can take an artificial crack which is under loading but has not started to grow. However, when the crack-tip is completely damaged and the crack growth is started, the crack-tip fields will be changed from Eqs. (40)-(43) for $m = 0$ to Eqs.(32)-(37) for $m \neq 0$.

So far a number of papers (Schovanec, 1986; Ang and Clements, 1987; Konda and Erdogan, 1994) on the stress intensity factor of a crack in the elastic medium with non-uniform elastic modulus have been published, they are mainly related to the fracture problems of functionally gradient materials. In particular, when the elastic modulus at the crack-tip is smaller (but not zero) than that of the other part of the material, the stress intensity factor has been found to be smaller than that of a crack in a uniform elastic medium (Ang and Clements, 1987).

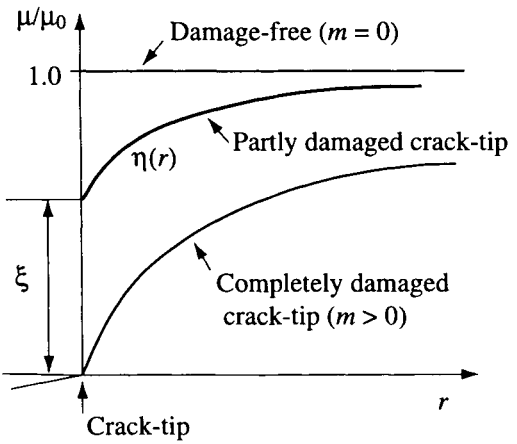

Figure 5. Distribution of elastic modulus for a partly damaged crack-tip

3.2 Case $0 < m < 3/4$

In this case, the crack-tip is completely damaged and the elastic modulus at the crack-tip becomes zero. However, as shown in Figure 2, the damage variable D decreases rapidly in the neighborhood of the crack-tip. Under this condition, we can find that the crack-tip stress still has a singularity of s ($-1/2 < s < 0$), because the exponent of r in stress fields (33) and (34) is smaller than 0, i.e.

$$-1/2 < (\sqrt{m^2+1}+m-2)/2 < 0 \tag{47}$$

Obviously, the intensity of the singularity has differed from the -1/2 singularity of the undamaged material due to the influences of damage. The larger the exponent m of the damage distribution is, the weaker singularity we have. Namely, for a growing crack influenced by the preceding damage field, K_{III} is no more a proper parameter to describe the intensity of the asymptotic stress field, and hence the parameter P_{III} defined in Eq. (35) should be employed. According to the present analysis, the parameter P_{III} contains two important factors of the preceding damage fields, i.e., damage exponent m and damage zone size r_0. Therefore, this parameter provides a novel possibility to describe the transient effects of crack growth under non-steady state; the transient effects can be naturally included into the parameter P_{III} of crack growth.

3.3 Case $m \geq 3/4$

Stress singularity at a crack-tip will disappear in this case, because the exponent s of r in stress fields (33) and (34) is now positive, i.e.

$$s = \sqrt{m^2+1}+m-2 \geq 0 \tag{48}$$

As observed in Figure 2, we have a moderate damage distribution in the vicinity of crack-tip when $m \geq 3/4$. This means that, when the decrease of the damage variable at the crack-tip is not so sharp, or not steeper than $r^{3/4}$, the crack-tip stress field will become non-singular.

From physical point of view, crack-tip stress should be finite rather than singular. Hitherto, this has been explained by considering the plastic zone in the front of crack-tip. However, the present analysis for the first time clarifies the important role of the preceding damage zone in the vanishing of the stress singularity. Moreover, the present analysis gives an analytical expression for the damage distribution that will lead to non-singular stress field. It should be noted that, the important effects of the damage zone on the stress singularity can not be clarified if a partly damaged crack-tip (Figure 5) is postulated in the

analysis (Wang and Chow, 1992).

As one of the most important problems in the development of the local approach of fracture based on CDM and FEM, the mesh-dependence due to stress singularity in front of crack-tip has been often discussed (Liu, Murakami and Kanagawa, 1994; Murakami and Liu, 1996). The present results elucidate an essential condition to ensure mesh-independent solution in local approach. Namely, for certain damage distribution ($m \geq 3/4$ in the present elastic damage case), the stress singularity and the related mesh-dependence will naturally disappear without use of any non-local numerical procedures (Pijaudier-Cabot and Bazant, 1986; Bazant and Pijaudier-Cabot, 1988; Chaboche, 1988).

4. NUMERICAL ANALYSIS FOR MORE GENERALDAMAGE DISTRIBUTIONS

The analyses in the preceding Section were conducted for an idealized radial distribution $g(r)$ of damage, as shown in Figure 6(a). Although this can be a good approximation to the damage fields in front of crack-tip, it is worth examining the effects of the damage distribution in the circumferential direction, particularly the effects of the damage "wake" behind the crack-tip. In this Section, we will discuss the effects of more general damage distribution by means of Finite Element Method (FEM). The validity of the analytical solution for circular damage field will be also discussed.

4.1 Damage distribution and finite element model

Finite element analysis will be performed for the following three kinds of damage distribution around a crack as shown in Figure 6:

1) Distribution A [Figure 6(a)]

This is the same radial distribution as that used in the analytical analysis of Section 2 and 3. The numerical analysis for this damage distribution is conducted in order to confirm the accuracy of the FEM analysis and to provide a basis for the comparison with other damage distributions. From Eqs. (2) and (25), we have the following elastic modulus in the circular damage zone with its center at the crack-tip:

$$\mu = \mu_0 (r / r_0)^m \tag{49}$$

where r_0 is damage size shown in Figure 6.

2) Distribution B [Figure 6(b)]

In this case, a wake zone is added to the above radial distribution A. Thus, inside the

damage zone shown in Figure 6(b), we have

$$\mu = \begin{cases} \mu_0 (r/r_0)^m & x \geq 0 \\ \mu_0 (y/r_0)^m & x < 0 \end{cases} \tag{50}$$

(3) Distribution C [Figure 6(c)]

In general, larger stress is induced in front of a crack-tip than the region lateral to the crack, and thus the damage develops more significantly in the direction of crack than in its circumferential direction. In view of this situation, a semi-elliptic damage zone in front of crack is assumed in this case as shown in Figure 6(c), where the length of the damage zone on the y-axis remains to be r_0 while that on the x-axis will be taken as kr_0 $(k>1)$. In this distribution, the elastic modulus inside the damage zone is given as follows:

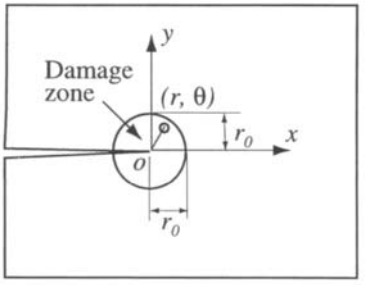

(a) Damage distribution A

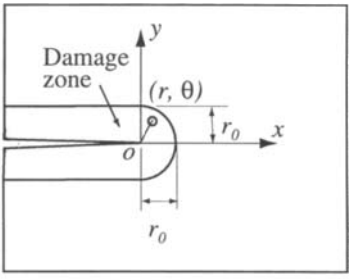

(b) Damage distribution B

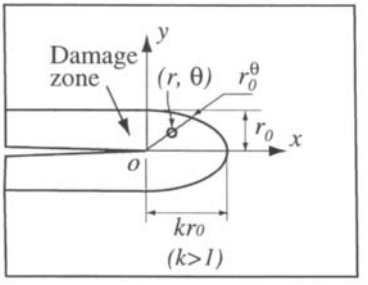

(c) Damage distribution C

Figure 6. Three damage distributions employed in the analyses

$$\mu = \begin{cases} \mu_0 (\sqrt{(x/k)^2 + y^2}/r_0)^m & x \geq 0 \\ \mu_0 (y/r_0)^m & x < 0 \end{cases} \tag{51}$$

In the succeeding finite element analysis, the elastic modulus at every Gaussian points inside the damage zone will be prescribed by one of the above damage distribution, Eqs. (49)-(51). For those Gaussian points outside the damage zone, the elastic modulus is taken to be μ_0.

A cracked specimen as shown in Figure 7 is implemented in the finite element calculations by use of ABAQUS code. The crack size a and the damage zone size r_0 of the specimen are taken as follows:

$$a = 0.1W \tag{52}$$

$$r_0 = 0.05a = 0.005W \tag{53}$$

This quite small damage zone size is selected in order to simulate the situation of a constrained damage field around an elastic crack.

The specimen is discretized by 135 20-node isoparametric elements. The partial finite element meshes around the crack-tip is shown in Figure 7. To ensure the accuracy of stress distribution inside the damage zone, the element size Δe (Figure 7) in front of crack-tip is controlled as small as

$$\Delta e = 0.02 r_0 \tag{54}$$

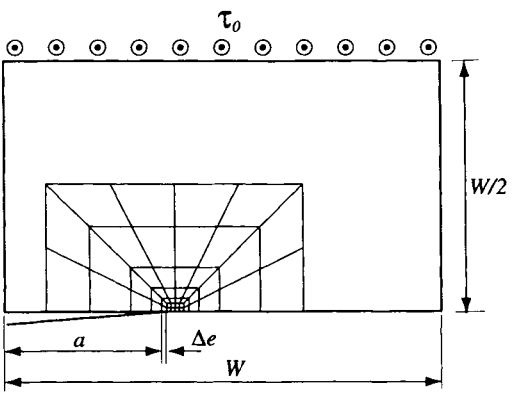

Figure 7. Specimen geometry and finite element meshes (part) at a crack-tip

4.2 Comparison between numerical and analytical solutions

Figure 8 shows comparison between numerical and analytical results of shear stress distribution on the crack line ($\theta = 0$) in front of a crack-tip, for the circular damage distribution of Figure 6(a). Let us first compare the results for the undamaged case ($m = 0$) where the numerical solution of crack-tip stress field can be compared with the well known K_{III}-field of fracture mechanics. Excellent agreement can be observed, and the maximum average error in the numerical results for τ_{yz} is smaller than 1.5%. This confirms that, the good accuracy of the numerical solution can be achieved by the use of the present finite element model.

Then, for the cases of damaged material ($m > 0$), similar comparison is observed in Fig 8. The theoretical curves of these cases are calculated by use of Eq. (34). Then, the values of P_{III} are obtained by best fitting the analytical equation (34) with the numerical results. The good correlation between the analytical and the numerical results is confirmed also for different m values. Then, the r-distribution of crack-tip stress field obeys a power law of $r^{(\sqrt{m^2+1}+m-2)/2}$, and thus the stress singularity is governed by the damage exponent m and disappears when $m \geq 0.75$.

4.3 Effects of more general damage distribution

Figure 9 shows the numerical results of the crack-tip stress fields obtained for the damage distribution A, B and C (with $k = 2.0$) of Figure 6. Several different values of expo-

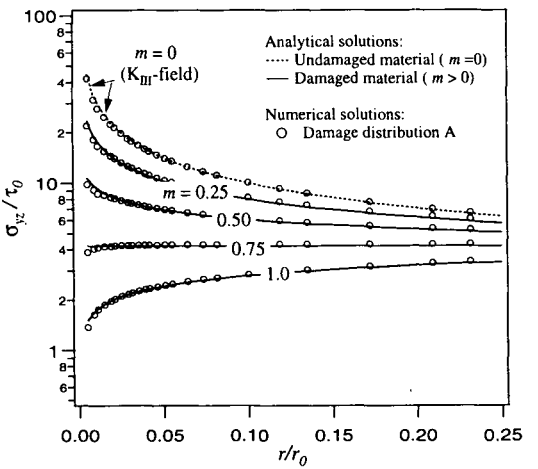

Figure 8. Comparison between numerical and an analytical stress distributions obtained for damage distribution A

nent m have been employed in these calculations. For a specific m value, the curves corresponding to the damage distribution A, B and C show almost same distribution to each other, although there exist some differences in stress values. These results implies that, for more general damage distribution, the analytical solution of Eqs. (33)-(34) can be employed also as a good approximation to describe the effects of damage distribution on the stress singularity in the front of a crack-tip.

In Figure 9, it is found that stress values are almost the same for the damage distribution B and C in a zone very close to the crack-tip. This implies that the shape of the damage zone has not apparent effects on the crack-tip stress fields. In contrast to this, the existence of a wake zone of the damage has salient influences on the stress fields. It is found that, the damage distribution A which contains no wake zone of damage gives a stress field about 10-30% larger than those of the damage distribution B and C. For obtaining a more precise asymptotic stress field for a growing crack surrounded by a damage zone, the distribution of the preceding damage, i.e., the wake zone of damage will play an essential role.

5. CONCLUSIONS

In order to elucidate the crucial effects of the preceding damage field on the stress singularity at a growing crack, elastic field of mode III crack was analyzed for three different distribution of the preceding damage. In the asymptotic analysis of Section 2 and 3,

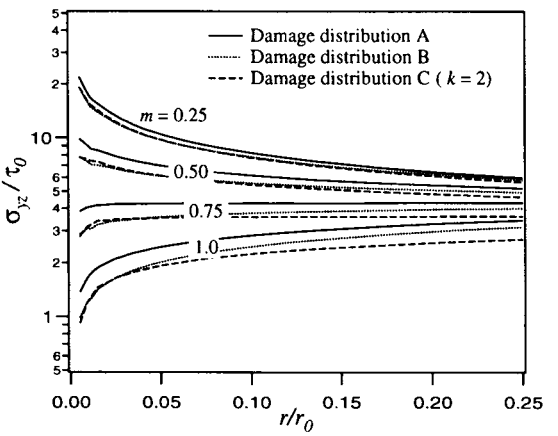

Figure 9. Comparison of stress distributions obtained by use of damage dustribution A, B and C

an idealized circular damage distribution represented by a power law function r^m of the distance r from the crack-tip was employed. The resulting analytical solution in this case elucidates that an elastic stress singularity is governed by the exponent m that specifies the essential characteristics of the damage distribution, and the singularity will disappear when m becomes larger than 0.75.

The results of Eqs. (33)-(34) of the present analysis revealed, for the first time, the important role of the preceding damage zone in the evaluation of the stress singularity at a growing crack. Although it has been inferred that the crack-tip stress should be zero in a damaged medium (Riedel, 1987; Riedel, 1990), the precise analytical behavior has not been clarified hitherto. However, according to the present analysis, the zero stress at the crack-tip was predicted for larger value of the exponent m of damage distribution.

These analytical results give us some important insight into the numerical simulation based CDM. The mesh-dependence of FEM analysis and other numerical difficulties in the crack growth analysis by local approach have been urgent problems for many years, and are closely related to the stress singularity. The present results indicates a new way to avoid these problems; i.e., the improvement of the damage evolution and the constitutive equations may furnish moderate damage distribution ($m \geq 3/4$ in the present elastic damage case), and thus may avoid the singularity in the numerical simulation.

In Section 4, FEM analysis was performed to investigate the effects of more general distributions of the preceding damage. According to the results of the analysis for these different distributions, no essentially differences in the stress singularity have been found. However, the important role of the wake zone of damage distribution (i.e., the damage distribution behind the crack-tip) has been revealed.

Although the present results are derived for a mode III crack in elastic medium subjected to damage, the similar problems for a mode I crack have been analyzed and will be published elsewhere.

Acknowledgments æ The authors are grateful for the financial support by the Ministry of Education, Science, Sports and Culture of Japan Under the Grant-in-Aid for Developmental Research (B) [No. 07555346] for the fiscal years of 1995 and 1996.

REFERENCES

Ang, W. T. and Clements, D. L. (1987). On some crack problems for inhomogeneous elastic materials. *International Journal of Solids and Structures.* **23**, 1089-1104.

Astafjev, V. I. and Grigorova, T. V. (1995). Stress and damage distribution near the tip of a crack

growing under creep. *Mechanics of Solids.* **30**, 144-149.

Bazant, Z. P. and Pijaudier-Cabot, G. (1988). Nonlocal continuum damage localization instability and convergence. *Journal of Applied Mechanics, Transaction of ASME.* **55**, 287-293.

Broek, D. (1974). *Elementary fracture mechanics*, Noordhoff, Groningen.

Chaboche, J. L. (1988). Phenomenological aspects of continuum damage mechanics. *Proc. 17th IUTAM*, Grenoble, France (Edited by Vol. pp.

Hutchinson, J. W. (1968). Singular behavior at the end of a tensile crack in a hardening material. *Journal of the Mechanics and Physics of Solids.* **16**, 13-31.

Irwin, G. R. (1957). *Journal of Applied Mechanics, Transaction of ASME.* **24**, 361.

Kachanov, L. M. (1986). *Introduction to Continuum Damage Mechanics*, Martinus Nijhoff, Dordrecht.

Konda, N. and Erdogan, F. (1994). The mixed mode crack problem in a homogeneous elastic medium. *Engineering Fracture Mechanics.* **47**, 533-545.

Lemaitre, J. and Chaboche, J. L. (1990). *Mechanics of Solid Materials*, Cambridge University Press, Cambridge.

Liu, Y., Murakami, S. and Kanagawa, Y. (1994). Mesh-dependence and stress singularity in finite element analysis of creep crack growth by continuum damage mechanics. *European Journal of Mechanics A/Solids.* **13**, 395-417.

Murakami, S. and Liu, Y. (1996). Local approach of fracture based on continuum damage mechanics and the related problems. *Material Science Research International.* **2**, 131-142.

Pijaudier-Cabot, G. and Bazant, Z. P. (1986). Nonlocal damage theory. *Journal of Engineering Mechanics, ASCE.* **113**, 1512-1533.

Rice, J. R. and Rosengren, G. F. (1968). *Journal of the Mechanics and Physics of Solids.* **16**, 1-12.

Riedel, H. (1987). *Fracture at High Temperatures*, Springer-Verlag, Berlin.

Riedel, H. (1990). Creep crack growth under small-scale creep conditions. *International Journal of Fracture.* **42**, 173-188.

Schovanec, L. (1986). A Griffith crack problem for an inhomogeneous elastic material. *Acta Mechanica.* **58**, 67-80.

Wang, J. and Chow, C. L. (1992). HRR fields for damaged material. *International Journal of Fracture.* **54**, 164-183.

Zhang, C. and Gross, D. (1993). Near-tip field of an anti-plane crack in a micro-cracked power-law solid. *International Journal of Fracture.* **60**, 107-120.

Zhang, X. T., Hwang, K. C. and Hao, T. H. (1993). Asymptotic solution of mode-III crack in damaged softening materials. *International Journal of Fracture.* **62**, 269-281.

Damage Mechanics in Engineering Materials
G.Z. Voyiadjis, J.-W.W. Ju and J.-L. Chaboche (Editors)
1998 Elsevier Science B.V.

Micromechanics of Fatigue Crack Initiation of Single Crystal under Plane Strain

T.H. Lin[a], K. Wong[b], and N.J. Teng[c]

[a,b,c]Department of Civil & Environmental Engineering, University of California, Los Angeles
P.O. Box 951593, Los Angeles, CA 90095-1593

The micromechanic analysis of a fatigue band in the most favorably oriented crystal at the free surface of a polycrystal is extended to the analysis of a single crystal under plane strain. The boundary tractions on the boundaries of the crystal embedded in the polycrystal are removed by applying equal and opposite tractions. The stress field caused by these opposite tractions is analyzed using finite element method. Extrusions on both sides the of single crystals as commonly observed is shown in the analytical calculations.

1. INTRODUCTION

Single crystals have been used in component parts of turbine engines. These parts are subject to repeated mechanical and thermal loadings. It has been found that about 90% of the catastrophic failures of these parts are due to fatigue of materials [1]. Hence, understanding the mechanism of these failures is essential to their reductions. The present study attempts to give a method to analyze the fatigue crack initiation of these single crystals.

Lin [2] and Lin et al. [3] have developed a physical model to analyze the high-cycle fatigue crack initiation of a face-centered cubic (f.c.c.) polycrystal. This model is amended to analyze the fatigue crack initiation of f.c.c. single crystals.

Single crystal tests show that under loading, slip occurs along certain directions on certain planes. This slip depends on the resolved shear stress and is independent of the normal stress on the sliding plane. The dependence of slip on the resolved shear stress, known as Schmid's law, has been shown by Parker [4] to hold also for cyclic loadings. Initial defects exist in all metals and cause an initial stress field, which gives an initial resolved shear stress field τ^i in the metal. The shear stress due to applied load is denoted by τ^a. When this τ^a combined with τ^i reaches the critical shear stress τ^c in some region, slip occurs to keep the resolved shear stress from exceeding the critical. After unloading, the slip remains and causes a residual resolved shear stress field τ^r. The total resolved shear stress is then

$$\tau = \tau^a + \tau^i + \tau^r \tag{1}$$

The governing condition to initiate or continue slip in a region is to have this resolved shear stress τ equal to τ^c.

To calculate the residual stress, the analogy between plastic strain and applied force is used [5]. It has been shown that the equivalent body force per unit volume along x_i-axis due to plastic strain e''_{ij} is

$$F_i = -C_{ijkl} e''_{kl,j} \tag{2}$$

where C_{ijkl} is the elastic constants of the metal. The repetition of alphabetic subscripts denotes summation and the subscript after a comma denotes differentiation with respect to the coordinate variable. The equivalent surface force per unit area along x_i-axis has been shown as

$$S_i = C_{ijkl} e''_{kl} \eta_j \tag{3}$$

where η_j is the cosine of the angle between the exterior normal to the surface and the x_j-axis. In the following analysis, the slip plane and the slip direction of the crystal is taken to form a 45° angle with the specimen axis.

Extrusions and intrusions have been observed to grow monotonically on fatigued specimens [6]. Kinematically, an extrusion forms when a positive shear strain occurs in a thin slice P and a negative shear strain in a closely located thin slice Q (see Figure 1). The initial stress field τ' favorable to this mode of slip is one having positive shear stress in P and negative in Q. Such an initial stress field can be provided by an initial tensile strain $e'_{\alpha\alpha}$ in R (the repetition of Greek subscript does not denote summation). Lin and Ito [7] suggested that the tensile strain $e'_{\alpha\alpha}$ in R along the slip direction α may be provided by a row of interstitial dipoles. Antonopoulos et al. [8] and Mughrabi et al. [9] have indicated that the ladder structure in a persistent slip band (PSB) can be described by an array of edge dislocation dipoles. A tensile loading τ_{22} on the polycrystal produces a positive τ^a in the whole crystal. Taking τ' to be positive in P and negative in Q, then $\tau' + \tau^a$ in P will first reach τ^c, prompting P to slide. This slip causes a residual shear stress $\tau^r_{\alpha\beta}$. The length of the crystal (along x_3-axis, normal to the plane of Figure 1) is assumed to be much longer than the band thickness. In the center length portion of the crystal, the slip and hence the plastic strain distributions along the band is assumed to be constant along the x_3-axis. This causes the deformation to be plane strain, and hence $\partial\tau_{\alpha 3}/\partial x_3 = 0$. Applying the equilibrium condition $\tau_{ij,j} = 0$ in terms of the (α,β,x_3) coordinates gives $\partial\tau_{\alpha\alpha}/\partial x_\alpha + \partial\tau_{\alpha\beta}/\partial x_\beta = 0$. The first term is generally small, so the second term is also small. Hence the change in $\tau^r_{\alpha\beta}$ across the small

band thickness (from P to Q) is very small. As a result, the slip in P reduces not only the positive shear stress in P, but also reduces the same amount of positive shear stress in Q. This decrease of positive shear stress is the same as increase of negative shear stress, causing Q to slide more readily during the reversed loading [7]. Similarly, the negative slip in Q reduces the negative shear stress not only in Q but also in P, thus causing P to slide more readily during the second forward loading. This process is repeated for every cycle and thus provides a natural gating mechanism to cause the alternate slip in P and Q, resulting in monotonic growth of the extrusion. Interchanging the signs of the initial stresses will produce an intrusion instead of an extrusion. This gating mechanism does not require the crystal to have more than one slip plane such as a f.c.c. crystal, hence is also applicable to hexagonal crystals.

The build-up of the slip strain $e''_{\alpha\beta}$ in P and Q is caused by $e^{i}_{\alpha\alpha}$ in R. This $e^{i}_{\alpha\alpha}$ causes an initial compression in R, which in turn causes positive $\tau^{i}_{\alpha\beta}$ in P and negative $\tau^{i}_{\alpha\beta}$ in Q. Under cyclic loading, the extrusion grows and R increases in length. This elongation causes the compression in R to decrease. There are 12 slip systems in a f.c.c. crystal. The change of direct stress $\tau_{\alpha\alpha}$ in R causes changes in resolved shear stress in all slip systems. When the decrease in compression in R becomes large, the applied stress can cause a second slip system to have shear stress reaching the critical value and slide. The plastic strain $e''_{\xi\eta}$ caused by slip in this secondary slip system has a tensor component just like $e^{i}_{\alpha\alpha}$ in causing the positive and negative $\tau^{i}_{\alpha\beta}$ in P and Q, respectively. The occurrence of the secondary slip system was recently clearly observed by Zhai et al. [10]. The 12 slip systems of a f.c.c. crystal are shown in Figure 2. The $\alpha\beta$ slip system in Figure 1 is called the primary slip system, which is identified as a_2 system in Figure 2. The secondary slip system due to the change of direct stress $\tau_{\alpha\alpha}$ under cyclic loading was found by Lin et al. [3] to be c_3. The plastic strain $e''_{\xi\eta}$ due to the slip has a tensor component $e''_{\alpha 3}$, which induces an equivalent force component F_3. The presence of F_3 requires the modification of the plane strain solution. A similar problem was shown in the analysis of prismatic bars by Lekhnitski [11] and is referred to as the generalized plane strain problem. This problem is defined as

$$u_i = u_i(x_1, x_2) \quad , \quad i = 1,2,3 \tag{4}$$

The stress in an isotropic elastic body is given as

$$\tau_{ij} = 2\mu\left[\frac{\upsilon}{1+2\upsilon}\delta_{ij}\Theta + \frac{1}{2}\left(u_{i,j} + u_{j,i}\right)\right] \tag{5}$$

where $\Theta = u_{1,1} + u_{2,2}$, μ is the shear modulus, and υ is the Poisson's ratio.

2. METHOD OF ANALYSIS

To analyze the fatigue band in a single crystal under generalized plane strain, consider a crystal embedded at a free surface of a polycrystal under alternate tension and compression. The sliding direction and the slip plane make 45° with the free surface and the loading axis (see Figure 1). The solutions of the plastic strain distributions in the fatigue band of the polycrystal have been shown by Lin et al. [3]. Melan [12] has given a plane stress solution of the stress field due to a given loading on a semi-infinite plate. His solution has been modified by Tung and Lin [13] for plane strain. This plane strain solution is then generalized to include the generalized plane strain deformation. Let $\tau_{ij}(\mathbf{x},\mathbf{x}'_k)$ be the stress at point $\mathbf{x}$ due to a unit force applied at point $\mathbf{x}'$ along the x_k-direction. The stress components are expressed in terms of the Airy stress functions, ϕ_k's, as

$$\tau_{11}(\mathbf{x},\mathbf{x}'_k)=\frac{\partial^2\phi_k}{\partial x_2^2}\ ,\quad \tau_{22}(\mathbf{x},\mathbf{x}'_k)=\frac{\partial^2\phi_k}{\partial x_1^2}\ ,\quad \tau_{12}(\mathbf{x},\mathbf{x}'_k)=\frac{\partial^2\phi_k}{\partial x_1\partial x_2}\ ,$$
$$\tau_{13}(\mathbf{x},\mathbf{x}'_k)=\tau_{23}(\mathbf{x},\mathbf{x}'_k)=0\ ,\quad \tau_{33}(\mathbf{x},\mathbf{x}'_k)=-\upsilon\left(\tau_{11}(\mathbf{x},\mathbf{x}'_k)+\tau_{22}(\mathbf{x},\mathbf{x}'_k)\right)\ ,\quad k=1,2 \tag{6}$$

$$\tau_{11}(\mathbf{x},\mathbf{x}'_k)=\tau_{22}(\mathbf{x},\mathbf{x}'_k)=\tau_{33}(\mathbf{x},\mathbf{x}'_k)=\tau_{12}(\mathbf{x},\mathbf{x}'_k)=0\ ,$$
$$\tau_{13}(\mathbf{x},\mathbf{x}'_k)=\frac{\partial\phi_k}{\partial x_1}\ ,\quad \tau_{23}(\mathbf{x},\mathbf{x}'_k)=\frac{\partial\phi_k}{\partial x_2}\ ,\qquad k=3 \tag{7}$$

where

$$\phi_1(\mathbf{x},\mathbf{x}')=-\left(p+q\right)\left(x_2-x_2'\right)\left(\theta_1+\theta_2\right)+\frac{1}{2}q\left(x_1-x_1'\right)\ln\frac{X_1}{X_2}+2p\frac{x_1x_1'(x_1+x_1')}{X_2} \tag{8}$$

$$\phi_2(\mathbf{x},\mathbf{x}')=-\left(p+q\right)\left(x_2-x_2'\right)\left(\theta_1+\theta_2\right)+\frac{1}{2}q\left(x_2-x_2'\right)\ln\frac{X_1}{X_2}-2p\frac{x_1x_1'(x_2-x_2')}{X_2} \tag{9}$$

$$\phi_3(\mathbf{x},\mathbf{x}')=-\frac{\ln X_1+\ln X_2}{4\pi} \tag{10}$$

and

$$p=\frac{1}{4\pi(1-\upsilon)}\ ,\quad q=p(1-2\upsilon)\ ,$$
$$X_1=\left(x_1-x_1'\right)^2+\left(x_2-x_2'\right)^2\ ,\quad X_2=\left(x_1+x_1'\right)^2+\left(x_2-x_2'\right)^2 \tag{11}$$

$$\theta_1=\arctan\left(\frac{x_2-x_2'}{x_1-x_1'}\right)\ -\pi\le\theta_1\le\pi\ ,\quad \theta_2=\arctan\left(\frac{x_2-x_2'}{x_1+x_1'}\right)\ -\frac{\pi}{2}\le\theta_2\le\frac{\pi}{2} \tag{12}$$

Equations (6) and (7) give the residual stress field, τ^r, in the surface crystal embedded in the polycrystal. This analysis also gives surface tractions on the grain boundaries (see

Figure 1). In a single crystal, the surface tractions are zero, and hence must be removed by applying equal and opposite tractions on the boundary. The stress field caused by the equal and opposite tractions is here solved by finite element method (FEM). Plastic strain occurs only in the fatigue band. The fatigue band is divided into a number of grids. The plastic strain in a grid in the left half of the crystal is denoted by $e_{ij}^{p(L)}$ and in the right half by $e_{ij}^{p(R)}$. The solution of the stress field in Figure 3(a) is the sum of the solution of Figures 3(b), (c), and (d). Figure 3(b) gives uniform stress. The stress field caused by plastic strain, $e_{ij}^{p(L)}$, is solved by the semi-infinite solid solution with the free surface at the left, as shown in Figure 4. This solution satisfies the condition of zero traction at the free surface and gives surface tractions on the right, top, and bottom planes (see Figure 4(b)). These tractions are removed by applying equal and opposite tractions as shown in Figure 4(c). The stress field due to the loading in Figure 4(c) is solved by FEM. With the plastic strain grid in the left half of the crystal, the equivalent forces induced by the plastic strain is relatively far from the considered crystal boundaries, and hence the variation of surface traction along the boundary is small, and the grids of the FEM does not need to be very fine. This will facilitate the FEM solution. Similarly, for the solution of Figure 3(d), the slid grid is in the right half. The free surface of the semi-infinite solid is taken to be at the right side. The initial strain e_{ij}^{i} has the same effect as the plastic strain, so the procedure for solving the residual stress field can be applied for solving the initial stress caused by initial strain in the fatigue band. This gives a method to calculate the influence coefficient of the stress in the mth grid due to a unit inelastic strain (plastic strain and initial strain) in the nth grid. The resolved shear stress τ is the sum of the initial stress τ^{i}, the applied stress τ^{a}, and the residual stresses, $\tau^{r(L)}$ and $\tau^{r(R)}$. This sum is equated to the critical shear stress, τ^{c}, and the incremental plastic strain distributions at different stages of loading are obtained.

3. EXPERIMENTAL OBSERVATIONS

Mecke and Blochwitz [14] observed the subgrain displacement in single nickel crystal under cyclic loading. These experiments were carried out under constant plastic strain amplitudes at room temperature. It is shown that the PSBs have penetrated across the whole crystal and extruded out on both sides as shown in figure 5. The case with extrusion protruding on one side and intrusion on the other side was not observed. Basinski et al. [15,16] tested copper single crystals at a constant plastic strain amplitude at room temperature under cyclic loadings. In these tests, both extrusions and intrusions are observed. Zhai et al. [17,18] performed fatigue experiments on aluminum single crystals under constant cyclic stress amplitude. Again, both extrusions and intrusions were observed on the free surfaces.

4. NUMERICAL CALCULATIONS

The analytical solution developed in Section 2 is here applied to analyze the single crystal tests. To simplify the calculation, a single fatigue band in the single crystal is considered (see Figure 1). The analytical method can readily be used to analyze multiple fatigue bands in the crystal. Referring to Figure 1(b), both P and Q are assumed to be 0.05 μm in thickness, and R to be 1.0 μm. The crystal is f.c.c. and is assumed to be elastically isotropic with shear modulus $\mu = 50$ *GPa* and the Poisson ratio $\upsilon = 0.3$. The critical shear stress, τ^c, is taken to be 200 *MPa*, and cyclic loading $\tau_{22} = 399.55$ *MPa*. An initial tensile strain was assumed to vary linearly from a maximum value at the center to zero at the two ends of a 1.4 mm segment in the fatigue band. This segment was divided into a number of grids, and each grid was approximated by a uniform initial tensile strain. This assumed initial tensile strain distribution was found to give a uniform initial resolved shear stress, τ^i. Thus a uniform τ^i of 0.5 *MPa* was used in the present analysis. The variations of the plastic strain in P and Q along the length of the fatigue band at different cycles of loading are shown in Figure 6.

Then an initial tensile strain of the same amount is assumed to be located at the left side. The variations of plastic strains were calculated and the results are shown in Figure 7. It is seen that both locations of the initial tensile strain give extrusions protruded out on both sides. If the initial tensile strain is replaced by an initial compression strain, intrusions instead of extrusions will occur on both sides. This seems to agree with the experimental observations.

5. CONCLUSIONS

As discussed previously, for an extrusion to protrude, the shear strain in P has to be positive and that in Q has to be negative near the occurrence of extrusion. This requires positive resolved shear stress in P and negative in Q. In turn, this requires a compressive stress in R to push the extrusion out. The occurrence of extrusion on both sides of the single crystal implies compression in R on both faces. A segment in R with an initial tension in the fatigue band tends to increase the length of the compressive stress in R under cyclic loadings. This is likely to spread this compression over the length of fatigue band and causes extrusion on both faces of the crystal.

Similarly, for an intrusion to occur on the left side, the shear strain in P must be negative and that in Q must be positive. This requires a tensile stress in R to pull the intrusion in. A segment in R with an initial compressive strain tends to increase the length of the tensile stress in R under cyclic loadings. The spread of the tension in R over the length of the fatigue band will result in intrusions on both faces. This gives the likeliness of intrusions on both faces.

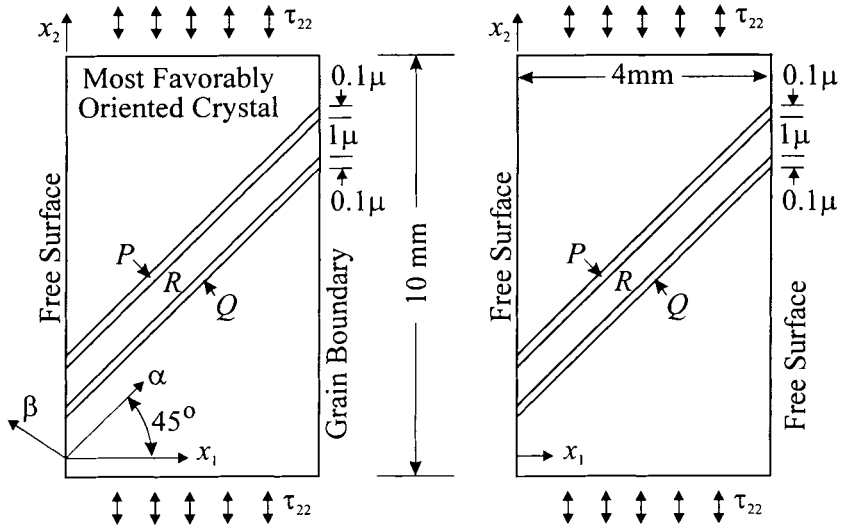

(a) A most favorably oriented crystal at free surface of a polycrystal.

(b) A single crystal under cyclic loading.

Figure 1. Micromechanic models of fatigue crack initiation.

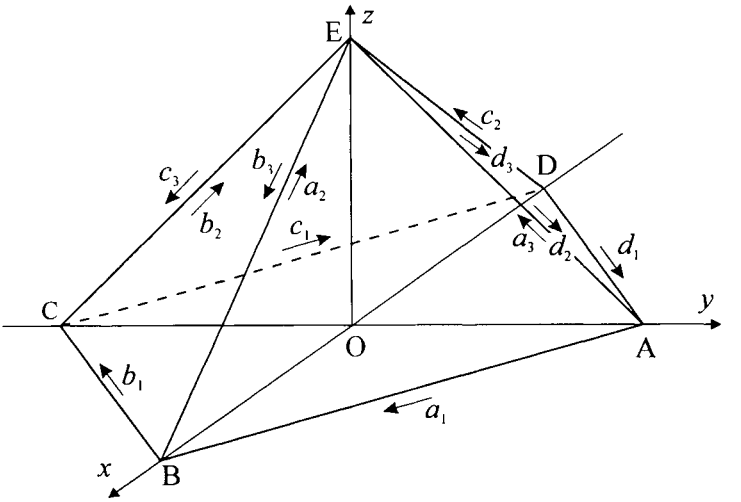

Figure 2. Crystallographic direction of a f.c.c. crystal.

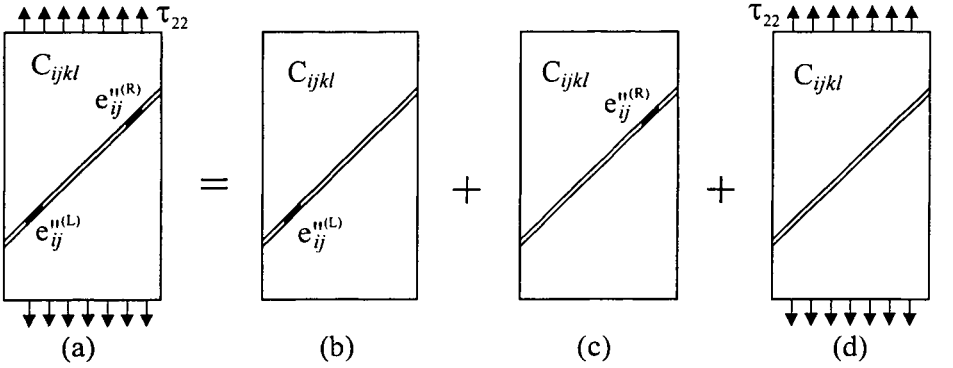

Figure 3. Procedure for decoupling the single crystal problem.

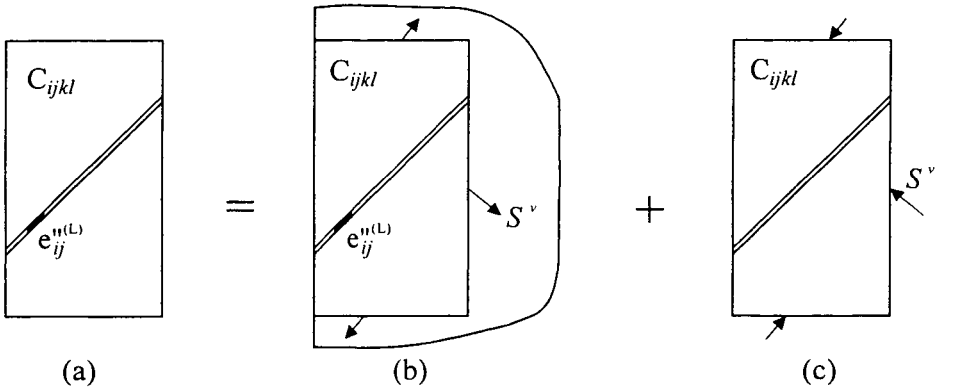

Figure 4. Removal of boundary tractions for a single crystal.

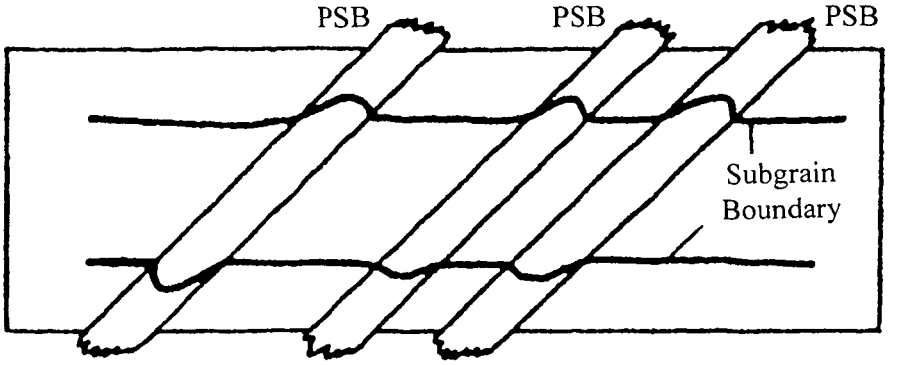

Figure 5. Extrusions observed in single crystal experiment [14].

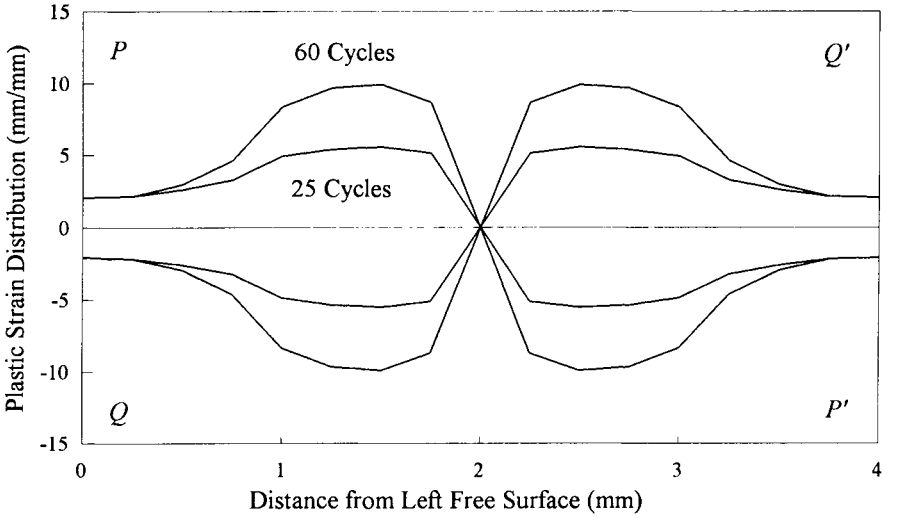

Figure 6. Plastic strain distribution with initial strain at center.

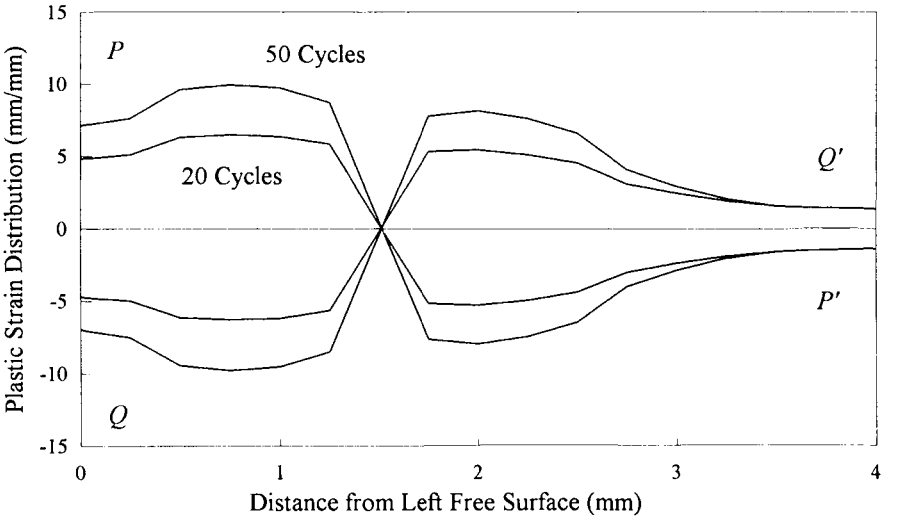

Figure 7. Plastic strain distribution with initial strain at left side.

ACKNOWLEDGMENT

This research was supported by the Air Force Office of Scientific Research through Grant F49629-96-1-0350. The interest of Dr. James Chang and Dr. Brian Sanders are gratefully acknowledged.

REFERENCES

1. A. Puskar and S.A. Golvin, Fatigue in Materials: Cumulative Damage Processes, Elsevier, (1985).
2. T.H. Lin, Adv. in Applied Mechanics, 29 (1992) 1-62.
3. T.H. Lin, S.R. Lin, and X.Q. Wu, Phil. Mag. A, 59 (1989) 1263-1276.
4. E.R. Parker, Mechanical Behavior of Materials in Elevated Temperatures, J.E. Dorn (ed.), McGraw-Hill (1961) 129-148.
5. T.H. Lin, Theory of Inelastic Structures, Wiley, New York (1968) 44-48.
6. P.J.E. Forsyth and C.A. Stubbington, J. Inst. Metals, 83 (1955) 395.
7. T.H. Lin and Y.M. Ito, Proc. U.S. Nat. Acad. Sci., 62 (1969) 631-635.
8. J.G. Antonopoulos, L.M. Brown, and A.T. Winter, Phil. Mag., 34 (1987) 549.
9. H. Mughrabi, R. Wang, K. Differt, U. Essmann, Fatigue Mechanism ASTM STP 811 (1983) 5-45.
10. T. Zhai, G.A.D. Briggs, and J.W. Martin, Acta Metall., 44 (1996) 3489-3496.
11. S.G. Lekhnitski, Theory of Elasticity of an Anisotropic Body, Holden-Day San Francisco (1963) 129-134.
12. E. Melan, *Zeitschrift fur angewandte Mathematik und Mechanik*, 12 (1932) 343-346; Correction in 20 (1940) 368.
13. T.K. Tung and T.H. Lin, J. Appl. Mech., 33 (1966) 363-370.
14. K. Mecke and C. Blochwitz, Phys. Stat. Sol. (A), 64 (1980) K5.
15. Z.S. Basinski, R. Pascual, and S.J. Basinski, Acta Metall., 31 (1983) 591-602.
16. Z.S. Basinski and S.J. Basinski, Acta Metall., 33 (1985) 1307-1317.
17. T. Zhai, S. Lin, and J.M. Xiao, Acta Metall. Mater., 38 (1990) 1687-1692.
18. T. Zhai, J.W. Martin, and G.A.D. Briggs, Acta Metall. Mater., 43 (1995) 3813-3825.

Damage Mechanics in Engineering Materials
G.Z. Voyiadjis, J.-W.W. Ju and J.-L. Chaboche (Editors)
© 1998 Elsevier Science B.V. All rights reserved.

The sliding crack model revisited

M. Basista[a] and D. Gross[b]

[a]Institute of Fundamental Technological Research, Polish Academy of Sciences,
Świętokrzyska 21, 00-049 Warsaw, Poland*

[b]Institute of Mechanics, Technische Hochschule Darmstadt,
Hochschulstrasse 1, 64289 Darmstadt, Germany

Abstract: Two-dimensional micromechanical sliding crack model of inelastic deformation in brittle solids under compression is reexamined within the thermodynamic framework with microstructural internal variables (Rice, 1971, 1975). Incremental stress-strain equations are derived for an elastic solid weakened by non-interacting sliding microcracks. Preliminary results of crack-crack interactions in the presence of frictional and cohesive resistance are also presented.

1. INTRODUCTION

It is well documented that nonlinear deformation and failure of brittle rocks involve the growth of microcracks from stress concentrators such as preexisting cracks and voids, inclusions, and dissimilar grain contacts. In unconfined compression tests the microcracks grow predominantly on the planes subparallel to the direction of loading. The final fracture in the form of splitting is commonly attributed to the unstable propagation of one or more of the largest and most favorably oriented cracks running longitudinally towards the specimen's ends. The failure is abrupt and inelastic strain at failure remains relatively small. In contrast, if a substantial lateral confinement is applied the deformation process is more complicated since it incorporates both brittle and ductile deformation modes. The final fracture (faulting) in a confined specimen results from the cooperative action of many small cracks that grow in a stable manner, interact and eventually form a dominant shear fault (crack band) at some angle to the maximum load axis. The stress - strain curve in this case visibly deviates from the straight line. The inelastic and elastic strains at failure (apex of the $\sigma - \varepsilon$ curve in the stress-controlled test) are typically of the same order of magnitude. Microstructural parameters, such as grain size, porosity, distribution of cleavage planes, initial crack density, etc., usually play an important role in the process of rock deformation.

*) Project partially supported by the State Committee for Scientific Research, Poland (Grant no. 7TO7A026) and Deutscher Akademischer Austauschdienst, Germany.

The microcrack growth under axial compression at low-to-moderate lateral pressures may occur according to several different mechanisms. Some of these mechanisms such as: frictional sliding on initial flaws producing secondary tension wings, tension cracking from isolated pores, pore collapse, have been extensively studied both experimentally and analytically (e.g. Brace and Bombolakis, 1963; Bieniawski, 1967; Walsh, 1965; Peng and Johnson, 1976; Nemat-Nasser and Horii, 1982, Horii and Nemat-Nasser, 1985a, 1986; Nemat-Nasser and Obata, 1988; Kachanov, 1982; Moss and Gupta, 1982; Steif, 1984, Zaitsev, 1985; Sammis and Ashby, 1986; Ashby and Hallam, 1986; Kemeny and Cook, 1991; Wang and Kemeny, 1993; Dyskin et al., 1995; Fanella and Krajcinovic, 1988; Ju, 1991; Zhao et al., 1993).

In this paper, attention is focused on the sliding crack model originated by Brace and Bombolakis (1963) and then widely used in the literature (for references see Basista and Gross, 1997a) to represent inelastic deformation of low-porosity rocks. It involves a rather complex sequence of events starting with the frictional sliding on the faces of preexisting (closed) flaws, followed by the curvilinear kinking from the crack tips, and completed by the subsequent mode-I growth of the kinked wings in the planes roughly parallel to the direction of dominant compressive stress. Depending on the sign of confining stress, the wing cracks may grow either in a stable (lateral compression) or unstable (lateral tension) manner.

The objective of this paper is to analytically derive the stress-strain relations for elastic material containing frictionally sliding microcracks under overall compressive stress. For this purpose, the thermodynamic framework with microstructural internal variables (Rice, 1971, 1975) is adopted. The authors' recent results (Basista and Gross, 1997a,b) are here summarized and further advanced by examining the interaction of frictional cracks.

2. INTERNAL VARIABLE REPRESENTATION OF SLIDING CRACK MODEL

Consider an isothermal deformation of a microcracked elastic solid subject to compressive principal stresses σ_1, σ_2 (compression is viewed negative). The analysis is confined to low lateral pressures $|\sigma_2| << |\sigma_1|$ so that strains may be considered infinitesimal and plastic effects may be neglected. Since the overall material response is nonlinear and stress-path dependent, an incremental formulation is necessary. For simplicity, the attention is focused on non-interacting slits embedded in a two-dimensional homogeneous and isotropic matrix. The sliding crack interaction will be addressed later in a separate section.

It is assumed that a macroscopically homogeneous deformation process can be suitably approximated by a sequence of constrained equilibrium states (Rice, 1971, 1975). As a consequence, it can be shown that the inelastic part of the macroscopic strain increment is related to the increments of internal variables at the microscale according to

$$d^{i}\varepsilon_{ij} = \frac{1}{V_0}\sum \frac{\partial f_\alpha(\boldsymbol{\sigma}, H)}{\partial \sigma_{ij}} d\xi_\alpha \tag{1}$$

where $f_\alpha = f_\alpha(\boldsymbol{\sigma}, H)$ is the set of thermodynamic forces conjugated to the internal variables ξ_α, $\boldsymbol{\sigma}$ is the tensor of applied stresses, H (for history) represents symbolically the current collection of values of ξ_α, V_0 denotes the volume of a representative volume element (RVE).

The summation in (1) extends over all sites of the RVE where the microstructural rearrangements take place. The total strain increment can be decomposed as

$$d\boldsymbol{\varepsilon} = d^e\boldsymbol{\varepsilon} + d^i\boldsymbol{\varepsilon} = \mathbf{M}:d\boldsymbol{\sigma} + d^i\boldsymbol{\varepsilon} \tag{2}$$

where $d^i\boldsymbol{\varepsilon}$ is given by (1). The instantaneous compliance tensor $\mathbf{M}$ is defined as

$$M_{ijkl} = \frac{\partial^2 \psi(\boldsymbol{\sigma}, H)}{\partial \sigma_{ij}\, \partial \sigma_{kl}}\Big|_{H \text{ fixed}} \tag{3}$$

Here, $\psi(\boldsymbol{\sigma}, H)$ is the specific complementary (Gibbs) energy given by

$$\psi(\boldsymbol{\sigma}, H) = \psi^0(\boldsymbol{\sigma}) + \Delta\psi(\boldsymbol{\sigma}, H) \;, \quad \psi^0 = \tfrac{1}{2}\sigma_{ij} M^0_{ijkl} \sigma_{kl} \tag{4}$$

where $\Delta\psi(\boldsymbol{\sigma}, H)$ denotes the inelastic part of ψ due to the frictional slip and the presence of wing cracks, M^0_{ijkl} is the elastic compliance of the matrix material. Note that for open cracks, the instantaneous compliance M_{ijkl} defined in (3) is the secant (effective) compliance which is, in fact, the unloading compliance. However, this conclusion ceases to be valid for closed frictional cracks considered in this paper (for details see Ju, 1991). This and related issues pertinent to the applicability of Rice's framework to the sliding crack mechanism of inelastic deformation are analyzed in more detail in Basista and Gross (1997a).

Frictional sliding on a preexisiting slit, which remains closed during the whole deformation cycle, leads to the formation of curvilinear tension wings. Similarly as in Nemat-Nasser and Obata (1988), the curvilinear wings are represented by the equivalent straight ones, as shown in Fig. 1. The orientation θ of the equivalent crack tip is yet to be determined maximizing K_I with respect to θ for a given wing length l.

The inelastic part of the specific complementary energy of a representative surface element (RSE) containing N non-interacting winged cracks is

$$\begin{aligned} \Delta\psi(\boldsymbol{\sigma}, H) &= \frac{N}{A_0}\left[\int_{-c}^{c}\int_{0}^{b(x_2')} \tau_{12}'(\boldsymbol{\sigma}, b)\, db\, dx_2' + 2\int_0^l G(\boldsymbol{\sigma}, l, \theta)\, dl\right] \\ &= \frac{N}{A_0}\left[2c\int_0^{\bar{b}} \tau_{12}'(\boldsymbol{\sigma}, \bar{b})\, d\bar{b} + \frac{1}{E_0'} 2\int_0^l \left(K_I^2 + K_{II}^2\right) dl\right] \end{aligned} \tag{5}$$

where: A_0 is the area of the RSE, σ_{ij}' are the actual stresses acting on PP' in the local coordinate system (x_1', x_2'), $2c$ is the length of the preexisting slit, l is the wing crack length, $b(x_2')$ is the relative slip displacement of the points on PP' with $\bar{b}$ being its average value over $2c$, G is the elastic energy release rate. As usual in the fracture mechanics notation

$E_0' = \begin{cases} E_0 & \text{for } \textit{plane stress} \\ E_0/(1-\nu_0^2) & \text{for } \textit{plane strain} \end{cases}$, with E_0 and ν_0 being Young's modulus and Poisson's ratio of the matrix material. The specific complementary energy is shown in a general form (5). Its integrated form, although analytic, is rather lengthy and is not displayed here.

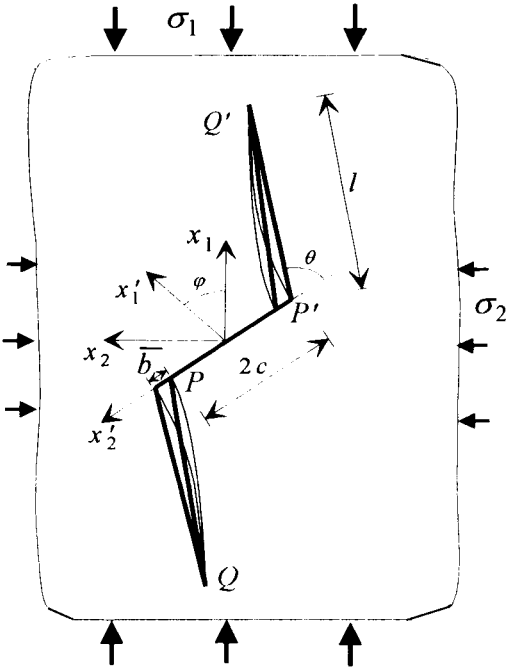

Figure 1. Sliding crack with tension wings.

Using (4) and (5), the inelastic change of ψ reads

$$d^i\psi = \frac{\partial\psi}{\partial\bar{b}}d\bar{b} + \frac{\partial\psi}{\partial l}dl + \frac{\partial\psi}{\partial\theta}d\theta$$
$$= \frac{N}{A_0}\left[\tau_{12}' 2c\, d\bar{b} + 2G\,dl + \frac{\partial}{\partial\theta}\left(2\int_0^l G\,dl\right)d\theta\right] = \frac{N}{A_0}\sum_{\alpha=1}^{3} f_\alpha d\xi_\alpha \tag{6}$$

From (6) the microfluxes and the conjugated thermodynamic forces for a single crack are

$$f_1 = \tau_{12}' 2c,\ d\xi_1 = d\bar{b};\quad f_2 = G,\ d\xi_2 = dl;\quad f_3 = \int_0^l \frac{\partial G}{\partial\theta}dl,\ d\xi_3 = d\theta \tag{7}$$

The explicit expressions for f_1, f_2, f_3 are contingent on the knowledge of the actual shear stress τ'_{12} acting on PP', and the stress intensity factors K_I and K_{II} at the wing crack tips.

From the superposition principle and the equilibrium of forces along PP' in the cross section $QPP'Q'$ (Fig.1) it follows that

$$\begin{aligned}&\tau^*_{12}\,2c - \left[\sigma_{11}\cos^2(\theta+\varphi) + \sigma_{22}\sin^2(\theta+\varphi) + \tau_{12}\sin 2(\theta+\varphi)\right]2l\sin\theta \\ &+\left[\tfrac{1}{2}(\sigma_{11}-\sigma_{22})\sin 2(\theta+\varphi) - \tau_{12}\cos 2(\theta+\varphi)\right]2l\cos\theta + 2\hat{F}_{el}(\bar{b},l) = 0\end{aligned} \tag{8}$$

where: $\tau^*_{12} = \tau'_{12} - \tau^r_{12}$ denotes the net shear stress that causes the slip on PP' after the cohesive and frictional resistance have been overcome, $\tau^r_{12} = -\frac{1}{2}\sin 2\varphi(\sigma_{11}-\sigma_{22}) + \tau_{12}\cos 2\varphi$ is the shear stress resolved on PP', σ_{11}, σ_{22}, τ_{12} are the applied stresses at infinity. The term $\hat{F}_{el}(\bar{b},l)$ in (8) represents the sum $\left(F^I_{el}\sin\theta + F^{II}_{el}\cos\theta\right)$ of the projections on PP' of the appropriate, as yet unknown, elastic restoring forces (or crack closing forces) F^I_{el}, F^{II}_{el} in mode I, II respectively. Anticipating subsequent differentiation of the thermodynamic forces f_α with respect to σ_{ij}, all three stress components σ_{11}, σ_{22}, τ_{12} were introduced into (8), although $\tau_{12} = 0$. In view of (7) and (8), the thermodynamic force conjugated to $d\bar{b}$ becomes

$$f_1 = \tau^r_{12}\,2c - \sigma_{11}\,2l\sin\varphi\cos(\theta+\varphi) + \sigma_{22}\,2l\cos\varphi\sin(\theta+\varphi) - \tau_{12}\,2l\cos(\theta+2\varphi) - 2\hat{F}_{el}(\bar{b},l) \tag{9}$$

The exact solution of the stress intensity factors (SIFs) at the curvilinear wing tips can be obtained only numerically (Horii and Nemat-Nasser, 1985a; Lauterbach and Gross, submitted). For the present modeling purposes, closed-form thus approximate solutions are required. Numerous approximations of K_I and K_{II} available in the open literature can be arranged in two classes: displacement-driven models (e.g. Steif, 1984; Nemat-Nasser and Obata, 1988) and force-driven models (Moss and Gupta, 1982; Zaitsev 1985; Horii and Nemat-Nasser, 1986; Kemeny and Cook, 1991). The key concepts of the displacement-driven vs. the force-driven idealization of the basic mechanism are depicted in Fig.2a,b, respectively.

In the displacement-driven model (Fig.2a), the rectilinear wings are pushed sideways by a rigid wedge whose dimensions depend on the preexisting crack length $2c$ and the varying average slip displacement $\bar{b}$. In this case, the SIFs involve complete elliptic integrals of the first and second kind: $K(k)$ and $E(k)$, with the modulus $k = \sqrt{l^2 + 2lc\cos\theta}/(l + c\cos\theta)$, cf. Tada et al. (1985). In general, these SIFs are not expressible by analytic functions except for a special case of *semi-infinite wedge* which, when translated into the present context, means two isolated (non-interacting) straight wing cracks. Strictly speaking, this is a realistic approximation only for the initial phase of kinking (very small wings). This special case was used as a basis in Nemat-Nasser and Obata (1988) for an analytical derivation of the inelastic strain from the respective crack opening displacements (CODs).

If the crack tips of a displacement-driven crack (Fig.2a) do not interact with each other (i.e. $l << c$) the modulus k is equal to zero. Consequently, the SIFs at the tips Q and Q' are expressible in the following form (e.g. Tada et al., 1985)

$$K_I(\bar{b},l,\sigma)=\frac{E_0'\bar{b}\sin\theta}{2\sqrt{2\pi(l+l^{**})}}+\sqrt{\frac{\pi l}{2}}\left[\sigma_{11}\cos^2(\theta+\varphi)+\sigma_{22}\sin^2(\theta+\varphi)+\tau_{12}\sin 2(\theta+\varphi)\right]$$

$$K_{II}(\bar{b},l,\sigma)=-\frac{E_0'\bar{b}\cos\theta}{2\sqrt{2\pi(l+l^{**})}}-\sqrt{\frac{\pi l}{2}}\left[\tau_{12}\cos 2(\theta+\varphi)-\tfrac{1}{2}(\sigma_{11}-\sigma_{22})\sin 2(\theta+\varphi)\right] \tag{10}$$

where $l^{**}=0.27c\pi^2/32$ is a nucleus wing length introduced in Nemat-Nasser and Obata (1988) to get proper asymptotic behavior of the above expressions in the short wing limit ($l\to 0$), i.e. to arrive at the Cotterell-Rice solution (Cotterell and Rice, 1980) for infinitesimal wings.

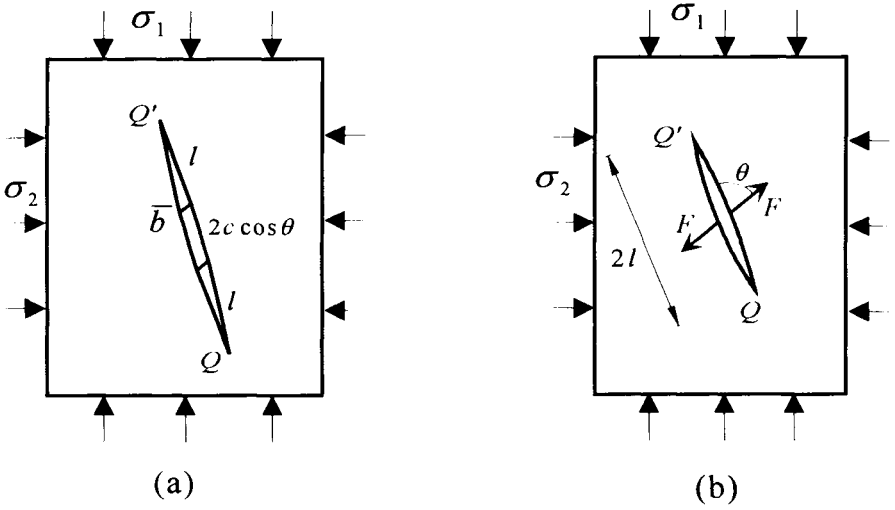

Figure 2. Idealizations of sliding crack (from Basista and Gross, 1997b): (a) Displacement-driven, (b) Force-driven.

In the reality, the original sliding crack $QPP'Q'$ (Fig.1) is displacement-driven: the SIFs at the wing tips are directly proportional to the relative slip of the slanted crack faces. However, when the preexisting crack undergoes forward- or backsliding, its wedging action upon the wings may equivalently be seen as force-driven (Nemat-Nasser and Obata, 1988). In such a case, the wedging effect the slip displacement exerts on the wings is represented by two collinear splitting forces $F=-2c\tau_{12}^{*}$. Assuming that the curvilinear wing cracks can be approximated by the straight ones whose orientation is to be determined from the maximization of K_I, the estimates of the SIFs at the wing tips in Fig.2b are (Horii and Nemat-Nasser, 1986)

$$K_I(F,l,\sigma) = \frac{F\sin\theta}{\sqrt{\pi(l+l^*)}} + \sqrt{\pi l}\left[\sigma_{11}\cos^2(\theta+\varphi) + \sigma_{22}\sin^2(\theta+\varphi) + \tau_{12}\sin 2(\theta+\varphi)\right]$$

$$K_{II}(F,l,\sigma) = \frac{-F\cos\theta}{\sqrt{\pi(l+l^*)}} - \sqrt{\pi l}\left[-\tfrac{1}{2}(\sigma_{11}-\sigma_{22})\sin 2(\theta+\varphi) + \tau_{12}\cos 2(\theta+\varphi)\right] \tag{11}$$

where $l^* = 0.27c$ plays the same role as l^{**} in the displacement-driven model.

3. DERIVATION OF STRAIN INCREMENT

The next step of the analysis consists in the calculation of the inelastic strain increment induced by the frictional sliding along the preexisting flaw, the wing crack extension and its simultaneous rotation. The wing crack rotation is a by-product of the modeling of the wing tip path. Recall that the curvilinear wing is traced as a sequence of inclined straight cracks whose orientations θ are determined maximizing K_I for a given wing length l. The wing length itself is calculated from the $K_I = K_{Ic}$ condition. The inelastic strain increments are obtained from the fundamental relation (1) using the derived microstructural thermodynamic forces (7), (9) and the approximate expressions for the SIFs (10), (11). It is essential that the conjugate forces f_α be symmetrized in components of σ and all three stress components be included when performing the differentiation in (1). After some computational effort, the final outcome in the global coordinates (x_1, x_2) reads (Basista and Gross, 1997b):

Strain increment due to frictional sliding ($\tilde{b}$ -driven and F-driven model alike)

$$d\varepsilon_{ij}^s = \omega_0 \begin{bmatrix} -\sin 2\varphi & \cos 2\varphi \\ \cos 2\varphi & \sin 2\varphi \end{bmatrix} d\tilde{b} + \omega_0 \begin{bmatrix} -2\sin\varphi\cos(\theta+\varphi) & \cos(\theta+2\varphi) \\ \cos(\theta+2\varphi) & 2\cos\varphi\sin(\theta+\varphi) \end{bmatrix} d\tilde{b}\,\tilde{l} \tag{12}$$

The following normalized quantities have been introduced in (12) and will be used in the sequel: $\omega_0 = Nc^2/A_0$, $\tilde{b} = \bar{b}/c$, $\tilde{l} = l/c$, where N is the number of non-interacting, active winged cracks in the representative surface element (RSE) of the area A_0, $\bar{b}$, l, c are marked in Fig.1. Note that parameter ω_0, which arises here in a natural manner from the structure of the potential $\Delta\psi$, is identical to the damage parameter introduced in Walsh (1965). In the literature, this parameter is also often referred to as the Budiansky-O'Connell (1976) crack density parameter.

Strain increment due to wing crack extension ($\tilde{b}$-driven)

$$d\varepsilon_{ij}^{c} = \frac{\omega_0}{2} g_1(\tilde{l}) \begin{bmatrix} -2\sin\varphi\cos(\theta+\varphi) & \cos(\theta+2\varphi) \\ \cos(\theta+2\varphi) & 2\cos\varphi\sin(\theta+\varphi) \end{bmatrix} \tilde{b}\, d\tilde{l}$$

$$+ \frac{\pi\omega_0}{2E_0'} \left\{ \begin{bmatrix} \left[4\sigma_1\cos^2(\theta+\varphi) + 4\sigma_2\sin^2(\theta+\varphi)\right] \begin{bmatrix} \cos^2(\theta+\varphi) & \frac{1}{2}\sin 2(\theta+\varphi) \\ \frac{1}{2}\sin 2(\theta+\varphi) & \sin^2(\theta+\varphi) \end{bmatrix} \\ -(\sigma_1-\sigma_2)\sin 2(\theta+\varphi) \begin{bmatrix} -\sin 2(\theta+\varphi) & \cos 2(\theta+\varphi) \\ \cos 2(\theta+\varphi) & \sin 2(\theta+\varphi) \end{bmatrix} \end{bmatrix} \right\} \tilde{l}\, d\tilde{l} \tag{13}$$

where $g_1(\tilde{l}) = \sqrt{\tilde{l}/(\tilde{l}+\tilde{l}^{\bullet\bullet})}$.

Strain increment due to wing crack rotation ($\tilde{b}$-driven)

$$d\varepsilon_{ij}^{\theta} = \omega_0 \begin{bmatrix} \sin\varphi\sin(\theta+\varphi) & -\frac{1}{2}\sin(2\varphi+\theta) \\ -\frac{1}{2}\sin(2\varphi+\theta) & \cos\varphi\cos(\theta+\varphi) \end{bmatrix} \tilde{b}\, h_1(\tilde{l})\, d\theta$$

$$+ \omega_0 \frac{\pi\tilde{l}^2}{E_0'} \begin{bmatrix} -\sin 2(\theta+\varphi)\sigma_1 & \frac{1}{2}\cos 2(\theta+\varphi)(\sigma_1+\sigma_2) \\ \frac{1}{2}\cos 2(\theta+\varphi)(\sigma_1+\sigma_2) & \sin 2(\theta+\varphi)\sigma_2 \end{bmatrix} d\theta \tag{14}$$

where $h_1(\tilde{l}) = \sqrt{\tilde{l}(\tilde{l}+\tilde{l}^{\bullet\bullet})} - \frac{\tilde{l}^{\bullet\bullet}}{2}\ln\left[\frac{2\tilde{l}}{\tilde{l}^{\bullet\bullet}} + 2\sqrt{\frac{\tilde{l}}{\tilde{l}^{\bullet\bullet}}\left(\frac{\tilde{l}}{\tilde{l}^{\bullet\bullet}}+1\right)} + 1\right]$.

Strain increment due to wing crack extension (F-driven)

$$d\varepsilon_{ij}^{c} = \frac{-4\omega_0\tau_{eff}}{E_0'} g_2(\tilde{l}) \begin{bmatrix} -2\sin\varphi\cos(\theta+\varphi) & \cos(\theta+2\varphi) \\ \cos(\theta+2\varphi) & 2\cos\varphi\sin(\theta+\varphi) \end{bmatrix} d\tilde{l}$$

$$+ \frac{\pi\omega_0}{E_0'} \left\{ \begin{bmatrix} \left[4\sigma_1\cos^2(\theta+\varphi) + 4\sigma_2\sin^2(\theta+\varphi)\right] \begin{bmatrix} \cos^2(\theta+\varphi) & \frac{1}{2}\sin 2(\theta+\varphi) \\ \frac{1}{2}\sin 2(\theta+\varphi) & \sin^2(\theta+\varphi) \end{bmatrix} \\ -(\sigma_1-\sigma_2)\sin 2(\theta+\varphi) \begin{bmatrix} -\sin 2(\theta+\varphi) & \cos 2(\theta+\varphi) \\ \cos 2(\theta+\varphi) & \sin 2(\theta+\varphi) \end{bmatrix} \end{bmatrix} \right\} \tilde{l}\, d\tilde{l} \tag{15}$$

where $g_2(\tilde{l}) = \sqrt{\tilde{l}/(\tilde{l}+\tilde{l}^{\bullet})}$

Strain increment due to wing crack rotation (F-driven)

$$d\varepsilon_{ij}^{\theta} = \omega_0 \frac{-8\tau_{eff}}{E_0'}\begin{bmatrix} \sin\varphi\sin(\theta+\varphi) & -\frac{1}{2}\sin(2\varphi+\theta) \\ -\frac{1}{2}\sin(2\varphi+\theta) & \cos\varphi\cos(\theta+\varphi) \end{bmatrix} h_2(\tilde{l})\,d\theta$$

$$+\omega_0 \frac{2\pi\tilde{l}^2}{E_0'}\begin{bmatrix} -\sin 2(\theta+\varphi)\sigma_1 & \frac{1}{2}\cos 2(\theta+\varphi)(\sigma_1+\sigma_2) \\ \frac{1}{2}\cos 2(\theta+\varphi)(\sigma_1+\sigma_2) & \sin 2(\theta+\varphi)\sigma_2 \end{bmatrix} d\theta \tag{16}$$

where $h_2(\tilde{l}) = \sqrt{\tilde{l}(\tilde{l}+\tilde{l}^*)} - \frac{\tilde{l}^*}{2}\ln\left[\frac{2\tilde{l}}{\tilde{l}^*} + 2\sqrt{\frac{\tilde{l}}{\tilde{l}^*}\left(\frac{\tilde{l}}{\tilde{l}^*}+1\right)}+1\right]$.

Having determined the inelastic strain it remains yet to compute the elastic part of the strain increment of the RSE containing isotropically distributed winged cracks. Within the present framework, this is done according to the relations (2) and (3) with the Gibbs potential determined by (5). The final form of the elastic part of strain tensor in the global coordinates reads

Elastic part of strain increment ($\tilde{b}$ -driven)

$$d^e\varepsilon_{ij} = M^0_{ijkl}\,d\sigma_{kl} + \omega_0 \frac{\pi\tilde{l}^2}{E_0'}\begin{bmatrix} d\sigma_{11}\cos^2(\theta+\varphi) & \frac{1}{4}(d\sigma_{11}+d\sigma_{22})\sin 2(\theta+\varphi) \\ \frac{1}{4}(d\sigma_{11}+d\sigma_{22})\sin 2(\theta+\varphi) & d\sigma_{22}\sin^2(\theta+\varphi) \end{bmatrix} \tag{17}$$

Elastic part of strain increment (F-driven)

$$d^e\varepsilon_{ij} = 2\,d^e\varepsilon_{ij}(\tilde{b}-driven) \tag{18}$$

The total strain increment comprises all the individual terms, namely

$$d\varepsilon_{ij} = d^e\varepsilon_{ij} + d\varepsilon_{ij}^s + d\varepsilon_{ij}^c + d\varepsilon_{ij}^{\theta} \tag{19}$$

A systematic discussion of the obtained equations (12)-(18) is provided in Basista and Gross (1997b).

So far in this section we were concerned with forward sliding in loading regime. If the effective shear stress on a preexisting crack diminishes for some reason $\left(d|\tau_{12}^*| < 0\right)$, then the sliding crack may undergo unloading. Various situations in unloading were analyzed in detail in Basista and Gross (1997a).

4. KINETIC EQUATIONS FOR INTERNAL VARIABLES

The preceding section has shown how the inelastic and elastic macroscopic strain are related to the particular microstructural rearrangements induced by the sliding crack mechanism. The microfluxes $d\xi_i$ and their conjugated thermodynamic forces f_i have been explicitly identified. The framework is now completed by the specification of kinetic relations for the rates $d\xi_i/dt$. Since no crack-crack interaction has been so far included in the present model, it suffices to consider kinetic equations for three microstructural internal variables $\tilde{b}, \tilde{l}, \theta$ resulting from the analysis of a single kinked crack. Consequently, the overall strain may be estimated afterwards using a simple averaging procedure that sums up the individual contributions of all active cracks while accounting for the assumed spatial distribution of the preexisting flaws.

In general, the slip displacement $\tilde{b}$ is to be computed from the forward- or backsliding activation condition, the wing length $\tilde{l}$ from the kinked crack instability condition, the orientation angle θ of the equivalent straight crack from the maximization analysis of K_I with respect to θ. The rates $\dot{\tilde{b}}, \dot{\tilde{l}}, \dot{\theta}$ expressed in terms of the applied stress rates $\dot{\sigma}_{ij}$ are obtained imposing the consistency requirements upon the above conditions.

It is assumed that frictional contact on PP' is governed by the Coulomb-Mohr law. Hence, the actual stresses acting on PP' at sliding are correlated according to

$$\tau'_{12} = \tau_c - \mu \sigma^r_{11} \tag{20}$$

where τ_c is the cohesion, μ is the coefficient of dry friction and $\sigma^r_{11} = \sigma_{11}\cos^2\varphi + \sigma_{22}\sin^2\varphi + \tau_{12}\sin 2\varphi$ is the resolved normal stress transmitted across PP'. The sliding activation condition is then obtained by combining the equilibrium equation (8) and the Mohr-Coulomb condition (20) for frictional glide to get

$$\begin{aligned}\Omega^s = {} & \sigma_{11}\left[\cos\varphi\left(\sin\varphi - \mu\cos\varphi\right) + \tilde{l}\cos(\theta+\varphi)\sin\varphi\right] \\ & - \sigma_{22}\left[\sin\varphi\left(\cos\varphi + \mu\sin\varphi\right) + \tilde{l}\sin(\theta+\varphi)\cos\varphi\right] \\ & + \tau_{12}\left[\cos 2\varphi + \mu\sin 2\varphi - \tilde{l}\cos(\theta+2\varphi)\right] + \tau_c + c^{-1}\hat{F}_{el} = 0\end{aligned} \tag{21}$$

As noticed by Moss and Gupta (1982), it is difficult to determine $\hat{F}_{el}$ because the stress-crack opening displacement relation for the entire kinked crack is not available. Consequently, some approximate solutions were sought. For example, Moss and Gupta (1982) neglected the initial slit ($c \to 0$), friction and cohesion and considered two limiting cases: $\theta \to 90°$ (locally, mode-I crack) and $\theta \to 0°$ (mode-II crack). Upon introducing a simplification that the wings grow parallel to the direction of the largest principal compressive stress σ_1 (i.e. $\theta + \varphi = \pi/2$), these authors obtained from (21) that

$$\hat{F}_{el} = \frac{\tilde{b} E'_0}{4} \tag{22}$$

Incidentally, an identical result was obtained in Basista and Gross (1997) while the derivation scheme itself was based on a somewhat different reasoning. Estimation of the elastic restoring forces makes the computation of $\tilde{b}$ (normalized average slip) straightforward. Furthermore, the kinetic equation for $\dot{\tilde{b}}$ can now be derived from the sliding activation equation (21) by time differentiation. It is perhaps interesting to note that the present considerations provide a micromechanical explanation of the lack of the normality rule in *macroscopic* constitutive equations for frictional materials. Kestin and Rice (1970) and Rice (1971) proved that the normality rule holds if a particular flux depends on the macroscopic stress only via its own thermodynamic force. It can be inferred from (7), (8) and (22) that such a dependence does not hold for a material with sliding cracks (Basista and Gross, 1997a). We recall also an alternative algorithm for computing $\tilde{b}$ proposed by Nemat-Nasser and Obata (1988). These authors did not analyze equilibrium of a slanted crack but derived $\tilde{b}$ from the duality of K_I factors by requiring that K_I of the displacement-driven model (10) be equal to that of the force-driven model (11) when the sliding mechanism is active.

The remaining kinematic variables $\tilde{l}$ and θ are obtained as functions of σ_{ij} from the following conditions:

$$\begin{cases} K_I = K_{IC} \\ \dfrac{\partial K_I}{\partial \theta} = 0 \end{cases} \tag{23}$$

Kinetic relations for $\dot{\tilde{l}}(\dot{\sigma}_{ij})$ and $\dot{\theta}(\dot{\sigma}_{ij})$ follow from (23) by time differentiation. The resulting equations are algebraically quite involved, thus were solved numerically using the symbolic algebra softwares. In the long wing limit these equations take much simpler forms and in uniaxial compression are even solvable analytically (Basista and Gross, 1997a).

5. AVERAGE STRESS-STRAIN RELATIONS

In the preceding sections, the preexisting cracks had fixed orientation and size. In order to compute overall stress-strain curves a homogenization procedure is necessary. Since crack interactions are not yet included, the overall stresses and strains may be approximated by simple area averages of the contributions of individual sliding cracks. Assuming a finite number of specific orientations of preexisting cracks, the average strain increment may be computed as in Nemat-Nasser and Obata (1988), from

$$d\bar{\varepsilon}_{ij} = \frac{1}{R}\sum_{r=1}^{R} d\varepsilon_{ij}\left(\varphi_r, \omega_0(\varphi_r)\right) \tag{24}$$

where R is the number of considered orientations φ_r. The strain increments under the summation sign in (24) are given by equations (12)-(19). For an isotropic distribution of preexisting cracks all crack orientations are likely to appear. From the symmetry arguments, it further follows that the shear strains in the global coordinate system (x_1, x_2) must vanish.

As an illustration of the developed constitutive theory, Basista and Gross (1997a) considered an example of uniaxial compression on Westerly granite specimens. The force-driven model mechanism (Fig.2b) was adopted for the computations of strain increments along the lines of Section 3. The following material parameters were assumed:

$$E_0 = 58000 \text{ MPa}, \quad \nu_0 = 0.23, \quad \sigma_{uc} = -204 \text{ MPa},$$
$$\mu = 0.65, \quad c = 5 \cdot 10^{-4} \text{ m}, \quad K_{IC} = 0.7 \text{ MPa}\sqrt{\text{m}}, \tag{25}$$
$$\tau_c = 12 \text{ MPa}, \quad \omega_0 = 0.375, \quad R = 90 .$$

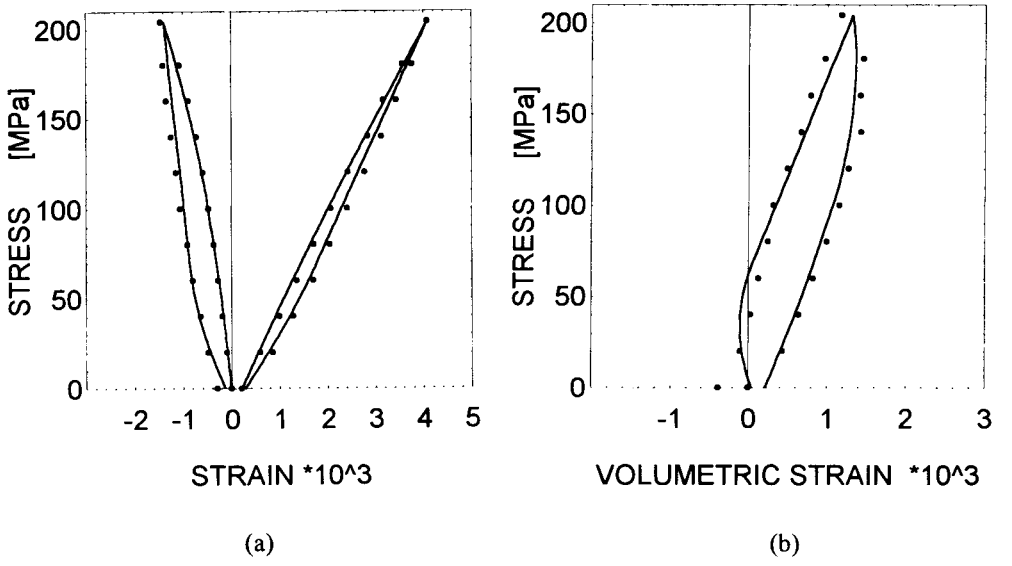

Figure 3. Analytical predictions (solid lines) from Basista and Gross (1997a) vs. test data on Westerly granite (Zoback and Byerlee, 1975).

In Fig.3a,b the obtained theoretical curves are compared with the experimental data of Zoback and Byerlee (1975). Simple as it is, this damage model predicts several qualitative features of the brittle response of granite: the overall trends in loading and unloading are well preserved, the lateral inelastic strain is substantially larger than its axial counterpart, the permanent set and hysteresis loops are accounted for. Note that the material parameters used in the computations are rather realistic and are documented in the referenced literature. Typically of all micromechanical models, the present formulation contains no fitting parameters

6. INTERACTION OF FRICTIONAL CRACKS

In this section, we shall report some preliminary results concerning the sliding cracks interaction effects and their incorporation in the present thermodynamic framework with microstructural internal variables. In general, crack interactions may be analyzed either

indirectly through one of the effective continua techniques (e.g. self-consistent method) or directly by formulating and solving an appropriate elasticity problem. In some simple cases of crack configurations, the integral equation method may successfully be employed to get the exact (analytical or numerical) solution to the elasticity problem in question. However, for large crack concentrations, the exact solution is practically out of our reach and the so called approximate direct methods offer a way out. Of several approximate direct methods dealing with crack-crack interactions (e.g. Gross, 1982; Horii & Nemat-Nasser, 1985b; Benveniste et al., 1989), the one proposed by Kachanov (1987) is chosen for its simplicity and accuracy.

Consider a plate of linear elastic material weakened by N arbitrarily located rectilinear closed cracks under overall compression. The present analysis of crack-crack interactions is confined to the *phase 1* (in the notation of Basista and Gross, 1997a) which stands for frictional sliding on preexisitng cracks with no tension wings yet. Within the present framework, the crack interaction effects (amplification or shielding) will influence the thermodynamic forces and the fluxes. In *phase 1*, it is sufficient to determine the actual shear stress (conjugate force) τ'_{12} along the preexisting crack, and the average slip displacement (internal variable) $\bar{b}$ from which the inelastic strains can be computed in the standard manner of Section 2.

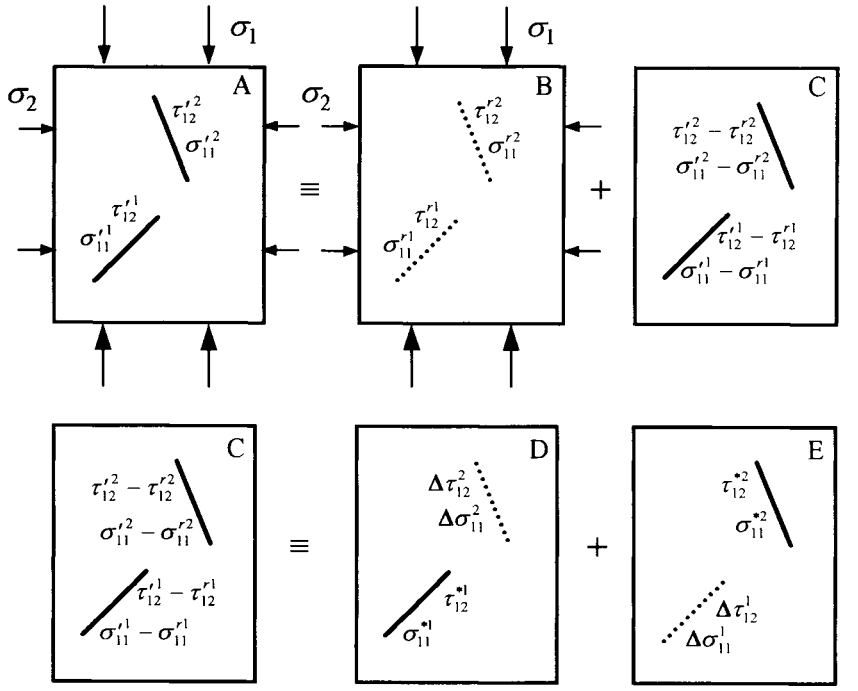

Figure 4. Superposition of stresses for two frictional cracks under compression.

The original Kachanov method has to be modified to account for cohesive-frictional sliding on closed cracks. In preparation for that, consider the superposition of stresses depicted in Fig.4. To facilitate the drawing, only two cracks are marked in Fig.4, whereas the equations to

follow are formulated for an arbitrary 2D array of N cracks. According to Kachanov (1987), the problem C can be represented as a superposition of N subproblems each involving only one isolated crack but loaded by unknown stresses τ_{12}^{*L}, σ_{11}^{*L}, (L=1,...,N). In contrast to open mode-I and mode-II cracks considered in Kachanov (1987, p.24), the signs of superimposed stresses in Fig.4 are strictly observed in order to avoid confusion among the several different stresses involved in the compression case. Recall that the continuum mechanics sign convention is used throughout this paper, i.e. compression is viewed negative. Consequently, for closed frictional cracks, it follows that

$$\tau_{12}^{*L} = \tau_{12}'^{L} - \left(\tau_{12}^{rL} + \Delta\tau_{12}^{L}\right) \tag{26}$$

$$\sigma_{11}^{*L} = \sigma_{11}'^{L} - \left(\sigma_{11}^{rL} + \Delta\sigma_{11}^{L}\right) = 0 \tag{27}$$

where $\tau_{12}'^{L}$, $\sigma_{11}'^{L}$ denote the actual (contact) shear and normal stresses existing on the faces of L-th crack, τ_{12}^{rL}, σ_{12}^{rL} are the resolved (due to the remote loading) shear and normal stresses along the line of L-th crack in a continuous material, $\Delta\tau_{12}^{L}$, $\Delta\sigma_{11}^{L}$ are the interaction terms, i.e. shear and normal stresses generated in the continuous material along the line of L-th crack by all other cracks.

The key assumption of the Kachanov method is that the unknown crack interaction stresses $\Delta\tau_{12}^{L}$, $\Delta\sigma_{11}^{L}$ are induced only by *uniform* average stresses (as yet also unknown) acting on the other cracks' faces. Denote by P_{ij}^{K} and T_{ij}^{K} the standard stress fields that are generated in the continuous material by the K-th crack loaded by uniform normal and shear tractions of unit intensity, respectively. The standard stress fields can be found in Kachanov (1987) or in the related papers that are referenced there. The crack interaction stresses, generated in the continuous material along the line of L-th crack, can be expressed as

$$\Delta\sigma_{11}^{L} = -n_i^{L}\left[P_{ij}^{K}\left\langle\sigma_{11}^{*K}\right\rangle + T_{ij}^{K}\left\langle\tau_{12}^{*K}\right\rangle\right]n_j^{L} \tag{28}$$

no sum over L; sum over $K = 1,\ldots,N$; $(K \neq L)$

$$\Delta\tau_{12}^{L} = -n_i^{L}\left[P_{ij}^{K}\left\langle\sigma_{11}^{*K}\right\rangle + T_{ij}^{K}\left\langle\tau_{12}^{*K}\right\rangle\right]m_j^{L} \tag{29}$$

where $\mathbf{n}$, $\mathbf{m}$ are the unit vectors normal and tangential to the crack; $\langle\ \rangle$ denotes the average value of the bracketed quantity. Averaging (28) and (29) leads to

$$\left\langle\Delta\sigma_{11}^{L}\right\rangle = -\Lambda_{11}^{KL}\left\langle\sigma_{11}^{*K}\right\rangle - \Lambda_{12}^{KL}\left\langle\tau_{12}^{*K}\right\rangle \tag{30}$$

$$\left\langle\Delta\tau_{12}^{L}\right\rangle = -\Lambda_{21}^{KL}\left\langle\sigma_{11}^{*K}\right\rangle - \Lambda_{22}^{KL}\left\langle\tau_{12}^{*K}\right\rangle \tag{31}$$

where Λ_{ij}^{KL} are the transmission factors (interaction matrices) defined as follows

$$\begin{aligned}
&\Lambda_{11}^{KL} = n_i^L \left\langle P_{ij}^K \right\rangle^L n_j^L, \quad \Lambda_{12}^{KL} = n_i^L \left\langle T_{ij}^K \right\rangle^L n_j^L; \qquad (K \neq L) \\
&\Lambda_{21}^{KL} = n_i^L \left\langle P_{ij}^K \right\rangle^L m_j^L, \quad \Lambda_{22}^{KL} = n_i^L \left\langle T_{ij}^K \right\rangle^L m_j^L; \qquad (K \neq L) \\
&\Lambda_{ij}^{KL} = 0; \quad (K = L)
\end{aligned} \tag{32}$$

In $(32)_{1,2}$ summation is extended over K, while no sum convention applies to L. For convenience, the notation of transmission factors in (32) has been slightly changed as compared with the original one in Kachanov (1987). For example Λ_{21}^{KL} denotes the average shear stress (lower index 2) on crack L due to unit normal stress (lower index 1) on crack K. In practical terms, computation of the above transmission factors requires integration of the standard stress fields caused by the K-th crack along the line of the L-th crack.

The actual stresses τ_{12}', σ_{11}' due to frictional contact on the L-th crack faces are interrelated through the Coulomb-Mohr law of dry friction, namely

$$\tau_{12}'^{L} = \tau_c - \mu \sigma_{11}'^{L} \tag{33}$$

Combining (33), (26) and (27) gives

$$\tau_{12}^{*L} = \left(\tau_c - \mu \sigma_{11}^{rL} - \tau_{12}^{rL}\right) - \left(\mu \Delta\sigma_{11}^{L} + \Delta\tau_{12}^{L}\right) \tag{34}$$

By averaging (34) and making use of (27), (30), (31), we obtain a system of N linear equations

$$\left(\delta^{KL} - \mu \Lambda_{12}^{KL} - \Lambda_{22}^{KL}\right)\left\langle \tau_{12}^{*K} \right\rangle = \left(\tau_c - \mu\sigma_{11}^{rL} - \tau_{12}^{rL}\right), \quad (K,L = 1,2,\ldots,N) \tag{35}$$

The right hand side of (35) specifies the remote loading conditions and the friction-cohesion resistance on the considered crack. The crack array geometry and the influence of friction on the transmission of shear stresses are reflected in the left hand part.

Equations (35) with the transmission factors (32) and a given loading $\left(\sigma_{11}^{rL},\ \tau_{12}^{rL}\right)$ constitute the governing system of equations for the average shear stresses $\left\langle \tau_{12}^{*K} \right\rangle$. To solve them, a numerical program, developed originally by Wagner and Gross (1988) for open cracks, has been extended here to account for the mode-II frictional sliding under overall compressive stresses. For a simple configuration of two inclined equal cracks (Fig.5a) under uniaxial compression, the obtained approximate solutions for $\left\langle \tau_{12}^{*} \right\rangle = \left\langle \tau_{12}^{*2} \right\rangle = -\left\langle \tau_{12}^{*1} \right\rangle$ have been compared with the 'exact' numerical results of Lauterbach and Gross (1997) who applied the BEM to solve the appropriate elastic boundary-value problem by means of the Kolosov-Muskhelishvili stress potentials. The curves in Fig.5b represent the average shear stresses acting on the individual cracks vs. the relative distance of crack tips. The solid lines depict the current results whereas the numerical solution of Lauterbach and Gross is marked by symbols.

Both solutions are practically indistinguishable. Note that for the most part configuration promotes shielding i.e. $\langle \tau_{12}^{*} \rangle$ diminishes as *d/c* becomes smaller.

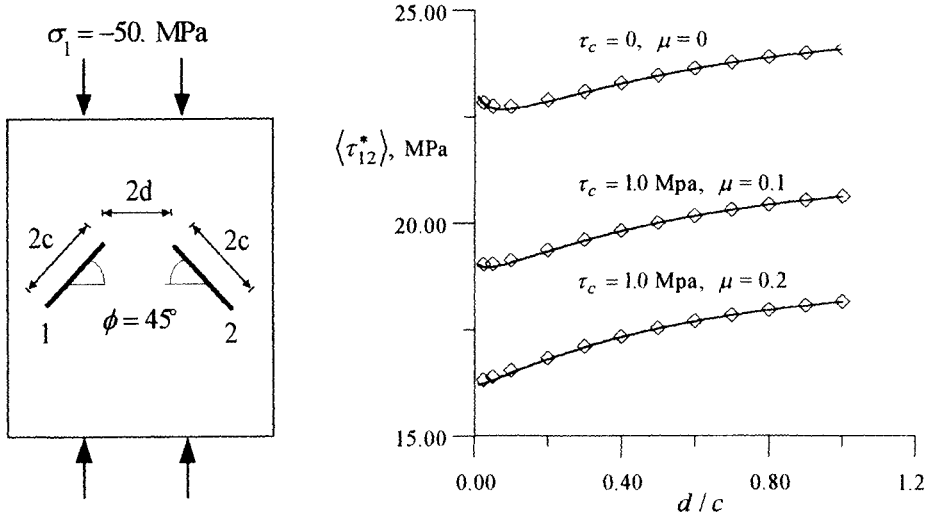

Figure 5. (a) Two symmetrically inclined cracks under uniaxial compression. (b) Average shear stresses $\langle \tau_{12}^{*} \rangle$ on crack faces vs. relative distance between crack tips.

Another illustrative example of two collinear inclined cracks is shown in Fig.6a,b. It is commonly known that collinear configurations of open cracks induce amplification of stresses and stress intensity factors. In case of frictional cracks this effect is maintained as seen in Fig. 6b.

Having computed the average stresses $\langle \tau_{12}^{*L} \rangle$, it is now possible to determine the actual shear stresses $\tau_{12}^{\prime L}$ (thermodynamic force in phase 1) acting on the L-th crack faces. This can be accomplished upon computing $\Delta\sigma_{11}^{L}$, $\Delta\tau_{12}^{L}$ from (28), (29), then τ_{12}^{*L} from (34), and finally $\tau_{12}^{\prime L}$ from (26).

The next step is to determine the average relative slip displacement (internal variable) $\langle b^{L} \rangle = \bar{b}^{L}$ of the points on crack faces. As stated in Kachanov (1987), the average displacement jump and the average tractions on a crack are interrelated through a simple (approximate) proportionality

$$\langle t_i^{*L} \rangle \approx -\left(E_0'/\pi c^{L}\right)\langle b_i^{L} \rangle \tag{36}$$

where $t_i^{*L} = \left(\sigma_{11}^{*L}, \tau_{12}^{*L}\right)$. The minus sign in (36) results from the sign conventions applied to stresses and displacement jumps. For the considered closed frictional cracks, it holds $\sigma_{11}^{*L} = 0$ and the proportionality (36) takes the form

$$\tilde{b}_2^L = \left\langle b_2^L \right\rangle / c^L = -\frac{\pi}{E_0'} \left\langle \tau_{12}^{*L} \right\rangle \tag{37}$$

Once the fluxes and conjugate forces are determined, the inelastic strain increments can be computed from the fundamental micro-macro transition relation (1).

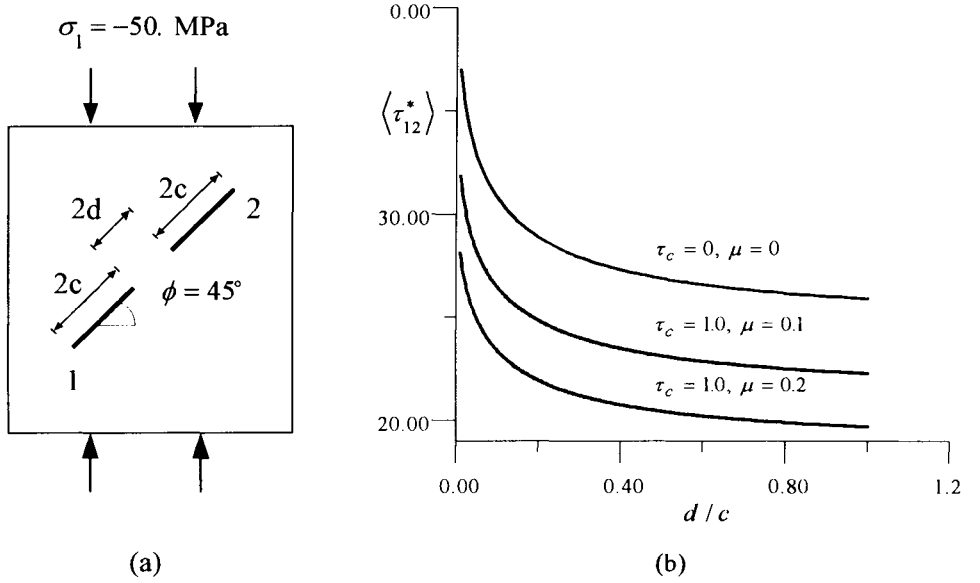

Figure 6. (a) Two collinear inclined cracks under uniaxial compression. (b) Average shear stresses $\left\langle \tau_{12}^{*} \right\rangle$ on crack faces vs. relative distance of crack tips.

7. CONCLUSIONS

In the first part of this paper, we have reviewed our recent results regarding the sliding crack model of brittle deformation within the context of Rice thermodynamic framework with microstructural internal variables. Two idealizations of the basic deformational micromechanism were analyzed: the displacement-driven model and the force-driven model. The entire sliding crack was considered with energy dissipation on the frictional sliding on preexisting flaws, the wing cracks extension, and the wing cracks rotation. The latter was introduced to mimic the curvilinear path of the wing tip propagation. Incremental stress-strain

equations were derived and applied to predict experimentally observed behavior of granite specimens in unconfined compression.

The second part was devoted to the interaction effects of sliding cracks examined within the Rice thermodynamic framework. So far, only *phase 1* (frictional sliding, no wings yet) was analyzed. The Kachanov (1987) strong interaction scheme was modified to account for frictional and cohesive resistance on closed cracks. Preliminary developments show that the model lends itself well to this method of modeling of crack-crack interactions.

8. REFERENCES

Ashby, M.F. and Hallam, S.D. (1986). The failure of brittle solids containing small cracks under compressive stress states. *Acta Metall.* **34**, 497-510.

Basista, M. and Gross, D. (1997a). The sliding crack model of brittle deformation: an internal variable approach. *Int. J. Solids Structures.* (in print)

Basista, M. and Gross, D. (1997b). Internal variable representation of microcrack induced inelasticity in brittle materials. *Int. J. Damage Mech.* (in print)

Benveniste, Y., Dvorak, G.J., Zarzour, J. and Wung, E.C.J. (1989). On interacting cracks and complex crack configurations in linear elastic media, *Int.J.Solids Structures* **25**, 1279-1293.

Bieniawski, Z.T. (1967). Mechanism of brittle fracture of rock. *Int. J. Rock Mech. Min. Sci.* **4**, 407-423.

Brace, W.F. and Bombolakis, E.G. (1963). A note on brittle crack growth in compression. *J. Geophys. Res.* **68**, 709-3713.

Cotterell, B. and Rice, J.R. (1980). Slightly curved or kinked cracks. *Int. J. Fracture* **16**, 155-169.

Dyskin, A.V., Germanovich, L.N., Jewell, R.J., Joer, H., Krasinski, J.S., Lee, K.K., Roegiers, J.-C., Sahouryeh, E. And Ustinov, K.B. (1995) Some experimental results on three-dimensional crack propagation in compression. In: *Mechanics of Jointed and Faulted Rock*, Rossmanith (ed.), Balkema Rotterdam, 91-96.

Fanella, D. and Krajcinovic, D. (1988). A micromechanical model for concrete in compression. *Engng. Fract. Mech.* **29**, 49-66.

Gross, D. (1982), Spannungsintensitaetsfaktoren von Risssystemen, *Ing. Archiv*, **51**, 301-310.

Horii, H. and Nemat-Nasser, S. (1985). Compression-induced microcrack growth in brittle solids: axial splitting and shear failure. *J. Geophys. Res.* **90**, 3105-3125.

Horii, H. and Nemat-Nasser, S. (1985). Elastic fields of interacting inhomogeneities, *Int. J. Solids Structures* **21**, 731-745

Horii, H. and Nemat-Nasser, S. (1986). Brittle failure in compression: splitting, faulting and brittle-ductile transition. *Phil. Trans. Roy. Soc. London* **319**, 337-374.

Ju, J.W. (1991). On two-dimensional self-consistent micromechanical damage models for brittle solids. *Int. J. Solids Structures* **27**, 227-258.

Kachanov, M. (1982). A microcrack model of rock inelasticity, Part I: Frictional sliding on microcracks. *Mech. Mater.* **1**, 19-27.

Kachanov, M. (1987). Elastic solids with many cracks-a simple method of analysis, *Int. J. Solids Structures* **23**, 23-43.

Kemeny, J.M. and Cook, N.G.W. (1991). Micromechanics of deformation in rocks. In *Toughening Mechanisms in Quasi-Brittle Materials* (Edited by S.P. Shah), pp. 155-188. Kluwer Academic Publishers.

Kestin, J.and Rice, J.R. (1970). Paradoxes in the application of thermodynamics to strained solids. In *Critical Review of Thermodynamics* (Edited by E.B. Stuart et al.), pp. 275-298. Mono Book Corp., Baltimore.

Lauterbach, B. and Gross D. (1997). Crack growth in brittle solids under compression. Submitted for publication.

Lauterbach, B. and Gross D. (1997). Private communication.

Moss, W.C. and Gupta, Y.M. (1982). A constitutive model describing dilatancy and cracking in brittle rock. *J. Geophys. Res.* **87**, 2985-2998.

Nemat-Nasser, S. and Horii, H. (1982). Compression-induced nonplanar crack extension with application to splitting, exfoliation and rockburst, *J.Geophys. Res.* **87**, 6805-6821.

Nemat-Nasser, S. and Obata, M. (1988). A microcrack model of dilatancy in brittle materials. *J. Appl. Mech.*, **55**, 24-35.

Peng, S. and Johnson, J.M. (1972). Crack growth and faulting in cylindrical specimens of chelmsford granite. *Int. J. Rock Mech. Min. Sci.* **9**, 37-86.

Rice, J.R. (1971). Inelastic constitutive relations for solids: an internal-variable theory and its application to metal plasticity. *J. Mech. Phys. Solids* **19**, 433-455.

Rice, J.R. (1975). Continuum mechanics and thermodynamics of plasticity in relation to microscale deformation mechanisms. In *Constitutive Equations in Plasticity* (Edited by A.S. Argon), pp. 23-79. The MIT Press, Cambridge, MA.

Sammis, C.G. and Ashby, M.F. (1986). The failure of brittle porous solids under compressive stress states. *Acta Metall.* **34**, 511-526.

Steif, P.S. (1984). Crack extension under compressive loading. *Eng. Fract. Mech.* **20**, 463-473.

Tada, H., Paris, P. and Irwin, G. (1985). *The Stress Analysis of Cracks Handbook*. Paris Productions Inc., St. Louis, MO.

Wagner, Ch. and Gross. D. (1988) Untersuchungen zur Wechselwirkung zwischen Defekten und einem Einzelriss. *DFG-Arbeitsbericht*, Gr 596/15-1, Institut fuer Mechanik, Technische Hochschule Darmstadt, Germany.

Walsh, J.B. (1965). The effect of cracks on the uniaxial elastic compression of rocks. *J. Geophys. Res.*, **70**, 399-411.

Wang, R. and Kemeny, J.M. (1993). Micromechanical modeling of tuffaceous rock for application in nuclear waste storage. *Int. J. Rock Mech. Min. Sci. and Geomech. Abstr.* **30**, 1351-1357.

Zaitsev, Y.V. (1985). Inelastic properties of solids with random cracks. In *Mechanics of Geomaterials* (Edited by Z. Bazant), Wiley.

Zhao, Y, Huang, J and Wang, R. (1993). Real-time SEM observations of the microfracturing process in rock during a compression test. *Int. J. Rock Mech. Min. Sci. and Geomech. Abstr.* **30**, 643-652.

Zoback, M.D. and Byerlee, J.D. (1975). The effect of cyclic differential stress on dilatancy in Westerly granite under uniaxial and triaxial conditions. *J. Geophys. Res.* **80**, 1526-1530.

This Page Intentionally Left Blank

Damage Mechanics in Engineering Materials
G.Z. Voyiadjis, J.-W.W. Ju and J.-L. Chaboche (Editors)
© 1998 Elsevier Science B.V. All rights reserved.

Damage evolution rule for multiaxial variable loading

Zenon MRÓZ[a] and Andrzej SEWERYN[b]

[a] Institute of Fundamental Technological Research,
Świętokrzyska 21, 00-049 Warsaw, Poland

[b] Białystok University of Technology, Faculty of Mechanics,
Wiejska 45 C, 15-351 Białystok, Poland

The damage accumulated within the material element is associated with the physical plane and predicted by the contact stress or strain rule. For singular stress or strains regimes a non-local failure or damage rule is used. The application to both monotonic and variable loading is provided. The theoretical model predictions are compared with the experimental data obtained for notched specimens under combined tension and shear loading varying monotonically or cyclically. The compliance variation is predicted from the known damage distribution on physical planes.

1. INTRODUCTION

The present work is concerned with the uniform formulation of damage and failure rules for materials subjected to monotonic or variable loading. A simple approach could be based on the elastic stress analysis with neglect of stress redistribution due to damage or plastic strains. The failure of brittle materials and high cycle fatigue problems could be treated within this approach. The local or non-local stress condition on the physical plane element is used to predict crack initiation or damage growth. This approach differs from the elastic fracture mechanics where the elastic energy release associated with the plane crack growth is used as a critical factor. However, the fracture mechanics assumptions do not allow for treatment of crack initiation processes from sharp notches, inclusions or grain boundary singularities. On the other hand, the proposed approach provides the simple tool to treat both crack initiation and propagation stages within the same constitutive assumptions. The experimental data validate the proposed model, though more ample empirical evidence is needed. The present model provides also the damage distribution on physical planes. The associated compliance variation can next be determined and the damage strain can be included in the analysis.

The present paper synthesizes and extends the previous authors results [1-8]. The comprehensive exposition of damage mechanics can be found in books by Lemaitre [10] and Krajcinowic [9].

2. NON-LOCAL BRITTLE FAILURE CRITERION

Consider an arbitrary physical plane Δ and the local coordinate system (ξ_1,ξ_2,ξ_3) (Fig.1). In the global coordinate system (x_1,x_2,x_3) the origin of the local system is specified by the position vector $\mathbf{x_0}(x_{01},x_{02},x_{03})$ and the unit normal vector $\mathbf{n}(n_1,n_2,n_3)$, specifies the plane orientation, where $n_i = \cos(\xi_3,x_i)$.

The stress and strain tensors $\underline{\sigma}$ and $\underline{\varepsilon}$ provide the traction and strain vectors Σ and E. In the local coordinate system we have

$$\Sigma_i(\tau_{n1},\tau_{n2},\sigma_n) = N_{ij}\sigma_{jk}n_k, \qquad E_i(\gamma_{n1},\gamma_{n2},\varepsilon_n) = N_{ij}\varepsilon_{jk}n_k, \tag{1}$$

where $N_{ij} = \cos(\xi_i,x_j)$ is the transformation matrix.
We have also

$$\begin{aligned}
&\sigma_n = \sigma_{ij}n_in_j, \quad \varepsilon_n = \varepsilon_{ij}n_in_j,\\
&\tau_{n\chi} = \sigma_{ij}t_{\chi i}n_j = \sigma_{ij}t_{\chi j}n_i = \frac{1}{2}\sigma_{ij}\left[t_{\chi i}n_j + t_{\chi j}n_i\right],\\
&\gamma_{n\chi} = \varepsilon_{ij}t_{\chi i}n_j = \varepsilon_{ij}t_{\chi j}n_i = \frac{1}{2}\varepsilon_{ij}\left[t_{\chi i}n_j + t_{\chi j}n_i\right],
\end{aligned} \tag{2}$$

where $t_{\chi i} = \cos(\xi_\chi,x_i)$, $\chi = 1, 2$.

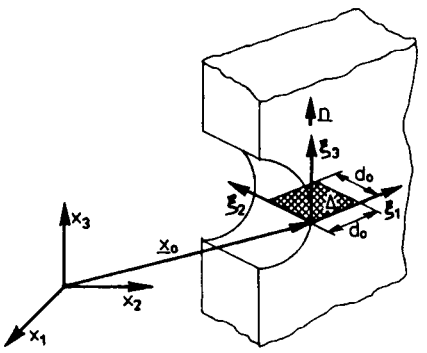

Fig. 1. Physical plane Δ with the associated local coordinate system (ξ_1,ξ_2,ξ_3), and the global reference system (x_1,x_2,x_3).

The resulting shear stress and strain in the plane Δ are expressed as follows

$$\tau_n = \left[\tau_{n1}^2 + \tau_{n2}^2\right]^{1/2}, \quad \gamma_n = \left[\gamma_{n1}^2 + \gamma_{n2}^2\right]^{1/2}. \tag{3}$$

Let us assume that the crack initiation and propagation process in the plane Δ depends on the contact stress and strain components, and also the damage accumulation on the physical plane. The stress condition of failure for monotonic loading is referred to the critical plane Δ_c on which the local stress failure function reaches a maximum, thus

$$R_{f\sigma} = \max_{(\mathbf{n},\mathbf{x_0})} R_\sigma(\sigma_n/\sigma_c, \tau_n/\tau_c) = 1, \tag{4}$$

where $R_{f\sigma}$ is the brittle failure factor; R_σ is the stress failure function, σ_c, τ_c are the failure stresses in tension and shear.

Let us note that the criterion (4) allows for specification of the critical load and also of crack location and orientation as the maximization process is carried out with respect to $\mathbf{x_0}$ and $\mathbf{n}$. The stress failure function is expressed in terms of contact traction components σ_n and τ_n. Depending on the material property this function can be assumed as normal or shear stress function or a combined function of different forms in tension and compression regimes, Fig.2.

Consider, for instance, an elliptic condition for $\sigma_n > 0$ and the Coulomb condition for $\sigma_n < 0$, thus

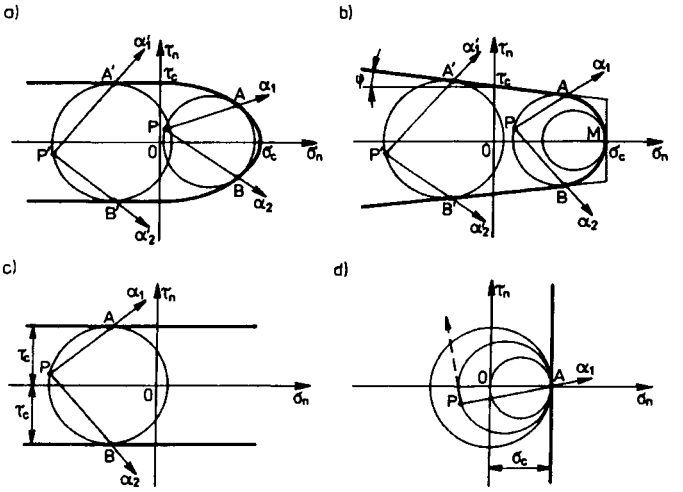

Fig.2. Stress brittle failure function in the stress plane: a) elliptic condition for normal tensile stress combined with the shear condition for compressive normal stress, b) Coulomb condition with tension cut-off, c) shear condition, d) tension condition

$$R_\sigma\left(\frac{\sigma_n}{\sigma_c},\frac{\tau_n}{\tau_c}\right)=\begin{cases}\left[\left(\dfrac{\sigma_n}{\sigma_c}\right)^2+\left(\dfrac{\tau_n}{\tau_c}\right)^2\right]^{0.5}, & \sigma_n\geq 0,\\ \dfrac{1}{\tau_c}\left(|\tau_n|+\sigma_n\tan\varphi\right), & \sigma_n<0.\end{cases} \tag{5}$$

The stress failure function can be presented in the (σ_n,τ_n) plane as the envelope of stress circles in the critical state. The critical planes α_1, α_2 are specified by the tangency points of the Mohr circle and the envelope, Fig.2. There are two critical planes for the Coulomb or shear stress condition and only one plane for the normal stress condition.

For large stress gradients or singular stress regimes such as those occurring at vertices of wedge shaped notches the non-local stress failure condition is applied by averaging the failure stress function over on area $d_0 \times d_0$, Fig.1, thus obtaining

$$R_{f\sigma}=\max_{(\mathbf{n},\mathbf{x}_0)}\overline{R}_\sigma\left(\sigma_n/\sigma_c,\tau_n/\tau_c\right)=\max_{(\mathbf{n},\mathbf{x}_0)}\left[\frac{1}{{d_0}^2}\int_0^{d_0}\int_0^{d_0}R_\sigma \mathrm{d}\xi_1\mathrm{d}\xi_2\right]=1, \tag{6}$$

where $\overline{R}_\sigma$ is the non-local failure function. An alternative non-local condition can be obtained by averaging stress components acting the plane Δ

$$\overline{\sigma}_n=\frac{1}{{d_0}^2}\int_0^{d_0}\int_0^{d_0}\sigma_n \mathrm{d}\xi_1\mathrm{d}\xi_2,\qquad \overline{\tau}_n=\frac{1}{{d_0}^2}\int_0^{d_0}\int_0^{d_0}\tau_n \mathrm{d}\xi_1\mathrm{d}\xi_2. \tag{7}$$

and substituting to (4), thus

$$R_{f\sigma} = \max_{(n,x_0)} \overline{R}_\sigma\left(\overline{\sigma}_n / \sigma_c, \overline{\tau}_n / \tau_c\right) = 1, \tag{8}$$

The size parameter d_0 (representing the size of the damage zone) can be specified by requiring the non-local condition (6) to be equivalent to the Griffith condition in the case of tensile crack propagation. This provides [1]

$$d_0 = \frac{2}{\pi}\left(\frac{K_{Ic}}{\sigma_c}\right)^2, \tag{9}$$

where K_{Ic} is the critical stress intensity factor in Mode I.

Assume now that the critical stress values σ_c and τ_c depend on temperature T_o and the accumulated damage $\omega_{n\sigma}$, so that

$$\sigma_c = \sigma_c\left(T_o, \omega_{n\sigma}\right) = \sigma_{co}\left(T_o\right)\left(1 - \omega_{n\sigma}\right)^p, \qquad \tau_c = \tau_c\left(T_o, \omega_{n\sigma}\right) = \tau_{co}\left(T_o\right)\left(1 - \omega_{n\sigma}\right)^p, \tag{10}$$

where σ_{co}, τ_{co} are the critical stress for the undamaged material and p is the material parameter. From (10) it follows that

$$\omega_{n\sigma} = 1 - \left(\frac{\sigma_c}{\sigma_{co}}\right)^{1/p} = 1 - \left(\frac{\tau_c}{\tau_{co}}\right)^{1/p} \tag{11}$$

and we assumed that the damage affects in the same way both critical stresses σ_c and τ_c.

A more general case can be treated when the coupled stress and plastic damage $\omega_{n\sigma}$, ω_{np} occurs accompanied by corrosive damage ω_{nh}. The effective damage on the plane Δ can be represented as follows

$$\Omega_{n\sigma} = \omega_{n\sigma} + \Phi_\sigma\left(\omega_{np}, \omega_{nh}\right). \tag{12}$$

and

$$\sigma_c = \sigma_{co}\left(T_o\right)\left(1 - \Omega_{n\sigma}\right)^p, \qquad \tau_c = \tau_{co}\left(T_o\right)\left(1 - \Omega_{n\sigma}\right)^p, \tag{13}$$

where Φ_σ provides the combined measure of plastic and corrosive damage.

The strain failure condition can be formulated analogously to the stress condition. Consider the failure strain function

$$R_{f\varepsilon} = \max_{(n,x_0)} R_\varepsilon\left(\varepsilon_n / \varepsilon_c, \gamma_n / \gamma_c\right) = 1, \tag{14}$$

where $R_{f\varepsilon}$ is the failure strain factor, and ε_c, γ_c are the critical normal and shear strains. The failure strain function can be assumed in the form

$$R_\varepsilon\left(\varepsilon_n / \varepsilon_c, \gamma_n / \gamma_c\right) = \left[\left(\frac{\langle\varepsilon_n\rangle}{\varepsilon_c}\right)^2 + \left(\frac{\gamma_n}{\gamma_c}\right)^2\right]^{0,5}. \tag{15}$$

where $\langle\varepsilon_n\rangle = \varepsilon_n$ for $\varepsilon_n > 0$ and $\langle\varepsilon_n\rangle = 0$ for $\varepsilon_n < 0$. The non-local failure condition can now be written as follows

$$R_{f\varepsilon} = \max_{(\mathbf{n},\mathbf{x}_0)} \overline{R}_\varepsilon\left(\varepsilon_n / \varepsilon_c, \gamma_n / \gamma_c\right) = \max_{(\mathbf{n},\mathbf{x}_0)}\left[\frac{1}{d_\varepsilon{}^2}\int_0^{d_\varepsilon}\int_0^{d_\varepsilon} R_\varepsilon \, d\xi_1 d\xi_2\right] = 1. \tag{16}$$

where the size parameter d_ε can be expressed by comparing (16) with the Griffith condition for the tensile crack. For the plane stress case we have

$$d_\varepsilon = \frac{2}{\pi}\left(\frac{(1-\nu)K_{Ic}}{\sigma_c}\right)^2. \tag{17}$$

Let us note that the stress and strain conditions are not equivalent and provide different predictions. In fact, the value of ε_n depends not only on σ_n but also on σ_{t1}, σ_{t2}, acting within the plane Δ.

3. EXPERIMENTAL ANALYSIS OF CRACK INITIATION IN NOTCHED ELEMENTS

Consider a plate with sharp wedge shaped notch of the angle 2β subjected to combined tension and shear. In the local coordinate system (r,ϑ), the stress and displacement fields can be presented in the form [11]

$$\begin{aligned} \sigma_{ij} &= (2\pi r)^{\lambda_I - 1} K_I^\lambda a_{ij}(\vartheta) + (2\pi r)^{\lambda_{II} - 1} K_{II}^\lambda b_{ij}(\vartheta), \\ q_i &= (2\pi r)^{\lambda_I} K_I^\lambda c_i(\vartheta) + (2\pi r)^{\lambda_{II}} K_{II}^\lambda d_i(\vartheta). \end{aligned} \tag{18}$$

where the singularity exponents λ_I and λ_{II} are specified from the characteristic equations

$$\lambda_I \sin 2\alpha + \sin 2\lambda_I \alpha = 0, \quad \lambda_{II} \sin 2\alpha - \sin 2\lambda_{II} \alpha = 0, \quad \alpha = \pi - \beta \tag{19}$$

and the generalized stress intensity factors for Mode I and Mode II are defined as follows

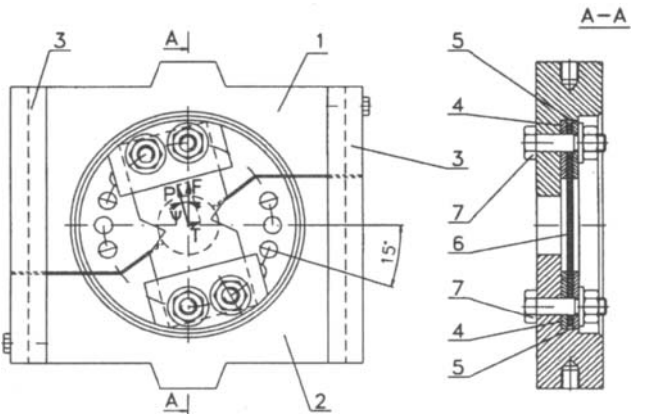

Fig.3. Special device for biaxial loading of plane specimens with notches

$$K_{\mathrm{I}}^{\lambda} = \lim_{\vartheta=0\, r\to 0}\left[(2\pi r)^{1-\lambda_{\mathrm{I}}}\sigma_{\vartheta\vartheta}(r,\vartheta)\right], \quad K_{\mathrm{II}}^{\lambda} = \lim_{\vartheta=0\, r\to 0}\left[(2\pi r)^{1-\lambda_{\mathrm{II}}}\tau_{r\vartheta}(r,\vartheta)\right]. \tag{20}$$

In order to analyze experimentally the crack initiation in notched specimens, a special device was constructed [8], Fig.3. The plane specimens are fixed in the device at an angle ψ with respect to the applied tensile force F. The tensile and shear forces acting on the transverse cross section are

$$T = F\sin\psi, \qquad P = F\cos\psi \tag{21}$$

The monotonic loading tests were carried out on polimethyl metacrylate (PMMA) specimens. Two notches of depth 25 mm were made symmetrically in the central specimen portion of width l_2 = 100 mm. The specimens length is l_1 = 200 mm, the distance between notch root s equals a = 50 mm and the radius of a semicircular notch equals r_0 = 25 mm. The specimen thickness is g = 5 mm.

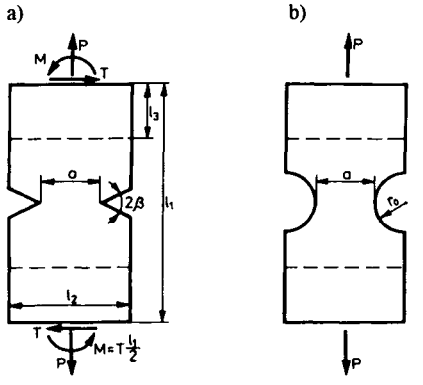

Fig.4. Plane specimens with: a) sharp notches, b) semicircular notches

The stress distribution and the generalized stress intensity factors K_{I}^{λ}, $K_{\mathrm{II}}^{\lambda}$ were determined numerically by using singular stress elements. The details of calculation are presented in the paper by Seweryn et al. [8]. The values of critical loads F_c at the crack propagation for varying loading angle ψ and the notch angle 2β are plotted in Figures 6a,d. The crack propagation direction ϑ_0 for varying angles and 2β are shown in Figures 5a,d. The value of the critical stress σ_c was identified by testing the specimen with the semicircular notch (2β = 180°, λ_{I} = 1) and assuming σ_c to correspond to crack initiation at notch root. It was further assumed that $0 < \sigma_\vartheta/\tau_c \le 1$. The non-local size parameters d_0 or d_ε were specified by determining the critical value of the stress intensity factor K_{Ic}. This value was specified in terms of generalized stress intensity factors $K_{\mathrm{Ic}}^{\lambda}$ for $2\beta = 20°\div 60°$ and the critical stress σ_c, thus

$$K_{\mathrm{Ic}} = \frac{\sigma_c}{2}\left(\frac{K_{\mathrm{Ic}}^{\lambda}}{\lambda_1\sigma_c}\right)^{\frac{1}{2(1-\lambda_1)}} \tag{22}$$

For PMMA the following values were obtained: σ_c = 115 MPa, K_{Ic} = 1.37 MPa m$^{-0.5}$, d_0 = 0.09 mm, d_ε = 0.038 mm.

It is seen that the use of the non-local stress condition (6) provides good correlation as regards to critical load variation with the loading angle ψ and the notch angle 2β. Similarly, the crack propagation orientation is well predicted by the non-local failure condition. On the other hand, the strain failure condition did not provide good correlation with the experimental data.

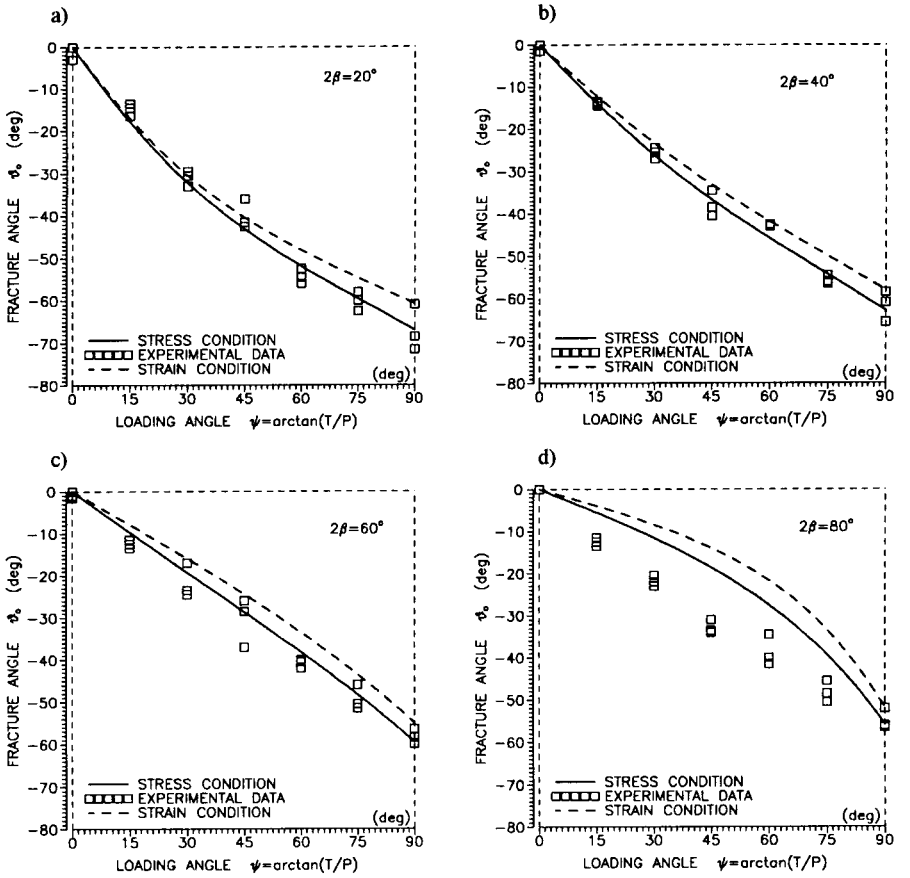

Fig.5. Crack initiation direction for specimens with notches of angles: a) 2β = 20°, b) 2β = 40°, c) 2β = 60°, d) 2β = 80° vs loading angle

4. STRESS CONDITION FOR DAMAGE ACCUMULATION

Let us now extend the analysis of the previous section by considering the accumulation of damage on the physical plane for variable loading conditions. The stress variation occurs within the elastic domain, so the compliance variation can be neglected and the damage growth can be related to elastic stress variation on the plane Δ, thus $d\omega_{n\sigma} = d\omega_{n\sigma}(\Sigma, d\Sigma, \Omega_{n\sigma})$.

Experimental data indicate that the high cycle fatigue damage occurs for stress path exceeding the threshold values of stress on the physical plane. We therefore introduce the damage initiation condition $R_{\sigma o}(\sigma_n, \tau_n, \Omega_{n\sigma}) = c$ specifying a domain in the plane σ_n, τ_n. The damage initiation function $R_{\sigma o}(\sigma_n/\sigma_o, \tau_n/\tau_o)$ is assumed to have the same form as the failure function $R_o(\sigma_n/\sigma_c, \tau_n/\tau_c)$. The critical stresses σ_c, τ_c are replaced by $\sigma_o \le \sigma_c$, $\tau_o \le \tau_c$, where σ_o, τ_o specify the damage initiation thresholds in pure tension and shear. The damage growth occurs when

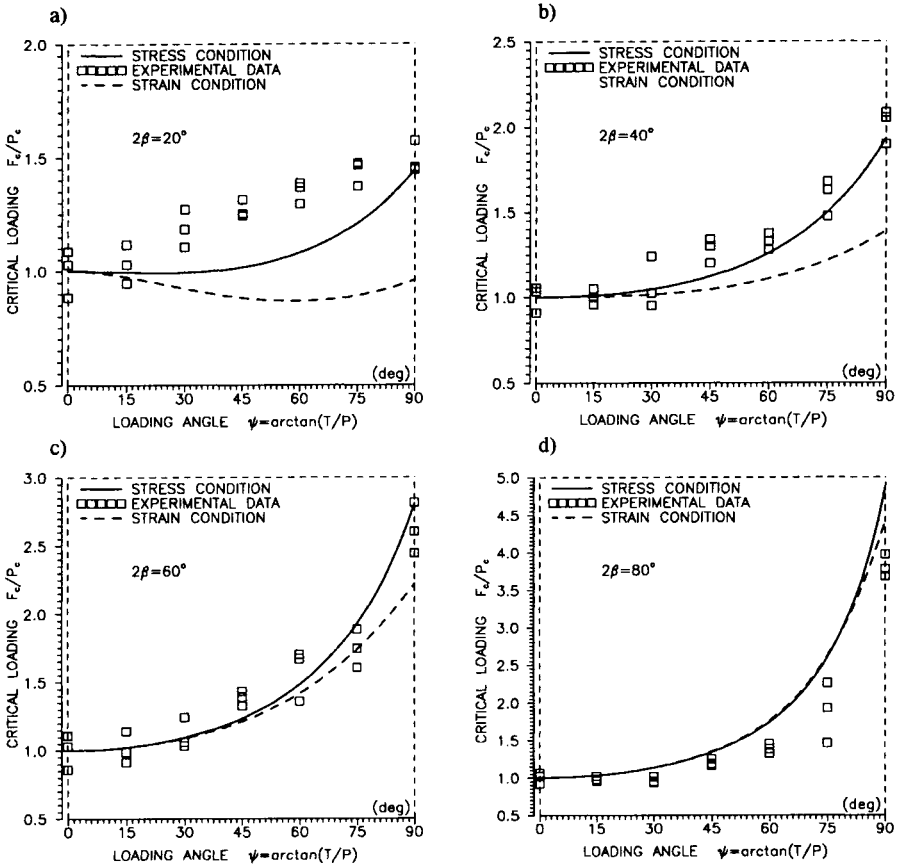

Fig.6. Critical load value F_c/P_c vs loading angle ψ for specimens with notches of angles: a) $2\beta = 20°$, b) $2\beta = 40°$, c) $2\beta = 60°$, d) $2\beta = 80°$

$$R_{f\sigma o} = \max_{(\mathbf{n},\mathbf{x}_0)} R_{\sigma o}\left(\frac{\sigma_n}{\sigma_o}, \frac{\tau_n}{\tau_o}\right) > 1, \tag{23}$$

where $R_{f\sigma o}$ is the damage initiation factor. For large stress gradients the non-local condition should be used, thus

$$\overline{R}_{f\sigma o} = \max_{(\mathbf{n},\mathbf{x}_0)} \overline{R}_{\sigma o}\left(\frac{\overline{\sigma}_n}{\sigma_o}, \frac{\overline{\tau}_n}{\tau_o}\right) = 1 \tag{24}$$

or

$$\overline{R}_{f\sigma o} = \max_{(\mathbf{n},\mathbf{x}_0)} \overline{R}_{\sigma o}\left(\frac{\sigma_n}{\sigma_o}, \frac{\tau_n}{\tau_o}\right) = \max_{(\mathbf{n},\mathbf{x}_0)}\left[\frac{1}{d_0^2}\int_0^{d_0}\int_0^{d_0} R_{\sigma o}\left(\frac{\sigma_n}{\sigma_o}, \frac{\tau_n}{\tau_o}\right) d\xi_1 d\xi_2\right] = 1. \tag{25}$$

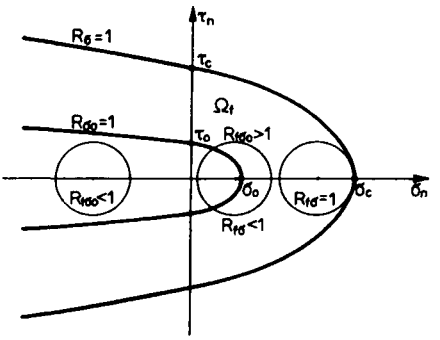

Fig.7. Local brittle failure and damage initiation curves in the stress plane

The stress values σ_0 and τ_0 depend on the temperature T_0 and the accumulated damage, so that

$$\begin{aligned} \sigma_0 &= \sigma_0\left(T_0, \omega_{n\sigma}\right) = \sigma_{00}\left(T_0\right)\left(1-\omega_{n\sigma}\right)^q, \\ \tau_0 &= \tau_0\left(T_0, \omega_{n\sigma}\right) = \tau_{00}\left(T_0\right)\left(1-\omega_{n\sigma}\right)^q, \end{aligned} \tag{26}$$

where q is the material parameter.

Consider now the domain of damage accumulation Ω_f, which in the plane (σ_n, τ_n) is bounded by the curves $R_{\sigma 0} = 1$ and $R_\sigma = 1$, Fig.7. Introduce the non-dimensional factor

$$R_{\sigma 0 c} = R_\sigma / R_{\sigma 0}. \tag{27}$$

The damage growth can now be expressed as follows

$$\mathrm{d}\omega_{n\sigma} = \Psi_\sigma\left(R_\sigma\right)\mathrm{d}\hat{R}_\sigma, \tag{28}$$

where

$$\mathrm{d}\hat{R}_\sigma = \begin{cases} \mathrm{d}R_\sigma & \text{for } \mathrm{d}R_\sigma > 0 \text{ and } R_{\sigma 0} > 1 \\ 0 & \text{for } \mathrm{d}R_\sigma \le 0 \text{ or } R_{\sigma 0} \le 1 \end{cases}, \tag{29}$$

and

$$\mathrm{d}R_\sigma = \frac{\partial R_\sigma}{\partial\left(\sigma_n / \sigma_c\right)}\mathrm{d}\left(\frac{\sigma_n}{\sigma_c}\right) + \frac{\partial R_\sigma}{\partial\left(\tau_n / \tau_c\right)}\mathrm{d}\left(\frac{\tau_n}{\tau_c}\right) = \frac{\partial R_\sigma}{\partial \sigma_n}\mathrm{d}\sigma_n + \frac{\partial R_\sigma}{\partial \tau_n}\mathrm{d}\tau_n + \frac{\partial R_\sigma}{\partial \Omega_{n\sigma}}\mathrm{d}\Omega_{n\sigma}, \tag{30}$$

where the last term accounting for damage effect can be neglected in most cases. The damage accumulation occurs for stress increment vectors directed into the exterior of the domain R_σ = const, Fig.8a.

An alternative specification of loading-unloading domains is shown in Figure 8b. The increment $\mathrm{d}\hat{R}_\sigma$ is now specified as follows

$$\mathrm{d}\hat{R}_\sigma = \frac{\partial R_\sigma}{\partial \sigma_n}\mathrm{d}\hat{\sigma}_n + \frac{\partial R_\sigma}{\partial \tau_{n1}}\mathrm{d}\hat{\tau}_{n1} + \frac{\partial R_\sigma}{\partial \tau_{n2}}\mathrm{d}\hat{\tau}_{n2} + \frac{\partial R_\sigma}{\partial \Omega_{n\sigma}}\mathrm{d}\Omega_{n\sigma}. \tag{31}$$

The stress increments $\mathrm{d}\hat{\sigma}_n, \mathrm{d}\hat{\tau}_{ni}$ $(i = 1, 2)$ are associated with the moving loading-unloading domain in the plane (σ_n, τ_{ni}). The full unloading occurs when the stress vector is directed into the interior of corner domain PAB, thus

$$\begin{aligned} \mathrm{d}\hat{\sigma}_n &= \mathrm{d}\sigma_n \quad \text{for} \quad \mathrm{d}\sigma_n \ge 0 \text{ and } \sigma_n \ge 0, \\ \mathrm{d}\hat{\sigma}_n &= 0 \quad\;\; \text{for} \quad \mathrm{d}\sigma_n < 0 \text{ or } \sigma_n < 0, \end{aligned} \tag{32a}$$

and

$$\begin{aligned} \mathrm{d}\hat{\tau}_{ni} &= \mathrm{d}\tau_{ni} \quad \text{for} \quad \tau_{ni}\mathrm{d}\tau_{ni} \ge 0, \\ \mathrm{d}\hat{\tau}_{ni} &= 0 \quad\;\; \text{for} \quad \tau_{ni}\mathrm{d}\tau_{ni} < 0. \end{aligned} \tag{32b}$$

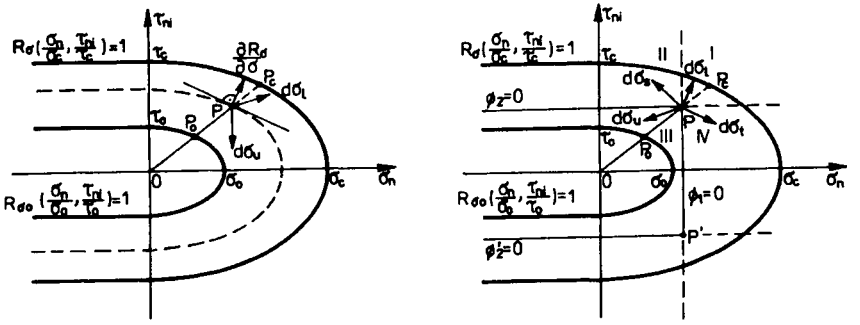

Fig.8. Damage initiation and stress failure curves in the (σ_n, τ_{ni}) - plane: a) loading-unloading domains specified by the curves R_σ = const, b) loading-unloading domains specified by straight lines σ_n,= const, τ_{ni} = const.

Moreover, the damage initiation condition is exceeded. The inequalities (32) specify four domains I, II, III and IV of full loading (I), shear loading - tension unloading (II), full unloading (III) and tension loading - shear unloading (IV).

For large stress gradients, the non-local condition is used, so that

$$\mathrm{d}\bar{\hat{R}}_\sigma = \frac{1}{d_0^{\,2}} \int_0^{d_0}\int_0^{d_0} \mathrm{d}\hat{R}_\sigma \, \mathrm{d}\xi_1 \mathrm{d}\xi_2 . \tag{33}$$

The form of the damage accumulation function $\Psi_\sigma(R_\sigma)$ was assumed as follows

$$\Psi_\sigma(R_\sigma) = A_\sigma \left(\frac{R_\sigma - R_{\sigma 0c}}{1 - R_{\sigma 0c}} \right)^{n_\sigma} \frac{1}{1 - R_{\sigma 0c}}, \tag{34}$$

where n_σ and A_σ are material parameters.

A simpler version of the model can be obtained by assuming σ_c and τ_c to be constant, $R_\sigma = R_\sigma(\sigma_n, \tau_n)$, and

$$\omega_{n\sigma} = \int_0^{\hat{R}_\sigma} \Psi_\sigma(R_\sigma)\, \mathrm{d}\hat{R}_\sigma , \tag{35}$$

The crack initiation condition occurs for the critical value of $\omega_{n\sigma}$, thus

$$R_\mathrm{d} = \max_{(\mathbf{n},\mathbf{x}_\theta)} \omega_{n\sigma} = 1. \tag{36}$$

For large stress gradients, the non-local condition (28) is applied.

The fatigue crack growth condition can be expressed similarly to (6), namely

$$\mathrm{d}a = \max_{(\mathbf{n},\mathbf{x}_\theta)} \left[A_\mathrm{d} \Psi_\sigma(\bar{R}_\sigma)\, \mathrm{d}\bar{\hat{R}}_\sigma \right], \tag{37}$$

where A_d is the parameter of crack growth.

Assume that the damage initiation corresponding to the condition $R_{\sigma 0}$ = 1, and the crack initiation corresponding to the condition $R_{\sigma 0}$ = 1 are expressed by similar functions,

$\frac{\sigma_o}{\sigma_c} = \frac{\tau_o}{\tau_c} = f$. Introduce within the domain Ω_f a one parameter family of curves R_σ = const ($f \le R_\sigma \le 1$). For the damage accumulation function (34), we have

$$R_d = \max_{(\mathbf{n},\mathbf{x}_0)} \left[\int_0^{\hat{R}_d} A_1 \left(\frac{R_\sigma - f}{1-f} \right)^{n_\sigma} \frac{d\hat{R}_\sigma}{1-f} \right] = 1. \tag{38}$$

where

$$\left(\frac{R_\sigma - f}{1-f} \right)^{n_\sigma} = \left(\frac{PP_o}{P_c P_o} \right)^{n_\sigma}. \tag{39}$$

and P, P_o, P_c are shown in Figure 8.

5. EXPERIMENTAL VERIFICATION OF NON-LOCAL FATIGUE CRACK INITIATION CONDITION

In this section we shall present the experimental data concerned with the crack initiation in plane elements with wedge shaped notches subjected to cyclically varying tension and shear. The specimen thickness is 5 mm, notch angles are $2\beta = 40°$, $80°$ and $180°$ (semicircular notch). Figure 4 presents the dimensions of specimen made of PMMA („Perspex"). The cyclic loading between zero and maximal force value with the frequency 3 Hz was executed in a specially designed device allowing for varying specimen orientation with respect to tensile force direction. The experimental details are provided by Molski and Seweryn [12].

The number of cycles corresponding to crack initiation at the notch root was specified by using the non-local crack initiation condition (33), (34) and the normal stress function R_σ. The crack initiation can now be expressed as follows

$$R_d = N_f \max_{(\vartheta)} \left[\left(\frac{\Delta\bar{\sigma}_{\vartheta\vartheta}(\vartheta) - \sigma_o}{\sigma_c - \sigma_o} \right)^{n_\sigma + 1} \right] = 1, \tag{40}$$

where r, ϑ are the polar coordinates with the origin at the notch vertex, N_f is the number of cycles corresponding to crack initiation. The averaged stress amplitude equals

$$\Delta\bar{\sigma}_{\vartheta\vartheta} = \frac{1}{d_0} \int_0^{d_0} \Delta\sigma_{\vartheta\vartheta}(\vartheta)\, dr. \tag{41}$$

Using the asymptotic representation of stress state near the notch vertex, we have

$$\Delta\bar{\sigma}_{\vartheta\vartheta} = \frac{\Delta K_I^\lambda f_I(\vartheta)}{\lambda_I (2\pi d_0)^{1-\lambda_I}} + \frac{\Delta K_{II}^\lambda f_{II}(\vartheta)}{\lambda_{II} (2\pi d_0)^{1-\lambda_{II}}}, \tag{42}$$

where ΔK_I^λ, ΔK_{II}^λ are the amplitudes of generalized stress intensity factors in wedge shaped notches. Equation (42) can be rewritten in the form

$$\Delta\bar{\sigma}_{\vartheta\vartheta} = \Delta F\left(\frac{\xi_{\mathrm{I}}(\beta) f_{\mathrm{I}}(\vartheta)}{\lambda_{\mathrm{I}}(2\pi d_0)^{1-\lambda_{\mathrm{I}}}}\cos\psi + \frac{\xi_{\mathrm{II}}(\beta) f_{\mathrm{II}}(\vartheta)}{\lambda_{\mathrm{II}}(2\pi d_0)^{1-\lambda_{\mathrm{II}}}}\sin\psi\right), \tag{43}$$

where coefficients ξ_{I} and ξ_{II} are determined from the numerical solution by the finite element method ($\xi_{\mathrm{I}} = K_{\mathrm{I}}^{\lambda} / P$, $\xi_{\mathrm{II}} = K_{\mathrm{II}}^{\lambda} / T$).

Table 1. Experimental results of fatigue tests for PMMA-specimens with V-notches [12]

No.	2β [deg]	ψ [deg]	ΔF [kN]	N_{f}
1	40	0	1,95	1
2	40	30	2,20	1
3	40	60	2,56	1
4	40	75	2,78	1
5	40	30	1,80	4
6	40	75	2,20	15
7	40	30	1,70	26
8	40	60	2,00	59
9	40	75	2,00	122
10	40	60	1,80	169
11	40	0	1,60	310
12	40	30	1,50	395
13	40	0	1,40	1832
14	80	0	2,25	1
15	80	30	2,64	1
16	80	60	3,35	1
17	80	75	5,03	1
18	80	75	4,02	3
19	80	0	1,90	19
20	80	30	2,10	48
21	80	60	2,50	53
22	80	75	2,75	126
23	80	30	1,80	528
24	80	0	1,70	579
25	180	0	11,50	1
26	180	0	8,00	266
27	180	0	6,50	2226

Introducing the effective normal stress amplitude

$$\Delta\sigma_{\mathrm{az}} = \max_{(\vartheta)} \Delta\bar{\sigma}_{\vartheta\vartheta}(\vartheta), \tag{44}$$

the number of cycles corresponding to crack initiation at the notch vertex is expressed from the simple relation

$$\log N_{\mathrm{f}} = -(n_\sigma + 1)\log\left(\frac{\Delta\sigma_{\mathrm{az}} - \sigma_{\mathrm{o}}}{\sigma_{\mathrm{c}} - \sigma_{\mathrm{o}}}\right). \tag{45}$$

It is seen that the non-local crack initiation condition provided simple relation for N_{f}, analogous to the one-dimensional condition. Figure 9 presents both the predicted curve and the experimental data. The values of the critical stress $\sigma_{\mathrm{c}} = 81.2$ MPa and of the size of damage zone $d_0 = 0.164$ mm were specified from the monotonic loading test. The value of σ_{o} and n_σ were specified from uniaxial fatigue tests, obtaining $n_\sigma = 10.7$ and $\sigma_{\mathrm{o}} = 21.6$ MPa. It is seen from Figure 9 that fair agreement was obtained between model prediction and experiment. The experimental points lie within 15% scatter layer with respect to the theoretical curve $\Delta\sigma_{\mathrm{az}}$ - N_{f} (only two experimental points for $2\beta = 80°$ and $\psi = 75°$ lie outside the scatter layer, which may be due to imperfection in specimen fabrication). The agreement can be regarded as satisfactory, noting that for static tests of PMMA the experimental scatter lies within the range ±12% (cf. Williams [13]).

It should be emphasized that the non-local crack initiation condition from sharp or rounded notches provides an effective tool for quantitative prediction. The crack propagation process can be treated in a similar way.

6. COMPLIANCE VARIATION OF THE DAMAGED MATERIAL

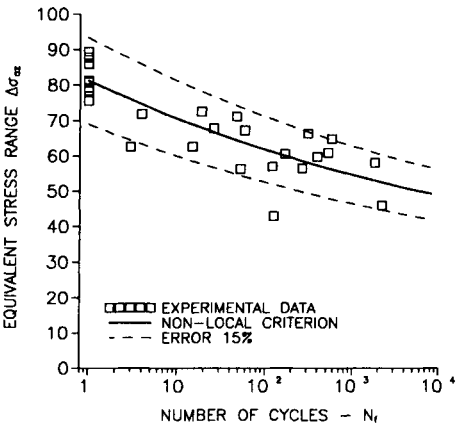

Fig.9. Equivalent stress range $\Delta\sigma_{az}$ vs number of cycles to fatigue crack initiation for biaxial loading (PMMA-specimens with V-notches) [12]

So far, we neglected the effect of compliance variation of the damaged material. However, for concrete, ceramics, and metals this variation may be significant in the later stage of damage accumulation, and effect the stress distribution. The problem of variation of the elastic compliance tensor due to damage was treated in numerous papers, cf. Budiansky and O'Connel [14], Ortiz and Popov [16], Horii and Nemat-Naser [15], Lubarda and Krajcinovic [17]. The compliance variation was related to the known damage tensor or crack density within the microelement.

In this section, we shall present the method of description of compliance variation due to damage distribution on all physical planes. Assume the strain decomposition

$$\varepsilon_{ij} = \varepsilon_{ij}^{\mathrm{e}} + \varepsilon_{ij}^{\mathrm{d}} = C_{ijkl}\sigma_{kl}, \tag{46}$$

where $\varepsilon_{ij}^{\mathrm{e}}$ is the elastic strain tensor of the undamaged material and C_{ijkl} is the compliance tensor of the damaged material. We have

$$\varepsilon_{ij}^{\mathrm{d}} = \left(C_{ijkl} - C_{ijkl}^{\mathrm{e}}\right)\sigma_{kl} = C_{ijkl}^{\mathrm{d}}\sigma_{kl}, \tag{47}$$

where C_{ijkl}^{e} is the compliance tensor of the undamaged material and C_{ijkl}^{d} is the compliance increment due to damage. For stress and strain increments (or rates) we have accordingly

$$\dot{\varepsilon}_{ij} = \dot{\varepsilon}_{ij}^{\mathrm{e}} + \dot{\varepsilon}_{ij}^{\mathrm{d}} = \left(C_{ijkl}^{\mathrm{e}} + C_{ijkl}^{\mathrm{d}}\right)\dot{\sigma}_{kl} + \dot{C}_{ijkl}^{\mathrm{d}}\sigma_{kl}. \tag{48}$$

The damage strains on the physical plane can be expressed as follows

$$\varepsilon_{n}^{\mathrm{d}} = C_{ijkl}^{\mathrm{d}}\sigma_{kl}n_i n_j, \quad \gamma_{n\alpha}^{\mathrm{d}} = \frac{1}{2}C_{ijkl}^{\mathrm{d}}\sigma_{kl}\left(t_{\alpha i}n_j + t_{\alpha j}n_i\right). \tag{49}$$

where $\alpha = 1, 2$. Noting that $n_k n_k = t_{1k}t_{1k} = t_{2k}t_{2k} = 1$, and using (3), the expressions (49) can be presented as follows

$$\begin{aligned}
\varepsilon_{n}^{\mathrm{d}} &= C_{ijkl}^{\mathrm{d}}n_i n_j n_k n_l \sigma_n = C_n^{\mathrm{d}}\sigma_n, \\
\gamma_{n1}^{\mathrm{d}} &= \frac{1}{4}C_{ijkl}^{\mathrm{d}}\left[\left(t_{1j}n_i + t_{1i}n_j\right)\left(t_{1l}n_k + t_{1k}n_l\right)\right]\tau_{n1} = C_{t1}^{\mathrm{d}}\tau_{n1}, \\
\gamma_{n2}^{\mathrm{d}} &= \frac{1}{4}C_{ijkl}^{\mathrm{d}}\left[\left(t_{2j}n_i + t_{2i}n_j\right)\left(t_{2l}n_k + t_{2k}n_l\right)\right]\tau_{n2} = C_{t2}^{\mathrm{d}}\tau_{n2},
\end{aligned} \tag{50}$$

where $C_n^{\mathrm{d}}, C_{t1}^{\mathrm{d}}, C_{t2}^{\mathrm{d}}$ represent the compliance variations due to normal and shear stresses on the physical plane.

Consider now a finite number N of circular cracks in a material element of volume V. The elastic energy of the element is a sum of elastic energy W^{e} in the undamaged material and the energy W^{d} due to damage, thus

$$W(\sigma) = W^{\mathrm{e}}(\sigma) + W^{\mathrm{d}}(\sigma) = W^{\mathrm{e}}(\sigma) + \sum_{\chi=1}^{N} W_{\chi}^{\mathrm{d}}(\sigma). \tag{51}$$

In the case of a single crack of radius l_χ within the plane Δ (Fig. 10), subjected to normal stress σ_n^χ, the energy portion W^{d} has the form (cf. Sneddon [18]):

$$W_{\chi}^{\mathrm{d}} = \frac{1}{2} d_{\mathrm{n}}(\nu, E)\, l_\chi{}^3 \left(\sigma_n^\chi\right)^2 H\left(\sigma_n^\chi\right), \tag{52}$$

where $d_{\mathrm{n}} = \dfrac{16\left(1-\nu^2\right)}{3E}$, $H\left(\sigma_n^\chi\right)$ is the Heaviside function, $H\left(\sigma_n^\chi\right) = \left\langle \sigma_n^\chi \right\rangle / \sigma_n^\chi$.

Accounting for the normal opening mode, the elastic energy is expressed as follows

$$W = \frac{1}{2}\int_V \sigma_{ij} C_{ijkl}^{\mathrm{e}} \sigma_{kl}\, \mathrm{d}V + \frac{1}{2}\sum_{\chi=1}^{N} d_{\mathrm{n}} l_\chi{}^3 \left(\sigma_n^\chi\right)^2 H\left(\sigma_n^\chi\right). \tag{53}$$

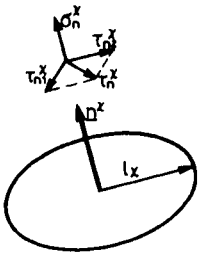

Fig.10. Circular cracks of radius l_χ

Consider a material element of volume V_{D} with N_{D} circular microcracks. Neglecting the effect of crack interaction the specific elastic energy of the elements equals

$$\frac{W}{V_{\mathrm{D}}} = \frac{1}{2}\sigma_{ij} C_{ijkl}^{\mathrm{e}} \sigma_{kl} + \frac{d_{\mathrm{n}}}{2V_{\mathrm{D}}} \sum_{\chi=1}^{N_{\mathrm{D}}} l_\chi{}^3 \left(n_i^\chi \sigma_{ij} n_j^\chi\right)^2 H\left(\sigma_n^\chi\right)$$

$$= \frac{1}{2}\sigma_{ij}\left(C_{ijkl}^{\mathrm{e}} + \frac{d_{\mathrm{n}}}{V_{\mathrm{D}}} \sum_{\chi=1}^{N_{\mathrm{D}}} l_\chi{}^3 n_i^\chi n_j^\chi n_k^\chi n_l^\chi H\left(\sigma_n^\chi\right)\right)\sigma_{kl} \tag{54}$$

where $\mathbf{n}^\chi$ is the unit normal vector specifying χ-th crack orientation.

The compliance increment due to microcracks can then be expressed as follows

$$C_{ijkl}^{d} = \frac{d_{\mathrm{n}}}{V_{\mathrm{D}}} \sum_{\chi=1}^{N_{\mathrm{D}}} l_\chi{}^3 n_i^\chi n_j^\chi n_k^\chi n_l^\chi H\left(\sigma_n^\chi\right). \tag{55}$$

If the crack density distribution $\rho_n(\mathbf{n})$ is specified together with the crack diameter distribution $l_n(\mathbf{n})$, the compliance increment due to damage can be presented in the form

$$C_{ijkl}^{\mathrm{d}} = \frac{d_{\mathrm{n}}}{2\pi a_{\mathrm{D}}} \int_{4\pi} \rho_n(\mathbf{n})\, l_n(\mathbf{n}) H(\sigma_n) n_i n_j n_k n_l\, \mathrm{d}\Omega = \int_{4\pi} G_n^{\mathrm{d}}(\mathbf{n})\, H(\sigma_n)\, n_i n_j n_k n_l\, \mathrm{d}\Omega, \tag{56}$$

where the element is assumed on a cylinder of the radius b_{D} and height a_{D}.

For a combined tension and shear loading, neglecting friction and dilatancy effect on the crack interfaces, the elastic energy increase due to damage equals

$$W_{\chi}^{\mathrm{d}} = \frac{1}{2} l_{\chi}{}^{3} \left[d_{\mathrm{n}}(\nu, E) \left(\sigma_n^{\chi} \right)^2 H\left(\sigma_n^{\chi} \right) + d_{\mathrm{t}}(\nu, E) \left(\tau_n^{\chi} \right)^2 \right], \tag{57}$$

where d_{n} and d_{t} depend on elastic stiffness parameters. The compliance tensor C_{ijkl}^{d} now equals

$$C_{ijkl}^{\mathrm{d}} = \frac{1}{V_{\mathrm{D}}} \sum_{\chi=1}^{N_{\mathrm{D}}} l_{\chi}{}^{3} \left(d_{\mathrm{n}}\, Q_{ijkl}^{\chi}\, H\left(\sigma_n^{\chi} \right) + d_{\mathrm{t}}\, T_{ijkl}^{\chi} \right) \tag{58}$$

where

$$Q_{ijkl}^{\chi} = n_i^{\chi} n_j^{\chi} n_k^{\chi} n_l^{\chi},$$

$$T_{ijkl}^{\chi} = \frac{1}{4} \left[\left(t_{1j}^{\chi} n_i^{\chi} + t_{1i}^{\chi} n_j^{\chi} \right) \left(t_{1l}^{\chi} n_k^{\chi} + t_{1k}^{\chi} n_l^{\chi} \right) + \left(t_{2j}^{\chi} n_i^{\chi} + t_{2i}^{\chi} n_j^{\chi} \right) \left(t_{2l}^{\chi} n_k^{\chi} + t_{2k}^{\chi} n_l^{\chi} \right) \right], \tag{59}$$

When the distributions $\rho_n(\mathbf{n})$ and $l_n(\mathbf{n})$ are known, the expression for C_{ijkl}^{d} becomes

$$C_{ijkl}^{\mathrm{d}} = \int_{4\pi} \left(G_n^{\mathrm{d}}(\mathbf{n})\, Q_{ijkl}\, H\left(\sigma_n \right) + G_t^{\mathrm{d}}(\mathbf{n})\, T_{ijkl} \right) \mathrm{d}\Omega. \tag{60}$$

where

$$G_t^{\mathrm{d}}(\mathbf{n}) = B_{\mathrm{t}}\, \rho_n(\mathbf{n})\, l_n(\mathbf{n}), \quad B_{\mathrm{t}} = \frac{d_{\mathrm{t}}}{2\pi a_{\mathrm{D}}}.$$

An alternative way of calculation of compliance increase due to damage distribution $\omega_n(\mathbf{n})$ was proposed by Seweryn and Mróz [7]. It is assumed that both normal and shear damage strains $\varepsilon_n^{\mathrm{d}} = \varepsilon_n^{\mathrm{d}}\left(\sigma_n, \omega_n \right)$, $\gamma_n^{\mathrm{d}} = \gamma_n^{\mathrm{d}}\left(\tau_n, \omega_n \right)$ are induced on the physical plane. Assume the following relationship between ω_n and $\varepsilon_n^{\mathrm{d}}$

$$\varepsilon_n^{\mathrm{d}} = A_{\mathrm{n}} \left(\frac{\omega_n}{1 - \omega_n} \right)^{q^*} \langle \sigma_n \rangle, \tag{61}$$

where A_{n}, q^* are material parameters..

Let us introduce the following distributions scalar and tensors [19]

$$C_{\mathrm{o}}^{\mathrm{d}*} = \int_{4\pi} C_n^{\mathrm{d}}(\mathbf{n})\, \mathrm{d}\Omega, \quad C_{ij}^{\mathrm{d}*} = \int_{4\pi} C_n^{\mathrm{d}}(\mathbf{n})\, n_i n_j\, \mathrm{d}\Omega, \quad C_{ijkl}^{\mathrm{d}*} = \int_{4\pi} C_n^{\mathrm{d}}(\mathbf{n})\, n_i n_j n_k n_l\, \mathrm{d}\Omega.. \tag{62}$$

The compliance tensor C_{ijkl}^{d} is now determined from the relation

$$C_{ijkl}^{\mathrm{d}} = \frac{315}{32\pi} \left(C_{ijkl}^{\mathrm{d}*} - \frac{2}{3} A_{ijkl} + \frac{C_{\mathrm{o}}^{\mathrm{d}*}}{21} I_{ijkl} \right), \tag{63}$$

where fourth order tensors A_{ijkl} and I_{ijkl} are defined as follows

$$\begin{aligned} A_{ijkl} &= \frac{1}{6} \left(\delta_{ij} C_{kl}^{\mathrm{d}*} + \delta_{kl} C_{ij}^{\mathrm{d}*} + \delta_{ik} C_{jl}^{\mathrm{d}*} + \delta_{il} C_{jk}^{\mathrm{d}*} + \delta_{jk} C_{il}^{\mathrm{d}*} + \delta_{jl} C_{ik}^{\mathrm{d}*} \right), \\ I_{ijkl} &= \frac{1}{3} \left(\delta_{ij} \delta_{kl} + \delta_{ik} \delta_{jl} + \delta_{il} \delta_{jk} \right). \end{aligned} \tag{64}$$

For the plane case the integration is performed over the circle of unit radius ($\Omega = 2\pi$, $d\Omega = d\vartheta$). Introducing the scalar C_o^{d*} and the tensors C_{ij}^{d*} i C_{ijkl}^{d*}

$$C_o^{d*} = \int_{2\pi} C_n^d(\vartheta)\, d\vartheta, \quad C_{ij}^{d*} = \int_{2\pi} C_n^d(\vartheta)\, n_i n_j\, d\vartheta, \quad C_{ijkl}^{d*} = \int_{2\pi} C_n^d(\vartheta)\, n_i n_j n_k n_l\, d\vartheta \tag{65}$$

the damage compliance tensor is specified as follows

$$C_{ijkl}^d = \frac{8}{\pi} C_{ijkl}^{d*} - \frac{6}{\pi} A_{ijkl} + \frac{C_o^{d*}}{2\pi} I_{ijkl}. \tag{66}$$

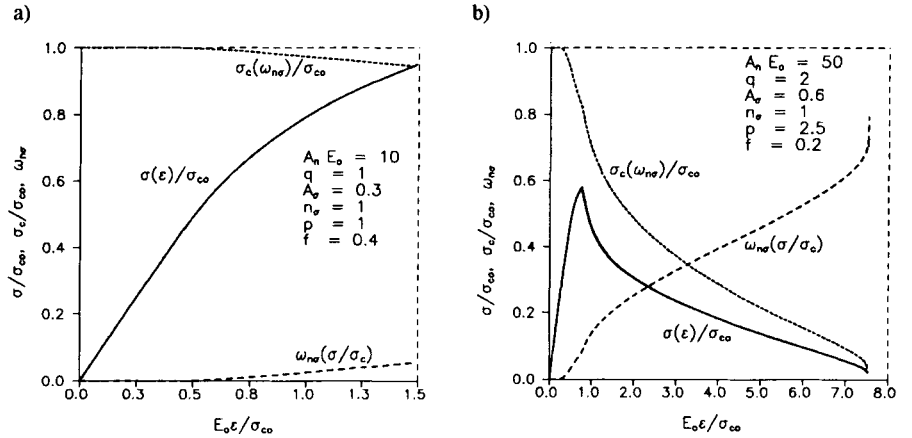

Fig.11. Diagrams of stress-strain, damage, and critical stress evolution for two different sets of material parameters [7]: a) $f = 0{,}4$, $p = 1$, $q = 1$, $A_\sigma = 0{,}3$, $n_\sigma = 1$, $A_n E_o = 10$; b) $f = 0{,}2$, $p = 2{,}5$, $q = 2$, $A_\sigma = 0{,}6$, $n_\sigma = 1$, $A_n E_o = 50$

Let us consider now the case of uniaxial tension for which the damage growth is dependent on the normal stress ($\sigma_o/\tau_c \to 0$). We have

$$d\hat{R}_\sigma = \frac{\langle d\sigma_n \rangle}{\sigma_{co}(1-\omega_n)^p} + \frac{p\langle \sigma_n \rangle\, d\omega_n}{\sigma_{co}(1-\omega_n)^{p+1}}. \tag{67}$$

and the growth of damage is specified by the relation

$$d\omega_n = \frac{\Psi_\sigma \langle d\sigma_n \rangle}{\sigma_c\left(1 - \Psi_\sigma \dfrac{p^* \langle \sigma_n \rangle}{\sigma_c(1-\omega_n)}\right)}, \tag{68}$$

where the damage accumulation function is

$$\Psi_\sigma = A_\sigma \left(\frac{\langle \sigma_n - \sigma_o \rangle}{\sigma_c(1-f)}\right)^{n_\sigma} \frac{1}{1-f}. \tag{69}$$

The resulting relation between the tensile stress and strain is obtained in the form

$$\sigma = \frac{\varepsilon E_o}{1 + A_n E_o \left(\frac{\omega_n}{1-\omega_n} \right)^{q^*} H(\sigma)}, \tag{70}$$

where E_o is the initial value of the Young modulus

Figures 11 present the stress-strain, and damage evolution curves and the variation of σ_e on the plane normal to tension axis. It is seen that depending on the values of $A_n E_o$, q^* and p the stress strain curves may have different character. In fact in Figure 11b the curve exhibits both stable and unstable (softening) response.

7. CONCLUDING REMARKS

The present paper provides the uniform treatment of damage accumulation and failure of materials for both monotonic and variable loading. Instead of formulating the constitutive equations for a volume element, the damage is associated with the physical plane and expressed in terms of contact stress components. The damage distribution $\omega_n(\mathbf{n})$ can then be described and the critical plane can be specified. The non-local failure condition and the damage growth rule provide the possibility to treat both regular and singular stress regimes. Also the crack initiation and propagation can be studied within the same constitutive assumptions. The present approach can then be applied to predict brittle failure of structural components with notches and also high cycle fatigue amplitudes for multiaxial loading. The prediction of compliance variation due to accumulated damage on physical planes enables the treatment of damage problems with account for stress redistribution due damage strains. The presented framework seems much simpler than the traditional damage models employing damage tensor state variables and representation of free energy in terms of strain and those variables, cf. Krajcinowic [9] or Lemaitre [10].

REFERENCES

1. Seweryn A. (1994), Brittle fracture criterion for structures with sharp notches, *Eng. Fract. Mech.*, **47**, 673-681.
2. Seweryn A. (1997), A non-local stress and strain energy release rate mixed mode fracture initiation and propagation criteria, (submited to *Eng. Fract. Mech*).
3. Seweryn A. (1997), *Damage accumulation and fracture of structural elements for complex state loading* (in Polish), Białystok University of Technology Publ., Białystok.
4. Seweryn A., Mróz Z. (1995), A non-local stress failure condition for structural elements under multiaxial loading, *Eng. Fract. Mech.*, **51**, 955-973.
5. Seweryn A., Mróz Z. (1996), A non-local stress failure and fatigue damage accumulation condition, In. *Multiaxial Fatigue and Design* (eds. Pineau A., Cailletaud G., Lindley T.C.), Mech. Eng. Publ., 259-280, London.

6. Seweryn A., Mróz Z. (1996), Damage accumulation and fracture criterion for complex state loading, *Arch. Machine Design*, **43**, 269-283.
7. Seweryn A., Mróz Z. (1997), On the criterion of damage evolution for variable multiaxial stress state, *Int. J. Solids Struct.* (in print).
8. Seweryn A., Poskrobko S., Mróz Z. (1997), Brittle fracture in plane elements with sharp notches under mixed-mode loading, *J. Eng. Mech. ASCE*, **123** (in print).
9. Krajcinowic D. (1996), *Damage mechanics*, Elsevier Science, Amsterdam.
10. Lemaitre J. (1992), *A Course on Damage Mechanics*, Springer Verlag, Berlin.
11. Seweryn A. and Molski K. (1996), Elastic stress singularities and corresponding generalised stress intensity factors for angular corners under various boundary conditions, *Eng. Fract. Mech.*, **55**, 529-556.
12. Molski K., Seweryn A. (1997), Fatigue and fracture of plane elements with sharp notches under biaxial loading, *Proc. 5th Int. Conf. on Biaxial/Multiaxial Fatigue & Fracture*, Cracow, Poland.
13. Williams J.G. (1984), *Fracture Mechanics of Polymers*, Ellis Horwood, Chichester.
14. Budiansky, B., and O'Connell, R.J. (1976), Elastic moduli of a cracked solid, *Int. J. Solids Struct.*, **12**, 81-97.
15. Horii, H., and Nemat-Nasser, S. (1983), Overall moduli of solids with microcracks: load-induced anisotropy, *J. Mech. Phys. Solids*, **31**, 155-171.
16. Ortiz M., Popov E.P. (1982), A physical model for the inelasticity of concrete, *Proc. Roy. Soc. Lond. A*, **383**, 101-125.
17. Lubarda V.A., Krajcinowic D. (1994), Tensorial representation of the effective elastic properties of the damaged materials, *Int. J. Damage Mech.*, **3**, 38-56.
18. Sneddon I.N. (1969), *Crack Problems in the Classical Theory of Elasticity*, J. Wiley, New York.
19. Lubarda V.A., Krajcinowic D. (1993), Damage tensors and the crack density distribution, *Int. J. Solids Struct.*, **30**, 2859-2877.

Acknowledgements - The investigation described in this paper is a part of the research project No. 7 T07C 006 12 sponsored by the Polish State Committee for Scientific Research.

Damage Mechanics in Engineering Materials
G.Z. Voyiadjis, J.-W.W. Ju and J.-L. Chaboche (Editors)
© 1998 Elsevier Science B.V. All rights reserved.

A Micromechanical Damage Model of Fiber Composites with Nonlinear Interface: Bulk, Tension and Compression Response

Z. Dong and A. J. Levy

Department of Mechanical, Aerospace and Manufacturing Engineering
Syracuse University, Syracuse, New York 13244

1. ABSTRACT

This paper describes a micromechanical model of the constitutive behavior of unidirectional fiber composites in which nonlinear behavior arises solely from the force-separation response of the interfaces. The direct method of composite materials theory is employed to obtain the effective property relations for a representative volume element while a local analysis of a solitary inclusion problem yields kinetic equations governing interface separation components. The resulting model, which involves no adjustable parameters, falls within the conceptual framework of continuum damage mechanics with "damage" variables that have a precise geometrical meaning. For equibiaxial loading the single damage variable is shown to be equivalent to the area density of voids surrounding the fibers. For complex planar loading more damage variables occur and these are shown to be the expansion coefficients arising in an eigenfunction representation of the average displacement jump at the inclusion-matrix interface. Local fields are determined by the dilute estimate and the Mori-Tanaka estimate assuming smooth interface response governed by a Needleman-type normal force-separation mechanism. Explicit results are presented for transverse uniaxial tension and transverse uniaxial compression loading of a composite reinforced by fibers in dilute concentration.

2. INTRODUCTION. PLANAR BULK RESPONSE.

In conventional damage models of brittle media the damage process typically involves the evolution of distributed cracking from a virgin reference state through complete failure defined in some physically meaningful, yet mathematically tractable, manner. By contrast the model described in this paper employs the term damage to mean the process by which the stiffness of a fiber composite degrades owing to the nonlinear separation of the interfaces beginning with initial interfacial cohesion (Fig.1a) through intermediate debonding (interface forces are active) (Fig.1b) and terminating with partial or complete decohesion (portions of the interface are essentially free of interface force) (Fig.1c). The present work concerns the behavior transverse to the fiber direction so that at the termination of the process (in which a significant part of the interface has lost cohesion) the composite may still support transverse load (primarily by the matrix) as well as axial load. The term damage is employed in this work because the

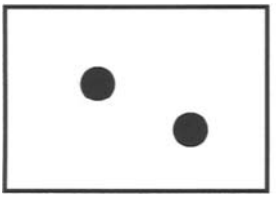

Fig.1a. Reference state.

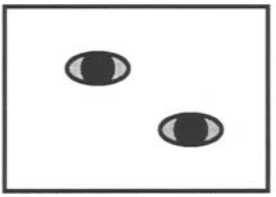

Fig.1b. Intermediate state.

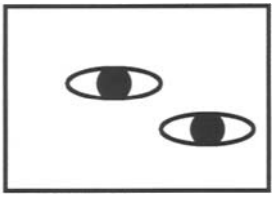

Fig.1c. Decohered state.

micromechanical model has the mathematical structure of continuum damage mechanics, i.e., a relation between stresses and strains and certain other "damage" variables which in turn are governed by their own kinetic equations relating them to stresses and/or strains. In practice, the direct method of composite materials theory is employed to yield an effective property relation for the representative volume element $\mathcal{B}$ (RVE) while interface jump boundary conditions of a local, solitary inclusion problem yield the kinetic equations.

2.1. Bulk response. The dilute estimate.

An illustration of this idea is contained in the following problem of planar bulk response of a unidirectional fiber composite in dilute concentration [1]. Thus, assume the existence of an RVE through which randomly distributed fibers embedded in a matrix phase may be modeled as effectively homogeneous and transversely isotropic. The effective transverse bulk modulus κ^* relates equibiaxial, transversely plane stresses and strains through the relation,

$$\sigma = 2\kappa^*\varepsilon\,, \tag{1}$$

where 2σ is the two dimensional trace ($tr_2\mathbf{S}$) of the stress tensor ($\mathbf{S}$) and 2ε is the plane strain dilatation given by the two dimensional trace of the strain tensor $\mathbf{E}$. A standard result of composite materials theory relates the effective moduli of the composite to the moduli and phase volume averages of the constituents provided the mean strain (or stress) in the fiber phase is know as a function of prescribed uniform boundary condition. If displacement discontinuities are allowed to develop at the fiber-matrix interfaces then the effective property relation depends on interfacial displacement jump components as well. Under these circumstances the relation assumes the form [2,3],

$$\varepsilon = \frac{1}{2\kappa^*}\sigma = \frac{1}{2\kappa^+}\sigma + c\left(\frac{1}{2\kappa^-} - \frac{1}{2\kappa^+}\right)\overline{\sigma}^- + \mathcal{A}\,, \tag{2}$$

where ε is the mean effective strain, σ is the mean stress, κ^+ (κ^-) is the bulk modulus of the matrix (fibers), and c is the fiber volume concentration defined by $\sum_{i=1}^{N} \mathrm{vol}(\Omega_i) \Big/ \mathrm{vol}(\mathcal{B})$. In (2) the quantity $\overline{\sigma}^-$ is the mean stress in the fiber phase,

$$\bar{\sigma} = \frac{\sum_{i=1}^{N} \mathrm{vol}(\Omega_i)\bar{\sigma}_i}{\sum_{i=1}^{N} \mathrm{vol}(\Omega_i)}, \tag{3}$$

while the quantity $\mathcal{A}$ characterizes the contributions of interfacial discontinuities to the mean effective strain and is given by,

$$\mathcal{A} = \frac{c\sum_{i=1}^{N} \int_{\partial\Omega_i} [\mathbf{u}] \bullet \mathbf{n}\, da}{2\sum_{i=1}^{N} \mathrm{vol}(\Omega_i)}. \tag{4}$$

Note that Ω_i is the region occupied by the i^{th} fiber with unit normal $\mathbf{n}$, $\bar{\sigma}_i$ is the mean stress in the i^{th} fiber and $[\mathbf{u}]$ indicates interface displacement jump. In order to apply (2), (3) and (4) one needs to know the displacement jump at each fiber-matrix interface as well as the mean stress in each of the fibers. The difficulty involved in obtaining these quantities has given rise to various and competing ad hoc estimates of local fields. Consider the situation where the fiber distribution is such that interaction effects between the fibers can be ignored. Under these circumstances *each* fiber can be regarded as isolated and subject to the same remotely applied equibiaxial stress field $\mathbf{S} = \sigma(\mathbf{e}_1 \otimes \mathbf{e}_1 + \mathbf{e}_2 \otimes \mathbf{e}_2 + 2\nu^{+}\mathbf{e}_3 \otimes \mathbf{e}_3)$ where unit vector $\mathbf{e}_3$ is directed along the fiber axis (Fig.2). Then (3) and (4) become,

$$\bar{\sigma} = \bar{\sigma}_i, \qquad \mathcal{A} = \frac{c}{2\mathrm{vol}(\Omega_i)} \int_{\partial\Omega_i} [\mathbf{u}] \bullet \mathbf{n}\, da, \quad i = 1,2,\ldots,N. \tag{5}$$

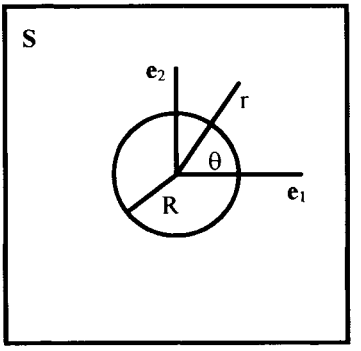

Fig.2. The solitary inclusion problem.

In order to complete the specification of the solitary fiber boundary value problem, assume that a Needleman-type [4,5] cohesive zone of vanishing thickness surrounds the fiber. If the interface is assumed uniform and incapable of supporting shear then the interface force-separation relation is given by,

$$\mathbf{s}_I(\mathbf{n};u) = f(u)\mathbf{n} \ , \tag{6}$$

where $u(=[u_r]/R)$ is the normalized radial component of the interface displacement jump. Now assume that the elastic fields are rotationally symmetric so that $u(=u_0)$ is uniform, independent of interface coordinate θ. (Note that depending on the form of f non symmetric solutions may exist to this problem as well [6,7,8]). Then (5_2) becomes simply $\mathcal{A}=cu_0$. Furthermore, it can be shown [1,9] that,

$$\begin{aligned} &\bar{\sigma}_i = f(u_0) \ , \ i = 1,2,\ldots,N \ , \\ &F(u_0;\sigma) = u_0 - \alpha_0\sigma + \alpha_1 f(u_0) = 0 \ , \end{aligned} \tag{7}$$

where the coefficients α_0, α_1 are dependent on the matrix and fiber elastic moduli. Combining (2) and (7) and noting that $\mathcal{A}=cu_0$ yields the system,

$$\begin{aligned} &\varepsilon = \hat{\varepsilon}(\sigma,\omega_0) = \alpha_2\sigma + \frac{\alpha_0}{\alpha_1}\omega_0 \ , \\ &F(\omega_0,\sigma) = \omega_0 - c\alpha_0\sigma + \alpha_1 c f(\omega_0) = 0 \ , \ c \neq 0 \ , \end{aligned} \tag{8}$$

where the coefficients α_i, i=0,1,2 are given by,

$$\alpha_0 = \frac{1}{2\kappa^+} + \frac{1}{2\mu^+} \ , \ \alpha_1 = \frac{1}{2\kappa} + \frac{1}{2\mu^+} \ , \ \alpha_2 = \frac{1}{2\kappa^+} + \frac{c(\kappa^+ - \kappa^-)(\mu^+ + \kappa^+)}{2\kappa^{+2}(\mu^+ + \kappa)} \ . \tag{9}$$

Equation (8_1) is the effective property relation and (8_2) is the kinetic equation governing the local evolution of interface separations. The quantity $\omega_0(=cu_0)$, regarded as the damage parameter, is a measure of the void area density in the plane of the cross section of the fibers. To see this simply note that cu_0 is $N\pi R[u_r]/\text{area}(\mathcal{B})$ (N is the total number of fibers) so that,

$$\frac{\text{total void area}}{\text{area}(\mathcal{B})} = 2\omega_0 + O(\omega_0^2) \ . \tag{10}$$

Thus to a term of order $O(\omega_0^2)$ ω_0 is one half the area density of voids. Note that while this correspondence is consistent with the original formulation of scalar damage as the area density of voids in a cross section (Rabotnov [10]) its meaning is nevertheless different. In the classical sense the void area density measures the loss of load bearing capability of material. The evolution of damage in this sense represents *both* the nucleation and growth of traction free defects. In the sense used in this paper the number of voids is fixed (by c) and equal to the number of fibers. Damage evolution in our sense means the growth of voids at the fiber-matrix

interface from initial coherence through complete decohesion when the voids are essentially traction free.

The system of equations (8) is complete once the functional form of the interface force law is prescribed since we assume that the elastic properties of the constituents and the fiber volume concentration are know a priori. Now assume that the interface force magnitude f is such that it is momotonically increasing on $(-\infty, u_{max})$, monotonically decreasing on (u_{max}, ∞) and such that $u_{max}>0$, $f(0)=0$, and Lim $f(u_0)=0$, $u_0 \uparrow u_v \in (u_{max}, \infty)$. By (8) the undamaged state $\omega_0=0$, corresponding to perfect interfacial coherence, coincides with the unloaded reference state. Furthermore, the fully damaged state is obtained from (8) by letting $f(\omega_0)=0$ for $\omega_0 \neq 0$ so that,

$$\omega_0 = c\alpha_0\sigma \text{ or } u_0 = u_v = \left(\frac{1}{2\kappa^+} + \frac{1}{2\mu^+}\right)\sigma ,$$
$$\varepsilon = \varepsilon_v = \frac{1}{2\kappa_v^*}\sigma = \left[\frac{1}{2\kappa^+} + c\left(\frac{1}{2\kappa^+} + \frac{1}{2\mu^+}\right)\right]\sigma . \tag{11}$$

In (11_1) u_v is just the normalized radial displacement of a solitary void while (11_2) is the stress-strain relation for a composite containing a dilute distribution of cylindrical voids. Note that if the fiber-matrix interfaces are regarded as rigidly bonded then $\omega_0=0$ for any load and (8_1) yields the stress-strain relation,

$$\varepsilon = \varepsilon_c = \frac{1}{2\kappa_c^*}\sigma = \left[\frac{1}{2\kappa^+} + \frac{c(\kappa^+ - \kappa^-)(\mu^+ + \kappa^+)}{2\kappa^{+2}(\mu^+ + \kappa^-)}\right]\sigma . \tag{12}$$

Equations (11_2) and (12) are consistent with well known results of voided and rigid interface composites [11].

Finally, it should be pointed out that the damage model is self consistent in the sense that an applied boundary strain yields an effective stiffness which is the inverse of the effective compliance obtained through (8). This has been demonstrated in [1].

2.2. Bulk response. The Mori-Tanaka estimate.

The Mori-Tanaka estimate [12] as applied to composite media [13] is one of a number of ad hoc models designed to incorporate aspects of inclusion-inclusion interaction at non dilute concentration in the estimation of the mean stress or strain in the inclusion phase. Unlike the self consistent and three phase estimates which surround the inclusion with an effective medium or an effective medium-matrix shell, the Mori-Tanaka estimate assumes that neighboring inclusions act to modify the matrix stress (or strain) field "seen" by a representative inclusion.

For the problem of bulk response this assumption means that we must estimate the mean fiber stress and interface displacement jump in a solitary fiber problem similar to that used in the dilute estimate except for the fact that the remotely applied stress is the mean stress in the matrix $\overline{\sigma}^+$. (Recall the relationship, for two phase composites,

$$\sigma = (1-c)\overline{\sigma}^{+} + c\overline{\sigma}^{-} \quad , \tag{13}$$

where σ is both the mean equibiaxial stress and the uniform boundary condition.) Thus, the relation (2) remains unchanged but (7) assumes the form,

$$\begin{aligned} &\overline{\sigma}_i = f(u_0) \ , \ i = 1,2,\ldots,N \ , \\ &F(u_0;\sigma) = u_0 - \alpha_0\overline{\sigma}^{+} + \alpha_1 f(u_0) = 0 \ . \end{aligned} \tag{14}$$

Now use (13) to eliminate $\overline{\sigma}^{+}$ in (14) noting that $\overline{\sigma}^{-} = \overline{\sigma}_i = f(u_0)$, i=1,2,...,N. Then the governing equations are of the form,

$$\begin{aligned} &\varepsilon = \hat{\varepsilon}(\sigma,\omega_0) = \hat{\alpha}_2\sigma + \frac{\hat{\alpha}_0}{\hat{\alpha}_1}\omega_0 \ , \\ &F(\omega_0,\sigma) = \omega_0 - c\hat{\alpha}_0\sigma + \hat{\alpha}_1 c f(\omega_0) = 0 \ , \end{aligned} \tag{15}$$

where the $\hat{\alpha}_i$ are given by,

$$\begin{aligned} &\hat{\alpha}_0 = \frac{1}{1-c}\left(\frac{1}{2\kappa'} + \frac{1}{2\mu'}\right), \quad \hat{\alpha}_1 = \frac{1}{1-c}\left(\frac{c}{2\kappa^{+}} + \frac{1-c}{2\kappa^{-}} + \frac{1}{2\mu^{+}}\right) \ , \\ &\hat{\alpha}_2 = \frac{1}{2\kappa'} + \frac{c(1-c)(\kappa' - \kappa^{-})(\mu^{+} + \kappa^{+})}{2\kappa^{+}(\mu^{+}\kappa^{+} + \kappa^{+}\kappa^{-} - c\mu'\kappa^{+} + c\mu'\kappa^{-})} \ . \end{aligned} \tag{16}$$

Equations (15) are identical in structure to (8) and, in fact, become them in the limit of small c, i.e., $\hat{\alpha}_0 = \alpha_0 + O(c)$, $\hat{\alpha}_1 = \alpha_1 + O(c)$, $\hat{\alpha}_2 = \alpha_2 + O(c^2)$. (Note that terms of order O(c) are neglected in $\hat{\alpha}_0, \hat{\alpha}_1$ since $\omega_0 = cu_0$.) Thus, consistent with the case of voided or rigid interface composites, the Mori-Tanaka estimate predicts the correct dilute approximation in the limit of small concentration. The system (15),(16) is also identical to that obtained from the three phase estimate and the composite cylinders model as given in [9].

Again as with the case of voided or rigid interface composites, the Mori-Tanaka estimate, applied to composites with non linear interfaces, is self consistent. To see this write relations analogous to (2) and (13) as,

$$\begin{aligned} &\sigma = 2\hat{\kappa}^{*}\varepsilon = 2\kappa^{+}\varepsilon + c(2\kappa^{-} - 2\kappa^{+})\overline{\varepsilon}^{-} - 2\kappa^{+}\Delta \ , \\ &\varepsilon - \Delta = (1-c)\overline{\varepsilon}^{+} + c\overline{\varepsilon}^{-} \ , \end{aligned} \tag{17}$$

where $\hat{\kappa}^{*}$ is the effective bulk modulus, ε is the uniform boundary strain (mean *effective* strain) and ε-Δ is the mean strain (recall $\Delta = cu_0$). We need to show that $\hat{\kappa}^{*} = \kappa^{*}$. First, solve the solitary fiber problem with remote "load" given by the mean strain in the matrix phase $\overline{\varepsilon}^{+}$. The solution to this problem along with some algebraic manipulation yields the desired result.

The limiting case of the voided composite follows from (15_2) by simply setting $f(\omega_0)$ equal to zero. Then $\omega_0 = c\hat{\alpha}_0\sigma$ or $u_0 = \hat{\alpha}_0\sigma$ which is the opening of a single void. The stress-strain relation for the voided composite then follows from (15_1),

$$\varepsilon_v = \left[\frac{2\kappa^+\mu^+(1-c)}{\mu^+ + c\kappa^+}\right]\sigma \ . \tag{18}$$

To obtain the stress-strain relation of a rigidly bonded composite let $\omega_0 = 0$ in (15_1) so that,

$$\varepsilon_c = \left[\frac{1}{2\kappa^+} + \frac{c(1-c)(\kappa^+ - \kappa^-)(\mu^+ + \kappa^+)}{2\kappa^+(\mu^+\kappa^+ + \kappa^+\kappa^- - c\mu^+\kappa^+ + c\mu^+\kappa^-)}\right]\sigma \ . \tag{19}$$

Both (18) and (19) are consistent with known results [14].

2.3. Predictions.

Predictions of composite response follows from (8) or (15) provided we prescribe the interface force magnitude (f). In this work we employ the physically based force law of Ferrante, Smith and Rose [15]. The physically based law, in the form originally used in [16], has the form,

$$f: u \rightarrow e\sigma_{MAX}(\beta u/\rho)\exp(-\beta u/\rho) \ , \tag{20}$$

where ρ is the characteristic length ratio δ/R, σ_{MAX} is the interface strength, and β is a fit parameter which can be arbitrarily fixed provided δ is considered as a phenomenological parameter (Fig.3). If the work of separation of interface force (20) is required to be the same

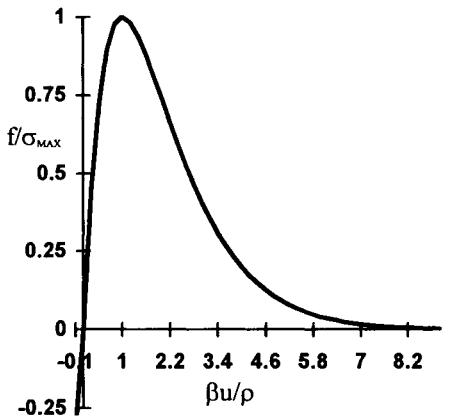

Fig.3. The interface force law.

as that for the third degree polynomial approximation of f then β assumes the value 4.8325. Note that (20) allows for a small amount of interpenetration when the interface is compressed.

In the two equations of the set (8) (or (15)) the damage parameter ω_0 can be eliminated to obtain a single equation involving the equibiaxial stress, equibiaxial strain and other physical and geometrical parameters describing the system. The resulting form provides no further insight so the sets (8) and (15) were plotted directly using MAPLE [17]. Fig.4 is a graph of the stress-strain response for a composite system consisting of an epoxy matrix reinforced by glass fibers. The interface strength (σ_{MAX}) is taken to be $\frac{1}{50}$ of the matrix elastic modulus and the force length parameter (ρ) is chosen to be 0.075. Both the dilute estimate and the Mori-Tanaka estimate are shown at different values of fiber volume concentration. Note that dilute estimate curves are only shown for values of fiber volume concentration (c) of .05 and .1. For values of c greater then .1 the dilute estimate yields predictions which may be regarded as unreliable in the sense that the stiffness at any strain value will be overestimated. The Mori-Tanaka estimate captures the phenomenon of composite instability under increasing stress owing to fiber-fiber interaction at large volume concentrations. Similar instability is observed in graphs of composite response at small force length ratios and small volume fiber concentrations [9]. The destabilizing mechanism is a consequence of the rapid descent of the interface force law (Fig. 3) which occurs under increasing interface separation in the solitary fiber problem (see [18]).

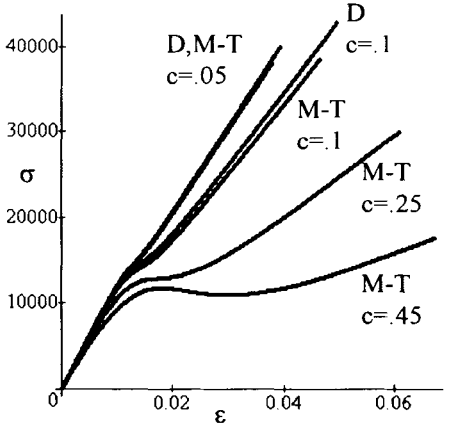

Fig.4. Bulk composite response. Dilute estimate (D), Mori-Tanaka estimate (M-T).
(κ =7291667psi, μ^-=4375000psi, κ^+=617284psi, μ^+=185185psi, σ_{MAX}=10000, ρ=.075)

3. GENERAL FORMULATION. TENSION AND COMPRESSION RESPONSE.

A general theory of the effective behavior of composites composed of linear elastic constituents with nonlinear interfaces has been presented in [1]. The following contains a brief outline of the theory for the special case in which the interfaces are assumed (i) uniform, independent of interface coordinate and (ii) perfectly smooth so that they do not support shear. The interface force law is then governed by (6).

3.1. General formulation.

Three dimensional analogs to effective property relations (2) and (17_1) are well known [2,3] and assume the form,

$$\begin{aligned}\overline{\mathbf{E}} &= \mathbf{K}^*[\overline{\mathbf{S}}] = \mathbf{K}^+[\overline{\mathbf{S}}] + c\left(\mathbf{K}^- - \mathbf{K}^+\right)[\overline{\mathbf{S}}^-] + \mathbf{A}\ , \\ \overline{\mathbf{S}} &= \mathbf{C}^*[\overline{\mathbf{E}}] = \mathbf{C}^+[\overline{\mathbf{E}}] + c\left(\mathbf{C}^- - \mathbf{C}^+\right)[\overline{\mathbf{E}}^-] - \mathbf{C}^+\mathbf{A}\ ,\end{aligned} \tag{21}$$

where $\mathbf{K}^*(\mathbf{C}^*)$ is the effective composite compliance(stiffness) and, as before, a +(–) superscript indicates a matrix(inclusion) field. (Note that tensor notation is consistent with Gurtin [19], e.g. $\mathbf{C}[\mathbf{E}] = C_{ijkl}E_{kl}\mathbf{e}_i \otimes \mathbf{e}_j$, $\mathbf{E}\mathbf{u}=E_{ij}u_j\mathbf{e}_i$, etc.) Analogous to (4) the displacement discontinuity tensor $\mathbf{A}$ represents the contribution of interfacial separation to the mean effective strain and is given by,

$$\mathbf{A} = \frac{c\sum_{i=1}^{N}\int_{\partial\Omega_i}\left([\mathbf{u}]\otimes\mathbf{n} + \mathbf{n}\otimes[\mathbf{u}]\right)\,da}{2\sum_{i=1}^{N} vol(\Omega_i)}\ . \tag{22}$$

As before $\overline{\mathbf{E}}^-(\overline{\mathbf{S}}^-)$ represents the mean inclusion strain(stress) taken over *all* the inclusions. If all inclusions are assumed to behave identically then these quantities can be regarded as mean values taken over a *single* inclusion. Note that this assumption has severe consequences in the prediction of realistic composite response (see Concluding Remarks).

The problem of estimating the mean inclusion strain(stress) $\overline{\mathbf{E}}^-(\overline{\mathbf{S}}^-)$ and the interface displacement jump $[\mathbf{u}]$ (for use in determining $\mathbf{A}$) requires the formulation and solution of an appropriate solitary inclusion problem. For the dilute estimate we consider the situation shown in Fig.3 where the remote stress is given by $\mathbf{S} = S_{11}\mathbf{e}_1\otimes\mathbf{e}_1 + S_{22}\mathbf{e}_2\otimes\mathbf{e}_2 + \nu^+(S_{11}+S_{22})\mathbf{e}_3\otimes\mathbf{e}_3$. (By the spectral decomposition theorem this is the most general planar remote loading.) The displacement field within, and external to, the inclusion may be written in the form,

$$\begin{aligned}\mathbf{u}^+(\mathbf{x}) &= \mathbf{u}_v(\mathbf{x}) - \int_{\partial\Omega}\mathbf{U}^+(\mathbf{x},\xi)\mathbf{s}_1(\mathbf{n};[\mathbf{u}](\xi))\,ds_\xi\ , \\ \mathbf{u}^-(\mathbf{x}) &= \int_{\partial\Omega}\mathbf{U}^-(\mathbf{x},\xi)\mathbf{s}_1(\mathbf{n};[\mathbf{u}](\xi))\,ds_\xi\ ,\quad \xi\in\partial\Omega\ ,\end{aligned} \tag{23}$$

where $\mathbf{U}^+$, $\mathbf{U}^-$ are the (presumed known) kernel functions generally dependent on the matrix and inclusion elastic moduli and derived, for example, from the Boussinesq-Flamant solution to the problem of a concentrated force acting at a point normal and (if interfacial shear is present) tangent to the boundary of an interior and exterior domain. The term $\mathbf{u}_v$ represents the void solution and depends linearly on the remote stress field $\mathbf{S}$. Matrix and inclusion displacement fields depend on the interfacial displacement jump through the interface force law (6) appearing in the integrals in (23). An integral equation governing the interfacial displacement

jump **[u]** is obtained by subtracting the equations in (23) and constraining the field point to reside on the interface,

$$\mathbf{[u](x)} = \mathbf{h(x)} + \int_{\partial\Omega} \mathbf{K(x,\xi)}\, \mathbf{s}_I(\mathbf{n};\mathbf{[u](\xi)})\, ds_\xi \ , \quad \mathbf{x},\xi \in \partial\Omega \ , \tag{24}$$

where the kernel **K** (as distinct from compliance **K**) is the negative of the sum of the kernel functions given in (23). The term **h** appearing in (24) is the displacement of the inner boundary of a void under remote load and is a linear function of both the remote stress **S** and the point **x** residing on the boundary. Additional equations enforcing rigid body equilibrium of the inclusion must be satisfied as well and these relations, given by,

$$\int_{\partial\Omega} \mathbf{s}_I(\mathbf{n};\mathbf{[u](\xi)})\, ds_\xi = \mathbf{0} \ , \quad \int_{\partial\Omega} \mathbf{r}(\xi) \times \mathbf{s}_I(\mathbf{n};\mathbf{[u](\xi)})\, ds_\xi = \mathbf{0} \ , \tag{25}$$

fix the rigid body modes of the displacement jump. (Note that (25_2) is automatically satisfied by interface force law (6).) Given an inclusion geometry and a specific form of interface-force separation law (e.g. (6) and (20)) a solution for the interface displacement jump is sought from (24) and (25). This quantity then determines the interface force vector $\mathbf{s}_I(\mathbf{n};\mathbf{[u](x)})$. Note that non linearities in the prescribed interface force-interface separation law yield a displacement jump which depends non linearly on the remote stress.

Quantities needed to complete the specification of the effective property relations (21) are the displacement discontinuity tensor **A** and the mean inclusion stress $\overline{\mathbf{S}}^-$. The interface displacement jump solution to (24) determines **A** directly through (22). The mean stress in the inclusion phase is computed from (23b) along with the stress displacement relations,

$$\overline{\mathbf{S}}^- = \frac{1}{\mathrm{vol}(\Omega)} \left[\lambda^- \int_\Omega (\mathrm{div}\mathbf{u}^-)\mathbf{I}\, dv + \mu^- \int_\Omega (\nabla\mathbf{u}^- + \nabla\mathbf{u}^{-T})\, dv \right] \ , \tag{26}$$

where λ^-, μ^- are the three dimensional Lame' moduli. (Note that $\overline{\mathbf{S}}^-$ ultimately depends upon the interface displacement jump through (23_2) and $\mathbf{s}_I(\mathbf{n};\mathbf{[u](x)})$.) Thus, provided we can determine the solution to the nonlinear integral equations (24) and (25), the effective response follows from (6), (21_1), (22), 23_2) and (26). A detailed analysis of (24), (25) has been carried out in [8] for different remote loadings. A sketch of the procedure is given below.

First, radial and angular components of (24) and (25_1) are written in the form,

$$\begin{aligned} u(\theta) &= h_r(\theta) + \int_0^{2\pi} f(u(\theta'))\, K_r(\theta,\theta')\, d\theta' \ , \\ v(\theta) &= h_\theta(\theta) + \int_0^{2\pi} f(u(\theta'))\, K_\theta(\theta,\theta')\, d\theta' \ , \\ \int_0^{2\pi} f(u(\theta'))\cos(\theta')\, d\theta' &= 0 \ , \qquad \int_0^{2\pi} f(u(\theta'))\sin(\theta')\, d\theta' = 0 \ , \end{aligned} \tag{27}$$

where u(v) is the normalized radial(angular) component of interface displacement jump $[u_r]/R([u_\theta]/R)$, $h_r(h_\theta)$ is the normalized radial(angular) component of displacement of inner boundary of a void and K_r, K_θ are (known) weakly singular kernel functions. For the interface force magnitude given by (20), (27_1) is a non linear integral equation of the Hammerstein type. Equation (27_2) is an integral expression which directly determines the tangential displacement jump once (27_1) has been solved. (Note that owing to the assumption of a perfectly smooth interface the tangential displacement (v) is completely determined by u.) The remaining equations (27_3) and (27_4) enforce rigid body force equilibrium of the inclusion.

In practice a solution to (27_1), (27_3) and (27_4) is sought in the form of an expansion of eigenfunctions of the kernel K_r. It can be shown that K_r has, through the bilinear formula, a mean convergent eigenfunction expansion in eigenvalues and orthonormal eigenfunctions given by,

$$\lambda_0 = \frac{-E^+E^-}{(1+\nu^-)(1-2\nu^-)E^+ + (1+\nu^+)E^-} ,$$

$$\lambda_{2n-1} = \lambda_{2n} = \frac{-(n^2-1)E^+E^-}{2n\left[(1-\nu^{-2})E^+ + (1-\nu^{+2})E^-\right] + (1+\nu^+)(1-2\nu^+)E^- - (1+\nu^-)(1-2\nu^-)E^+} ,$$

$$\varphi_0 = 1/\sqrt{2\pi}, \quad \varphi_{2n-1} = \cos n\theta/\sqrt{\pi}, \quad \varphi_{2n} = \sin n\theta/\sqrt{\pi} , \quad n = 2,3,\ldots$$

If we preclude the possibility of rigid displacement of the inclusion we can assume that even, symmetric solutions may be approximated by the finite series expansion,

$$u = u_0 + \sum_{i=1}^{n} u_{4i-1} \cos 2i\theta , \tag{28}$$

which identically satisfies (27_3), (27_4). Substitution of (28) into (27_1) yields a set of n+1 non linear algebraic equations ($G(u_0,u_{4i-1})=0$ i=1,2,...,n) governing the expansion coefficients u_i,

$$\begin{aligned}
&u_0 - \frac{1}{2\pi\lambda_0}\int_0^{2\pi} f(u_0, u_{4i-1}; \theta')d\theta' - h_0 = 0, \\
&u_3 - \frac{1}{\pi\lambda_3}\int_0^{2\pi} f(u_0, u_{4i-1}; \theta')\cos 2\theta' d\theta' - h_3 = 0, \\
&u_{4j-1} - \frac{1}{\pi\lambda_{4j-1}}\int_0^{2\pi} f(u_0, u_{4i-1}; \theta')\cos 2j\theta' d\theta' = 0, \quad j = 2,3,\ldots,
\end{aligned} \tag{29}$$

where $h_r=h_0+h_3\cos 2\theta$ and h_0, h_3 are linear in the remote load ratio's S_{11}/E^+, S_{22}/E^+. (For a discussion of convergence properties of the solution (28) see [8].) The expansion for $v(\theta)$ is taken in the form,

$$v(\theta) = v_0 + \sum_{i=1}^{n} v_{4i} \sin 2i\theta , \tag{30}$$

where the equations governing the coefficients follow directly from (27_2) and are of the form,

$$v_0 = 0\,,$$
$$v_{4n} = \frac{1}{\pi}\int_0^{2\pi} h_\theta(\theta)\sin 2n\theta d\theta + \frac{C+2C'n}{\pi(4n^2-1)}\int_0^{2\pi} f(u_k;\theta)\cos 2n\theta d\theta, \quad n = 1,2,.... \tag{31}$$

The coefficients C, C' are given explicitly in [8] and are functions of matrix and inclusion elastic moduli.

The eigenfunction expansions (28) and (30), and the equations governing the expansion coefficients ((29) and (31)) represent the kinetic equations in a micromechanical damage model of the mechanical response of fiber composites which "damage" by loss of cohesion at the fiber-matrix interfaces. (A virtually identical formulation applies to particulate composites as well. The only constraint on the geometry of the reinforcement phase being the tractability in forming the kernel functions $\mathbf{U}^+$, $\mathbf{U}^-$, $\mathbf{K}$ in integral equations (23) and (24) and the ease in evaluating the mean inclusion stress $\bar{\mathbf{S}}^-$ in representation (26).) It follows from (22), (28) and (30) that the displacement discontinuity tensor $\mathbf{A}$ has the form,

$$\mathbf{A} = c\left[\left(u_0 + \frac{1}{2}u_3 - \frac{1}{2}v_4\right)\mathbf{e}_1 \otimes \mathbf{e}_1 + \left(u_0 - \frac{1}{2}u_3 + \frac{1}{2}v_4\right)\mathbf{e}_2 \otimes \mathbf{e}_2\right]. \tag{32}$$

It can be shown that (23_2) and (26) imply that components of the mean inclusion stress $\bar{\mathbf{S}}^-$ are given by,

$$\bar{S}_{11}^- = \frac{1}{2\pi}\int_0^{2\pi} f(u(\theta'))[1+\cos 2\theta']\,d\theta', \quad \bar{S}_{22}^- = \frac{1}{2\pi}\int_0^{2\pi} f(u(\theta'))[1-\cos 2\theta']\,d\theta',$$
$$\bar{S}_{12}^- = \frac{1}{2\pi}\int_0^{2\pi} f(u(\theta'))\sin 2\theta'\,d\theta' \quad \bar{S}_{33}^- = \frac{\nu^-}{\pi}\int_0^{2\pi} f(u(\theta'))\,d\theta'. \tag{33}$$

Because of the expansion (28) the mean inclusion stress is a function of the expansion coefficients, i.e., $\bar{\mathbf{S}}^-(u_0, u_{4i-1})$. The effective property relation (21_1) is in the form of a stress-strain relation depending on expansion coefficients u_0, u_{4i-1}, v_{4i} which assume the role of damage parameters. These variables are governed by the non linear relations (29) and (31), i.e., the kinetic equations. Thus, the damage parameters represent the expansion coefficients in an eigenfunction representation of the interface displacement jump in a solitary inclusion problem. Note that an entirely equivalent formulation of this problem begins with the effective property relation (21_2). The remote boundary condition in the related solitary inclusion problem is then an applied strain. It can be proved (see [1]) that the effective stiffness $\mathbf{C}^*$ determined in this way is the inverse of the effective compliance $\mathbf{K}^*$ determined as in the previous discussion. Thus, non linear interface response preserves self consistency.

The general formulation just described was developed for dilute concentrations of inclusions. In order to capture some of the effects of inclusion-inclusion interaction the Mori-Tanaka estimate can be implemented within this framework in a manner similar to that given in section

2.2. We need only consider the solitary inclusion problem depicted in Fig. 3 since the form of the effective property relations (21) remain unchanged (of course the functional forms of **A** and $\overline{\mathbf{S}}^-$ will change). Consider the integral equations (24) and (25) (or (27)) governing the interface displacement jump. The quantity **h** is the displacement of the inner boundary of a void and is linear in remote load **S**. No other term in these equations depends on the remote loading. The Mori-Tanaka estimate is obtained simply by replacing **S** in **h** by $\overline{\mathbf{S}}^+$ which may be expressed in terms of **S** and $\overline{\mathbf{S}}^-$ by the tensor analog of (13). This process requires a readjustment of the integral equations (24) and (25) (or (27)). In this paper we will not pursue this idea any further and the following section will present results for uniaxial tension and compression based only on the dilute estimate. Future work will present explicit results for the Mori-Tanaka estimate.

3.2. Uniaxial tension and compression.

Consider the case of uniaxial tension transverse to the fiber direction, i.e., $\mathbf{S} = \sigma(\mathbf{e}_1 \otimes \mathbf{e}_1 + \nu^+ \mathbf{e}_3 \otimes \mathbf{e}_3)$, $\sigma>0$. Then, for the response in the load direction ($\varepsilon=E_{11}$) the effective property relation (21_1) becomes,

$$\varepsilon = \left(\frac{1}{4\mu^+} + \frac{1}{4\kappa^+}\right)\sigma + c\left(\frac{1}{4\mu^-} - \frac{1}{4\mu^+}\right)(\overline{S}_{11}^- - \overline{S}_{22}^-) + c\left(\frac{1}{4\kappa^-} - \frac{1}{4\kappa^+}\right)(\overline{S}_{11}^- + \overline{S}_{22}^-) + A_{11} \ , \qquad (34)$$

and, for the planar response transverse to the load direction,

$$E_{22} = \left(\frac{1}{4\kappa^+} - \frac{1}{4\mu^+}\right)\sigma + c\left(\frac{1}{4\mu^-} - \frac{1}{4\mu^+}\right)(\overline{S}_{22} - \overline{S}_{11}) + c\left(\frac{1}{4\kappa^-} - \frac{1}{4\kappa^+}\right)(\overline{S}_{11}^- + \overline{S}_{22}^-) + A_{22} \ , \qquad (35)$$

where A_{11}, A_{22} are given by (32). The quantity $\overline{S}_{11}^-$ is just $\overline{\sigma}^-$ appearing in (33). Now the system governing the n+1 mode approximation (n+1 normal modes, n tangential modes) consists of equations (6), (20), (29), (31), (32), (33) and (34). (Note that for tension loading h_0, h_3 in (29) are given by $h_0 = (1-\nu^{+2})\sigma/E^+$, $h_3=2h_0$.) Because the tangential expansion coefficients depend on the normal coefficients through (31) they can be eliminated from (32). Then the system of equations to be solved may be written symbolically as,

$$\begin{aligned} &\varepsilon = F(\sigma;\omega_j)\,, \\ &G_i(\sigma;\omega_j) = 0\,, \quad i,j = 0,1,\ldots,n \ , \end{aligned} \qquad (36)$$

where the ω_j are normalized expansion coefficients arising in the normal separation at the interface, i.e., $\omega_i=cu_i$. In order to obtain predictions of composite response a computer program, employing the Newton-Raphson method together with the composite Simpson 1/3 Rule, was written to integrate (36) numerically. First, local solutions for the interface separation (ω_j) are sought (from (36_2)) for fixed constitutive parameters under increasing uniaxial load σ. Hadamard stability (stability in energy) of the equilibria is assessed through an examination of eigenvalues of the matrix of partial derivatives of $G_i(\sigma;\omega_j)$ and stable and

unstable solution branches are pieced together to form the evolution of mode multipliers with load (see [8] for more details). The stress strain curve $\varepsilon(\sigma)$ follows directly from (36_1). Computations were carried out for an n value of 3, which corresponds to 4 normal modes (1, cos2θ, cos4θ, cos6θ) and 3 tangential modes (sin2θ, sin4θ, sin6θ). Fig. 5 represents a graph of composite tensile response for a range of values of force length ratio $\rho(=\delta/R)$. The void solutions [20],

$$\frac{\mu^*}{\mu^+} = 1 - \frac{6k^+ + 8\mu^+}{3k^+ + \mu^+}c + O(c^2) \ , \qquad \frac{\kappa^*}{\kappa^+} = 1 - \frac{3k^+ + 4\mu^+}{3\mu^+}c + O(c^2) \ , \tag{37}$$

and the rigid interface solutions [20],

$$\frac{\mu^*}{\mu^+} = 1 - \frac{c}{[\mu^+/(\mu^+ - \mu^-)] - (k^+ + \frac{7}{3}\mu^+)/(2k^+ + \frac{8}{3}\mu^+)} + O(c^2) \ , \qquad \frac{\kappa^*}{\kappa^+} = 1 - \frac{c}{[\kappa^+/(\kappa^+ - \kappa^-)] - (k^+ + \frac{1}{3}\mu^+)/(k^+ + \frac{4}{3}\mu^+)} + O(c^2) \tag{38}$$

are used to get the limiting behavior for uniaxial tension through the relation $\varepsilon = (1/4\mu^* + 1/4\kappa^*)\sigma$ and these curves bound the nonlinear interface solutions. (Note that k appearing in the above formulas is the three dimensional bulk modulus.) In particular the stiffness of the rigid interface composite is greater than the maximum stiffness of the nonlinear interface composite owing to the allowance of interface slip during interface debonding. Furthermore, the stiffness of the voided composite is less than the minimum stiffness of the nonlinear interface composite owing to the compressive action of the matrix on the fibers normal to the direction of maximum interface separation. (Material interpenetration at fiber

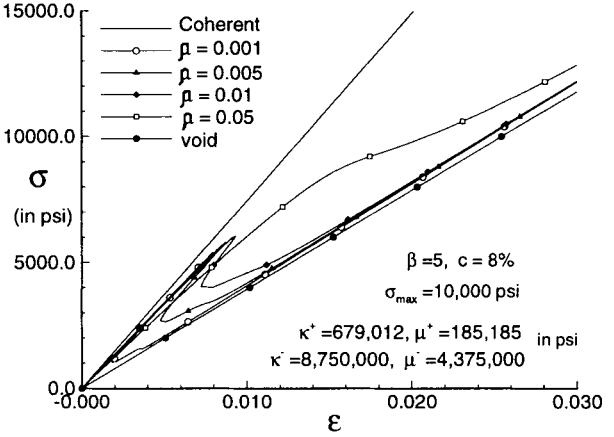

Fig. 5. Composite response for various force length ratios. Uniaxial tension.

matrix interfaces is resisted through the interface force law f (Fig.3).) An inspection of the curves in Fig. 5 indicates the effect of force length parameter on response. Thus, decreasing ρ, i.e., decreasing the range of action of the interface force, precipitates an abrupt transition in composite response at increasing stress. This aggregate behavior corresponds to bifurcation of equilibrium interface separation in the solitary inclusion problem arising from the local effect of rapid descent of the interface force separation law for each interface.

The behavior just described is qualitatively similar to the response of the nonlinear composite subject to pure shear [1]. It is also similar to the equibiaxial stress problem although in that case, the limiting rigid composite solution and the void solution are recovered exactly by the nonlinear composite upon initial application of the load (rigid composite stiffness) and asymptotically as the interface force approaches zero (voided composite stiffness). This is because the interface separations are rotationally symmetric and tangential interface force and displacement jump are zero. Note that under equibiaxial loading the normal component of fiber-matrix interface force carries matrix stresses to the fibers. In contrast, only a part of the matrix stresses arising from tensile load is transmitted to the fibers by the normal component of interface force. The remaining portion would be born by the tangential component of interface force. Because it is absent in the constitutive characterization of the interface employed here, the composite response is more compliant. This same state of affairs exists under pure shear loading [1] only to an even greater degree. Note that the equibiaxial response curves are exact in the sense that only one symmetrical mode arises in the description of interface separation. By contrast, tensile response requires an infinite number of modes to exactly characterize interface separation.

Finally, Fig. 6 shows composite response under a uniaxial compressive load $\sigma<0$ given the same constitutive parameters used previously. Under uniaxial compressive loading a symmetric solution to the solitary inclusion problem indicates that the interface will separate in regions approximately perpendicular to the load line while regions of matrix and inclusion boundary parallel to the load line will be in mechanical contact Levy [7]. Because this separation action is indirect, caused essentially by the Poisson effect, the influence of debonding on the overall effective response is minimal (as indicated in Fig. 6).

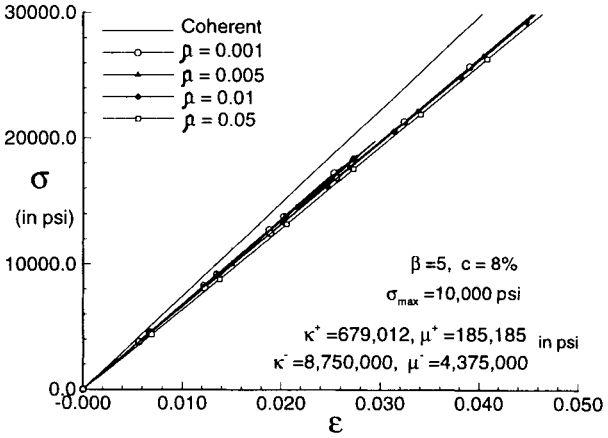

Fig. 6. Composite response for various force length ratios. Uniaxial compression.

4. CONCLUDING REMARKS.

This paper describes a micromechanical damage model of a two phase composite material composed of linear elastic constituents which interact through non linear interface forces. Within this framework damage is defined as the loss of cohesion at the inclusion-matrix interfaces and is measured by coefficients in a series representation of the displacement jump at a representative interface. The attractiveness of this approach is that no adjustable parameters appear in the model which requires only that the elastic properties of the phases and the properties of a representative interface (e.g. interface strength, work of separation, etc.) be specified. As has been demonstrated, the model is capable of handling dilute distributions of inclusions as well as larger inclusion volume fractions through the Mori-Tanaka estimate. Although the paper has concentrated primarily on unidirectional fiber composites the framework is virtually identical for particulate composites.

The specification of the dilute estimate or the Mori-Tanaka estimate is just one assumption which needs to be made a priori. Another, is the form of the interface constitutive relation. In this paper we have employed a force law (20) derived from a potential so that the results obtained may be unrealistic if the loading is reversed. This problem can be dealt with by proposing a more realistic interface force law within the same conceptual framework utilized here. The phenomenon of matrix inelasticity is more difficult to address within the proposed micromechanical framework. Alternative models combining micromechanics and continuum damage concepts in an elastoplastic setting do however exist (see [21]).

A more severe assumption employed by the proposed model is that the damage process indicated in Fig. 1 is representative, i.e., at each level of remote loading *every* inclusion has precisely the same void surrounding it. (This hypothesis is built into the model through the process of solving a solitary inclusion problem and employing the local fields as representative of all inclusions in the composite.) Progressive debonding is therefore not accounted for in the model and to include it would require the solution to an isolated multi particle system or some other hypothesis concerning the inclusion fields arising in (21). Future work will address this important issue.

5. REFERENCES.

1. Z. Dong and A.J. Levy, J. Mech. Phys. Solids, Submitted.

2. Y. Benveniste, Mech. Mat., **4** (1985) 197.

3. J. Aboudi, Composites Science and Technology, **28** (1987) 103.

4. A. Needleman, J. Appl. Mech., **54** (1987) 525.

5. A. Needleman, Ultramicroscopy, **40** (1992) 203.

6. A.J. Levy, J. Mech. Phys. Solids, **43** (1995) 1003.

7. A.J. Levy, in *Contemporary Research in the Mechanics and Mathematics of Materials.* (eds. R.C. Batra-M.F. Beatty), CIMNE, Barcelona, 1996.

8. A.J. Levy, Phil. Trans. R. Soc. Lond. **A**, (1997) in press.

9. A.J. Levy, J. Appl. Mech., **63** (1996) 357.

10. Y.N. Rabotnov, Proceedings of the Twelfth International Congress of Applied Mechanics, Stanford University, 1969.

11. Z. Hashin, Theory of fiber reinforced materials. NASA CR-1974 **31**,1972.

12. T. Mori and K. Tanaka, Acta Metallurgica., **21** (1973) 571.

13. Y. Benveniste, Mech. Mat. **6** (1987) 147.

14. Z. Hashin and B.W. Rosen, J. Appl. Mech. **31**,(1964) 223.

15. J. Ferrante, J.R. Smith & J.H. Rose, in *Microscopic Aspects of Adhesion and Lubrication* (ed. J.M. Georges), Elsevier, Amsterdam, 1982.

16. A. Needleman, J. Mech. Phys. Solids, **38** (1990) 289.

17. MAPLE Waterloo Maple Software, Waterloo, 1996.

18. A.J. Levy, J. Mech. Phys. Solids, **42** (1994) 1087.

19. M.E. Gurtin, in *Mechanics of solids* (ed. C. Truesdell), **2**, Springer Verlag, Heidelberg, 1984.

20. S. Nemat-Nasser and M. Hori, *Micromechanics: Overall Properties of Heterogeneous Materials*, North-Holland, Amsterdam, 1993.

21. G.Z. Voyiadjis and T. Park, J. Eng. Mech., **121** (1995) 1209.

This Page Intentionally Left Blank

PART II

LOCALIZATION AND DAMAGE

This Page Intentionally Left Blank

Damage Mechanics in Engineering Materials
G.Z. Voyiadjis, J.-W.W. Ju and J.-L. Chaboche (Editors)
© 1998 Elsevier Science B.V. All rights reserved.

Dynamic localized fracture in inelastic solids

Piotr Perzyna

Centre of Mechanics, Institute of Fundamental Technological Research,
Polish Academy of Sciences, Świętokrzyska 21, 00-049 Warsaw, Poland

Abstract

The paper aims at the investigation of ductile localized fracture phenomena in dynamic adiabatic processes in inelastic solids. Particular attention is focused on the dependence of fracture phenomenon upon the evolution of constitutive properties of the material. The micro-damage mechanism is treated as a sequence of nucleation, growth and coalescence of microcracks.

To accomplish in one model the description of the rate sensitivity of the material and rate dependent micro-damage mechanism the theory of thermoviscoplasticity is developed within a framework of the rate type covariance material structure with finite set of internal state variables. This theory takes into consideration the effects of micro-damage mechanism and thermomechanical coupling. The rate dependent, internal state variables approach has the exciting feature of being directly connected to the evolution of microstructural properties of the material. The relaxation time is used as characteristic time which can thus be viewed as a regularization parameter, or as a micromechanical parameter to be determined from physical experimental observations. By assuming that the relaxation time tends to zero the rate independent thermoplastic response of the material with rate independent micro-damage mechanism is considered. The dynamic fracture criterion within localized shear band region is proposed. This criterion implies that the fracture is the time dependent process, i.e. it depends strongly on time duration of the stress impulse.

Rate dependency (viscosity) allows the spatial differential operator in the governing equations to retain its ellipticity, and the initial-value problem is well-posed. The viscoplastic regularization procedure assures the stable integration algorithm by using the finite element method. Particular attention is focused on the well-posedness of the evolution problem (the initial-boundary value problem) as well as on its numerical solutions. Convergence, consistency and stability of the discretised problem are discussed. The validity of the Lax equivalence theorem is examined.

Utilizing the finite element method and ABAQUS system for regularized elasto-viscoplastic model the numerical investigation of the three dimensional dynamic adiabatic deformation in particular body is presented. Two particular examples have been considered, namely dynamic adiabatic processes for a thin-walled steel tube and for a thin steel plate. In each case a thin shear band region of finite width which undergoes significant deformations and temperature rise has been determined. Its evolution until occurrence of final fracture has been simulated. It has been investigated how the localized fracture mode depends on various constitutive parameters (namely the relaxation time and the irreversibility coefficient).

1. INTRODUCTION

In technological dynamical processes fracture can occur as a result of an adiabatic shear band localization generally attributed to a plastic instability generated by thermal softening and intrinsic micro-damage mechanism during plastic deformation.

Hartley, Duffy and Hawley (1987), Marchand and Duffy (1988), Marchand, Cho and Duffy (1988) and Cho, Chi and Duffy (1988) made microscopic observations of the shear band localization on the thin-walled steel tubes in a split Hopkinson torsion bar. Three different steels were tested. Dynamic deformation in shear was imposed to produce shear bands. It was found whenever the shear band led to fracture of the specimen, the fracture occurred by a process of void nucleation, growth and coalescence. No cleavage was observed on any fracture surface, including the most brittle of the steel tested. This is presumably due to the thermal softening of the shear band material that results from the local temperature rise and micro-damage mechanism occurring during deformation process.

Adiabatic shear banding in 4340 steel under pure shear loading in split Hopkinson torsion bar using a high-speed photography was studied by Giovanola (1988). It was found that shear localization occurs in two sequential stages over width of 60 μm and 20 μm, respectively. Strain rates approaching $1.4 \cdot 10^6$ s^{-1} were measured in the band and temperature elevation was in excess of 1000^0C. Fractographic and metallographic observations have shown that the mechanism of shear fracture by microvoid nucleation and growth may, at least in certain situations, provide a plausible explanation for the formation of wite etching bands. General conclusion from experimental observations of Giovanola (1988) is that the thermomechanical strain localization and micro-damage mechanisms become the main cooperative phenomena responsible for adiabatic shear band localized fracture.

Chakrabarti and Spretnak (1975) investigated the localized fracture mode for tensile steel sheet specimens simulating both plane stress and plane strain processes. The material used in their study was AISI 4340 steel. The principal variable in this flat specimen test was the width to thickness ratio. Variation in specimen geometry produces significant changes in stress state, directions of shear bands and ductility. They found that fracture propagated consistently along the shear band localized region.

In recent years Zbib and Jurban (1992) have investigated numerically a three dimensional problem involving the development of shear bands in a steel bar pulled in tension and Batra and Zhang (1993) the three-dimensional dynamic thermomechanical deformations of a 4340 steel thin tube twisted in a split Hopkinson bar at nominal strain rate of 1000, 2500 and 25000 s^{-1}.

The papers by Perzyna and Duszek-Perzyna (1994), Perzyna (1994, 1995), Lodygowski and Perzyna (1996, 1997) and Lodygowski (1996) presented the application of a recently developed viscoplastic-damage type constitutive theory for high strain rate flow process and ductile fracture to the problems of shear band localization and fracture of dynamically loaded thin-walled tubes experiencing strain rates ranging between $10^{-1} - 10^4$ s^{-1} and the investigation of localized fracture phenomena in thin and thick plates undergoing adiabatic dynamic and isothermal quasi-static processes.

The main objective of the present paper is the investigation of the influence of some

constitutive parameters on shear band localization phenomena.

In chapter 2 the formulation of the initial–boundary value problem (evolution problem) and development of a constitutive model within a thermodynamic framework of the rate type material structure with internal state variables are given. Such important effects as the micro–damage mechanism and thermomechanical coupling are taken into consideration. It has been assumed that the intrinsic micro–damage mechanism consists of the nucleation, growth and coalescence of microvoids. The rate dependent evolution equation for the porosity parameter has been postulated. Discussion of cooperative phenomena, i.e. thermomechanical coupling and micro–damage mechanism is given. The fracture criterion is presented and the description of an adiabatic inelastic flow process is given.

Numerical solutions of the initial–boundary value problem (evolution problem) are discussed in chapter 3. Well–posedness of the evolution problem is presented. Discretisation in space and time is proposed and convergence, consistency and stability are examined. The Lax equivalence theorem is formulated.

Chapter 4 is devoted to the numerical investigation of shear band localization fracture. Two particular examples have been considered, namely dynamic adiabatic processes for a thin–walled steel tube and for a thin steel plate. All formulated initial boundary value problems (evolution problems) have been solved numerically by means of finite element method and ABAQUS system, cf. chapter 5. In each case particular attention has been focused on a thin shear band region of finite width which undergoes significant deformations and temperature rise. Its evolution until occurrence of fracture has been simulated.

In chapter 6 the influence of some constitutive parameters on localized fracture phenomena have been investigated. The paper closes with some conclusions in chapter 7.

2. INITIAL–BOUNDARY VALUE PROBLEM (EVOLUTION PROBLEM)

2.1. Formulation of the evolution problem

Find φ as function of t and $\mathbf{x}$ satisfying*

$$\begin{array}{ll} \text{(i)} & \dot{\varphi} = \mathcal{A}(t,\varphi)\varphi + \mathbf{f}(t,\varphi); \\ \text{(ii)} & \varphi(0) = \varphi^0(\mathbf{x}); \\ \text{(iii)} & \text{The boundary conditions.} \end{array} \tag{1}$$

A strict solution of (1) with $\mathbf{f}(t,\varphi) \equiv 0$ (i.e. the homogeneous evolution problem) is defined as a function $\varphi(t) \in \mathrm{E}$ (a Banach space) such that

$$\varphi(t) \in \mathcal{D}(\mathcal{A}), \quad \text{for all} \quad t \in [0, t_f], \tag{2}$$

$$\lim_{\Delta t \to 0} \| \frac{\varphi(t+\Delta t) - \varphi(t)}{\Delta t} - \mathcal{A}\varphi(t) \|_{\mathrm{E}} = 0 \quad \text{for all} \quad t \in [0, t_f].$$

*We shall follow here some fundamental results which have been discussed in Richtmyer and Morton (1967), Strang and Fix (1973), Richtmyer (1978), Ionescu and Sofonea (1993) and Dautray and Lions (1993).

The boundary conditions are taken care of by restricting the domain $\mathcal{D}(\mathcal{A})$ to elements of E that satisfy those conditions; they are assumed to be linear and homogeneous, so that the set $\mathbf{S}$ of all φ that satisfy them is a linear manifold; $\mathcal{D}(\mathcal{A})$ is assumed to be contained in $\mathbf{S}$.

The choice of the Banach space E, as well as the domain of $\mathcal{A}$, is an essential part of the formulation of the evolution problem.

2.2. Rate type constitutive structure for an elastic–viscoplastic damaged material

The main objective is to develop the rate type constitutive structure for an elastic–viscoplastic material in which the effects of the micro-damage mechanism and thermomechanical coupling are taken into consideration.

Let us introduce the axioms as follows:

(i) Axiom of the existence of the free energy function in the form

$$\psi = \hat{\psi}(\mathbf{e}, \mathbf{F}, \vartheta; \boldsymbol{\mu}), \tag{3}$$

where $\mathbf{e}$ is the Eulerian strain tensor, $\mathbf{F}$ the deformation gradient, ϑ a temperature field and $\boldsymbol{\mu}$ denotes the internal state variable vector.

(ii) Axiom of objectivity (spatial covariance). The constitutive structure should be invariant with respect to any diffeomorphism $\boldsymbol{\xi} : \mathcal{S} \to \mathcal{S}$, where $\mathcal{S}$ denotes the actual (spatial) configuration of a body $\mathcal{B}$, cf. Marsden and Hughes (1983).

(iii) The axiom of entropy production. For any regular process ϕ_t, ϑ_t, $\boldsymbol{\mu}_t$ of a body $\mathcal{B}$ the constitutive functions are assumed to satisfy the reduced dissipation inequality

$$\frac{1}{\rho_{Ref}}\boldsymbol{\tau} : \mathbf{d} - (\eta\dot{\vartheta} + \dot{\psi}) - \frac{1}{\rho\vartheta}\mathbf{q} \cdot \operatorname{grad}\vartheta \geq 0, \tag{4}$$

where ϕ_t is the function of motion, ρ and ρ_{Ref} denote the mass density in the actual and reference configuration, respectively, $\boldsymbol{\tau}$ is the Kirchhoff stress tensor, $\mathbf{d} = \mathbf{d}^e + \mathbf{d}^p$ the rate of total deformation, η denotes the specific (per unit mass) entropy and $\mathbf{q}$ is the heat vector field.

Let us postulate $\boldsymbol{\mu} = (\boldsymbol{\zeta}, \xi)$, where $\boldsymbol{\zeta}$ denotes the new internal state vector which describes the dissipation effects generated by viscoplastic flow phenomena and ξ is the volume fraction porosity parameter and takes account for micro-damage mechanism.

Let us introduce the plastic potential function for damaged material in the form cf. Shima and Oyane (1976) and Perzyna (1984, 1986)

$$f = \frac{J_2}{\kappa_0^2} + n\xi\left(\frac{J_1}{\kappa_0}\right)^2; \tag{5}$$

where $J_1 = \tau^{ab} g_{ab}$, $J_2 = \frac{1}{2}\tau'^{ab}\tau'^{cd} g_{ac} g_{bd}$, κ_0 denotes the yield stress of the matrix material, $n = n(\vartheta)$ is the temperature dependent material function and $\mathbf{g}$ denotes the metric tensor in $\mathcal{S}$.

Let us postulate the evolution equations as follows† ($\mathrm{L}_{\boldsymbol{v}}$ defines the Lie derivative with respect to the velocity field and the dot denotes the material derivative)

$$\mathbf{d}^p = \Lambda \mathbf{P}, \quad \mathrm{L}_{\boldsymbol{v}} \boldsymbol{\zeta} = \Lambda \mathbf{Z}, \quad \dot{\xi} = \Xi, \tag{6}$$

where for the elastic–viscoplastic model of a material we assume (cf. Perzyna (1963, 1971, 1994, 1995))

$$\Lambda = \frac{1}{T_m} \langle \Phi(f - \kappa) \rangle, \tag{7}$$

T_m denotes the relaxation time for mechanical disturbances and κ is the isotropic work-hardening parameter, Φ is the empirical overstress function and the bracket $\langle \cdot \rangle$ defines the ramp function, the material function $\mathbf{Z}$ is intrinsically determined by the constitutive assumptions postulated, the scalar valued evolution function Ξ has to be determined and the tensor function $\mathbf{P}$ is defined as follows.

$$\mathbf{P} = \frac{1}{2} \frac{\partial f}{\partial \boldsymbol{\tau}}. \tag{8}$$

The isotropic hardening–softening material function κ is assumed in the form cf. Perzyna (1984, 1986) and Nemes, Eftis and Randles (1990)

$$\kappa = \{q + (1 - q) \exp[-h(\vartheta) \in^p]\}^2 \left[1 - \left(\frac{\xi}{\xi^F}\right)^{\frac{1}{2}}\right], \tag{9}$$

where $q = \frac{\kappa_1}{\kappa_0}$, κ_0 and κ_1 denote the yield and saturation stress of the matrix material (both can be temperature dependent functions), respectively, $h = h(\vartheta)$ is the temperature dependent strain hardening function for the matrix material, $\in^p = \int_0^t (\frac{2}{3} \mathbf{d}^p : \mathbf{d}^p)^{\frac{1}{2}} dt$ is the equivalent plastic deformation and ξ^F denotes the value of porosity at which the incipient fracture occurs. The overstress viscoplastic function Φ is postulated in the form (cf. Perzyna (1963, 1971))

$$\Phi(f - \kappa) = (f - \kappa)^m, \quad \text{where } m = 1, 3, 5, \ldots \tag{10}$$

The axioms (i)–(iii), the energy balance equation and the evolution equations (6) lead to the rate equations as follows

$$\begin{aligned} \mathrm{L}_{\boldsymbol{v}} \boldsymbol{\tau} &= \mathcal{L}^e : \mathbf{d} - \mathcal{L}^{th} \dot{\vartheta} - [(\mathcal{L}^e + \mathbf{g}\boldsymbol{\tau} + \boldsymbol{\tau}\mathbf{g}) : \mathbf{P}] \frac{1}{T_m} \langle (f - \kappa)^m \rangle, \\ \rho c_p \dot{\vartheta} &= -\mathrm{div}\mathbf{q} + \frac{\vartheta \rho}{\rho_{Ref}} \frac{\partial \boldsymbol{\tau}}{\partial \vartheta} : \mathbf{d} + \chi \boldsymbol{\tau} : \mathbf{d}^p + \lambda \dot{\xi}, \end{aligned} \tag{11}$$

where

† For precise definition of the finite elasto–plastic deformation see Duszek–Perzyna and Perzyna (1994) and Perzyna (1995).

$$\mathcal{L}^e = \rho_{Ref}\frac{\partial^2\hat{\psi}}{\partial\mathbf{e}^2}, \quad \mathcal{L}^{th} = -\rho_{Ref}\frac{\partial^2\hat{\psi}}{\partial\mathbf{e}\partial\vartheta}, \quad c_p = -\vartheta\frac{\partial^2\hat{\psi}}{\partial\vartheta^2}, \tag{12}$$

the irreversibility coefficient χ is defined by

$$\chi = -\rho\left(\frac{\partial\hat{\psi}}{\partial\boldsymbol{\zeta}} - \vartheta\frac{\partial^2\hat{\psi}}{\partial\vartheta\partial\boldsymbol{\zeta}}\right)\cdot\mathbf{Z}\frac{1}{\boldsymbol{\tau}:\mathbf{P}}, \tag{13}$$

λ denotes the generalized force conjugates to the internal state variable ξ and is determined by the relation

$$\lambda = -\rho\left(\frac{\partial\hat{\psi}}{\partial\xi} - \vartheta\frac{\partial^2\hat{\psi}}{\partial\vartheta\partial\xi}\right). \tag{14}$$

To make possible numerical investigation of the three-dimensional dynamic adiabatic deformations of a body for different ranges of strain rate we introduce some simplifications of the constitutive model.

(i) By analogy with the infinitesimal theory of elasticity we postulate linear elastic properties of the material, i.e.

$$(\mathcal{L}^e)^{abcd} = G\left(g^{ac}g^{db} + g^{cb}g^{da}\right) + \left(K - \frac{2}{3}G\right)g^{ab}g^{cd} + \tau^{bd}g^{ac}, \tag{15}$$

where G and K denote the shear and bulk modulus, respectively.

(ii) It is assumed that

$$\mathcal{L}^{e^{-1}} : \mathcal{L}^{th} = \theta\mathbf{g}, \tag{16}$$

where θ is the thermal expansion coefficient in the elastic range.

It is noteworthy that the influence of the evolution of microvoids on elastic properties of the material is not taken into account.

2.3. Intrinsic micro-damage process

The intrinsic micro damage process consists of nucleation, growth and coalescence of microvoids (microcracks). Recent experimental observation results (cf. Shockey et al. (1985)) have shown that coalescence mechanism can be treated as nucleation and growth process on a smaller scale. This conjecture simplifies very much the description of the intrinsic micro-damage process by taking account only of the nucleation and growth mechanisms. Then the porosity or the void volume fraction parameter ξ can be determined by $\dot{\xi} = \left(\dot{\xi}\right)_{nucl} + \left(\dot{\xi}\right)_{grow}$.

Physical considerations (cf. Curran et al. (1987) and Perzyna (1986)) have shown that the nucleation of microvoids in dynamic loading processes which are characterized by very short time duration is governed by the thermally-activated mechanism. Based on this heuristic suggestion we postulate for rate dependent plastic flow

$$\left(\dot{\xi}\right)_{nucl} = \frac{1}{T_m} h^*(\xi,\vartheta)\left[\exp\frac{m^*(\vartheta)\mid \sigma - \sigma_N(\xi,\vartheta,\in^p)\mid}{k\vartheta} - 1\right], \tag{17}$$

where k denotes the Boltzmann constant, $h^*(\xi,\vartheta)$ represents a void nucleation material function which is introduced to take account of the effect of microvoid interaction, $m^*(\vartheta)$ is a temperature dependent coefficient, $\sigma = (1/3)J_1$ is the mean stress and $\sigma_N(\xi,\vartheta,\in^p)$ is the porosity, temperature and equivalent plastic strain dependent threshold stress for microvoid nucleation.

For the growth mechanism we postulate (cf. Johnson (1981), Perzyna (1986), Perzyna and Drabik (1989, 1995) and Nemes et al. (1990))

$$\left(\dot{\xi}\right)_{grow} = \frac{1}{T_m}\frac{g^*(\xi,\vartheta)}{\sqrt{\kappa}}\left[\sigma - \sigma_{eq}(\xi,\vartheta,\in^p)\right], \tag{18}$$

where $T_m\sqrt{\kappa}$ denotes the dynamic viscosity of a material, $g^*(\xi,\vartheta)$ represents a void growth material function and takes account for void interaction and $\sigma_{eq}(\xi,\vartheta,\in^p)$ is the porosity, temperature and equivalent plastic strain dependent void growth threshold mean stress.

Equations (17) and (18) determine the evolution function Ξ postulated in Eq. $(6)_3$.

2.4. Cooperative phenomena (thermomechanical coupling and micro–damage mechanism)

For adiabatic process ($\mathbf{q} = 0$) Eq. $(11)_2$ takes the form

$$\rho c_p \dot{\vartheta} = \vartheta\frac{\rho}{\rho_{Ref}}\frac{\partial \boldsymbol{\tau}}{\partial \vartheta} : \mathbf{d} + \chi\boldsymbol{\tau} : \mathbf{d}^p + \lambda\dot{\xi}. \tag{19}$$

The first term on the right–hand side of Eq. (19) has not a dissipative nature and is of the second order when compared with the internal dissipation terms. Its contribution to internal heating is small. This may suggest that in some considerations it can be neglected. However this nondissipative term will have important influence on the propagation and interaction of stress waves in inelastic damaged solids.

The second term on the right–hand side of Eq. (19) represents the rate of internal dissipation due to plastic flow process while the last term gives the contribution to the rate of internal dissipation generated by the intrinsic micro–damage mechanism.

When the nondissipative term is neglected then Eq. (19) takes the form

$$\rho c_p \dot{\vartheta} = \chi\boldsymbol{\tau} : \mathbf{d}^p + \lambda\dot{\xi}. \tag{20}$$

From Eq. (20) we can compute the irreversibility coefficient χ. It gives

$$\chi = \frac{\rho c_p \dot{\vartheta} - \lambda\dot{\xi}}{\boldsymbol{\tau} : \mathbf{d}^p}. \tag{21}$$

For $\lambda = 0$, i.e. when the influence of the intrinsic micro–damage mechanism is not taken into consideration, Eq. (21) takes the form

$$\chi = \frac{\rho c_p \dot{\vartheta}}{\boldsymbol{\tau} : \mathbf{d}^p}. \tag{22}$$

For this particular case the irreversibility coefficient χ has a simple interpretation as the heat rate conversion to plastic work rate fraction. However Eq. (21) shows that the remaining work rate is attributed to the energy rate lost for micro–damage effects.

When modelling thermomechanical behaviour of materials χ is usually assumed to be a constant in the range $0.85 - 0.95$ (a practice that dates back to the work of Taylor and Quinney (1934)).

Recent experimental investigations performed by Mason, Rosakis and Ravichandran (1994) by using a Kolsky (split Hopkinson) pressure bar and a high-speed infrared detector array have clearly shown that this assumption may not be correct for all metals.

The reason for this considerable discrepancy is clearly visible from Eq. (21). The rate of the lost energy $\lambda\dot{\xi}$ implied by the intrinsic micro–damage mechanism is responsible for the decreasing of χ.

Mason, Rosakis and Ravichandran (1994) observed that the irreversibility coefficient χ depends of strain and strain rate in a range of metals. Their experimental observations have significant implications in the study of the conditions preceding and governing adiabatic shear band formation and shear band growth as well as on the establishment of a criterion governing dynamic fracture mode selection in rate sensitive materials.

2.5. Fracture criterion

We base the fracture criterion on the evolution of the porosity internal state variable.

Let us assume that for $\xi = \xi^F$ catastrophe takes place (cf. Perzyna (1984)), that is

$$\kappa = \hat{\kappa}(\in^p, \vartheta, \xi) \mid_{\xi=\xi^F} = 0. \tag{23}$$

It means that for $\xi = \xi^F$ the material looses its stress carrying capacity. The condition (23) describes the main feature observed experimentally that the load tends to zero at the fracture point. It is noteworthy that the isotropic hardening–softening material function $\hat{\kappa}$ proposed in particular form (9) satisfies the fracture criterion (23).

2.6. Adiabatic inelastic flow process

The evolution problem (1) describes an adiabatic inelastic flow process provided

$$\boldsymbol{\varphi} = \begin{bmatrix} \phi \\ \boldsymbol{v} \\ \rho_M \\ \boldsymbol{\tau} \\ \xi \\ \vartheta \end{bmatrix}, \quad \mathbf{f} = \begin{bmatrix} \boldsymbol{v} \\ 0 \\ \frac{\rho_M}{1-\xi}\Xi \\ \left[\left(\frac{\chi}{\rho_M(1-\xi)c_p}\mathcal{L}^{th}\boldsymbol{\tau} + \mathcal{L}^e + \mathbf{g}\boldsymbol{\tau} + \boldsymbol{\tau}\mathbf{g}\right) : \mathbf{P}\right]\frac{1}{T_m}\langle(f-\kappa)^m\rangle - \frac{\lambda\Xi}{\rho_M(1-\xi)c_p}\mathcal{L}^{th} \\ \Xi \\ \frac{\chi}{\rho_M(1-\xi)c_p}\boldsymbol{\tau} : \mathbf{P}\frac{1}{T_m}\langle(f-\kappa)^m\rangle + \frac{\lambda}{\rho_M(1-\xi)c_p}\Xi \end{bmatrix},$$

$$\mathcal{A} = \begin{bmatrix} 0 & 0 & 0 & 0 & 0 & 0 \\ 0 & 0 & \frac{1}{\rho_M^0(1-\xi_0)}\frac{\boldsymbol{\tau}}{\rho_M}\mathrm{grad} & \frac{\mathrm{div}}{\rho_M^0(1-\xi_0)} & \frac{\boldsymbol{\tau}\,\mathrm{grad}}{\rho_M^0(1-\xi_0)(1-\xi)} & 0 \\ 0 & -\rho_M\mathrm{div} & 0 & 0 & 0 & 0 \\ 0 & \mathbb{E} : \mathrm{sym}\frac{\partial}{\partial\mathbf{x}} + 2\mathrm{sym}(\boldsymbol{\tau} : \frac{\partial}{\partial\mathbf{x}}) & 0 & 0 & 0 & 0 \\ 0 & 0 & 0 & 0 & 0 & 0 \\ 0 & \frac{\vartheta}{c_p\rho_{Ref}}\frac{\partial\boldsymbol{\tau}}{\partial\vartheta} : \mathrm{sym}\frac{\partial}{\partial\mathbf{x}} & 0 & 0 & 0 & 0 \end{bmatrix}. \tag{24}$$

It is noteworthy that the spatial operator $\mathcal{A}$ has the same form as in elastodynamics of damaged material while all dissipative effects generated by viscoplastic flow phenomena influence the process through the nonlinear function $\mathbf{f}$.

3. NUMERICAL SOLUTION OF THE EVOLUTION PROBLEM

3.1. Well–posedness of the evolution problem

The homogeneous evolution problem (i.e. for $\mathbf{f} \equiv 0$) is called well posed (in the sense of Hadamard) if it has the following properties:

(i) The strict solutions are uniquely determined by their initial elements;

(ii) The set Y of all initial elements of strict solutions is dense in the Banach space E;

(iii) For any finite interval $[0, t_0]$, $t_0 \in [0, t_f]$ there is a constant $K = K(t_0)$ such that every strict solution satisfies the inequality

$$\|\boldsymbol{\varphi}(t)\| \leq K\|\boldsymbol{\varphi}^0\|, \quad \text{for} \quad 0 \leq t \leq t_0. \tag{25}$$

The inhomogeneous evolution problem (1) will be called well posed if it has a unique solution for all reasonable choices of $\boldsymbol{\varphi}^0$ and $\mathbf{f}(t, \boldsymbol{\varphi})$ and if the solution depends continuously, in some sense, on those choices.

It is possible to show (cf. Richtmyer (1978)) that strict solutions exists for sets of $\boldsymbol{\varphi}^0$ and $\mathbf{f}(\cdot)$ that are dense in E and E_1 (a new Banach space), respectively.

Let us consider first undamaged material (i.e. we assume $\Xi \equiv 0$). For this case the spatial operator $\mathcal{A}$ has strictly the form as in elastodynamics. Then, for the proof of the well–posedness of the homogeneous evolution problem (for $\mathbf{f} \equiv 0$) we can use the results obtained in elastodynamics. Next, we can extent the results to elasto–viscoplasticity by considering the nonhomogeneous evolution problem (when $\mathbf{f} \neq 0$) and by superposing suitable smoothness assertions for the nonlinear function $\mathbf{f}$ (cf. Ionescu and Sofonea (1993) and Perzyna (1994, 1995)).

3.2. Discretisation in space and time

We must approximate (1) twice. First, when E is infinite dimensional, we must replace $\mathcal{A}$ by an operator $\mathcal{A}_h$ which operates in a finite dimensional space $V_h \subset \mathrm{E}$, where, in general, $h > 0$ represents a discretisation step in space, such that $\dim(V_h) \to \infty$ as $h \to 0$. Second, we must discretise in time, that is to say choose a sequence of moments t_n (for example $t_n = n\Delta t$, where Δt is time step) at which we shall calculate the approximate solution.

Let us introduce the following semi–discretised (discrete in space) problem.

$$\left.\begin{array}{l} \text{Find } \boldsymbol{\varphi}_h \in \mathcal{C}^0([0, t_0]; V_h) \text{ ($\mathcal{C}^0$ denotes the space of functions} \\ \text{continuous on } ([0, t_0], V_h)) \text{ satisfying} \\ \frac{d\boldsymbol{\varphi}_h(t)}{dt} = \mathcal{A}_h\boldsymbol{\varphi}_h(t) + \mathbf{f}_h(t), \\ \boldsymbol{\varphi}_h(0) = \boldsymbol{\varphi}_{0,h}. \end{array}\right\} \tag{26}$$

The operator $\mathcal{A}_h$ for the finite element method can be obtained by a variational formulation approach. The discrete equations are obtained by the Galerkin method at particular points in the domain.

Finally, we shall define a method allowing us to calculate $\varphi_h^n \in V_h$, an approximation to $\varphi_h(t_n)$ starting from φ_h^{n-1} (we limit ourselves to a two-level scheme). Then we can write

$$\varphi_h^{n+1} = C_h(\Delta t)\varphi_h^n + \Delta t \mathbf{f}_h^n, \qquad \varphi_h^0 = \varphi_{0,h} \tag{27}$$

where we introduce the operator $C_h(\Delta t) \in \mathcal{L}(V_h)$ ($\mathcal{L}$ is the set of continuous linear mapping of V_h with values in V_h) and where $\mathbf{f}_h^n$ approximates $\mathbf{f}_h(t_n)$.

We shall always assume that the evolution problem (1) is well posed and there exists a projection R_h of E into V_h such that

$$\lim_{h \to 0} | R_h\varphi - \varphi |_{\mathrm{E}} = 0 \qquad \forall \varphi \in \mathrm{E}. \tag{28}$$

3.3. Convergence, consistency and stability

The first fundamental question is that of the convergence, when h and Δt tend to zero, of the sequence $\{\varphi_h^n\}$, the solution (27), towards the function $\varphi(t)$, the solution of (1). Let us restrict our consideration, for the moment, to the case where $\mathbf{f}(t) \equiv 0$.

Definition 1. The scheme defined by (27) will be called convergent if the condition

$$\varphi_{0,h} \to \varphi^0 \quad \text{as} \quad h \to 0 \tag{29}$$

implies that

$$\varphi_h^n \to \varphi(t) \quad \text{as} \quad \Delta t \to 0, \quad n \to \infty \quad \text{with} \quad n\Delta t \to t \tag{30}$$

for all $t \in]0, t_0[$, $t_0 \in [0, t_f]$, where φ_h^n is defined by (27) and $\varphi(t)$ is the solution of (1). All this holds for arbitrary φ^0.

The study of the convergence of an approximation scheme involves two fundamental properties of the scheme, consistency and stability.

Definition 2. The scheme defined by (27) is called stable, if there exists a constant $K \geq 1$ independent of h and Δt such that

$$\|(C_h(\Delta t))^n R_h\|_{\mathcal{L}(\mathrm{E})} \leq K \quad \forall n, \Delta t \quad \text{satisfying} \quad n\Delta t \leq t_0. \tag{31}$$

In the Definition 1 and 2 there occur two parameters h and Δt. It may be that the scheme is not stable (or convergent) unless Δt and h satisfy supplementary hypotheses of the type $\Delta t / h^\alpha \leq$ constant, $\alpha < 0$, in which case we call the scheme **conditionally stable**. If the scheme is stable for arbitrary h and Δt we say that it is **unconditionally stable**.

Definition 3. The scheme defined by (27) will be called consistent with equation (1) if there exists a subspace $Y \subset \mathrm{E}$ dense in E, such that for every $\varphi(t)$ which is a solution of (1) with $\varphi^0 \subset Y$ (and $\mathbf{f} \equiv 0$) we have

$$\lim_{h\to 0,\Delta t\to 0} \left| \frac{C_h(\Delta t)R_h\varphi(t)-\varphi(t)}{\Delta t} - \mathcal{A}\varphi(t) \right|_{\mathrm{E}} = 0. \tag{32}$$

We can now state the Lax equivalence theorem (cf. Richtmyer and Morton (1967), Strang and Fix (1973) and Dautray and Lions (1993)).

Theorem. Suppose that the evolution problem (1) is well-posed for $t \in [0, t_0]$ and that it is approximated by the scheme (27), which we assume consistent. Then the scheme is convergent if and only if it is stable.

The proof of the Lax equivalence theorem can be found in Dautray and Lions (1993).

4. EXAMPLES OF THE EVOLUTION PROBLEM

4.1. Adiabatic dynamic process for thin steel tube

Cho, Chi and Duffy (1988) tested the specimens machined in the shape of thin-walled tubes with integral hexagonal flanges for gripping. Torsional loading at high strain rates was applied in a torsional Kolsky bar (split-Hopkinson bar).

We idealize the initial-boundary value problem (cf. Lodygowski and Perzyna (1997)) by assuming the specimen in the shape of thin-walled tube.

The initial conditions are taken in the form

$$\begin{aligned} &\phi(\mathbf{x},0)=0, \quad \boldsymbol{v}(\mathbf{x},0)=0, \quad \rho(\mathbf{x},0)=\rho_{Ref}=\rho_M^0(1-\xi_0), \\ &\boldsymbol{\tau}(\mathbf{x},0)=0, \quad \xi(\mathbf{x},0)=\xi_0, \quad \vartheta(\mathbf{x},0)=\vartheta_0=\text{constant in } \mathcal{B}. \end{aligned} \tag{33}$$

That is, the body is initial at rest, is stress free at a uniform temperature ϑ_0 and the initial porosity at every material point is ξ_0.

For the boundary conditions, we assume

$$\begin{aligned} \boldsymbol{\tau}\cdot\mathbf{n} &= 0 \text{ on the inner and outer surfaces of the tube,} \\ \mathbf{q}\cdot\mathbf{n} &= 0 \implies \operatorname{grad}\vartheta\cdot\mathbf{n}=0 \text{ on all bounding surfaces,} \\ \boldsymbol{v}(x_1,x_2,0,t) &= 0, \quad \boldsymbol{v}(x_1,x_2,\mathrm{L},t) = \omega^*(t)\left(x_1^2+x_2^2\right)^{\frac{1}{2}}\mathbf{n}^*, \end{aligned} \tag{34}$$

where $\mathbf{n}$ is a unit outward normal to the respective surfaces, $\omega^*(t)$ is the angular speed of the end surface $x_3 = \mathrm{L}$ of the tube, and $\mathbf{n}^*$ is a unit vector tangent to the surface $x_3 = \mathrm{L}$. It is assumed that

$$\omega^*(t) = \begin{cases} \omega_0^* t/20, & 0 \le t \le 20\mu\mathrm{s}, \\ \omega_0^*, & t > 20\mu\mathrm{s}. \end{cases} \tag{35}$$

The rise time of 20 μs is typical for torsional tests done in a split Hopkinson bar (cf. Batra and Zhang (1993)).

The following values for various material parameters are assumed (AISI 1018 cold rolled steel)

$$\begin{array}{llll} \rho_M = 7860 \text{ kg/m}^3, & c_p = 460 \text{ J/kg}^0\text{C}, & G = 80 \text{ GPa}, & \\ K = 210 \text{ GPa}, & \kappa_0 = 237 \text{ MPa}, & \kappa_1 = 1.2\cdot\kappa_0, & \vartheta_0 = 293 \text{ K}, \\ h = const = 5.15, & n = const = 1.25, & m = 5 \text{ (for } \vartheta = 0), & m = 4.7 \text{ (for } \vartheta = 353 \text{ K}). \end{array}$$

Two parameters, namely the relaxation time T_m and the irreversibility coefficient χ, have been changed in the range as follows

$$T_m = 2.5 \cdot 10^{-2} - 2.5 \cdot 10^{-8} \text{ s for } 272 < \vartheta \leq 353 \text{ K},$$
$$T_m = 1.0 \cdot 10^{-2} - 1.0 \cdot 10^{-8} \text{ s for } \vartheta > 353 \text{ K},$$
$$\chi = 0.6 - 0.9.$$

The tube has been twisted at nominal shear strain rates ranging $10^3 - 10^4$ s^{-1}.

For the particular example considered it has been assumed $\xi = 0$ (no influence of the micro-damage mechanism) and $\omega_0^* = 253$ s^{-1}.

4.2. Adiabatic dynamic processes for thin steel plate

We idealized the initial-boundary value problem investigated by Chakrabarti and Spretnak (1975) by assuming the velocity driven adiabatic process for a thin steel plate ($12.7 \times 25.4 \times 0.33$ mm). The material of a plate is AISI 4340 steel. The following values for material parameters are assumed: $\sigma_M = 7850$ kg/m^3, E (Young's modulus) = 200 MPa, the yield stress is 1634 kPa at reference temperature $\vartheta_0 = 293$ K, 1310 kPa at $\vartheta = 343$ K, 1006 kPa at $\vartheta = 482$ K, $c_p = 4.6$ kJ/kg K, $\xi_0 = 0.04$, $\xi^F = 0.3$, $m = 1$.

The relaxation time T_m and the irreversibility coefficient χ are assumed to change in the ranges as follows: $T_m = 2.5 \cdot 10^{-2} - 2.5 \cdot 10^{-6}$ s, $\chi = 0.6 - 0.9$.

The symmetry of the boundary conditions is strictly keeping, to one edge of the plate constant velocity is applied $v = 10$ m/s and the other edge is motionless ($v = 0$).

5. NUMERICAL COMPUTATION RESULTS

5.1. Thin steel tube

The aforestated initial-boundary value problem has been solved by using the wide spectrum of ABAQUS possibilities (cf. Lodygowski et al. (1994) and Lodygowski and Perzyna (1996)).

The half of the specimen (the thin walled cylinder) is modelled via both multilayer shell and three-dimensional brick elements with 4 layers in radial direction. In circumferential direction the model consists of 24 segments with 10 elements on the depth.

To avoid the reflection of waves and to model the influence of the rest of the specimen it has been postulated that the additional spring and mass elements are taken into consideration.

In Figs. 1–4 the evolution of the plastic equivalent strain in different laminates for various pairs of the relaxation time T_m and the irreversibility coefficient χ has been visualized.

5.2. Thin steel plate

For adiabatic dynamic process the specimen (a thin sheet) is modelled via 800 (20×40) shell elements. Dynamic explicit method is used (more than 120 000 inc.), cf. Glema et al. (1997).

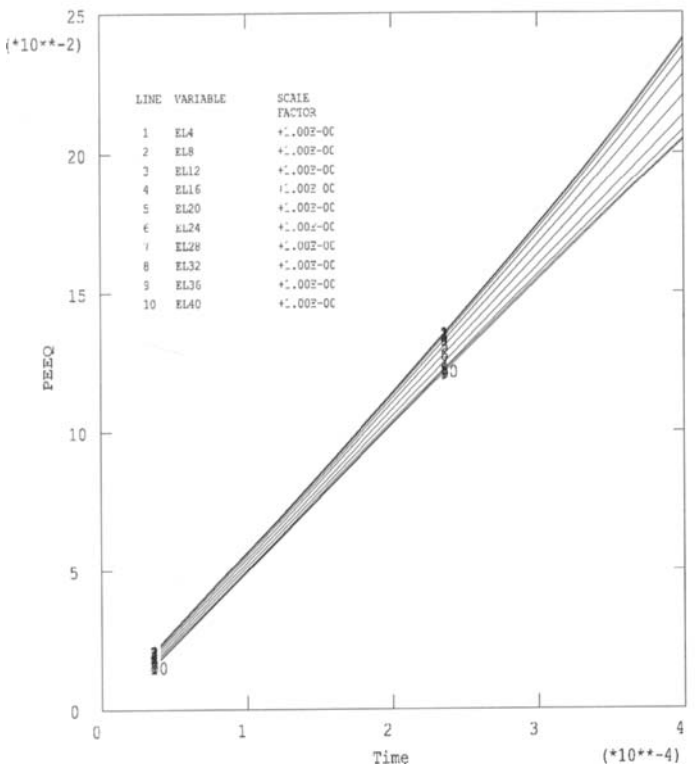

Figure 1. Evolution of the plastic equivalent strain in different laminates, for $T_m = 2.5 \cdot 10^{-2}$ s and $\chi = 0.9$.

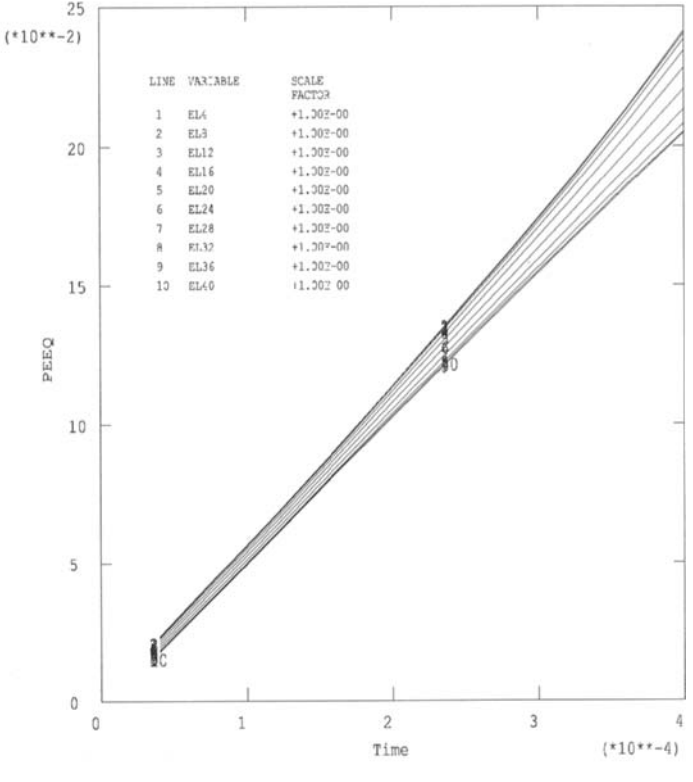

Figure 2. Evolution of the plastic equivalent strain in different laminates, for $T_m = 2.5 \cdot 10^{-2}$ s and $\chi = 0.6$.

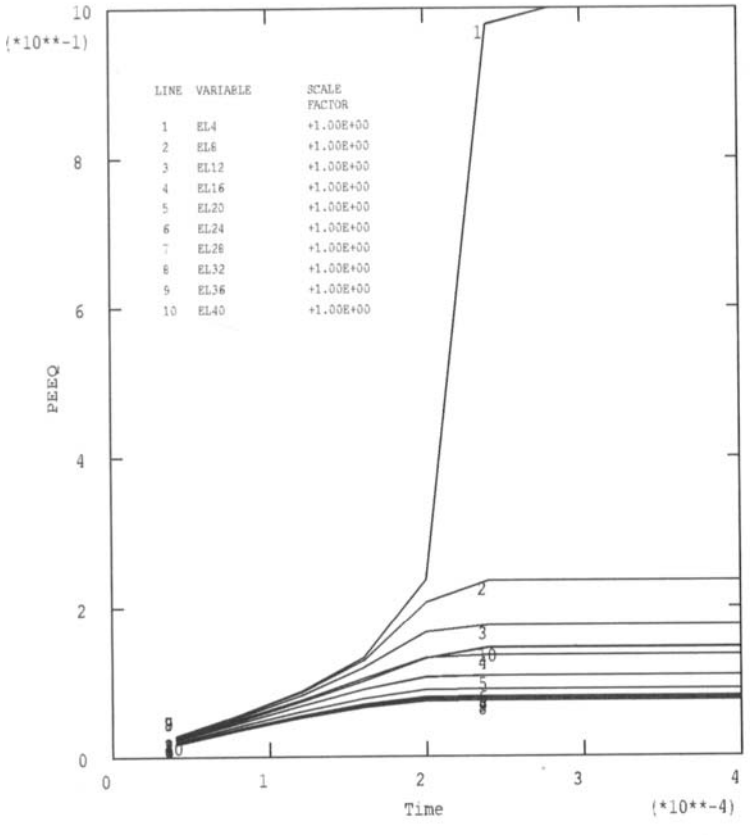

Figure 3. Evolution of the plastic equivalent strain in different laminates, for $T_m = 2.5 \cdot 10^{-6}$ s and $\chi = 0.9$.

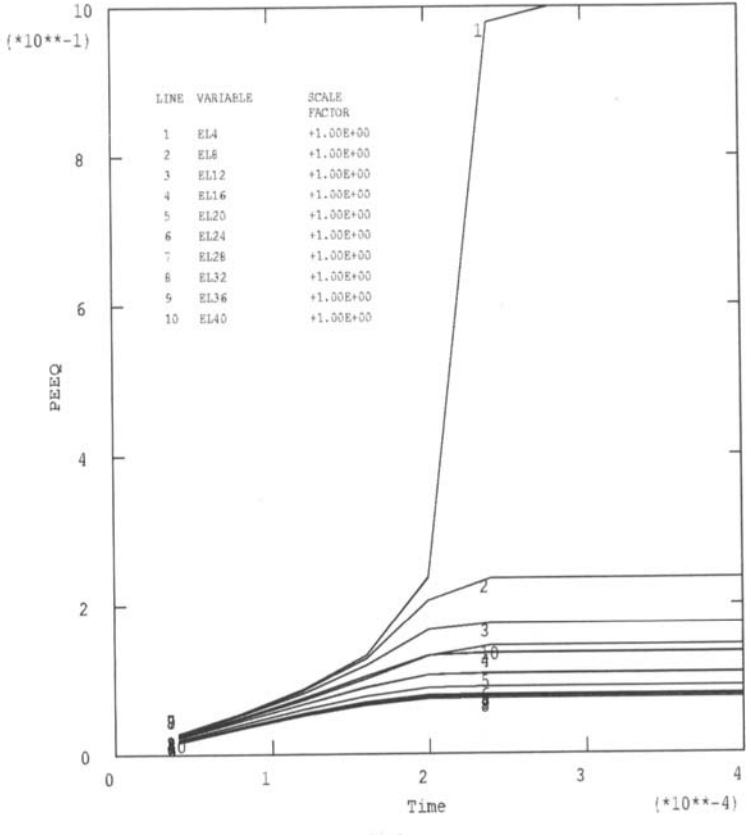

Figure 4. Evolution of the plastic equivalent strain in different laminates, for $T_m = 2.5 \cdot 10^{-6}$ s and $\chi = 0.6$.

In Fig. 5 the deformed meshes for various relaxation time T_m have been presented. The distribution of the equivalent plastic deformation along the longer edge of the plate is shown in Fig. 6. The modes of fracture for different relaxation time T_m have been visualized in Fig. 7.

6. DISCUSSION OF THE INFLUENCE OF CONSTITUTIVE PARAMETERS

From the results obtained for adiabatic processes for thin steel tube and for thin steel plate it has been proved that the width of the shear band region and the temperature rise vary very much with the relaxation time assumed. It has been also observed that the distribution of the equivalent plastic deformation and the modes of fracture along the shear band region are very much affected by the relaxation time. It has been clearly shown that the wave propagation and interaction and the deformation process and as the result the localization of plastic deformation along the shear band are very much depended on the assumed value for the relaxation time. Since the relaxation time can be viewed either as a regularization parameter or as a microstructural parameter to be determined basing on physical foundations and experimental observations hence the identification of this parameter has a great importance for proper constitutive modelling for localization and fracture phenomena. It has been found that localization anf fracture phenomena are not so much affected by the irreversibility coefficient.

7. FINAL COMMENTS

It has been proved that the localization of plastic deformation phenomenon in an elastic viscoplastic solid body can arise only as the result of the reflection and interaction of waves. It has different character then that which occurs in a rate independent elasto-plastic solid body (cf. Perzyna (1994, 1995)). Rate dependency (viscosity) allows the spatial difference operator in the governing equations to retain its ellipticity and the initial value problem is well-posed. Viscosity introduces implicitly a length-scale parameter into the dynamical initial-boundary value problem and hence it implies that the localization region is diffused when compared with an inviscid plastic material. The introduced length-scale is proportional to the relaxation time. The main feature of the developed theoretical model is the possibility of the investigation of the entire process considered. Under dynamic loading conditions the propagation of deformation in the specimen considered establishes heterogeneous distributions of stress and strain, causing the location of the instability regions in the form of shear bands. These regions vary with the imposed strain rate and are affected by the assumed value of the relaxation time (or viscosity parameter). Thus the evolution of the localized shear band region until occurrence of fracture has been simulated. It has been also proved that the insensitivity of the results to mesh refinement is apparent whether material softening in present or not.

Figure 5. Deformed meshes for various relaxation times A) $T_m = 2.5 \cdot 10^{-2}$; B) $T_m = 2.5 \cdot 10^{-3}$; C) $T_m = 2.5 \cdot 10^{-4}$; D) $T_m = 2.5 \cdot 10^{-5}$ s; E) $T_m = 2.5 \cdot 10^{-6}$ s.

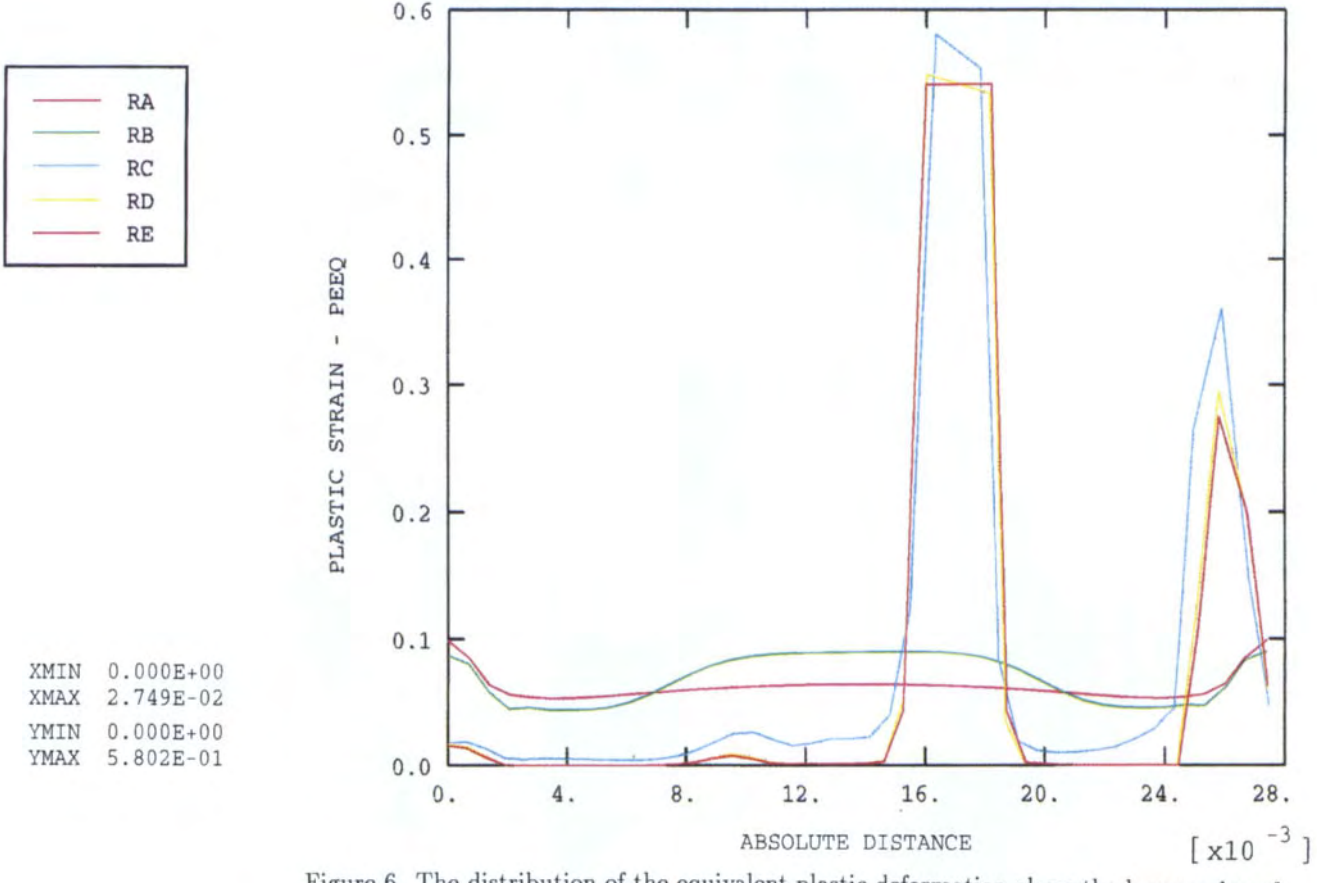

Figure 6. The distribution of the equivalent plastic deformation along the longer edge of the plate for various relaxation times A) $T_m = 2.5 \cdot 10^{-2}$; B) $T_m = 2.5 \cdot 10^{-3}$; C) $T_m = 2.5 \cdot 10^{-4}$; D) $T_m = 2.5 \cdot 10^{-5}$ s; E) $T_m = 2.5 \cdot 10^{-6}$ s.

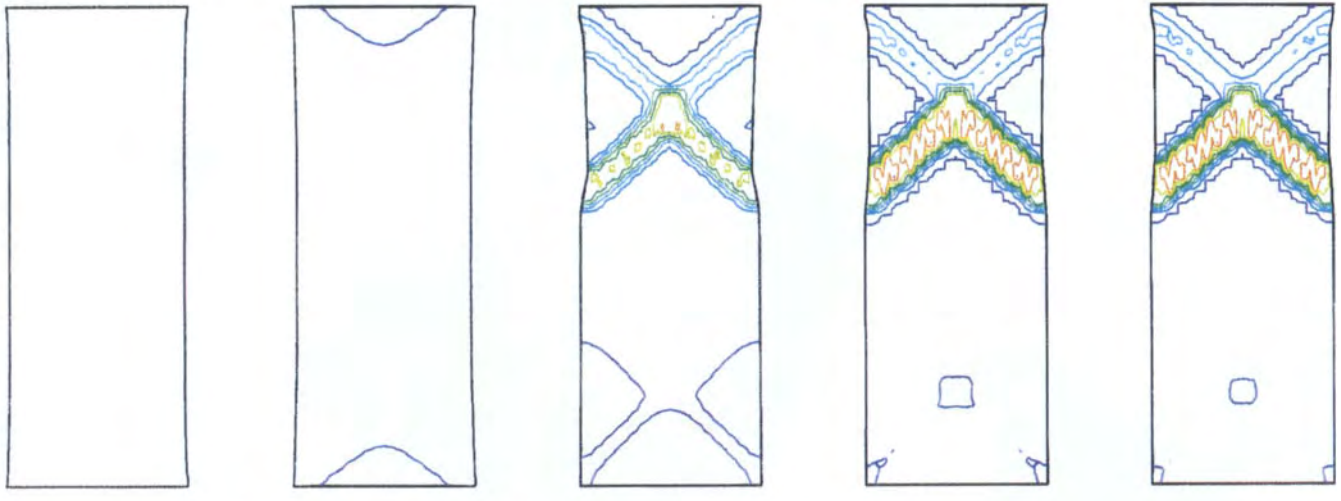

Figure 7. The modes of fracture for various relaxation times A) $T_m = 2.5 \cdot 10^{-2}$; B) $T_m = 2.5 \cdot 10^{-3}$; C) $T_m = 2.5 \cdot 10^{-4}$; D) $T_m = 2.5 \cdot 10^{-5}$ s; E) $T_m = 2.5 \cdot 10^{-6}$ s.

ACKNOWLEDGMENT

The paper has been partly prepared within the research programme sponsored by the Committee of Scientific Research under Grant 7 T07 A013 10.

REFERENCES

1. R.C. Batra and X. Zhang, On the propagation of a shear band in a steel tube, *J. Engng. Materials and Technology*, 116 (1994) 155–161.
2. A.K. Chakrabarti and J.W. Spretnak, Instability of plastic flow in the direction of pure shear, *Metallurgical Transactions*, 6A (1975) 733–747.
3. K. Cho, Y.C. Chi and J. Duffy, Microscopic observations of adiabatic shear bands in three different steels, Brown University Report, 1988.
4. D.R. Curran, L. Seaman and D.A. Shockey, Dynamic failure of solids, *Physics Reports*, 147 (1987) 253–388.
5. R. Dautray and J.L. Lions, Mathematical Analysis and Numerical Methods for Science and Technology, Vol. 6. Evolution Problems II, Springer, Berlin, 1993.
6. M.K. Duszek–Perzyna and P. Perzyna, Analysis of the influence of different effects on criteria for adiabatic shear band localization in inelastic solids, in.: Material Instabilities: Theory and Applications, AMD–Vol. 183/MD–Vol.50, ASME, pp.59–85, 1994.
7. J.H. Giovanola, Adiabatic shear banding under pure shear loading, *Mechanics of Materials*, 7 (1988) 59–87.
8. A. Glema, R. Łodygowski and P. Perzyna, Effects of microdamage in plastic strain localization, XIII Polish Conference on Computer Methods in Mechanics, Poznań, Poland, 5–8 May, 1997, Proc., pp. 451–458, 1997.
9. K.A. Hartley, J. Duffy and R.H. Hawley, Measurement of the temperature profile during shear band formulation in steels deforming at high strain rates, *J. Mech. Phys. Solids*, 35 (1987) 283–301.
10. I.R. Ionescu and M. Sofonea, Functional and Numerical Methods in Viscoplasticity, Oxford, 1993.
11. J.N. Johnson, Dynamic fracture and spallation in ductile solids, *J. Appl. Phys.*, 52 (1981) 2812–2825.
12. T. Łodygowski, On avoiding of spurious mesh sensitivity in numerical analysis of plastic strain localization, *Computer Assisted Mechanics and Engineering Sciences*, 2 (1995) 231–248.
13. T. Łodygowski, M. Lengnick, P. Perzyna and E. Stein, Viscoplastic numerical analysis of dynamic plastic strain localization for a ductile material, *Archives of Mechanics*, 46 (1994) 1–25.
14. T. Łodygowski and P. Perzyna, Numerical modelling of localized fracture of inelastic solids in dynamic loading processes, *Int. J. Num. Meth. Engng.*, (1996) (in print).
15. T. Łodygowski and P. Perzyna, Localized fracture of inelastic polycrystalline solids under dynamic loading processes, *International J. Damage Mechanics*, (1997) (in print).
16. A. Marchand, K. Cho and J. Duffy, The formation of adiabatic shear bands in an AISI 1018 cold–rolled steel, Brown University Report, 1988.
17. A. Marchand and J. Duffy, An experimental study of the formation process of adiabatic shear bands in a structural steel, *J. Mech. Phys. Solids*, 36 (1988) 251–283.
18. J.E. Marsden and T.J.R. Hughes, Mathematical Foundations of Elasticity, Prentice–Hall, Englewood Cliffs, New York, 1983.

19. J.J. Mason, A.J. Rosakis and R. Ravichandran, On the strain and strain rate dependence of the fraction of plastic work converted to heat: an experimental study using high speed infrared detectors and the Kolsky bar, *Mechanics of Materials*, 17 (1994) 135–145.
20. J.A. Nemes, J. Eftis and P.W. Randles, Viscoplastic constitutive modelling of high strain-rate deformation, material damage and spall fracture, *J. Appl. mech.*, 57 (1990) 282–291.
21. P. Perzyna, The constitutive equations for rate sensitive plastic materials, *Quart. Appl. Math.*, 20 (1963) 321–332.
22. P. Perzyna, Thermodynamic theory of viscoplasticity, *Advances in Applied Mechanics*, 11 (1971) 313–354.
23. P. Perzyna, Constitutive modelling of dissipative solids for postcritical behaviour and fracture, *ASME J. Eng. Materials and Technology*, 106 (1984) 410-419.
24. P. Perzyna, Internal state variable description of dynamic fracture of ductile solids, *Int. J. Solids Structures* 22 (1986) 797-818.
25. P. Perzyna, Adiabatic shear band localization fracture of solids in dynamic loading processes, in.: Proc. of Int. Conference on Mechanical and Physical Behaviour of Materials under Dynamic Loading, Oxford, September 26–30, 1994; (ed. J.Harding), Les Editions de Physique Le Ulis, pp. 441-446, 1994.
26. P. Perzyna, Instability phenomena and adiabatic shear band localization in thermoplastic flow processes, *Acta Mechanica*, 106 (1994) 173–205.
27. P. Perzyna, Interactions of elastic–viscoplastic waves and localization phenomena in solids, in.: IUTAM Symposium on Nonlinear Waves in Solids, August 15–20, 1993, Victoria, Canada; (eds. J.L. Wegner and F.R. Norwood), ASME, pp. 114 121, 1995.
28. P. Perzyna and A. Drabik, Description of micro damage process by porosity parameter for nonlinear viscoplasticity, *Arch. Mechanics*, 41 (1989) 895–908.
29. P. Perzyna and A. Drabik, Micro–damage mechanism in adiabatic processes, *Int. J. Plasticity*, (1997) (submitted for publication).
30. P. Perzyna and M.K. Duszek Perzyna, Phenomenological modelling of adiabatic shear band localization fracture of solids in dynamic loading processes, in.: Localized Damage III; Computer Aided Assessment and Control, (eds. M.H. Aliabadi, A. Carpinteri, S.Kalisky, D.J.Cartwright), Computational Mechanics Publications., Southampton, pp. 579–588, 1994.
31. R.D. Richtmyer, Principles of Advance Mathematical Physics, Vol. I, Springer, New York, 1978.
32. R.D. Richtmyer and K.W. Morton, Difference Methods for Initial–Value Problems, John Wiley, New York, 1967.
33. S. Shima and M. Oyane, Plasticity for porous solids, *Int. J. Mech. Sci.*, 18 (1976) 285 291.
34. D.A. Shockey, L. Seaman and D.R. Curran, The microstatistical fracture mechanics approach to dynamic fracture problem, *Int. J. Fracture*, 27 (1985) 145–157.
35. G. Strang and G.J. Fix, An Analysis of the Finite Element Method, Prentice–Hall, Englewood Cliffs, 1973.
36. G.I. Taylor and H. Quinney, The latent energy remaining in a metal after cold working, *Proc. R. Soc. Lond.*, A143 (1934) 307–326.
37. H.M. Zbib and J.S. Jurban, Dynamic shear banding: A three–dimensional analysis, *Int. J. Plasticity*, 8 (1992) 619-641.

Damage Mechanics in Engineering Materials
G.Z. Voyiadjis, J.-W.W. Ju and J.-L. Chaboche (Editors)
© 1998 Elsevier Science B.V. All rights reserved.

Macromechanical Description of Micro–Shear Banding

R.B. Pęcherski

Institute of Fundamental Technological Research, Polish Academy of Sciences,
Świętokrzyska 21, 00–049 Warsaw, Poland, rpecher@ippt.gov.pl

Physical model of shear strain rate produced by active micro–shear bands in metals is formulated and mathematical idealization of micro–shear bands system by means of the theory of singular surface of order one is proposed. Extension of the known averaging procedure over the representative volume element traversed by the strong discontinuity surface of a vortex sheet type is presented. Constitutive description of small elastic and large plastic deformations within the framework of two surface plasticity model with internal yield surface connected with kinematic hardening anisotropy and the external surface approximating the generic micro–shear banding surface is proposed. The idea of the multiple potential surfaces forming a vertex on the smooth external surface is applied to display the connection with the geometric pattern of micro–shear bands.

1. INTRODUCTION

Metallographic observations reveal that in heavily deformed metals, in particular under highly constrained conditions which can appear in technological shaping operations, a multiscale hierarchy of shear banding occurs. Also at the advanced stage of ductile fracture, while void coalescence takes place, the behaviour of the ligaments between the voids is controlled by the formation of micro–shear bands. The new mechanism of deformation progressively replaces crystallographic multiple slip and twinning also at small strains, if they are preceded by the alteration of the scheme of straining. The change of deformation mode contributes to the development of strain induced anisotropy and modifies material properties. Therefore, macromechanical description of micro–shear banding is important for adequate constitutive modelling of inelastic strain and damage processes in metallic solids.

Theoretical analysis of large plastic deformations of metals accounting for active

micro–shear bands requires careful analysis of averaging procedures and proper setting of the resulting description within continuum theory of materials. Formulation of a complete theory based on the precise micro–to–macro transition remains an open question. An attempt to tackle the averaging procedure over the RVE with micro–shear bands was presented in [1], where the macroscopic measure of velocity gradient accounting for micro–shear banding was derived. The derivation is based on the physical model relating macroscopic shear strain rate with microstructural features of micro–shear bands, mathematical idealization of a system (cluster) of active micro–shear bands as propagating singular surface of order one, having properties of a vortex sheet, and the extension of the known averaging procedure applied to the representative volume element (RVE), which is traversed by the discontinuity surface. This makes possible to derive in a more rigorous manner the constitutive relations of plasticity accounting for macroscopic effects of micro–shear bands, which were obtained previously under certain simplifying assumptions, [2–4]. The double surface plasticity model, proposed in [4] and [5], has been extended and corroborated in this study. The internal yield surface is connected with nonlinear kinematic hardening model of Armstrong–Frederick type while the external surface corresponds with the saturation of the back stress effect. It appears that this phenomenon can be correlated with massive formation of micro–shear bands. Basing on the idea of the "extremal surface", presented by Hill [6], the concept of the generic micro–shear banding surface was introduced, which can be approximated by means of the class of the external limit surfaces. The model proposed shows that the contribution of active micro–shear bands with their characteristic geometric pattern, transmitted to the macroscopic level, produce the non–coaxiality between principal directions of stress and rate of plastic deformations. The relation for plastic spin appears in a natural way as an effect of this non–coaxiality. It transpires that depending on the contribution of the mechanisms involved in plastic flow, a fully active range, separated from the elastic range by a truly nonlinear zone called the partially active range, may exist. A new physical insight is given into the linear and nonlinear flow laws, in rates of deformation and stress, known in the theory of plasticity. The idea of multiple potential surfaces forming a vertex on the smooth external surface is applied to connect the fully active range and the partially active range with the definite geometric pattern of micro–shear bands. This leads to the new non–associated plastic flow rules accounting for the effects of micro–shear banding. The possibilities of certain simplifications and perspectives of the application of the theoretical model vis–à–vis the results presented recently in the literature are discussed.

2. PHYSICAL MOTIVATION

The term micro–shear band is understood as a long and very thin (of order 0.1 μm) sheet–like region of concentrated plastic shear, crossing grain boundaries without deviation and forming a definite pattern in relation to the principal directions of strain. The experimental information about mechanical behaviour and related structural features is reviewed, e.g. in [2–3] and [7–8], where the comprehensive list of references is given. The metallographic observations reveal the hierarchy of plastic slip processes: from coplanar dislocation groups moving collectively along active slip systems, through slip lammellae and slip bands to coarse slip bands, which may further transform into transgranular micro–shear bands and form clusters (packets) of micro–shear bands of the thickness of order $(10 \div 100)$ μm. The clusters of micro–shear bands, produced for instance in rolling, form the planar structures, which are usually inclined by the angle φ of about $\pm 35^{\circ}$ to the rolling plane and are orthogonal to the specimen lateral face. There can be, however, considerable deviations from this value within the 15° to 50° range. It is worthy to stress that the problem of specifying the angle is complicated by the difficulty of distinguishing the most recently formed micro–shear bands from those that were formed earlier and subsequently rotated with material towards the rolling plane, cf. [3] and [7–8]. This is related with the important observation, stressed in [8] and discussed also in [3], that a particular micro–shear band operates only once and develops rapidly to its full extent. The micro–shear bands, once formed, do not contribute further to the increase in plastic shear strain. Thus, it appears that the successive generations of active micro–shear bands competing with the mechanism of multiple crystallographic slip are responsible for plastic strain in metals.

The discussion of experimental observations concerning micro–shear bands geometry leads to the hypothesis, which says that it is typical of the clusters of active micro–shear bands that their planes are rotated relative to the respective planes of maximum shear stress by a certain angle β, which is usually of the order $(5 \div 15)^{\circ}$. This deviation angle plays essential rôle in the phenomenological theory of plastic deformations accounting for the effects of micro–shear banding and will be considered as a statistically averaged micro–shear bands orientation parameter, transmitting to the macroscopic level the geometry of their spatial pattern. The experimental observations show that the spatial pattern of micro–shear bands does not change for loading conditions that deviate within limits from the proportional loading path, i.e. the load increments are confined to a certain cone, in particular wedge–shaped region, the angle of which can be determined experimentally. For instance, according to Dybiec [9], in the polycrystalline Cu the

critical angle δ_c of this cone is of the order 22°. However, more drastic change of the loading scheme produces the change of the spatial orientation of micro–shear bands. This is supported by the results presented in [10], where after cross rolling two families of micro–shear bands inclined by about $\pm\ 35^\circ$ to the most recent rolling direction were observed. The existence of the deviation angle β is characteristic for the micro–shear bands produced in the deformation processes carried under nearly isothermal conditions. Thermal shear bands, i.e. the mode of plastic flow localization governed by a coupled thermoplastic mechanism, have also been studied by many authors. In particular, the so–called "adiabatic shear bands" are often reported to coincide with the trajectories of maximum shear stress, what results in $\beta = 0$, [11].

3. CONTINUUM MECHANICS DESCRIPTION OF MICRO–SHEAR BANDING

3.1. Macroscopic averaging in plasticity of metals

Problem of macroscopic averaging in plasticity of metals was discussed in [1], where also the bibliography of the earlier papers was given. The averaging procedure and micro–to–macro transition, studied within the framework of finite strain theory in [12] and [13] lead to the following relations for the macroscopic measures of the deformation gradient $\mathbf{F}$ and its rate $\dot{\mathbf{F}}$, which are averaged over the reference configuration V_o of the RVE and can be expressed by means of surface data

$$\mathbf{F} \equiv \{\mathbf{f}\} = \frac{1}{V_o}\int_{V_o} \mathrm{Grad}\chi_m \, dV_o = \frac{1}{V_o}\int_{\partial V_o} \mathbf{x} \otimes \boldsymbol{\nu}_o \, dA_o \,, \tag{1}$$

$$\dot{\mathbf{F}} \equiv \{\dot{\mathbf{f}}\} = \frac{1}{V_o}\int_{V_o} \mathrm{Grad}\dot{\chi}_m \, dV_o = \frac{1}{V_o}\int_{\partial V_o} \dot{\chi}_m \otimes \boldsymbol{\nu}_o \, dA_o \,, \tag{2}$$

where the symbol χ_m denotes the microscopic field of motion of the material point $\mathbf{X}_m$ in the reference configuration of the RVE into its current position $\mathbf{x}_m = \chi_m(\mathbf{X}_m, t)$, and the microscopic field of velocity $\mathbf{v}_m$ is determined in the current configuration

$$\mathbf{v}_m = \mathbf{v}_m(\mathbf{x}_m, t) = \mathbf{v}_m\big(\chi_m(\mathbf{X}_m, t), t\big) \equiv \dot{\chi}_m(\mathbf{X}_m, t) \,. \tag{3}$$

The presented averaging procedure is valid under the general assumption that the dominant mechanism of plastic deformation corresponds to multiple crystallographic slip. In such a case, the theory describing kinematics and constitutive structure of finite

elastic–plastic deformation of crystalline solids is well established and the transition between the microscopic and macroscopic levels is well understood, (cf. [1] for more detailed discussion and pertinent references). As it was stressed in [3] and [5], the situation changes when additional mechanism of the multiscale system of shear banding is taken into consideration.

3.2. Physical model of shear strain rate produced by active micro–shear bands

Consider a certain RVE containing the region of progressive shear banding, depicted schematically in Fig. 1a, where the traces of successive clusters of micro–shear bands are shown. The arrow points to the direction of the expansion of the region. According to the physical motivation discussed above, at this level of observation the clusters of active micro–shear bands can be considered as elementary carriers of plastic strain.

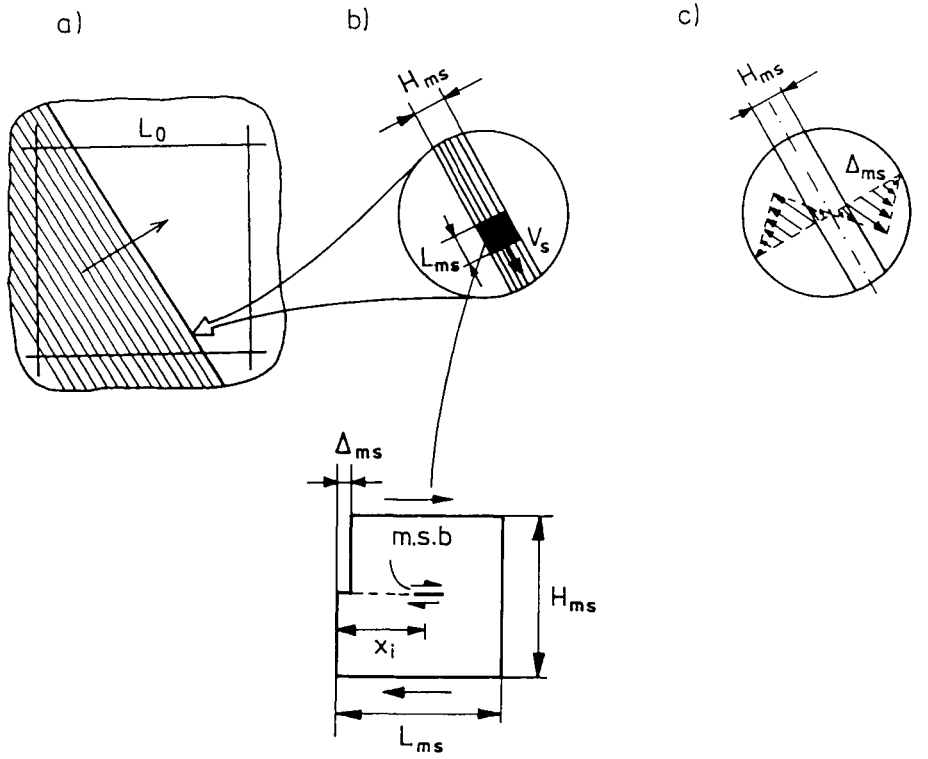

Figure 1. Schematic illustration of the multiscale system of shear banding.

In Fig. 1b, the "magnification" of the shear banding area is "zoomed in" and the related fundamental mechanism of plastic shear is illustrated. The cluster of micro–shear bands

has the active zone of the thickness H_{ms} and the width L_{ms}, in which the passage of active micro–shear bands results in the local perturbation, Δ_{ms}, of the microscopic displacement field, $\mathbf{u}_m = \mathbf{x}_m - \mathbf{X}_m$, moving with the speed V_s as a distortion wave. The possible profile of the local perturbation, Δ_{ms}, is depicted in Fig. 1c.

Consider a set of N_{ms} active micro–shear bands of similar orientation and produced within the time period $\Delta\tau$, which can be considered as an infinitesimal increment of "time–like parameter" t in the macroscopic description. As it is depicted schematically in Fig. 1b, such a system (cluster) of micro–shear bands produces the microscopic shear strain γ_{ms}, which is given by the following relation

$$\gamma_{ms} = \frac{\Delta_{ms}}{H_{ms}}, \qquad \Delta_{ms} = \frac{B_{ms} N_{ms}}{L_{ms}} \bar{x}_{ms}, \qquad \bar{x}_{ms} = \frac{1}{n} \sum_{i}^{N_{ms}} x_i, \tag{4}$$

where B_{ms} is the total displacement produced by a single micro–shear band and $\bar{x}_{ms}$ denotes the average distance that N_{ms} micro–shear bands have moved in the active zone. The width of the active zone L_{ms} can be determined by the length of the path that micro–shear bands passed with an average speed v_{ms} during the time period $\Delta\tau$. Assuming that the distance $\bar{x}_{ms}$ and the number of active micro–shear bands N_{ms} can change during the propagation of the active zone we have from (4)

$$\dot{\gamma}_{ms} = \frac{B_{ms}}{L_{ms} H_{ms}} \left(N_{ms} \dot{\bar{x}}_{ms} + \bar{x}_{ms} \dot{N}_{ms} \right), \tag{5}$$

where the dot denotes differentiation with respect to the "time–like parameter" t. Let us observe that under the simplifying assumption that the speed of micro–shear bands in the active zone of the cluster is approximately the same, the rate $\dot{\bar{x}}_{ms}$ can be identified with the speed v_{ms} of the head of a single micro–shear band, $\dot{\bar{x}}_{ms} \equiv v_{ms}$, (cf. [1], where the model of a single micro–shear band is studied). If the number of active micro–shear bands operating in the active zone of a single cluster can be assumed constant, (5) takes the form which is formally similar to the Orowan relation, (cf. [1])

$$\dot{\gamma}_{ms} = B_{ms} \rho_{ms} v_{ms}, \qquad \rho_{ms} = \frac{N_{ms}}{L_{ms} H_{ms}}, \tag{6}$$

where ρ_{ms} corresponds to the density of micro–shear bands operating within the active zone of the cluster. This is the number of active micro–shear bands that cut through a unit cross–sectional area.

3.2. System of active micro–shear bands as a surface of strong discontinuity

The foregoing discussion of physical nature of micro–shear banding process support the following hypothesis:

The passage of micro–shear bands within the active zone of the cluster, results in the perturbation of the microscopic displacement field Δ_{ms} *travelling with the speed* V_s, *which produces a discontinuity of the microscopic velocity field in the RVE it traverses. The progression of clusters of micro–shear bands can be idealized mathematically by means of a singular surface of order one propagating through the macro–element (RVE) of the continuum.*

The necessary mathematical formalism of the theory of propagating singular surfaces is given, e.g. in [14], [15] and [16]. The theory allows to identify the postulated discontinuity surface of the microscopic velocity field $\mathbf{v}_m$ in the RVE as a singular surface moving in the region V_o of the reference configuration of the body given by the equation $\Sigma(t) : G(\mathbf{X}_m, t) = 0$, where for each instant of "time–like parameter" $t \in I \subset R$, the surface $\Sigma(t) \subset V_o$ has the dual counterpart $S(t) \subset V$, in the spatial configuration of the RVE, $S(t) : g(\mathbf{x}_m, t) = 0$, i.e. the material points $\mathbf{X}_m \in \Sigma(t)$ occupy the places $\mathbf{x}_m \in S(t)$ at a given instant t. There exists the jump discontinuity of derivatives of the function of motion χ_m, i.e. of the microscopic velocity field $[\dot{\chi}_m] \neq \mathbf{0}$ and the deformation gradient $[\mathbf{f}] \neq \mathbf{0}$, which are assumed smooth in each point of $V_o \times I$ excluding the discontinuity surface

$$[\dot{\chi}_m] = \dot{\chi}_m^+ - \dot{\chi}_m^- \neq \mathbf{0}\,, \qquad [\mathbf{f}] = \mathbf{f}^+ - \mathbf{f}^- \neq \mathbf{0}\,. \tag{7}$$

According to [14] and [16] the considered surface of strong discontinuity of microscopic velocity field fulfills the properties of a vortex sheet with the jump discontinuity of the first derivatives of χ_m given by

$$[\mathbf{v}_m] = V_S\, \boldsymbol{s}\,, \qquad [\mathbf{f}] = -\frac{V_S}{U}\, \boldsymbol{s} \otimes \boldsymbol{n}\, \mathbf{f}\,, \quad \text{for} \quad U \neq 0\,, \tag{8}$$

where $\boldsymbol{s}$ and $\boldsymbol{n}$ are, respectively, the unit tangent and the unit normal vectors to the discontinuity surface $S(t)$ while U corresponds to the local speed of propagation of $S(t)$.

Similarly, for the material counterpart of a singular surface $\Sigma(t)$ the compatibility relations take the form

$$[\dot{\chi}_m] = V_S\, s\,, \quad [\mathbf{f}] = -\frac{V_S}{U_N}\, s \otimes N \quad \text{for} \quad U_N \neq 0\,, \tag{9}$$

where N is the unit normal vector to the discontinuity surface $\Sigma(t)$ and U_N is the normal component of the surface velocity (cf. [15], p. 96).

3.4. Macroscopic measure of the rate of deformation produced by micro–shear banding

According to the analysis in [1], the averaging procedure (2) of the microscopic velocity field $\dot{\chi}_m$ over the macro–element V_o can be generalized for the macroscopic RVE traversed by the singular surface of vortex sheet type with the velocity jump of the magnitude V_S. Then, the macroscopic measures of deformation gradient $\mathbf{F}$ and its rate $\dot{\mathbf{F}}$ are expressed by means of surface data in the following way

$$\mathbf{F} \equiv \frac{1}{V_o} \int_{\partial V_o - \Sigma(t)} \mathbf{x}_m \otimes \nu_o \, dA_o\,, \tag{10}$$

where according to (1), $\mathbf{F} = \mathbf{F}$ and due to (2) and $(9)_1$

$$\dot{\mathbf{F}} = \frac{1}{V_o} \int_{V_o} \mathrm{Grad}\dot{\chi}_m \, dV_o + \frac{1}{V_o} \int_{\Sigma(t)} V_S\, s \otimes N \, dA_o\,, \tag{11}$$

and in the spatial form

$$\mathbf{L} \equiv \frac{1}{V} \int_{\partial V - S(t)} \mathbf{v}_m \otimes \nu \, dA = \frac{1}{V} \int_V \mathrm{grad}\mathbf{v}_m \, dV + \frac{1}{V} \int_{S(t)} V_S\, s \otimes n \, dA\,, \tag{12}$$

where $\mathbf{L}$ denotes the macroscopic measure of velocity gradient, averaged over the macro–element V traversed by the vortex sheet $S(t)$. The averaging formula (12) enables us to account for the contribution of micro–shear banding in the macroscopic measure of velocity gradient produced at finite elastic–plastic strain. According to (12), the velocity gradient $\mathbf{L}$ is decomposed as follows

$$\mathbf{L} = \mathbf{L} + \mathbf{L}_{MS}, \quad \mathbf{L} = \frac{1}{V} \int_V \mathrm{grad}\mathbf{v}_m \, dV, \quad \mathbf{L}_{MS} = \frac{1}{V} \int_{S(t)} V_S s \otimes n \, dA. \tag{13}$$

Assuming that the singular surface $S(t)$ forms a plane traversing volume V, with the

unit vectors $\boldsymbol{s}$ and $\boldsymbol{n}$ held constant, $(13)_3$ results in $\mathbf{L}_{MS} = \dot{\gamma}_{MS}\, \boldsymbol{s} \otimes \boldsymbol{n}$, where the macroscopic shear strain rate $\dot{\gamma}_{MS}$ is determined according to (6) by the microscopic variables as an average over the RVE

$$\dot{\gamma}_{MS} = \frac{1}{V}\int_{S(t)} H_{ms}\dot{\gamma}_{ms}\,dA = \frac{1}{V}\int_{S(t)} H_{ms} B_{ms} \rho_{ms} v_{ms}\,dA . \tag{14}$$

Assuming for simplicity that the structural parameter B_{ms} and the speed v_{ms} are constant over the surface $S(t)$, we have

$$\dot{\gamma}_{MS} = B_{ms} v_{ms} \rho_{MS} , \qquad \rho_{MS} = \frac{1}{V}\int_{S(t)} H_{ms}\rho_{ms}\,dA . \tag{15}$$

The symbol ρ_{MS} denotes the macroscopic volume density of micro–shear bands that operate within the sequence of clusters sweeping the RVE. The density ρ_{MS} may change with "time–like parameter" t, for the magnitudes of H_{ms} and ρ_{ms} are, in general, various for different clusters and (15) takes the following equivalent form, [1]

$$\dot{\gamma}_{MS} = B_{ms} L_{ms} \dot{\rho}_{MS} . \tag{16}$$

The derived relations are valid for a single system of micro–shear bands. This can be generalized for the case of a double shearing system

$$\mathbf{L} = \mathbf{L} + \sum_{i=1}^{2} \dot{\gamma}_{MS}^{(i)}\, \boldsymbol{s}^{(i)} \otimes \boldsymbol{n}^{(i)} , \tag{17}$$

where $\dot{\gamma}_{MS}^{(i)}$ is the macroscopic shear strain rate and $\boldsymbol{s}^{(i)}$, $\boldsymbol{n}^{(i)}$ are the respective unit vectors of the "i"th shearing system. It worthy to note, that (17) is valid only under the simplifying assumption that the active micro–shear bands in both systems operate in the time period, which corresponds to a sufficiently small increment of "time–like parameter" in the macroscopic description. Otherwise, the sequence of events should be taken into considerations. The above relations provide the following macroscopic measures of the rate of plastic deformations and plastic spin produced by active micro–shear bands

$$\mathbf{D}_{MS}^{p} = \frac{1}{2}(\mathbf{L}_{MS} + \mathbf{L}_{MS}^{T}) , \qquad \mathbf{W}_{MS}^{p} = \frac{1}{2}(\mathbf{L}_{MS} - \mathbf{L}_{MS}^{T}) . \tag{18}$$

The discussed averaging procedure over the RVE with the singular surface allows to account for the characteristic geometric pattern of micro–shear bands which is transmitted upwards through a multiscale hierarchy of observational levels.

3.4. The meaning of "yield" within the context of micro–shear banding

It was recognized in [2–4] that in the plasticity model accounting for the effects of micro–shear bands the meaning of "yield" is not a trivial one and requires more detailed analysis. The precise connection of the nominal yield points with intrinsic material properties was discussed earlier by Hill in [6] and [17], where the idea of an "extremal surface" was proposed. Let us imagine that after a given prestrain of the RVE of a polycrystalline aggregate, further glide hardening on the active slip systems of its constituent grains is suspended. In general, due to constraint hardening, the incremental plastic flow under constant overall load is still precluded. However, as it was observed in [6], special configurations of internal micro–stresses and yield vertices are possible that together admit one or more fields of strain rate which are compatible with zero stress rate. According to Hill [18], such fields correspond to intrinsic eigenstates and are associated with incipient branching of constitutive relation between increments of objective stress and strain. If the micro–shear bands are understood as an effect of special configuration of internal micro–stresses that accumulate at grain boundaries till the glide hardening on the active slip systems is suspended and then abruptly release producing, under constant overall load, the field of plastic deformation rate $\mathbf{D}^{p}_{MS}$ as a self–induced deformation mode, the similarity with the intrinsic eigenstates, discussed in [6] and [18], can be observed. As is emphasized in [6], the "extremal surface" is not a single yield surface but is rather an assemblage of yield points for physically distinct states of the RVE, none of which can be reached from any other via purely elastic paths in the stress space. Then, the following observation correlates the properties of the "extremal surface" with the mechanism of micro–shear banding:

The properties of the "extremal surface" conform with the mechanism of micro–shear banding. The yield state approaching a certain state on the "extremal surface" can be related with the formation of a particular spatial pattern of micro–shear bands. Another state occupying the "extremal surface" pertains to another spatial pattern of micro–shear bands. The transition from one state to the other is not possible via a purely elastic path, for an accumulated plastic strain is necessary to produce the new set of micro–shear bands characterized, in general, by another geometric pattern. Such an "extremal surface" forms the generic micro–shear banding surface.

Based on the aforementioned discussion, a simplified model with two limit surfaces can be introduced. The preliminary study of such a model of plastic flow with an external surface taking into account the onset of shear–banding and the internal yield surface, which is related with the back stress anisotropy was presented in [4] and [5].

4. CONSTITUTIVE DESCRIPTION

4.1. Basic concepts and relations of elasto–plasticity of structured solids

Consider a polycrystalline aggregate as a continuum body. An infinitesimal neighbourhood of a material point $\mathbf{X}$ of this body corresponds to the aforementioned RVE, which is sufficient for a valid continuum mechanics description of gross elastic–plastic behaviour. The dominant orientation of the crystalline lattice in the RVE is represented by director vectors. We can choose an arbitrary triad of orthogonal unit vectors that will serve as a reference frame for the description of anisotropic properties and elastic behaviour of material element. The director vectors define the structure of continuous body. The different visualizations of such a triad are discussed in [19–24], where more detailed discussion and further references can be found. The assumption that the continuum is endowed with the structure in the form of the director vectors leads to the Mandel's concepts of the local, relaxed, intermediate isoclinic configurations, plastic spin and structure corotational rate. Due to this, the decomposition of the deformation gradient $\mathbf{F}$ becomes unique $\mathbf{F} = \mathbf{EP}$, where $\mathbf{E}$ denotes the elastic transformation from the intermediate isoclinic configuration to the current one and $\mathbf{P}$ is the plastic transformation from the reference configuration to the isoclinic one. The derivation of the macroscopic measure of the velocity gradient $\mathbf{L}$ and its decomposition (13) makes possible to formulate in a more rigorous manner the constitutive equations of elastoplasticity with an account of micro–shear banding. The following kinematical relations can be derived, (cf. [1]):

$$\mathbf{D} = \mathbf{D}^{e} + \mathbf{D}^{p} = \mathbf{D}^{e} + \mathbf{D}^{p}_{S} + \mathbf{D}^{p}_{MS}, \qquad \mathbf{W} = \mathbf{W}^{e} + \mathbf{W}^{p} = \mathbf{W}^{e} + \mathbf{W}^{p}_{S} + \mathbf{W}^{p}_{MS}, \tag{19}$$

where $\mathbf{D}^{p}_{S}$ and $\mathbf{W}^{p}_{S}$ correspond, respectively, to the rate of plastic deformation and plastic spin produced by crystallographic multiple slip. Observe that according to (13), if the contribution of micro–shear bands is negligible, we have $\mathbf{D}^{p}_{MS} = \mathbf{W}^{p}_{MS} = \mathbf{0}$.

Further analysis will be confined to isothermal processes with small elastic strains. Then, due to the polar decomposition $\mathbf{E} = \mathbf{V}^{e}\mathbf{R}^{e}$ and logarithmic elastic strain $\varepsilon = \ln \mathbf{V}^{e}$ the following approximate relations can be obtained, (cf. e.g. [5]):

$$\mathbf{D}^{p} = \mathbf{R}^{e}\{\dot{\mathbf{P}}\mathbf{P}^{-1}\}_{s}\mathbf{R}^{eT}, \qquad \mathbf{W}^{p} = \mathbf{R}^{e}\{\dot{\mathbf{P}}\mathbf{P}^{-1}\}_{a}\mathbf{R}^{eT}, \qquad \mathbf{D}^{e} = \dot{\varepsilon} + \varepsilon\,\mathbf{W}^{e} - \mathbf{W}^{e}\,\varepsilon, \tag{20}$$

with the elasticity equation

$$\overset{o}{\tau} = \mathcal{L} : \mathbf{D}^{e}, \qquad \overset{o}{\tau} = \dot{\tau} - \mathbf{W}^{e}\tau + \tau\,\mathbf{W}^{e}, \qquad \mathcal{L} = \rho_{k}\frac{\partial^{2}\Phi}{\partial\varepsilon\;\partial\varepsilon}, \qquad \mathbf{W}^{e} = \dot{\mathbf{R}}^{e}\mathbf{R}^{eT}. \tag{21}$$

The symbol $\mathcal{L}$ denotes the fourth–order tensor of elastic moduli and Φ is the free energy

function per unit mass, assumed in the form $\Phi(\varepsilon, \hat{\mathbf{A}}) = \Phi_1(\varepsilon) + \Phi_2(\hat{\mathbf{A}})$, where $\hat{\mathbf{A}}$ is the set of internal variables taken with respect to the isoclinic configuration.

4.2. Model of plastic flow with nonlinear evolution of kinematic hardening

Let us consider the description of elastic–plastic behaviour of metallic solids with two limit surfaces. The internal yield surface f is connected with nonlinear kinematic hardening anisotropy and the external surface $\mathcal{F}$ is related with the micro–shear banding, cf. Fig. 2. It is sufficient for further study to assume the model of small elastic and finite plastic deformations with the following set of internal variables:

$$\hat{\mathbf{A}} =: \{\hat{\boldsymbol{\alpha}}, \hat{s}\}, \quad \mathbf{A} =: \{\boldsymbol{\alpha}, s\}, \quad \boldsymbol{\alpha} = \mathbf{R}^e \hat{\boldsymbol{\alpha}} \mathbf{R}^{eT}, \quad s = \hat{s}, \tag{22}$$

related with the isoclinic and current configurations, respectively. The tensor variable $\boldsymbol{\alpha}$, often called the deviatoric back stress, describes kinematic hardening effect (the translation of the yield surface) and the scalar variables $s =: \{\kappa, K, \rho_{MS}^{(i)}\}$, $i = 1, 2$, represent the isotropic hardening parameters κ and K, as well as, the macroscopic volume density of micro–shear bands $\rho_{MS}^{(i)}$ that operate within the sequence of clusters of the "i"th shearing system sweeping the RVE. The Huber – Mises criterion accounting for kinematic hardening is assumed to approximate the internal yield surface f and the constitutive equations at the yield point take the form:

$$f(\tau', \boldsymbol{\alpha}, \kappa) = \frac{1}{2}(\tau' - \boldsymbol{\alpha}):(\tau' - \boldsymbol{\alpha}) - \kappa^2 = 0, \qquad \dot{\kappa} = b(\kappa_s - \kappa)\dot{\bar{\gamma}}_S, \qquad \kappa(0) = \kappa_o, \tag{23}$$

$$\mathbf{D} = \mathbf{D}^e + \mathbf{D}_S^p = (\mathcal{L}^{-1} + \frac{1}{2h}\boldsymbol{\mu}_f \otimes \boldsymbol{\mu}_f):\overset{\circ}{\boldsymbol{\tau}}, \quad \boldsymbol{\mu}_f = \frac{1}{\sqrt{2}k}(\tau' - \boldsymbol{\alpha}), \tag{24}$$

$$\overset{\circ}{\boldsymbol{\alpha}} = (\sqrt{2}\, h_a' \boldsymbol{\mu}_f - c_r \boldsymbol{\alpha})\dot{\bar{\gamma}}_S, \quad \boldsymbol{\alpha}(0) = \boldsymbol{\alpha}_o, \quad \dot{\bar{\gamma}}_S = (2\mathbf{D}_S^p:\mathbf{D}_S^p)^{\frac{1}{2}}, \tag{25}$$

where τ' is the deviator of the Kirchhoff stress τ, and κ_s is a material constant representing a saturation value for κ, whereas b corresponds to a constant controlling the pace of saturation. The internal variable κ determines the "size" of the yield surface, (i.e. $\kappa = \frac{1}{\sqrt{2}}R$, where R is the radius of the Huber–Mises cylinder). The combined plastic hardening modulus h reads:

$$h = h_i + h_a, \qquad h_i = b(\kappa_s - \kappa), \quad h_a = h_a' - \frac{1}{\sqrt{2}} c_r \boldsymbol{\mu}_f:\boldsymbol{\alpha}. \tag{26}$$

The form of the nonlinear kinematic hardening rule $(25)_1$ was proposed originally for small strains by Armstrong and Frederick [25] and applied further in the studies on cyclic plasticity (cf. e.g. Chaboche [26]). The material constant c_r is related with the

saturation of the back stress effect while accumulated plastic strain increases. The scalar multiplier j fulfills the conditions $j = 1$ if $\mu_f : \overset{\circ}{\tau} \geq 0$ and $j = 0$ if $\mu_f : \overset{\circ}{\tau} < 0$. The objective rate of the kinematic hardening parameter $\boldsymbol{\alpha}$ reads

$$\overset{\circ}{\boldsymbol{\alpha}} = \dot{\boldsymbol{\alpha}} - \mathbf{W}^e\boldsymbol{\alpha} + \boldsymbol{\alpha}\mathbf{W}^e, \qquad \mathbf{W}^e = \mathbf{W} - \mathbf{W}^p. \tag{27}$$

The additional constitutive equation for the plastic spin $\mathbf{W}^p$ is necessary to determine the spin $\mathbf{W}^e$ of the rotation of the structure. In the study by Paulun and Pęcherski [27] the relation for plastic spin was derived, which can be applied for the case of nonlinear kinematic hardening rule $(25)_1$ in the following form

$$\mathbf{W}_S^p = \frac{3}{(h_a'^2 + \sqrt{3}\,\bar{\alpha}h_a')^{\frac{1}{2}}}(\boldsymbol{\alpha}\mathbf{D}^p - \mathbf{D}^p\boldsymbol{\alpha}), \qquad \bar{\alpha} = (\tfrac{1}{2}\,\boldsymbol{\alpha}:\boldsymbol{\alpha})^{\frac{1}{2}}. \tag{28}$$

More detailed discussion on the proper formulation of the relation for plastic spin for the case of kinematic hardening rule $(25)_1$ and of its special form for $c_r = 0$, known as Prager–Ziegler law, is given in [22] and [27], where further references can be found.

4.3. Approximation of the generic micro–shear banding surface

Let us observe that the nonlinear hardening rule $(25)_1$ implicitly introduces the second limit surface, for $\overset{\circ}{\boldsymbol{\alpha}} = \mathbf{0}$ leads to, (cf. [26]):

$$\mathcal{F}(\tau', \mathcal{K}) = \frac{1}{2}(\tau' : \tau') - \mathcal{K}^2 = 0, \qquad \dot{\mathcal{K}} = B(\mathcal{K}_s - \mathcal{K})\dot{\bar{\gamma}}_S, \qquad \mathcal{K}(0) = \mathcal{K}(\Gamma_{MS}) + \frac{h_a'}{c_r}, \tag{29}$$

where $\mathcal{K}$ is the "size" of the limit surface, (i.e. $\mathcal{K} = \frac{1}{\sqrt{2}}\,\mathcal{R}$, where $\mathcal{R}$ is the radius of the external surface), $\mathcal{K}_s$ is a material constant representing a saturation value for $\mathcal{K}$, and B is a material constant controlling the pace of saturation. The parameter $\mathcal{K}$ can be determined from the observations of micro–shear bands formation. According to the recent studies of Oliferuk et al. [28] the saturation of internal micro–stresses can be correlated with massive formation of micro–shear bands. This is related with certain amount of plastic strain $\bar{\gamma}_S = \Gamma_{MS}$, accumulated along a given deformation path. Assuming that the internal micro–stresses can be represented on the macroscopic level by the back stress $\boldsymbol{\alpha}$, we can determine the material constant c_r, which relates the saturation of the back stress effect with micro–shear banding. In this way, the resulting limit surface $\mathcal{F}$ of radius $\mathcal{R}$ comes into contact, at the loading point, with the generic micro–shear banding surface. The discussed results of deformation tests complemented with metallographic observations reveal that the onset of micro–shear bands is strongly

dependent upon the change of loading scheme and the resulting deformation path, (cf. eg. [5]). Therefore, the class of external limit surfaces, determined for different loading histories, should be considered. This is depicted in Fig. 2, where the external limit surfaces $\mathcal{F}_A$ and $\mathcal{F}_B$ arrive at the micro–shear banding surface. The points of contact are pertinent to the respective stress states τ'_A and τ'_B, which have been reached for different loading paths $\mathcal{L}_A$ and $\mathcal{L}_B$. According to (29), the general functional relations $\Gamma_{MS} = \mathcal{G}(\mathcal{L})$ and $c_\tau = \mathcal{C}(\mathcal{L})$ should be used to determine the family of external surfaces, which approximate locally the generic micro–shear banding surface. Systematic experimental investigations are necessary to asses the change of Γ_{MS} and c_τ for different loading paths.

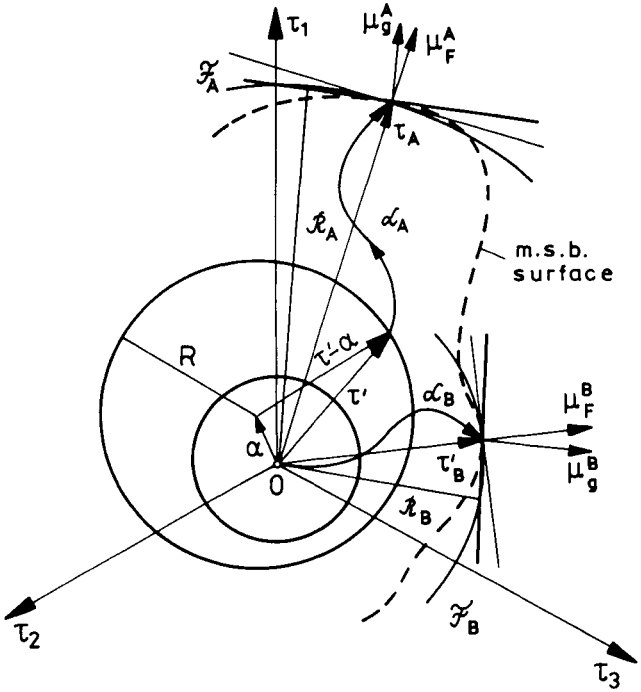

Figure 2. The generic micro–shear banding (m.s.b.) surface approximated by the class of the external limit surfaces $\mathcal{F}$ obtained for different loading paths $\mathcal{L}$.

4.4. Derivation of plastic flow laws accounting for micro–shear banding

According to Hill [6], the macroscopic constitutive equations describing elastic–plastic deformations of polycrystalline aggregates are either thoroughly or partially incrementally nonlinear. Depending on the contribution of the mechanisms

involved in plastic flow, a region of fully active loading, called also a fully active range, separated from the total unloading (elastic) range by a truly nonlinear zone corresponding to the partially active range, may exist. According to the works [6], [29] and [30] the following hypothesis is formulated, [3]:

For continued plastic flow with the deviations from proportional loading contained within a certain cone of stress rates that corresponds to the fully active range, the incremental plastic response can be assumed as linearly dependent on the stress increment. Inside the fully active range the spatial pattern of micro–shear bands is fixed, whereas in the partially active range the spatial pattern of active micro–shear bands is changing following the orientation of the maximum shear stress plane. This is associated with the thoroughly nonlinear relation between the rates of plastic deformations and stress.

The connection of the fully active range and partially active range with the geometric pattern of micro–shear bands is necessary to specify the relation for the rate of plastic deformations for different loading paths. Due to the fact that the multiple sources of plasticity are dealt with, the theory of multimechanisms with multiple plastic potentials can be considered. The concept of multiple potential surfaces forming a vertex on the smooth limit surface was studied earlier by Mróz [31] within the framework of non–associated flow laws. In our case, the existence of the following plastic potentials related with the mechanisms responsible for plastic flow can be postulated, (cf. [3]):

(i) The plastic potential g_0 *that reproduces at the macroscopic level the crystallographic multiple slips and is associated with the external surface approximated by means of the Huber–Mises locus* $\mathcal{F} = g_0$.

(ii) The non–associated plastic potentials g_1 *and* g_2 *that approximate at the macroscopic level the multiplicity of plastic potential functions related with the clusters of active micro–shear bands.*

The plastic potential functions g_1 and g_2 display the geometry of the considered micro–shear bands systems and result in two separate planes that form in the space of principal stresses τ_i, i = 1, 2, 3, a vertex at the loading point on the smooth Huber–Mises cylinder $\mathcal{F}$. The planes are defined by normals $\mathbf{N}_i$, which can be expressed in terms of the unit vectors $\boldsymbol{s}^{(i)}$, $\boldsymbol{n}^{(i)}$, i = 1, 2, defining the "i"th system (cluster) of micro–shear bands $\mathbf{N}_i = \frac{\sqrt{2}}{2}(\boldsymbol{s}^{(i)} \otimes \boldsymbol{n}^{(i)} + \boldsymbol{n}^{(i)} \otimes \boldsymbol{s}^{(i)})$. As it is shown in Fig. 3, the normals $\mathbf{N}_i$, i = 1, 2, can be expressed in terms of the unit normal $\boldsymbol{\mu}_F$ and the unit tangent $\mathbf{T}$ to the limit surface $\mathcal{F}(\tau', K)$ at the loading point

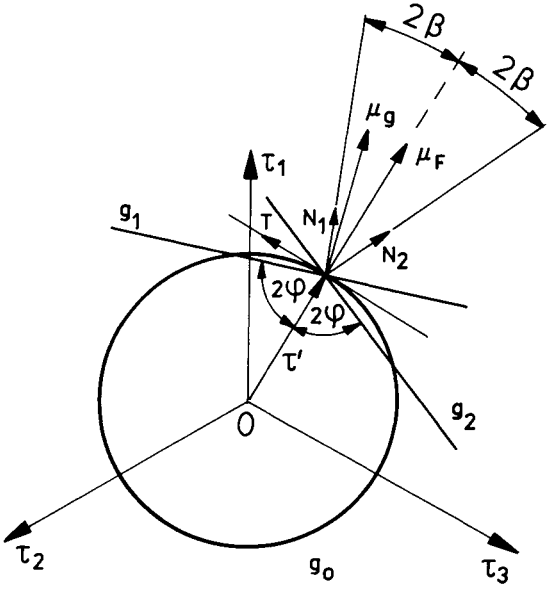

Figure 3.The projection of the Huber–Mises cylinder $\mathcal{F} = g_0$ and the potential planes g_1 and g_2 onto the deviatoric plane and the plastic cone defined by the angle β.

$$\mathbf{N}_1 = \cos 2\beta\, \boldsymbol{\mu}_F + \sin 2\beta\, \mathbf{T}\,, \qquad \mathbf{N}_2 = \cos 2\beta\, \boldsymbol{\mu}_F - \sin 2\beta\, \mathbf{T}\,, \tag{31}$$

$$\boldsymbol{\mu}_F = \frac{1}{\sqrt{2}\mathcal{K}}\,\boldsymbol{\tau}', \qquad \mathbf{T} = \mathcal{N}\,\overline{\boldsymbol{\tau}\left(\frac{\boldsymbol{\tau}'}{\bar{\tau}}\right)} = \mathcal{N}\,[\overset{\circ}{\boldsymbol{\tau}}' - (\overset{\circ}{\boldsymbol{\tau}}:\boldsymbol{\mu}_F)\boldsymbol{\mu}_F], \qquad \bar{\tau} = \left(\tfrac{1}{2}\boldsymbol{\tau}':\boldsymbol{\tau}'\right)^{\frac{1}{2}}. \tag{32}$$

where due to

$$\|\overset{\circ}{\boldsymbol{\tau}}' - (\overset{\circ}{\boldsymbol{\tau}}':\boldsymbol{\mu}_F)\,\boldsymbol{\mu}_F\|^2 = \overset{\circ}{\boldsymbol{\tau}}':\overset{\circ}{\boldsymbol{\tau}}' - (\overset{\circ}{\boldsymbol{\tau}}':\boldsymbol{\mu}_F)^2, \qquad \overset{\circ}{\boldsymbol{\tau}}:\boldsymbol{\mu}_F = \|\overset{\circ}{\boldsymbol{\tau}}\|\cos\delta, \tag{33}$$

the mormalization factor $\mathcal{N}$ is given by $\mathcal{N} = (\|\overset{\circ}{\boldsymbol{\tau}}\|\sin\delta)^{-1}$. According to $(19)_1$ and (31), the relation for the rate of plastic deformation takes form

$$\mathbf{D}^p = \mathbf{D}^p_{\boldsymbol{\mu}} + \mathbf{D}^p_{\mathbf{T}} = \frac{\sqrt{2}}{2}\,\dot{\gamma}^*\,\boldsymbol{\mu}_F + \frac{\sqrt{2}}{2}\,\dot{\epsilon}_{MS}\,\mathbf{T}\,, \tag{34}$$

where

$$\dot{\gamma}^* = \dot{\bar{\gamma}}_S + \dot{\gamma}_{MS}, \qquad \dot{\gamma}_{MS} = \cos 2\beta(\dot{\gamma}^{(1)}_{MS} - \dot{\gamma}^{(2)}_{MS}), \qquad \dot{\epsilon}_{MS} = \sin 2\beta(\dot{\gamma}^{(1)}_{MS} + \dot{\gamma}^{(2)}_{MS})\,. \tag{35}$$

This is depicted in Fig. 3 showing the plastic wedge–shaped region, within which the all possible rates of plastic deformation $\mathbf{D}^p$ are confined. Observe that only the normal component of the rate of plastic deformations contributes to the change of the radius of

the limit surface $\mathcal{F}(\tau', \mathcal{K})$ and the consistency condition, $\dot{\mathcal{F}} = 0$, yields

$$\dot{\gamma}^* = \frac{\sqrt{2}}{2}\frac{\overset{\circ}{\tau} : \mu_F}{H}, \qquad H = B(\mathcal{K}_s - \mathcal{K}) . \tag{36}$$

The following active micro–shear bands fractions, $f_{MS}^{(1)}$, $f_{MS}^{(2)}$, of the rate of plastic shearing $\dot{\gamma}^*$, are introduced, respectively,

$$\dot{\gamma}_{MS}^{(1)} \cos 2\beta = f_{MS}^{(1)} \dot{\gamma}^*, \qquad -\dot{\gamma}_{MS}^{(2)} \cos 2\beta = f_{MS}^{(2)} \dot{\gamma}^*, \tag{37}$$

where due to $(34)_1$ and for $\dot{\gamma}^* > 0$ the following constraints hold

$$\frac{\dot{\gamma}_S}{\dot{\gamma}^*} + f_{MS}^{(1)} + f_{MS}^{(2)} = 1 , \quad f_{MS}^{(1)} + f_{MS}^{(2)} \in [0, 1], \quad f_{MS}^{(1)}, f_{MS}^{(2)} \in [0, 1]. \tag{38}$$

Basing on the observation that the micro–shear bands can be active only in the case of continued plastic flow, i.e. when loading condition is fulfilled, it is assumed that for $\dot{\gamma}^* = 0$, $f_{MS}^{(1)} = f_{MS}^{(2)} = 0$. The all possible special cases resulting from the conditions (38) are discussed in [3]. The fractions $f_{MS}^{(1)}$, $f_{MS}^{(2)}$ display the stochastic character of the active micro–shear bands formation during the deformation process and can be determined within the framework of internal variables approach. In particular, accounting for (16) and (37) allows us to relate the fractions $f_{MS}^{(i)}$ with the pertinent macroscopic densities of micro–shear bands $\rho_{MS}^{(i)}$, i = 1, 2, which can be considered as internal variables given by the following evolution equations

$$\dot{\rho}_{MS}^{(i)} = \Gamma^{(i)}(\tau, \kappa, \mathcal{K}, \alpha, \rho_{MS}^{(i)})\dot{\gamma}^*, \qquad \rho_{MS}^{(i)}(0) = \rho_o^{(i)}, \tag{39}$$

what results in

$$f_{MS}^{(i)} = B_{ms} L_{ms} \Gamma^{(i)}(\tau, \kappa, \mathcal{K}, \alpha, \rho_{MS}^{(i)}), \qquad i = 1, 2. \tag{40}$$

Proper specification of the evolution functions $\Gamma^{(i)}$ remains an open problem and needs further studies. Certain microscopic models lead to the conjecture that shear banding may contribute to the rate of plastic deformation as a sequence of the generations of active micro–shear bands governed by logistic equation (Verhulst equation), taken from the population dynamics, (cf. [32]).

According to (32) and (34–37), the rate of plastic deformation takes the form, which is formally similar to the hypoelastic case of J_2 deformation theory but accounting for partially active range enables unloading, (cf. [2]):

$$D^p = \frac{\overset{\circ}{\tau} : \mu_F}{2H}\mu_F + \frac{1}{2H}\left[\overset{\circ}{\tau}' - (\overset{\circ}{\tau} : \mu_F)\,\mu_F\right], \tag{41}$$

$$_1$$

$$\frac{1}{H_1} = \begin{cases} \dfrac{\overset{\circ}{\tau} : \mu_F}{H} \dfrac{f_{MS} \tan 2\beta}{\|\overset{\circ}{\tau}'\| \sin\delta} & , \ \delta \in (\delta_c, \frac{\pi}{2}] \quad \text{partially active range} \\ \dfrac{1}{H \tan\delta_c} f_{MS} \tan 2\beta & , \ \delta \in [0, \delta_c] \quad \text{fully active range.} \end{cases} \tag{42}$$

The second term in (41) is responsible for the non–coaxiality between the principal directions of stress and rate of plastic deformations and H_1 plays the rôle of the non–coaxiality modulus, which in the case of the fully active range, i.e. for $\delta \in [0, \delta_c]$, is formally similar to the Mandel–Spencer non–coaxiality modulus discussed earlier within the context of plastic behaviour of single crystals and geological materials, (cf. [3]). The symbol $f_{MS} = f_{MS}^{(1)} - f_{MS}^{(2)}$, $f_{MS} \in [-1, 1]$, denotes the nett fraction of the active micro–shear bands that contribute to the total rate of plastic shearing. The corresponding relation for plastic spin in the case of micro–shear banding reads, (cf. [3]):

$$\mathbf{W}^p_{MS} = \frac{f_{MS}\ \chi(\delta)}{4\bar{\tau}\ H\ \cos 2\beta} (\overset{\circ}{\tau}\tau - \tau\overset{\circ}{\tau}), \qquad \chi(\delta) = \begin{cases} \operatorname{ctan}\delta\ , & \delta \in (\delta_c, \frac{\pi}{2}] \\ \operatorname{ctan}\delta_c, & \delta \in [0, \delta_c] \end{cases}. \tag{43}$$

Equivalently, for the yield point τ' reaching the limit surface $\mathcal{F}(\tau', \mathcal{K})$, the following new form of non–associated plastic flow rule can be derived, (cf. [5]):

$$\mathbf{D} = \mathbf{D}^e + \mathbf{D}^p = (\mathcal{L}^{-1} + \frac{i}{2H} \mu_g \otimes \mu_F) : \overset{\circ}{\tau}, \tag{44}$$

$$\mu_g = \begin{cases} (1 - f_{MS} \tan 2\beta \operatorname{ctan}\delta)\ \mu_F + \dfrac{f_{MS} \tan 2\beta}{\sin\delta} \rho & , \ \delta \in (\delta_c, \frac{\pi}{2}] \\ (1 - f_{MS} \tan 2\beta \operatorname{ctan}\delta_c)\ \mu_F + \dfrac{f_{MS} \tan 2\beta}{\sin\delta_c} \rho_c & , \ \delta \in [0, \delta_c] \end{cases}, \qquad \rho = \frac{\overset{\circ}{\tau}}{\|\overset{\circ}{\tau}\|}, \tag{45}$$

where $i = 1$ if $\mu_F : \overset{\circ}{\tau} \geq 0$ and $i = 0$ if $\mu_F : \overset{\circ}{\tau} < 0$, whereas ρ_c is such that $\arccos(\rho_c : \mu_F) = \delta_c$. Observe that for $\delta \in [0, \delta_c]$, the following inverted form of (44) exists

$$\overset{\circ}{\tau} = \mathcal{L} : \Big(1 - \frac{i_1\ \mu_g \otimes \lambda_F}{2H + \mu_g : \lambda_F} \Big) : \mathbf{D}, \tag{46}$$

where $i_1 = 1$ if $\lambda_F : \mathbf{D} \geq 0$ and $i_1 = 0$ if $\lambda_F : \mathbf{D} < 0$, $\qquad \lambda_F = \mathcal{L} : \mu_F$.

In the partially active range, i.e. for $\delta \in (\delta_c, \frac{\pi}{2}]$, the constitutive equation (44) is thoroughly nonlinear. According to (47), the resulting potential surface g_f is determined by the normal μ_g, cf. Fig. 2, where the fraction f_{MS} is the controlling parameter of the non–associated plastic flow law. If $f_{MS} = 0$, (46) transforms into the J_2 flow law. The magnitude of $f_{MS} \in [-1, 1]$ can fluctuate in the course of plastic flow. However, the

assumption that f_{MS} is kept constant during the deformation process can be considered as a useful first approximation.

5. CONCLUDING REMARKS

In [2], the model accounting for the double shear system with related yield planes, intersecting at the Huber–Mises yield locus, was briefly mentioned as an alternative approach. Notwithstanding the fact that the additional yield conditions related with shear banding have no firm physical and experimental foundations, such an approach could be considered as an attractive approximation simplifying theoretical and computational analysis of boundary value problems. This found confirmation in recent studies, [33], where the similar approach, based on the assumption that the contribution of crystallographic multislip, represented by the J_2 flow law, and micro–shear banding allows to the additive composition of pertinent rates of plastic deformation, was presented independently. The authors proposed "a dual yield constitutive model involving both the J_2 flow and a threshold shear stress based–flow", which was incorporated in a finite element program capable of handling large strains and rotations. The results of simulation of shear band localization occurring in a uniaxially loaded plane strain specimen show that relatively simple phenomenological approach, capturing the most essential features of micro–shear banding, can lead to satisfactory approximation of material behaviour. The implementation of the presented constitutive description into the known models describing the porous material failure by void growth to coalescence, [34–36], could appear useful in more accurate prediction of damage processes.

Acknowledgement

This work was supported by the Committee for Research (KBN) Poland, under the research project No. 7 T07A 017 08.

6. REFERENCES

1. R.B. Pęcherski, Arch. Mech., 49 (1997) 385.
2. R.B. Pęcherski, Proc. IUTAM Symposium, Finite Inelastic Deformations, Hannover, 1991, D. Besdo and E. Stein (eds.), Springer, Berlin, 1992, 167.
3. R.B. Pęcherski, Arch. Mech., 44, (1992) 563.
4. R.B. Pęcherski, ZAMM, 75, (1995) 203.
5. R.B. Pęcherski, J. Mat. Process. Technol., 60 (1966) 35.
6. R. Hill, J. Mech. Phys. Solids, 15 (1967) 779.
7. A. Korbel, Advances in Crystal Plasticity, D.S. Wilkinson and J.D. Embury

(eds.), Canadian Institute of Mining and Metallurgy, 1992, 42.
8. M. Hatherly and A.S. Malin, Scripta Metall., 18 (1984) 449.
9. Dybiec, H. – private communication.
10. K. Pieła and A. Korbel, Mat. Sci. Forum, 217–222 (1996) 1037.
11. Y. Bai and B. Dodd, Adiabatic Shear Localization, Pergamon Press, Oxford, 1992.
12. R. Hill, Proc. R. Soc. Lond., A 326 (1972) 131.
13. K.S. Havner, Finite Plastic Deformation of Crystalline Solids, Cambridge University Press, Cambridge, U.K., 1992.
14. C. Truesdell and R.A. Toupin, The Classical Field Theories, Encyclopaedia of Physics, III/1, S. Flügge (ed.), Springer–Verlag, Berlin, 1960.
15. A.C.Eringen and E.S. Suhubi, Elastodynamics, Academic Press, New York, 1974.
16. W. Kosiński, Field Singularities and Wave Analysis in Continuum Mechanics, Polish Scientific Publishers, Warszawa and Ellis Horwood, Chichester, 1986.
17. R. Hill, Math. Proc. Camb. Phil. Soc., 85 (1979) 179.
18. R. Hill, Math. Proc. Camb. Phil. Soc., 93 (1983) 177.
19. J. Mandel, Plasticité Classique et Viscoplasticité, C.I.S.M., Udine, Springer, 1972.
20. J. Mandel, Foundations of Continuum Thermodynamics, J.J. Delgado Domingos et al (eds.), McMillan, London, 1974, 283.
21. M. Kleiber and B. Raniecki, Plasticity Today, Modelling, Methods and Applications, A. Sawczuk and G. Bianchi (eds.), Elsevier, London, 1985, 3.
22. R.B. Pęcherski, Arch. Mech., 40 (1988) 807.
23. S. Cleja–Ţigoiu and E. Soós, Appl. Mech. Rev., 43 (1990) 131.
24. J.F. Besseling and E. Van Der Giessen, Mathematical Modelling of Inelastic Deformation, Chapman & Hall, London, 1994.
25. P.J. Armstrong and C.O. Frederick, G.E.G.B. Report RD/B/N 731 (1966).
26. J.L. Chaboche, Int. J. Plasticity, 2 (1986) 149.
27. J.E. Paulun and R.B. Pęcherski, Arch. Appl. Mech., 62, (1992) 386.
28. W. Oliferuk, A. Korbel and M.W. Grabski, Mat. Sci. Engn., A220 (1996) 123.
29. J. Christoffersen and J.W. Hutchinson, J. Mech. Phys. Solids, 27 (1979) 465.
30. H. Petryk, J. Mech. Phys. Solids, 37 (1989) 265.
31. Z. Mróz, J. de Mécanique, 2 (1963) 21.
32. R.B. Pęcherski, ZAMM, 72 (1992) T250.
33. N.Ramakrishnan and S.N. Atluri, Mechanics of Materials, 17 (1994) 307.
34. V. Tvergaard, Advances in Applied Mechanics, J.W. Hutchinson and T.Y. Wu (eds.), Academic Press, New York, 1990, 83.
35. P. Perzyna, J. Engng. Mat. Technol., 106 (1994) 410.
36. R. Lammering, R.B. Pęcherski and E. Stein, Arch. Mech., 42 (1990) 347.

Damage Mechanics in Engineering Materials
G.Z. Voyiadjis, J.-W.W. Ju and J.-L. Chaboche (Editors)
© 1998 Elsevier Science B.V. All rights reserved.

Some Remarks on Gradient and Nonlocal Damage Theories

R. de Borst[a,b], M.G.D. Geers[b,c], R.H.J. Peerlings[b] and A. Benallal[d]

[a] Koiter Institute Delft/Faculty of Civil Engineering, Delft University of Technology, P.O. Box 5048, 2600 GA Delft, The Netherlands

[b] Faculty of Mechanical Engineering, Eindhoven University of Technology, Eindhoven, The Netherlands

[c] Faculty of Civil Engineering, Royal Military Academy, Brussels, Belgium

[d] Laboratoire de Mécanique et Technologie, ENS de Cachan, Cachan, France

1. INTRODUCTION

Starting in the early 1980s a tremendous amount of activity has been devoted to developing numerical methodologies which are able to trace the entire load-deflection path up to and including complete failure of a specimen or a structural part or component. Different formalisms have been used for this purpose, such as plasticity for metals and soils, being physically more appealing for these materials, and damage theories for more brittle materials such as concrete, ceramics, certain fibre-reinforced polymers and rocks under low confining pressures. In either formalism a descending branch in the stress-strain curve is introduced at a generic stage of the deformation process to simulate the loss of load-carrying capacity at progressive straining. These approaches are macroscopic in the sense that the globally observed descending load-deflection curve is translated into local 'softening' stress-strain relations. Thus, a homogenized response is obtained of microscopic processes which occur in the material.

A mathematical consequence of such macroscopic models, which are normally based on continuum mechanics, is that at a certain threshold level of loading the governing differential equations locally lose ellipticity (or hyperbolicity if dynamic loading conditions are considered). Consequently, the boundary or initial value problem becomes ill-posed [1], and analytical as well as numerical solutions become meaningless. A host of solutions has been suggested to remedy this deficiency of the standard continuum approach. For high-speed phenomena the inclusion of the inherent rate dependence of a material seems natural, see for instance Needleman [2] for metals, Loret and Prévost [3] for soils and Sluys [4-6] for concrete. For granular materials a revival of the Cosserat continuum has been witnessed, and micromechanical foundations for applying such a theory have been established [7]. Numerical approaches have been elaborated that can be implemented in standard finite element codes in a straightforward fashion [8,9]. For cracking in concrete and ceramics, but also for describing void growth in metals nonlocal theories have been suggested either in an integral format or in a differential format. For a simple elastic-damaging formalism a nonlocal theory in an integral

format has been proposed by Pijaudier-Cabot and Bazant [10]. Aifantis and his colleagues [11-15] and Schreyer and Chen [16] have proposed gradient plasticity theories, which were cast into a numerical format by de Borst and co-workers [17-20]. More recently, Mühlhaus *et al.* [21] have proposed a gradient theory within a damage mechanics framework, and numerical approaches that are related to this theory have been described in [22,23]. A somewhat different formalism was advocated in [24,25], including a robust numerical implementation.

In this contribution we shall consider enriched damage theories in which the damage is coupled to (isotropic) elasticity. Firstly, we shall briefly summarize standard damage theories and nonlocal damage theories in an integral format. Based on the latter class of theories a family of gradient-enhanced damage theories will be derived. For the particular case where higher-order gradients of a local equivalent strain are introduced, a refinement is described, which remedies the problem of artifical widening of the damage zone in progressive stages of the loading process [26,27]. A concise description of the numerical implementation of this model will be given. Finally, a comparison will be carried out between some gradient damage theories and a nonlocal damage theory in an integral format.

2. ELASTICITY-BASED DAMAGE MODELS

Damage mechanics theory can be used to describe degradation and failure of structural materials and components. In its simplest form, it degrades the elastic properties, in particular Young's modulus with the accumulation of damage [28]:

$$\boldsymbol{\sigma} = (1-\omega)\mathbf{D}\boldsymbol{\varepsilon} \tag{1}$$

with $\boldsymbol{\sigma}$ the stress tensor, $\boldsymbol{\varepsilon}$ the strain tensor, $\mathbf{D}$ the virgin elastic stiffness tensor, and ω a scalar-valued internal variable, which reflects the amount of damage which the material has experienced. It starts at zero (undamaged state) and grows to one (complete loss of integrity) as a function of a scalar-valued history parameter κ, which represents the most severe deformation the material has experienced: $\omega = \omega(\kappa)$. The history parameter initiates at a threshold level κ_i and damage growth is possible if the damage loading function

$$f(\varepsilon_{eq}, \kappa) = \varepsilon_{eq} - \kappa \tag{2}$$

vanishes. In particular, the damage loading function f and the growth rate of the history parameter κ have to satisfy the Kuhn-Tucker loading-unloading conditions

$$f \leq 0 \quad , \quad \dot{\kappa} \geq 0 \quad , \quad f\dot{\kappa} = 0 \tag{3}$$

In eq. (2) ε_{eq} is the local equivalent strain. For metals, the local energy release rate due to damage is often substituted [29], i.e. $\varepsilon_{eq} = {}^1\!/_2\boldsymbol{\varepsilon}^T\mathbf{D}\boldsymbol{\varepsilon}$, while for pressure-sensitive materials, it can be a function of the positive principal strains [30]

$$\varepsilon_{eq} = \sqrt{\sum_{i=1}^{3} (< \varepsilon_i >)^2} \tag{4}$$

with $< \cdot >$ the Macauley brackets.

3. NONLOCAL DAMAGE MODELS

In a nonlocal generalization the equivalent strain ε_{eq} is normally replaced by a spatially averaged quantity [10],

$$f(\bar{\varepsilon}_{eq}, \kappa) = \bar{\varepsilon}_{eq} - \kappa \tag{5}$$

where the nonlocal average strain $\bar{\varepsilon}_{eq}$ is computed as:

$$\bar{\varepsilon}_{eq}(\mathbf{x}) = \frac{1}{V_r(\mathbf{x})} \int_V g(\mathbf{s}) \varepsilon_{eq}(\mathbf{x}+\mathbf{s})\, dV \ , \quad V_r(\mathbf{x}) = \int_V g(\mathbf{s})\, dV \tag{6}$$

with $g(\mathbf{s})$ a weight function, e.g., the error function,

$$g(s) = \frac{1}{\sqrt{2\pi} l} e^{-s^2/2l^2} \tag{7}$$

and $\mathbf{s}$ a relative position vector pointing to the infinitesimal volume dV. Alternatively, the locally defined history parameter κ may be replaced in the damage loading function f by a spatially averaged quantity:

$$f(\varepsilon_{eq}, \bar{\kappa}) = \varepsilon_{eq} - \bar{\kappa} \tag{8}$$

where the nonlocal history parameter $\bar{\kappa}$ follows from:

$$\bar{\kappa}(\mathbf{x}) = \frac{1}{V_r(\mathbf{x})} \int_V g(\mathbf{s}) \kappa(\mathbf{x}+\mathbf{s})\, dV \ , \quad V_r(\mathbf{x}) = \int_V g(\mathbf{s})\, dV \tag{9}$$

The Kuhn-Tucker conditions can now be written as:

$$f \le 0 \ , \quad \dot{\bar{\kappa}} \ge 0 \quad , \quad f\dot{\bar{\kappa}} = 0 \tag{10}$$

4. GRADIENT DAMAGE MODELS

Nonlocal constitutive relations can be considered as a point of departure for constructing gradient models. Again, this can either be done by expanding the equivalent strain ε_{eq} of (6), or by applying an expansion with respect to the history parameter κ of (9). We will first consider the expansion of κ and then we will do the same for ε_{eq}. Expanding the kernel κ into a Taylor series we obtain for an isotropic, infinite medium

$$\bar{\kappa} = \kappa + c\nabla^2\kappa \tag{11}$$

where higher-order terms have been omitted. The gradient constant c is a material parameter of the dimension length squared. It can be related to the averaging volume and then becomes dependent on the precise form of the weight function g. For instance, for a one-dimensional continuum and taking the error function (7), we obtain $c = {}^1\!/_2 l^2$. It is recalled, that in this paper we adopt a phenomenological view in which $\sqrt{c}$ reflects the length scale of the failure process that we wish to describe macroscopically.

A special case of the above theory is obtained by assuming a linear relation between the local history parameter κ and the local damage variable ω:

$$\kappa = \kappa_i + M\omega \,, \tag{12}$$

with κ_i representing a threshold value below which there is no damage growth, and M a constant [22]. Now, the damage loading function changes into

$$f = \varepsilon_{eq} - \kappa_i - M(\omega + c\nabla^2\omega) \tag{13}$$

and ω can be taken as the independent variable in finite element implementations [22,23].

In a fashion similar to the derivation of gradient damage models based on the averaging of the history parameter κ, we can elaborate a gradient approximation of the local equivalent strain ε_{eq}. If we truncate after the second-order terms and carry out the integration implied in (6) under the assumption of isotropy, the following relation ensues:

$$\bar{\varepsilon}_{eq} = \varepsilon_{eq} + c\nabla^2\varepsilon_{eq} \tag{14}$$

This formulation has a severe disadvantage when applied in a finite element context, namely that it requires computation of second-order gradients of the local equivalent strain ε_{eq}. Since this quantity is a function of the strain tensor and since the strain tensor involves first-order derivatives of the displacements, third-order derivatives of the displacements have to be computed, which necessitates C^1-continuity of the shape functions. As a possible remedy, a two-field formulation can be set up, in which the local equivalent strain ε_{eq} is replaced by an independent, continuous field variable, say $\bar{\varepsilon}_{eq}$. Applying the divergence theorem then leads to a formulation in which only C^0-continuous shape functions are necessary. A more elegant solution is obtained by differentiating eq. (14) twice and substituting the result into eq. (14). Again neglecting fourth-order terms then leads to

$$\bar{\varepsilon}_{eq} - c\nabla^2\bar{\varepsilon}_{eq} = \varepsilon_{eq} \tag{15}$$

When $\bar{\varepsilon}_{eq}$ is discretized independently and use is made of the divergence theorem, a C^0-interpolation for $\bar{\varepsilon}_{eq}$ suffices [24].

Recently, Geers [26,27] has shown that formulation (15), in which the gradient parameter c is a constant, is deficient in the sense that for progressive damage an artificial spreading of the damage zone occurs that is orthogonal to the direction of crack propagation. For the example of a Compact Tension Test, shown in Figure 1, the computed damage distributions are shown in Figures 2 and 3 for two different stages in the loading process. Figure 2 shows that initially a small, narrow damage zone arises. However, upon further crack propagation, this zone evolves into a broad band of damage, Figure 3, which is physically unacceptable, since after a full crack has formed ($\omega = 1$) the surrounding material should unload and not be stretched further. To accommodate this observation, Geers [26,27] has proposed to replace the constant parameter c in eq. (15) by ζ,

$$\bar{\varepsilon}_{eq} - \zeta\,\nabla^2\bar{\varepsilon}_{eq} = \varepsilon_{eq} \tag{16}$$

which is a function of the local strain state, e.g.,

$$\zeta = c\,(\varepsilon_{eq} / \varepsilon_{\zeta}) \quad \text{if} \quad \varepsilon_{eq} \le \varepsilon_{\zeta} \quad \text{else} \quad \zeta = c \tag{17}$$

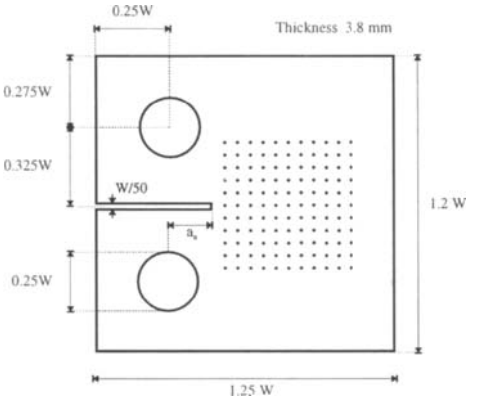

Figure 1. Compact Tension Specimen.

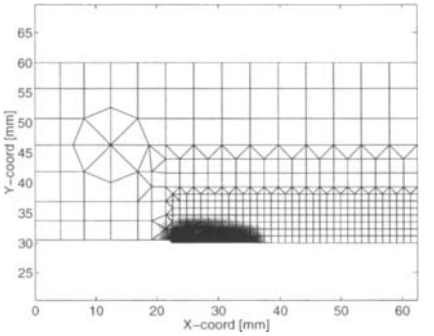

Figure 2. Widening of damage zone: onset of damage evolution.

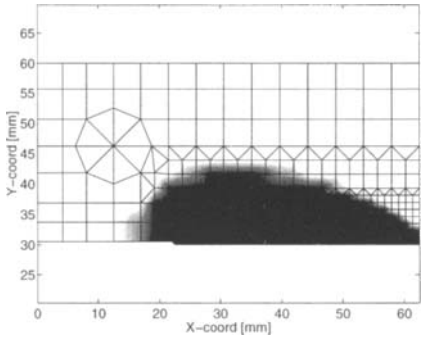

Figure 3. Widening of damage zone: progressive damage evolution.

In this fashion, the gradient activity ζ grows with increasing local strains. If local unloading occurs due to stress relief because of the nearby existence of fully developed crack the nonlocal interaction decreases again through its coupling to the local strain state ε_{eq}. This is demonstrated in Figures 4 and 5, where the same specimen is analysed as in Figures 1-3, but now

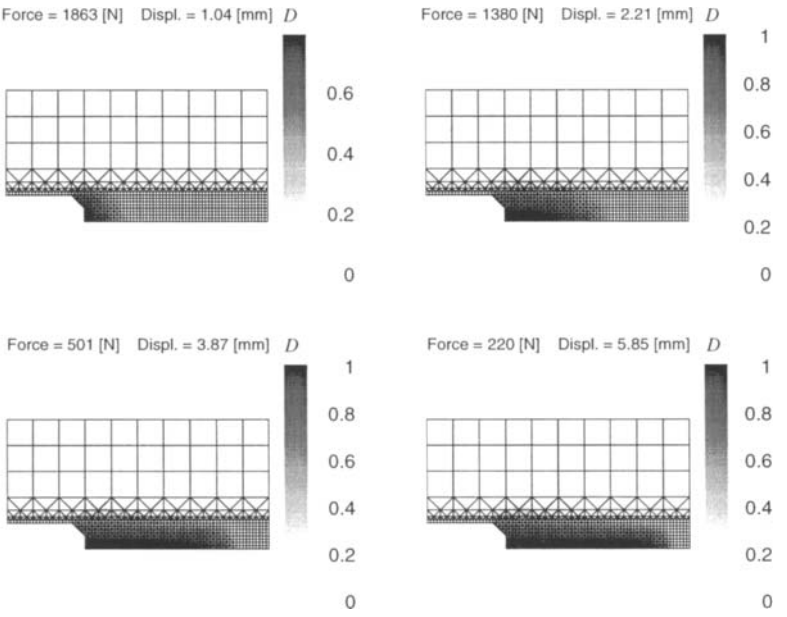

Figure 4. Damage evolution with an evolution law for the gradient activity ζ.

with the evolution law (17) for the gradient activity ζ instead of the constant gradient parameter c. From Figure 4 we observe that the damage zone remains confined to the original width which it occupied during the initial localization process. The evolution of the variable gradient activity ζ is visualized in Figure 5 for different stages of the loading process. We clearly observe a decrease of the gradient activity, and therefore of the nonlocal interaction, after the crack tip has passed and when the local crack growth has been completed. Indeed, in a phenomenological manner the observation is modelled that the nonlocal effect is related to phenomena as microcracking, crack bridging, debonding of the fibres and fibre pull-out, which gradually vanish upon growth to a full crack.

5. FINITE ELEMENT ASPECTS

For the formulation of the incremental boundary value problem in gradient-enhanced continua we introduce the displacement vector $\mathbf{u}$, the strain tensor in a vector form $\boldsymbol{\varepsilon}$ and the stress tensor in a vector format $\boldsymbol{\sigma}$. Under the assumption of small deformations, we have the equilibrium equations for a body occupying a volume V

$$\mathbf{L}^{\mathrm{T}}\boldsymbol{\sigma} + \mathbf{b} = \mathbf{0} \tag{18}$$

the kinematic equations

$$\boldsymbol{\varepsilon} = \mathbf{L}\mathbf{u} \tag{19}$$

and constitutive equations, cf. eq. (1) for simple, isotropic damage. $\mathbf{b}$ is a body-force vector

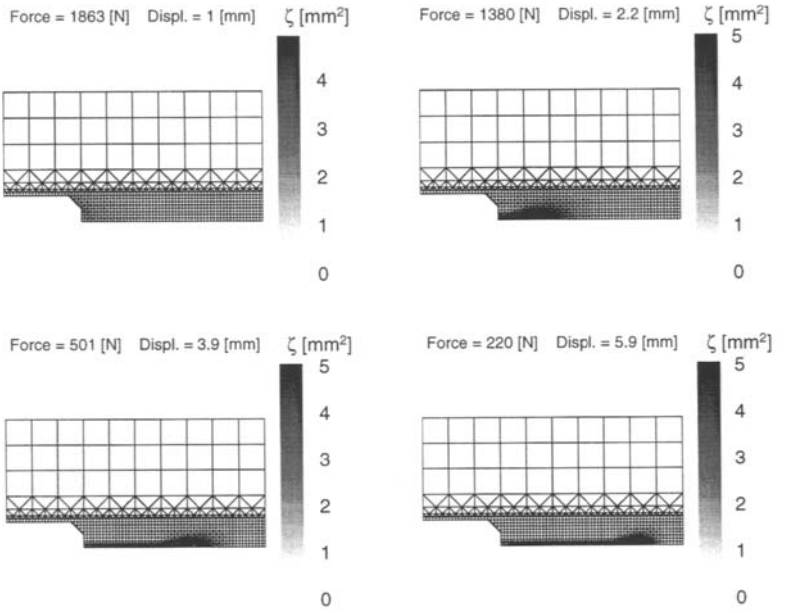

Figure 5. Evolution of the gradient activity ζ upon progressive deformation.

and $\mathbf{L}$ is a differential operator matrix which connects the strains to the displacements. To complete the incremental boundary value problem we have standard static and kinematic boundary conditions on complementary parts of the body surface S.

For the development of the finite element formulation of the gradient-enhanced damage model we start by transforming the governing equations for motion (18) and the 'nonlocal' equivalent strain $\bar{\varepsilon}_{eq}$, eq. (16), into a weak form:

$$\int_V \delta\mathbf{u}^T(\mathbf{L}^T\boldsymbol{\sigma} + \mathbf{b})\,dV = 0 \tag{20}$$

$$\int_V \delta\bar{\varepsilon}_{eq}(\bar{\varepsilon}_{eq} - \zeta\nabla^2\bar{\varepsilon}_{eq} - \varepsilon_{eq})\,dV = 0 \tag{21}$$

where the δ-symbol denotes the variation of a quantity. Using the divergence theorem, the standard boundary conditions with $\mathbf{t}$ the boundary tractions, and assuming a non-standard boundary condition of the form $\mathbf{n}^T(\zeta\nabla\bar{\varepsilon}_{eq}) = 0$, we obtain

$$\int_V (\mathbf{L}\delta\mathbf{u})^T\boldsymbol{\sigma}\,dV = \int_V \delta\mathbf{u}^T\mathbf{b}\,dV + \int_S \delta\mathbf{u}^T\mathbf{t}\,dS \tag{22}$$

$$\int_V [\delta\bar{\varepsilon}_{eq}\,\bar{\varepsilon}_{eq} + (\nabla\delta\bar{\varepsilon}_{eq})^T(\zeta\nabla\bar{\varepsilon}_{eq}) + \delta\bar{\varepsilon}_{eq}(\nabla\zeta)^T\nabla\bar{\varepsilon}_{eq} - \delta\bar{\varepsilon}_{eq}\,\varepsilon_{eq}]\,dV = 0 \tag{23}$$

According to eq. (23), gradients of ζ have to be computed. This is most elegantly accom-

plished by replacing ζ in eq. (23) by a continuous field variable z, such that

$$\int_V [\delta\bar{\varepsilon}_{eq}\,\bar{\varepsilon}_{eq} + (\nabla\delta\bar{\varepsilon}_{eq})^T(z\nabla\bar{\varepsilon}_{eq}) + \delta\bar{\varepsilon}_{eq}(\nabla z)^T\nabla\bar{\varepsilon}_{eq} - \delta\bar{\varepsilon}_{eq}\,\varepsilon_{eq}]\,dV = 0 \tag{24}$$

subject to the constraint

$$\int_V \delta z(z - \zeta)\,dV = 0 \tag{25}$$

A three-field theory is now obtained with the basic variables $\mathbf{u}$, $\bar{\varepsilon}_{eq}$ and z.

The set of equations (22), (24) and (25) is highly nonlinear and must be solved using an iterative procedure at structural level. The Newton-Raphson procedure is widely used for this purpose and has also been adopted in this study. This algorithm requires the linearization of the above set of equations. Care must be exercised that this linearization is carried out in a consistent fashion, since else the quadratic convergence of the method is lost. This linearization process has been carried out by Geers [26,27] and is briefly summarized below.

Since the damage variable ω is a function of the history parameter κ, which is coupled to the nonstandard equivalent strain $\bar{\varepsilon}_{eq}$, we have

$$d\omega = \frac{\partial\omega}{\partial\kappa}\frac{\partial\kappa}{\partial\bar{\varepsilon}_{eq}}\,d\bar{\varepsilon}_{eq} \tag{26}$$

and we can linearize the constitutive equation (1) as

$$d\boldsymbol{\sigma} = (1 - \omega_{i-1})\mathbf{D}\mathbf{L}d\mathbf{u} - \left(\frac{\partial\omega}{\partial\kappa}\right)_{i-1}\left(\frac{\partial\kappa}{\partial\bar{\varepsilon}_{eq}}\right)_{i-1}\mathbf{D}\boldsymbol{\varepsilon}_{i-1}d\bar{\varepsilon}_{eq} \tag{27}$$

where the d-symbol denotes the iterative changes of a variable from iteration i – 1 to i and the kinematic relation (19) has been used. We now substitute eq. (27) into eq. (22) to obtain

$$\int_V \delta\mathbf{u}^T\mathbf{L}^T\left[(1 - \omega_{i-1})\mathbf{D}\mathbf{L}d\mathbf{u} - \left(\frac{\partial\omega}{\partial\kappa}\right)_{i-1}\left(\frac{\partial\kappa}{\partial\bar{\varepsilon}_{eq}}\right)_{i-1}\mathbf{D}\boldsymbol{\varepsilon}_{i-1}d\bar{\varepsilon}_{eq}\right]dV$$

$$= \int_V \delta\mathbf{u}^T\mathbf{b}\,dV + \int_S \delta\mathbf{u}^T\mathbf{t}\,dS - \int_V (\mathbf{L}\delta\mathbf{u})^T\boldsymbol{\sigma}_{i-1}\,dV \tag{28}$$

In a similar fashion we can linearize eqs (24) and (25) as

$$-\int_V \delta\bar{\varepsilon}_{eq}\left(\frac{\partial\varepsilon_{eq}}{\partial\boldsymbol{\varepsilon}}\right)_{i-1}\mathbf{L}d\mathbf{u}\,dV + \int_V [\delta\bar{\varepsilon}_{eq}d\bar{\varepsilon}_{eq} + \delta\bar{\varepsilon}_{eq}(\nabla z_{i-1})^T\nabla d\bar{\varepsilon}_{eq} + \delta(\nabla\bar{\varepsilon}_{eq})^T z_{i-1}\nabla d\bar{\varepsilon}_{eq}]\,dV$$

$$+ \int_V [\delta\bar{\varepsilon}_{eq}(\nabla\bar{\varepsilon}_{eq,i-1})^T\nabla dz + \delta(\nabla\bar{\varepsilon}_{eq})^T\nabla\bar{\varepsilon}_{eq,i-1}dz]\,dV =$$

$$-\int_V \delta\bar{\varepsilon}_{eq}[\bar{\varepsilon}_{eq,i-1}+(\nabla\bar{\varepsilon}_{eq,i-1})^T\nabla z_{i-1}-\varepsilon_{eq,i-1}]\,dV-\int_V \delta(\nabla\bar{\varepsilon}_{eq})^T\nabla\bar{\varepsilon}_{eq,i-1}z_{i-1}\,dV \tag{29}$$

and

$$\int_V \delta z\left[-\left(\frac{\partial\zeta}{\partial\varepsilon_{eq}}\right)_{i-1}\left(\frac{\partial\varepsilon_{eq}}{\partial\boldsymbol{\varepsilon}}\right)_{i-1}\mathbf{L}d\mathbf{u}+dz\right]dV=-\int_V \delta z(z_{i-1}-\zeta_{i-1})\,dV \tag{30}$$

The finite element discretization is now rather straightforward. We interpolate the displacements $\mathbf{u}$, the nonstandard equivalent strain $\bar{\varepsilon}_{eq}$ and the gradient activity z by

$$\mathbf{u}=\mathbf{N}_a\mathbf{a} \tag{31}$$

$$\bar{\varepsilon}=\mathbf{N}_\varepsilon\bar{\boldsymbol{\varepsilon}}_{eq} \tag{32}$$

$$z=\mathbf{N}_z\mathbf{z} \tag{33}$$

with $\mathbf{N}_a$, $\mathbf{N}_\varepsilon$ and $\mathbf{N}_z$ matrices which contain the interpolation polynomials for the displacements, the nonstandard equivalent strains and the gradient activity, respectively, and $\mathbf{a}$, $\bar{\boldsymbol{\varepsilon}}_{eq}$ and $\mathbf{z}$ vectors that contain the nodal degrees of freedom for the displacements, the nonstandard equivalent strains and the gradient activity. The strains $\boldsymbol{\varepsilon}$ and the gradients of $\bar{\varepsilon}_{eq}$ and z are then obtained as

$$\boldsymbol{\varepsilon}=\mathbf{B}_a\mathbf{a} \tag{34}$$

$$\nabla\bar{\varepsilon}_{eq}=\mathbf{B}_\varepsilon\bar{\boldsymbol{\varepsilon}}_{eq} \tag{35}$$

$$\nabla z=\mathbf{B}_z\mathbf{z} \tag{36}$$

where $\mathbf{B}_a=\mathbf{L}\mathbf{N}_a$, $\mathbf{B}_\varepsilon=\nabla\mathbf{N}_\varepsilon$ and $\mathbf{B}_z=\nabla\mathbf{N}_z$ contain the derivatives of the respective shape functions. Substitution of eqs (31)-(36) into the linearized equations (28)-(30) and requiring that the result holds for any kinematically admissible discrete nodal variation $\delta\mathbf{a}$, $\delta\bar{\boldsymbol{\varepsilon}}_{eq}$ and $\delta\mathbf{z}$ then results in

$$\begin{bmatrix}\mathbf{K}_{aa} & \mathbf{K}_{a\varepsilon} & \mathbf{0}\\ \mathbf{K}_{\varepsilon a} & \mathbf{K}_{\varepsilon\varepsilon} & \mathbf{K}_{\varepsilon z}\\ \mathbf{K}_{za} & \mathbf{0} & \mathbf{K}_{zz}\end{bmatrix}\begin{bmatrix}d\mathbf{a}\\ d\bar{\boldsymbol{\varepsilon}}_{eq}\\ d\mathbf{z}\end{bmatrix}=\begin{bmatrix}\mathbf{f}_a\\ \mathbf{f}_\varepsilon\\ \mathbf{f}_z\end{bmatrix} \tag{37}$$

with the vectors $\mathbf{f}_a$, $\mathbf{f}_\varepsilon$ and $\mathbf{f}_z$ defined as

$$\mathbf{f}_a=\int_V \mathbf{N}_a^T\mathbf{b}\,dV+\int_S \mathbf{N}_a^T\mathbf{t}\,dS-\int_V \mathbf{B}_a^T\boldsymbol{\sigma}_{i-1}dV \tag{38a}$$

$$\mathbf{f}_\varepsilon=-\int_V(\mathbf{N}_\varepsilon^T\mathbf{N}_\varepsilon\bar{\boldsymbol{\varepsilon}}_{eq,i-1}+\mathbf{N}_\varepsilon^T\bar{\boldsymbol{\varepsilon}}_{eq,i-1}^T\mathbf{B}_\varepsilon^T\mathbf{B}_z\mathbf{z}_{i-1}+\mathbf{B}_\varepsilon^T\mathbf{B}_\varepsilon\boldsymbol{\varepsilon}_{eq,i-1}\mathbf{N}_z\mathbf{z}_{i-1}-\mathbf{N}_\varepsilon^T\varepsilon_{eq,i-1})\,dV \tag{38b}$$

$$\mathbf{f}_z = -\int_V \mathbf{N}_z^{\mathrm{T}}(\mathbf{N}_z\mathbf{z}_{i-1} - \zeta_{i-1})\,\mathrm{d}V \tag{38c}$$

and the tangential submatrices

$$\mathbf{K}_{aa} = \int_V (1 - \omega_{i-1})\mathbf{B}_a^{\mathrm{T}}\mathbf{D}\mathbf{B}_a\,\mathrm{d}V \tag{39a}$$

$$\mathbf{K}_{a\varepsilon} = \int_V \left(\frac{\partial\omega}{\partial\kappa}\right)_{i-1}\left(\frac{\partial\kappa}{\partial\bar{\varepsilon}_{eq}}\right)_{i-1}\mathbf{B}_a^{\mathrm{T}}\mathbf{D}\boldsymbol{\varepsilon}_{i-1}\mathbf{N}_\varepsilon\,\mathrm{d}V \tag{39b}$$

$$\mathbf{K}_{\varepsilon a} = -\int_V \mathbf{N}_\varepsilon^{\mathrm{T}}\left(\frac{\partial\varepsilon_{eq}}{\partial\boldsymbol{\varepsilon}}\right)_{i-1}\mathbf{B}_a\,\mathrm{d}V \tag{39c}$$

$$\mathbf{K}_{\varepsilon\varepsilon} = \int_V (\mathbf{N}_\varepsilon^{\mathrm{T}}\mathbf{N}_\varepsilon + \mathbf{N}_\varepsilon^{\mathrm{T}}\mathbf{z}_{i-1}\mathbf{B}_z^{\mathrm{T}}\mathbf{B}_\varepsilon + \mathbf{B}_\varepsilon^{\mathrm{T}}\mathbf{N}_z\mathbf{z}_{i-1}\mathbf{B}_\varepsilon)\,\mathrm{d}V \tag{39d}$$

$$\mathbf{K}_{\varepsilon z} = \int_V (\mathbf{N}_\varepsilon^{\mathrm{T}}\bar{\boldsymbol{\varepsilon}}_{eq,i-1}^{\mathrm{T}}\mathbf{B}_z^{\mathrm{T}}\mathbf{B}_z + \mathbf{B}_\varepsilon^{\mathrm{T}}\mathbf{B}_\varepsilon\bar{\boldsymbol{\varepsilon}}_{eq,i-1}\mathbf{N}_z)\,\mathrm{d}V \tag{39e}$$

$$\mathbf{K}_{za} = -\int_V \mathbf{N}_z^{\mathrm{T}}\left(\frac{\partial\zeta}{\partial\varepsilon_{eq}}\right)_{i-1}\left(\frac{\partial\varepsilon_{eq}}{\partial\boldsymbol{\varepsilon}}\right)_{i-1}\mathbf{B}_a\,\mathrm{d}V \tag{39f}$$

$$\mathbf{K}_{zz} = \int_V \mathbf{N}_z^{\mathrm{T}}\mathbf{N}_z\,\mathrm{d}V \tag{39g}$$

6. NONLOCAL VERSUS GRADIENT DAMAGE MODELS

To gain some insight into the properties of the nonlocal versus the gradient damage models, a dispersion analysis is now carried out for a one-dimensional bar of infinite length [6,31]. We shall briefly summarize the main results of such an investigation that has been carried out for the nonlocal damage model with averaging on the equivalent strain and a constant internal length scale l, and the two related gradient models (explicit and implicit format, eqs (14) and (15), respectively) [25].

In a dispersion analysis a perturbation of the form

$$\delta u = \hat{u}e^{\mathrm{i}k(x - c_f t)} \tag{40}$$

is introduced into the governing set of equations, namely the equation of motion, the kinematic relation and the constitutive model, which have been combined to give a single expression in terms of the axial displacement of the bar and have been linearized around a homogeneous deformation state indicated with the subscript 0. In eq. (40) k is the wave number, c_f is the

corresponding phase velocity and $\hat{u}$ is the amplitude of the perturbation. The following expressions are obtained for the phase velocity [25]:

❑ Non-local damage model, eq. (6):

$$c_f = c_e \sqrt{1 - \omega_0 - \varepsilon_0 \left(\frac{\partial \omega}{\partial \kappa}\right)_0 e^{-k^2/2l^2}} \tag{41}$$

❑ Gradient damage model in explicit format, eq. (14):

$$c_f = c_e \sqrt{1 - \omega_0 - \varepsilon_0 \left(\frac{\partial \omega}{\partial \kappa}\right)_0 (1 - {}^1/_2 k^2 l^2)} \tag{42}$$

❑ Gradient damage model in implicit format, eq. (15):

$$c_f = c_e \sqrt{1 - \omega_0 - \varepsilon_0 \left(\frac{\partial \omega}{\partial \kappa}\right)_0 (1 + {}^1/_2 k^2 l^2)^{-1}} \tag{43}$$

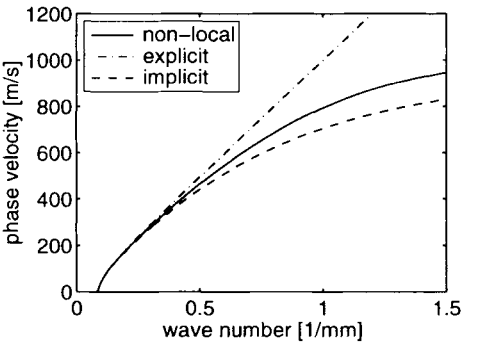

Figure 6. Wave velocity as function of wave number.

In eqs (41)-(43) c_e is the elastic wave velocity, ε_0 is the existing strain level and ω_0 is the corresponding value of the damage parameter. The following material data were used: a Young's modulus E = 20,000 MPa, a density such that c_e = 1000 m/s, a linear degrading damage model with an initial value κ_i = 0.0001, a value κ_c = 0.0125 at which the local load-carrying capacity is exhausted, and an internal length scale $l = \sqrt{2}$ mm. Taking a strain level $\varepsilon_0 = \kappa_i$, the curves of Figure 6 are obtained.

We observe that all three models result in a cut-off wave number below which loading waves cannot propagate, i.e. the wave speed becomes imaginary. This phenomenon was also found for gradient-enhanced plasticity models [4,6,20]. However, the cut-off wave number now depends on the existing strain level, and as seen in Figure 7, the critical wave length becomes smaller for increasing deformation, in contrast to gradient plasticity where it remains constant. Also, the three different damage models start to differ at increasing strain levels. The most salient observation is that while the nonlocal damage model and the gradient model in an implicit format approach a zero wave length, and therefore a physically realistic vanish-

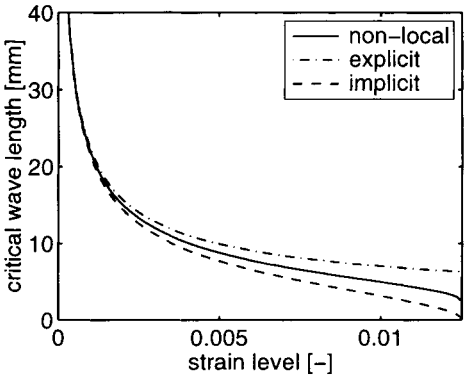

Figure 7. Cut-off wave length as function of strain level.

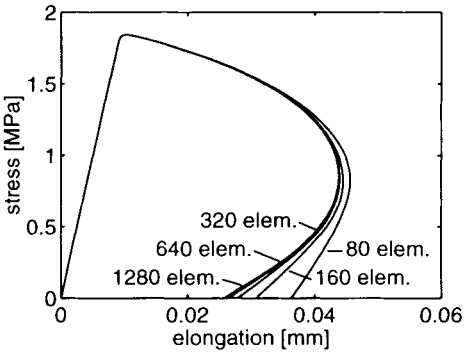

Figure 8. Load-deflection curves at mesh refinement (implicit gradient model).

ing localization zone for large strain levels, this is not so for the gradient damage model in an explicit format, thus precluding a gradual transition into a line crack.

Next, we consider a bar with a finite length, L = 100 mm, and take an imperfection (10% reduction of the cross sectional area A) in the centre 10 mm of the bar. Now, for reasons mentioned above, numerical computations have been carried out only for the implicit gradient damage model and for the nonlocal damage model, but not for the explicit gradient damage model. In the first case a full constrained Newton-Raphson procedure was adopted [24], while a secant stiffness method was used for the nonlocal damage model. It appeared that the nonlocal damage model requires a less fine discretization than the implicit gradient damage model, as the results for an 80 element and for a 160 element discretization already coincide in the nonlocal approach, while this is not the case for the implicit gradient model, Figure 8. On the other hand, convergence in terms of equilibrium iterations is much better for the gradient model, and fully converged solutions could be obtained until almost a zero residual load level, Figures 8 and 9. The equilibrium-finding iterative procedure for the nonlocal model fails at a non-zero residual load level. In fact, for finer discretizations the iterative procedure diverges at an earlier stage in the loading process. Figure 9 compares the load-deflection curves for both

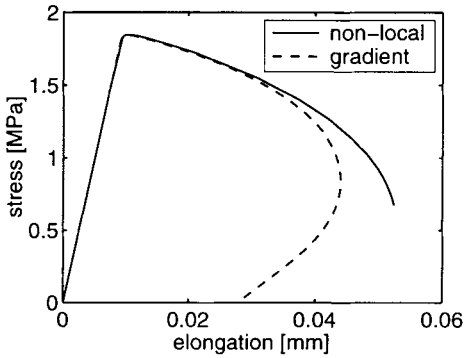

Figure 9. Comparison of the nonlocal and implicit gradient models.

models for a discretization of 320 elements. We observe that upon further loading, the differences between both models become more pronounced and that at a certain stage convergence is lost for the nonlocal damage model.

7. CONCLUDING REMARKS

A family of gradient-enhanced damage models has been described where the damage is coupled to elasticity. Although they can be related to nonlocal damage models in an integral format, their properties are in some cases quite different from those of nonlocal integral-type damage models, as has been shown by dispersion analyses and by a simple one-dimensional example. For a particular gradient-enhanced damage model an enhancement has been suggested, which eliminates the widening of the damage zone which is observed upon fracture propagation in enhanced damage models where the internal length scale remains constant. For this model, a computationally efficient scheme has been described, which opens the way to large-scale computations.

REFERENCES

[1] A. Benallal, R. Billardon and G. Geymonat (1988) Some mathematical aspects of the damage softening rate problem, in J. Mazars and Z.P. Bazant (eds.), *Cracking and Damage,* Elsevier, Amsterdam and London, pp. 247-258.

[2] A. Needleman (1988) Material rate dependence and mesh sensitivity in localization problems, *Comp. Meth. Appl. Mech. Eng.* **67** , 69-86.

[3] B. Loret and J.H. Prévost (1990) Dynamic strain localization in elasto-(visco-)plastic solids, Part 1, *Comp. Meth. Appl. Mech. Eng.* **83** , 247-273.

[4] L.J. Sluys (1992) *Wave propagation, localisation and dispersion in softening solids,* Dissertation, Delft University of Technology, Delft.

[5] L.J. Sluys and R. de Borst (1992) Wave propagation and localisation in a rate-dependent cracked medium - Model formulation and one-dimensional examples, *Int. J. Solids Structures* **29** ,

2945-2958.
[6] L.J. Sluys and R. de Borst (1992) Dispersive properties of gradient-dependent and rate-dependent media, *Mech. Mater.* **18** , 131-149.
[7] H.-B. Mühlhaus and I. Vardoulakis (1987) The thickness of shear bands in granular materials, *Geotechnique* **37** , 271-283.
[8] R. de Borst (1991) Simulation of strain localisation: A reappraisal of the Cosserat continuum, *Engng. Comput.* **8** , 317-332.
[9] R. de Borst (1993) A generalisation for J_2-flow theory for polar continua, *Comp. Meth. Appl. Mech. Eng.* **103** , 347-362.
[10] G. Pijaudier-Cabot and Z.P. Bazant (1987) Nonlocal damage theory, *J. Engng. Mech.* **113** , 1512-1533.
[11] E.C. Aifantis (1984) On the microstructural origin of certain inelastic models, *J. Engng. Mater. Technol.* **106** , 326-334.
[12] E.C. Aifantis (1987) The physics of plastic deformation, *Int. J. Plasticity* **3** , 211-247.
[13] E.C. Aifantis (1992) On the role of gradients in the localization of deformation and fracture, *Int. J. Engng. Sci.* **30** , 1279-1299.
[14] H.-B. Mühlhaus and E.C. Aifantis (1991) A variational principle for gradient plasticity, *Int. J. Solids Structures* **28** , 845-858.
[15] I. Vardoulakis and E.C. Aifantis (1991) A gradient flow theory of plasticity for granular materials, *Acta Mechanica* **87** , 197-217.
[16] H.L. Schreyer and Z. Chen (1986) One-dimensional softening with localization, *J. Appl. Mech.* **53** , 791-797.
[17] R. de Borst and H.-B. Mühlhaus (1992) Gradient-dependent plasticity: Formulation and algorithmic aspects, *Int. J. Num. Meth. Eng.* **35** , 521-539.
[18] R. de Borst and J. Pamin (1996) Some novel developments in finite element procedures for gradient-dependent plasticity, *Int. J. Num. Meth. Eng.* **39** , 2477-2505.
[19] R. de Borst and J. Pamin (1996) Gradient plasticity in numerical simulation of concrete cracking, *Eur. J. Mechanics: A/Solids,* **15** , 295-320.
[20] L.J. Sluys, R. de Borst and and H.-B. Mühlhaus (1993) Wave propagation, localization and dispersion in a gradient-dependent medium, *Int. J. Solids Structures* **30** , 1153-1171.
[21] H.-B. Mühlhaus, R. de Borst, L.J. Sluys and J. Pamin (1994) A thermodynamic theory for inhomogeneous damage evolution, in H.J. Siriwardane and M.M. Zaman (eds.), *Computer Methods and Advances in Geomechanics,* Balkema, Rotterdam and Boston, pp. 635-640.
[22] R. de Borst, A. Benallal and O.M. Heeres (1996), A gradient-enhanced damage approach to fracture, *J. de Physique IV,* **C6** , 491-502.
[23] C. Comi, Computational modelling of gradient-enhanced damage in quasi-brittle materials, *Mech. Coh.-frict. Mat.* , submitted for publication.
[24] R.H.J. Peerlings, R. de Borst, W.A.M. Brekelmans and J.H.P. de Vree (1996) Gradient-enhanced damage for quasi-brittle materials, *Int. J. Num. Meth. Eng.* **39** 3391-3403.
[25] R.H.J. Peerlings, R. de Borst, W.A.M. Brekelmans, J.H.P. de Vree and Spee, I. (1996) Some observations on localisation in non-local and gradient damage models, *Eur. J. Mech./A: Solids,* **15** , 937-954.
[26] M.G.D. Geers (1997) *Experimental Analysis and Computational Modelling of Damage and Fracture,* Dissertation, Eindhoven University of Technology, Eindhoven.
[27] M.G.D. Geers, R. de Borst, W.A.M. Brekelmans and R.H.J. Peerlings, Strain-based transient-gradient damage model for failure analyses, *Comp. Meth. Appl. Mech. Eng.* , accepted for publication.
[28] J.C. Simo and J.W. Ju (1987) Strain and stress-based continuum damage models: I. Formulation, *Int. J. Solids Structures* **23** , 821-840.
[29] J. Lemaitre and J.L Chaboche (1990) *Mechanics of Solid Materials,* Cambridge University Press, Cambridge.
[30] J. Mazars and G. Pijaudier-Cabot (1989). Continuum damage theory - application to concrete, *J. Eng. Mech.* **115** , 345-365.
[31] A. Huerta and G. Pijaudier-Cabot (1994) Discretization influence on the regularization by two localization limiters, *J. Eng. Mech.* **120** , 1198-1218.

Damage Mechanics in Engineering Materials
G.Z. Voyiadjis, J.-W.W. Ju and J.-L. Chaboche (Editors)
© 1998 Elsevier Science B.V. All rights reserved.

Catastrophic slip phenomena in crystalline materials

A.Korbel *, K.Korbel *, R.B.Pęcherski **

* Academy of Mining and Metallurgy, Kraków, Mickiewicza 30, Poland
** Institute of Fundamental Problems of Technics , Warszawa, Świętokrzyska 21, Poland

In the work the experimental observations on single and polycrystalline metals are used to show the need for a new approach to crystal plasticity in which three aspects of slip: mechanistic, geometrical and structural are incorporated. A particular attention is paid to the effect of a sequential operation of slip systems. The arguments that the change in the deformation bearing systems leads to the catastrophic coarse slip in single crystals and to shear banding in polycrystalline metals are provided. The model of the sequential multi-system slip is shown along with the results of the numerical calculations of the crystal behavior. The criterion for micro-shear banding is discussed on the basis of the features of micro-shear bands in metallic materials.

1. INTRODUCTION

Except of particular conditions, like high temperature and/or very low stress, plastic flow of crystalline materials results from slip. The experimental studies, briefly summarized in [1] show that localization of strain has to be considered as the particular mode of plastic flow which in a single crystal receives the form of catastrophic (coarse) slip, while in polycrystals it takes the form of a trans-granular shear (shear band). Appearance of such forms of slip clearly points to the evolution of slip extent during deformation. Hence, the analytical account for this evolution may be an alternative way to predict the global performance of crystals during plastic yielding. In such approach three aspects of slip: mechanistic, geometrical and structural, must be simultaneously taken into consideration in order to obtain coherent and fully consistent with experimental facts description of the crystal behavior. It seems to be the way to predict the strain hardening of crystals oriented for a single system glide, the latent hardening effects and the condition of the change from a fine (homogeneous) slip behavior into a coarse , localized slip. The experimentally proved role of the coarse slip within individual grains of a polycrystalline aggregate as a precursor of micro shear bands strengthens the idea that shear banding is the latest stage of the slip evolution and makes that the analytical description of slip behavior in a single crystal may provide the basis for prediction of the global behavior of polycrystals.

In this work the experimental observations on single and polycrystalline metals are used to show the need for a new approach to crystal plasticity in which the already mentioned

aspects of slip in crystals are incorporated. The numerical analysis is aimed to predict the formation and evolution of the crystal substructure and, consequently, the evolution of slip features in the course of straining. To accomplish this goal it is assumed that slip in a crystal (individual grain of a polycrystalline aggregate) begins in one system, and activation of secondary systems has a sequential character and varies in tact with evolution of the scheme of loading . The latter is defined from the geometry of slip (geometrical constraints) which via reaction (elastic) stress, the crystal reorientation and throughout the slip criterion activates the secondary slip systems and controls the amount of shear in the operating systems. The first analytical results are compared with experimental observations of slips in single crystals. The meaning of the sequential multi-system slip is discussed in terms of the accumulation of dislocations in particular systems (obstacles pattern), associated evolution of slip, the stability of the substructure and the conditions for the breakdown in the slip evolution law into catastrophic (trans-substructural) coarse slip and into micro-shear band.

2. THE NATURE AND EVOLUTION OF SLIP - experimental basis for modelling

At the background of the analysis there are some common and fundamental experimental observations. The first is that slip is a highly anisotropic form of the response of crystal to the applied load. Therefore, slip begins in that of the crystallographically equivalent systems in which the lattice resistance to shear (movement of dislocations) is the least and in which the resolved shear stress is the highest. Hence the criterion for slip [2] which may be written in the following generalized form:

$$\tau = \sigma : \mathbf{b} \otimes \mathbf{n}, \qquad (1)$$

selectively chooses a slip system at the onset of plastic yielding. This causes that in most (if not all) cases of the scheme of loading the first amount of slip occurs in one slip system. This argument may be used also for the case of a symmetrical orientation of crystal in which the resolved shear stress is the same for a few systems, simply because the ideal symmetrical orientation is highly unlike. In addition, because of the lattice imperfections, even then the local conditions favor the choice of a single system slip.

In a microstructural scale slip is a physical act which comprises generation and movement of dislocations in the common plane. The extent of these elementary slip events - area swept or the mean free path of the dislocation glide λ, and the number of dislocations generated ρ - are the intrinsic features of slip. They have the topological representation in the pattern of slip lines on the crystal surface. The effect of several evenly distributed slip events in a system is equivalent to the homogeneous shear $\gamma = (b \cdot N \cdot \lambda \cdot dA/V)$ of the body or in a simplified form $\gamma = b \cdot \rho \cdot \lambda$ (Orovan relationship). An associated effect is the accumulation of dislocations, which gives rise to the formation of substructure (the obstacles network).

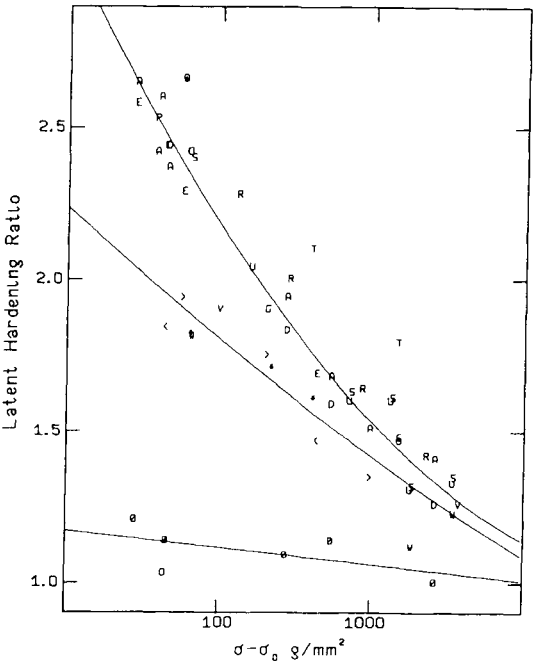

Fig.1. The latent hardening effect after Basinski & Jackson [3]

Therefore, if the criterion for the slip is met, then some amount of shear is carried by the slip system leading to accumulation of dislocations in the active slip plane. In consequence, the initial equivalence of crystallographically identical systems is lost. This structural aspect of slip is well exposed by the latent hardening ratio (the value of flow stress in a secondary system to that in the deformation bearing one). As it is shown in Fig.1, this ratio jumps dramatically from the value 1 (before deformation) to the value of the order of 3 if a small slip takes place in the „primary system". This fact prompts one to accept that activation of the other system, which is necessary in order to accomplish the requested permanent change of the crystal shape, follows in a sequential manner.

This is the most important experiment born conclusion, which has to be at the background of the construction of a model of evolution of crystals behavior. Such an approach to crystal plasticity is substantially different from the so far developed models, which rely upon the assumption of a simultaneous multi-system slip, and especially those based upon Taylor [4} or Bishop and Hill [5] arguments. The basic difference concerns the identification of the operative slip systems and the amount of shear in each of them, and consequently, it pertains to the associated structural effects like rotation of the crystal lattice relative to the loading system and accumulation of dislocations in different slip planes (formation and stability of the obstacles network). In the case of a sequential operation of slip systems, it is impossible to predict „a priori" which systems are brought into operation and how big is the shear they carry until the geometrical aspect of slip and the associated evolution of the loading scheme are considered. This statement meets a very convincing

experimental evidence in the observations of slip activity, evolution of slip extent and strain hardening of a single crystal oriented for a single slip in the uniaxial tension experiment.

Let us , therefore, briefly summarize the observations for a FCC crystal loaded along the <145> lattice direction. Then, while rising the tensile force, the yield criterion is met only for one of the twelve crystallographically equivalent systems - [101](111). The orientation of the crystal causes that the applied load favors slip only in this system over a very large (of the order of 50%) elongation of the crystal, making that this system is the deformation bearing system. Inspection of the tensile characteristics of such an oriented crystal, like that quoted after Basinski [6] in Fig.2, shows that already after small deformation (stage of easy glide) the hardening rate rises very quickly to the level of $10^{-2}\,\mu$ which is the highest rate of strain hardening of the crystal. The extent of the easy glide increases to several percent of crystal elongation with the increase of the initial critical slip stress as it was shown for the first time in the pioneer works of Sachs and co-workers on single crystals of Cu, Cu-Zn and Ag-Au alloy single crystals [7-9]. This stage is commonly interpreted as the range of the single slip activity just because of the lack of hardening and very large, strain independent slip extent (length of slip lines) [10]. Accumulation of dislocations in the primary system leads to formation of the obstacles network in the form of parallel dislocation walls along active slip planes, which do not interfere with the slip on parallel slip planes in-between the walls. A sudden rise of the hardening in a transient region between the first and the second stage of deformation has to be, therefore, associated with the appearance of slip in secondary systems (forest hardening).

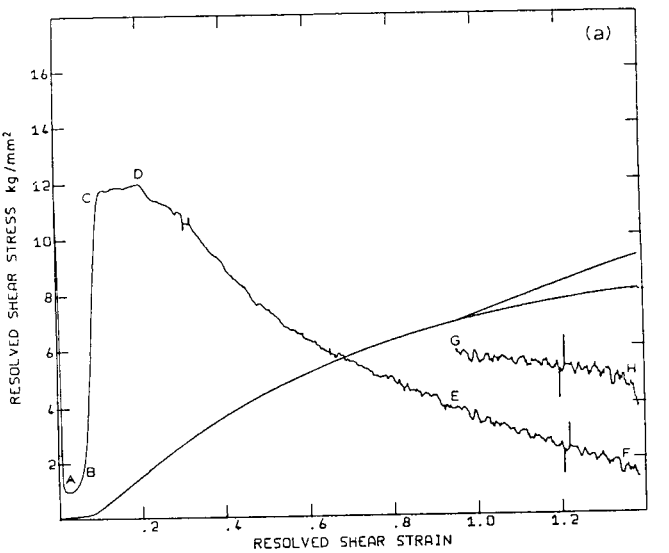

Fig.2 Tensile characteristics of a single slip oriented Cu single crystal and variation of strain hardening rate in the course of straining after [6].

Figure 3 shows the slip line pattern at the beginning (a) and at the end of the easy glide stage of the deformation (b) of Cu-Al crystal proving that the slip line length in this stage is constant and that progress in straining results from the increase of the number of slip events (number of slip lines) in the same system.

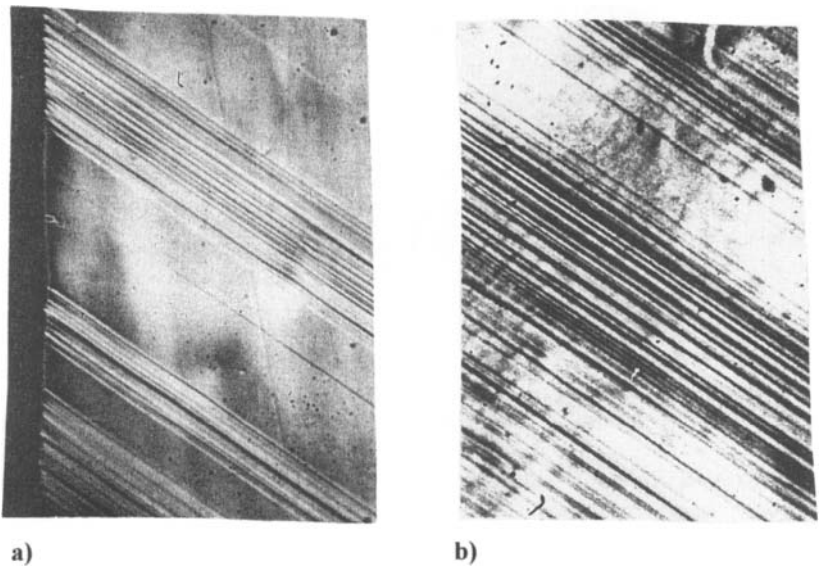

Fig.3. Slip patterns in Cu-Al single crystal at the beginning (a), and at the end of the easy glide (b).

The onset of the second stage of deformation coincides with the beginning of the slip evolution, as it is shown in Fig.4 [10]. It has been found that the slip line length is inversely proportional to the second stage deformation of the crystal [6,10]. The experimental observations clearly show that the transient from the first to the second stage of a single crystal hardening is associated with slip in the secondary [011](111) system which is termed the conjugate system to emphasize that it comes into operation in a feedback with the primary system. Dislocations accumulating in this system form the obstacles network for slip in the primary system (Fig.5) giving rise to slip evolution and the strain hardening (Fig.2).

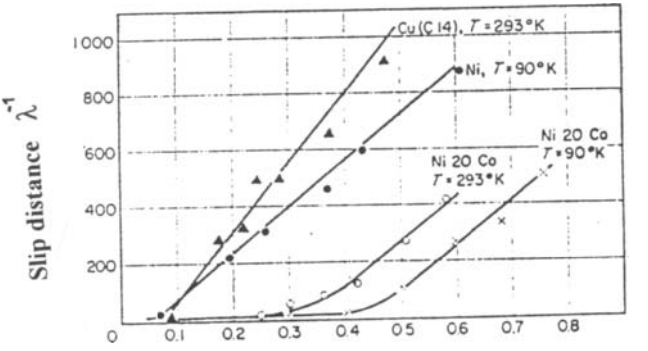

Fig.4. The evolution of the slip length in the primary system in the course of straining of FCC

Fig.5 Slip pattern typical for the second stage of deformation (the highest strain hardening) in Cu-Al single crystal showing the slip activity in the primary and the conjugate systems.

There is a very important experimental information that the orientation factor for slip in the conjugate system is then 2.5 times smaller than that in the primary system, and along with the latent hardening ratio (about 2.5) it makes that the applied stress at the moment of conjugate slip activation has to be roughly 6 times higher than that being measured . In terms of the applied stress argument it is impossible to justify the slip, proved also experimentally in the „cross slip" system. For these systems the orientation factor is zero and it remains zero throughout the second stage of deformation of a single crystal for typical orientations with tensile axis lying in the cross slip plane. There exists, therefore, other cause of the activation of the secondary systems than the sole applied stress. Slip in the secondary systems has to be therefore considered as the accommodating slip, which is driven by the reaction stress resulting from the forbidden components of the deformation tensor under tensile conditions. This reaction stress has to be precisely evaluated in order to identify the secondary slip systems, the sequence of their operation and the amount of shear they carry in every instant of sequential operation. This has been recently exposed in an analytical work on the effect of sequential slip upon the description of the plastic deformation of crystals[11]. It is shown there that only under very special conditions the simultaneous double system slip yields the same result as a sequential operation of these systems. Fig.6 gives a simple illustration of the effect of the amount of the shear increment $d\gamma$ (the same for each system) upon the rotation of the two initially orthogonal edges of a hypothetical crystal after the commutative operation of two slip systems symmetrically disposed within the crystal. From this figure one can find that for the same cumulated deformation in the systems the geometrical change of the crystal faces is not unique and depends upon the value of the strain increments in the systems.

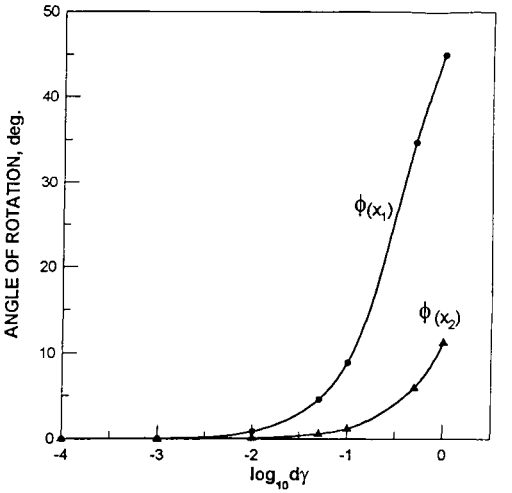

Fig.6. The effect of the increment of deformation during sequential operation of two symmetrically disposed slip systems upon the rotation of edges of a hypothetical crystal.

From the point of view of the evolution of the slip behavior the answer to the question which system and when comes into operation and how much shear it carries is crucial. This conclusion meets support in the results of the strain path change experiments on single and polycrystalline metals which have to be considered as the second most important information about the nature of slip in crystals. Jakson and Basinski [3] have shown that the plastic flow during the subsequent deformation (i.e. in a sample taken from the parent crystal after it had undergone some initial plastic deformation) was unstable if the secondary deformation employed a slip system different than that used in the primary straining. The slip in a secondary system took then the form of a coarse slip which extended across the existing substructure (obstacles network). These facts point to a mechanical instability of the dislocation substructure during the slip in a secondary system providing, however, that the secondary system becomes the deformation bearing one. This last statement follows the experimental observation of the so called „overshoot instability" which is observed often to terminate uniform deformation during tension of single crystals when the orientation factor becomes the highest for the secondary (conjugate) system.[12].

The observations of the behavior of single crystals of alloys subjected to tension in the symmetrical (double system slip) orientation [7, 13] (Fig.7) and Basinski's observations that in such orientation the tensile axis passes several times the symmetry [001]-[111] line during straining [14] provide another proof that the operation of slip systems is sequential and that some critical amount of shear in a system is needed to destabilize the existing substructure. It results in the catastrophic trans-substructural coarse slip development. Such a response of slip to the change of the deformation bearing system suggests that the collapse of the substructure which opens the way for the catastrophic slip (by making an easy path for the dislocation

motion) is a direct effect of the slip geometry. This may happen in the case of a dislocation wall made of primary dislocation dipoles . Rotation of the wall due to slip in a secondary, noncoplanar system leads to the collapse of the wall if the opposite dipole segments are brought to the common slip plane. This may happen provided that the shear in the secondary system is sufficiently large. This, in turn, means that the criterion for coarse slip is met when the deformation conditions lead to a change of the deformation bearing system and may be met if the accommodating slip destabilizes the obstacles network.

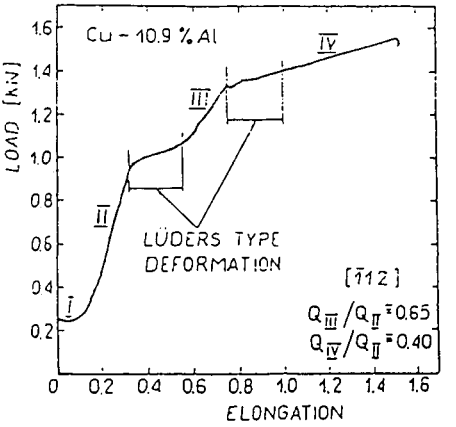

Fig.7. The tensile stress-strain curve of Cu-Al single crystal oriented for double system slip [13].

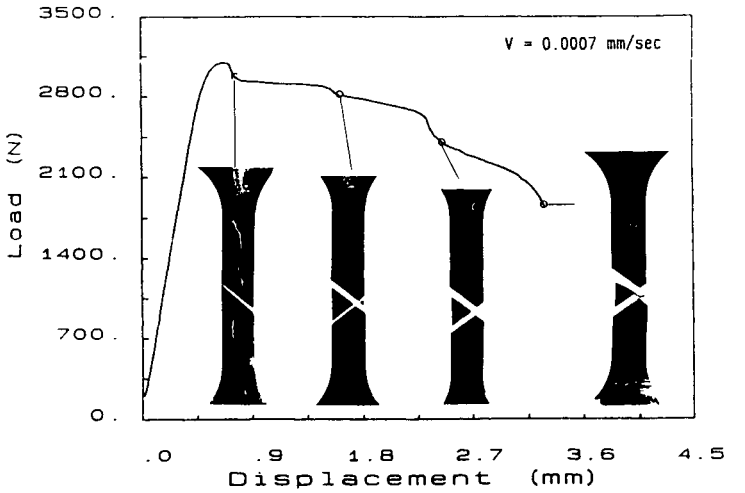

Fig.8. The tensile characteristics and macroscopic shear bands in polycrystalline iron formed during tension after primary rolling deformation [15].

Such a purely geometric (athermal) effect of the sequential slip must be taken into consideration in order to understand the evolution of the metal substructure and its stability in the course of deformation. This argument is valid also for polycrystals. The experiments

performed on polycrystalline metals clearly show that the change of the scheme of straining, which on the level of an individual grain means the change in the deformation bearing system, leads to the macroscopic strain localization in shear bands [15-19]. The example of such a response of the slip to the change of the scheme of straining from rolling to tension along the transverse direction is shown in Fig.8

Optical microscope observations show that the macroscopic band is composed of a set of parallel micro-shear bands, maintaining the same position in the sample as the macroscopic band (Fig.10). They show also that formation of micro-shear bands in polycrystals is preceded by formation of coarse slip bands within individual grains whose positions follow the orientation of crystallographically preferred slip systems [o-k-g]. Such a behavior could be forecast on the basis of the already given arguments. Basinski and Jackson argued [3] that in polycrystals „since due to grain boundary constraints the slip system operative in individual grains will be forced to change as the deformation proceeds". Such changes must promote coarse slip within grains, which develops along with the homogeneous fine slip deformation. A simultaneous operation of two modes of slip may account for the fact that the strain hardening rate in polycrystals is never as high as in the second stage of a single crystal deformation. The argument used by Basinski and Jackson addresses the criterion for coarse slip development (precursors of micro shear bands) to the effect of secondary slip. At the same time, the activation of a secondary slip system is ascribed to the constraints induced evolution of the stress state in the material. Therefore, either an analytical or a numerical account for the constraints effect on the choice of the operating slip system within individual grains seems to be the key to understand the performance of the polycrystalline metals. The conversion of coarse slip event into a micro-shear band appears in such circumstances as the next stage of the slip evolution which possesses its own characteristic features. The very peculiar feature of this mode of deformation is that deformation is concentrated within the very narrow (0.1 - 0.2μm) layers (micro shear bands) which extend across several grains of a polycrystalline aggregate keeping the same position in the material as is shown in Fig.9.

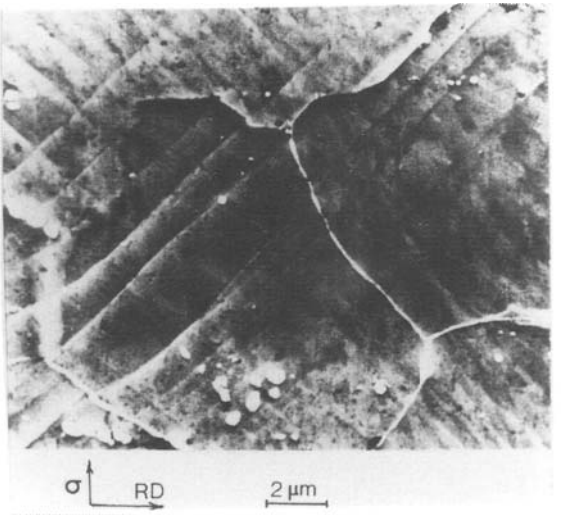

Fig.9. Microstructure features of shear banding in Armco iron [15].

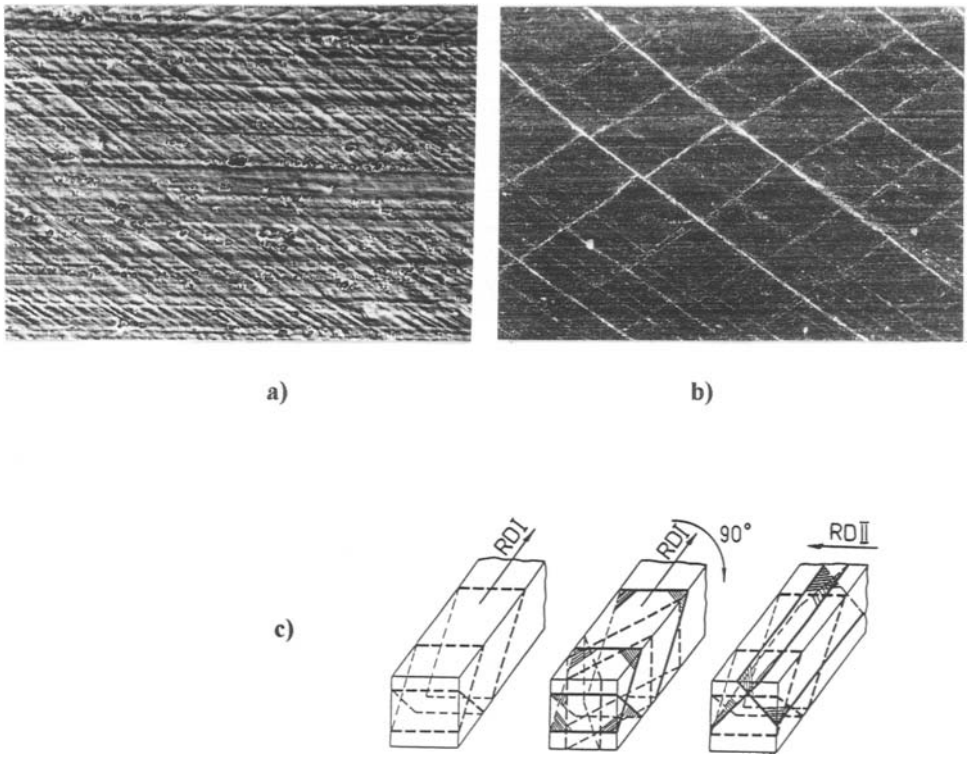

Fig.10. Different spatial distribution of micro-shear bands in Aluminum alloy (a,b) and the effect of the scheme of loading upon their orientation in the sample[17].

The position of shear bands in the material is sensitive to the scheme of loading, but not to the material structure and texture [15-18]. These properties of micro shear bands, along with the experimental evidence that the deformation within the band is a simple shear deformation [19], prompts one to accept that slip in crystals may also occur in other than the crystallographically preferred slip systems. The experiments reveal that the conditions allowing to activate another - „non-easy" system are closely connected with the structure destabilization due to the change of the deformation path . A criterion for activation of non-easy slip systems and transmission of slip across a grain boundary has already been proposed [20]. Practical use of such a criterion is , however, conditioned by the first demand - formation of a „soft path" for a catastrophic (highly cooperative) movement of dislocations.

It is worth mentioning that these properties of micro-shear bands, and in particular the possibility to induce this mode of deformation by the change of the scheme of loading, which also controls the position of micro-shear bands in the material, have already been used in the control of the metal structure [17,18,21]. In Fig.10 some examples of shear bands in polycrystalline Aluminum alloy are shown. They were induced in different spatial

distributions and orientations in the samples. The results of the experiments with formation of natural metal-matrix-composites [22] by decomposition of the unstable matrix along deliberately induced micro-shear bands indicate that the practical knowledge in this area exceeds theoretical considerations. That is why in our approach to crystal plasticity the emphasis is put on these experimental facts which concern the slip behavior. It seems that just these facts provide the instruction how to model the evolution of the structural features and mechanical performance of crystals. In particular they show that there are three distinct forms of the slip in polycrystalline metals which undergo the evolution in the course of straining. A fine, fully structure controlled slip breaks down into a catastrophic (trans-substructural) coarse slip and the coarse slip evolves into a trans-granular shear (polycrystals). These forms show different properties, hence the criteria for the breakdown from one to the other form have to be considered separately. Therefore, at the beginning it is necessary to find the appropriate model of the fine (multi-sytem) slip in a single crystals and identify the reasons of its breakdown into a catastrophic slip. Such a model must be based upon the features and consequences of crystallographically determined slips. In turn, the criterion for shear banding (polycrystals) should resolve itself into the identification of the conditions under which a coarse slip is able to continue across several grains regardless their orientation. The basic assumption which has to be made then is, that there are the conditions for activation the slip in non easy slip systems. These two different models of slip will be, therefore, considered separately. The first as the „Sequential slip based model" and the second as the „Criterion for a trans-granular shear".

3. SEQUENTIAL SLIP BASED MODEL - the first numerical results.

The experimental facts justify the postulate that the change from a homogeneous deformation into unstable, localized one, which is equivalent to the change from the fine, evenly distributed slip into a catastrophic coarse slip, may be considered as resulting from the sequential operation of slip systems. Therefore, the criterion for such a catastrophe should be sought in the evolution of the amount of slip in operative systems in every instant of their sequential activation along with identification of these systems and the moments of their activation. The advantage of such approach to crystal plasticity is that it gives a chance to trace the evolution of the total density of dislocations accumulated in the crystal and also the distribution of the dislocations among different systems. Hence, the most important properties of crystal, like flow stress and latent hardening ratio, and their evolution in the course of straining which are required for modeling [23], may be numerically found. Agreement of the calculated and experimental data is then the premise that this approach to the crystal plasticity and, in particular, to plastic flow instability in crystals is correct. The first step in the analysis was, therefore, to model the mechanical performance of a single fcc crystal oriented (tension) for a single slip glide which is the best experimentally documented case of crystal deformations.

The scheme of calculation was as follows: from an increment $d\gamma$ of a simple shear in the primary system the geometrical changes of the crystal and its spatial orientation, while non-constrained by the loading system, were calculated from the deformation gradient tensor $\mathbf{F}_{pl}$ of the primary homogeneous slip. Then, the necessary rotation and elastic distortions of

the crystal to make it match with the tensile system were evaluated. The reaction stresses, responsible for such matching were determined via elastic shear modulus. The applied tensile stress was then supplemented by the reaction stress components and, from the generalized slip criterion (eq.1), the values of the shear stress in the crystallographically allowed systems were calculated. The increment of the strain in the primary system was taken in such a way that the generated constraints were too low to activate a secondary system until a few incremental shears in the primary system took place. The back stress in the primary system (from the constraints) was balanced by the increase of the tensile stress, so that the yield criterion in the system was sustained. Density of the dislocation ρ_s in the system was determined using the Orovan relationship. The initial slip distance λ was taken from the experiments [6,10], and the spacings between slip events were calculated by taking into account that the number of dislocations emitted from a source is proportional to the shear stress in the system and the free path of dislocations. In this way the mesh-length of the primary dislocation network (obstacles pattern for the secondary systems) was estimated. As a result the current critical shear stress for slip in a secondary system (proportional to the square root of the primary dislocation density) and the free path of dislocation glide in such a system were found . Every time the evolution of the stress state led to activation of the secondary system (the most stressed one in which the slip criterion was met), the increment of slip was found from the argument that the secondary slip replaces elastic distortions by plastic deformation (releases the reaction stresses) and tends to restore the initial scheme of loading. The density of the dislocations stored in the secondary system was then calculated allowing to evaluate the structural (forest) hardening of the primary system. The rise of the applied stress in order to overcome this effect was the measure of the macroscopic rate of strain hardening of the crystal. The final product of the calculation procedure is the flow stress - strain dependence as shown in Fig. 11.These curves were found for different values of the initial critical shear stress in the primary system (respectively 5, 10 and 20 MPa) and different initial free path of the dislocation glide 0.1mm and 1 mm, respectively, and the shear modulus 40000 MPa. Hence, the results may be compared with experimental FCC single crystals tensile curves. The parallel result was the identification of the operating slip systems.

These curves reveal the experimentally found features of the tensile deformation of single crystals for the chosen orientation. The easy glide region of deformation was found to be sensitive to the initial critical shear stress of slip, and the value of the strain hardening rate in this stage was found to be of the order of 10^{-3} μ in tact with experimental observations. The rate of the strain hardening in the second stage, which again, in tact with measurements is not constant throughout this stage, reaches the experimentally found value of the order of 10^{-2} μ.

The most important information for verification of the model comes from the identification of the operative slip systems. Within the range of strains tested by the model, it is found that the secondary slip employs the conjugate $[011](\bar{1}\bar{1}1)$ and the cross plane $[011](1\bar{1}1)$ systems and that they operate alternatively with the primary system. This result is, therefore, fully consistent with experimental observations and it seems to be the first analytically predicted effect.

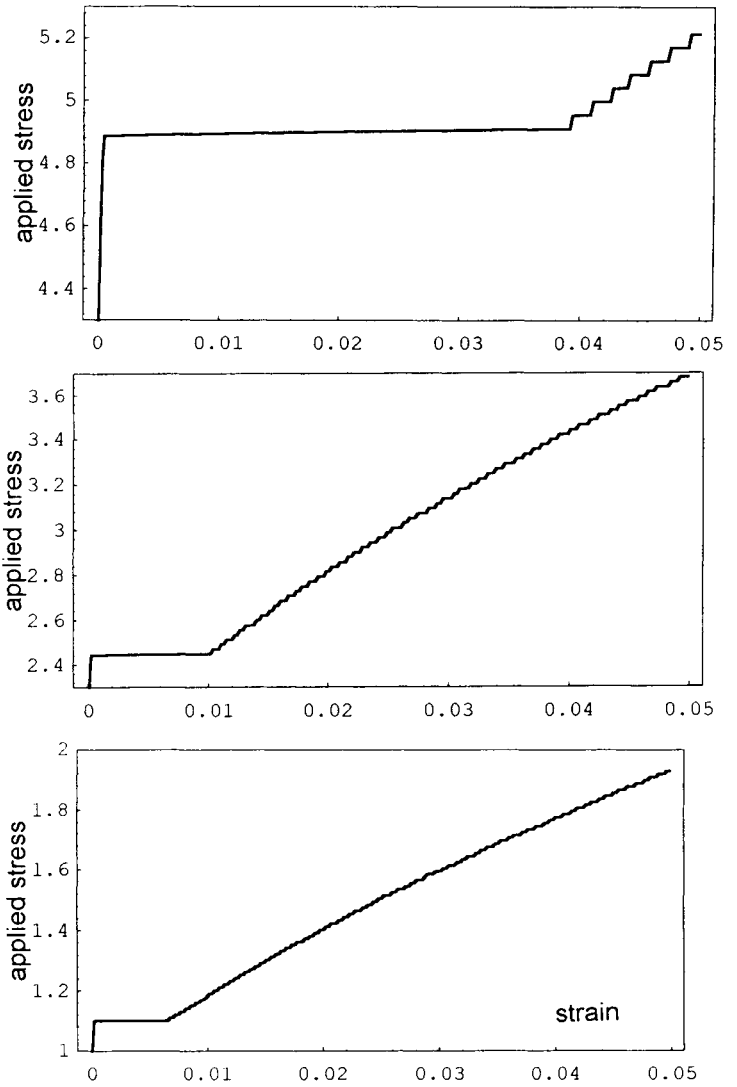

Fig.11. Calculated stress-strain curves for different value of τ_{crit} and λ

The additional verification of the model was obtained when the procedure had been used to identify the accommodating slip systems in the other, experimentally documented case. Twinning in the Cu-Al single crystal reflects such a case. The mechanical effect of twinning, which takes place under the overshoot instability conditions is marked on the tensile characteristics by the instability point (the second in Fig.7) . The twinning system employs then the conjugate $(\bar{1}\bar{1}1)$ plane and $[\bar{1}21]$ the twinning direction. Already a very thin plate of twin which carries the very large (0.707) shear, in the tensile test has to be

accommodated by slip in a secondary slip systems. The numerical calculations indicate that these systems are: the critical plane system $[0\bar{1}1](\bar{1}11)$ and the two cross plane systems [011] $(1\bar{1}1)$ and $[\bar{1}01](111)$. Fig.12 shows the slip pattern on the surface of a partly twinned crystal. Identification of the slip traces has shown that they belong to a critical and to two (white and dark) cross plane systems. These results justify the conclusion that exact account for the role of the „geometrical" constraints is crucial for prediction of the operative slip system, the sequence and the moment of activation and the amount of shear they carry. It seems also justified to believe that within the proposed model such an account is possible.

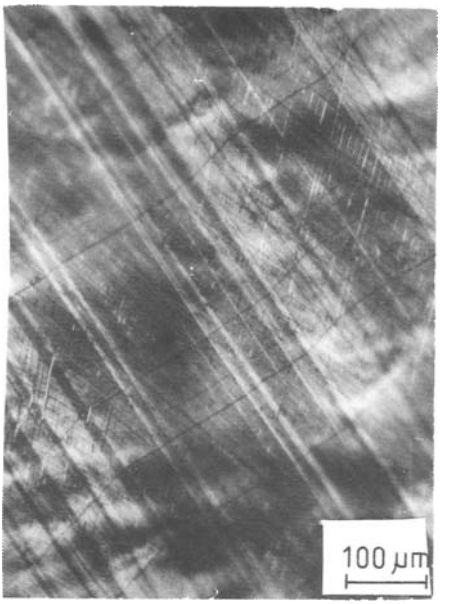

Fig.12. Slip pattern on the surface of Cu-Al crystal partly twinned during tensile deformation

As a comment to these results it is necessary to emphasize that the mechanism of glide was considered athermal. There are two arguments behind this assumption. The first comes from the experimental data which show that the strain hardening rate of crystals in the first and in the second stage of deformation is temperature independent [6]. The second argument results from the mechanism of slip. The elementary slip event consists of the emission of the dislocations from a source and their cooperative movement which is governed by the long range applied and interaction stresses. From this point of view, thermal activation, which at this stage has not been yet taken into consideration, is associated rather with the rearrangement (relaxation) of the already stored dislocations than with their thermally assisted glide. Such an rearrangement definitely helps to destabilize the obstacles network, but this effect appears important for the third stage of single crystal deformation (stage of dynamic recovery) the onset of which is temperature and strain rate dependent [6].

A monotone decrease of the hardening rate in this stage coincides with concomitant fine and coarse slips in the primary (deformation bearing) system. There is, therefore, a good reason to believe that the decrease of hardening rate results from successive replacement of the fine, homogeneous slip by a localized coarse slip. The most convincing argument for this observation has been provided by Cottrell and Stokes [24]. They showed that the rise of the temperature in the course of straining of the crystal results in the catastrophic coarse slip which in such circumstances takes the form of the propagating Luders front or develops into a neck.

4. CRITERION FOR TRANS-GRANULAR SHEAR

The already mentioned observations of the morphological features of shear bands delivered a clear suggestion about the mechanism of this mode of deformation. They have lead to the idea that a micro-shear band results from the conversion of an avalanche like (catastrophic) movement of dislocations which develops along a soft path in the crystal. Such a highly cooperative movement possesses the property of the stress pulse traveling across the crystal. The formation of the micro-shear bands resolves itself into the criterion for non-dispersive transmission of the stress pulse across a grain boundary [20]. The term „non-dispersive transmission" means that the shear carried by a dislocation avalanche, which develops in a crystallographically favorable system, does not disperse at a grain boundary, but continues along non-easy systems across several grains. It also means, that such a pulse results from the superposition of the stress fields of dislocations, and therefore it has to be a complex local stress state. This conclusion has been proved by the experiments on the Aluminum and the Fe-Ni alloys. The shear band induced fracture of the sheet of polycrystalline metal (Fig. 14), while leaving the deformation zone during the rolling [22] , and formation of the martensite along shear bands during rolling [18] provide a clear evidence for very large tensile stress along the normal to the plane of shear. From such an experiment it was possible, also, to deduce that shear bands possess a wavy nature. The experiments with the shear bands induced martensite show, for example, that there must be a communication system between separate martensitic plates. Otherwise it would be very difficult to understand why they arrange along the common micro- shear bands.

Fig. 13. Fracture along shear bands during rolling of Aluminum alloy [22].

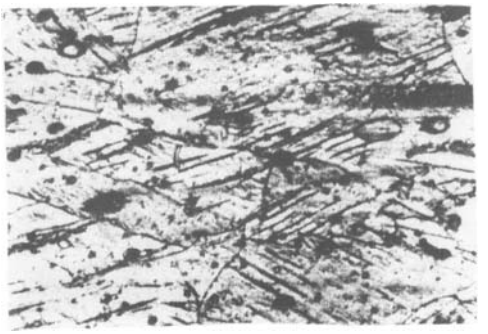

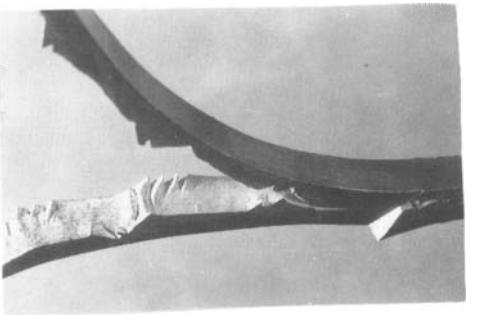

Fig. 14. Stress induced (rolling) formation plates of martensite in Fe-30Ni alloy [18].

Therefore, an analytical account for such a criterion needs that the physical mechanism of slip (movement of dislocation) to be taken into considerations. The starting point of the analysis is the profile of internal stress associated with a pile-up configuration of dislocations. Two extreme momentary situations (Fig. 15) may be considered. In the case (a) the pile-up stress may relax due to the activation of slip system in a neighboring grain. Then the stress pulse amplitude will never reach the static pile-up stress, which may be orders of magnitude large than the applied stress. This case can be classified as a dissipative transmission of the pulse throughout the grain boundary. In the case (b) the second grain does not „see" the stress concentration, except the very last moment of the pile-up formation. The peak stress may be of the order of the theoretical strength, required for homogeneous nucleation of dislocations (high enough to activate slip in a non-easy system).

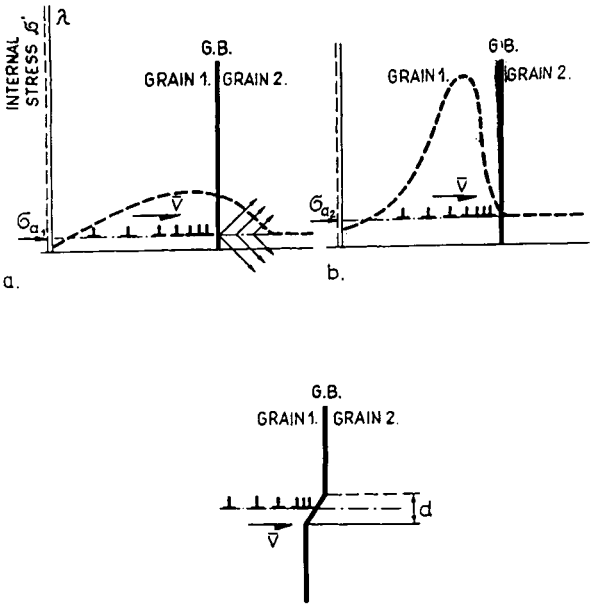

Fig. 15. A hypothetical dispersive (a) and non-dispersive transmission of the stress pulse of a group of dislocations through the grain boundary [20].

A numerical distinction between these two case can be performed on the basis of the rate of stress increase in the location on the grain boundary. The stress rate $d\sigma/dt$ may be written:

$$d\sigma/dt = (d\sigma/dx) \cdot (dx/dt) \qquad (2)$$

The right hand terms of the expression are the stress gradient at the grain boundary (caused by the approaching group of dislocations, and the velocity V_g of the group, respectively).

The position dependent gradient of the stress in the group of dislocations and the velocity of the group are the controlling factors for the grain boundary stressing rate, but only if there is no relaxation of stresses due to slip in the neighboring grain. This means that non-dissipative transmission of the stress pulse through the grain boundary is possible when the rate of the stressing is higher than the highest available (critical) rate of the stress transmission. This critical rate of the stress transmission is, in turn, determined by the velocity of sound in a metal, which for a shear stress wave is $c = (\mu/\rho_m)^{1/2}$, where μ is shear modulus and ρ_m the material proper density. Here, „c" is the velocity of the displacement of a material point du/dt; thus, the critical rate of stressing can be found via the well known relationship between displacement, strain and stress. These yield the following relation:

$$\sigma_{crit} = c \cdot (\mu/D) \tag{3}$$

or

$$\sigma_{crit} = (\mu/D) \cdot ((\mu/\rho m)^{1/2} \ . \tag{4}$$

The quantity D in the formula is the thickness of the zone of shearing (thickness of the micro-shear band). The criterion for the non-dispersive stress transmission, as well as for the highest peak stress of the pile-up, takes the form:

$$(d\sigma/dx)_{GB} \cdot Vg \quad > \quad \mu^{3/2} / (b \cdot \rho_m^{1/2}) \tag{5}$$

When fulfilled, the pile-up stress may reach the theoretical value, which is transmitted with sonic velocity in a neighboring grain in the form of the stress pulse. Audible acoustic emission heard during a jerky flow in some materials during tension may be considered as the proof of highly dynamic nature of shear banding for which the proposed criterion may be applied.

5. FINAL REMARKS

The proposed model of the plastic flow in crystals is based upon a step by step numerical analysis of the evolution of the crystal behavior in the course of straining. Therefore, it should be considered as an alternative, with respect to a „constitutive" modeling, way of the account for catastrophic phenomena in crystalline materials. A criterion for the catastrophic plastic flow is sought in the evolution of intrinsic properties (slip distance, number of dislocations engaged in a slip event) of the slip, but not in the evolution of global features of the material. Such an approach offers some definite advantages. First of all it is free from empirical data except of those which concerns the initial (prior to straining) material features. Instead, it makes possible to evaluate the evolution of the material

properties. The criterion of strain localization specifies the conditions which must be met locally in order to initiate that process. Therefore it is not a probabilistic criterion but is addressed to the location in the material from which the localization may develop. The meaning of this statement is well exposed by the experiments with shear banding in a fine and coarse grain material [15]. It was shown that in a fine grain material the zone of macroscopic localization is composed of very densely spaced microbands. In the coarse grain material such a zone is discontinuous (Fig.16) what points to the crystallographic origin of shear bands. Then, the continuos or discontinuous development of localization depends on the number (population) of grains in which the conditions for catastrophic slip are reached.

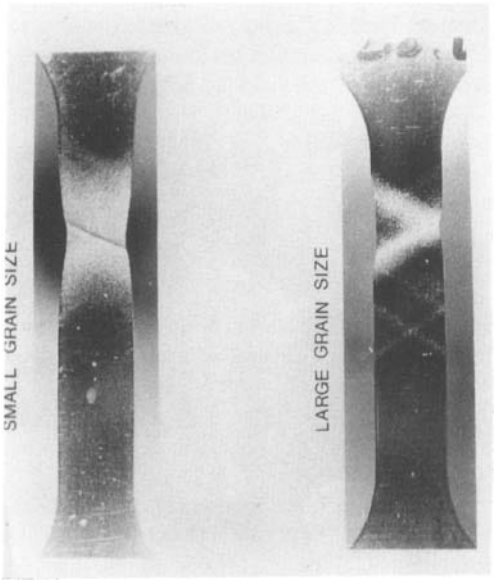

Fig.16. Continues and discontinues distribution of shear bands during necking in a fine and coarse grain Armco Iron [15].

It seems, therefore, justified to focus upon the modelling of the mechanical behavior of single crystals in different loading conditions (crystal orientation, scheme of loading, temperature) in order to identify the circumstance under which the development of a catastrophic flow is especially easy.

Acknowledgment.

The Authors wish to express their thank to the State Committee for Scientific Research for financial support of the work (Research Grant No 017 08).

REFERENCES

1. A.Korbel, Crystals Plasticity, Canadian Inst.Mining & Metallurgy (1992), 42.
2. E.Schmid and W.Boas, Kristallpastizitat mit besonderer Berucksichtigung mit Metalle, Springer-Verlag (1935).
3. P.J.Jackson and Z.S.Basinski, Can. J. Phys., 45 (1967) 707.
4. G.I.Taylor, J.Inst. Metals, 62 (1938) 218.
5. J.F.W.Bishop and R.Hill, Phil. Mag., 43 (1951) 414.
6. S.J.Basinski mand Z.S.BasinZeitsski, Dislocations in Solids, 4 (1979) 261.
7. M.Masima and G.Sachs, chrift fur Physik, 50 (1928) 11.
8. V.Goler and G.Sachs, Zeitschrift fur Physik, 55 (1929) 581.
9. G.Sachs and J.Weerts, Zeitschrift fur Physik, 60 (1930) 473.
12. Z.S.Basinski, M.Szczerba,.D.Embury, Phil.Mag., in press.
10. S.Mader and H.Seeger, Acta Metall., 8 (1960) 513.
11. K.Korbel, R.Pęcherski and A.Korbel, will be published.
13. A.Korbel and M.Szczerba, Rev. Phys. Appl., 23 (1988) 706.
14. Z.S.Basinski, private information.
15. A.Korbel and P.Martin, Acta Metall., 36 (1988) 2575.
16. A.Korbel and P.Martin, Acta Metall., 34 (1986)1905.
17. A.Korbel and K.Piełа, Materials. ScienceForum, 217 (1996) 1037.
18. A.Korbel and F.Ciura, Solid Mechanics and its Applications, 46 (1996) 107.
19. A.Korbel and M.Richert, Strength of Materials, The Japan Inst. Metals (1994) 271.
20. A.Korbel, Scripta Metall., 24 (1990) 1229.
21. W.Bochniak, A.Korbel, Strength of Materials, The Japan Inst. Metals (1994) 579.
22. A.Korbel, W.Bochniak, F.Ciura, H.Dybiec and K.Piełа, Extraction and Processing Division, TMS Publication, B.Mishra Ed. (1997) 301.
23. D.Pierce, R.J Asaro and A.Needleman, Acta Metall., 30 (1982)1087.
24. A.H.Cottrell and R.J.Stokes, Proc. roy. Soc., A233 (1955) 17.

This Page Intentionally Left Blank

PART III

DAMAGE IN BRITTLE MATERIALS

This Page Intentionally Left Blank

Damage Mechanics in Engineering Materials
G.Z. Voyiadjis, J.-W.W. Ju and J.-L. Chaboche (Editors)
© 1998 Elsevier Science B.V. All rights reserved.

A comparative study of isotropic and anisotropic descriptions of damage in concrete structures

S. Fichant, C. La Borderie, and G. Pijaudier-Cabot[1]

Laboratoire de Mécanique et Technologie , ENS Cachan / CNRS / Université P. et M. Curie, 61 avenue du Président Wilson, F-94235 Cachan cedex, France.
[1] member, Institut Universitaire de France

Abstract : Scalar damage models are very often implemented in computational analyses in order to predict the responses and failure modes of concrete and reinforced concrete structures. In most situations, however, damage is not isotropic but rather geometrically oriented. Therefore, there as been many questions about the pertinence and range of applicability of isotropic, scalar, damage models for describing a degradation process which is strongly geometrically oriented. In order to assess what are the limitations of such a simplifying assumption, a comparative study is presented. The scalar damage model is compared with another model where damage induced orthotropy is taken into account. Structural analyses on bending beams, compression-shear and tension-shear concrete panels are discussed. Although it may appear to be simplistic, the scalar damage model provides accurate predictions when failure is due to uniaxial extension. Crack closure introduces an additional anisotropy which is important in compression-shear problems. Finally, damage induced anisotropy seems important when failure is due to multiaxial extension, such as in shear-tension problems.

1. INTRODUCTION

Quasi-brittle materials such as concrete exhibit a non linear stress-strain response mainly because of micro-cracking. In most cases, these microcracks are oriented with respect of the applied stress history (Shah and Maji 1989, Torrenti et al. 1989): in uniaxial tension microcraks develop perpendicularly to the tensile stress; in compression, splitting cracks parallel to the direction of the compressive stress appear. In constitutive models, it is usually recognised that microcracks open in a plane which is perpendicular to the direction of the maximum principal tensile stress (Rots 1988, De Borst and Nauta 1985, Govindjee et al. 1995) or controlled by the principal strain directions (see e.g. Simo and Ju 1987, Berthaud et al. 1990). The development of microcracks results in a progressive degradation of the elastic stiffness of the material. The degraded elastic operator is not

expected to remain isotropic but to become gradually anisotropic. This phenomenon is called damage-induced anisotropy.

Starting in the 80's, several anisotropic damage models have been developed for quasi-brittle materials. Among many proposals Krajcinovic and Fonseka (1981) used damage vectors, Sidoroff (1981), Chaboche et al. (1994), Mazars and Pijaudier-Cabot (1989), Dragon and Mroz (1979), Valanis (1991) used a second order tensor, Ortiz (1985), Simo and Ju (1987), Yazdani and Schreyer (1990), and more recently Carol et al. (1994) proposed to consider that damage is a fourth order tensor. Each proposal yields a specific type of anisotropy. For instance, with a second order tensor the damaged material becomes orthotropic. Their variety is somewhat puzzling because it is difficult to compare the predicted type of damage-induced anisotropy with experimental data and therefore it is difficult to provide a proper method for choosing the most appropriate type of damage variable.

From a theoretical point of view, it seems appropriate that rational methods for the derivation of the type of damage variables should be devised. Ladeveze (1983) proposed a general technique of approximation of the elastic stiffness of a damaged material. The method introduces two damage surfaces which characterise the unidirectional stiffness and the compressibility of the material for any loading direction. The elastic moduli are derived using an approximation technique similar to a weighted residual method. A second technique is based on the microplane approach proposed for quasi-brittle materials by Bazant (see e.g. Bazant and Prat 1989). The elastic (or tangent) stiffness of the material is obtained from the relationship between the stress and the strain vectors for any arbitrary microplane direction. The construction of the stiffness results from a energy based equivalence. Damage is defined at the microplane level and the relation with the global elastic stiffness of the material was elucidated by Carol et al. (1991). They arrived at the definition of a fourth order damage tensor where the damage variables at the microplane level appear and simplifications can be performed.

In Ladeveze's proposal, it is already stated that the definition of the damage surfaces should be envisioned with respect to experimental observations: without any other discriminating data, the simple knowledge of a uniaxial response of the material (axial strain vs. axial stress) cannot provide anything but a one scalar isotropic damage model. For the same experiment, the additional knowledge of the axial strain vs. transverse strain curve yields a two scalar isotropic damage model. Fichant et al. (1997) combined the simple features of the microplane approach with the approximation of damage surfaces in the same spirit as Ladeveze's approach. They derived a simplified microplane-type model where the behaviour of the damaged material is discretised along a finite set of directions and interpolated in between them. The elastic behaviour of the damaged material depends on the interpolation used for the distribution of damage in each direction of the material. With a infinite number of discretisation directions, the microplane model is recovered. As a consequence, the degree of interpolation of the damage surface can be related to the experimental knowledge of the mechanical response of the material considered.

Interestingly, these methods provide also a common ground from which different type of models starting from different discretisation levels (and thus different types of damage-induced anisotropy) can be compared. In view of the simplicity of implementation of a scalar model, it can be appealing to disregard the

crack orientation, provided the numerical predictions do not really differ from those of a more realistic model which incorporates damage-induced anisotropy. In this paper, we will focus attention on this issue and we will try to sort out cases where a simple, scalar approach yields sufficiently accurate results.

2. PRINCIPLE OF THE CONSTITUTIVE MODELS

The models that are going to be compared are based on the approximation of the relationship between the overall stress (latter simply denoted as stress) and the effective stress in the material defined by the equation:

$$\sigma'_{ij} = C^0_{ijkl}\varepsilon_{kl} \quad \text{or} \quad \sigma'_{ij} = C^0_{ijkl}\left(C^{damaged}\right)^{-1}_{klmn}\sigma_{mn} \tag{1}$$

where σ_{ij} is the overall stress component, σ'_{ij} is the effective stress component, and $C^{damaged}_{ijkl}$ is the stiffness of the damaged material, and C^0_{ijkl} is the initial stiffness of the undamaged material, assumed to be isotropic, linear and elastic. Let us define the relationship between the stress and the effective stress along a finite set of directions of unit vectors n:

$$\begin{aligned} \sigma &= (1-d(n))n_i\sigma'_{ij}n_j \\ \tau &= (1-\delta(n))\sqrt{\sum_{i=1}^{3}\left(\sigma'_{ij}n_j - \left(n_k\sigma_{kl}n_l\right)n_i\right)^2} \end{aligned} \tag{2}$$

where σ and τ are the normal and tangential components of the stress vector respectively, and two damage surfaces are introduced:

$$S_d(n):\ n \rightarrow d(n) \text{ and } S_\delta(n):\ n \rightarrow \delta(n) \tag{3}$$

$d(n)$ and $\delta(n)$ are scalar valued quantities which introduce the effect of damage in the relation between the effective stress vector and the overall stress vector. The basis of the model is the numerical interpolation of these surfaces. They are approximated by the knowledge of $d(n)$ and $\delta(n)$ for a finite set of directions.

The stress is solution of the virtual work equation :

$$\begin{aligned} &\text{find } \sigma_{ij} \text{ such that } \forall \varepsilon^*_{ij} \\ &\frac{4\pi}{3}\sigma_{ij}\varepsilon^*_{ij} = \int_S \left(\left[(1-d(n))n_k\sigma'_{kl}n_in_i + (1-\delta(n))\left(\sigma'_{ij}n_j - n_k\sigma'_{kl}n_in_i\right)\right]\cdot\varepsilon^*_{ij}n_j\right)d\Omega \end{aligned} \tag{4}$$

The model is similar to a microplane model which is kinetically constrained (Bazant and Ozbolt, 1990). The most important difference with the microplane model is that in the absence of damage, Eq. (4) yields exactly the stiffness matrix of an isotropic material, without the need for integrating numerically. We will now consider that the two damage surfaces are identical: $d(n)=\delta(n)$. The simplest approximation, which does not yield isotropy, corresponds to an ellipsoidal damage

surface: this surface is characterised by three principal directions and by the values of three damage scalars d_i along these directions. The isotropic damage model will be deduced from the anisotropic one simply by assuming that the damage surface is spherical instead of being ellipsoidal.

The evolution of the elastic constants due to damage growth is given, in both isotropic and orthotropic approximations, by the evolution of the damage surfaces. Initially, the damage surface (Eq. 3) is reduced to a point $d(n) \equiv 0$. Once damage starts to grow, it becomes an ellipsoidal or spherical surface. The evolution of damage is controlled by a loading surface f:

$$f(n) = n\varepsilon n - \varepsilon_d - \chi(n) \tag{5}$$

where χ is an hardening softening variable which is interpolated in the same fashion as the damage surface. The threshold of damage is given by the strain ε_d. The evolution of the damage surface is defined by an evolution equation inspired that of an isotropic model (Mazars and Pijaudier-Cabot, 1989):

$$\begin{cases} \text{if } f(n^*) = 0 \text{ and } n^* \dot{\varepsilon} n^* > 0 \text{ then } \begin{cases} \dot{d}(n^*) = \left[\dfrac{\varepsilon_d (1 + a(n^* \varepsilon n^*))}{(n^* \varepsilon n^*)^2} \exp(-a(n^* \varepsilon n^* - \varepsilon_d) \right] n^* \dot{\varepsilon} n^* \\ \dot{\chi}(n^*) = n^* \dot{\varepsilon} n^* \end{cases} \\ \text{else } \dot{d}(\bar{n}^*) = 0, \ \dot{\chi}(n^*) = 0 \end{cases} \tag{6}$$

The model parameters are the initial radius of the surface $\chi(n)$ which is assumed to be isotropic initially since the undamaged material is isotropic and the parameter a. The first parameter can be related to the tensile strength of the material if one assumes that damage in uniaxial tension occurs at the peak stress and the second will be related to the fracture energy of the material in the same spirit as smeared crack models (Rots 1988). Note that the vectors n^* are the three principal directions of the *incremental* strain whenever damage grows. The new damage surface is the combination of two surfaces: the one corresponding to the initial damage surface, and the surface corresponding to the incremental growth of damage. The principal directions of the macroscopic stress tensor are not necessarily the same as the principal directions of the strain tensor in the anisotropic model (Fichant et al., 1997).

It is important to remark that the model parameters in the evolution laws of damage *do not depend on the level of interpolation*. In the comparisons, this characteristic will be essential because any discretisation level will provide exactly the same uniaxial material response in tension.

3. ANISOTROPIC PLASTIC-DAMAGE MODEL

Degradation of the stiffness due to progressive microcracking is one among several important features of the behaviour of concrete. Plastic strains are observed experimentally. When the loading history is not monotonic, damage deactivation occurs due to microcrack closure. It seems important to take into account these

phenomena in order to carry out the comparison between the isotropic and anisotropic damage models.

3.1. Damage - plasticity coupling

In view of the form of the damage model, elasto-plastic damage can be introduced at several levels. In the microplane approach, plasticity is coupled to damage at the microplane level (Bazant and Prat, 1989). In other phenomenological models (see e.g. Ju 1989, Lemaitre 1984) the coupling between damage and plasticity is introduced in the definition of the free energy of the material. Because we wish to separate the approximation of damage from plasticity, we will use the second technique. Note that damage will only affect the elastic part of the behaviour, which means that locally plasticity (microcraks sliding) and damage (microcrack opening) are assumed to be uncoupled as far as their evolution is concerned. This will introduce also a great simplicity in the computational implementation (Ju 1989, Benallal et al. 1991).

In the present approach, we decompose the strain increment in an elastic and plastic one:

$$d\varepsilon_{ij} = d\varepsilon_{ij}^{e} + d\varepsilon_{ij}^{p} \tag{7}$$

and damage is introduced in the elastic part of the stress-strain response:

$$\sigma_{ij} = C_{ijkl}^{damaged} \varepsilon_{kl}^{e} \tag{8}$$

Note that from now on the elastic strain ε_{ij}^{e} will replace the total strain ε_{ij} is the equations (5,6) defining the evolution of damage. We assume that the evolution of the plastic strain is controlled by a yield function which is expressed in term of the effective stress in the undamaged material. Because plasticity is indexed on the effective stress, it will not interact with the specific approximations used for the damage models. Among the various possibilities in the choice of a yield function, we have chosen to implement a yield function due to Nadai (1950) inspired from the Drucker-Prager criterion. The two constants in the Nadai criterion are given the following values: $\beta = 1.16$ and $\gamma = 0.4$.

The evolution of the plastic strain is defined according to the normality rule and the hardening rule is given by:

$$w = qp^{r} + w_0 \tag{9}$$

where q and r are model parameters and w_0 defines the initial reversible domain in the stress space.

3.2. Crack closure effects

Crack closure effects are of importance when the material is subjected to alternated loads. During load cycles, micro cracks close progressively and the tangent stiffness of the material should increase while damage is kept constant. Within isotropic damage modelling, one solution is to introduce two damage scalars, instead of one, in order to separate the mechanical effect of micro

cracking depending on the sign of the stress. Here, a separation of the stress tensor into a positive and negative part is introduced:

$$\sigma = \langle\sigma\rangle^{+} + \langle\sigma\rangle^{-} \tag{10}$$

where $<\sigma>^{+}$, and $<\sigma>^{-}$ are the positive and negative part (polar decomposition) of the stress tensor (for a scalar $<x>^{+} = x$ if $x>0$ and $<x>^{+} = 0$ if $x<0$). The influence of damage, introduced in Eqs. (2) of the model, is modified:

$$\sigma_{ij} n_j = (1 - d(n))\langle\sigma\rangle^{t}_{+\,ij} n_j + (1 - d_c(n))\langle\sigma\rangle^{t}_{-\,ij} n_j \tag{11}$$

$d_c(n)$ defines a new damage surface which describes the influence of tensile damage on the response of the material in compression. Because this new variable refers to the same state of degradation as in tension, there is a relation between $d_c(n)$ and $d(n)$. The new damage surface defining $d_c(n)$ is directly deduced from the damage surface $d(n)$. It is an ellipsoidal surface with the same principal direction as the surface defining $d(n)$ and along each principal direction i, we have the relation:

$$d_c^i = \left(\frac{d_j(1-\delta_{ij})}{2}\right)^{\alpha}, \; i \in [1,3] \tag{12}$$

where δ_{ij} is the kronecker symbol and α is a model parameter. Note that the two surfaces $d_c(n)$ and $d(n)$ are spherical in the case of isotropic damage.

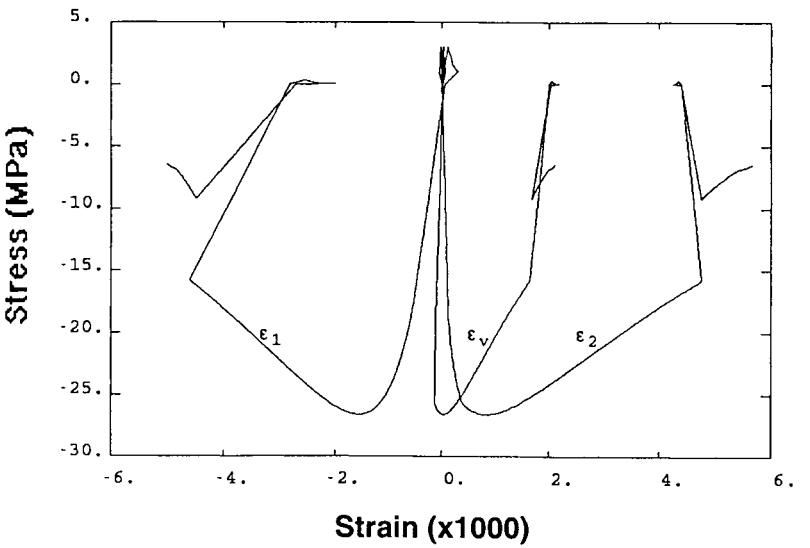

Figure 1 : Uniaxial tension-compression response of the anisotropic model.

3.3. Response of the model and computational aspects

For the two approximations of the damage surface, the constitutive relations contain 6 model parameters in addition to the Young's modulus of the material and the Poisson's ratio. The first series of 3 parameters $(\varepsilon_d, a, \alpha)$ deals with the evolution of damage in tension and in compression. The second series of three parameters involved in the plastic part of the constitutive relation is (q, r, w_0). They are obtained from a fitting of the uniaxial compression response of concrete once the parameters involved in the damage part of the constitutive relations have been obtained.

The two damage models exhibit strain softening. In order to circumvent some of the difficulties involved with softening in the computations, we have chosen to control that the energy dissipation due to cracking in uniaxial tension be constant whatever the finite element size during localisation (see e.g. Rots 1988).

Figure 1 shows a typical uniaxial compression-tension response of the model corresponding to a standard concrete with a tensile strength of 3 MPa and a compressive strength of 40 MPa. The set of model parameters is:

$$E = 30000\ MPa,\ \nu = 0.2,\ a = 1000,\ \alpha = 12, \varepsilon_d = 10^{-4},\ r = 0.5,\ q = 7000 MPa,\ W_0 = 26.4 MPa$$

The anisotropic model reproduces quite well (qualitatively) the evolution of the longitudinal and of the transverse strains with the stress. With the isotropic model, that is assuming that the damage surface in Eq. (3) is a sphere, the same good description of the axial stress-axial strain curve would be obtained with the same model parameters. The axial stress-transverse strain curve would be, however, different because the (elastic) Poisson's ratio of the material would not be affected by damage.

The anisotropic model and the isotropic model have been implemented in the finite element code Castem 2000. Given the strain and the strain increment, the plastic strain increment is computed first. Because it depends on the effective stress only, the plastic strain increment is independent of damage. We have used for plasticity a classical return mapping algorithm (Ortiz and Simo 1986, Simo and Taylor 1986). The plane stress constraint is added in the computation of the plastic multiplier (Aravas 1987). Once the increment of plastic strain has been computed, the incremental damage is computed explicitly from Eqs. (5,6) and the new state of stress is obtained from Eq. (4) (for more details see Fichant, 1996).

4. FINITE ELEMENT COMPUTATIONS AND COMPARISONS

We are going now to compare the isotropic and anisotropic models on three types of structural analyses. At the level of the constitutive relations, a comparison has been performed by Fichant et al. (1997) revealing that the shear response of the anisotropic damage model differs substantially from that of the isotropic one. This observation was based on the analysis of the material response to a strongly non radial loading history proposed by Willam et al. (1986). For situations where the loading history does not yield severe non radial stress or strain histories, we will see that the results can be quite different.

4.1. Single edge notched beam

The first comparison deals with the single edge notched concrete beam tested by Schlangen (1993). This type of experiment has been simulated extensively in the literature using smeared crack models and plasticity based models (see e.g. Rots 1988, Feenstra 1993). The geometry of the beam and loading apparatus is schematised on Fig. (2). The load F is applied on the testing apparatus so that the point load close to the notch is F_1=10/11 F and the point load near the beam end is F_2=1/11 F.

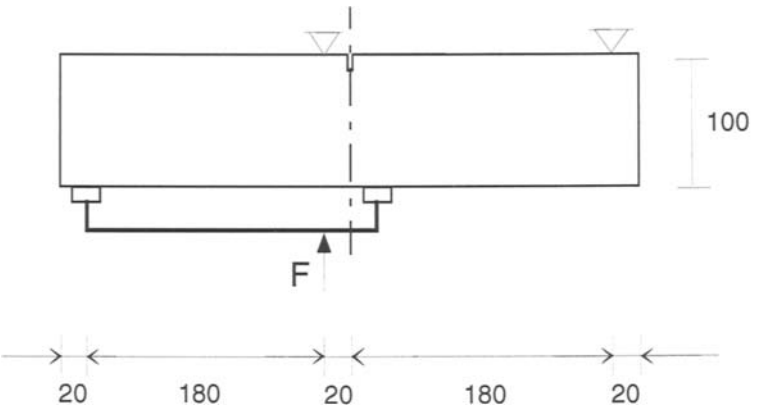

Figure 2: Single-edged notched beam : geometry and loads.

The material properties used in the simulations are the same as those chosen in Feenstra's analysis (1993):

For concrete :

Young's modulus: $E = 35000$ MPa
Poisson's Ratio: $\nu = 0.15$
Tensile strength : $f_t = 2.8$MPa which yields $\varepsilon_d = 0.76\ 10^{-4}$
Fracture energy : $G_f = 0.07$N/mm
Compressive strength : $f_c = 36.5$ MPa

other model parameters :

$\alpha = 12$
$r = 0.5, q = 7000MPa, w_0 = 26.4MPa$

For the loading apparatus (steel beam)

Young's modulus: $E = 200000$ MPa
Poisson's Ratio: $\nu = 0.3$

Figure 3 shows the plot of the applied load F versus the crack mouth sliding displacement (CMSD). We have plotted on this figure the experimental data, the computations performed with the isotropic and anisotropic plastic damage models and with the rotating crack model (Feenstra, 1993). Considering the experimental dispersion, the three predictions are quite equivalent, except for large displacements.

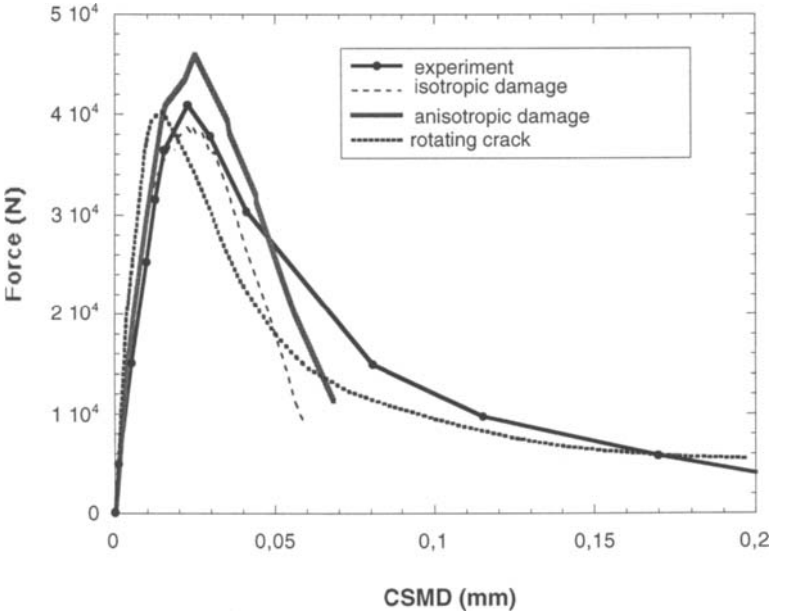

Figure 3 : Single-edged notched beam : load vs. CMSD response.

The predicted distributions of damage are also quite similar. It should be noted that, the two damage models are sensitive to mesh alignment when damage localises to form a crack. The regularisation employed here avoids mesh-size dependence but not mesh-alignment effects. In this experiment, damage essentially occurs due to extensions. The two damage models provide the same material response in uniaxial tension, therefore it is not surprising that the models provide approximately the same result.

4.2. Compression shear experiments

Compression shear experiments have been performed by Fichant on plain concrete I-shaped panels (Clément et al. 1994, Fichant 1996). The geometry of the panels and the loading system is shown on Fig. (4).

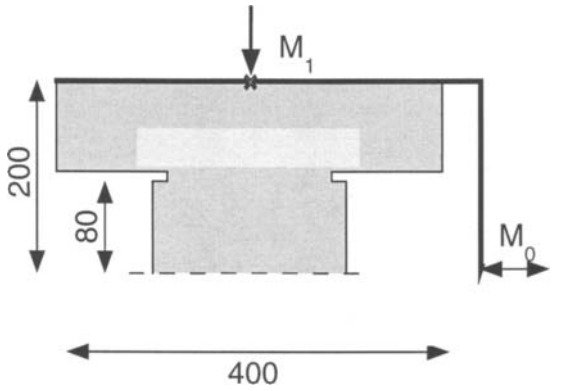

Figure 4 : Compression shear test: specimens tested (dimensions in mm).

The panel thickness is 60 mm. Notches were cut on most of specimens in order to control crack propagation and to avoid multiple cracking as much as possible. The tests were designed so that diagonal shear cracks propagate in the specimen subjected to alternated shear loads.

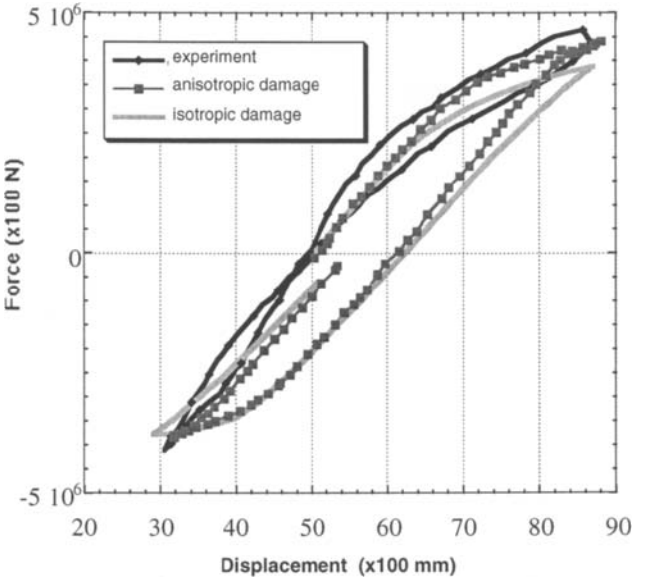

Figure 5: Compression shear test: experimental and predicted responses.

From the experimental viewpoint, applying shear requires the combination of two loads in two orthogonal directions. The biaxial testing frame for these experiments was a Schenk multiaxial testing system. The vertical load, denoted M_1 on Fig. (4) was applied with two hydraulic jacks and the lateral loads denoted as M_0 were applied with another pair of jacks. The vertical compression force was constrained to remain constant (75KN). The horizontal loads were applied under displacement controlled conditions.

The material properties of concrete and the corresponding model parameters were the same as those of in the previous computation. Only one half of the plate was considered with a central symmetry of the displacements. Figure 5 shows the comparison between the experiment and the two predictions of the isotropic and anisotropic damage models. Again, the numerical predictions are quite similar. In both simulations, two independent diagonal crack systems develop in the plate, same as in the experiments. The first one when the horizontal load is negative and the second one when it becomes positive. Figure 6 shows the distribution of damage for the isotropic damage model. It is interesting to note that although the isotropic damage model does not contain any directional information, it provides a very accurate prediction of the damage system. Because of damage deactivation, the first damage band does not affect the material response when the shear load is reversed. Hence, the two damage bands propagate independently. In the stress-strain relations, the crack closure effect which introduces effectively a damage-induced anisotropy, is the most important feature in this example.

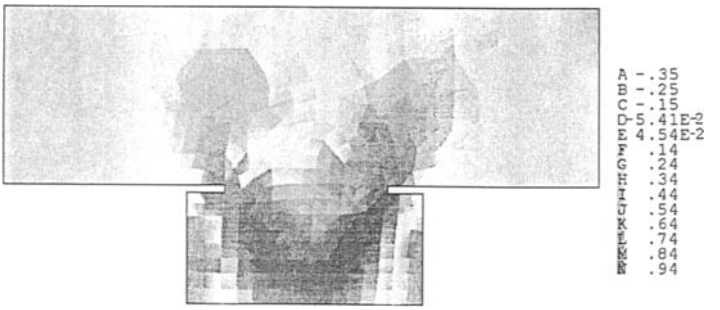

Figure 6: compression shear test : map of damage at the end of the loading history with the isotropic model

4.3. Double edged notched specimen

On tension shear problems, the predictions of the two models should not be as close because damage deactivation may not occur. In order to investigate this possibility, computations on the double edged notched specimens tested by Nooru-Mohamed (1992) have been performed. Figure 7 shows the specimen geometry of the plain concrete panels tested. Their thickness was 50 mm. The panels were loaded by a shear force denoted as P_s first. This load was kept constant while uniaxial tension was applied to the specimen. The tensile force P was controlled by

the relative tensile displacement δ measured in between two points A and A' as shown on the figure.

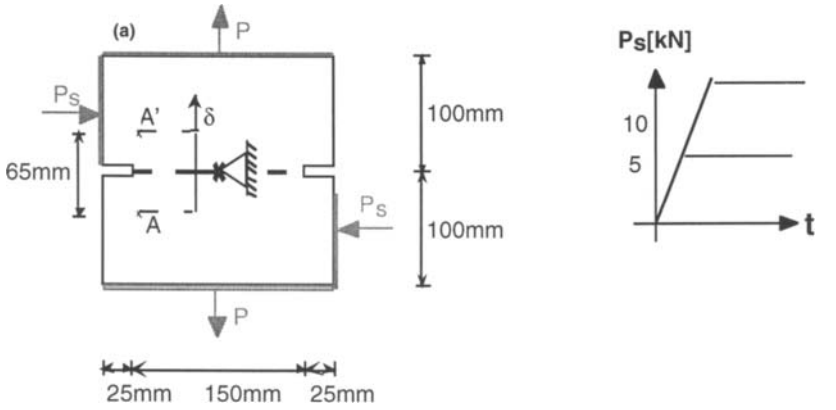

Figure 7 : Double-edged notched specimen : geometry and loads.

In order to focus on the differences between the two damage models, we have removed plasticity from the constitutive relations. The material properties of concrete and the model parameters used in the computations are:

Young's modulus: $E = 30000$ MPa, Poisson's Ratio: $\nu = 0.2$
Tensile strength : $f_t = 3$MPa which yields $\varepsilon_d = 1\ 10^{-4}$
Fracture energy : $G_f = 0.1$N/mm
Compressive strength : $f_c = 36.5$ MPa, $\alpha = 12$

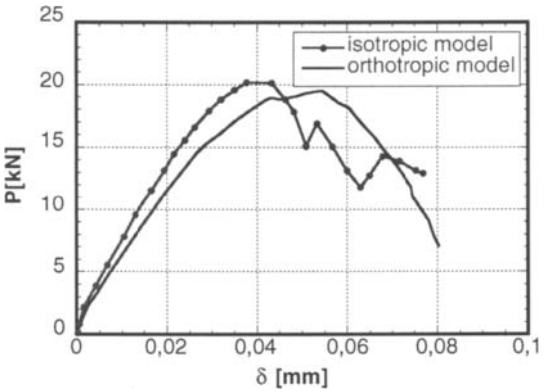

Figure 8 : Double-edged notched specimen: tensile load vs. vertical displacement for P_S=5 KN.

Two tests have been considered with different values of the shear force: P_s = 5 KN and P_s = 10 KN. Figures (8,9) show the predictions according to the two constitutive relations in both cases. The maximum tensile loads are quite similar for the lowest shear force and the predictions of the two models differ as shear is increased. It is interesting to compare the evolution of the maximum tensile force: the data indicate that the maximum tensile force should decrease by 15 % as shear is increased. The computations with the isotropic damage model yield exactly the contrary. With the anisotropic model, there is very a slight decrease of the tensile load. The reason for these differences is better illustrated on the maps of damage.

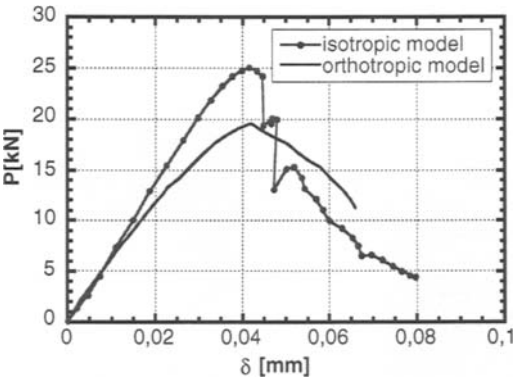

Figure 9 : Double-edged notched specimen: tensile load vs. vertical displacement for P_S=10 KN.

For the smallest shear load, horizontal cracks develop in the center of the plate. Both models provide reasonably accurate predictions compared to the experiments. When P_s = 10 KN, two curved cracks should develop according to the experimental observation (Fig. 10). Still, the isotropic model predicts that horizontal cracks should propagate while the curved crack propagation is better approached with the anisotropic damage model.

5.CONCLUDING REMARKS

Isotropic (scalar) damage models are simple to develop and can be easily fitted from uniaxial experiments. At the same time, damage-induced anisotropy is delicate to characterise experimentally. It increases the number of model parameters to be experimentally determined, at least in the context of phenomenological models where damage is a second order or a fourth order tensor. Although it is legitimate to argue that the definition of a damage variable should indeed incorporate some directional information, it is interesting to sort out

situations where an isotropic model may yield equally good predictions in structural analyses.

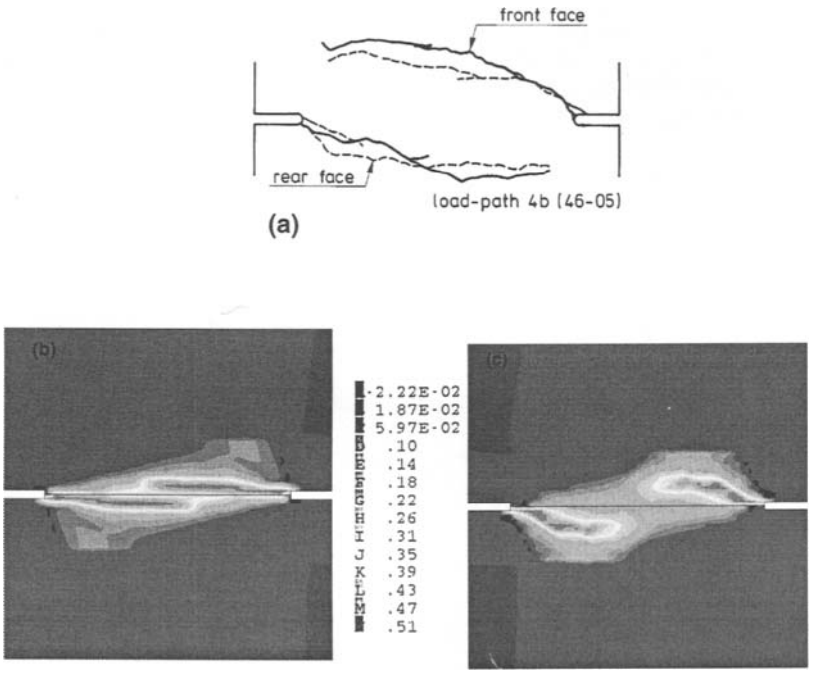

Figure 10 : Double-edged notched specimen: damage according to the experiment (a), to the isotropic damage model (b), and to the anisotropic model for P_S=10 KN.

When the failure mode is essentially controlled by uniaxial tension, we found that damage-induced anisotropy is not required. In fact, damage deactivation due to crack closure is more important as it introduces anisotropy of the elastic stiffness. Damage induced anisotropy seems important when the material is locally subjected to multiaxial extensions, as in the shear tension problems. It is also expected that anisotropy is of central importance in situations where the loading history is severely non radial with an incremental growth of damage. This particular point remain to be validated with other comparisons on structural analyses.

6. BIBLIOGRAPHY

Aravas, N. (1987), On The Numerical Integration of a Class of Pressure Dependent Plasticity Models, Int. J. Num. Meth. Engrg., Vol. 24, pp. 1395-1416.

Bazant, Z.P. and Ozbolt, J. (1990), Nonlocal Microplane Model for Fracture, Damage and Size Effect in Structures, J. of Engrg. Mech. ASCE, Vol. 116, pp. 2485-2505.
Bazant, Z.P. and Prat, P.C. (1988), Microplane Model for Brittle-Plastic Material I: Theory, J. Engrg. Mech. ASCE, Vol. 114, pp. 1672-1702.
Benallal, A., Billardon, R. and Lemaitre, J. (1991), Continuum Damage Mechanics and Local Approach to Fracture : Numerical Procedures, Comp. Meth. in Appl. Mech. and Engrg., Vol. 92, pp. 141-155.
Berthaud, Y., Laborderie, C., and Ramtani S. (1990), Damage Modelling and Crack Closure Effects, Damage Mechanics in Engrg. Materials, J.W. Ju et al. Eds., ASME AMD Vol. 109, pp. 263-276.
Carol, I., Rizzi, E., and Willam, K. (1994), A Unified Description of Elastic Degradation and Damage Based on a Loading Surface, Int. J. Solids and Struct., Vol. 31, pp. 2835-2865.
Carol, I., Bazant, Z.P. and Prat P.C., Geometrical Damage Tensor Based on Microplane Model, J. of Engrg. Mech. ASCE, Vol. 117, 1991, pp. 2429-2448.
Chaboche, J.L., Lesne, P.M., and Maire, J.F. (1994), Phenomenological Damage Mechanics of Brittle Materials with Description of the Unilateral Damage Effect, in Fracture and Damage in Quasibrittle Structures, Z.P. Bazant et al. eds., E&FN Spon Pubs, London, pp. 75-84.
Clément, J.L., Fichant, S., Laborderie, C., Pijaudier-Cabot, G. and Tailhan, J.L. (1994), Experiments on Pre-Damaged Specimens, report of Brite-Euram project P-3275 "Failure Mechanics of Fibre-Reinforced Concrete and Pre-Damaged Structures", Laboratoire de Mécanique et Technologie, Cachan, France.
De Borst ,R. and Nauta, P. (1985), Non Orthogonal Cracks in Smeared Finite Element Models, Engrg. Comput., Vol. 2, pp. 35-46.
Dragon, A. and Mroz, Z. (1979), A Continuum Model for Plastic-Brittle Behaviour of Rock and Concrete, Int. J. Engrg. Sci., Vol. 17, pp. 121-137.
Feenstra, P.H. (1993), Computational Aspects of Biaxial Stress in Plain and Reinforced Concrete, Dissertation, Delft University of Technology, the Netherlands.
Fichant, S., Pijaudier-Cabot, G. and La Borderie, C. (1997), Continuum Damage Modelling : Approximation of Crack Induced Anisotropy, Mech. Res. Comm., Vol. 24, pp. 109-114.
Fichant, S. (1996), Endommagement et anisotropie induite du béton de structures. Modélisations approchées, thèse de Doctorat de l'ENS Cachan, Cachan, France.
Govindjee S., Kay, G.J., and Simo, J.C. (1995), Anisotropic Modelling and Numerical Simulation of Brittle Damage in Concrete, Int. J. Numerical Methods in Engrg., Vol. 38, pp. 3611-3633.
Ju, J.W. (1989), On Energy-Based Coupled Elastoplastic Damage Theories: Constitutive Modelling and Computational Aspects, Int. J. Solids and Struct., Vol. 25, pp. 803-833.
Krajcinovic, D., and Fonseka, G.U. (1981), The Continuous Damage Theory of Brittle Materials, J. of Applied Mech. ASME, Vol. 48, pp. 809-824.
Ladevèze, P. (1983), Sur une théorie de l'endomagement anisotrope, Int. Report n°34, Laboratoire de Mécanique et Technologie, Cachan, France.
Lemaitre, J. (1984), How to Use Damage Mechanics, Nuclear Engrg. and Design, Vol. 80, pp. 233-245.
Mazars, J. and Pijaudier-Cabot, G. (1989), Continuum Damage Theory - Application to Concrete, J. Engrg. Mech. ASCE, Vol. 115, pp. 345-365.

Nadai, A. (1950), Theory of Flow and Fracture of Solids, Vol. 1, second edition, Mc Graw Hill, New York, p. 572.
Nooru-Mohamed, M.B. (1992), Mixed-Mode Fracture of Concrete : An Experimental Approach, Doctotal Dissertation, Delft University of Technology, the Netherlands.
Ortiz, M. (1985), A Constitutive Theory for the Inelastic Behaviour of Concrete, Mechanics of Materials, Vol. 4, pp. 67-93.
Ortiz, M. and Simo, J.C. (1986), An Analysis of a New Class of Integration Algorithm for Elastoplastic Constitutive Relations, Int. J. Num. Meth. Engrg., Vol. 23, pp. 353-366.
Pijaudier-Cabot, G. (1995), Nonlocal Damage, in Continuum Models for Matrials with Microstructures, H.B. Muhlhaus editor, Wiley Pubs, pp. 105-144.
Rots, J. G. (1988), Computational Modelling of Concrete Fracture, Doctotal Dissertation, Delft University of Technology, the Netherlands.
Schlangen, E. (1993), Experimental and Numerical Analysis of Fracture Processes in Concrete, Doctotal Dissertation, Delft University of Technology, the Netherlands.
Shah, S.P. and Maji, A. (1989), Experimental Observation of Cracking and Damage, in "Cracking and Damage", J. Mazars and Z.P. Bazant eds., Elsevier Pubs, pp. 15-29.
Sidoroff, F. (1981), Description of Anisotropic Damage Application to Elasticity, in Proc. IUTAM Symp. on Physical Nonlinearites in Structural Mechanics, J. Hult and J. Lemaitre eds., Springer Pubs, Berlin, pp. 237-244.
Simo, J.C. and Ju, J.W. (1987), Strain- and Stress-Based Continuum Damage Models - I Formulation, Int. J. Solids and Struct., Vol. 23, pp. 821-840.
Simo, J.C., and Taylor, R.L. (1986), Return Mapping Algorithm for Plane Stress Elastoplasticity, Int. J. Num. Meth. Engrg., Vol. 22, pp. 649-670.
Torrenti, J.M., Desrues, J., Acker, P. and Boulay C. (1989), Application of strereophotogrammetry to the Strain Localisation in Concrete Compression, in "Cracking and Damage", J. Mazars and Z.P. Bazant eds., Elsevier Pubs, pp. 30-41.
Valanis, K.C. (1991), A Global Damage Theory and the Hyperbolicity of the Wave Problem, ASME J. of Applied Mech., Vol. 58, pp. 311-316.
Willam K., Pramono E., and Sture S. (1986), Fundamental Issues of Smeared Crack Models, Proc. Int. Conf. of Fracture and Rocks, Shah S.P. and Swartz S.E. eds., Springer-Verlag, pp. 142-157.
Yazdani, S., and Schreyer, H.L. (1990), Combined Plasticity and Damage Mechanics Model for Plain Concrete, J. Engrg. Mech. ASCE, Vol. 116, pp. 1435-1450.

Damage Mechanics in Engineering Materials
G.Z. Voyiadjis, J.-W.W. Ju and J.-L. Chaboche (Editors)
© 1998 Elsevier Science B.V. All rights reserved.

Advanced Thermomechanical Constitutive Models for Airfield Concrete Pavement under High Temperatures

J. W. Ju and Y. Zhang

Department of Civil and Environmental Engineering, University of California, Los Angeles, CA 90095-1593, U.S.A.

An axisymmetric thermomechanical constitutive model is proposed for airfield concrete pavement under very rapid heating and cooling processes due to high-temperature exhaust gas from axisymmetric vectored thrust engines. Newman's crack growth model is applied to estimate the delamination (thermal spalling) time of the airfield concrete pavement at various locations due to the internal pore pressure. Furthermore, coupled heat and mass transfer in concrete pavement is considered.

1. INTRODUCTION

The ordinary Portland cement (OPC) concrete has been widely used in airbase facilities such as airfield runways and parking aprons. During the take-off and landing of advanced aircraft, OPC concrete airfield pavement is subjected to extremely rapid transient high-temperature loadings as well as thermal cycles of heating and cooling due to very hot exhaust gas emanating from modern vectored thrust engines (VTE), or auxiliary power units (APU), etc. Examples are the AV-8B Harrier, F/A-18, and the next generation Joint Strike Fighters (JSF). In particular, the exhaust gas temperature of a VTE could rapidly reach over 800 ^{0}C, and the corresponding exhaust velocity could go beyond 600 m/s.

Damage to airfield concrete pavement could be in the form of thermomechanical "spalling" or "scaling" of concrete runways and launch pads due to transient (monotonic or cyclic) high temperature loadings. Alternatively, "scaling" of concrete parking aprons could occur due to coupled thermal-mechanical-chemical degradation effects from heat and oils; cf. McVay, Smithson and Manzione (1993). Scaling refers to thin plate-like pieces or lamina that flake or peel off from the damaged concrete surfaces. By contrast, spalling refers to small, thin pancake-shaped pieces which explode into the air because of very large steam pressure in pores, high thermal gradients and large compressive thermal stresses (parallel to the surface in the pavement). Specifically, compressive stresses produce not only concrete crushing, but also a bulging instability (similar to buckling) of the top layer. Under these severe thermomechanical loadings, internal *microcracks* nucleate and propagate in concrete, leading to progressive delamination at some shallow depth beneath the pavement surface.

Thermomechanical behavior and properties of concretes at elevated temperatures have been studied in the past four decades primarily owing to the interests in heat resistance of concretes in

fire engineering, and conventional as well as nuclear electric power plants. We refer to Bazant et al. (1982) for an extensive literature review on high-temperature behavior of OPC and refractory concretes. Among the temperature-dependent properties of OPC concretes at high temperatures discussed by Bazant et al. (1982), important aspects include dehydration of cement, increase of porosity, moisture content, thermal expansion and shrinkage, pore steam pressure, loss of strength, thermal cracking due to thermal incompatibility, degradation of elastic moduli, thermal creep, heat capacity, thermal conductivity and thermal diffusivity, and explosive thermal spalling due to excessive pore steam pressure, etc.

2. AXISYMMETRIC HEAT CONDUCTION MODEL

2.1 Transient temperature distribution

When the airfield concrete pavement is subjected to vectored thrust from an axisymmetric engine nozzle, an axisymmetric heat conduction formulation can be employed. Due to the wide temperature range (say from 25 ^{0}C to 700 ^{0}C) considered, we must consider the density ρ, the specific heat c and the thermal conductivity K of concrete as functions of the temperature T. The axisymmetric heat conduction equation takes the form:

$$\rho c \frac{\partial T}{\partial t} = \frac{\partial}{\partial r}\left(K\frac{\partial T}{\partial r}\right) + \frac{K}{r}\frac{\partial T}{\partial r} + \frac{\partial}{\partial z}\left(K\frac{\partial T}{\partial z}\right) \tag{1}$$

In this study, the temperature history $T_s(t)$ at the pavement surface ($z = 0$) is prescribed based on experimental data. The heat flux is approximated as zero at the bottom pavement; i.e., $q = K\frac{\partial T}{\partial z} \approx 0$. Moreover, the heat flux at $r/R = 0$ and $r/R = \infty$ (the radial far field) is approximated as zero; i.e., $q = K\frac{\partial T}{\partial r} \approx 0$. For simplicity, the initial temperature in the concrete pavement is assumed to be $T_0 = 25$ ^{0}C.

We employ a conditionally stable *explicit* finite difference scheme to solve Eq. (1). We can obtain the following temperature solution:

$$T_{jl}^{n+1} = T_{jl}^{n} + \frac{\Delta t}{\rho_{jl}^{n} c_{jl}^{n}}\left\{\frac{K_{(j+\frac{1}{2})l}^{n}\left[T_{(j+1)l}^{n} - T_{jl}^{n}\right] - K_{(j-\frac{1}{2})l}^{n}\left[T_{jl}^{n} - T_{(j-1)l}^{n}\right]}{(\Delta r)^2} + \frac{K_{jl}^{n}}{r_{jl}}\frac{\left[T_{(j+1)l}^{n} - T_{jl}^{n}\right]}{\Delta r}\right.$$

$$\left. + \frac{K_{j(l+\frac{1}{2})}^{n}\left[T_{j(l+1)}^{n} - T_{jl}^{n}\right] - K_{j(l-\frac{1}{2})}^{n}\left[T_{jl}^{n} - T_{j(l-1)}^{n}\right]}{(\Delta z)^2}\right\} \tag{2}$$

For the foregoing explicit scheme, the von Neumann heuristic stability criterion takes the form:

$$\Delta t \leq \min_{j,l,n}\left[\frac{\rho_{jl}^{n} c_{jl}^{n} (\Delta_r)^2 (\Delta_z)^2}{K_{jl}^{n}\left(2(\Delta_r)^2 + 3(\Delta_z)^2\right)}\right] \tag{3}$$

Based on available experimental data from the literatures, we employ the following numerical values for varying thermal properties of the concrete pavement. (a) $\rho(T)$ changes linearly from 1.45 g/cm^3 at 105 ^{0}C to 1.3 g/cm^3 at 850 ^{0}C (Harmathy, 1970); (b) $c(T)$ increases linearly from 0.23 cal/g.^{0}C at 25 ^{0}C to 0.26 cal/g.^{0}C at 1000 ^{0}C (Harmathy and Allen, 1973); and (c) the thermal conductivity $K(T)$ changes linearly from 1.26 kcal/m.hr.^{0}C at 25 ^{0}C to 1.01 kcal/m.hr.^{0}C at 1000 ^{0}C.

A comparison is displayed in Figure 1 between the actual experimental data (Rish and McVay, 1994) and our model predictions for the temperatures versus time at different depths with $r/R = 0$ (the center line).

2.2 Pore pressure distribution

For simplicity, pores in concrete are modeled as spherical microvoids fully saturated with water at this time. Our formulation here follows the ASME Steam Tables; see, Keenan et al. (1978), Meyer et al. (1993). Specifically, during the saturation state (the K-function), the reduced saturation pressure becomes

$$\frac{P_K(r,z,t)}{P_{c1}} = exp\left\{\frac{1}{\theta}\,\frac{\sum_{i=1}^{5} k_i(1-\theta)^i}{1+k_6(1-\theta)+k_7(1-\theta)^2} - \frac{(1-\theta)}{k_8(1-\theta)^2+k_9}\right\} \tag{4}$$

where $\theta = (T(r,z,t)+273.15)/T_{c1}$, $P_{c1} = 22.12$ MPa, and $T_{c1} = 647.3$ ^{0}K. The constants in Eq. (4) are $k_1 = -7.691234564$, $k_2 = -26.08023696$, $k_3 = -168.1706546$, $k_4 = 64.23285504$, $k_5 = -118.9646225$, $k_6 = 4.167117320$, $k_7 = 20.97506760$, $k_8 = 10^9$, and $k_9 = 6$.

By contrast, above the critical temperature, the pore pressure follows the L-function:

$$\frac{P_L(r,z,\ t)}{P_{c1}} = L_0 + L_1\theta + L_2\theta^2 \tag{5}$$

where $L_0 = 15.74373327$, $L_1 = -34.17061978$, and $L_2 = 19.31380707$.

2.3 Thermoelastic stress-strain relationship with void effects

For a linear elastic concrete pavement with many spherical microvoids, the additional strain $\overline{\epsilon}^d$ due to the void effects can be approximately rendered as

$$\overline{\epsilon}^d = \frac{1}{2V}\sum_k \left[\int_s (\mathbf{u}\otimes\mathbf{n}+\mathbf{n}\otimes\mathbf{u})\,dS\right]^{(k)} \tag{6}$$

where V denotes the (sufficiently large) representative volume, $\sum$ denotes a summation operator over all voids, $\mathbf{u}$ denotes the displacement vector, $\mathbf{n}$ signifies the outward normal vector associated with $\mathbf{u}$, and S signifies the void surface.

The stress-strain relationship with void effects will be:

$$\begin{Bmatrix} \epsilon_{xx} \\ \epsilon_{yy} \\ \epsilon_{zz} \\ 2\epsilon_{yz} \\ 2\epsilon_{zx} \\ 2\epsilon_{xy} \end{Bmatrix} = \frac{1}{E^*} \begin{bmatrix} 1 & -\nu^* & -\nu^* & 0 & 0 & 0 \\ -\nu^* & 1 & -\nu^* & 0 & 0 & 0 \\ -\nu^* & -\nu^* & 1 & 0 & 0 & 0 \\ 0 & 0 & 0 & 2(1+\nu^*) & 0 & 0 \\ 0 & 0 & 0 & 0 & 2(1+\nu^*) & 0 \\ 0 & 0 & 0 & 0 & 0 & 2(1+\nu^*) \end{bmatrix} \begin{Bmatrix} \sigma_{xx} \\ \sigma_{yy} \\ \sigma_{zz} \\ \sigma_{yz} \\ \sigma_{zx} \\ \sigma_{xy} \end{Bmatrix} + \phi PC \begin{Bmatrix} 1 \\ 1 \\ 1 \\ 0 \\ 0 \\ 0 \end{Bmatrix} + \alpha \Delta T \begin{Bmatrix} 1 \\ 1 \\ 1 \\ 0 \\ 0 \\ 0 \end{Bmatrix} \tag{7}$$

where E^* and ν^*, respectively, are the effective elastic Young's modulus and Poisson's ratio with void effects:

$$E^* = \frac{E}{1 + \phi A} \tag{8}$$

$$\nu^* = \frac{\nu + \phi B}{1 + \phi A} \tag{9}$$

Here, E is the virgin elastic Young's modulus without voids, ν is the virgin elastic Poisson's ratio without voids, P is the internal pore pressure, α denotes the linear thermal expansion coefficient, ΔT denotes the temperature change, and

$$A \equiv \frac{3(1-\nu)(9+5\nu)}{2(7-5\nu)} \tag{10}$$

$$B \equiv \frac{3(1-\nu)(1+5\nu)}{2(7-5\nu)} \tag{11}$$

$$C \equiv \frac{(1+\nu)}{2E} \tag{12}$$

$$\phi \equiv \frac{4\pi}{3V} \sum_{i=1}^{N} \bar{R}_i^3 \tag{13}$$

Obviously, ϕ is the void volume fraction. Moreover, $\bar{R}$ denotes the void radius.

Here, we synthesize available experimental data from the literatures and adopt the following properties: $E^* = 34{,}475\left[1 - 0.00139(T - T_0) + 4.48 \times 10^{-7}(T - T_0)^2\right]$ MPa (Cruz, 1966),

$\nu^* = 0.27 - 0.000453(T - T_0)$ (Marechal, 1972), and $\alpha = 1.3 \times 10^{-5}/^0$C (Cruz and Gillen, 1980).

We assume that the radial displacements are zero at $r = 0$ and $r = \infty$ (or a large distance compared to R, the radius of the nozzle). Similarly, we assume that the displacements in the radial and axial directions are zero at $z = \infty$ (or a large distance compared to the thickness of the pavement).

To calculate the stress distributions inside the concrete pavement, we employ the axisymmetric 4-node linear elastic finite element codes for each specific time t. The radial stress distribution at $r/R = 0$ is shown in Figure 2 for various time.

3. A CRACK GROWTH MODEL

According to the Newman's crack growth model (Newman, 1971; Tada, et al., 1985), tension microcracks may be induced from microvoids when the vapor pressures inside spherical microvoids increase to a certain level. The Mode I crack tip quasi-static stress intensity factor due to the vapor pressure inside a microvoid reads

$$K_{Is} = P(r, z, t)\sqrt{\pi a}\, F\left(\frac{a}{a + \bar{R}}\right) \tag{14}$$

where a is the crack length, $\bar{R}$ is the microvoid radius, and $F(s) = 1+(1-s)(0.5+0.743(1-s)^2)$.

The quasi-static crack growth criterion takes the form:

$$K_{Is} \geq K_{Ic} \tag{15}$$

where K_{Ic} is the Mode I fracture toughness of concrete (taken as a constant, 200 KN/$m^{3/2}$). For simplicity, we assume an initial crack length $a_0 = 0.1\bar{R}$ for a microvoid in our calculation. From Ju and Zhang (1997) and the present study, we find that the dynamic crack growth velocity $\dot{a}$ is very high, approximately 2,000 m/sec. Therefore, once a crack propagates from the perimeter of a pore, it practically takes no time to reach the delamination (thermal spalling) state.

It is known that tension cracks grow in the general direction of maximum compression. As was discussed in the previous section and figures, the in-plane stress state in the plane parallel to the concrete surface is compressive. Therefore, cracks are expected to grow from pressured voids along the direction parallel to the concrete pavement surface.

A pore size distribution curve was provided by Meyer-Ottens (1975), which is adopted here to estimate the pore sizes. Since the *largest* pore size is the dominant factor, the pore size under consideration is taken as $\bar{R} = 5\mu m$. It is emphasized again that the crack growth speed is very fast and the delamination occurs instantaneously as soon as Eq. (15) is satisfied.

To illustrate the behavior of the proposed simple delamination model, Figure 3 shows the time to delamination versus r/R at the airfield concrete pavement surface. Figure 4 displays the time to delamination versus various depths at $r/R = 0$.

4. COUPLED HEAT AND MASS TRANSFER IN CONCRETE

To model the mass (moisture and exhaust) and heat transfer through concrete, coupled partial differential equations must be solved concerning the conservation of moisture, exhaust and energy.

4.1 Coupled governing equations of heat and mass transfer in concrete

Let us assume a single potential which governs the moisture flux J_w and gas flux J_g:

$$J_w = -\frac{a_w}{g}\nabla p_w \tag{16}$$

$$J_g = -\frac{a_g}{g}\nabla p_g \tag{17}$$

The heat flux takes the form:

$$q = -k\nabla T \tag{18}$$

where k is the heat conductivity of concrete.

The conservation of mass for moisture requires that

$$\frac{\partial w}{\partial t} = -\nabla \cdot J_w + \frac{\partial w_d}{\partial t} \tag{19}$$

where w is the moisture concentration, w_d is the total mass of free (evaporable) water that has been released into the pore by dehydration, and w_d is obtained from experimental data.

The conservation of mass for gas requires that

$$\frac{\partial G}{\partial t} = -\nabla \cdot J_g \tag{20}$$

where G is the gas concentration.

The balance of heat leads to

$$\rho C\frac{\partial T}{\partial t} - C_{wa}\frac{\partial w}{\partial t} - C_w J_w \cdot \nabla T - C_{ga}\frac{\partial G}{\partial t} - C_g J_g \cdot \nabla T = -\nabla \cdot q \tag{21}$$

where ρ, C are the mass density and isobaric heat capacity of concrete (including its chemically combined water, but excluding its free water), C_{wa} is heat of sorption of free water, C_w is the isobaric heat capacity of bulk (liquid) water, C_{ga} is the heat of sorption of gas, and C_g is the isobaric heat capacity of gas.

4.2 Equations of state of pore water and gas

For nonsaturated (partially saturated) concrete, we have $p_w \leq p_s(T)$. Here, $p_s(T)$ is the saturation pressure of water at temperature T. Bazant et al. (1978) provided the following semi-empirical expression by fitting the test data. For $h \leq 0.96$, we write

$$\frac{w}{c} = \left(\frac{w_1}{c}h\right)^{\frac{1}{m(T)}} \tag{22}$$

where

$$h = \frac{p_w}{p_s(T)} \tag{23}$$

$$m(T) = 1.04 - \frac{T'}{22.34 + T'} \tag{24}$$

$$T' = \left(\frac{T + 10}{T_0 + 10}\right)^2 \tag{25}$$

Here, T is the temperature (^oC) and $T_0 = 25^oC$. Further, c is the mass of (anhydrous) cement of concrete (kg/m^3) and w_1 is the saturation water content at 25^oC. It is convenient to determine w_1/c accurately for a given concrete mix.

For saturated concrete, we have $p_w \geq p_s(T)$. For $h \geq 1.04$, we write

$$w = \frac{\epsilon}{\nu} \tag{26}$$

where ν is the specific volume of water, and ϵ is the available pore space for water by taking into account the increase in pore space resulting from elastic volume expansion, decrease in adsorbable water and/or partial dehydration.

For $0.96 \leq h \leq 1.04$, we use the linear interpolation to calculate w.

For gas content, we use the following equation to calculate G:

$$G = \frac{p_g \epsilon (1 - s)}{R_g(T + 273.15)} \tag{27}$$

where R_g is the gas constant and s is the volume fraction of liquid water in pore.

4.3 Numerical simulation

For simplicity, only one dimensional heat and mass transfer problem will be considered here. We employ the explicit finite difference scheme to solve this problem. For any explicit finite difference scheme, we must consider the stability criterion of the numerical solution.

The initial water content in concrete is $95kg/m^3$, and the saturation water content in concrete w_1 at 25^oC is $100kg/m^3$. The cement content is $300kg/m^3$. The initial porosity of concrete at 25^oC is 0.15. The water permeability of concrete at 25^oC is $a_{wo} = 5.0 \times 10^{-13}$.

Pore pressure histories at different depths are plotted in Figure 5. In addition, the water content histories at different depths are displayed in Figure 6. We observe that the drying rate near the concrete pavement surface (the heating surface) is very high. This is due to the high heating rate of the concrete pavement surface by the exhaust gas from the aircraft vectored thrust nozzle. The type of aircraft engine determines the heating rate of the concrete pavement surface.

ACKNOWLEDGMENTS.

This work is sponsored by the Air Force Office of Scientific Research under research grant number F49620-96-1-0384 (Program Manager: Capt. Michael Chipley). The support and interest of Capt. Michael Chipley are gratefully acknowledged.

REFERENCES

1. BAZANT, Z. P., AND THONGUTHAI, W., (1978), "Pore pressure and drying of concrete at high temperature", *J. Eng. Mech. Div.*, ASCE, **104 (5)**, 1059–1079.

2. BAZANT, Z. P., CHERN, J. C., ABRAMS, M. S., AND GILLEN, M. P., (1982), "Normal and refractory concretes for LMFBR applications – Vol. 1: Review of literature on high-temperature behavior of Portland cement and refractory concretes", *Electric Power Research Institute Technical Report* NP-2437, Vol. 1, June 1982, Electric Power Research Institute.

3. CRUZ, C. R., (1966), "Elastic properties of concrete at high temperature", *J. PCA Res. & Dev. Lab.*, PCA Bull. **191**, 37–45.

4. CRUZ, C. R. AND GILLEN, M., (1980), "Thermal expansion of Portland cement paste, mortar and concrete at high temperatures", *Fire and Materials*, **4 (2)**.

5. HARMATHY, T. Z., (1970), "Thermal properties of concrete at elevated temperature", ASTM *J. of Materials*, **5**, 47–74.

6. HARMATHY, T. Z. AND ALLEN, L. W., (1973), "Thermal properties of selected masonry unit concretes", *J. ACI*, **70**, 132–142.

7. JU, J. W., AND ZHANG, Y., (1997), "A thermomechanical model for airfield concrete pavement under transient high temperature loadings", *Int. J. of Damage Mechanics*, in press.

8. KEENAN, J. H., KEYES, F. G., HILL, P. G., AND MOORE, J. G., (1978), "Steam tables: thermodynamic properties of water including vapor, liquid, and solid phases: International Systems of units–S.I.", John Wiley & Sons, New York.

9. MARECHAL, J. C., (1972), "Variations in the modulus of elasticity and Poisson's ratio with temperature", *Concrete for Nuclear Reactors*, **1**, ACI SP-34, 495–503.

10. MCVAY, M. C., SMITHSON, L., D., AND MANZIONE, C., (1993), "Chemical damage to airfield concrete aprons from heat and oils", *ACI Materials Journal*, **90 (3)**, 253–258.

11. MEYER, C. A., MCCLINTOCK, R. B., SILVESTRI, G. J., AND SPENCER, R. C., JR., (1993), "ASME steam tables: thermodynamic and transport properties of steam", 6th ed., ASME Press, New York.

12. MEYER-OTTENS, C., (1975), "On the problem of spalling of concrete structural components under fire-induced stress", *Deutscher Ausschuss fuer Stahlbeton*, No. **248**, Berlin, Germany.

13. NEWMAN, J. C., (1971), "An improved method of collocation for the stress analysis of cracked plates with various shaped boundaries", NASA Technical Note, NASA TN D-**6376**.

14. RISH, J. W., III, AND MCVAY, M. C., (1994), "Moisture release and migration in concrete due to vectored thrust", Annual Task Report for AFOSR Contract No. 93WL004.

15. TADA, H., PARIS, P. C., AND IRWIN, G., (1985), "The stress analysis of crack handbook", 2nd edition, Paris Production Incorporated.

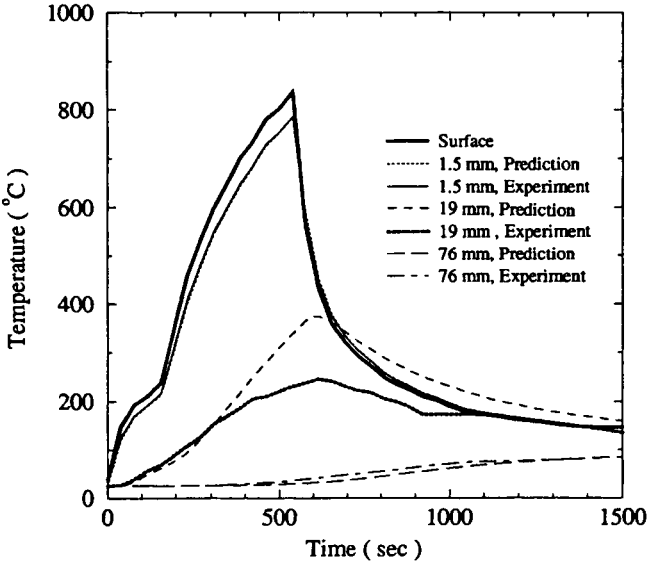

Figure 1. A comparison between the experimental data and predictions on temperature history at $r/R = 0$.

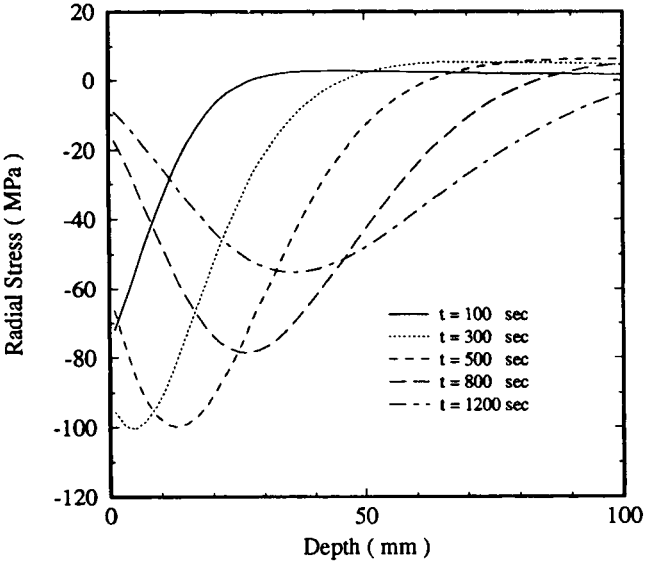

Figure 2. The radial stress distribution at $r/R = 0$.

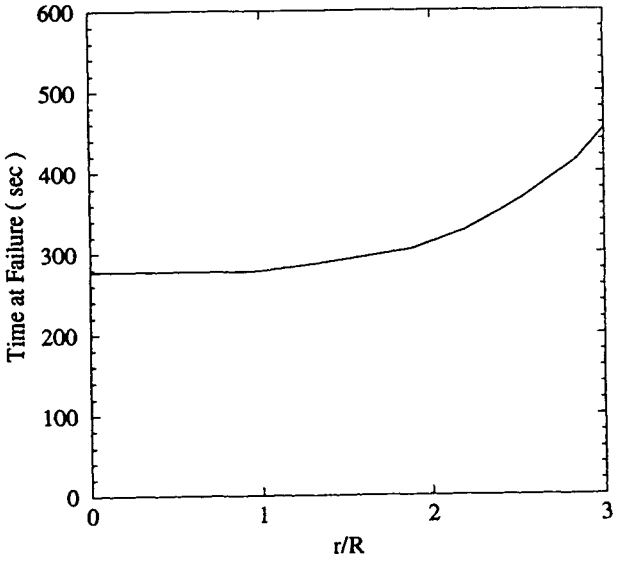

Figure 3. The time to delamination failure as a function of r/R at the surface.

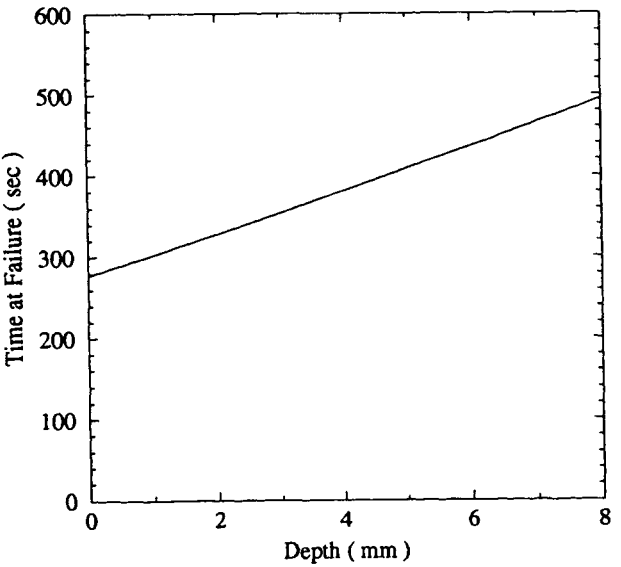

Figure 4. The time to delamination failure as a function of the depth at $r/R = 0$.

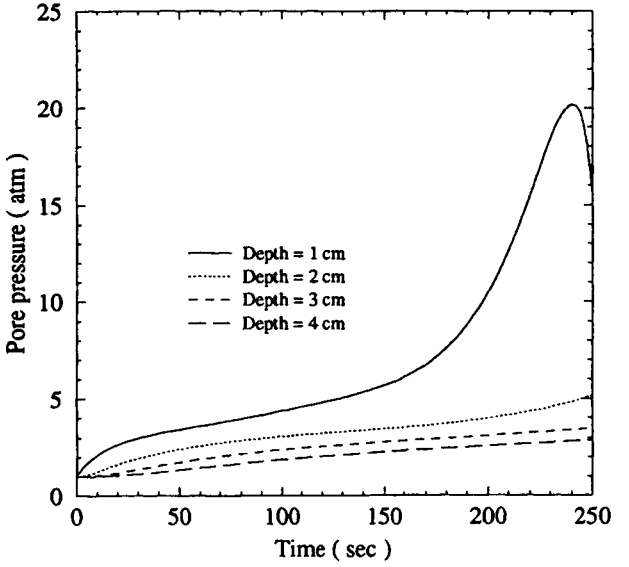

Figure 5. The pore pressure histories at different depths.

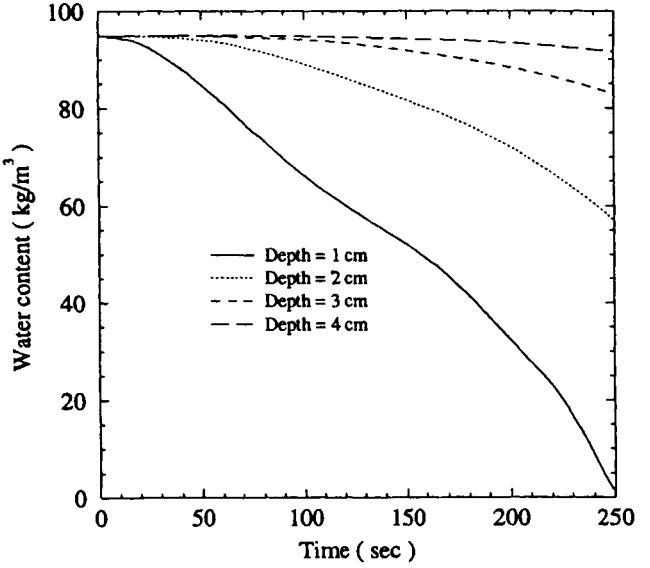

Figure 6. The water content histories at different depths.

Damage Mechanics in Engineering Materials
G.Z. Voyiadjis, J.-W.W. Ju and J.-L. Chaboche (Editors)
© 1998 Elsevier Science B.V. All rights reserved.

Mechanical behavior of thin-film coating/substrate systems under nanoindentation

Jackie Li[a], Alex Hsieh[b] and Tsu-Wei Chou[a]

[a]Center for Composite Materials, and Department of Mechanical Engineering, University of Delaware, Newark, DE 19716, U.S.A.

[b]Army Research Laboratory, Weapons and Materials Research Directorate, AMSRL-WM-MA, Aberdeen Proving Ground, MD 21005-5069, U.S.A.

This paper investigates the mechanical behavior of thin-film coating/substrate systems under nanoindentation testing. Experimental results have demonstrated the different failure mechanisms of material systems consist of hard-coating on soft substrate and soft-coating on hard substrate. An analytical model using Hankel's transform method is introduced to examine the displacement and stress fields of a thin-film coating/substrate system with perfect interfacial bonding under an axisymmetrical compressive loading on the coating surface. The present analysis can account for the influence of the film thickness and the material properties of the substrate. This knowledge of the stress fields provides the basis of understanding of the failure mechanisms of thin-film coating/substrate systems. Finally, the influence of Poisson's ratios of the film and the substrate are discussed in detail.

1. INTRODUCTION

Thin-film coatings have been used extensively in industry for a variety of purposes, for example, protection of the substrate materials from mechanical, thermal and chemically aggressive environment. Nanoindentation tests have been used to measure the mechanical properties of coatings and their bonding to the substrate. Two types of coating are considered in the present study: hard-coating on a soft-substrate such as diamond-like carbon (DLC) coating on polycarbonate, and soft-coating on a hard-substrate such as DLC on silicon. Distinct failure mechanisms have been observed for these two types of coating

systems through nanoindentation tests. In order to better understand the failure of coating/substrate systems, an analytical model using Hankel's transform [1] have been developed to evaluate the elastic fields due to nanoindentation. In most of the existing works, the substrate material is often treated as a rigid body [2-4], and numerical iteration [5, 6] and finite element methods [3,4, 7-10] have been adopted for the analyses.

In this paper, first, we present the experimental observations of nanoindentation fracture for both hard- and soft-coating/substrate systems. Then, the analytical elastic solution, which are capable of accounting for the influences of the thin-film thickness and material properties, are presented to explain the failure behavior of the coating/substrate systems. Finally, the Poisson's ratio effect of the coating/substrate system is discussed in details.

2. EXPERIMENTAL OBSERVATIONS

Nanoindentation tests for thin-film coating/substrate systems were conducted at the Oak Ridge National Laboratory, and the load-displacement relations of the coating/substrate systems have been obtained [11]. The coating and substrate material properties can then be evaluated using the load-displacement data and the continuous stiffness measurement technique developed by Oliver and Pethica [12]. Also failure mechanisms can be observed microscopically during the indentation test, which are recapitulated in the following.

Diamond-like carbon (DLC) thin film coating material was deposited on the substrates of silicon and polycarbonate through ion beam deposition. The thickness of DLC coating was varied from 0.1 μm to 2μm to examine its influence.

Nanoindentation experiments were performed at room temperature with a Berkovich indenter. Here the specimens of DLC/Si with 2μm and 0.1μm coating thickness, and DLC/polycarbonate with 0.1μm coating thickness were used in the nanoindentation tests. The following elastic properties of coatings and substrates are quoted from reference [11].

TABLE 1. Elastic properties of coatings and substrates

Material	Elastic modulus (GPa)	Poisson's Ratio
DLC (in DLC/Si)	110	0.2
Silicon	200	0.2
DLC(in DLC/polycarbonate)	38	0.2
Polycarbonate	3	0.35

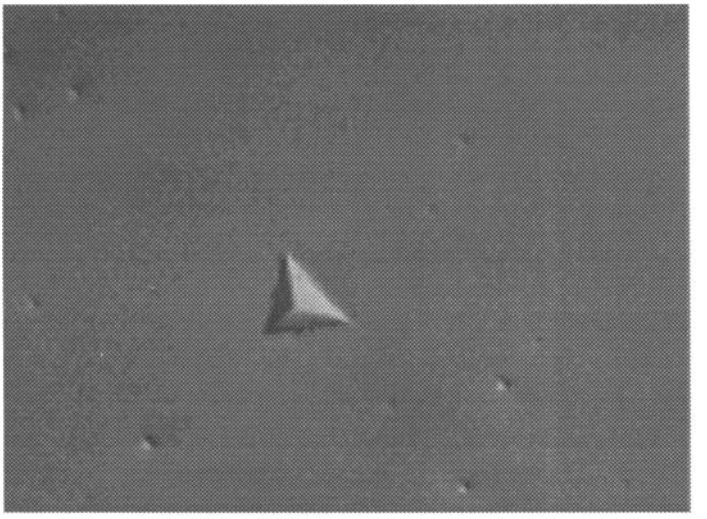

(a)

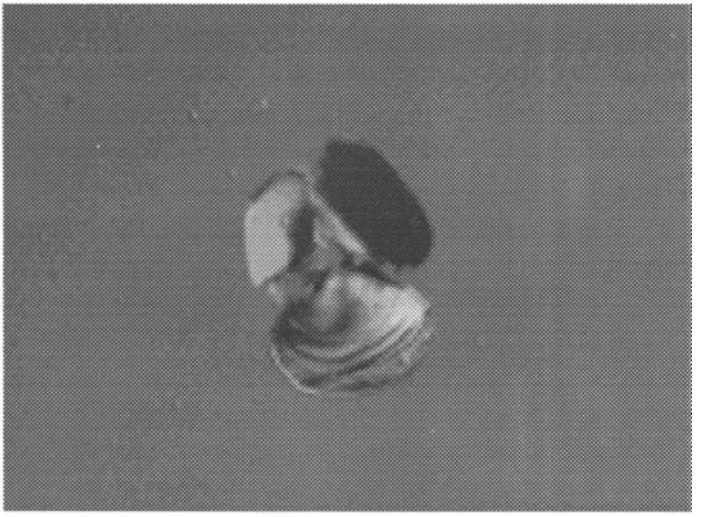

(b)

Fig.1. Micrographs of 2μm indentation depth on DLC/Si system with DLC coating thickness: (a) t=2μm, and (b) t=0.1μm [11].

From the above Table, DLC/Si and DLC/polycarbonate clearly represent the elastically soft-coating/hard-substrate system and hard-coating/soft-substrate system, respectively.

These two material systems exhibit totally different failure phenomena under nanoindentation tests. Figure 1(a) and (b) show the micrographs of 2μm indentation depth of DLC/Si with 2μm and 0.1μm coating thickness, respectively. In Fig. 1(a) no failure is observed since the DLC coating is considerably thicker and the indentation depth is not high enough to cause any fracture. However, when the thickness of the DLC coating becomes very thin, delamination around the edge of the contact zone in the DLC/Si system can be observed very clearly in Fig. 1(b).

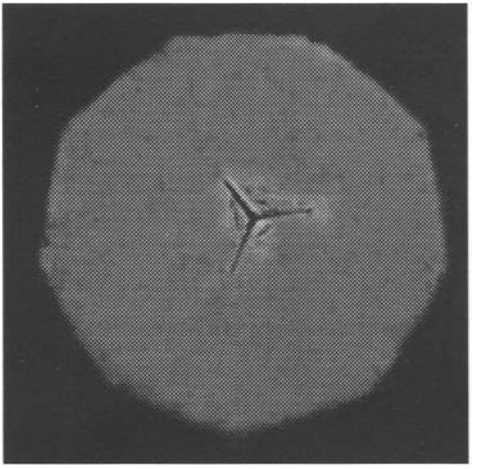

Fig.2 Micrograph of 4μm indentation depth on DLC/polycarbonate with 0.1μm DLC coating thickness [11].

On the other hand, Fig. 2 shows the major cracks in the film along the three edges of the pyramid-shaped Berkovich indenter and micro cracks in the film around the contact zone for DLC/polycarbonate. The contrast between Fig.1(b) and Fig.2 indicates that delamination is the dominant failure mode in soft-coating system, whereas film cracking occurs first in the hard-coating system. The knowledge of the stress fields in the coating/substrate systems under nanoindentation will give better insight of their failure behavior.

3. THEORETICAL MODELING

Li and Chou [13] recently have developed an analytically elastic solution of thin-film coating/substrate system under an axisymmetric loading by using Hankel's transform technique. Their approach is adopted in the present study. Instead of solving the elastic fields due to Berkovich indentation, we consider the indentation problem of the coating/substrate system under an axisymmetric loading shown in Fig.3. This is motivated by the work of Gao and Wu [14], who have pointed out that an axisymmetric cylindrical punch can be used to model nonaxisymmetrical indenters (e.g. Vickers and Berkovich indenters) due to the insensitivity of the stress distribution to indenter cross sectional shape.

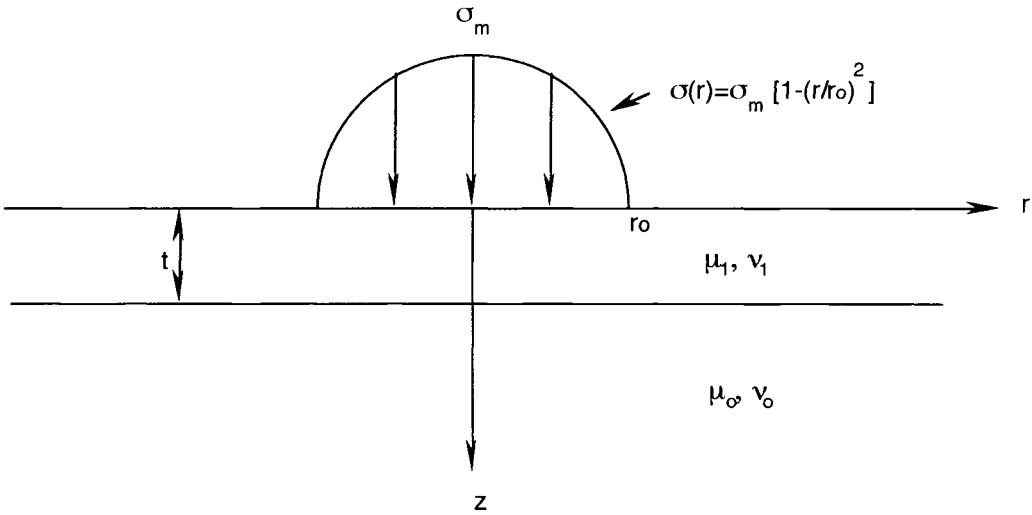

Fig.3 A schematic diagram of a coating/substrate system under an axisymmetric loading

In Fig.3, the thin-film is denoted as phase 1, and phase 0 is for the half-space substrate. Both phases are assumed to be isotropic and perfectly bonded to each other. The elastic shear modulus and Poisson's ratio are written as μ_i and ν_i for the i-th phase. The coating thickness, radius of the contact zone, and the maximum loading stress are denoted as t, r_0, and σ_m, respectively. Here we choose the cylindrical polar coordinates (r, θ, z) to describe the axisymmetric problem with respect to z-axis, and the stress components are σ_r, σ_θ, σ_z, $\tau_{r\theta}$, $\tau_{\theta z}$ and τ_{zr}.

The symmetry condition with respect to the z-axis implies that $\tau_{r\theta}$ and $\tau_{\theta z}$ vanish, and the equilibrium equations are reduced to

$$\frac{\partial \sigma_r}{\partial r} + \frac{\partial \tau_{rz}}{\partial z} + \frac{1}{r}(\sigma_r - \sigma_\theta) = 0 \tag{1}$$

$$\frac{\partial \tau_{rz}}{\partial r} + \frac{\partial \sigma_z}{\partial z} + \frac{\tau_{zr}}{r} = 0. \tag{2}$$

By introducing a stress function Φ, the stress components can be expressed in terms of Φ as follows:

$$\begin{aligned}
\sigma_r &= \lambda \nabla^2 \Phi_z - 2(\lambda + \mu)\Phi_{rrz} \\
\sigma_z &= (3\lambda + 4\mu)\nabla^2 \Phi_z - 2(\lambda + \mu)\Phi_{zzz} \\
\sigma_\theta &= \lambda \nabla^2 \Phi_z - 2(\lambda + \mu)\frac{1}{r}\Phi_{rz} \\
\tau_{zr} &= (\lambda + 2\mu)\frac{\partial}{\partial r}\nabla^2 \Phi - 2(\lambda + \mu)\Phi_{zzr}
\end{aligned} \tag{3}$$

where λ is the Láme constant, and $\Phi_{rrz} = \partial^3 \Phi / \partial r^2 \partial z$. In the case of axial symmetry, $\nabla^2 \equiv \frac{\partial^2}{\partial r^2} + \frac{1}{r}\frac{\partial}{\partial r} + \frac{\partial^2}{\partial z^2}$. Then the compatibility equation can be written as

$$\nabla^4 \Phi = 0. \tag{4}$$

Following Harding and Sneddon [14], the Hankel's transform is applied to solve the above biharmonic equation

$$G = \int_0^\infty \Phi r J_0(\xi r) dr \tag{5}$$

where $J_0(\xi r)$ is a Bessel function of the first kind of order 0. Thus, Equation (4) is reduced to an ordinary differential equation

$$\left(\frac{d^2}{dz^2} - \xi^2\right)^2 G = 0. \tag{6}$$

The solution of Eq.(6) is easily obtained as

$$G = (A + Bz)e^{\xi z} + (C + Dz)e^{-\xi z} \tag{7}$$

where A, B, C and D are constants which are in general functions of ξ and can be determined from the boundary conditions. By inverting Hankel's transform, the stress function can be solved as

$$\Phi = \int_0^\infty \xi G J_0(\xi r) d\xi . \tag{8}$$

Based upon Eq.(8), the stress fields then can be obtained from Eqs. (3).

For the material systems considered here, the stress function Φ needs to be found for the coating as well as the substrate. Thus, instead of four coefficients in Eq. (8) there are eight coefficients denoted as A_0, B_0, C_0, D_0, A_1, B_1, C_1, and D_1, where the subscripts 0 and 1 represent the substrate and coating phase, respectively. Since all the stresses and displacements vanish when $z \to \infty$, A_0 and B_0 must be zero, and the remaining six coefficients can be determined from the boundary and interfacial continuity conditions.

The boundary loading conditions in the indentation problem considered here are expressed as

$$\sigma_z(r,0) = -q(r), \qquad \tau_{zr}(r,0) = 0 \tag{9}$$

where the negative sign in the first equation indicates a compression, and the function q(r) can be further expressed in terms of Hankel's transform as

$$q(r) = \int_0^\infty \bar{q}(\xi) \xi J_0(\xi r) d\xi . \tag{10}$$

Perfect bonding at the interface between the film and the substrate is assumed. Then the interfacial continuity conditions at the plane $z = t$ are given as

$$\begin{aligned} u_1(r,t) &= u_0(r,t) & w_1(r,t) &= w_0(r,t) \\ \sigma_{z1}(r,t) &= \sigma_{z0}(r,t) & \tau_{zr1}(r,t) &= \tau_{zr0}(r,t) \end{aligned} \tag{11}$$

By using the boundary and interface conditions (9) and (11), and following the derivation of Li and Chou [13], the stress components are obtained as

$$\sigma_{ri}(\rho,\varsigma)=\frac{1}{t^2}\int_0^\infty \bar{q}(\xi)\left[\bar{\sigma}_{ri}^{*}(\eta,\varsigma)+\frac{\bar{\sigma}_{ri}(\eta,\varsigma)}{D(\eta)}\right]\eta J_0(\rho\eta)d\eta$$
$$-\frac{1}{\rho t^2}\int_0^\infty \bar{q}(\xi)\left[\bar{\sigma}_{ri}^{*}(\eta,\varsigma)+\frac{\bar{\sigma}_{ri}(\eta,\varsigma)}{D(\eta)}\right]J_1(\rho\eta)d\eta \tag{12}$$

$$\sigma_{\theta i}(\rho,\varsigma)=\frac{1}{t^2}\int_0^\infty \bar{q}(\xi)\frac{\bar{\sigma}_{\theta i}(\eta,\varsigma)}{D(\eta)}\eta J_0(\rho\eta)d\eta$$
$$+\frac{1}{\rho t^2}\int_0^\infty \bar{q}(\xi)\left[\bar{\sigma}_{\theta i}^{*}(\eta,\varsigma)+\frac{\bar{\sigma}_{\theta i}(\eta,\varsigma)}{D(\eta)}\right]J_1(\rho\eta)d\eta \tag{13}$$

$$\sigma_{zi}(\rho,\varsigma)=\frac{1}{t^2}\int_0^\infty \bar{q}(\xi)\left[\bar{\sigma}_{zi}^{*}(\eta,\varsigma)+\frac{\bar{\sigma}_{zi}(\eta,\varsigma)}{D(\eta)}\right]\eta J_0(\rho\eta)d\eta \tag{14}$$

$$\tau_{rzi}(\rho,\varsigma)=\frac{1}{t^2}\int_0^\infty \bar{q}(\xi)\left[\bar{\tau}_{rzi}^{*}(\eta,\varsigma)+\frac{\bar{\tau}_{rzi}(\eta,\varsigma)}{D(\eta)}\right]\eta J_1(\rho\eta)d\eta \tag{15}$$

where

$$\bar{\sigma}_{r1}^{*}(\eta,\varsigma)=\frac{1}{2}e^{-\varsigma\eta},\qquad \bar{\sigma}_{r0}^{*}(\eta,\varsigma)=0$$

$$\bar{\sigma}_{r1}(\eta,\varsigma)=\frac{1}{2}\left\{\left[-a+3b+2b(2+\varsigma)\eta-4b(1-\varsigma)\eta^2\right]e^{-(2-\varsigma)\eta}-2ab(1+\varsigma\eta)e^{-(4-\varsigma)\eta}\right.$$
$$\left.-(3-2\varsigma\eta)e^{-\varsigma\eta}+2b\left[2-(2+\varsigma)\eta+2\varsigma\eta^2\right]e^{-(2+\varsigma)\eta}-abe^{-(4+\varsigma)\eta}\right\}$$

$$\bar{\sigma}_{r0}(\eta,\varsigma)=-\frac{2\gamma_0}{\alpha}\left\{\left[-c+3d-2\left(c-d(2+\varsigma)\right)\eta\right]e^{-\varsigma\eta}\right.$$
$$\left.+\left[ac-3bd+2bd(2+\varsigma)\eta+4bd(1-\varsigma)\eta^2\right]e^{-(2+\varsigma)\eta}\right\} \tag{16}$$

$$\bar{\sigma}_{r1}^{'}(\eta,\varsigma)=\frac{1}{2}\left\{\left[-a+b\gamma_1+2b(2\gamma_2+\varsigma)\eta-4b(1-\varsigma)\eta^2\right]e^{-(2-\varsigma)\eta}-2ab(\gamma_2+\varsigma\eta)e^{-(4-\varsigma)\eta}\right.$$
$$\left.-(\gamma_1-2\varsigma\eta)e^{-\varsigma\eta}+2b\left[2\gamma_0-(2\gamma_2+\varsigma)\eta+2\varsigma\eta^2\right]e^{-(2+\varsigma)\eta}-abe^{-(4+\varsigma)\eta}\right\}$$

$$\bar{\sigma}_{r0}^{'}(\eta,\varsigma)=-\frac{2\gamma_0}{\alpha}\left\{\left[-c+d\gamma_3-2\left(c-d(1-\varsigma)\right)\eta\right]e^{-\varsigma\eta}\right.$$
$$\left.+\left[ac-bd\gamma_3+2bd(2\gamma_4+\varsigma)\eta+4bd(1-\varsigma)\eta^2\right]e^{-(2+\varsigma)\eta}\right\}$$

with

$$\eta = \xi t, \quad \varsigma = z/t, \quad \text{and} \quad \rho = r/t$$

$$D(\eta) = 1 - (a + b + 4b\eta^2)e^{-2\eta} + abe^{-4\eta}$$

$$a = \frac{(3-4\nu_0)\alpha - (3-4\nu_1)}{1+(3-4\nu_0)\alpha}, \quad b = \frac{\alpha - 1}{\alpha + (3-4\nu_1)}, \quad \alpha = \frac{\mu_1}{\mu_0}$$

$$\gamma_0 = 1-\nu_1, \quad \gamma_1 = 3-4\nu_1, \quad \gamma_2 = 1-2\nu_1, \quad \gamma_3 = 3-4\nu_0 \tag{17}$$

and $\gamma_4 = 1-2\nu_0$

$$c = \frac{\alpha}{\alpha+\gamma_1}, \quad d = \frac{\alpha}{\gamma_3\alpha+1}.$$

Also,

$$\bar{\sigma}^{\bullet}_{\theta 1}(\eta,\varsigma) = \bar{\sigma}^{\bullet}_{r1}(\eta,\varsigma), \quad \bar{\sigma}^{\bullet}_{\theta 0}(\eta,\varsigma) = 0$$

$$\bar{\sigma}_{\theta 1}(\eta,\varsigma) = -2\nu_1\left[-(1+2\eta)be^{-(2-\varsigma)\eta} + abe^{-(4-\varsigma)\eta} + e^{-\varsigma\eta} - (1-2\eta)be^{-(2+\varsigma)\eta}\right]$$

$$\bar{\sigma}_{\theta 0}(\eta,\varsigma) = -\frac{8\nu_0\gamma_0 d}{\alpha}\left[e^{-\varsigma\eta} - (1-2\eta)be^{-(2+\varsigma)\eta}\right]$$

$$\bar{\sigma}^{'}_{\theta 1}(\eta,\varsigma) = \bar{\sigma}^{'}_{r1}(\eta,\varsigma), \qquad \bar{\sigma}^{'}_{\theta 0}(\eta,\varsigma) = \bar{\sigma}^{'}_{r0}(\eta,\varsigma) \tag{18}$$

and

$$\bar{\sigma}^{\bullet}_{z1}(\eta,\varsigma) = -\bar{\sigma}^{\bullet}_{r1}(\eta,\varsigma), \quad \bar{\sigma}^{\bullet}_{z0}(\eta,\varsigma) = 0$$

$$\bar{\sigma}_{z1}(\eta,\varsigma) = \frac{1}{2}\left\{\left[a+b+2b(2-\varsigma)\eta + 4b(1-\varsigma)\eta^2\right]e^{-(2-\varsigma)\eta} - 2ab(1-\varsigma\eta)e^{-(4-\varsigma)\eta}\right.$$
$$\left.-(1+2\varsigma\eta)e^{-\varsigma\eta} - 2b\left[(2-\varsigma)\eta + 2\varsigma\eta^2\right]e^{-(2+\varsigma)\eta} + abe^{-(4+\varsigma)\eta}\right\}$$

$$\bar{\sigma}_{z0}(\eta,\varsigma) = \frac{2\gamma_0}{\alpha}\left\{-\left[c+d+2\left(c-d(1-\varsigma)\right)\eta\right]e^{-\varsigma\eta}\right.$$
$$\left.+\left[ac+bd-2bd(2-\varsigma)\eta + 4bd(1-\varsigma)\eta^2\right]e^{-(2+\varsigma)\eta}\right\} \tag{19}$$

$$\bar{\tau}^{*}_{rz1}(\eta,\varsigma)=\bar{\sigma}^{*}_{z1}(\eta,\varsigma),\qquad \bar{\tau}^{*}_{rz0}(\eta,\varsigma)=0$$

$$\bar{\tau}_{rz1}(\eta,\varsigma)=\frac{1}{2}\left\{\left[-a+b+2b\varsigma\eta-4b(1-\varsigma)\eta^{2}\right]e^{-(2-\varsigma)\eta}-2ab\varsigma\eta e^{-(4-\varsigma)\eta}\right.$$
$$\left.+(1-2\varsigma\eta)e^{-\varsigma\eta}-2b(1-\varsigma\eta+2\varsigma\eta^{2})e^{-(2+\varsigma)\eta}+abe^{-(4+\varsigma)\eta}\right\}$$

$$\bar{\tau}_{rz0}(\eta,\varsigma)=\frac{2\gamma_0}{\alpha}\left\{-\left[c-d+2(c-d(1-\varsigma))\eta\right]e^{-\varsigma\eta}\right.$$
$$\left.+\left[ac-bd+2bd\varsigma\eta+4bd(1-\varsigma)\eta^{2}\right]e^{-(2+\varsigma)\eta}\right\}. \tag{20}$$

For the coating/substrate system, the stress distribution on the loading surface is unknown, and it is difficult to determine from the displacement profile. Thus, in order to simulate the non-uniform loading distribution of the indentation problem, the following form of surface loading is assumed and shown in Fig.3:

$$q(r)=\begin{cases}\sigma_m\left[1-\left(\dfrac{r}{r_0}\right)^{2}\right] & r\le r_0\\ 0 & r>r_0\end{cases} \tag{21}$$

where σ_m is the maximum stress at $r=0$, and r_0 is the loading contact radius. Then $q(r)$ in Hankel's transform domain, $\bar{q}(\xi)$, can be written as

$$\bar{q}(\xi)=2\frac{\sigma_m t^{2}}{\rho_0}\left[\frac{2}{\eta^{3}}J_1(\rho_0\eta)-\frac{\rho_0}{\eta^{2}}J_0(\rho_0\eta)\right] \tag{22}$$

where $\rho_0=r_0/t$ and $\eta=\xi t$. Then the components of stress can be solved accordingly.

4. RESULTS

Now we use the above elastic solution to calculate the stress fields of DLC/Si and DLC/polycarbonate systems. Figure 4 shows the normalized radial and hoop stresses along the axisymmetric z-axis with $t=r_0$ for both coating/substrate systems, and the bulk substrate materials Si and polycarbonate. Due to the symmetry of loading with respect to the z-axis, the radial and hoop stresses along the z-axis in this case are identical. The elastic properties of the materials are taken from Table 1. The horizontal line at $z/t=1$ indicates the interface. The radial and hoop stresses for both bulk materials of Si and polycarbonate (dashed lines) are continuous, while the stresses in DLC/Si and DLC/polycarbonate (solid lines) show

discontinuity across the interface due to the mismatch of material properties. Also the radial (hoop) stress reaches the maximum in tension in the DLC coating film at the interface for DLC/polycarbonate. This result provides the analytical basis of film cracking (Fig.2) in the hard-coating system. But for the soft-coating/hard-substrate system (e.g. DLC/ Si), instead of film cracking, delamination occurs first (see Fig. 1(b)).

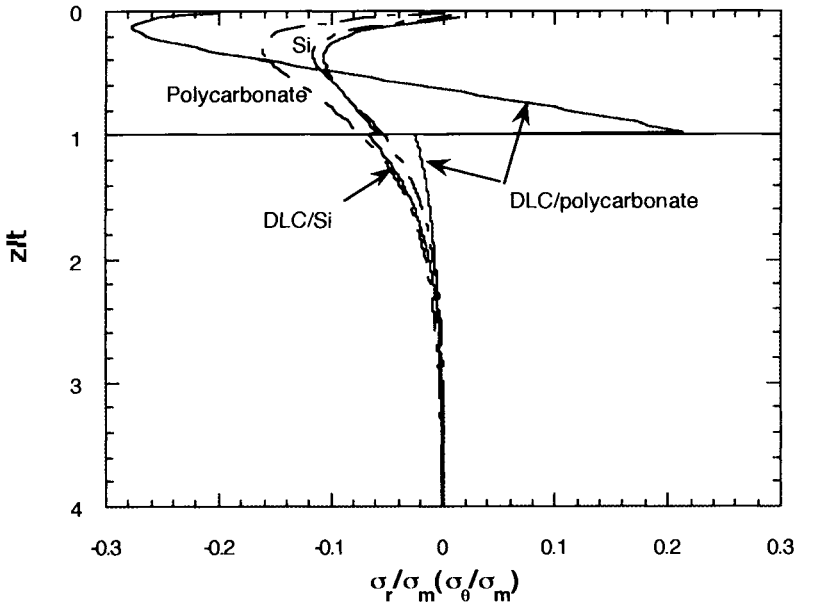

Fig.4 Radial (hoop) stress distribution along the z-axis

Figure 5 shows the shear stress distribution along the r-axis at the interface ($z=t$) with $t=r_0$. The maximum shear stress occurs near the edge of loading contact zone for all the coating/substrate and bulk substrate systems. The DLC/Si system shows the highest value of the maximum shear stress, which is apparently responsible for the interfacial delamination shown in Fig.1(b).

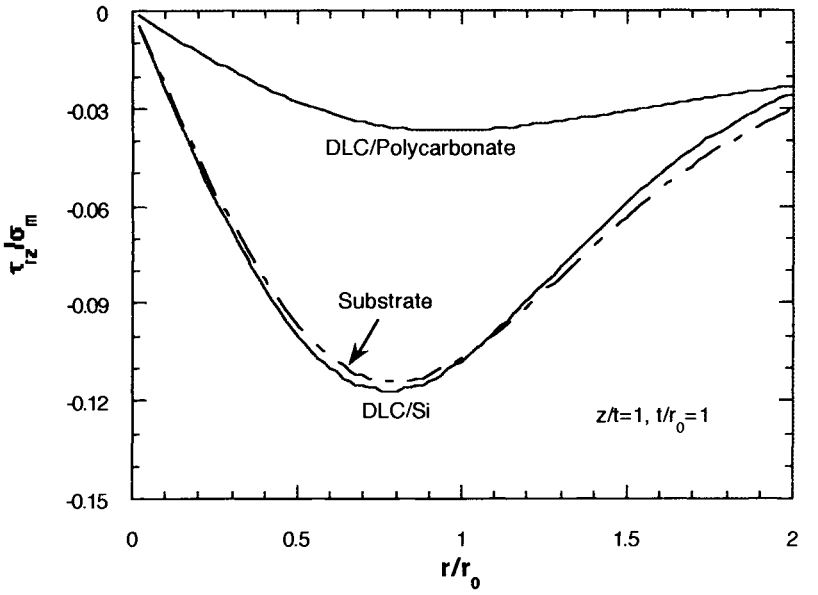

Fig. 5 Shear stress distribution along the r-axis at the interface

Finally, we consider the effect of Poisson's ratio on the coating/substrate system. Figure 6 shows the normalized radial and hoop stresses along the axisymmetric z-axis with $t=r_0$. This time the shear moduli of the coating and the substrate are assumed to be identical ($\mu_1=\mu_0$), and the Poisson's ratio of the substrate $\nu_0=0.33$, and the Poisson's ratio of the film coating ν_1 assumes the values of 0.1, 0.2 and 0.5. The change of the normal stress due to the difference of Poisson's ratios between the thin film and the substrate is not as significant as that shown in Fig. 4. Particularly, when $\nu_1>\nu_0$ (dash-dotted line in Fig.6), the normal radial stress in the film is always compressive, which cannot induce cracking in the film. It should also be noted that the Young's moduli of the film and the substrate are different when the Poisson's ratio of the film changes. From the relation of $E_i=2\mu_i(1+\nu_i)$, one can find that $E_1>E_0$, when $\nu_1>\nu_0$; these result can also be used to define a hard-coating ($E_1>E_0$), and a soft-coating ($E_1<E_0$). However, since Poisson's ratio $\nu \leq 0.5$ in general,

the ratio of the Young's moduli between the coating and the substrate can not be greater than 1.5. As a result, cracks are unlikely to occur in the film of a coating/substrate system due to the difference of the Poisson's ratios between the two phases.

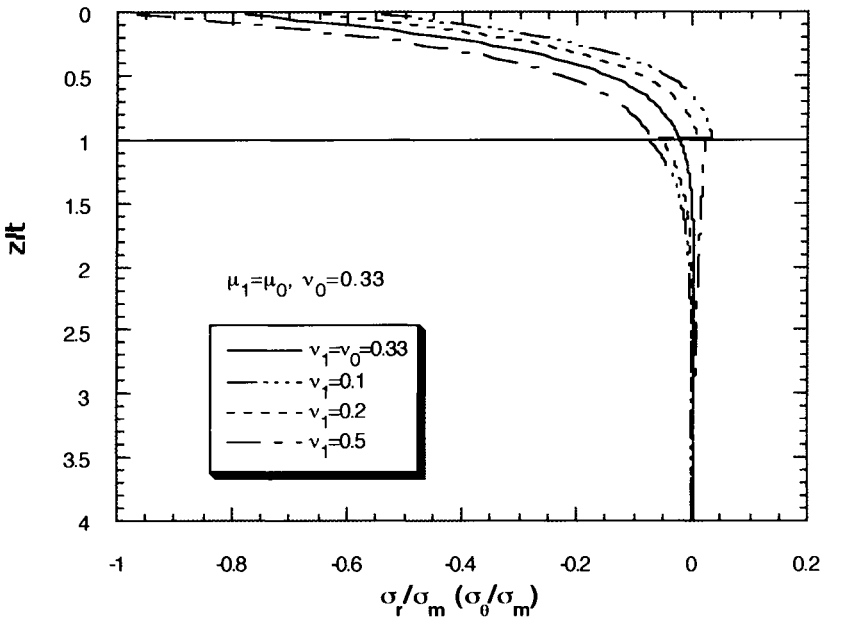

Fig.6 The influence of Poisson's ratio on the radial (hoop) stress distribution along the z-axis

The effect of Poisson's ratio on the shear stress field of the coating/substrate systems has also been examined. Figure 7 shows the shear stress distributions in the film of the coating/substrate system at the interface with $t=r_0$, $\mu_1=\mu_0$, and $\nu_0=0.33$. As ν_1 increases the maximum value of the shear stress also increases. For $\nu_1>\nu_0$, the shear stress of the coating system is greater than that of the bulk substrate material itself. As a result, interfacial delamination is likely to occur.

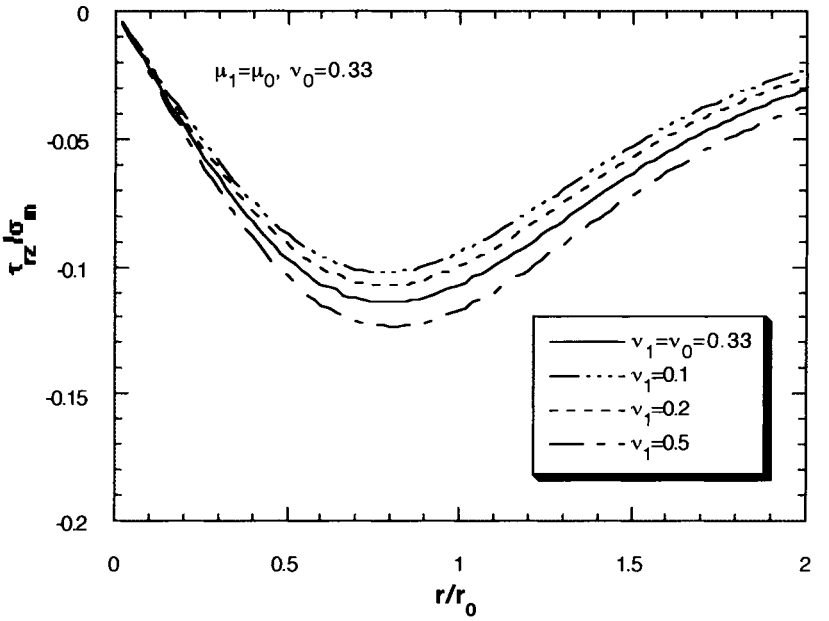

Fig.7 Influence of the Poisson's ratio on shear stress of the coating/substrate system.

5. CONCLUSIONS

In this paper we have examined the elastic stress field of coating/substrate systems under nanoindentation and its implication on failure mechanisms. Delamination in soft-coating/hard-substrate systems such as DLC/Si has been observed, while film cracking occurs in hard-coating/soft-substrate systems such as DLC/polycarbonate. Results of the elastic stress analysis show that the maximum shear stress occurs near the loading contact zone at the interface for the DLC/Si system, which is responsible for film delamination. On the other hand, the existence of tensile radial stress in the film near the interface for the hard-coating/soft-substrate DLC/polycarbonate system is the main reason for the cracks in the hard film. Finally, Poisson's ratio effects on stress field of the coating/substrate system have been examined. As a conclusion, The difference of the Poisson's ratio between the coating and substrate may cause film delamination if the Poisson's ratio of the film is

greater than that of the substrate. However, Poisson's ratio effect is insufficient to cause film cracking.

ACKNOWLEDGMENT

Tsu-Wei Chou would like to thank the U.S. Army Research Laboratory for partial support of this work.

REFERENCES

1. Sneddon, I.N. (1951). *Fourier Transforms*. McGraw-Hill, New York.
2. Matthewson, M.J. (1981). Axi-Symmetric Contact on Thin Compliant Coatings, *J. Mech. Phys. Solids* **29** (2), 89-113.
3. Ritter, J.E., Lardner, T.J., Rosenfeld, L. and Lin, M.R. (1989). Measurement of Adhesion of Thin Polymer Coatings by Indentation, *J. Appl. Phys.* **66** (8), 3626-3634.
4. Jayachandran, R., Boyce, M.C. and Argon, A.S. (1995). Mechanics of the Indentation Test and Its Use to Assess the Adhesion of Polymeric Coatings, *Adhesion Measurement of Films and Coatings*, Edited by K.L. Mittal, VSP, 189-215.
5. Chui, Y.P. and Hartnett, M.J. (1983). A Numerical Solution for Layered Solid Contact Problems with Application to Bearings, *ASME J. Lub. Tech.* **105**, 585-590.
6. O'Sullivan, T.C. and King, R.B. (1988). Sliding Contact Stress Field Due to a Spherical Indenter on a Layered Elastic Half-Space, *ASME J. Tribology* **110**, 235-240.
7. Komvopoulos, K., Saka, N. and Suh, N.P. (1987). The Role of Hard Layers in Lubricated and Dry Sliding, *ASME J. Tribology* **109**, 223-231.
8. Komvopoulos, K. (1989). Elastic-Plastic Finite Element Analysis of Indented Layered Media, *ASME J. Tribology* **110**, 430-439.
9. Kral, E.R., Komvopoulos, K. and Bogy, D.B. (1995). Finite Element Analysis of Repeated Indentation of an Elastic-Plastic Layered Medium by a Rigid Sphere, Part I. Surface Results, *ASME J. Appl. Mech.* **62**, 20-28.
10. Kral, E.R., Komvopoulos, K. and Bogy, D.B. (1995). Finite Element Analysis of Repeated Indentation of an Elastic-Plastic Layered Medium by a Rigid Sphere, Part II. Subsurface Results, *ASME J. Appl. Mech.* **62**, 29-42.
11. Li, J., Thostenson, E.T., Chou, T.-W. and Riester, L. (1997). Experimental and Analytical Study on Thin-Film Coating/Substrate Systems by Nanoindentation,

submitted to *J. Mat. Res.*

12. Oliver, W.C. and Pethica, J.B. (1989). U.S. Patent No. 4,848,141.
13. Li, J. and Chou, T.-W. (1997). Elastic Field of a Thin-Film/Substrate System Under an Axisymmetric Loading, *Int. J. Solids & Structures*, (in press).
14. Harding, J.W. and Sneddon, I.N. (1945). The elastic stresses produced by the indentation of the plane surface of a semi-infinite elastic solid by a rigid punch, *Proc. Camb. Phil. Soc.* **41**, 16-26.

Damage Mechanics in Engineering Materials
G.Z. Voyiadjis, J.-W.W. Ju and J.-L. Chaboche (Editors)
© 1998 Elsevier Science B.V. All rights reserved.

On the Continuum Description of Damage in Fiber-Reinforced Composites

D. Boudon-Cussac, A. Burr and F. Hild[a]

[a]Laboratoire de Mécanique et Technologie
ENS de Cachan / CNRS / Université Paris VI
61, avenue du Président Wilson, F-94235 Cachan Cedex, France

In this paper, the derivation of a mechanism-based constitutive law is presented to model the mechanical behavior of fiber-reinforced composites. It allows to account for matrix-cracking, interfacial debonding and sliding in the framework of Continuum Damage Mechanics. Applications are performed on a unidirectional SiC/SiC composite and on concrete specimens.

1. INTRODUCTION

The basic mechanisms related to the degradation of brittle matrices reinforced by continuous or discontinuous fibers and submitted to monotonic loading histories are matrix-cracking, interfacial debonding and sliding, and eventually fiber breakage and fiber pull-out. These mechanisms induce stiffness losses and inelastic strains. The latter are studied within the framework of Continuum Damage Mechanics (CDM) by using micromechanical analyses. An explicit expression of the Helmholtz free energy density is derived. In particular, internal variables are carefully chosen to describe the degradation mechanisms and written in an appropriate format to allow the derivation of constitutive equations applicable to structural calculations.

The model is used to analyze experimental data obtained on SiC matrices unidirectionally reinforced by continuous SiC fibers. The evolution laws are derived by using micromechanical parameters. The same model is used to study the behavior of an unreinforced concrete. To avoid localized damage, a prismatic concrete specimen is loaded by aluminum bars glued on two opposite lateral faces. In particular, the effect of glue between the aluminum bars and the concrete specimen is discussed and modeled. Furthermore, the model is utilized to study the behavior of concrete specimen reinforced by short fibers made of steel and aligned along the loading direction. This composite is loaded by using a similar technique as that used to analyze unreinforced concrete. The effect of the addition of short fibers is discussed.

2. PHYSICAL MODEL

Loading a composite consisting of a brittle matrix supported by stronger fibers, usually causes multiple matrix-cracking [1] accompanied by debonding and sliding at the

fiber-matrix interface. Because of stress redistribution between the fiber and matrix, the cracking density usually saturates. Matrix-cracking is responsible for the decrease of stiffness observed in experiments on Brittle Matrix Composites (BMCs), relief of residual stresses due to processing and sliding at the fiber-matrix interface are the source of irreversible strains.

2.1. The Unit Cell

The cell illustrated in Fig. 1 and first proposed by Aveston and Kelly [2] has stood the test of time with the introduction of a debond energy at the front of the slipping region [3]. This unit cell constitutes the basis for formulating constitutive equations suitable for finite element calculations used in design studies.

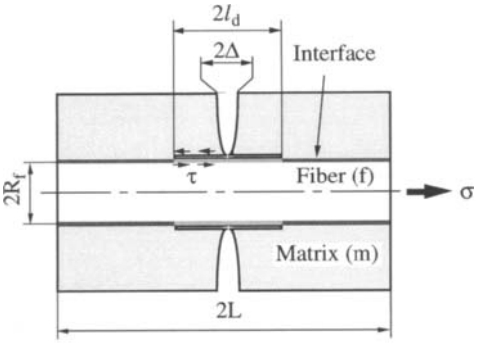

Figure 1. Elementary Cell.

In the unit cell shown in Fig. 1 the elastic moduli of the fiber and matrix are E_f and E_m respectively, the volume fraction of the fiber is f and R_f is the fiber radius. The elastic modulus of the undamaged composite is $E = fE_\mathrm{f} + (1-f)E_\mathrm{m}$. Matrix-cracking occurs when the matrix stress reaches a material value σ_mc [1,4] and the average distance between cracks is denoted by $2L$. The debond length at the fiber/matrix interface is $2l_\mathrm{d}$, and the interface is assumed to have a constant shear strength τ. The critical energy release rate to extend an interface crack is $\mathcal{G}_\mathrm{d}$. Following Hutchinson and Jensen [3], this critical energy release rate $\mathcal{G}_\mathrm{d}$ can be represented as a debond strength σ_d which introduces simplicity in later calculations

$$\sigma_\mathrm{d} = 2\sqrt{\frac{(1-f)E_\mathrm{m}E_\mathrm{f}\mathcal{G}_\mathrm{d}}{R_\mathrm{f}E}} \tag{1}$$

To define the state of the unit cell, the values for the crack spacing $2L$, the slip length $2l_\mathrm{d}$ and the interface properties τ and σ_d must be known. The latter are unknown material parameters but are assumed to be constant. Residual stresses are introduced during processing so that the stress level in the matrix σ^*_pm is an additional unknown.

The statistical nature of the distribution of crack distances and debond lengths discussed in Ref. [5] is not considered herein. For the sake of simplicity, it is assumed that the average crack distance $2L$ and the corresponding debond length $2l_d$ are sufficient to characterize the state of the material.

2.2. Interrogation of First Loading Response

On first loading, the initial response of the composite is elastic when the modulus is E. On reaching the matrix-cracking stress σ_{mc}, matrix-cracking occurs which is accompanied by matrix-fiber interface debonding and slip. From the partial unloading tests shown in Fig. 2, it is possible to measure the current elastic modulus $E(1-D)$ and the total irreversible or inelastic strain. The relationship between the damage variable D and the crack spacing $2L$ may be estimated from micromechanics following the model of Cox [6] and Aveston and Kelly [2]

$$D = \frac{\Omega}{1+\Omega} \tag{2}$$

in which the dimensionless quantities are defined by

$$\Omega = \frac{\omega}{A}\tanh\left(\frac{1}{\omega}\right) \quad , \quad \omega = \frac{R_f}{\beta L} \quad , \quad A = \frac{fE_f}{(1-f)E_m} \quad , \quad \beta^2 = \frac{2G_m E}{(1-f)E_m E_f \ln\left(\frac{R_m}{R_f}\right)} \tag{3}$$

where G_m is the shear modulus of the matrix and $2R_m$ the average distance between fibers ($f = R_f^2/R_m^2$, see Fig. 1). Since the damage variable D is readily measured, Eqn. (2) provides a means of determining indirectly the crack spacing $2L$.

The crack opening displacement Δ_c following matrix-cracking consists of two contributions, viz. Δ_e is the elastic opening due to cracking, and Δ_p is the opening due to the relief of the residual stresses due to processing. The crack opening displacement Δ_e resulting from elastic deformations is given by the relationship [7,8]

$$\frac{(1-f)E_m}{E}\frac{\Delta_e}{L} = \frac{\sigma D}{E(1-D)} \tag{4}$$

By using the model of Cox [6] and Aveston and Kelly [2], the crack opening displacement Δ_p is accompanied by the irreversible strain ϵ_r

$$\epsilon_r = \frac{(1-f)E_m}{E}\frac{\Delta_p}{L} = \frac{\epsilon_{pm}D}{1-D} \quad \text{with } \epsilon_{pm} = \frac{\sigma^*_{pm}}{E_m} \tag{5}$$

and by the relief of initially stored energy

$$\psi_r = -\frac{E\epsilon_{pm}^2 D}{2(1-D)} = -\frac{1}{2}\epsilon_{pm}E\epsilon_r \tag{6}$$

When interface slip occurs, it is accompanied by an additional crack opening displacement Δ_s. The latter gives rise to a self-balancing stress field along the slip length $2l_F$ ($\leq 2l_d$) in the matrix, $\sigma_m(z)$ and in the fiber, $\sigma_f(z)$, for which the corresponding elastic

strains are denoted by $\epsilon_m(z)$ and $\epsilon_f(z)$, respectively. The self-balancing stress fields cause inelastic strains

$$\epsilon_i = \frac{(1-f)E_m}{E}\frac{\Delta_s}{L} = \frac{1}{L}\int_0^L \epsilon_f(z)dz \tag{7}$$

The total crack opening displacement Δ is the sum of three contributions

$$\Delta = \Delta_e + \Delta_p + \Delta_s \tag{8}$$

The crack closure condition is simply expressed as $\Delta = 0$. Debonding and friction also cause elastic energy to be stored in the material. The expression for the non-recoverable energy is found to be

$$\psi_d = \frac{EA}{2L}\int_0^L \epsilon_f^2(z)dz \tag{9}$$

The explicit calculation of the integral is left to a later stage. Equation (9) is concerned with the residual stress due to debonding and sliding. Normally there is an initial residual stress in many composite systems due to processing. The presence of the two residual stress fields induces a coupling term $\psi_{d|p}$ in the total non-recoverable energy density ψ_s. If the residual stress field due to processing is constant along the total length of the composite, the non-recoverable energy density $\psi_{d|p}$ can be expressed as

$$\psi_{d|p} = -\epsilon_i E \epsilon_{pm} \tag{10}$$

Equation (10) shows that the inelastic strain ϵ_i and the misfit strain ϵ_{pm} are sufficient to measure the energy resulting from the coupling.

3. THE CONTINUUM REPRESENTATION

Since the objective of the paper is to obtain mechanism-based constitutive equations which are suitable for finite element calculations, the results of the model are reformulated by using the techniques of Continuum Mechanics and the concept of state variables [9,10]. The model described in the preceding section helps to define the state variables and to calculate the free energy density (also called state potential) from which the corresponding forces can be deduced. Finally, the evolution laws have to be written.

3.1. State Potential for Unidirectional Composites

The free energy density for a given state is calculated by performing two elastic calculations following approaches introduced by Volterra [11], and used to analyze the elastic behavior of homogeneous and isotropic media [11,12], and the influence of inclusions in an infinite medium [13]. The first step consists of calculating the elastic energy when a crack is introduced and the unbroken part (f) is moved with respect to the broken part (m) by an additional amount Δ_s over a length $2l_f = 2l_d$ with no external load. The derivation of the non-recoverable energy ψ_s has been determined in the previous section and is rewritten as follows

$$\psi_s = \frac{E\epsilon_i^2}{2d} - \epsilon_i E \epsilon_{pm} - \frac{E\epsilon_{pm}^2 D}{2(1-D)} \tag{11}$$

where the general expression of the damage variable d is given by

$$d = \frac{1}{A}\left[\frac{1}{L}\int_0^L \epsilon_{\mathrm{f}}(z)dz\right]^2 / \left[\frac{1}{L}\int_0^L \epsilon_{\mathrm{f}}^2(z)dz\right] \tag{12}$$

By using the micromechanical model with a debond strength σ_{d} and a constant shear strength τ defined previously, the inelastic strain ϵ_{i} and the damage variable d are expressed as

$$\epsilon_{\mathrm{i}} = \lambda_{\mathrm{d}} T_{\mathrm{d}} (1 + \Sigma_{\mathrm{d}}) \quad , \quad d = \frac{\lambda_{\mathrm{d}}}{A}\left[1 + \frac{1}{3}(1 + \Sigma_{\mathrm{d}})^{-2}\right]^{-1} \tag{13}$$

where the dimensionless groups λ_{d}, T_{d} and Σ_{d} are given by

$$\lambda_{\mathrm{d}} = \frac{l_{\mathrm{d}}}{L} \quad , \quad T_{\mathrm{d}} = \frac{\tau l_{\mathrm{d}}}{R_{\mathrm{f}} E_{\mathrm{f}}} \quad , \quad \Sigma_{\mathrm{d}} = \frac{\sigma_{\mathrm{d}} R_{\mathrm{f}}}{\tau l_{\mathrm{d}}} \tag{14}$$

The value of the square bracket of Eqn. (13.2) varies between 1 and 4/3 for a high and low debond energy material [14] respectively, which means that the value of the dimensionless group Σ_{d} has little effect on d.

The second step consists of an elastic loading of a cracked system with friction prevented. The recoverable part of the Helmholtz free energy density becomes

$$\psi_{\mathrm{e}} = \frac{E(1-D)}{2}\left[\epsilon - \epsilon_{\mathrm{i}} - \frac{\epsilon_{\mathrm{pm}} D}{1-D}\right]^2 \tag{15}$$

The total free energy density is the sum of the two components (11) and (15) of energy density. The total free energy density can be expressed by using four state variables which are the total strain ϵ, and three internal variables, viz. the damage variable D modeling the loss of stiffness due to cracking, the inelastic strain ϵ_{i} due to debonding and sliding, the damage variable d measuring the amount of non-recoverable energy due to debonding and slip

$$\psi = \frac{E(1-D)}{2}\left[\epsilon - \epsilon_{\mathrm{i}} - \frac{\epsilon_{\mathrm{pm}} D}{1-D}\right]^2 + \frac{E\epsilon_{\mathrm{i}}^2}{2d} - \epsilon_{\mathrm{i}} E \epsilon_{\mathrm{pm}} - \frac{E\epsilon_{\mathrm{pm}}^2 D}{2(1-D)} \tag{16}$$

The forces associated with the state variables are given by

$$\sigma = \frac{\partial \psi}{\partial \epsilon} \quad , \quad Y = -\frac{\partial \psi}{\partial D} \quad , \quad X = -\frac{\partial \psi}{\partial \epsilon_{\mathrm{i}}} \quad , \quad y = -\frac{\partial \psi}{\partial d} \tag{17}$$

Equation (17.1) defines the macroscopic stress σ and Eqn. (17.2) the energy release rate density Y associated with matrix-cracking. The energy release rate density Y is proportional to the square of a modified 'effective stress' $(\sigma + E\epsilon_{\mathrm{pm}})/(1-D)$. Similarly, Eqn. (17.3) defines the back stress X associated with sliding whose exact value depends upon the interfacial properties. Equation (17.4) defines the energy release rate density y associated to the residual stresses due to debonding and sliding.

3.2. State Potential for 2D Composites

A 2D formulation requires an anisotropic damage description [15]. In the case of cracking perpendicular to the fiber direction, the generalization is straight forward since the only compliance change is given in the fiber direction, and therefore only one scalar anisotropic damage variable is needed and the previous 1D analysis is still relevant. For a 0/90 layered or woven composite, the Helmholtz free energy density depends upon the damage variables modeling matrix-cracking in the 0 and 90-degree 'layers'

$$\psi_{\mathrm{e}} = \frac{1}{2}\, \underline{\underline{\epsilon}}_{\mathrm{e}} : \underline{\underline{\underline{\underline{E}}}}(D_{\mathrm{m}}^{0}, D_{\mathrm{m}}^{90}) : \underline{\underline{\epsilon}}_{\mathrm{e}} \tag{18}$$

where $\underline{\underline{\epsilon}}_{\mathrm{e}}$ denotes the elastic strain tensor, ':' the contraction with respect to two indices, $\underline{\underline{\underline{\underline{E}}}}$ the elastic stiffness tensor of the damaged composite (i.e., it depends upon the matrix-cracking damage variables D_{m}^{0} and D_{m}^{90} [15]).

A second order tensor is needed to model the inelastic strains due to debonding and slip. In the case of a 2D composite, a first order approximation only requires the in-plane components (i.e., $\epsilon_{\mathrm{i}11}$, $\epsilon_{\mathrm{i}22}$, and $\epsilon_{\mathrm{i}12}$) of the inelastic strain tensor $\underline{\underline{\epsilon}}_{\mathrm{i}}$. Since each operative slip system can be integrated separately in terms of energetic contributions, the internal damage variables can be defined separately for each inelastic strain term. Therefore there are as many debond damage terms as non-vanishing inelastic strain components [15]

$$\psi_{\mathrm{d}} = \frac{E_{11}}{2}\frac{\epsilon_{\mathrm{i}11}^{2}}{d_{11}} + \frac{E_{22}}{2}\frac{\epsilon_{\mathrm{i}22}^{2}}{d_{22}} + \frac{G_{12}}{2}\frac{\epsilon_{\mathrm{i}12}^{2}}{d_{12}} \tag{19}$$

where E_{11}, E_{22}, are the Young's moduli along the 1- and 2-directions, respectively, and G_{12} is the shear modulus in the 1-2 plane. In the case of cracking perpendicular to the fiber direction, only one inelastic strain component is different from zero, viz. the normal component along the fiber direction. Similarly, only one scalar debond damage variable is needed.

Equation (10) is used to derive the generalized coupling term $\psi_{\mathrm{d|p}}$ for 2D composites

$$\psi_{\mathrm{d|p}} = -\,\underline{\underline{\epsilon}}_{\mathrm{i}} : \underline{\underline{\underline{\underline{E}}}} : \underline{\underline{\epsilon}}_{\mathrm{pm}} \tag{20}$$

where $\underline{\underline{\underline{\underline{E}}}}$ is the stiffness tensor of the undamaged material. It is worth noting that the misfit strain tensor $\underline{\underline{\epsilon}}_{\mathrm{pm}}$ is an average tensor on the composite level to be computed for each specific architecture. Lastly, the relief of initially stored energy by the residual stresses due to processing is expressed as a generalization of Eqn. (6)

$$\psi_{\mathrm{r}} = -\frac{1}{2}\, \underline{\underline{\epsilon}}_{\mathrm{pm}} : \underline{\underline{\underline{\underline{E}}}} : \underline{\underline{\epsilon}}_{\mathrm{r}} \left(\underline{\underline{\epsilon}}_{\mathrm{pm}}, D_{\mathrm{m}}^{0}, D_{\mathrm{m}}^{90}\right) \tag{21}$$

where the irreversible strain tensor $\underline{\underline{\epsilon}}_{\mathrm{r}}$ depends upon the misfit strain tensor $\underline{\underline{\epsilon}}_{\mathrm{pm}}$ and the damage state described by D_{m}^{0} and D_{m}^{90}.

The Helmholtz free energy density depends upon the damage variables modeling matrix-cracking, the inelastic strain tensor as well as the damage variables modeling debonding and sliding

$$\psi = \frac{1}{2}\,\underline{\underline{\epsilon}}_{\rm e} : \underline{\underline{\underline{\underline{E}}}}(D_{\rm m}^0, D_{\rm m}^{90}) : \underline{\underline{\epsilon}}_{\rm e} + \frac{E_{11}}{2}\frac{\bar{\epsilon}_{\rm in11}^2}{d_{11}} + \frac{E_{22}}{2}\frac{\bar{\epsilon}_{\rm in22}^2}{d_{22}} + \frac{G_{12}}{2}\frac{\bar{\epsilon}_{\rm in12}^2}{d_{12}} - \underline{\underline{\epsilon}}_{\rm i} : \underline{\underline{\underline{\underline{E}}}} : \underline{\underline{\epsilon}}_{\rm pm} - \frac{1}{2}\,\underline{\underline{\epsilon}}_{\rm pm} : \underline{\underline{\underline{\underline{E}}}} : \underline{\underline{\epsilon}}_{\rm r}\left(\underline{\underline{\epsilon}}_{\rm pm}, D_{\rm m}^0, D_{\rm m}^{90}\right) \quad (22)$$

with

$$\underline{\underline{\epsilon}}_{\rm e} = \underline{\underline{\epsilon}} - \underline{\underline{\epsilon}}_{\rm i} - \underline{\underline{\epsilon}}_{\rm r}\left(\underline{\underline{\epsilon}}_{\rm pm}, D_{\rm m}^0, D_{\rm m}^{90}\right) \quad (23)$$

where $\underline{\underline{\epsilon}}$ is the total strain tensor. The associated forces are defined by

$$\underline{\underline{\sigma}} = \frac{\partial \psi}{\partial \underline{\underline{\epsilon}}} \quad (24)$$

$$Y_{\rm m}^0 = -\frac{\partial \psi}{\partial D_{\rm m}^0} \quad , \quad Y_{\rm m}^{90} = -\frac{\partial \psi}{\partial D_{\rm m}^{90}} \quad (25)$$

$$\underline{\underline{X}} = -\frac{\partial \psi}{\partial \underline{\underline{\epsilon}}_{\rm i}} \quad (26)$$

$$y_{11} = -\frac{\partial \psi}{\partial d_{11}} \quad , \quad y_{22} = -\frac{\partial \psi}{\partial d_{22}} \quad , \quad y_{12} = -\frac{\partial \psi}{\partial d_{12}} \quad (27)$$

Equations (24), (25), (26) and (27) constitute a generalization of Eqns. (17.1), (17.2), (17.3) and (17.4).

3.3. The Evolution Laws

The final step in establishing the model is to determine the growth laws $F_{\rm D}, F_{\rm i}, F_{\rm d}$ which relate the state variables $(D, \epsilon_{\rm i}, d)$ to their associated forces (Y, X, y)

$$D = F_{\rm D}(Y) \quad , \quad \epsilon_{\rm i} = F_{\rm i}(X) \quad , \quad d = F_{\rm d}(y) \quad (28)$$

To be thermodynamically admissible, the intrinsic dissipation $\mathcal{D}$ must be positive

$$\mathcal{D} = Y\,\dot{D} + X\,\dot{\epsilon}_{\rm i} + y\,\dot{d} \geq 0 \quad (29)$$

It can be shown that this condition is satisfied in the present case.

The evolution laws will be identified for two different BMCs, viz. a unidirectional SiC/SiC composite and a reinforced concrete. The identification procedure is based upon the experimental results of a loading/partial unloading test (Fig. 2) from which the current value of the elastic modulus $E(1-D)$ and the total inelastic strain $\epsilon_{\rm i} + \epsilon_{\rm r}$ can be measured. A similar approach is used to identify the parameters of the evolution laws of 2D composites. A detailed description of the procedure can be found in Ref. [16].

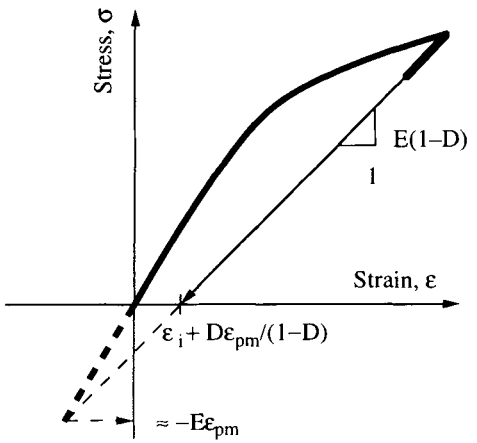

Figure 2. Schematic stress/strain curve with partial unloading.

4. SiC/SiC COMPOSITE

The first material to be analyzed is a unidirectional SiC/SiC composite. This material has been extensively studied so that many experimental data are available. In particular, the change of the average crack density with the applied stress has been measured [17] even though the task is tedious and needs special care to get reliable data [18]. The initial cracking condition can be written as

$$Y = Y_c \tag{30}$$

From Eqns. (17.2) and (30), the matrix-cracking stress σ_{mc} is found to be

$$\frac{\sigma_{mc}}{E} + \epsilon_{pm} = \sqrt{\frac{2Y_c}{E}} \tag{31}$$

This relationship is a transcription in the framework of CDM of the well-known expression derived in Linear Elastic Fracture Mechanics [4]. The Cox' Model (see Eqns. (2) and (3), $1 > 2.5\ \omega$) predicts that there is a linear relationship between the damage quantity $D/(1-D)$ and the average crack density ω

$$\frac{D}{1-D} = \frac{\omega}{A} \tag{32}$$

The micromechanics associated with crack spacing is complex and involves statistical calculations [19]. Instead of following this route, use is made of the experimental observation of Domergue [17] that the crack density ω satisfies the following evolution law

$$\omega = \frac{\sigma - \sigma_c}{\sigma_0} \quad \text{with} \quad \sigma_0 = \frac{(\sigma_F - \sigma_{mc})\,\beta L_F}{R_f} \tag{33}$$

The normalizing constants L_F and σ_F are the values of L and σ at failure before saturation occurs. If saturation occurs, the previous constants are the values of L and σ at saturation. By eliminating the crack density ω from the last two equations and by using Eqn. (17.2) for Y in Eqn. (33) combined to Eqn. (32), the evolution law for D in terms of Y becomes

$$D = \frac{2\sqrt{Y} + \sqrt{Y_0} - \sqrt{Y_c} - \sqrt{\left(2\sqrt{Y} + \sqrt{Y_0} - \sqrt{Y_c}\right)^2 - 4\sqrt{Y}\left(\sqrt{Y} - \sqrt{Y_c}\right)}}{2\sqrt{Y}}$$
$$\text{with} \quad \sqrt{2EY_0} = A\sigma_0 \tag{34}$$

To get the onset of interfacial debonding (when $l_d = 0$), the dependence of the dimensionless group T_d with the applied stress σ is needed

$$T_d = \frac{1}{2A}\left(\frac{\sigma - \sigma_{id}}{E}\right) \tag{35}$$

where the stress σ_{id} describing the onset of interfacial debonding can be calculated

$$\frac{\sigma_{id}}{E} + \epsilon_{pm} = \frac{A\sigma_d}{E_f} \tag{36}$$

The growth law for the inelastic strain ϵ_i has been defined by Eqn. (28.2) with the definition of the back stress X given in Eqn. (17.3). By eliminating the debond length l_d between Eqns. (13) and (35), and the crack spacing $2L$ (Eqns. (3.2) and (33)), the relationship between ϵ_i and the applied stress σ becomes

$$\epsilon_i = \frac{B\left(\sigma - \sigma_{mc}\right)}{4A^2\sigma_0}\left[\left(\frac{\sigma}{E} + \epsilon_{pm}\right)^2 - \left(\frac{A\sigma_d}{E_f}\right)^2\right] \quad \text{with} \quad B = \frac{\beta E_f}{\tau} \tag{37}$$

It is possible formally to develop the relationship (28.2), but from a computation point of view, it is easier to use directly the result of the micromechanics given in Eqn. (37).

The growth law of the interfacial damage d can be written as a function of its associated force y. Instead, the evolution law is given as a function of the applied stress σ

$$d = \frac{B\left(\sigma - \sigma_{mc}\right)\left(\sigma - \sigma_{id}\right)}{2A^2\sigma_0 E}\left[1 + \frac{1}{3}\left\{1 + 2\frac{A\sigma_d}{E_f}\left(\frac{\sigma - \sigma_{id}}{E}\right)^{-1}\right\}^{-2}\right]^{-1} \tag{38}$$

The first key parameter to determine is the misfit strain ϵ_{pm}. Usually at the onset of matrix-cracking, the inelastic strains are very small so that the value of the misfit stress $E\epsilon_{pm}$ is obtained by searching the intersection of the unloading line with the elastic response of the material (see Fig. 2). The accuracy of the measurement of this quantity can be checked by using the first partial unloadings. In the present case, the following estimate is found

$$\epsilon_{pm} = 5.8 \times 10^{-4} \pm 4 \times 10^{-5} \tag{39}$$

The value of the misfit strain is in good agreement with that obtained by using an identification technique based upon the analysis of hysteresis loops [14]. The difference in coefficients of thermal expansion is then on the order of $\Delta\alpha \cong 1.5 \times 10^{-6} \pm 10^{-7}$ K^{-1} when the temperature variation $\Delta T = 1000$ K. The value of $\Delta\alpha$ is expected for SiC/SiC composites obtained by CVI [17].

The experimental relationship observed between D and Y is shown in Fig. 3. From this curve the values of the dimensionless parameters $\sqrt{2Y_c/E}$ and $\sqrt{2Y_0/E}$ can be obtained

$$\sqrt{\frac{2Y_c}{E}} = 1.07 \times 10^{-3} \pm 3 \times 10^{-6} \quad \text{and} \quad \sqrt{\frac{2Y_0}{E}} = 3.7 \times 10^{-4} \pm 8 \times 10^{-6} \tag{40}$$

from which the matrix-cracking stress σ_{mc} can be derived immediately and has the value 275 ± 1 MPa, which is in good agreement with experimental observations [17].

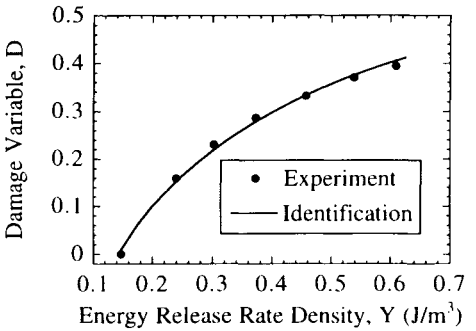

Figure 3. Damage variable D versus its associated force Y for a SiC/SiC composite.

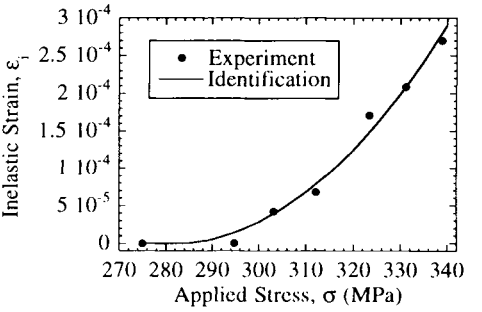

Figure 4. Inelastic strain ϵ_i versus applied stress σ for a SiC/SiC composite.

Equations (37) and (38) contain the dimensionless parameters $B/4A^2$ and $A\sigma_d/E_f$. They are identified by using the inelastic strain due to debonding and sliding alone. By fitting the experimental data of Fig. 4, the values of the dimensionless parameters are

$$\frac{B}{4A^2} = 73 \times 10^3 \pm 9 \times 10^3 \quad \text{and} \quad \frac{A\sigma_d}{E_f} = 1.7 \times 10^{-3} \pm 2 \times 10^{-5} \tag{41}$$

Since all the dimensionless parameters have been identified, the value of the dimensionless group λ_d can be computed

$$\lambda_d = \frac{l_d}{L} = B\omega T_d \tag{42}$$

At saturation, λ_d is equal to unity so that the value for the saturation stress σ_{sat} is

$$\sigma_{sat} = 490 \text{ MPa} > \sigma_F = 340 \text{ MPa} \tag{43}$$

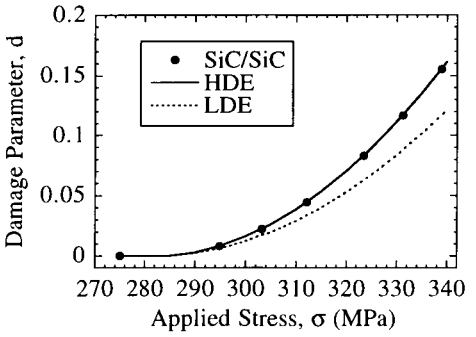

Figure 5. Damage variable d versus applied stress σ for a SiC/SiC composite.

Another output of the identification is the variation of the damage variable d with the applied stress σ. Figure 5 compares the response of a high debond energy (HDE) material, a low debond energy (LDE) material and the analyzed SiC/SiC composite. The behavior of the SiC/SiC composite coincides with the response given by an HDE material. This result was also found by Evans et al. [14]. On the other hand, it has been shown that layered alumina with carbon/epoxy prepregs is an LDE composite [20].

In the previous sections, the only discussed features were associated with monotonic loading conditions. As a consequence of the previous identification, the inelastic strains upon complete unloading (referred to as permanent strains and denoted by ϵ_{p}) are predictions since they were not used to tune the model. Unloading from the maximum stress $\sigma_{\max}$ to a stress $\sigma_{\max} - \Delta\sigma$ is accompanied by reverse slip from the extremity of the debonded region (the reverse slip length is $2l_{\mathrm{u}}$). The expressions of the inelastic strain $\Delta\epsilon_{\mathrm{i}}$ decrement is given by

$$\Delta\epsilon_{\mathrm{i}} = -2\lambda_{\mathrm{u}} T_{\mathrm{u}} \tag{44}$$

where the dimensionless group T_{u} measures the average strain due to reverse slip over a distance l_{u}

$$T_{\mathrm{u}} = \frac{\tau l_{\mathrm{u}}}{E_{\mathrm{f}} R_{\mathrm{f}}} = \frac{\Delta\sigma}{4EA} \tag{45}$$

and λ_{u} is defined as

$$\lambda_{\mathrm{u}} = \frac{l_{\mathrm{u}}}{L} = B\omega T_{\mathrm{u}} \tag{46}$$

Equation (44) is valid provided the reverse slip length l_{u} is less than the debond length l_{d}. When the reverse slip length l_{u} is equal to the debond length l_{d}, reverse slip no longer evolves. If $\Delta\sigma_{\mathrm{a}}$ denotes the stress decrement at which slip arrest occurs then

$$\frac{\Delta\sigma_{\mathrm{a}}}{E} = 4AT_{\mathrm{d}} \tag{47}$$

When $\Delta\sigma \geq \Delta\sigma_a$, the inelastic strain decrement is

$$\Delta\epsilon_i = -2\lambda_d T_d - \frac{\Delta\sigma - \Delta\sigma_a}{AE}\lambda_d \tag{48}$$

When the material behaves in an HDE regime, slip arrest is very likely to occur. This property can be noticed when the hysteresis loops have a parabolic and a subsequent linear portion. In the present case, slip arrest was always involved. Figure 6 shows that the predicted values of the permanent strains are in good agreement with the measured ones.

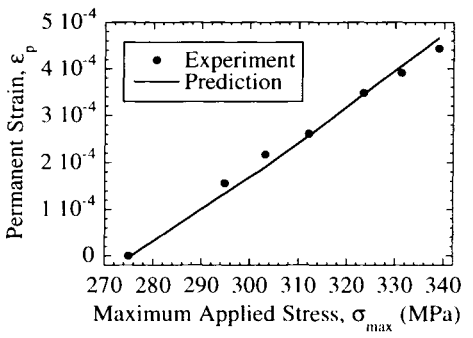

Figure 6. Permanent strain ϵ_p versus maximum applied stress σ_{max} for a SiC/SiC composite.

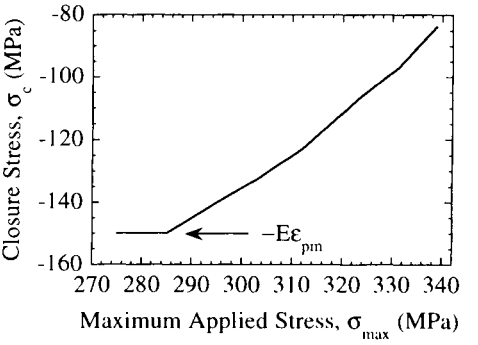

Figure 7. Crack closure stress σ_c versus maximum applied stress σ_{max} for a SiC/SiC composite.

Lastly, the crack closure condition is analyzed. No data are available to compare the predictions with experimental data. By using Eqns. (4), (5), (7) and (8), the crack closure condition $\Delta = 0$ can be rewritten as

$$\epsilon_i(\sigma_c) + \frac{(\sigma_c + E\epsilon_{pm})\,D}{E(1-D)} = 0 \tag{49}$$

where σ_c denotes the closure stress, $\epsilon_i(\sigma_c)$ the inelastic strain at the current stress level and D the damage variable at the maximum stress level σ_{max}. Geometrically, this condition is given by the intersection of the stress/strain curve with the elastic response ($\sigma = E\epsilon$) of the material: see Fig. 2. Equation (49) shows that the crack closure condition depends upon all the active mechanisms. In particular, when friction is prevented (i.e., $\epsilon_i = 0$), the closure stress ($\sigma_c = -E\epsilon_{pm}$) is independent of the damage variable D. This result was used to identify the misfit strain ϵ_{pm} (see Fig. 2). Furthermore, the crack closure stress only vanishes when the misfit strain vanishes. Under this hypothesis, the closure condition reduces to the two equivalent conditions: $\sigma_c = 0$ and $\epsilon_c = 0$, where ϵ_c is the closure strain.

In Fig. 7, the predicted values of the closure stress are plotted. When the maximum stress is less than the debond stress (i.e., $\sigma_{id} = 285$ MPa) the closure stress is equal to $-E\epsilon_{pm} = -150$ MPa as expected by the model. As the maximum stress increases, the closure stress increases too.

5. CONCRETE SPECIMEN

The identification of the constitutive law of monolithic as well as fiber-reinforced concrete in tension is difficult from a direct uniaxial test. Early localization occurs and leads to the formation of one macrocrack. A special tension test allowing the Identification of Diffuse Damage (referred to as 'ID2') was first proposed by L'Hermite [21], then devised by Bazant and Pijaudier-Cabot [22], Mazars et al. [23,24]. This technique consists of gluing 8 × 8 × 250 mm^3 aluminum bars on 38 × 80 × 160 mm^3 concrete prismatic specimens (Fig. 8) to avoid the formation of a single crack. In the identification procedure, the previous authors assume that the interface between the aluminum bars and the concrete specimen is infinitely strong ($\sigma_d \to \infty$) and that the strain is uniform in the bars. Under these assumptions, the underlying behavior of concrete is deduced in a straight forward manner [22 24]. In the present case, the effect of the interface will be explicitly considered and discussed.

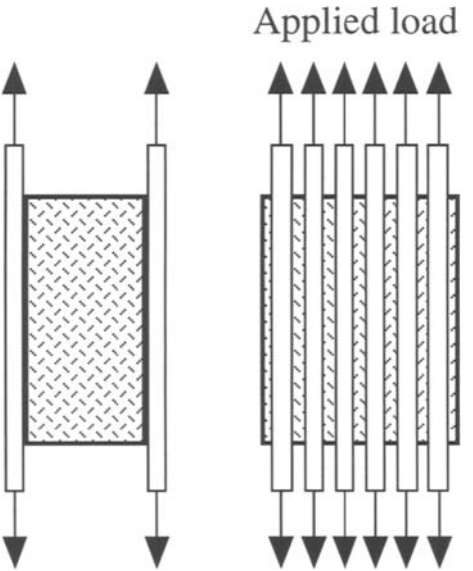

Figure 8. Schematic of an ID2 specimen.

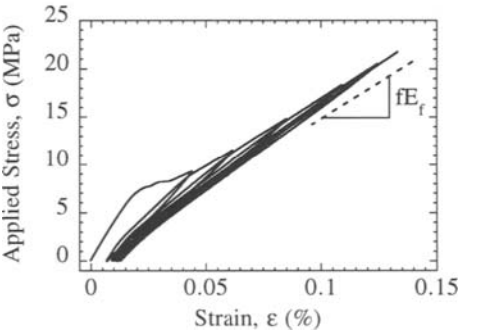

Figure 9. Stress/strain response of an ID2 concrete specimen ($f_{sf} = 0.\%$) loaded in tension.

The aim of this section is to analyze this experimental technique by using the model of Section 3. The effect of short fibers added in a concrete matrix is also discussed. In

the tested concrete specimens, four different volume fractions (f_{sf}) of short steel fibers are considered: $0., 0.1, 0.3$ and 0.6%. The fibers are aligned along the loading direction.

5.1. Analysis of Unreinforced Concrete

In this subsection, experimental data obtained for two ID2 specimens made of unreinforced concrete ($f_{sf} = 0.\%$) are analyzed. As a first approximation, this specimen can be described by the unit cell introduced in Section 2. In the present case however, the residual stresses due to processing can be neglected. The state variables still are ϵ, D, ϵ_i and d on a macroscopic scale and the associated forces are σ, Y, X and y, respectively. Unload/reload sequences in tension (Fig. 9) are performed. The damage variable D, the inelastic strain ϵ_i as well as the permanent strain ϵ_p are measured as a function of the applied stress σ.

Figure 9 shows that at the end of the test, the composite behavior approaches that of the volume fraction of aluminum bars (denoted by fE_f in the figure). It is therefore expected that, contrary to the analyzed SiC/SiC composite, saturation occurs. This feature will be discussed later on.

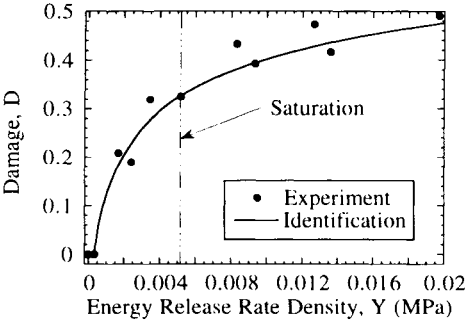

Figure 10. Damage variable D versus its associated force Y for two ID2 concrete specimens ($f_{sf} = 0.\%$).

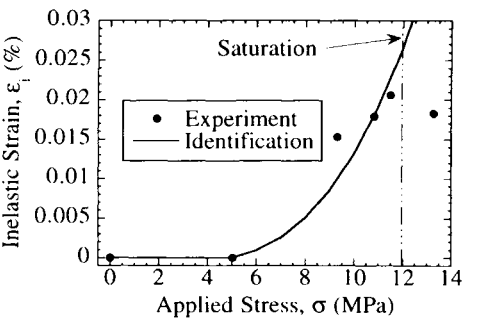

Figure 11. Inelastic strain ϵ_i versus applied stress σ for two ID2 concrete specimens ($f_{sf} = 0.\%$).

The identification procedure uses the same information as that used in the analysis of the unidirectional SiC/SiC composite (viz. the damage variable D and the inelastic strain ϵ_i). The experimental relationship observed between D and Y is given in Fig. 10. From this curve the values of the following dimensionless parameters can be obtained

$$\sqrt{\frac{2Y_c}{E}} = 1.3 \times 10^{-3} \pm 10^{-5} \quad \text{and} \quad \sqrt{\frac{2Y_0}{E}} = 4.4 \times 10^{-4} \pm 6 \times 10^{-5} \tag{50}$$

from which the matrix-cracking stress σ_{mc} can be derived immediately and has the value 5.1 ± 0.4 MPa, which is in good agreement with the experimental observations of Fig. 9.

The dimensionless parameters $B/4A^2$ and $A\sigma_d/E_f$ are identified by using the inelastic strain due to debonding and sliding. By fitting the experimental results of Fig. 11, the values of the dimensionless parameters are

$$\frac{B}{4A^2} = 12 \times 10^3 \pm 10^3 \quad \text{and} \quad \frac{A\sigma_d}{E_f} \cong 0 \tag{51}$$

The fact that σ_d is vanishingly small indicates that the specimen behaves in a low debond energy (LDE) regime. Therefore, the usual assumptions made to identify the underlying behavior of concrete (i.e., $\sigma_d \to \infty$) cannot be used in the present case. The analysis of the change of the inelastic strain shows that there is a change in the evolution pattern for a stress greater than 12 MPa, indicating the onset of cracking saturation.

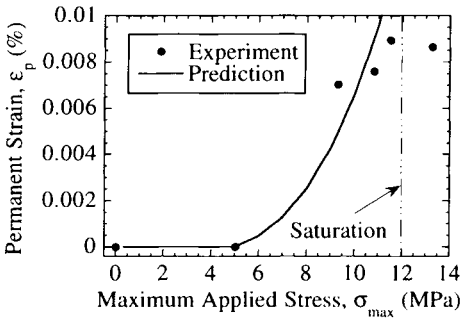

Figure 12. Permanent strain ϵ_p versus maximum applied stress σ_{max} for two ID2 concrete specimens ($f_{sf} = 0.\%$).

When the composite behaves in an LDE regime and the residual stresses are negligible, there exists a very simple relationship between the inelastic strain ϵ_i and the corresponding permanent strain ϵ_p

$$\epsilon_i = 2\epsilon_p \tag{52}$$

Figure 12 shows that the predictions of the change of the permanent strain with the applied stress is in reasonable agreement with the experiments. Figures 11 and 12 consistently show that the saturation stress is equal to 12 MPa. On the other hand, Fig. 10 shows that the prediction, *a priori* only valid up to saturation, can be further extended. Beyond the saturation level, the behavior of the ID2 specimen is mainly driven by the aluminum bars and the interface between the bars and the concrete parallelepiped (Fig. 9). It is worth remembering that the interface is weak (indicated by the LDE regime): the underlying behavior of concrete is very difficult to deduce since the stress state in concrete is not uniform along the loading direction.

5.2. Analysis of Reinforced Concrete

The effect of the addition of short fibers is discussed in this subsection by comparing the response of specimens with and without short fibers.

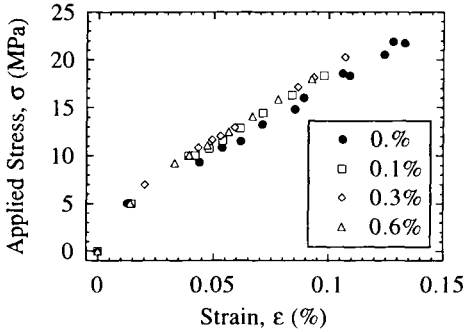

Figure 13. Comparison of stress/strain responses of ID2 concrete specimens loaded in tension when $f_{sf} = 0., 0.1, 0.3$ and 0.6%.

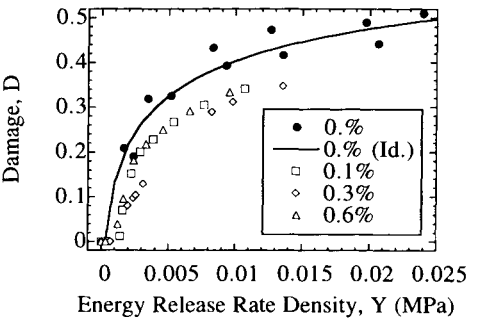

Figure 14. Damage variable D versus its associated force Y for ID2 specimens ($f_{sf} = 0., 0.1, 0.3$ and 0.6%). The symbols are experimental data and the solid line is the identification when $f_{sf} = 0.\%$.

The comparison at a purely macroscopic level consists of plotting the stress/strain responses for different volume fractions of short fibers ($f_{sf} = 0., 0.1, 0.3$ and 0.6%). Figure 13 shows that the volume fraction $f_{sf} = 0.\%$ constitutes a lower bound to the stress/strain behavior. However the effect of the volume fraction is not very important.

The experimental relationship observed between D and Y is shown in Fig. 14. The effect of the addition of short fibers becomes more significant. However, the most important feature is the presence of short fibers but not their relative volume fraction. This result indicates that the cracks are probably bridged but by very few short fibers so that the actual value of the volume fraction is unimportant.

Similarly, Fig. 15, shows that the overall inelastic strain is more influenced by the presence of short fibers rather than their respective volume fraction. Lastly, Fig. 16 shows the prediction of the change of the permanent strain with the maximum stress. A similar effect of the short fiber volume fraction can be observed. The prediction is in reasonable agreement with all the experimental data up to the saturation level (i.e., 12 MPa).

6. SUMMARY

A Continuum Damage Mechanics formulation has been applied to fiber-reinforced Composites. In addition to the total strain, the internal variables which define the state of the material have been identified. Matrix-cracking is described by one damage variable,

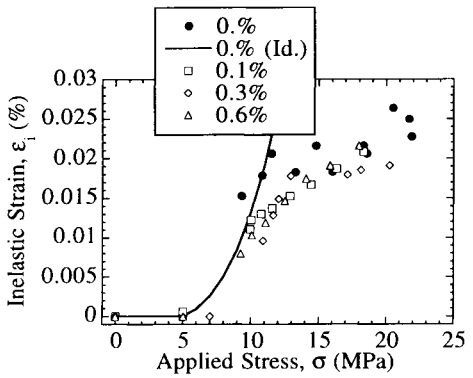

Figure 15. Inelastic strain ϵ_i versus applied stress σ for ID2 specimens (f_{sf} = 0., 0.1, 0.3 and 0.6%).The symbols are experimental data and the solid line is the identification when f_{sf} = 0.%.

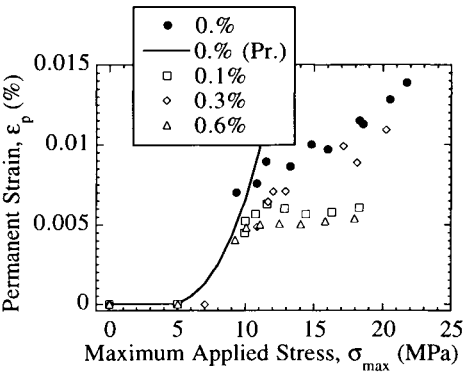

Figure 16. Permanent strain ϵ_p versus maximum applied stress σ_{max} for ID2 specimens f_{sf} = 0., 0.1, 0.3 and 0.6%.The symbols are experimental data and the solid line is the prediction when f_{sf} = 0.%

debonding and sliding are modeled by an inelastic strain and another damage variable measuring the amount of non-recoverable energy. These variables are related to microscopic quantities introduced to analyze the degradation mechanisms of BMCs.

Micromechanical parameters are exhibited to model matrix-cracking, interfacial debonding and sliding. Their identification is discussed by analyzing the mechanical behavior of a unidirectional SiC/SiC composite. This composite behaves in a large debond energy regime in which the stress levels related to the debond strength are significantly higher than those related to sliding.

Conversely, concrete specimens reinforced by aluminum bars exhibit a low debond energy regime. The classical identification procedure cannot be used to infer the behavior of concrete from the response of the composite system. Furthermore, this type of experiment is more sensitive to the presence or the lack of short fibers in concrete than the actual volume fraction (up to 0.6%). However, in some other cases, the effect of fiber volume fraction can be more significant (e.g., three point flexure tests [25]).

The framework presented in this paper has been extended to model layered as well as woven fiber-reinforced composites. The nature of the different internal variables have been discussed. The same formalism can also be used to model high temperature applications in which the change of residual stresses as well as creep mechanisms need to be incorporated [26]. This work is still in progress.

REFERENCES

1. J. Aveston, G. A. Cooper and A. Kelly, in Proceedings National Physical Laboratory: Properties of Fiber Composites, IPC Science and Technology Press, Surrey (UK), (1971) 15.
2. J. Aveston and A. Kelly, J. Mater. Sci. 8 (1973) 352.
3. J. W. Hutchinson and H. M. Jensen, Mech. Mater. 9 (1990) 139.
4. B. Budiansky, J. W. Hutchinson and A. G. Evans, J. Mech. Phys. Solids 34 [2] (1986) 167.
5. A. Burr, P. Feillard and F. Hild, C. R. Acad. Sci. Paris Série IIb [t. 323] (1996) 377.
6. H. L. Cox, Br. J. Appl. Phys. 3 (1952) 72.
7. A. A. Valuenko and M. L. Kachanov, Mekh. Tverdogo Tela 4 (1971) 159.
8. A. C. F. Cocks and F. A. Leckie, in Advances in Applied Mechanics, Academic Press, New-York (USA), (1987), 239.
9. J. R. Rice, J. Mech. Phys. Solids 19 (1971) 433.
10. P. Germain, Q. S. Nguyen and P. Suquet, ASME J. Appl. Mech. 50 (1983) 1010.
11. V. Volterra, Annales Scientifiques de l'Ecole Normale Supérieure, Paris (France) 24 [3] (1907) 401.
12. A. E. H. Love, Cambridge University Press, Cambridge (UK), 1927.
13. J. D. Eshelby, Proc. Roy. Soc. London A 241 (1957) 376.
14. A. G. Evans, J.-M. Domergue and E. Vagaggini, J. Am. Ceram. Soc. 77 [6] (1994) 1425.
15. A. Burr, F. Hild and F. A. Leckie, Arch. Appl. Mech. 65 [7] (1995) 437.
16. A. Burr, F. Hild and F. A. Leckie, Eur. J. Mech. A/Solids 16 [1] (1997) 53.
17. J.-M. Domergue, PhD dissertation, University of California, Santa Barbara, 1995.
18. S. Jansson and F. A. Leckie, Acta Metall. Mater. 40 [11] (1993) 2967.
19. W. A. Curtin, Acta Metall. Mater. 41 [5] (1993) 1369.
20. F. Hild, A. Burr and F. A. Leckie, Int. J. Solids Struct. 33 [8] (1996) 1209.
21. S. L'Hermite, in Proceedings 4th International Symposium on the Chemistry of Cement, Washington DC (USA), (1960) 659.
22. Z. P. Bazant and G. Pijaudier-Cabot, ASCE J. Eng. Mat. 115 [4] (1989) 755.
23. J. Mazars and Y. Berthaud, C. R. Acad. Sci. Paris Série II [t. 308] (1989) 579.
24. J. Mazars, Y. Berthaud and S. Ramtani, Eng. Fract. Mech. 35 [4/5] (1990) 629.
25. D. Boudon-Cussac, PhD dissertation, University Paris VI, 1996.
26. A. Burr, F. Hild and F. A. Leckie, in Proceedings JNC10, D. Baptiste and A. Vautrin (eds.), AMAC, Paris (France), (1996) 1275.

Damage Mechanics in Engineering Materials
G.Z. Voyiadjis, J.-W.W. Ju and J.-L. Chaboche (Editors)
© 1998 Elsevier Science B.V. All rights reserved.

A mesocrack damage and friction coupled model for brittle materials

A. Dragon and D. Halm

Laboratoire de Mécanique et de Physique des Matériaux (UMR CNRS 6617), ENSMA, Téléport 2, BP 109, 86960 Futuroscope Cedex, France

A three-dimensional model of anisotropic damage by mesocrack growth, Halm and Dragon [1], is first summarized in its extended version. It is employing a second-order tensorial damage variable and considering damage (i.e. generation and growth of decohesion microsurfaces) as the unique dissipative mechanism. The model – concerning rate-independent, small strain, isothermal behaviour – reduces any system of mesocracks to three equivalent orthogonal sets and leads to a form of orthotropy. It allows to take into account residual effects due to damage itself. To account for elastic moduli recovery due to crack closure phenomena a compromise solution has been advanced between micromechanical considerations imposing a fourth-order crack-related tensor and macroscopic modelling efficiency. The formulation maintains the orthotropy of the effective properties, instead of eventual general form of anisotropy. Unlike some models which do not avoid (or rectify a posteriori) discontinuity of the stress-strain response, the approach herein ensures a priori the stress continuity and allows to express a convenient macroscopic opening-closure criterion.

The foregoing model is in the present work considered as coupled with a form of friction-induced plasticity. To account for the friction effects on microcrack lips a new internal variable is introduced to capture the corresponding dissipative mechanism. The thermodynamic potential (free-energy function) is enlarged and modified by introducing two additional terms related to the stored energy due to frictional sliding. The evolution law of the latter is formulated in the space of corresponding thermodynamic forces through a standard scheme. Numerical simulations for complex loading paths are successively performed and compared with available experimental data.

1. INTRODUCTION

The specific stress-stain response of brittle materials such as rocks, plain concrete, ceramics, glasses can be inferred in large degree from their predominant damage micromechanism, namely multiple micro- and mesocrack incipience and growth. The progressive, microcrack orientation dependent degradation of elastic moduli at the macroscopic level is commonly accompanied with the events like volumetric dilatancy, induced anisotropy, irreversible strain after unloading, more pronounced in the direction of preponderant microcracking. The unilateral effect consisting in elastic moduli recovery due to crack closure under the compressive load is a characteristic feature of cyclic behaviour of the materials at stake.

When considering the crack closure for a microcrack system in a brittle solid under mechanical loading one can trace a link between complex multistage loading and unloading curves observed experimentally and the friction resistance at the crack lips level and subsequent frictional sliding and/or eventual crack opening. In such a way the unloading process for a damaged material can be itself friction-locked and possibly dissipative (if followed by frictional sliding). The inelastic unloading is just a particular event revealing the coupling effect of damage by microcracking with a form of plasticity generated by the frictional sliding on closed multiple

crack set. It has received some attention in the past, see f.ex. Kachanov [2], Horii and Nemat-Nasser [3], Ju [4], Krajcinovic et al. [5], Andrieux et al. [6], Gambarotta and Lagomarsino [7], Fond and Berthaud [8]. For the most part the papers cited represent instructive micromechanical analyses leading to models covering limited spectre of stress-strain paths (two-dimensional, axisymmetric, etc.). The purpose of this paper is to address – in an overview manner – basic issues of 3D-modelling employing an internal variable formalism for the joint process of anisotropic damage by microcraking and frictional sliding at closed microcracks. The aim is to provide an efficient, reasonably simple, macroscopic – whereas strongly micromechanically stimulated – model. The approach presented is based on the anisotropic damage model proposed by Dragon, see Dragon et al. [9] and extended by Halm and Dragon [1] to include the unilateral effect concerning normal stiffness recovery with respect to a microcrack plane.

An outline of the remainder of this paper is as follows : in Section 2 is summarized the existing model by Halm and Dragon for anisotropic damage by microcracking with normal unilateral effect. In Section 3 are considered basic issues of a new, non-classical modelling of frictional sliding. The latter is built under general loading conditions involving various dissipative configurations : frictional sliding for constant damage for closed microcracks, frictional sliding and evolving damage for closed microcracks, damage with no frictional sliding for open cracks, combinations of above for multiple crack systems. In fact, in the present model, multiple systems of parallel cracks are reduced to three orthogonal equivalent systems thus inducing a form of orthotropy (instead of eventual more general anisotropy), according to Dragon et al. [9], see also Kachanov [10]. The friction model given herein allows avoiding some inconveniences of the Coulomb model though strong affinities persist. It is presented in itself in Section 3 whereas the full damage/friction coupling is discussed and recapitulated in Section 4. Some example calculations are shown further (Section 5) to demonstrate various features of the coupled model and to make comparison with experimental data. The model presented is aimed to provide an efficient and consistent tool for structural analysis accounting for basic dissipative phenomena in brittle solids. Emphasis is put on reasonable simplicity and on accessible identification of material constants from prevalent laboratory tests.

2. ANISOTROPIC DAMAGE AND NORMAL UNILATERAL EFFECT

This Section outlines the salient features of the anisotropic damage model by Halm and Dragon [1] which forms the framework for further developments presented in Sections 3 and 4. An objective of the damage model summarized below is to describe – in a realistic and structural calculus applicable manner – the process of mesocrack-induced anisotropic degradation and relative behaviour of an elastic rock-like 'brittle' solid. It stipulates evaluation of effective elastic moduli of a material with microcracks and an adequate description of the evolution of damage. The emphasis has been put on an "open" formulation of the model to allow further extensions and couplings. It is based on the hypotheses and developments ordered below in the items from (i) to (v) :

(i) A single damage internal variable is constituted by a symmetric, second-order tensor $\mathbf{D}$ indicating orientation of microcrack set(s) as well as the dissipative mechanism under consideration, namely generation and growth of decohesion microsurfaces :

$$\mathbf{D} = \sum_i d^i(s)\,\mathbf{n}^i \otimes \mathbf{n}^i \qquad (1)$$

The scalar density $d^i(s)$ is proportional to the extent s of decohesion surface and the unit normal vector $\mathbf{n}^i$ describes orientation of the i-th set of parallel crack-like defects. The form (1) is motivated by micromechanical considerations (see e.g. Kachanov [2,10]) but in the context here the density d(s) is reckoned as a macroscopic quantity. The expression (1) is in itself a guiding interpretation of damage-related internal variable $\mathbf{D}$. Since $\mathbf{D}$ is a symmetric second-

order tensor it has three positive eigenvalues D_k (k = 1, 2, 3) and three orthogonal eigenvectors $\mathbf{v}^k$. This means that any system of microcracks (1), decomposed into 1,...,i,...n of subsystems of parallel mesocracks can be reduced to three equivalent orthogonal sets of cracks characterized by densities D_k and normal vectors $\mathbf{v}^k$:

$$\mathbf{D} = \sum_{k=1}^{3} D_k \, \mathbf{v}^k \otimes \mathbf{v}^k \tag{2}$$

(ii) The damage-dependent strain energy (free energy per unit volume) $w(\boldsymbol{\varepsilon},\mathbf{D})$ generates a form of elastic orthotropy – in connection to three eigensystems (2) – for $\mathbf{D} \neq \mathbf{0}$; w is assumed a linear function of $\mathbf{D}$ and in this way corresponding to non-interacting cracks hypothesis. On the other hand it contains linear and quadratic terms in $\boldsymbol{\varepsilon}$. A particular invariant form given below comprises a single linear term reading g $\mathrm{tr}(\boldsymbol{\varepsilon}.\mathbf{D})$, g = const, corresponding to damage-induced residual phenomena. The macroscopic residual stress for $\boldsymbol{\varepsilon} = \mathbf{0}$ is thus explicitly obtained. Inversely, for $\boldsymbol{\sigma} = \mathbf{0}$, non-zero residual strain is induced.

(iii) Under predominantly compressive loading favourably oriented cracks close leading to an elastic moduli recovery phenomenon in the direction normal to the closed cracks. It is called here normal unilateral effect – in the absence of frictional sliding (the latter, when accounted for later, will induce a 'shear' recovery effect as well) – and requires more involved damage characterization. In fact, for a set of cracks constrained against opening a fourth-order tensorial density is necessary for a rigorous, micromechanically motivated description. A compromise solution has been advanced in [1] between micromechanical considerations imposing an additional fourth-order damage variable and macroscopic modelling efficiency. The formulation maintains the orthotropy of the effective, elastic properties – instead of eventual more general anisotropy induced by a new fourth-order damage tensor – and the fourth-order entity $\hat{\mathbf{D}}$, necessary to account for the normal unilateral effect, is directly assembled with the eigenvalues and eigenvectors of $\mathbf{D}$:

$$\hat{\mathbf{D}} = \sum_{k=3}^{3} D_k \, \mathbf{v}^k \otimes \mathbf{v}^k \otimes \mathbf{v}^k \otimes \mathbf{v}^k \tag{3}$$

(iv) A single scalar simultaneous invariant of $\hat{\mathbf{D}}$ and $\boldsymbol{\varepsilon}$ completes the expression of the free energy (thermodynamic potential), with no additional material constant with respect to the basic form $w(\boldsymbol{\varepsilon},\mathbf{D})$ postulated in (ii). Rigorous continuity analysis in the framework of multilinear elasticity (for a given damage state), recast in [1], leads to a simple microcrack closure condition for an equivalent set, namely : $\mathbf{v}^k.\boldsymbol{\varepsilon}.\mathbf{v}^k \leq 0$. The detailed expression of $w(\boldsymbol{\varepsilon},\mathbf{D})$ including the normal unilateral effect is :

$$\begin{aligned} w(\boldsymbol{\varepsilon},\mathbf{D}) = {} & \frac{1}{2}\lambda(\mathrm{tr}\,\boldsymbol{\varepsilon})^2 + \mu\,\mathrm{tr}(\boldsymbol{\varepsilon}.\boldsymbol{\varepsilon}) + g\,\mathrm{tr}(\boldsymbol{\varepsilon}.\mathbf{D}) + \alpha\,\mathrm{tr}\,\boldsymbol{\varepsilon}\,\mathrm{tr}(\boldsymbol{\varepsilon}.\mathbf{D}) + 2\beta\,\mathrm{tr}(\boldsymbol{\varepsilon}.\boldsymbol{\varepsilon}.\mathbf{D}) \\ & - (\alpha+2\beta)\boldsymbol{\varepsilon} : \left[\sum_{k=1}^{3} H(-\mathbf{v}^k.\boldsymbol{\varepsilon}.\mathbf{v}^k)\, D_k \mathbf{v}^k \otimes \mathbf{v}^k \otimes \mathbf{v}^k \otimes \mathbf{v}^k \right] : \boldsymbol{\varepsilon} \end{aligned} \tag{4}$$

where H is the classical Heaviside function ; α, β are material constants related to modified elastic moduli for a given damage state. λ and μ are conventional Lamé constants for elastic (non damaged) solid matrix.

The corresponding damage-influenced orthotropic elasticity representation $\boldsymbol{\sigma}(\boldsymbol{\varepsilon},\mathbf{D})$ and the damage driving (thermodynamic) force $\mathbf{F}^{D}$ are determined by partial derivation :

$$\boldsymbol{\sigma} = \frac{\partial w}{\partial \boldsymbol{\varepsilon}} = \lambda(\mathrm{tr}\boldsymbol{\varepsilon})\mathbf{1} + 2\mu\boldsymbol{\varepsilon} + g\mathbf{D} + \alpha\left[\mathrm{tr}(\boldsymbol{\varepsilon}.\mathbf{D})\mathbf{1} + (\mathrm{tr}\boldsymbol{\varepsilon})\mathbf{D}\right] + 2\beta\,(\boldsymbol{\varepsilon}.\mathbf{D} + \mathbf{D}.\boldsymbol{\varepsilon}) - 2(\alpha+2\beta)\sum_{k=1}^{3} H(-\mathbf{v}^k.\boldsymbol{\varepsilon}.\mathbf{v}^k)D_k(\mathbf{v}^k.\boldsymbol{\varepsilon}.\mathbf{v}^k)\mathbf{v}^k \otimes \mathbf{v}^k \tag{5}$$

$$\mathbf{F}^{D} = -\frac{\partial w}{\partial \mathbf{D}} = -g\boldsymbol{\varepsilon} - \alpha(\mathrm{tr}\boldsymbol{\varepsilon})\boldsymbol{\varepsilon} - 2\beta(\boldsymbol{\varepsilon}.\boldsymbol{\varepsilon}) + (\alpha+2\beta)\sum_{k=1}^{3} H(-\mathbf{v}^k.\boldsymbol{\varepsilon}.\mathbf{v}^k).(\mathbf{v}^k.\boldsymbol{\varepsilon}.\mathbf{v}^k)^2\,\mathbf{v}^k \otimes \mathbf{v}^k \tag{6}$$

In spite of the presence of the Heaviside function $H(-\mathbf{v}^k.\boldsymbol{\varepsilon}.\mathbf{v}^k)$, w, $\boldsymbol{\sigma}$ and $\mathbf{F}^{D}$ remain continuous when passing from the open mesocracks configuration to the closed mesocracks configuration and vice versa.

(v) The evolution of $\mathbf{D}$, corresponding to the brittle, splitting-like crack kinetics, has been found to follow the normality rule with respect to a criterion in the space of components of the proper thermodynamic force (affinity) $\mathbf{F}^{D}$. The damage evolution is thus following the principle of maximum (damage) dissipation, see also Govindjee et al. [11], and is related here to tensile (positive) straining $\boldsymbol{\varepsilon}^{+}$ and to actual damage pattern. The particular damage criterion $f(\mathbf{F}^{D},\mathbf{D}) \le 0$ is explicitly dependent on the part $\mathbf{F}^{D1+} = -g\boldsymbol{\varepsilon}^{+} = \mathbf{F}^{D} - \mathbf{F}^{D2} - \mathbf{F}^{D1-}$ of the driving force $\mathbf{F}^{D}.\mathbf{F}^{D1}$ is the strain energy release rate term related to residual 'locked' effects : $\mathbf{F}^{D1} = -g\boldsymbol{\varepsilon}$, $\mathbf{F}^{D2}$ represents the remaining recoverable energy release rate. The former term is decomposed into the splitting part $\mathbf{F}^{D1+} = -g\boldsymbol{\varepsilon}^{+}$, $\boldsymbol{\varepsilon}^{+} = \mathbf{P}^{+}:\boldsymbol{\varepsilon}$, with $\mathbf{P}^{+}$ a positive fourth-order projection tensor selecting positive eigenvalues from strain, and the non-splitting part $\mathbf{F}^{D1-} = -g(\boldsymbol{\varepsilon} - \boldsymbol{\varepsilon}^{+})$. The damage criterion and rate-independent damage evolution law are thus as follows :

$$f\left(\mathbf{F}^{D} - \mathbf{F}^{D2} - \mathbf{F}^{D1-},\mathbf{D}\right) = \sqrt{\frac{1}{2}\,\mathrm{tr}\left[\left(\mathbf{F}^{D} - \mathbf{F}^{D2} - \mathbf{F}^{D1-}\right).\left(\mathbf{F}^{D} - \mathbf{F}^{D2} - \mathbf{F}^{D1-}\right)\right]} + B\,\mathrm{tr}\left[\left(\mathbf{F}^{D} - \mathbf{F}^{D2} - \mathbf{F}^{D1-}\right).\mathbf{D}\right] - \left(C_o + C_1\mathrm{tr}\,\mathbf{D}\right) \le 0 \tag{7}$$

$$\dot{\mathbf{D}} = \Lambda_D \frac{\partial f}{\partial \mathbf{F}^{D}} = \begin{cases} 0 & \text{if } f < 0 \text{ or } f = 0,\ \dot{f} < 0 \\ \Lambda_D\left[\dfrac{\boldsymbol{\varepsilon}^{+}}{\sqrt{2\,\mathrm{tr}(\boldsymbol{\varepsilon}^{+}.\boldsymbol{\varepsilon}^{+})}} + B\mathbf{D}\right] & \text{if } f = 0 \text{ and } \dot{f} = 0 \end{cases} \quad ;\ \Lambda_D \ge 0 \tag{8}$$

Remarks :

The fourth-order tensor $\hat{\mathbf{D}}$ depends entirely on $\mathbf{D}$ (see definition (3)) ; it does not require a separate evolution law.

In numerical calculations any loading path is considered as a collection of $\mathbf{D}$-proportional segments. The form of Eqn (6) is valid for such a segment, i.e. for a given configuration of principal directions of $\mathbf{D}$.

The model, non-linear as it is, contains eight material constants only : λ, μ, α, β, g, B, C_o and C_1. Seven of them can be relatively easily determined from axisymmetric triaxial

compression test with unloading, see Dragon et al. [9]. In particular, C_o and C_1 are determined from the corresponding non-linear damage loading portion of experimental curves. The identification of α and β exploits the unloading portions considered as elastic according to the hypotheses (i)-(v) of the foregoing frictionless damage-elastic version. The point where the unloading is performed should correspond to pronounced oriented damage, but has to be reasonably far from the bifurcation-onset point to avoid interference.

To determine B one should resort to a two-segment loading path experiment. The second loading is to be performed off the first-segment damage-induced anisotropy axes. One can see from (8) that B intervenes as a sort of a damage-drag constant moderating the **D**-principal axes tendency to follow $\boldsymbol{\varepsilon}^+$-axes in complex non-proportional loading involving $\boldsymbol{\varepsilon}^+$-axes rotation.

An operational, structural analysis approach employing the concept of damage should combine an efficient damage model implemented in robust computer algorithm associated with proper tools for detection and control of bifurcation phenomena. The latter indicate eventual transition from distributed damage to surface-like localization considered as a precursor of macroscopic fracture. In any case bifurcation events point out an ill-posedness of the problem and necessity of remaking a computational scheme. Actually, the basic model presented, i.e. the one summarized above *except* the last, unilateral effect related term in $w(\boldsymbol{\varepsilon},\mathbf{D})$ put up in eqn (4), was extensively tested for its capacities to generate physically sound localized failure mechanisms, see e.g. [9,12]. The very fair predictions in this field obtained for homogeneous stress-strain paths as well as for boundary-value problems related to rock engineering applications have prompted further developments of the model itself including its coupling with a form of mesocrack-friction-induced plasticity as put forward in the next section.

3. MESOCRACK FRICTION INDUCED PLASTICITY

The unilateral normal effect included in the model summarized in Section 2 allows a moduli recovery in the direction normal to the closed mesocracks. It fails to capture a shear moduli recovery parallelly to the crack plane resulting from some blocking of mesocrack lips displacement due to roughness and corresponding friction phenomena. Experimental data involving loading-unloading cycles for specimens subject to torsion and hydrostatic compression for instance show hysteretic effects generated by such a blocking and subsequent frictional sliding on closed mesocrack lips. The beginning of unloading is characterized by a quasi-vertical curve while further decreasing slope is linked to progressive sliding, see f.ex. Pecqueur [13]. Some attempts of micromechanical modelling of the phenomena deserve attention , [2-8]. However they are not directly operational for an efficient structural analysis. Some of earlier attempts (Kachanov [2], Horii and Nemat-Nasser [3]) consider the influence of friction on effective moduli but do not provide satisfactory treatment of sliding evolution. Most of existing approaches are limited to two-dimensional analyses, as e.g. [6], with the notable exception of the more recent work by Gambarotta and Lagomarsino [7].

3.1. Elastic-damage-and-friction response

The global strain expression for a representative volume of elastic solid of stiffness **C** containing microcracks (assumed plane and quasi-circular for simplicity) can be written as a sum of the solid matrix contribution $\boldsymbol{\varepsilon}^o$ and the crack contribution $\boldsymbol{\varepsilon}^c$:

$$\boldsymbol{\varepsilon} = \mathbf{C}^{-1} : \boldsymbol{\sigma} + \frac{1}{2V}\sum_i \left(\langle \mathbf{b} \rangle \otimes \mathbf{n} + \mathbf{n} \otimes \langle \mathbf{b} \rangle\right)^i s^i = \boldsymbol{\varepsilon}^o + \sum_i \boldsymbol{\varepsilon}^{ci} \tag{9}$$

with the crack displacement discontinuity $\mathbf{b}^i$ being averaged ($\langle \mathbf{b}^i \rangle$) for the microcrack set i. For closed sliding cracks, as long as the orientation $\mathbf{n}^i$ is preserved, $\langle \mathbf{b}^i \rangle$ is orthogonal to $\mathbf{n}^i$:

$$\langle \mathbf{b}^i \rangle = \xi^i \mathbf{g}^i \quad , \quad \mathbf{g}^i \perp \mathbf{n}^i \quad \text{if} \quad \mathbf{n}^i = \text{const.} \tag{10}$$

with ξ^i representing the amount of sliding in the direction $\mathbf{g}^i$. One can write furthermore :

$$\boldsymbol{\varepsilon}^{ci} = \frac{s^i}{2V}\,\xi^i\left(\mathbf{g}^i \otimes \mathbf{n}^i + \mathbf{n}^i \otimes \mathbf{g}^i\right) \tag{11}$$

Hence, for the microcrack system i, the sliding variable is chosen in the form :

$$\boldsymbol{\gamma}^i = \frac{s^i \xi^i}{V}\,\mathrm{sym}\,(\mathbf{n}\otimes\mathbf{g})^i\,, \tag{12}$$

the symmetrisation being operated for the expression in parentheses. The similarity with (1) is striking : as for **D**, the form of $\boldsymbol{\gamma}$ is motivated by micromechanics ; as for d(s) the quantity $\frac{s^i \xi^i}{V}$ cannot be explicitly calculated in the framework of macroscopic model. Moreover, as any system of microcracks represented by **D** reduces to three equivalent sets according to (2), the sliding tensor $\boldsymbol{\gamma}$ can be written in the analogous manner :

$$\boldsymbol{\gamma} = \sum_{k=1}^{3} \frac{s^k \xi^k}{V}\,\mathrm{sym}\,(\mathbf{v}\otimes\boldsymbol{\gamma})^k = \sum_{k=1}^{3} \boldsymbol{\gamma}^k$$

where $\mathbf{v}^k$, k = 1,2,3 are **D**-eigenvectors.

Let us consider, for a while, a single system of mesocracks characterized by the only principal non zero component D_3 and the normal (eigenvector) $\mathbf{v}^3$. The objective here is to argue for an enlarged form of the free-energy function $w(\boldsymbol{\varepsilon};\mathbf{D},\boldsymbol{\gamma})$ accounting for the frictional blocking and sliding effects for closed crack sets.

From (4), (5) one can infer that the anisotropic damage-induced shear moduli are entirely determined by μ (solid matrix shear modulus) and the term $2\beta\mathrm{tr}(\boldsymbol{\varepsilon}.\boldsymbol{\varepsilon}.\mathbf{D})$. Hence, for the damage configuration at stake ($D_1=D_2=0$; $D_3 \neq 0$) one obtains :

$$\begin{cases} \sigma_{13} = 2\mu\varepsilon_{13} + 2\beta D_3 \varepsilon_{13} \\ \sigma_{23} = 2\mu\varepsilon_{23} + 2\beta D_3 \varepsilon_{23} \end{cases}$$

The degradation of moduli in the normal direction to the open crack set is described in the *conjugate* manner by the α-term as well as the β-one. The expression of the Young modulus E_3 for the damage configuration as above is

$$E_3 = \lambda + 2\mu + 2\alpha D_3 + 4\beta D_3 - \frac{(\lambda + \alpha D_3)^2}{\lambda + \mu}$$

Let us consider the transition from open cracks to closed ones, assuming friction resistant lips when in contact. The crack-open form of (4), with $H(-\mathbf{v}^3.\boldsymbol{\varepsilon}.\mathbf{v}^3)=0$ applies for the former case. When the cracks are closed and blocked by friction resistance at a given $\boldsymbol{\gamma}$, the shear modulus μ is recovered and this should be properly reflected in the new modified expression $w(\boldsymbol{\varepsilon};\mathbf{D},\boldsymbol{\gamma})$. The β-term should be counterbalanced in this expression. The α-term, having no influence on shear moduli, enters as before. Additional invariants including $\boldsymbol{\gamma}$ can be only simultaneous $(\boldsymbol{\gamma},\mathbf{D})$-invariants as there is no sliding on crack lips in the absence of damage. As from (15) one infers $\mathrm{tr}\,\boldsymbol{\gamma} = 0$ and $\mathrm{tr}(\boldsymbol{\gamma}.\mathbf{D}) = 0$ (for conservative damage axes), only two simultaneous invariants of $\boldsymbol{\varepsilon}$, $\boldsymbol{\gamma}$ and **D** convey useful information. They are : $\mathrm{tr}(\boldsymbol{\varepsilon}.\boldsymbol{\gamma}.\mathbf{D})$ and

$\mathrm{tr}(\boldsymbol{\gamma}.\boldsymbol{\gamma}.\mathbf{D})$. The argument for the quantity including β in the last term of (4) was to restitute the normal stiffness reduced by the term $2\beta\mathrm{tr}(\boldsymbol{\varepsilon}.\boldsymbol{\varepsilon}.\mathbf{D})$ in the first line of (4), but since this latter term is going to be counterbalanced, the former quantity has to disappear from w. Doing so allows one to write the expression $w(\boldsymbol{\varepsilon};\mathbf{D},\boldsymbol{\gamma})$ for closed friction-resistant crack lips in the form :

$$\begin{aligned} w(\boldsymbol{\varepsilon},\mathbf{D},\boldsymbol{\gamma}) = {} & \frac{1}{2}\lambda(\mathrm{tr}\boldsymbol{\varepsilon})^2 + \mu\mathrm{tr}(\boldsymbol{\varepsilon}.\boldsymbol{\varepsilon}) + g\mathrm{tr}(\boldsymbol{\varepsilon}.\mathbf{D}) + \alpha\mathrm{tr}\boldsymbol{\varepsilon}\,\mathrm{tr}(\boldsymbol{\varepsilon}.\mathbf{D}) \\ & - \alpha(\boldsymbol{\varepsilon} : \hat{\mathbf{D}} : \boldsymbol{\varepsilon}) + \eta_1\mathrm{tr}(\boldsymbol{\varepsilon}.\boldsymbol{\gamma}.\mathbf{D}) + 2\eta_2\mathrm{tr}(\boldsymbol{\gamma}.\boldsymbol{\gamma}.\mathbf{D}) \end{aligned} \tag{13}$$

η_1 and η_2 are material constants to be identified.

From the micromechanics viewpoint there are infinity of crack-closure paths possible (straight, slantwise, mixed,...). The macroscopic model continuity requires w and $\boldsymbol{\sigma}$-functions continuity. This leads to the following condition at the closure-point :

$$\begin{cases} \boldsymbol{\varepsilon}.\mathbf{D} = \boldsymbol{\gamma}.\mathbf{D} \\ \mathbf{D}.\boldsymbol{\varepsilon} = \mathbf{D}.\boldsymbol{\gamma} \end{cases} \quad \Leftrightarrow \quad \gamma_{ij} = \mathrm{sym}(\varepsilon_{ik}\nu_k\nu_j) \qquad \text{at closure-point} \tag{14}$$

The latter formula constitutes an initialization for the sliding variable $\boldsymbol{\gamma}$ and can be explained as follows : at closure point, the sliding quantity $\boldsymbol{\gamma}$ is equal to the strain $\boldsymbol{\varepsilon}$ in the crack plane, the matrix transmits its deformation to the crack.

According to the continuity conditions for multilinear elasticity (Wesolowski [14], Curnier et al. [15]) already employed in [1] in the context of unilateral normal effect, see eqns (4)-(6) Sect. 2, the jump of effective elastic stiffness $[[\mathbf{C}^*]]$ between open crack (the corresponding energy is designated by w° below) and closed crack respective configurations should be a singular operator. It is sufficient that its all second-order determinants be equal to zero.

In the present context –eqn (13) at the very closure point, taking into account (14) – $[[\mathbf{C}^*]]$ is given as follows :

$$[[\mathbf{C}^*]] = \left.\frac{\partial^2 w}{\partial\boldsymbol{\varepsilon}\partial\boldsymbol{\varepsilon}}\right|_{\boldsymbol{\gamma},\mathbf{D}} - \left.\frac{\partial^2 w^\circ}{\partial\boldsymbol{\varepsilon}\partial\boldsymbol{\varepsilon}}\right|_{\mathbf{D}} ;$$

$$[[C^*_{ijkl}]] = \left(\frac{1}{2}\eta_1 + \eta_2 - \beta\right)\left(\delta_{ik}D_{jl} + \delta_{jl}D_{ik} + \delta_{il}D_{jk} + \delta_{jk}D_{il}\right) - 2\alpha\hat{D}_{ijkl}$$

The above-mentioned singularity requirement and an additional stronger condition applied by Halm and Dragon [16] (in the way similar as in [1]) lead respectively to

$$\begin{cases} \frac{1}{2}\eta_1 + \eta_2 - \beta = 0 \\ \eta_1 = 4\beta \end{cases} \tag{15}$$

The free-energy $w(\boldsymbol{\varepsilon};\mathbf{D},\boldsymbol{\gamma})$ can now be written as follows (for either open or closed cracks)

$$\begin{aligned} w(\boldsymbol{\varepsilon};\mathbf{D},\boldsymbol{\gamma}) = {} & \frac{1}{2}\lambda(\mathrm{tr}\boldsymbol{\varepsilon})^2 + \mu\,\mathrm{tr}(\boldsymbol{\varepsilon}.\boldsymbol{\varepsilon}) + g\,\mathrm{tr}(\boldsymbol{\varepsilon}.\mathbf{D}) + \alpha\mathrm{tr}\,\boldsymbol{\varepsilon}\,\mathrm{tr}(\boldsymbol{\varepsilon}.\mathbf{D}) + 2\beta\,\mathrm{tr}(\boldsymbol{\varepsilon}.\boldsymbol{\varepsilon}.\mathbf{D}) \\ & + \mathrm{H}(-\mathbf{v}.\boldsymbol{\varepsilon}.\mathbf{v})\left[-2\beta\mathrm{tr}(\boldsymbol{\varepsilon}.\boldsymbol{\varepsilon}.\mathbf{D}) - \alpha\boldsymbol{\varepsilon} : \hat{\mathbf{D}} : \boldsymbol{\varepsilon} + 4\beta\mathrm{tr}(\boldsymbol{\varepsilon}.\boldsymbol{\gamma}.\mathbf{D}) - 2\beta\mathrm{tr}(\boldsymbol{\gamma}.\boldsymbol{\gamma}.\mathbf{D})\right] \end{aligned} \tag{16}$$

The expression (16) can be generalized to three non-interactive equivalent crack sets represented by eigenvectors $\mathbf{v}^k$ associated with the principal components D_k, k=1,2,3. One can select the k-th set using the following projection operator $\mathbf{L}^k$:

$$\mathbf{L}^k = \mathbf{v}^k \otimes \mathbf{v}^k \otimes \mathbf{v}^k \otimes \mathbf{v}^k$$
$$\mathbf{D}^k = D_k \mathbf{v}^k \otimes \mathbf{v}^k = \mathbf{L}^k : \mathbf{D} \tag{17}$$

This allows to write counterpart equations of (4)-(6) independently for each equivalent set, all possible configurations being included (open or closed, sliding or non sliding sets) :

$$w(\boldsymbol{\varepsilon},\mathbf{D},\boldsymbol{\gamma}) = \frac{1}{2}\lambda(tr\boldsymbol{\varepsilon})^2 + \mu tr(\boldsymbol{\varepsilon}.\boldsymbol{\varepsilon}) + g tr(\boldsymbol{\varepsilon}.\mathbf{D}) + \alpha tr(\boldsymbol{\varepsilon}) tr(\boldsymbol{\varepsilon}.\mathbf{D}) + 2\beta tr(\boldsymbol{\varepsilon}.\boldsymbol{\varepsilon}.\mathbf{D})$$
$$+ \sum_{k=1}^{3} H(-\mathbf{v}^k.\boldsymbol{\varepsilon}.\mathbf{v}^k)\left[-\alpha\boldsymbol{\varepsilon} : (D_k \mathbf{L}^k) : \boldsymbol{\varepsilon} - 2\beta tr(\boldsymbol{\varepsilon}.\boldsymbol{\varepsilon}.\mathbf{D}^k) + 4\beta tr(\boldsymbol{\varepsilon}.\boldsymbol{\gamma}^k.\mathbf{D}^k) - 2\beta tr(\boldsymbol{\gamma}^k.\boldsymbol{\gamma}^k.\mathbf{D}^k)\right] \tag{18}$$

$$\boldsymbol{\sigma} = \frac{\partial w}{\partial \boldsymbol{\varepsilon}} = \lambda(tr\boldsymbol{\varepsilon})\mathbf{1} + 2\mu\boldsymbol{\varepsilon} + g\mathbf{D} + \alpha\left[tr(\boldsymbol{\varepsilon}.\mathbf{D})\mathbf{1} + (tr\boldsymbol{\varepsilon})\mathbf{D}\right] + 2\beta\,(\boldsymbol{\varepsilon}.\mathbf{D} + \mathbf{D}.\boldsymbol{\varepsilon})$$
$$+ \sum_{k=1}^{3} H(-\mathbf{v}^k.\boldsymbol{\varepsilon}.\mathbf{v}^k)\left[-2\alpha D_k (\mathbf{v}^k.\boldsymbol{\varepsilon}.\mathbf{v}^k)(\mathbf{v}^k \otimes \mathbf{v}^k) - 2\beta(\boldsymbol{\varepsilon}.\mathbf{D}^k + \mathbf{D}^k.\boldsymbol{\varepsilon}) + 2\beta(\boldsymbol{\gamma}^k.\mathbf{D}^k + \mathbf{D}^k.\boldsymbol{\gamma}^k)\right] \tag{19}$$

$$\mathbf{F}^D = -\frac{\partial w}{\partial \mathbf{D}} = -g\boldsymbol{\varepsilon} - \alpha(tr\boldsymbol{\varepsilon})\boldsymbol{\varepsilon} - 2\beta(\boldsymbol{\varepsilon}.\boldsymbol{\varepsilon}) + \sum_{k=1}^{3} H(-\mathbf{v}^k.\boldsymbol{\varepsilon}.\mathbf{v}^k)\left[\alpha(\mathbf{v}^k.\boldsymbol{\varepsilon}.\mathbf{v}^k)^2 \mathbf{v}^k \otimes \mathbf{v}^k + 2\beta\mathbf{L}^k : (\boldsymbol{\varepsilon}.\boldsymbol{\varepsilon})\right.$$
$$\left. - 4\beta\mathbf{L}^k : (\boldsymbol{\varepsilon}.\boldsymbol{\gamma}^k) + 2\beta\mathbf{L}^k : (\boldsymbol{\gamma}^k.\boldsymbol{\gamma}^k)\right] \tag{20}$$

As each equivalent set of the normal $\mathbf{v}^k$ is to be considered independently, the corresponding affinity (thermodynamic force) is :

$$\mathbf{F}^{\gamma^k} = -\frac{\partial w}{\partial \boldsymbol{\gamma}^k} = H(-\mathbf{v}^k.\boldsymbol{\varepsilon}.\mathbf{v}^k)\left[-2\beta(\boldsymbol{\varepsilon}.\mathbf{D}^k + \mathbf{D}^k.\boldsymbol{\varepsilon}) + 2\beta(\boldsymbol{\gamma}^k.\mathbf{D}^k + \mathbf{D}^k.\boldsymbol{\gamma}^k)\right] \tag{21}$$

The remark concerning eqn (6), Section 2, stating its validity for a **D**-proportional segment, i.e. for a given configuration of principal direction of **D**, is still in force for eqn (20).

3.2. Sliding criterion and evolution

The model herein considers frictional non-sliding/sliding phenomena on mesocrack lips on a macroscopic scale, by an approach similar to that to damage, notwithstanding the micromechanical background and interpretations of **D** and $\boldsymbol{\gamma}$. So, the Coulomb criterion form, function of the corresponding shear and normal tractions on a crack lip, employed in micromechanical models (Horii and Nemat-Nasser [3], Andrieux et al. [6], Gambarotta and Lagomarsino [7]), is methodologically less suitable in the present context. The pertinent thermodynamic affinity governing frictional sliding on an equivalent system k, (k=1,2,3) is the entity $\mathbf{F}^{\gamma^k}$ defined above as the strain energy release-rate with respect to $\boldsymbol{\gamma}^k$.

The frictional non sliding/sliding complementary law is based on the hypotheses as follows :

(i) The sliding criterion depends explicitly on the norm of the tangential part $\mathbf{F}^{\gamma Tk}$ of the "force" $\mathbf{F}^{\gamma k}$ and on the normal strain $\mathbf{v}^k.\boldsymbol{\varepsilon}.\mathbf{v}^k$ consecutively to the strain-related representation of the energy w and the crack-closure criterion at stake ($\mathbf{v}^k.\boldsymbol{\varepsilon}.\mathbf{v}^k \le 0$).

(ii) Contrarily to inconsistencies relative to the normality rule in the classical Coulomb framework affected by appearance of a normal separating velocity (cf. for example Michalowski and Mroz [17], Curnier [18]) a standard scheme in the space of forces conjugate to $\boldsymbol{\gamma}^k$ keeps physical pertinence. The normality rule appears to relate the frictional sliding rate to the tangential force $\mathbf{F}^{\gamma Tk}$ indicating its leaning to the crack plane (for a $\mathbf{D}^k$-proportional loading segment).

Consequently, the corresponding convex reversibility domain $h^k \le 0$ can be written as

$$h^k\left(\mathbf{F}^{\gamma k}, \mathbf{v}^k.\boldsymbol{\varepsilon}.\mathbf{v}^k\right) = h^k\left(\mathbf{F}^{\gamma k} - \mathbf{F}^{\gamma Nk}, \mathbf{v}^k.\boldsymbol{\varepsilon}.\mathbf{v}^k\right) = \sqrt{\frac{1}{2}\mathrm{tr}\left[\left(\mathbf{F}^{\gamma k} - \mathbf{F}^{\gamma Nk}\right).\left(\mathbf{F}^{\gamma k} - \mathbf{F}^{\gamma Nk}\right)\right]} + \rho\mathbf{v}^k.\boldsymbol{\varepsilon}.\mathbf{v}^k \le 0$$
$$\text{if } \mathbf{v}^k.\boldsymbol{\varepsilon}.\mathbf{v}^k \le 0 \quad (22)$$

where ρ is a material constant, a strain-related friction coefficient in the space $(\mathbf{F}^{\gamma k}, \boldsymbol{\varepsilon})$ and

$$\mathbf{F}^{\gamma k} = \mathbf{F}^{\gamma Tk} + \mathbf{F}^{\gamma Nk} \quad ; \quad \mathbf{F}^{\gamma Tk} = \mathbf{F}^{\gamma k} - (\mathbf{v}^k.\mathbf{F}^{\gamma k}.\mathbf{v}^k)\,\mathbf{v}^k \otimes \mathbf{v}^k$$
$$\mathbf{F}^{\gamma Nk} = (\mathbf{v}^k.\mathbf{F}^{\gamma k}.\mathbf{v}^k)\,\mathbf{v}^k \otimes \mathbf{v}^k \quad (23)$$

The normality rule for $\dot{\boldsymbol{\gamma}}^k$ is then

$$\dot{\boldsymbol{\gamma}}^k = \Lambda_\gamma^k \frac{\partial h^k\left(\mathbf{F}^{\gamma k} - \mathbf{F}^{\gamma Nk}, \mathbf{v}^k.\boldsymbol{\varepsilon}.\mathbf{v}^k\right)}{\partial \mathbf{F}^{\gamma k}} = \begin{cases} 0 & \text{if } h^k < 0 \text{ or } h^k = 0,\ \dot{h}^k < 0 \\ \Lambda_\gamma^k \dfrac{\mathbf{F}^{\gamma Tk}}{\sqrt{2\mathrm{tr}\left(\mathbf{F}^{\gamma Tk}.\mathbf{F}^{\gamma Tk}\right)}} & \text{if } h^k = 0 \text{ and } \dot{h}^k = 0,\ \Lambda_\gamma^k \ge 0 \end{cases} \quad (24)$$

Detailed comments on salient aspects of the criterion $h^k = 0$ in the strain space are given by Halm and Dragon [16]. Figure 1 shows the corresponding form together with a hardening-like phenomenon (for $\boldsymbol{\gamma}^k \neq 0$) in reduced stress space $(\sigma_{33}, \sigma_{13})$. The similitude between the actual yield surface and the Coulomb one can be clearly noticed. In connection with the crack opening/closure condition (a single crack system $D_3 \neq 0$ is considered for illustration) the cone $h^k = 0$ is shifted to the left : it corresponds to negative value of σ_{33} at the closure point. The correspondence of (22) with the Coulomb locus can be pointed out furthermore when comparing ρ with the conventional Coulomb coefficient ρ_c. For the stress and sliding configuration depicted in Fig. 1, the Coulomb locus is $|\sigma_{13}| + \rho_c\sigma_{33} = 0$ and

$$\rho_c = \frac{\rho\mu}{|\beta| D_3 A} \qquad \text{with} \qquad A = \lambda(1 - 2\nu) + 2\mu - 2\alpha\nu D_3 \quad (25)$$

By examining the complete set (18)-(24) of the equations of the model, one can see that the frictional sliding does not sweep away the relative simplicity of the enlarged model (see the end of Section 2). Only one additional constant ρ adds to eight material constants $(\lambda,\mu,\alpha,\beta,C_o,C_1,g,B)$. It can be stressed that ρ (as ρ_c above) governs the slope of the cone in Fig. 1, an example illustrating the general form (22). However, ρ is not here the unique slope-governing factor. In the example considered the slope is inversely proportional to D_3 thus implying that a higher crack density is favouring sliding amount.

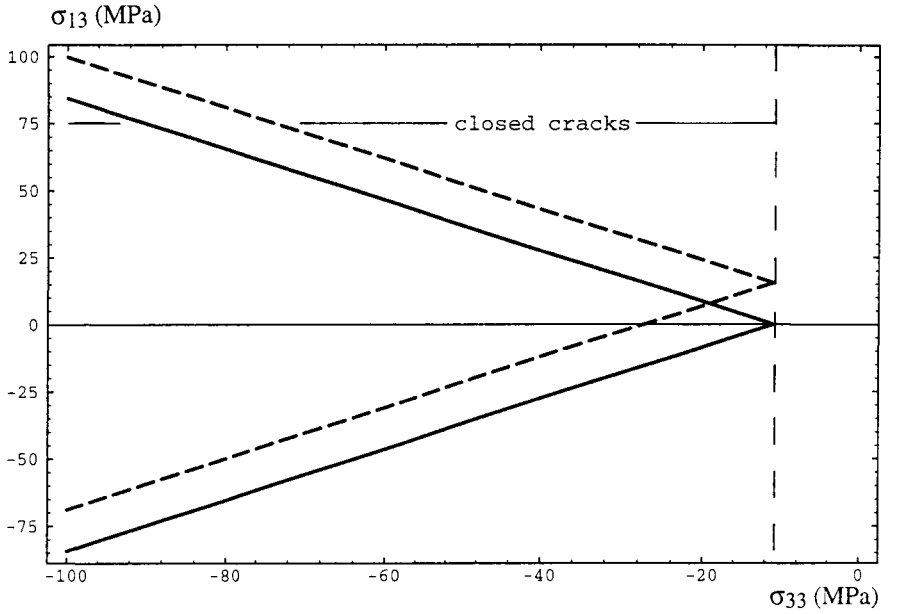

Figure 1. Frictional sliding criterion and the relative sliding-induced hardening mechanism in the reduced stress-space (σ_{33}, σ_{13}).

4. DAMAGE AND FRICTIONAL SLIDING INTERACTION. FULLY COUPLED MODEL

The model completed in Section 3 incorporating friction-induced blocking and sliding on equivalent mesocrack-sets is valid for a given ('freezed') damage state or for conservative damage evolution ($\mathbf{D}^k$-proportional loading paths). It has proved conclusive in representing multistage loading-and-unloading dissipative cycles due to blocking-and-sliding sequences, see Halm and Dragon [16] for illustrations. In particular a dissipative unloading blocking-and-sliding sequence could be obtained while for the same stress-strain cycle the frictionless model of Section 2 gave purely elastic unloading.

The splitting-like damage kinetics considered in Section 2 is approximately valid for closed sliding mesocracks even when some branching occurs see for example Horii and Nemat-Nasser [19] for some experimental insight. This type of kinetics will be still considered as the predominant mechanism furthest for $\mathbf{D}^k$-non-proportional loading. This means the complementary damage law (7)-(8) being reconducted for more complex stress-strain paths involving varying $\mathbf{D}^k$ orientations. However, as the frictional blocking-and-sliding is inevitably affecting the stress-strain response, so f.ex. the stress threshold corresponding to damage criterion f=0 is subsequently affected. For example in the stress subspace analogous to that of Fig. 1, the frontier f=0 corresponding to closed cracks under frictional blocking/sliding is farther beyond the limit for frictionless cracks, see e.g. Fig. 9 in [16].

This is mostly the sliding complementary rule (22)-(24) which needs to be perfected to describe fairly the $\mathbf{D}^k$-non-proportional loading paths. If the principal axes of $\mathbf{D}^k$ rotate the orthogonality $\boldsymbol{\gamma}^k : \mathbf{D}^k=0$ is no longer true and discontinuities may arise, especially for crack closure-opening transition. So, an enhanced form of $h^k \leq 0$ needs to account for the $\mathbf{D}^k$-axes

rotation. The form (22), depending on $\mathbf{F}^{\gamma Tk}$, produced – via normality rule (24) – sliding $\dot{\boldsymbol{\gamma}}^k$ *in* the mesocrack plane. A judicious modification of this basic assumption should be compatible with sliding and damage departure from the actual mesocrack equivalent plane. This is achieved by means of the following partition of $\mathbf{F}^{\gamma k}$, given below for a single crack set of normal $\mathbf{v}^k$:

$$\begin{aligned}\mathbf{F}^{\gamma k} = \mathbf{F}^{\gamma Tk} + \mathbf{F}^{\gamma Nk} &= \underbrace{\mathbf{F}^{\gamma Tk} + 4\beta(\boldsymbol{\gamma}^k : \mathbf{D}^k)\mathbf{v}^k \otimes \mathbf{v}^k} - 4\beta(\boldsymbol{\varepsilon} : \mathbf{D}^k)\,\mathbf{v}^k \otimes \mathbf{v}^k \\ &= \qquad \mathbf{F}^k \qquad\quad - 4\beta(\boldsymbol{\varepsilon} : \mathbf{D}^k)\,\mathbf{v}^k \otimes \mathbf{v}^k\end{aligned} \tag{26}$$

$\mathbf{F}^k$ is the appropriate part of $\mathbf{F}^{\gamma k}$ to enter the more general expression of $h^k \le 0$ suitable for the model including $\mathbf{D}^k$-axes rotation. First, one obtains that for $\mathbf{D}^k$-proportional loading $\mathbf{F}^k$ reduces to $\mathbf{F}^{\gamma Tk}$ (as $\boldsymbol{\gamma}^k : \mathbf{D}^k = 0$) and the new representation h^k ($\mathbf{F}^k$, $\mathbf{v}^k.\boldsymbol{\varepsilon}.\mathbf{v}^k$) reduces to (22). Secondly, the above-mentioned, crucial stress continuity problem is effectively dealt with. In fact, comparing (14),(21),(23),(26), one can see that the closure-opening transition point for sliding crack-set can be alternatively defined as

$$\mathbf{F}^k = \mathbf{F}^{\gamma k} = \mathbf{0} \qquad \Leftrightarrow \qquad \boldsymbol{\varepsilon}.\mathbf{D}^k + \mathbf{D}^k.\boldsymbol{\varepsilon} = \boldsymbol{\gamma}^k.\mathbf{D}^k + \mathbf{D}^k.\boldsymbol{\gamma}^k \tag{27}$$

Despite the fact that the above equation represents weaker condition than (14), it allows to verify the singularity requirement for [[C*]] (cf. Section 3.1) leading to the stress continuity.

It can be remarked that though $\boldsymbol{\gamma}^k:\mathbf{D}^k \neq 0$ as equivalent crack-axes rotate no additional invariants are necessary in the strain energy expression (18). This is not required by the continuity considerations (see above) and it brings neither significant information. For example, introducing tr $\boldsymbol{\varepsilon}$ tr ($\boldsymbol{\gamma}^k.\mathbf{D}^k$), tr $\boldsymbol{\gamma}^k$ ($\boldsymbol{\gamma}^k.\mathbf{D}^k$) and $\boldsymbol{\gamma}^k : \mathrm{D}_k\,\mathbf{L}^k : \boldsymbol{\gamma}^k$ does not convey more record on shear moduli degradation than existing invariants tr ($\boldsymbol{\varepsilon}.\boldsymbol{\gamma}^k.\mathbf{D}^k$) and tr ($\boldsymbol{\gamma}^k.\boldsymbol{\gamma}^k.\mathbf{D}^k$).

The above considerations lead to the following improved expression for the sliding complementary rule :

$$h^k(\mathbf{F}^k, \mathbf{v}^k.\boldsymbol{\varepsilon}.\mathbf{v}^k) = \sqrt{\frac{1}{2}\mathrm{tr}(\mathbf{F}^k.\mathbf{F}^k)} + \rho\mathbf{v}^k.\boldsymbol{\varepsilon}.\mathbf{v}^k \le 0 \tag{28}$$

$$\dot{\boldsymbol{\gamma}}^k = \Lambda_\gamma^k \frac{\partial h(\mathbf{F}^k, \mathbf{v}^k.\boldsymbol{\varepsilon}.\mathbf{v}^k)}{\partial \mathbf{F}^{\gamma k}} = \begin{cases} \mathbf{0} & \text{if } h^k < 0 \text{ or } h^k = 0\,,\ \dot{h}^k < 0 \\ \Lambda_\gamma^k \dfrac{\mathbf{F}^k}{\sqrt{2\mathrm{tr}(\mathbf{F}^k.\mathbf{F}^k)}} & \text{if } h^k = 0 \text{ and } \dot{h}^k = 0\,,\ \Lambda_\gamma^k \ge 0 \end{cases} \tag{29}$$

The direction of $\dot{\boldsymbol{\gamma}}^k$ is thus allowed to leave the equivalent crack-set plane consecutively to the rotation of the latter. In such a manner $\mathbf{D}^k$-non-proportional loading can be followed by the model which takes into account the interaction of the two dissipative mechanisms : damage and frictional sliding. The corresponding combined dissipation is

$$\mathcal{D} = \mathbf{F}^D : \dot{\mathbf{D}} + \sum_{k=1}^{3} \mathbf{F}^{\gamma k} : \dot{\boldsymbol{\gamma}}^k \tag{30}$$

Despite of the corresponding normality rules, i.e. the formulae (8) and (29) respectively for damage growth and frictional sliding, and the convexity characterizing the domains $f \le 0$ and $h \le 0$ one should check the non-negativity of $\mathcal{D}$ in the process of numerical integration. This is because of the partition of the respective thermodynamic forces, i.e. the sole parts $\mathbf{F}^D$–$\mathbf{F}^{D2}$–$\mathbf{F}^{D1}$ and $\mathbf{F}^{\gamma k} - \left[-4\beta\,(\boldsymbol{\varepsilon} : \mathbf{D}^k)\,\mathbf{v}^k \otimes \mathbf{v}^k\right]$ entering respectively into the corresponding damage and

sliding-yield functions. The convex domains at stake should contain their origin respectively in the $\mathbf{F}^D$- space and in $\mathbf{F}^{\gamma k}$-space to ensure thermodynamically admissible evolutions (one can note in this point some analogy with the kinematic hardening rule in classical plasticity). In this respect the algorithmic approximation of the coupled model should control the dissipation issue for each step and integration point. The incremental procedure leading to numerical integration of the equations of the model can be summarized as follows :

(i) It can be performed in the standard strain discretization for the loading path under finite consideration ; at time t^n the set $\boldsymbol{\varepsilon}^n$, $\boldsymbol{\sigma}^n$, $\mathbf{D}^n$, $\boldsymbol{\gamma}^{kn}$ is known.

(ii) For each damage equivalent system, the normal strain $\mathbf{v}^k.\boldsymbol{\varepsilon}.\mathbf{v}^k$ is checked.

(iii) If $\mathbf{v}^k.\boldsymbol{\varepsilon}.\mathbf{v}^k > 0$ (open crack-set), $\boldsymbol{\gamma}^k$ vanishes and if $f = 0$, the increment of $\mathbf{D}$ is calculated from the discretized form of (8).

(iv) If $\mathbf{v}^k.\boldsymbol{\varepsilon}.\mathbf{v}^k \leq 0$ (closed crack-set), both criteria $f \leq 0$, $h^k \leq 0$ are checked ; the increments $\Delta\boldsymbol{\gamma}^k$ and $\Delta\mathbf{D}$ are simultaneously calculated from (8) and (29).

(v) The integration of the two evolution rules above is performed by an implicit algorithm whose numerical stability is well confirmed. Moreover the implicit procedure has been found particularly advantageous for a large class of damage models (Cormery, [20]) as being naturally compatible with their constitutive formulation. In the present model one can notice the low numerical coupling degree between $\boldsymbol{\gamma}^k$ and $\mathbf{D}$: $\mathbf{D}^n$ is obtained, independently of $\boldsymbol{\gamma}^{kn}$, by a simple "naturally implicit" algorithmic approximation of (8). Once $\mathbf{D}^n$ is calculated, $\boldsymbol{\gamma}^{kn}$ is determined by iterative procedure from (29).

For completeness, the coupled rate-independent anisotropic damage-frictional sliding constitutive equations are summarized in Table 1.

Table 1
Rate-independent anisotropic damage-frictional coupled model

Free energy : (per unit volume)

$$w(\boldsymbol{\varepsilon};\mathbf{D},\boldsymbol{\gamma}) = \frac{1}{2}\lambda(\mathrm{tr}\boldsymbol{\varepsilon})^2 + \mu\,\mathrm{tr}\,(\boldsymbol{\varepsilon}.\boldsymbol{\varepsilon}) + g\,\mathrm{tr}(\boldsymbol{\varepsilon}.\mathbf{D}) + \alpha\,\mathrm{tr}\boldsymbol{\varepsilon}\,\mathrm{tr}(\boldsymbol{\varepsilon}.\mathbf{D}) + 2\beta\,\mathrm{tr}(\boldsymbol{\varepsilon}.\boldsymbol{\varepsilon}.\mathbf{D})$$
$$+ \sum_{k=1}^{3} H(-\mathbf{v}^k.\boldsymbol{\varepsilon}.\mathbf{v}^k)\Big[-\alpha\boldsymbol{\varepsilon} : (D_k\mathbf{L}^k) : \boldsymbol{\varepsilon} - 2\beta\mathrm{tr}(\boldsymbol{\varepsilon}.\boldsymbol{\varepsilon}.\mathbf{D}^k) + 4\beta\mathrm{tr}(\boldsymbol{\varepsilon}.\boldsymbol{\gamma}^k.\mathbf{D}^k)$$
$$- 2\beta\,\mathrm{tr}(\boldsymbol{\gamma}^k.\boldsymbol{\gamma}^k.\mathbf{D}^k)\Big]$$

Stress-strain and internal variable relations :

$$\boldsymbol{\sigma} = \frac{\partial w}{\partial \boldsymbol{\varepsilon}}, \text{ see (19)} \; ; \; \mathbf{F}_D = -\frac{\partial w}{\partial \mathbf{D}}, \text{ see (20)} \; ; \; \mathbf{F}^{\gamma k} = -\frac{\partial w}{\partial \boldsymbol{\gamma}^k}, \text{ see (21)}$$

for details

Damage complementary rule :

$$f(\mathbf{F}^D - \mathbf{F}^{D2} - \mathbf{F}^{D1}, \mathbf{D}) \leq 0 \quad , \text{ see (7) for details}$$

$$\dot{\mathbf{D}} = \Lambda_D \frac{\partial f}{\partial \mathbf{F}^D} = \Lambda_D \left[\frac{\boldsymbol{\varepsilon}^+}{\sqrt{2\mathrm{tr}(\boldsymbol{\varepsilon}^+.\boldsymbol{\varepsilon}^+)}} + B\mathbf{D} \right] \quad , \quad \Lambda_D \geq 0$$

$\mathbf{D}$-consistency :

$$\dot{f}\,\Lambda_D = 0$$

Frictional sliding related plasticity :

$$h^k(\mathbf{F}^k, \mathbf{v}^k.\boldsymbol{\varepsilon}.\mathbf{v}^k) = \sqrt{\frac{1}{2}\mathrm{tr}(\mathbf{F}^k.\mathbf{F}^k)} + \rho\,\mathbf{v}.\boldsymbol{\varepsilon}.\mathbf{v}^k \leq 0, \text{ see (23), (26)}$$

for detailed form of $\mathbf{F}^k$

$$\dot{\boldsymbol{\gamma}}^k = \Lambda_\gamma^k \frac{\partial h^k}{\partial \mathbf{F}^{\gamma k}} = \Lambda_\gamma^k \frac{\mathbf{F}^k}{\sqrt{2\mathrm{tr}(\mathbf{F}^k.\mathbf{F}^k)}} \quad , \quad \Lambda_\gamma^k \geq 0$$

$\boldsymbol{\gamma}^k$-consistency :

$$\dot{h}^k \Lambda_\gamma^k = 0$$

5. APPLICATION : ROCK-LIKE SOLIDS

To illustrate the model pertinency two selected numerical examples are provided below. They are concerned with brittle rock behaviour and examine the effect of loading involving necessarily the closed mesocrack related phenomena thus bringing forward the efficiency of the fully coupled model.

The first example is the analysis of a homogeneous stress-strain path relative to the third step of the complex loading programme as follows :

- Step 1 : Uniaxial tension, $\sigma_3 > 0$, induces damage $D_3 > 0$ (a set of parallel mesocracks of normal 3).
- Step 2 : Unloading then reloading under compression beyond the crack closure threshold are considered. The corresponding numerical simulation is strain-controlled ; $\varepsilon_{33} < \varepsilon_{11} = \varepsilon_{22}$.
- Step 3 : Upon a given (freezed) configuration (ε_{33},$\varepsilon_{11} = \varepsilon_{22}$) corresponding to mesocracks closure is superposed additional shear strain-controlled loading : $\varepsilon_{13} = \varepsilon_{23}$ and subsequent unloading. Three loading-unloading cycles are simulated. In Figure 2 the corresponding σ_{13}vs ε_{13} loading and unloading curves are plotted. Damage growth, accompanied with principal **D**-axes rotation is calculated for each loading cycle. Friction blocking or sliding effects are accounted for.

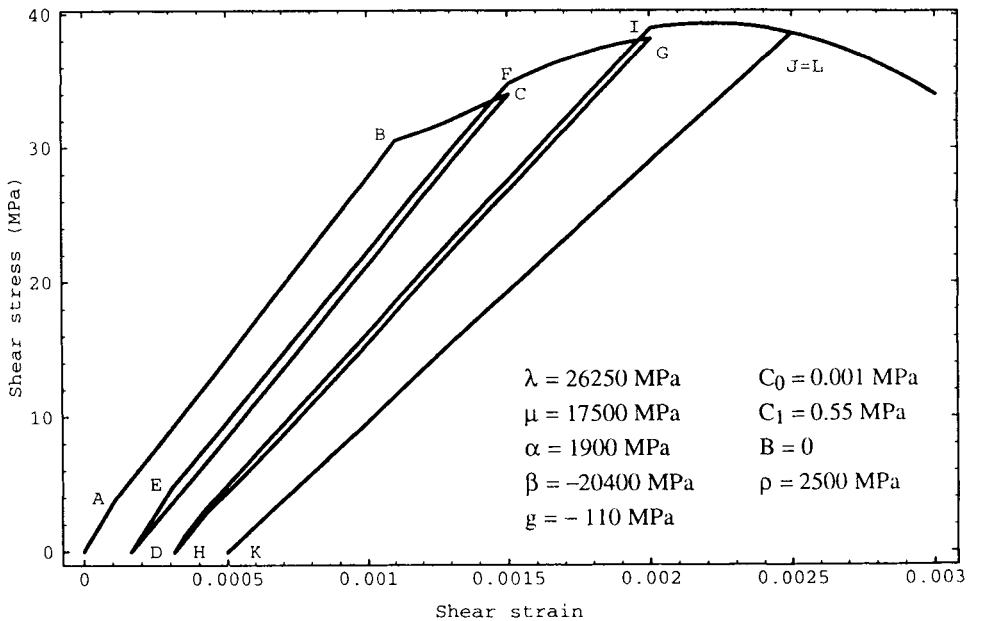

Figure 2. Shear stress (σ_{13})-shear strain (ε_{13}) loading and unloading cycles corresponding to damage and frictional sliding variations. Non-proportional damage growth is simulated preceded by an initial tension-induced damage ($D_3 > 0$) and subsequent compression-induced crack closure. Complex hysteresis for the two incipient cycles (A-B-C-D-E-F and F-G-H-I) is followed by purely elastic unloading and loading (J-K-L ; J=L).

The initial stiffened portion O-A is due to friction-induced blocking effect corresponding to recovery of the solid elastic shear modulus μ. Beyond A frictional sliding is evolving, the slope of the portion A-B is lower than the slope 0-A. From B to C damage growth accompanied with frictional sliding occurs. The loading path at stake is a **D**-non-proportional one ; there is some rotation of equivalent crack-axes and a complex damage state is brought about. The C-D portion represents slightly non-linear unloading curve. In fact this is a multiform unloading process with successive sliding sequences : blocking on one equivalent set, two remaining sets open, followed by closure of a second one and frictional sliding on one then two sets, etc. The non-linearity of C-D is hardly visible on the graphic representation. The segment D-E represents again (as OA) a blocking stage followed by sliding E-F, damage F-G, etc. For the third cycle a purely elastic unloading J-K and loading K-L (L=J) are noticed. This kind of elastic shakedown should be further analysed and compared to reliable experimental data, [21]. Here, the simulated curve σ_{13}vs.ε_{13} is presented to illustrate the capacity of the model to deal with multiple stage loading/unloading loops involving, eventually coupled damage-and-sliding effects. The material under consideration is Fontainebleau sandstone.

The second example refers to experimental tests by Pecqueur [13] consisting in a torsional loading applied to hollow cylinder specimens under hydrostatic compression. The cylinder is cut in a brittle rock (Vosges sandstone). In fact, the torque vs. angular deformation curve plotted in Figure 3 (solid line) concerns the central, quasi-homogeneous part with respect to stress-strain distribution. The corresponding calculations concern a pre-damaged material with a set of mesocracks perpendicular to the cylinder axis in compression-induced closure range. Again, an initial stiffened portion is observed corresponding to friction-related blocking phenomenon (stage I). It is followed by stage II where frictional sliding evolution is noticed. This explains the reduced slope observed in Figure 2, the solid line leaning closely to the experimental one. Finally, for stage III, the simultaneous complex damage growth and sliding take place and the slope becomes even smaller. The calculated coupled damage growth and sliding effect is somewhat larger than experimentally observed but the overall agreement is quite satisfactory for the coupled damage and sliding model. The same simulation (with the same initial damage level and configuration) has been carried out for the sole anisotropic damage (frictionless) model of Section 2. The curves clearly indicate that the hypothesis of perfectly lubricated cracks underestimates the torque value whereas friction stiffens the material and predicts a behaviour closer to experiment. Note also that the drop (stage III) is much more pronounced for the frictionless model.

6. CONCLUDING REMARKS

Some of the basic issues concerning inelastic behaviour of brittle materials like rocks and concrete have been presented and explored in the framework of rate-type constitute theory with internal variables. In fact, inelasticity in such materials results from the evolution of a large number of internal (micro-)and/or mesocracks accompanied with microscopic frictional effects, volumetric dilatancy and strong pressure sensitivity. The corresponding continuum damage models attempting to capture the progressive degradation of mechanical properties attributable to evolution of multiple defects and accounting for irreversible frictional sliding over the internal crack surfaces are referred to the extended framework of damage-elastoplastic constitutive theory including the classical rate theory of elastoplastic deformation of crystalline materials as well as the non-linear theories of progressively mesofracturing solids. Such a global vision of non-linear mechanics of materials has been recently postulated by Lubarda and Krajcinovic [22].

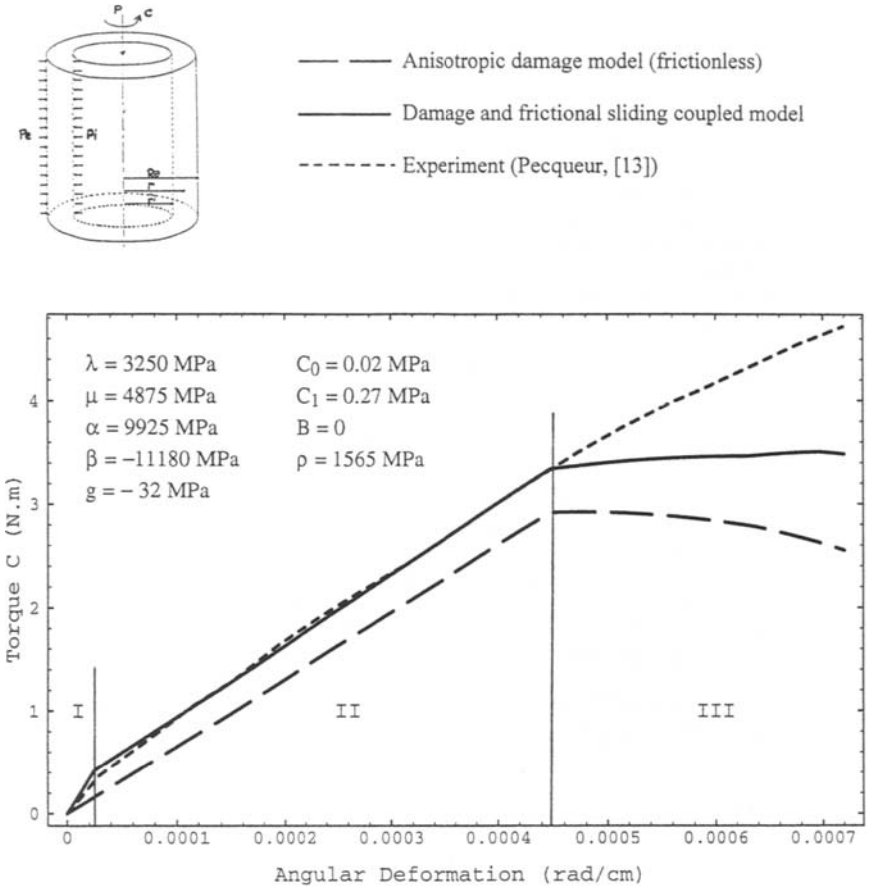

I : crack blocking, shear moduli recovery.
II : frictional sliding on crack lips (weakened shear moduli).
III : frictional sliding + damage growth.

Figure 3. Torsional load versus angular deformation response for hollow cylinder example. The solid line gives the homogeneous response of the model when both damage and frictional blocking/sliding (for closed mesocracks) are taken into account. It appears fairly close to experimental response (Pecqueur, [13]). The latter effectively happens to be homogeneous in the central third.

The model presented here provides a realistic description of anisotropic damage evolution by multiple mesocrack-growth and of irreversible frictional sliding-related plasticity. It constitutes an efficient instrument for structural analysis due to its relative simplicity (a small number of material parameters to identify) and its modular character allowing to treat engineering problems at various level of complexity. The first, basic level concerns modelling the anisotropic degradation by mesocrack growth, Dragon et al. [9]. The second level consists in accounting for the normal moduli recovery with respect to equivalent mesocrack-sets (Section 2 herein). Some cyclic and pressure overloading phenomena can be well approximated by this version, see Halm and Dragon [1]. The damage and frictional blocking/sliding coupled model proposed above allows to treat complex loading paths with rotating loading and damage axes (torsional loading for example). Some successful structural analysis applications including three-dimensional detection of damage localization have been performed by employing the basic version. Further study concerns enhanced integration of pre-existing and/or 'virtual' damage phenomena susceptible to emerge on the mesoscale of a material at early stages of loading and thus to affect strongly its further resistance to failure.

REFERENCES

1. D. Halm and A. Dragon, Int. J. Damage Mech., 5 (1996) 384.
2. M. Kachanov, Mech. Mat., 1 (1982) 19.
3. H. Horii and S. Nemat-Nasser, J. Mech. Phys. Solids, 31 (1983) 151.
4. J. Ju, Int. J. Solids Structures, 27 (1991) 227.
5. D. Krajcinovic, M. Basista, D. Sumarac, in Damage Mechanics of Composite Materials, R. Talreja (editor), 1-51, Elsevier, Amsterdam, 1994.
6. S. Andrieux, Y. Bamberger and J.J. Marigo, J. Mécanique Théorique et Appl., 5 (1986) 471.
7. L. Gambarotta and S. Lagomarsino, Int. J. Solids Structures, 30 (1993) 177.
8. C. Fond and Y. Berthaud, Int. J. Fracture, 74 (1995), 1.
9. A. Dragon, F. Cormery, T. Désoyer and D. Halm, in Localization and Bifurcation Theory for Soils and Rocks, R. Chambon et al. (eds), 127-140, Balkema, Rotterdam, 1994.
10. M. Kachanov, Appl. Mech. Rev., 45 (1992) 304.
11. S. Govindjee, G.J. Kay, J.C. Simo, Int. J. Num. Meth. Engng., 38 (1995) 3611.
12. A. Dragon and D. Halm, in Engineering Mechanics (Proc. ASCE 10th Conference), S. Sture (editor), Vol. 2, 702-705, ASCE, New York, 1995.
13. G. Pecqueur, PhD thesis, Lille Univ., 1995.
14. Z. Wesolowski, Arch. Mech., 4 (1969), 449.
15. A. Curnier, Q. He and P. Zysset, J. Elasticity, 37 (1995), 1.
16. D. Halm and A. Dragon, European J. Mechanics A/Solids, (1997) to appear.
17. R. Michalowski and Z. Mroz, Arch. Mech., 30 (1978) 259.
18. A. Curnier, Int. J. Solids Structures, 20 (1984) 637.
19. H. Horii and S. Nemat-Nasser, J. Geophys. Res., 90B4 (1985) 3105.
20. F. Cormery, PhD thesis, Poitiers Univ., 1994.
21. A. Dragon and D. Halm, forthcoming.
22. V.A. Lubarda and D. Krajcinovic, Int. J. Plasticity, 11 (1995) 763.

Damage Mechanics in Engineering Materials
G.Z. Voyiadjis, J.-W.W. Ju and J.-L. Chaboche (Editors)
© 1998 Elsevier Science B.V. All rights reserved.

Anisotropic damage model for the triaxial creep behaviour of plain concrete

E. Papa and A. Taliercio

Department of Structural Engineering, Politecnico di Milano
Piazza Leonardo da Vinci 32, 20133 Milan, Italy

A viscoplastic model with damage was developed to describe the mechanical behaviour of plain concrete subjected to sustained multiaxial stresses of high intensity. The model is characterized by inelastic strains due to plasticity and damage and by a second-order damage tensor. The evolution laws for these variables are formulated by extending the proposal of other authors for metals and rocksalt. The procedure to obtain the main model parameters from experiments is also outlined. The reliability of the model was assessed through comparisons with available test results.

1. INTRODUCTION

The present work is originated by an extensive experimental research program carried out at the Department of Structural Engineering of Milan Technical University (Politecnico). This program investigates the behaviour of plain concrete subjected to high sustained triaxial loading, either cyclic or constant in time. Concrete cylinders were tested in a triaxial cell, in which axial load and lateral pressure could be independently varied; further details on the testing apparatus can be found in [1]. The research aimed at obtaining a better understanding of the complex phenomena that take place in concrete at high stress levels, in view of more rationally exploiting the properties of concrete and its possible application within a broader range of stresses.

The main results of the research (reported in [2-4]) can be summarized as follows: (a) at high stress levels, creep effects, associated with the maximum stress attained during cycles, dominate over dynamic effects, provided that the cycle amplitude does not exceed about 30% of the maximum stress; (b) if the cycle amplitude is a given fraction of the static triaxial strength at different values of the confining pressure, fatigue life is positively affected by an increase in lateral confinement only if the hydrostatic stress does not exceed a certain level [4]; (c) the decrease in stiffness (i.e., the material damage) is mostly affected by the maximum deviatoric stress attained during the pre-loading phase that precedes the cyclic or creep test [3]; (d) damage evolves significantly only during the tertiary creep stage [3]; (e) specimens submitted to triaxial tests that do not fail within a maximum prescribed time, experience a *decrease* in strength if they are reloaded to failure in uniaxial compression: the decrease is as more important as higher the previously applied lateral confinement was [2]; (f) specimens submitted to uni- and triaxial tests that do not fail within a maximum prescribed time, experience an *increase* in strength if they are reloaded to failure with the same confinement

previously applied: the increase is as more important as higher the applied lateral confinement was and can even attain 30÷35% of the static strength of the virgin specimens.

The description of the above phenomena requires having mathematical models available, capable of accounting for the material damage, the damage-induced creep acceleration and, possibly, the evolution of the elastic and the failure domain of the material resulting from creep. No model was found in the literature specifically formulated to describe the triaxial creep behaviour of concrete at high stress levels. Indeed, a number of (elastic-) viscoplastic models exists, conceived for relatively homogeneous materials such as metals, rocksalt and clay. A reason for this is that for metals the problem arises of creep failure at elevated temperature, whereas thermally-induced creep strains can be the origin of local failures in underground waste isolation deposits excavated in rock salt. Additionally, some models for clay exist capable of describing the evolution of the elastic domain of the material following creep. In a preliminary work [5] the problem was tackled of assessing whether these models can be applied to concrete the heterogeneous nature of which is likely to be associated with damage phenomena different from crystalline materials. It was concluded that, from a phenomenological point of view, the same evolution laws that govern the evolution of creep-induced damage in metals and rocksalt are appropriate to concrete and that similarities exist between creep-induced "hardening" in clay and concrete. A model capable of simultaneously accounting for creep strains, damage variable(s) and an evolving elastic domain, however, is presently missing.

The model presented in this work is a viscoplastic model with damage, obtained as an extension of the model proposed by the authors for static and cyclic loads [6,7]. The model is featured by two second-order damage tensors, representative of surface damage induced by tensile and compressive strains. A viscoplastic potential is introduced in order to obtain the evolution laws for damage and permanent strains. These strains are considered as the sum of inelastic strains due to plasticity and inelastic strains due to damage.

A discussion about the identification of the model parameters is presented in the last Sections of the paper, where some comparisons with available experimental results are also depicted. These results confirm the reliability of the presented model.

2. THE MODEL PROPOSED: THEORETICAL DEVELOPMENTS

The model proposed by the authors in [6,7] for quasi-static loading is able to reproduce the *unilateral behaviour* of concrete; this expression indicates the fact that, during loads histories involving changes in sign of the applied stress, the loss in stiffness associated with cracks opened in tension is recovered when cracks close after the stress has turned to compression [e.g. 8]. Accordingly, two *independent* damage tensors were introduced, ω^T, ω^C, which account for damage induced by tensile and compressive strains, respectively. Since further treatments will cover triaxial compression tests, volumetric damage will be assumed to be negligible in loading conditions where all principal stresses are compressive.

Allowing for unilaterality, the following expressions is proposed for the Helmoltz free energy of the material:

$$\rho\psi^{el} = \frac{3}{2}(k_0 - 2G_0)tr^2\mathbf{e} + G_0 tr\left[(1-\omega^T)^{1/2}\cdot\mathbf{e}^T\cdot(1-\omega^T)^{1/2}\cdot\mathbf{e}^T\right] + G_0 tr\left[(1-\omega^C)^{1/2}\cdot\mathbf{e}^C\cdot(1-\omega^C)^{1/2}\cdot\mathbf{e}^C\right] \quad (1)$$

$\mathbf{e}^T$ (resp. $\mathbf{e}^C$) must be intended as the tensor having the same positive (resp. negative) eigenvalues as the elastic strain tensor $\mathbf{e}$, and vanishing possible other eigenvalues. k_0 and G_0 are the bulk and shear modulus respectively of the undamaged material.

Derivation of eq. (1) respect to $\mathbf{e}$ gives the stress-strain relationship:

$$\sigma = \left[(k_0 - 2G_0)tr(\mathbf{e})\right]\mathbf{1} + 2G_0[(1-\omega^T)^{1/2}\cdot\mathbf{e}^T\cdot(1-\omega^T)^{1/2}] + 2G_0[(1-\omega^C)^{1/2}\cdot\mathbf{e}^C\cdot(1-\omega^C)^{1/2}] \quad (2)$$

Derivation of eq. (1) with respect to the damage variables yields the damage driving forces conjugate to ω^T and ω^C:

$$\mathbf{Y}^T = -\frac{\partial(\rho\psi^{el})}{\partial\omega^T} = G_0\mathbf{e}^T\cdot\mathbf{e}^T; \qquad \mathbf{Y}^C = -\frac{\partial(\rho\psi^{el})}{\partial\omega^C} = G_0\mathbf{e}^C\cdot\mathbf{e}^C; \quad (3a,b)$$

Note that tensors $\mathbf{Y}^T$ and $\mathbf{Y}^C$ have the same principal directions as $\mathbf{e}$: accordingly, both ω^T and ω^C also have the same principal directions.

Once that the intensive variables conjugated to the extensive ones have been defined through a suitable thermodynamic potential, the evolution laws for the state variables must be introduced. When damageable materials are dealt with, it is customary to substitute nominal stresses with "effective stresses", which are increased respect to the nominal ones to allow for the reduction in load-carrying material section [9]. Here, the effective stress tensor $\hat{\sigma}$ is defined as the tensor having $\hat{\sigma}_\alpha = \sigma_\alpha / (1-\omega_\alpha^{II})$ as eigenvalues, meaning that $\omega_\alpha^{II} = \omega_\alpha^C$ if the corresponding principal elastic strain is compressive, whereas $\omega_\alpha^{II} = \omega_\alpha^T$ if such strain is tensile.

For the description of the inelastic response of the material, several authors showed that the theory of viscoplasticity with mixed hardening is able to reproduce the creep behaviour of metals and rocksalt [9,10]. Supposing to apply this theory to concrete, the following viscoplastic potential Ω_p is introduced:

$$\Omega_p = A_0\frac{K}{N+1}\left\langle\frac{\hat{X}_{eq} - R}{K}\right\rangle^{N+1} \quad (4)$$

with

$$\hat{X}_{eq} = \sqrt{\frac{3}{2}}\left\|\hat{\mathbf{S}} - \mathbf{B}\right\|. \quad (5)$$

$\hat{\mathbf{S}}$ is the deviator of the effective stress tensor $\hat{\sigma}$, defined as

$$\hat{\mathbf{S}} = \hat{\sigma} - \frac{1}{3}tr(\hat{\sigma})\mathbf{1}. \quad (6)$$

B is the tensor of the kinematic hardening variables (backstress tensor); R is the isotropic hardening scalar variable; K is a normalizing stress variable (dragstress); A_0 and N are material constants. The evolution laws for **B**, R and K will be described later.

Derivation of the potential with respect to the stress tensor yields the plastic strain rate:

$$\dot{\varepsilon}^p = \frac{\partial \Omega_p}{\partial \sigma} = \frac{3}{2} A_0 \left\langle \frac{\hat{X}_{eq} - R}{K} \right\rangle^N \frac{\hat{S} - B}{\hat{X}_{eq}} \tag{7}$$

The plastic strains (7) are not sufficient to characterize the creep behaviour of concrete subjected to high stresses. Indeed, if creep tests with unloading-reloading cycles are performed, the linear domain is found to expand. If the time at constant stress is sufficiently long, the stress point can re-enter the linear domain, although creep strains do not stabilize as eq. (7) would predict (see Fig. 1). Consequently, the total inelastic strain rate is considered as sum of two contributions:

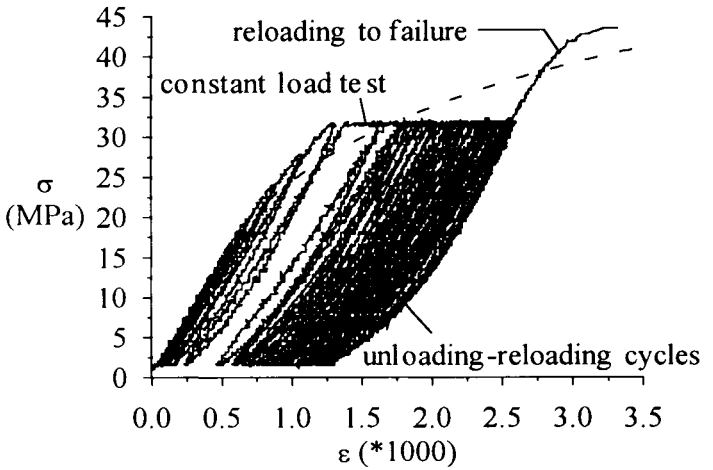

Figure 1 - Uniaxial creep test at 90% of ultimate strength with unloading and reloading cycles. The dashed line represents the boundary of the linear field.

$$\dot{\varepsilon}^i = \dot{\varepsilon}^p + \dot{\varepsilon}^d \tag{8}$$

The second term, $\dot{\varepsilon}^d$, is considered to be associated with damage, according to the proposal of Herrmann & Kestin [11]. Also this contribution is assumed to be irreversible and, as a first approximation, it will be supposed to be of the form $\dot{\varepsilon}^d = f(\omega, \dot{\omega})$.

For the damage evolution law, an expression is used similar to that proposed by Bodner [12] for metals, and later extended by Chan *et al.* [13] to rock salt. Its applicability to concrete has been verified in [5].

Starting form these observations, the expression of the potential of dissipation can be completed by adding to Ω_p a second term Ω_d, that accounts for the dissipation due to damage and for damage-induced inelastic strains:

$$\Omega_d = a_0^T \mathrm{tr}\left[\omega^T \cdot \dot{\omega}^T \cdot \hat{\sigma}\right] + a_0^C \mathrm{tr}\left[\omega^C \cdot \dot{\omega}^C \cdot \hat{\sigma}\right] + \frac{a_1^T}{a_3^T+1} \mathrm{tr}\left[\omega^T \cdot \left(\tilde{\omega}^T\right)^{a_2^T} \cdot \left(\mathbf{Y}^T\right)^{a_3^T+1}\right] + \frac{a_1^C}{a_3^C+1} \mathrm{tr}\left[\omega^C \cdot \left(\tilde{\omega}^C\right)^{a_2^C} \cdot \left(\mathbf{Y}^C\right)^{a_3^C+1}\right] \tag{9}$$

a_0^H, a_1^H, a_2^H, a_3^H (>0), with H=T or C, are material constants; $\tilde{\omega}^T$ and $\tilde{\omega}^C$ are two second-order tensors with eigenvalues $\tilde{\omega}_\alpha^H$ (α=I,II,III) related to the eigenvalues of ω^H by the relation $\tilde{\omega}_\alpha^H = -\ln \omega_\alpha^H$. Derivation of Ω_d respect to the stress tensor yields the damage-induced inelastic strains:

$$\dot{\varepsilon}^d = \frac{\partial \Omega_d}{\partial \sigma} = a_0^T \omega^T \cdot \dot{\omega}^T \cdot \left(\mathbf{1} - \omega^T\right)^{-1} + a_0^C \omega^C \cdot \dot{\omega}^C \cdot \left(\mathbf{1} - \omega^C\right)^{-1} \tag{10}$$

If the damage components take small values (less than about 0.2), the associated inelastic strain given by this equation is almost identical to that computed according to the relation proposed by Herrmann & Kestin [11].

Derivation of Ω_d respect to the damage driving forces gives the evolution laws of damage in tension and compression:

$$\dot{\omega}^T = \frac{\partial \Omega_d}{\partial \mathbf{Y}^T} = a_1^T \omega^T \cdot \left(\tilde{\omega}^T\right)^{a_2^T} \cdot \left(\mathbf{Y}^T\right)^{a_3^T} \tag{11a}$$

$$\dot{\omega}^C = \frac{\partial \Omega_d}{\partial \mathbf{Y}^C} = a_1^C \omega^C \cdot \left(\tilde{\omega}^C\right)^{a_2^C} \cdot \left(\mathbf{Y}^C\right)^{a_3^C} \tag{11b}$$

Note that damage increases for any value of the damage driving forces, but its evolution can be extremely slow when the damage variables and the damage driving forces (that is, the effective stress) take small values.

In order to complete the model, it is necessary to define the evolution laws for the plastic variables **B**, R and K. Starting from the expressions proposed in [10], we can write:

$$\dot{R} = A_3 \left(1 - R/R'\right) \dot{\varepsilon}_{eq}^p \tag{12}$$

$$\dot{K} = A_5 \left(1 - K/K'\right) \dot{\varepsilon}_{eq}^p \tag{13}$$

with

$$\dot{\varepsilon}_{eq}^p = \sqrt{\frac{2}{3}} \left\| \dot{\varepsilon}^p \right\| \tag{14}$$

As far as the kinematic hardening variable is concerned, the original proposal by Aubertin [10] reads

$$\dot{\mathbf{B}} = A_1 \left[\dot{\varepsilon}^p - \frac{\dot{\varepsilon}^p_{eq}}{B'_{eq}} \mathbf{B} \right] \tag{15}$$

with

$$B'_{eq} = B_0 (\dot{\varepsilon}^p_{eq} / \dot{\varepsilon}_0)^{1/N} \tag{16}$$

B_0 being a material parameter.

According to this proposal, the plastic strains rates (7) are purely deviatoric. Application of this expression to triaxial creep tests on concrete cylinders, however, was found to be inappropriate since axial and diametral creep strains could not be simultaneously well described; we will return later on this point in Section 4. A similar problem was encountered by Chan *et al.* [14] with an isotropic damage model formulated for the creep of rocksalt. This inconsistency was explained by those authors by assuming non-associativity for the damage-induced creep strains. Here it is proposed to modify eq. (15) by setting

$$\dot{\mathbf{B}} = \mathbf{A}^1 \left[\dot{\varepsilon}^p - \frac{\dot{\varepsilon}^p_{eq}}{B'_{eq}} \mathbf{B} \right] \tag{17}$$

where $\mathbf{A}^1$ is now a second order tensor that shares with $\dot{\varepsilon}^p$ and $\mathbf{B}$ the principal directions. In particular, for triaxial tests on cylinders, the two nonvanishing significant values of $\dot{\mathbf{B}}$ read:

$$\dot{B}_1 = A^1_1 \dot{\varepsilon}^p_1 - \frac{A^1_1}{B'_{eq}} \dot{\varepsilon}^p_{eq} B_1 \tag{18a}$$

$$\dot{B}_2 = A^1_2 \dot{\varepsilon}^p_2 - \frac{A^1_2}{B'_{eq}} \dot{\varepsilon}^p_{eq} B_2 \tag{18b}$$

In eqns. (12,13,16,18), B'_{eq}, R' and K' represent the saturation values of the relevant variables, while A^1_1, A^1_2, A_3, A_5, B_0 and $\dot{\varepsilon}_0$ are material parameters. Finally, note that the evolution of these variables depends only on the plastic component of the permanent strains.

Two examples will be presented to illustrate the model capabilities. In Fig. 2 the simulation is shown of uniaxial creep tests at different fractions of the uniaxial compressive strength, σ_c. The model correctly accounts for the increase in creep time to failure with decreasing stress level. In particular, at σ less than about $0.5\sigma_c$ the time for which the material sustains the applied stress is apparently unbounded. Also note that the three stages of primary (or transient), secondary (or steady-state) and, possibly, tertiary creep are reproduced by the model.

Fig. 3 shows the influence of the lateral confinement upon the creep time to failure, t_f, as predicted by the model in the simulation of triaxial creep tests on cylinders at 90% of the static strength for a given ratio r between confining pressure and axial stress. The trend of t_f with r is not monotonic and is somehow consistent with the experimentally observed trend of the fatigue life with r [4]. This can be explained by considering that, in the simulated tests, an increase in r is matched both by an increase in hydrostatic compression and in deviatoric stress: these two stress components have opposite effects on fatigue life and creep time to failure; depending on which of these two effects dominates, t_f can either increase or decrease with r.

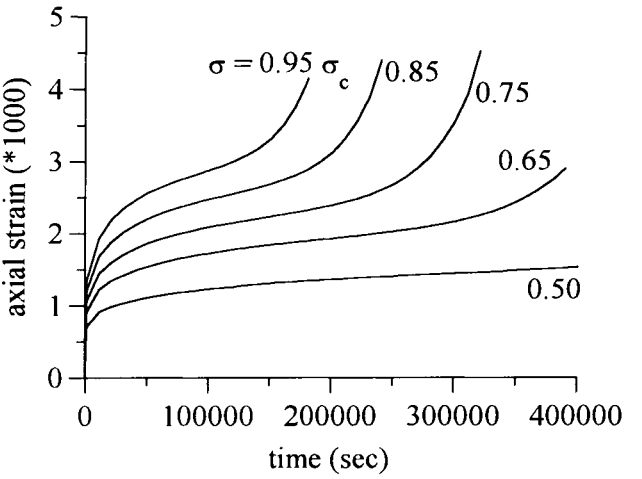

Figure 2 - Simulation of uniaxial creep tests at different stress levels.

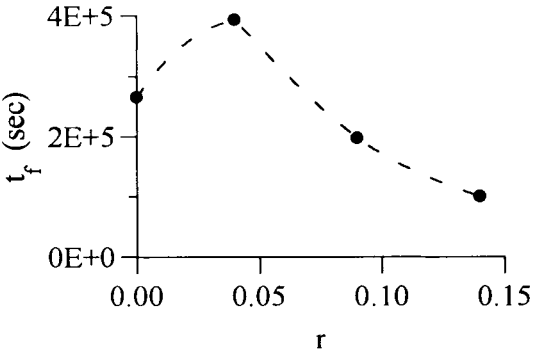

Figure 3 - Predicted creep time to failure, t_f, vs. ratio r between confining pressure and axial stress for triaxial creep tests at 90% of the triaxial static strength for a given r.

3. PARAMETER IDENTIFICATION

For sake of illustration, the procedure to identify the model parameters will be now discussed with reference to triaxial tests on cylinders.

The model parameters are partly associated with the plastic behaviour of the material and partly associated with damage phenomena. Thus, in principle it would be necessary to have experimental data available from creep tests where damage phenomena are negligible, to separately identify the first set of parameters. Nevertheless, experiments show that the damage evolution becomes significant only after the primary and secondary creep stages are concluded. Consequently, the parameters pertinent to the viscoplastic behaviour of the material can be identified during these two phases. On the contrary, the material constants that define damage and damage-induced inelastic strains can be obtained by data from the final phase of the tests (tertiary creep).

The evolution of the parameters B'_{eq}, R' and the coefficients A_1^1, A_2^1, A_3 that define the evolution laws of B_1, B_2 and R can be identified considering uni- and triaxial creep tests with loading and reloading cycles during the pre-loading phase and at different times of the creep test. Referring to the inelastic part of strains only, the amplitude of the current elastic domain can be determined from the extension of vertical segment of the σ-ε^p plot during the loading-reloading phase. Note that, in principle, extension tests could also be required to completely define the linear domain. For sake of simplicity, here it is assumed that the elastic limit in tension is unaffected by permanent strains. The mid-point of the elastic segment gives the value of B_1 and B_2. The values of A_1^1 and A_2^1 depend on the initial slope of the B_1-ε_1^p and B_2-ε_2^p plots, while A_3 is the initial slope of the R–ε_{eq}^p curve.

The parameter A_0 can be derived from the initial slope of the primary creep curve. By knowing the experimental value of $\dot{\varepsilon}_1^p$, which is practically constant during the secondary creep phase, the values of K' and N can be obtained by eq. (7).

Fig. 4 shows the identification of K' and N by using the results of six triaxial tests with different values of the ratio r. The experimental values of r and $\dot{\varepsilon}_1^p$ are reported in Table 1. Since no unloading-reloading cycles were performed during these tests, the values of R' and B'_{eq} were obtained by extrapolation from the results of uniaxial tests including such cycles.

Since A_5 determines the velocity at which K reaches its saturation value K', this value can be obtained based on the duration of the primary creep stage, while the constants $\dot{\varepsilon}_0$ and B_0 in eq. (16) depend on the initial plastic threshold.

As far as the parameters that govern the damage evolution are concerned, a_1^H and a_3^H are obtained through the values of the creep time to rupture of the material at different stress levels, while a_2^H controls the velocity of the damage evolution (H=T or C).

Finally, the parameters a_0^H are obtained from eq. (10) removing from the total inelastic strain the plastic contribution, identified by eq. (7).

Table 1 - Experimental values of the secondary creep rate in the triaxial tests employed for the identification of the model parameters

test no.	r	$\dot{\varepsilon}_1^p$ (sec^{-1})
1819-28	0.04	3.75e-10
1825-16	0.04	2.5e-10
1824-40	0.10	1.5e-9
1825-24	0.10	1.25e-9
1819-38	0.14	2.5e-9
1825-28	0.14	1.75e-9

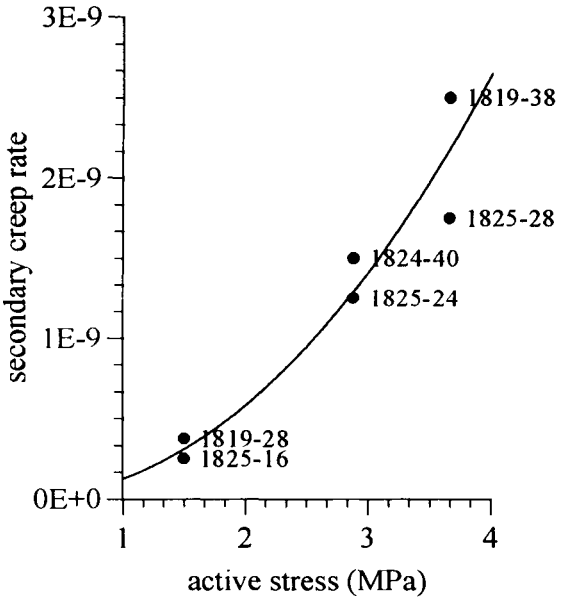

Figure 4 - Identification of parameters K' and N through the plot of the secondary creep rate versus the active stress $\hat{X}_{eq} - R$.

4. NUMERICAL SIMULATIONS

The parameters identified from triaxial creep tests, according to the procedure illustrated in the previous section, were also used to simulate uniaxial tests on three concrete specimens tested at constant stress equal to 95% of the ultimate static strength. The relevant results are shown in Fig. 5a,b. Fig. 5a shows plots of the axial and lateral strain versus time, while in Fig. 5b the volumetric strain is plotted versus the axial strain. On account of the experimental

scatter, the computed model response seems to average the experimental data from the three tests fairly well. In particular, note that the model is able to capture the phenomenon of dilatancy that precedes failure, owing to the anisotropic description of damage.

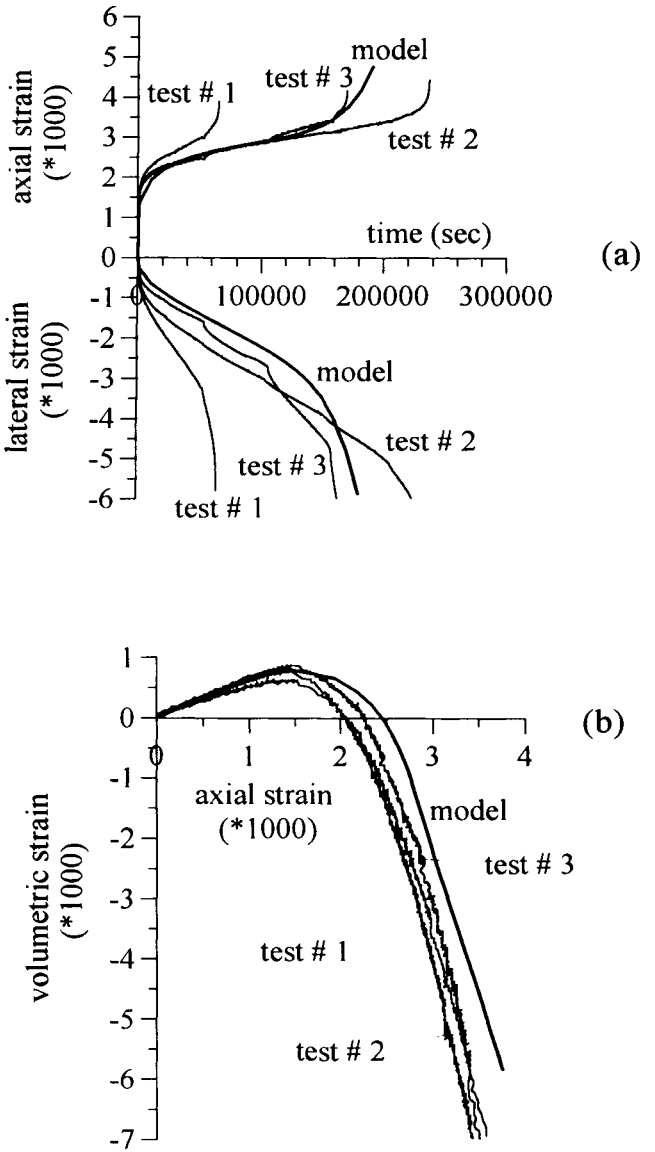

Figure 5 - Uniaxial creep tests at 95% of the static strength: numerical simulation of three experiments. (a) axial and lateral strain vs. time; (b) volumetric vs. axial strain.

It is worth emphasizing that different values for the parameter A_1^1 and A_2^1 had to be employed for the evolution laws of B_1 and B_2, whereas according to the original proposal from [10] these values would be equal. Indeed, Fig. 6 shows the numerical evolution of lateral strain vs. time: the dashed line is obtained assuming $A_1^1 = A_2^1$, while using two different values for A_1^1 and A_2^1 gives the solid line. This picture shows clearly that the original viscoplastic model, with purely deviatoric plastic strains, when applied to concrete, is unable to simultaneously describe the evolution of both the axial and the lateral strain.

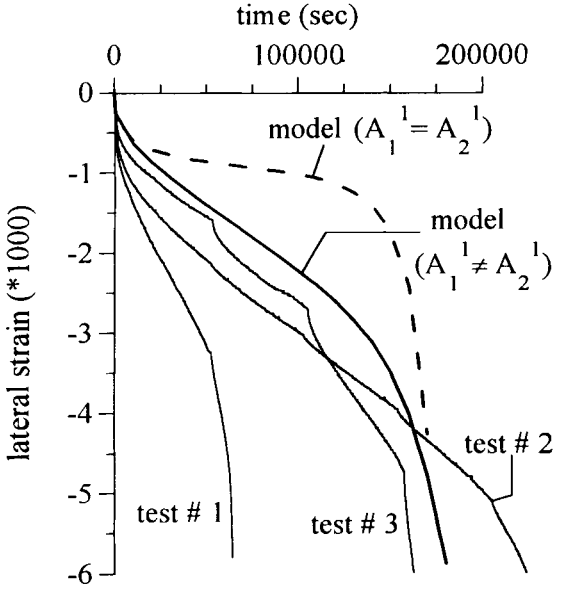

Figure 6 - Lateral strain during uniaxial creep tests at 95% of the static strength; experimental data from three tests and theoretical predictions with equal and different values for A_1^1 and A_2^1

Fig. 7 shows the evolution of damage variables ω_1^C and ω_2^T in time in the simulation of the uniaxial creep tests: note that their values are significant only after the end of secondary creep. Also note that ω_2^T increases faster than ω_1^C. These features of the numerical model are consistent with the experimental finding not only for creep tests but also for cyclic tests [3].

Finally, by using the same parameters, two triaxial creep tests with r = 0.14 at 90% of the triaxial static strength were modeled [3]. The tested specimens did not fail within 400000 seconds, so that the tertiary creep stage is missing in both tests. The experimental results and the obtained simulation are reported in Fig. 8. Here again, note that the numerical response is in good agreement with the experimental data.

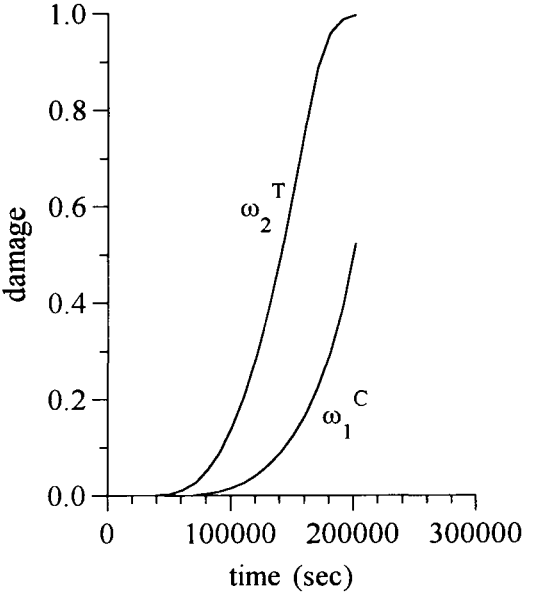

Figure 7 - Evolution of the damage variables during the uniaxial creep tests simulated in Fig. 3.

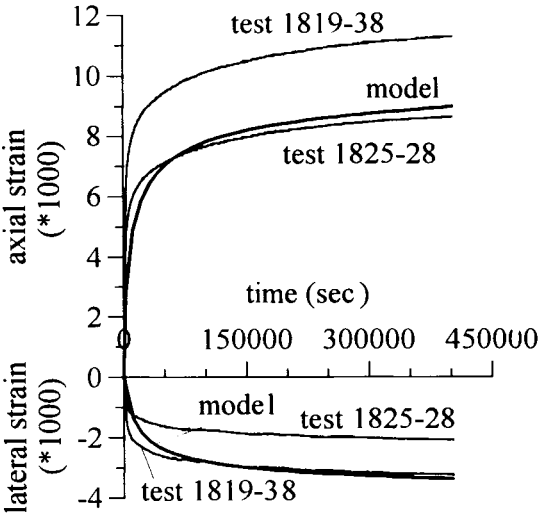

Figure 8 - Numerical simulation of two triaxial creep tests (r=0.14) at 90% of the static strength.

5. CONCLUDING REMARKS

A model able to describe the behaviour of concrete subjected to sustained elevated triaxial loading has been proposed. For this aim, the phenomena due to plasticity have been coupled to damage through the definition of a suitable viscoplastic potential. The evolution laws of permanent strains and damage variables are thermodynamically consistent, since they were obtained by derivation of this potential. In this model viscoelastic strains are neglected and creep strains are considered to be entirely unrecoverable: this is an assumption common to other theoretical models developed for metals and rocksalt subjected to high constant stress (see e.g. [10,13]). A procedure to identify the model constants and variables has been outlined. The reliability of the model has been assessed through comparisons with results of uni- and triaxial tests.

The model is featured by an important number of parameters; the procedure to identify these parameters, however, is not impractical since they define the evolution laws of variables which possess a clear physical meaning.

Although in principle the model is able to describe quite general load histories, the laws proposed for the evolution of the damage variables during creep tests are inappropriate to describe monotonic tests. Indeed, if creep tests are correctly modeled, damage turns out to be unrealistically negligible during the pre-loading phase and during reloading to failure for specimens that did not fail at constant stress. On account of the latter remark, the residual strength of the material upon re-loading turns out to be unrealistically high respect to experiments. Future developments will aim at formulating evolution laws applicable with a broader range of tests.

The remarks recalled in the Introduction based on the results of a number of creep tests were used as guidelines to formulate a theoretical model qualitatively accounting for the salient features of the behaviour of concrete at high sustained stresses, namely the evolution of the elastic domain with permanent strains and the occurrence of damage phenomena. Work is presently in progress to establish specific relationships between any single loading parameters and the change in stiffness and strength of the material.

ACKNOWLEDGMENTS

This work was developed within the framework of a research program supported by MURST, the Italian Ministry for University.

REFERENCES

1 A. Cividini, A. Taliercio, G. Sacchi, R. Bellotti, G. Ferrara and P. Rossi, Materials & Structures, 25 (1992) 490.
2 A. Taliercio and E. Gobbi, Mag. Concr. Res., 48 (1996) 157.
3 A. Taliercio and E. Gobbi, Mag. Concr. Res., 49 (1997) in press.
4 A. Taliercio and E. Gobbi, Mag. Concr. Res. (1997) to appear.
5 E. Papa, A. Taliercio and E. Gobbi, Materials & Structures, (1997) to appear.
6 E. Papa and A. Taliercio, Proc. XII Natl. Conf. of the Italian Assoc. of Theoretical and Applied Mechanics (1995), V, 141.

7 E. Papa and A. Taliercio, Engng. Frac. Mech., 55 (1996) 163.
8 C. La Borderie, Y. Berthaud and G. Pijaudier-Cabot, Proc. 2nd Int. Conf. on Computer aided analysis and design of concrete structures, Zell am See (Austria), (1990) 975
9 J. Lemaitre and J.L. Chaboche, Mécanique des matériaux solides, Dunod-Bordas, Paris, 1985.
10 M. Aubertin, D.E. Gill and B. Ladanyi, Mechanics of Materials, 11 (1991) 63.
11 G. Herrmann and J. Kestin. Proc. Conf. on Strain localization and size effects due to damage and cracking, Z.P. Bazant and J. Mazars (Eds.), Elsevier, London, (1988) 228.
12 S.R. Bodner, Plasticity Today, A. Sawczuk and G. Bianchi (Eds.), Elsevier, London, (1985) 471.
13 K.S.Chan, S.R. Bodner, A.F. Fossum, and D.E. Munson, Mechanics of Materials, 14 (1992) 1.
14 K.S.Chan, N.S. Brodsky, A.F. Fossum, S.R. Bodner and D.E. Munson, Int. J. Plasticity, 10 (1994) 623.

Damage Mechanics in Engineering Materials
G.Z. Voyiadjis, J.-W.W. Ju and J.-L. Chaboche (Editors)
© 1998 Elsevier Science B.V. All rights reserved.

Damage and fracture modeling of 4D CC composites

P. Ladevèze[a], X. Aubard[b], C. Cluzel[ac] and L. Guitard[a]

[a]Laboratoire de Mécanique et Technologie E.N.S. de Cachan/C.N.R.S./Univ. P. et M. CURIE
61, avenue du Président Wilson 94235 CACHAN Cedex (FRANCE)

[b]Société Européenne de Propulsion -
Le Haillan - BP 37 - 33165 St MEDARD-EN-JALLES (FRANCE)

[c]IUT GMP EVRY - Cours Mrg Roméro 91000 EVRY (FRANCE)

A mechanical material model is derived for 4D Carbon/Carbon composites. By using an anisotropic damage mechanics approach, a very simple mathematical model of the material mechanical behavior, based on some remarkable experimentally-observed properties, is built at the macroscopic scale. The identification of the material parameters is presented. The predictions of the model are then compared to different tests. Fiber yarn debonding near edges is also studied through a material mesomodel, with the mesoconstituents being: the fiber yarns, the matrix and the interfaces. Initial results are shown for a tension specimen.

1. INTRODUCTION

The material under study was manufactured by S.E.P. (Société Européenne de Propulsion) and is a 4D Carbon-Carbon composite comprising four reinforcement directions parallel to the largest diagonals of a cube. These materials, called SEPCARB 4D, are used in the throat nozzles of solid propulsion systems (Fig. 1) owing to their excellent thermo-mechanical properties and their high resistance to ablation [1]. Structures made of SEPCARB 4D are submitted to very high thermal gradients (from 20°C to 3000°C) as well as to complex mechanical stresses. The aim of this study is to accurately model the thermo-mechanical behavior of these materials, and in particular their damage mechanisms, in order to predict the response of industrial structures.

The macroscopic behavior of this material is highly anisotropic and non-linear. Several types of degradations are observed inside the material and near the edges. Studying these degradations at the micro scale seems to be infeasible because of the 4D structure of the material. Also the material has a complicated behavior and very little information is available to build a behavior model. Thus, the approach adopted seeks to make the best use of the avalaible information herein. A very simple mathematical material model has first been derived for multiaxial loadings as a consequence of some remarkable experimentally-observed properties and the material geometry. The anisotropic continuum damage mechanics theory introduced by Ladevèze [2] is applied with the central focus being to derive the simplest damage kinematics. Anelastic phenomena are taken into account by a plastic like model.

Identifying the material constants and functions characterizing the studied 4D CC composite is a rather difficult task. Fiber debonding near the edge is very significant in tensile tests and affects the results of these tests. Proceeding further in the test analysis, a study of these edge effect phenomena is in progress. The model is still three-dimensional, but it takes into account the material heterogeneity and complicated architecture. As in [3-4], the model is developed at the meso-scale, intermediate between the macro scale of the structure and the micro scale of the fiber. For each meso-constituent (fiber yarns, matrix and interfaces), a mechanical model is used. To rebuild a homogeneous behavior from the meso model, a method based on the asymptotic development theory for periodic media is carried out.

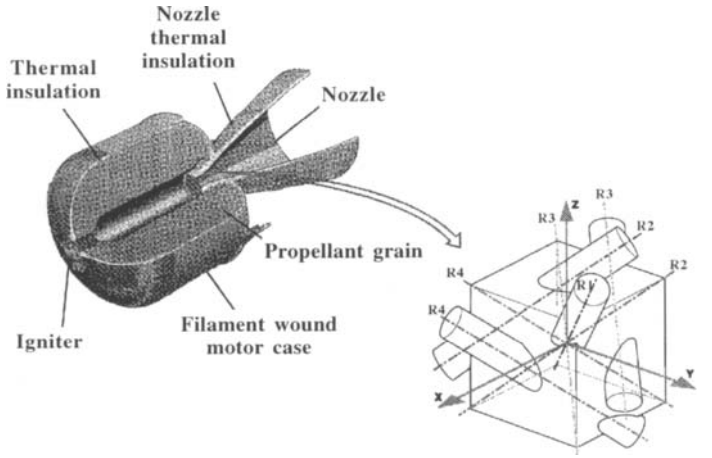

Figure 1: Nozzle throat and Sepcarb 4D composite

2. MATERIAL AND MAIN EXPERIMENTAL FEATURE

The reinforcement yarns (fibers/matrix) have variable diameters, which are typically between 1 and 3mm. They are positioned in four directions parallel to the larger diagonals of a cube (Fig. 1). One defines the X, Y and Z axis oriented perpendicularly to the cube faces, with the base (X',Y',Z) obtained by a 45° rotation of (X,Y,Z) around Z and the vectors $R_{i,i\in\{1,2,3,4\}}$ of the reinforcement directions.

This material has a non-linear anisotropic behavior, as shown in Figure 2, where the presented experimental results (stress - longitudinal strain) were obtained in tension in directions X, X' and R_i to ambient temperature. For a loading in a direction of reinforcement, both transversal and longitudinal strains increase linearly with the stress until a brittle failure. Responses to tension with cycling stresses in the X and X' directions show behavior with damage and anelastic strains. Damage of the Sepcarb 4D is attributed mainly to the mechanisms of Yarn/Matrix interface degradations.

Results from tension tests conducted by S.E.P. in the X-direction on specimens with circular sections of different diameters (Fig. 3) show that Yound's modulus and failure stress increase with the section dimensions of specimen.

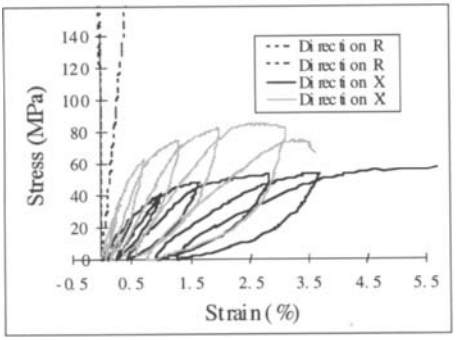

Figure 2: Experimental responses of the internal behavior obtained in tension in the X, X' and R directions

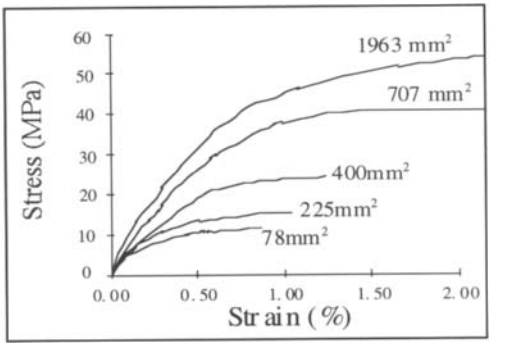

Figure 3: Stress-strain curves of tension tests in the X-direction, at ambient temperature; influence of the size of specimen section (S.E.P. results)

The failure surface of the large section specimen reveals two zones (Fig. 4):

-a rather flat central zone of yarn failure, and
-a peripheral zone approximately 15mm in width showing an irregular surface with yarn debonding.

In contrast, the failure surface of the specimen with 10 and 30-mm diameters seems to indicate only the presence of the zone of high debonding. These two zones allow assuming different variations for degradations occuring far from a free surface and near the edges. This phenomenon is attributed to the edge effect which modifies the stress distribution both in matrix and yarns close to a free surface.

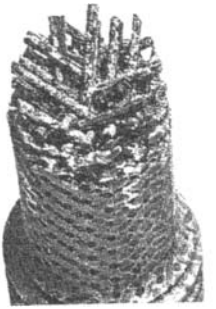

Figure 4a: Failure surface of a circular cylindrical specimen with a section diameter of 30mm (S.E.P.)

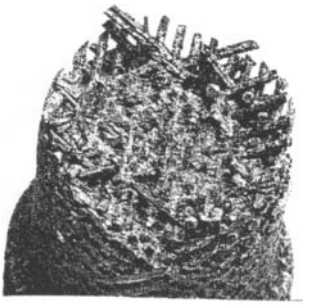

Figure 4b: Failure surface of a circular cylindrical specimen with a section diameter of 50mm (S.E.P.)

To approach a model of the Sepcarb 4D mechanical behavior, one have to dissociate both the internal behavior and the yarn debonding initiated near the edges. The initial study, presented below, aims to the model and identify, at the macroscopic scale, the "internal" behavior of

Sepcarb 4D. The second study concerns more specifically the phenomenon of yarn debonding linking to free edge effects. In order to take into account the material heterogeneity and complex architecture, the model, such as in [3-4], is developed at the mesoscopic scale, intermediate between the macro scale of the structure and the micro scale of the fiber.

3. MACROSCOPIC MODELING OF THE FAR-EDGE SEPCARB 4D MECHANICAL BEHAVIOR

3.1. Hypotheses

This modeling approach is based on the responses obtained with the tension tests conducted on the large-section specimens. These different responses (Fig. 2) display the very high anisotropy of the mechanical behavior. This anisotropy is due to the reinforcement orientations which are much stiffer than the matrix. Therefore, for a loading in a direction of reinforcement, was obtained a linear evolution, until a brittle failure, of the transversal and longitudinal strains as a function of the longitudinal stress. Because of the symmetry of the yarn orientations, the Young's modulus is identical for each direction of reinforcement. Symmetries induced by the yarn orientations also impose the same material behavior for the directions X, Y and Z. Figure 2 shows, for tension tests in these directions, a behavior with damage and anelastic strains.

3.2. Modeling of the elastic behavior and damage kinematics

The description of Sepcarb 4D behavior in the elastic domain is developed using the classical Hooke tensor with only 3 coefficients. The spatial disposition and orientations of the reinforcements impose, by symmetry, a cubic elastic behavior. In Figure 5, the variation of Young's modulus $E(\vec{n})$ is represented, as calculated with Hooke's tensor, and shows the high anisotropy induced by the reinforcements.

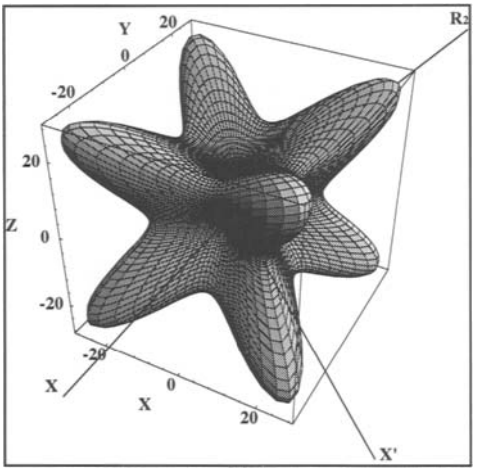

Figure 5: Variation of Young's modulus; surface $E(\vec{n}).\vec{n}$

In the cube basis, the orthotropic basis of the material in which the 3 directions X, Y and Z are equivalent, the inverse of the elastic tensor (denoted K) can be written very easily with Young's modulus in the X-direction (denoted E), Poisson's ratio XY (denoted ν) and the XY shear modulus (denoted G).

$$\mathbf{K}^{-1}:\begin{vmatrix} \frac{1}{E} & -\frac{\upsilon}{E} & -\frac{\upsilon}{E} & 0 & 0 & 0 \\ & \frac{1}{E} & -\frac{\upsilon}{E} & 0 & 0 & 0 \\ & & \frac{1}{E} & 0 & 0 & 0 \\ & & & \frac{1}{2G} & 0 & 0 \\ & & & & \frac{1}{2G} & 0 \\ & & & & & \frac{1}{2G} \end{vmatrix}_{(X,Y,Z)}$$

To describe the degradation state of the material, damage mechanics [5] is used and, in particular, its extension to anisotropic damage as proposed by Ladevèze [2] and already used for different composites [6-7-8]; the Hooke's tensor variation is used as a damage indicator. The main problem is to define the internal variables of damage. *Two, and only two, assumptions* are introduced:

- the longitudinal modulus and Poisson coefficients remain constant for tension tests in each direction of reinforcement, and
- the material, even after being damaged, behaves similarly in the 4 directions of yarns, which supposes a homogeneous distribution of the degradations in the 4 directions; the distribution damage types have already been observed on 3D C-C composites [4].

In order to take into account these assumptions, a barycentric representation, based on the four unit vectors $\underline{R}_{i,i\in\{1,2,3,4\}}$ defining the reinforcement directions, is introduced. It is shown that, from the strain energy [9], the Hooke's tensor $\mathbf{K}$ can be described with the following coefficients:

$$\mathrm{Tr}\left[\mathbf{K}^{-1}.\left[\underline{R}_i.\underline{R}_j{}^t\right]_{sym}.\left[\underline{R}_k.\underline{R}_l{}^t\right]_{sym}\right],(i,j,k,l)\in\{1,2,3,4\}^4 \qquad (1)$$

Since the 4 directions of reinforcement have been assumed to play identical roles, even for the damaged material, the coefficients defined in (1) can be reduced to the following seven:

$$\begin{aligned} a &= \mathrm{Tr}\left[\mathbf{K}^{-1}.\left(\underline{R}_1.\underline{R}_1{}^t\right).\left(\underline{R}_1.\underline{R}_1{}^t\right)\right] \\ b &= \mathrm{Tr}\left[\mathbf{K}^{-1}.\left(\underline{R}_1.\underline{R}_1{}^t\right).\left(\underline{R}_1.\underline{R}_2{}^t\right)_{sym}\right] \\ c &= \mathrm{Tr}\left[\mathbf{K}^{-1}.\left(\underline{R}_1.\underline{R}_1{}^t\right).\left(\underline{R}_2.\underline{R}_3{}^t\right)_{sym}\right] \\ d &= \mathrm{Tr}\left[\mathbf{K}^{-1}.\left(\underline{R}_1.\underline{R}_1{}^t\right).\left(\underline{R}_2.\underline{R}_2{}^t\right)\right] \end{aligned} \qquad \begin{aligned} e &= \mathrm{Tr}\left[\mathbf{K}^{-1}.\left(\underline{R}_1.\underline{R}_2{}^t\right)_{sym}.\left(\underline{R}_1.\underline{R}_2{}^t\right)_{sym}\right] \\ f &= \mathrm{Tr}\left[\mathbf{K}^{-1}.\left(\underline{R}_1.\underline{R}_2{}^t\right)_{sym}.\left(\underline{R}_1.\underline{R}_3{}^t\right)_{sym}\right] \\ g &= \mathrm{Tr}\left[\mathbf{K}^{-1}.\left(\underline{R}_1.\underline{R}_2{}^t\right)_{sym}.\left(\underline{R}_3.\underline{R}_4{}^t\right)_{sym}\right] \end{aligned} \qquad (2)$$

These seven coefficients are not independent. Relationship (3) which binds the 4 vectors $\underline{R}_i$ reveals 4 relationships between the seven parameters:

$$\sum_{i=1}^{4}\underline{R}_i=\underline{0},\ \text{avec}\ \sqrt{3}\underline{R}_1:\begin{vmatrix}1\\1\\1\end{vmatrix},\sqrt{3}\underline{R}_2:\begin{vmatrix}-1\\1\\-1\end{vmatrix},\sqrt{3}\underline{R}_3:\begin{vmatrix}-1\\-1\\1\end{vmatrix},\sqrt{3}\underline{R}_4:\begin{vmatrix}1\\-1\\-1\end{vmatrix}\Rightarrow\begin{cases}a+3b=0\\d+b+2c=0\\e+2f+b=0\\c+g+2f=0\end{cases} \qquad (3)$$

Three independent coefficients that completely describe the elastic behavior are obtained and we choose:

$$a = \frac{E + G(1 - 2\upsilon)}{3EG} \geq 0$$

$$d = \frac{-E + 3G(1 - 2\upsilon)}{9EG} \tag{4}$$

$$e = \frac{E + G(3 + 2\upsilon)}{9EG} \geq 0$$

This choice allows taking into account directly the experimental information obtained in the reinforcement directions. The coefficient "a" is by definition the inverse of the Young's modulus of the material in a reinforcement direction. It is therefore a constant elastic parameter denoted "a_0". The coefficient "d", which is linked to the transverse modulus X'R of the Sepcarb 4D, is constant as well and denoted "d_0". The damage kinematics are then determined and associated to the latter coefficient. The parameter "e", positive by definition, is selected. h is defined as a damage scalar coefficient, varying from 1 to infinity, equal to the fraction of the initial value of "e" to the value corresponding to a damage state of the material:

$$a = a_0 = E(R_i)^{-1}$$

$$\frac{-\upsilon_{RiY'}}{E_{R_i}} = \frac{9d - a}{16} \Rightarrow d = d_0 \tag{5}$$

$$e = e_0 h$$

3.3. Damage force - Damage evolution law

The thermodynamic force Y_h associated with the parameter h is defined classically from the elastic strain energy of the damaged material in the following way:

$$E_d = \frac{3}{8}a_0(-A_1 + 6A_3 + 3A_2) + \frac{9}{8}d_0(A_1 - 2A_3 + A_2) + \frac{9}{4}e_0 h(A_1 - A_2) \tag{6}$$

with: $A_1 = \sigma_{XX}^2 + \sigma_{YY}^2 + \sigma_{ZZ}^2$, $A_2 = \sigma_{XX}\sigma_{YY} + \sigma_{XX}\sigma_{ZZ} + \sigma_{ZZ}\sigma_{YY}$, and $A_3 = \sigma_{XY}^2 + \sigma_{YZ}^2 + \sigma_{XZ}^2$

$$Y_h = \left.\frac{\partial E_d}{\partial h}\right|_{\sigma_{ij} = cst} \tag{7}$$

The dissipation due to the damage is written: $\omega = Y_h.\dot{h}$. The state of damage with quasi-static loading is assumed to depend on the maximum force; one therefore has:

$$h = f(\underline{Y}_h), \text{ with: } \underline{Y}_h(t) = \sup_{\tau<t}(Y_h(\tau)). \tag{8}$$

The damage evolution law "$\underline{Y}_h$ -> h" is an experimentally-identified material characteristic.

3.4. Anelastic strain modeling

The micro defect, i.e. the damage, leads to sliding with friction in the matrix and in the interfaces and thus to anelastic strains. More generally, it is possible to obtain coupling phenomena between damage and anelasticity. One way to model these phenomena is to apply plasticity mechanical modelling. The notion which seems to work quite well is to build the model from quantities which are called "effective": the effective stress tensor $\tilde{\sigma}$ and the effective anelastic strain rate $\dot{\tilde{\varepsilon}}^p$ [10].

The effective stress is chosen; it defines the coupling between the classical stress and the damage state which is involved in anelastic strains. One particular choice which will be pursued herein is:

$$\tilde{\sigma} = \mathbf{K}_0.\mathbf{K}^{-1}.\sigma \text{ , with } \mathbf{K}_0 \text{ the initial Hooke tensor} \tag{9}$$

The effective anelastic strain rate is defined from the anelastic dissipation in the following way:

$$\mathrm{Tr}\left[\tilde{\sigma}.\dot{\tilde{\varepsilon}}^p\right] = \mathrm{Tr}\left[\sigma.\dot{\varepsilon}^p\right]. \tag{10}$$

The anelastic model results from the following hypotheses:

- the behavior in the 4 reinforcement directions is only elastic,
- the hardening is assumed to be isotropic, and
- the limit of the elastic domain is defined with an anisotropic threshold which is written:

$$f\left(\tilde{\sigma},\tilde{R}\right) = \sqrt{\mathrm{Tr}\left[\mathbf{H}.\tilde{\sigma}.\tilde{\sigma}\right]} - \tilde{R}(\tilde{p}) - \tilde{R}_0 \tag{11}$$

with **H** being a fourth-order tensor which defines the coupling between the different stresses.

By analogy with damage (like for damage, anelastic strains are blocked in the directions of reinforcements), a system of representation of the anelastic behavior is used with the reinforcement directions explicitly. The **H** tensor is then similar to the Hooke's tensor. Introducing the blocking, which was experimentally observed, of the longitudinal and transversal anelastic strains for a loading in a given yarn direction, it can be shown in [9] that **H** is entirely defined with only 1 parameter and thus:

$$f\left(\tilde{\sigma},\tilde{R}\right) = \sqrt{2\left(\tilde{\sigma}_{XX}{}^2 + \tilde{\sigma}_{YY}{}^2 + \tilde{\sigma}_{ZZ}{}^2 - \tilde{\sigma}_{XX}\tilde{\sigma}_{YY} - \tilde{\sigma}_{XX}\tilde{\sigma}_{ZZ} - \tilde{\sigma}_{YY}\tilde{\sigma}_{ZZ}\right)} - \tilde{R}(\tilde{p}) - \tilde{R}_0 \tag{12}$$

Anelastic flow law is obtained from the threshold function by:

$$\dot{\tilde{\varepsilon}}_{ij}^p = \dot{\tilde{p}}\frac{\partial f}{\partial \tilde{\sigma}_{ij}}\bigg|_{R=Cst} \quad \text{with } \dot{p} \geq 0,\ f \leq 0 \text{ and } \dot{p}f = 0 \tag{13}$$

The effective accumulated anelastic strain rate is then:

$$\dot{\tilde{p}} = \frac{1}{\sqrt{3}}\sqrt{\dot{\tilde{\varepsilon}}_{XX}^{p\ 2} + \dot{\tilde{\varepsilon}}_{YY}^{p\ 2} + \dot{\tilde{\varepsilon}}_{ZZ}^{p\ 2}} \tag{14}$$

The anelastic model is completely defined once the hardening function: "$\tilde{R}(\tilde{p}) - \tilde{R}_0$" as been experimentally identified.

3.5. Model parameters identification

3.5.1. Experimental method

To experimentally identify the internal behavior, tension tests conducted on the specimens with large diameter are used, along with more detailed tests in which edge degradations are blocked mechanically. In order to block yarn debonding, a thin layer of resin epoxy (with a thickness of about 0.02mm) has been deposited on the specimen tested in the L.M.T. laboratory. The initial longitudinal elastic modulus identified in this manner is greater than the modulus obtained with the non-coated specimen (even, despite the small dimensions of the section of the coated specimen). In contrast, the maximum stress values obtained are less than the one obtained with the specimen with large sections. The phenomenon of debonding, although blocked during the first part of the tests, has occurred. The curves presented in Figure 6 allow us, in comparing the results of tests conducted on coated specimens with those conducted on the large-section specimens, to define the limit of the influence of the resin on edge effects (which defines the limit of the identification of the model parameters). This limit corresponds to the appearance of unstuck marks of the resin on the coated specimen, marks which were visually observed during the tests (Fig. 7).

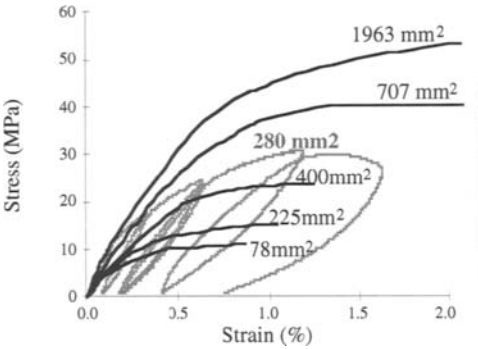

Figure 6: Comparison of results of tension test conducted with specimens of several sizes and on a specimen coated with a resin epoxy.

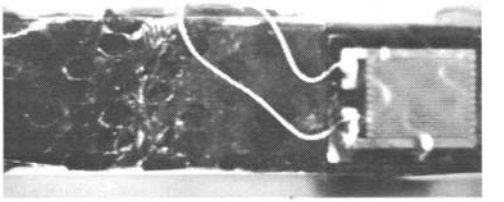

Figure 7: Face of a damaged specimen: yarn debonding and unstuck resin

3.5.2. Elastic parameters and damage evolution law

The simplicity of the defined model allows carrying out the complete identification of the material parameters with only 2 tension tests with cycling: the first one in a reinforcement direction, and the other one in the X-direction. For each cycle, one obtains the maximum value

of the stress, the longitudinal strain and 2 transversal strains measured perpendicularly to the longitudinal direction.

With a test in a direction of reinforcement, the values of the constant elastic parameters a_0 and d_0 are obtained. Transverse and longitudinal responses obtained from a tension test in the X-direction yield the value of the parameter "e" as well as its evolution. For each unloading, two values of the variable h are derived, with one taking into account the longitudinal elastic modulus, and the other one taking into account the transverse elastic modulus (15). Values of the associated variable Y_h are obtained from the maximum value of the stress for each unload.

$$\frac{1}{E} = \frac{3}{8}\left(-a_0 + 3d_0 + 6e\right)$$
$$\frac{-\upsilon}{E} = \frac{9}{16}\left(a_0 + d_0 - 2e\right) \qquad (15)$$

Figure 8 presents the results generated from two tests. The points obtained from both the longitudinal and transverse responses provide the same evolution for the parameter h. This result constitutes an important validation of the approach used to build the internal model presented. The curve identified from this graph is a straight line.

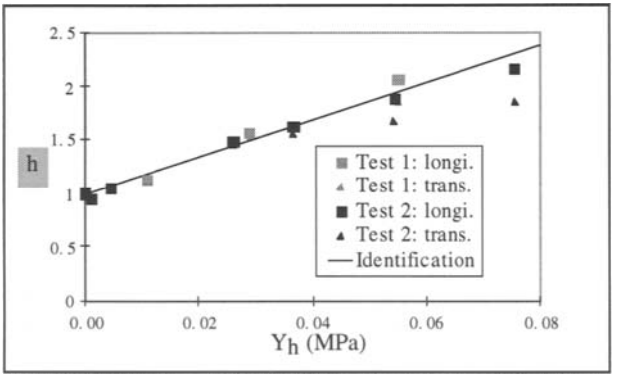

Figure 8: Identification of the damage evolution law

3.5.3. Identification of the plastic model

The hardening function is derived by calculating the values of "p" from the anelastic strain measures, along with the values of "$\tilde{R}(\tilde{p}) + \tilde{R}_0$" from the maximum value of the stress reached before each unload. The results obtained from 2 tests are presented in Figure 9. The identified curve is a straight line.

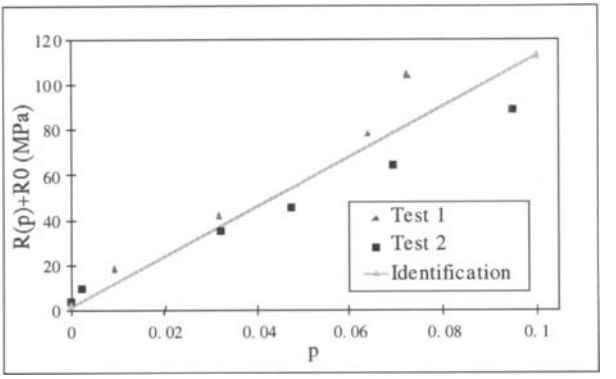

Figure 9: Identification of the hardening function

3.6. Correlation calculations/tests

To use the presented model, the classic elastic moduli is defined in the initial basis (X, Y, Z) using the relationships between the barycentric moduli and the classic moduli:

$$E = \frac{8}{3(-a_0 + 3d_0 + 6e)}, \quad G = \frac{4}{9(a_0 - d_0)} \quad \text{and} \quad \nu = \frac{-a_0 - d_0 + 2e}{-a_0 + 3d_0 + 6e} \tag{16}$$

The model has been identified at S.E.P. for temperatures between 0° and 2500 °C and introduced into the F.E. computation code MARC. It has been validated by different comparisons tests/calculations (4-point bending test, tube being submitted to an internal pressure). Figure 10 presents results obtained both experimentally and numerically for a 4-point bending test conducted at 1000 °C.

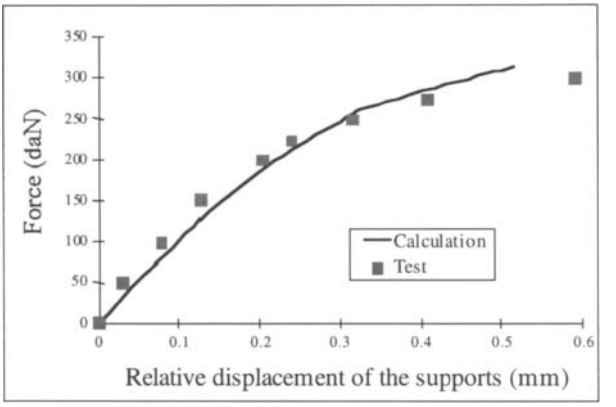

Figure 10: Test/calculation results for a 4-point bending test at 1000°C

4. STUDY OF THE DEBONDING PHENOMENON

4.1. Mesoscopic scale

Observations of the specimen failure surfaces (Fig. 4) and the edge surfaces of the specimens (Fig. 7) show a yarn debonding and slipping in the composite respectively. The aim of this second study is to understand the origin and the evolution of this degradation in cooection with the local redistribution of the stresses near a free surface. A study at a mesoscopic scale allows taking into account the composite structure (organization of the yarns) and easily modeling the mechanisms of degradation. Such an approach has already been used in the study of Carbon/Carbon composites such as 3D Aérolor [4] and 3D EVO [3]. These studies, carried out at the mesoscopic scale, have made it possible to understand the importance of the interface in composite material damage.

The description of the Sepcarb 4D at the mesoscopic scale uses 3 meso-constituents, which are:

- the yarns, cylindrical with a circular section,
- the matrix that fills the voids imposed by the presence of yarns in 4 directions (in the case of the Sepcarb 4D, the matrix has a continuous volume), and
- the interfaces that transmit efforts between yarns and matrix.

Damage is held constant in each meso-constutuent of the cells defining the structure. The model thus defined is consistent; results of numerical computations are independent of the mesh.

4.2. Modeling of the meso-constituent mechanical behavior

To simplify the modeling process, it is initially assumed that the major damage phenomenon is the yarn/matrix interfaces degradation. A brittle, transverse isotropic elastic model is therefore chosen for the yarn behavior and an isotropic elastic behavior for the matrix. For the interface, results of many studies conducted on the problem of yarn/matrix interface debonding in composites [11-14] are utilized. The behavior is elastic with damage; totally damaged sliding with friction is modeled with the Coulomb law. A brittle damage threshold is chosen to characterize the interface degradation. The threshold is defined as a quadratic criterion on the normal and tangeant stresses of the interface:

$$\left(\frac{\sigma_N - \sigma_S}{\sigma_C}\right)^2 + \left(\frac{\tau}{\tau_C}\right)^2 = 1 \qquad (17)$$

4.3. Modeling of the geometry

The Sepcarb 4D is manufactured with cylindrical yarns of circular sections. Their spatial orientations define a priori a punctual contact surface. It can be noticed from the photograph of a plane normal to X (Fig. 12) that the yarns, after the material manufacturing, have a rather hexagonal-shaped section. One also notices that the angles between 3 directions of yarns projected on a plane perpendicular to the fourth direction are 60° (Fig. 11). We have therefore chosen to model the yarn geometry by a cylindrical form with a hexagonal section. The contact zone between two yarns is thus surfacic in the form of a rhombus.

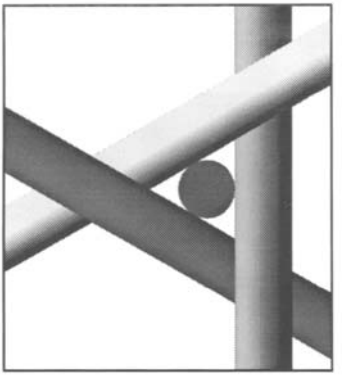

Figure 11: Visualization of the angles between the projections, in a plane perpendicular to one axis of the yarns

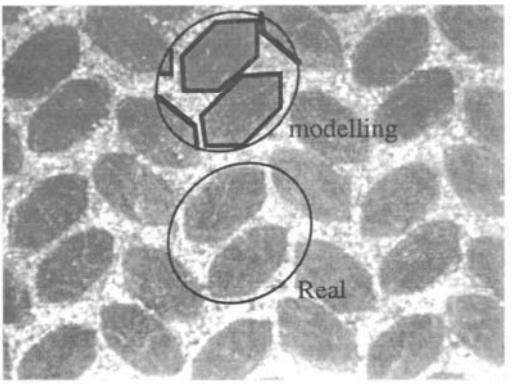

Figure 12: Plane of normal X, modeling of the yarn geometry

4.4. 3D computation of a specimen

In order to take into account experimental results showing the influences of a free edge, the structure chosen is a specimen in tension-compression. To simplify the development of the mesh, the section chosen is square, instead of the circular shape of the specimen used by S.E.P.

The dimensions of the section are between 10 and 50mm inclusive and are linked to the material periodicity. Specimen length is approximately 250mm. Since the total length of the specimen is high compared to the section dimensions and the period (between 5 and 10mm, depending on the direction), the effects due to the loading (imposed displacement) on heads is assumed not to modify the response of the specimens medium zone. The area studied is thus reduced by utilizing the periodicity with a technique of asymptotic development.

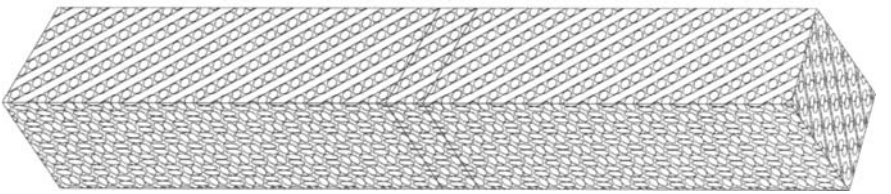

Figure 13: Homogeneous zone of a specimen

This technique introduced in [15-16] is primarily intended to separate local effects (to the level of an elementary cell) from global effects (macroscopic loading). Technically, an asymptotic development to the solution of the mechanical problem is being performed. One can find in [17] an implementation of the technique for the study of edge effects in composite material structures. This technique has been used in [4] to develop an approach to the mesoscopic scale of Carbon/Carbon composites which are periodic in 3 directions. The technique of asymptotic developments is utilized for homogeneous plates in [18] and for stratified Carbon/Carbon composite 2D periodics in [3]. Here, a technique adapted to beam 1D periodics is developed; it will be described in a later paper.

The mechanical problem obtained is solved numerically by the F. E. method. Because of the complexity of the structure, we have chosen not to use an automatic three-dimensional mesher to build the mesh, so as to more easily manage the number, the size and the form of the finite elements. In order to use interface elements, the meshes of the different substructures (yarn and matrix) are made compatible Several sizes have been drawn up for the mesh. Figure 15 displays the coarsest mesh of a period of the homogeneous area of a specimen.

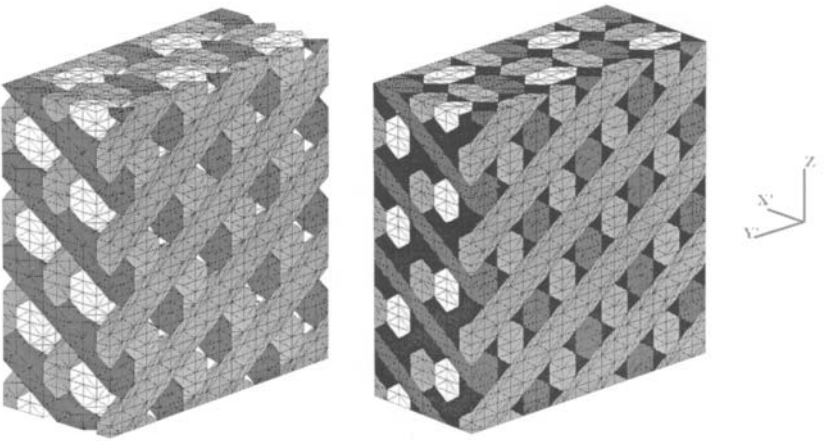

Figure 14: Coarse mesh of the section specimen of direction X'

4.5. Computational tool

To study the influence of edge effects, the structure (a period of the homogeneous zone of a specimen) has to be large enough. The finite-element discretized problem thus assume a very large size (50,000 dof for the mesh presented in Figure 14, with the discretisation being the coarsest, and the section of the specimen being only about 200mm^2). Moreover, it is non-linear because of the behavior (contact with friction) of yarn/yarn and yarn/matrix interfaces. Using a numerical method adapted to such problems then becomes necessary.

The computational strategy proposed by P. Ladevèze [19] is used herein. This approach is based on a formulation and on a strategy that are well-suited to the use of parallel computers. Here, what is sought in the use of this parallelism is, above all, a high degree of both modularity and flexibility in the description of the problem. The principles of this method are detailed in [20]. It leads to a decomposition of the structure into sub-structures and interfaces. The aim is to construct a mechanical and "parallel" algorithm in relying on the mechanical properties of the problem. The contact-type non-linearities are treated in a local and mixed manner through a constitutive law associated with the interfaces. Unlike classical techniques for solving contact and friction problems, this approach does not introduce additional variables (such as Lagrange multipliers) into the global resolution of the problem; these non-linearities are treated locally at the interfaces. More over, this approach leads to a reduction in problem size and costs for larger problems [20], even on sequential computers.

The development of the approach has led to the development, by L. CHAMPANEY, of a semi-industrial prototype software (COFAST 3D). This software has been implemented in the industrial calculation code CASTEM 2000 (developed by CEA: Commissariat à l'Energie Atomique [21]) and uses its pre- and post-processing functions (meshing, stiffness matrice

construction, visualization). Specific procedures have been added in order to use the flexibility of the approach: research and automatic construction of the geometry of interfaces, adapted post-processing procedures.

4.6. Mechanical characteristics of the meso-constituents

The yarn longitudinal Young's modulus has been identified experimentally by S.E.P. [1]. Initially, in order to obtain values of the other mechanical characteristics of the meso-constituents, we have been relying on values presented in [4], with respect to another Carbon/Carbon composite.

The method of identifying mechanical characteristics of the meso-constituents is similar to the one presented in [4]. Tests on sticks are in progress. A traction test will allow obtaining the longitudinal Young's modulus and Poisson's coefficient ν_{12} (with 1 being the longitudinal direction of a yarn). The value of the shear coefficient G_{12} is evauated with a torsion test. The other elastic characteristics will be obtained from the initial macroscopic values of the elastic modulus of the material, using a homogenization technique by the asymptotic development of 3D periodical media, with the interfaces being assumed perfect.

4.7. Initial results

The results presented hereafter are currently almost all qualitative. Nevertheless, the first numerical computations allow validating the different choices made. Indeed, the main effects owing to the presence of the edge problem are obtained.

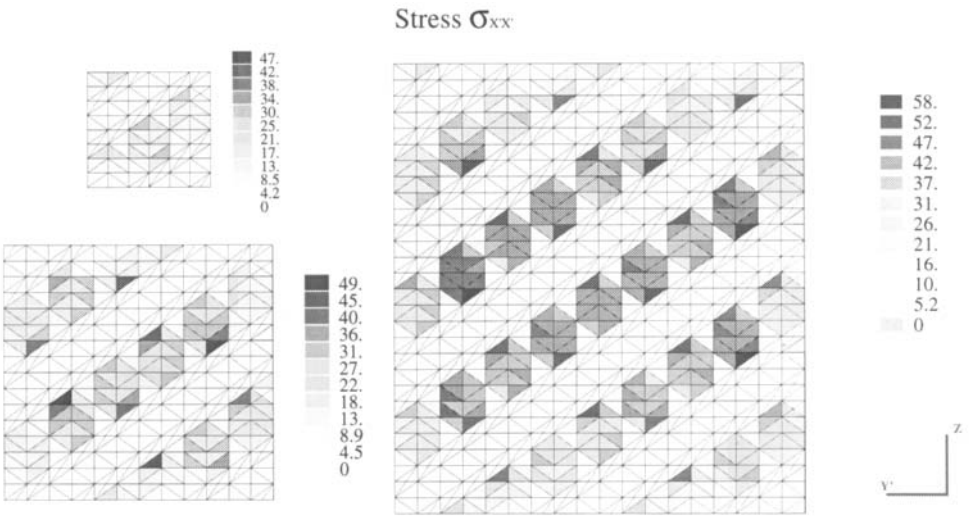

Figure 15: Component X'X' of the stress field in 3 sections with different sizes for the same macroscopic strain.

With an elastic computation (the interfacial behavior is held to be perfect), the presence of the edge effect can already be observed. Figure 15 displays the tension/compression stress fields obtained with 3 sections of different sizes for the same macroscopic strain. One can see very clearly (Fig. 15) on the large section an evolution, between the edge and the heart of the

section, of the stress value in the yarns not perpendicular to the direction of loading. One also notices that the maximum value of the stress increases with the dimensions of the section. These differences in the stress fields presented have an influence on the specimen stiffness, with the stiffness being defined by the ratio of the mean over a period of the tension/compression stress field to the macroscopic strain. The calculated stiffness increases with the section area (Table 1). Therefore, the experimental phenomenon of the initial longitudinal modulus sensitivity to the dimensions of the specimen section is exposed.

Section	1	2	3
Longitudinal modulus (GPa)	11.7	16.6	22

Table 1: Computation results: stiffness value of the specimen as a function of the section size of the specimen.

A second phenomenon observed is the evolution, as a function of the section dimensions, of the specimens, of the maximum stress attained with a tension test. Figure 16 shows the curves (longitudinal strain - longitudinal stress intensity) obtained with the 3 sections presented. The degradation threshold of the interfacial behavior (initially perfect and then frictional contact) chosen for these initial calculations is a limit on the interfacial shear stress value. The experimental phenomenon of specimen stiffening as the specimen dimensions increase is described.

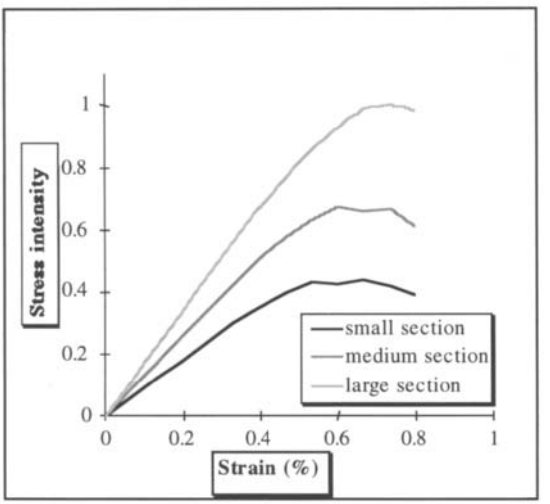

Figure 16: Macroscopic curves (longitudinal strain - stress intensity) obtained by computation

5. CONCLUSIONS AND PERSPECTIVES

An initial model of the internal mechanical behavior of Sepcarb 4D composites has been proposed and identified. In order to easily take into account the prefered directions which are the 4 directions of reinforcements, a model of non-linear behavior has been developed using a

system of barycentric coordination. The elasto-plastic type model with damage thus obtained is very simple since it necessitates only three elastic coefficients, one curve to describe the damage evolution and one curve to describe anelasticity. The identification of this model necessitates only 2 tension tests, a test in a direction of reinforcement with longitudinal and transversal strain measures and an off-yarn axis test with a measure of the longitudinal strain. An experimental point of view towards strengthening the specimen edges allows a simplified identification. The edge effects have been fixed only partially; a stronger protection of the edges is envisaged. Another solution consists of taking into account the influence of the debonding during testing.

The material is then studied at a smaller scale, called the mesoscopic scale, which corresponds to the scale of the material constituents: the fiber yarns, the matrix and their interfaces. A simple model of the mechanical behavior of these meso-constituents is developed: brittle transverse isotropic elastic for the yarns, isotropic elastic for the matrix, and perfect then contact with friction after a brutal damage for the interfaces. With this model, the influence on some of the mechanical macroscopic characteristics (initial Young's modulus and failure stress) of the specimen section dimensions is obtained.

Nevertheless, the results obtained are still only qualitative. In order to carry out a more precise study, it is thus necessary to verify several points: the influence of the mesh size on results, and the influence of the interface degradation criterion, in taking into account the normal stress in the interface, seems to help model the confinement of the material far from a free surface.

ACKNOWLEDGEMENTS

The authers are indebted to DGA for its financial support.

REFERENCES

1. L. Delneste, B. Pérez, An inelastic finite element model of 4D Carbon-Carbon Composites, AIAA Journal Volume 21, Number 8, August 1983, 1983, pp. 1143-1149.

2. P. Ladevèze, On an anisotropic damage theory, Failure criteria of structured media, proceedings of the CNRS International Colloquium n° 351, Villard de Lans, France 1983, J.P. Boehler Editor, A.A Balkema Publishers, 1993, pp. 355-365.

3. P. Ladevèze, O. Allix, C. Cluzel, Damage modelling at the macro and meso scales for 3D composites, Damage in Composite Materials, G. Z. Voyiadjis (Editor), Elsevier Science Publishers B.V., 1993, pp. 195-215.

4. J. P. Dumont, P. Ladevèze, M. Poss, Y. Rémond, Damage mechanics for 3D composites, International Journal of composite structures, Vol 8,1987, 1987, pp. 119-141.

5. J. Lemaitre, A course on damage mechanics, Springer Ed., 1992.

6. P. Ladevèze, M. Poss, L. Proslier, Damage and fracture of tridirectional composites, Proceedings of the 4th International Conference in composite materials, Progress in science and engineering of composites, Volume 1 Tokyo, 1982, pp. 649-658.

7. A. Gasser, P. Ladevèze, M. Poss, Damage mechanisms of a woven Sic/Sic composite: modelling and identification, Composite Science and Technology, V 56 -7, 1996, pp. 779-784.

8. P. Ladevèze, E. L. Dantec, Damage modelling of the elementary ply for laminated composites, Composite Science and Technology, 43-3, 1992, pp. 257-267.

9. X. Aubard, C. Cluzel, L. Guitard, P. Ladevèze, Modelling of the mechanical behavior of 4D C-C composite materials, Special issue of Composite Science and Technology, 1996, to appear.

10. P. Ladevèze, Inelastic strain and damage, in Damage Mechanics of Composite Materials, Ch. 4, Ed R. Talreja, Elsevier, 1994, pp. 117-138.

11. J. W. Hutchinson, H. M. Jensen, Model of fiber debonding and pull-out in brittle composites with friction, Mechanics of materials, 1990, pp. 139-165.

12. P. D. Jero, R. J. Kerans, Effect of interfacial roughness on the frictional stress measured using push-out tests, Journal of the American Ceramic Society, 1991, pp. 2793-2801.

13. A. Domnanovich, H. Peterlik, K. Kromp, Determination of interface parameters for Carbon/Carbon composites by the fiber-bundle pull-out test, Composite Science and Technology, 1996, pp. 1017-1029.

14. P. Brenet, F. Conchin, G. Fantozzi, P. Reynaud, D. Rouby, C. Tallaron, Mesure directe de la contrainte de pontage d'une fissure, une nouvelle approche du comportement à la rupture de composites Céramiques-Céramiques, Comptes-rendus des neuvièmes Journées nationales sur les composites, J.P. Favre & A. Vautrin (eds), AMAC publication, 1994, pp. 1073-1082.

15. E. Sanchez-Palencia, Non-homogeneous media and vibration theory, Lect. Not. Phys., 127, Springer, Heidelberg, 1980.

16. G. Duvaut, Analyse fonctionnelle et mécanique des milieux continus, Theory and Applied Mechanics, Ed. W. KOITER, North Holland, 1976.

17. C. Auriel, G. Boubal, P. Ladevèze, Sur une méthode de calcul des effets locaux, Comptes rendus des JNC3 A. Corvino, C. Bathias, A.R. Bunsell, D. Menkès & G. Verchery eds, Pluralis Publication, Paris, 1982, pp. 279-288.

18. D. Caillerie, Plaques élastiques minces à structures périodiques de période et d'épaisseur comparable, Compte Rendu de l'Académie des Sciences Paris, 1982, pp. 159-162.

19. P. Ladevèze, Mécanique non linéaire des structures : nouvelle approche et méthode de calcul non-incrémentale, Hermes, Paris, 1996.

20. L. Champaney, J. Y. Cognard, D. Dureisseix, P. Ladevèze, Large-scale applications on parallel computers of a mixed domain decomposition method, Computational Mechanics, Vol. 19 n°4, 1997, pp. 253-263.

21. P. Verpaux, T. Charras, A. Millard, CASTEM 2000 une approche moderne du calcul des structures, Calcul des structures et intelligence artificielle (FOUET, J.M., LADEVEZE, P., OHAYON, R., Eds.), Pluralis, 1988, pp. 261-271.

This Page Intentionally Left Blank

PART IV

DAMAGE IN METALS AND METAL MATRIX COMPOSITES

This Page Intentionally Left Blank

Damage Mechanics in Engineering Materials
G.Z. Voyiadjis, J.-W.W. Ju and J.-L. Chaboche (Editors)
© 1998 Elsevier Science B.V. All rights reserved.

Prediction of damaged behavior and failure of a metal matrix composite using a multiscale approach

K. Derrien*, D. Baptiste*, D Guedra-Degeorges**
* Laboratory LM3, ENSAM, CNRS URA 1219, 151 Bd de l'Hôpital 75013 Paris France
Email : baptiste@paris.ensam.fr
** Aérospatiale, Centre Commun de Recherche, 12 rue Pasteur 92152 Suresnes France

INTRODUCTION :

The aerospace industry has demonstrated the feasibility of particulate reinforced MMC structural components, taking advantages of the stiffness, fatigue and friction properties of these materials. MMC prototype component have been introduced in helicopters and aircraft's, and series production will soon become a reality.
As MMCs are very heterogeneous materials, their mechanical properties are highly dependent on their composition: matrix, type and volume fraction of reinforcement, interface between matrix and particles. In order to extend the range of industrial application of MMCs, it is therefore necessary to develop micromechanical models predicting their macroscopic mechanical behavior from their composition. These models will be key tools for the development and optimization of these materials.
Our objective is to predict the tensile behavior, the damage and the failure of an aluminum X2080 reinforced by different volume fraction of silicon carbide, using a micro-macro relationship.

1 Materials and experimental results :

The first stage of this study has been an experimental characterization of powder metallurgy MMCs: aluminum alloy and associated unreinforced aluminum matrix. The results are used as input and validation data for the model.
The materials were made by a powder blending and extruded route.X2080 and X2080 + SiCp (15 and 20%) extruded round bars were used.
All the materials were both T4 heat treated.
The microstructure of MMCs has been characterized using image analysis. The particles are almost aligned in the extrusion direction.
Their average diameter is 12μm, their aspect ratio is 1,5.

The mechanical properties of the matrix and MMC's have been measured from tensile tests. Results are reported in the following table:

Table 1 :
Mechanical Properties

Material	E (GPa)	σult (MPA)	A (%)	ν
Matrix X2080	75	530	19	0.32
X2080+15% SiCp	100	545	6	0.27
X2080+20% SiCp	105	540	3.6	0.28

Introduction of SiC particles in the aluminum alloy results:
- in an increase of the material Young's modulus (high E value of SiC)
- in a decrease in the material ductility

Fractographic investigation fractography has revealed that fracture surface consists of microvoids of sizes ranging from the micron to ten microns. The origin of these voids has been attributed to fracture of either the SiC particles or the inclusions and precipitates.
Ductile failure consists of void nucleation, growth and coalescence stages, the relative importance of each stage should determine the macroscopic ductility of the material.

In order to determine the microstructural damage mechanisms at the origin of the MMC static behavior, tensile tests in-situ in a scanning electron microscope have been carried out..
In the MMCs studied, the main damage mechanism is particle failure which appears in the largest particles or in the most elongated ones just before the macroscopic yield stress of the material. New particles are broken until failure of the specimen which takes place by linking of the microcracks initiated in the matrix from the broken particles.
The fracture plane of most particles is normal to the macroscopic loading axis, indicating that the particles are broken because of the local tensile stress induced in the particle.

Generally statistical criteria are used to describe particles fracture. In this study a Weibull law has been chosen, in which the two important parameters are the particle size and the maximum principal stress in the particle.
The size and aspect ratio distributions of broken particles have been measured during the in-situ tensile tests, the results are used to determine the Weibull parameters of the SiC particles.

The accumulated number of the broken particles increases with the plastic strain imposed to the MMC.In the following graph (fig 1) , the evolution of the ratio of broken particles with the macroscopic plastic strain is plotted as a function of their size and aspect ratio. Larger particles are fractured first at lower strain level , then followed by smaller sized ones at higher strain levels.

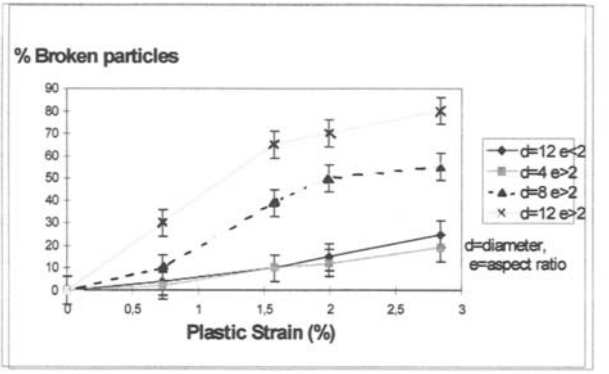

Fig 1 : *Number of broken particles function of the macroscopic strain for different diameter and aspect ratio*

2 Prediction of the tensile behavior of MMCs :

In a second stage of the study, the micromechanical model has been developed and validated with the above mentioned experimental data. The input of the model are, the mechanical properties of the particles which are considered as elastic brittle, the mechanical properties of the matrix which is considered as elastoplastic, the histograms of size and aspect ratio of the particles, the damage criterion at the origin of the failure.
The micromechanical model used to predict the tensile mechanical behavior of MMCs is based on Mori and Tanaka's method and takes into account the plasticity of the matrix and the damage of the constituents.

2 1 Micromechanical model:

Mori and Tanaka's method is based on Eshelby's original work. Its main assumption is contained in the strain localization relation which defines the load sharing between the different constituents. This localization relation is expressed by [1]:

$$\varepsilon_r = T_r \varepsilon_0$$
$$T_r = \left[L_r + L_0\left(S_r^{-1} - I\right)\right]^{-1} L_0 S_r \qquad (1)$$

ε_0, L_0 and ε_r, L_r are the average strain and stiffness tensor of the matrix and the r-th reinforcement respectively. Sr is the Eshelby's tensor.

If a uniform stress Σ is applied to the material, it was shown that the average local stress over the composite is equal to Σ, the corresponding strain in the material is noted E and we have:

$$\begin{aligned} \Sigma &= c_0\langle\sigma\rangle_0 + c_1\langle\sigma\rangle_1 \\ E &= c_0\langle\varepsilon\rangle_0 + c_1\langle\varepsilon\rangle_1 \end{aligned} \tag{2}$$

$\langle\ \rangle_i$ means the volume average value in the volume of the phase i

As a result, the estimation of the composite stiffness tensor can be written as:

$$L = \left(c_0L_0 + \sum_{r=1}^{r=n} c_rL_rT_r\right)\left(c_0I + \sum_{r=1}^{r=n} c_rT_r\right)^{-1} \tag{3}$$

2 2 Elastoplastic behaviour :

The model is extended to the elastoplastic behavior using the concept of secant moduli.
The theory makes use of a linear comparison material, whose elastic moduli at every instant are chosen to coincide with the average secant moduli of the matrix to reflect its elastoplastic behavior state. Following Eshelby's equivalent inclusion principle and Mori-Tanaka's mean field method, the composite is subsequently replaced by the comparison material filled with equivalent transformation strains. The matrix behavior is identified from the tensile stress-strain curve of the unreinforced alloy and the composite stress-strain curve is determined step by step by varying progressively the matrix secant modulus.
This approach differs from the original one proposed by Tandom and Weng [2] by the new definition of the matrix effective stress. The effective stress is not defined in terms of the averaged stress in the matrix alone but in terms of the average elastic distortional energy in the matrix [3-4] .
It can be evaluated from the variation of the effective compliance with respect to the variation of the local shear modulus such as:

$$\sigma_e^2 = \frac{3}{2}\langle\sigma':\sigma'\rangle_0 = \Sigma:\left(-\frac{3\mu_0^2}{c_0}\frac{\delta M}{\delta\mu_0}\right):\Sigma \tag{4}$$

where M is the composite compliance tensor and μ_0 the local shear modulus.

While the original theory [2], is not acceptable for porous materials under a high triaxiality (effective stress is calculated directly from mean deviatoric stress and therefore vanishes under an hydrostatic tension), the new theory is suitable for application for porous materials and high triaxiality loading conditions. Compared to the secant moduli based on the average matrix stress, the proposed method always gives softer predictions in the case of uniaxial loading.

2 3 Damage evolution:

The fracture probability of each particles is a function of its volume V_r and of the maximum principal stress σ_r.
The Weibull's law can be written [5-6]:

$$P_r(\sigma_r, V_r) = 1 - \exp\left(-\frac{V_r}{V_u}\left(\frac{\sigma_r}{\sigma_u}\right)^m\right) \quad (5)$$

m, σ_u, are called shape and scale parameters.
V_r and V_u are the volume of the rth group and that of the reference group for which the Weibull's parameters are determined respectively.
in our case we have [7]:
σ_u=1500MPa
m=4
V_0 is the volume for a particle of diameter 10μm

The number of broken particles are increasing functions of the macroscopic load (Fig 2).
We choose to replace the broken particles by penny shaped cracks located perpendicular to the loading direction and which are oblate spheroids with the major axe being equal to the radius of particles and the minor axe being a function of the external load (Fig 3).

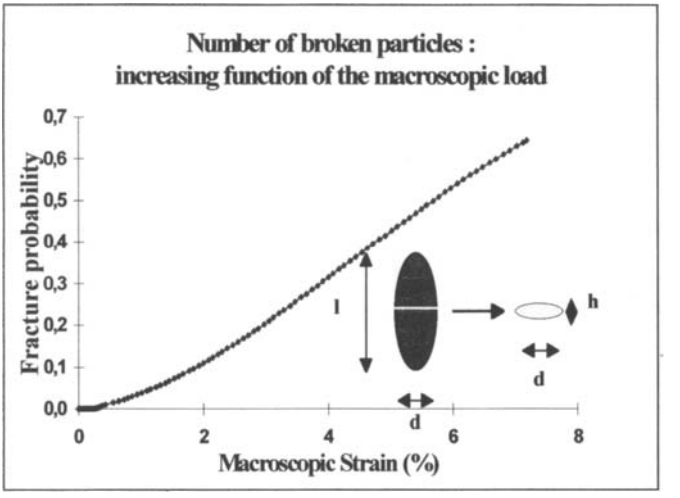

Fig 2 : *Number of broken particles*

The analytical value of the crack opening displacement h is :

$$h = 2b\varepsilon^*_{33} \quad (6)$$

ε^* is the eigenstrain in the crack.

Using Mori Tanaka's method, we have :

$$\varepsilon_r^* = \left(L_0(I - S_r)\right)^{-1}(\sigma_0 - \sigma_r) \tag{7}$$

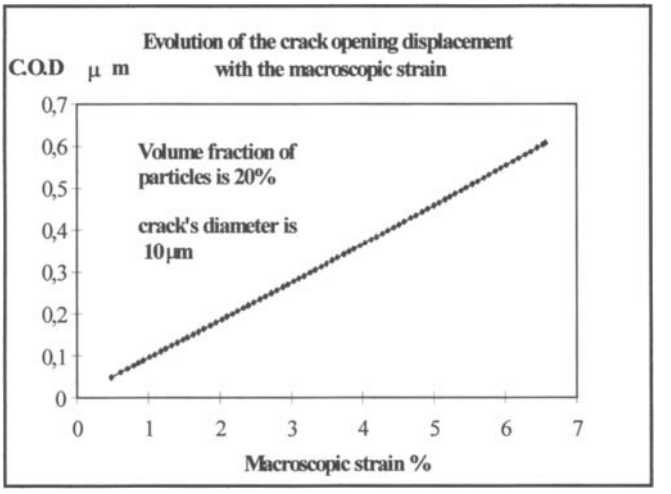

Fig 3 : *Evolution of the C.OD for penny-shape*

The tensile stress-strain curve is calculated step by step by varying progressively the matrix secant modulus and introducing broken particles.
composite elastic moduli are a function of the volume fraction of both unbroken and broken particles. since the number of broken particles is a function of external macroscopic loading, the evolution of Young's modulus can be predicted during the simulation of a stress-strain curve.

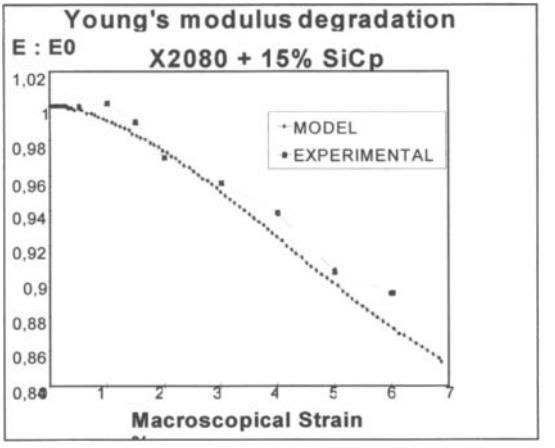

Fig 4 : *Young's modulus evolution during a tensile test*

3 Prediction of failure :

Regions of the matrix adjacent to broken particles are sites with high hydrostatic tension and hence the nucleation of cavities is expected. The failure between adjacent broken particles appears to occur by intense growth of these cavities in the matrix. The origin of these microvoids is attributed to failure of inclusions and precipitates. The nucleation and growth of these cavities near the penny-shaped cracks is governed by high value of the strain near the crack tip in shear bands.
In order to predict the failure we have to calculate the growth of these voids.
Macroscopic failure is governed by a critical volume fraction of voids.

3 .1 Stress and strain fields near the crack :

The strain distribution at the crack tip is obtained from HRR solution.
Following the HRR solution, the equivalent plastic strain $\varepsilon^p(r,\theta)$ of the dominant J region is represented by [8] :

$$\varepsilon^p(r,\theta) = \left(\frac{J}{\sigma_y I_n r}\right)^{\frac{N}{N+1}} \varepsilon^p(N,\theta) \qquad (8)$$

r : distance from the crack tip
σ_y : yield strength
I_n : integral constant

The original HRR solution is not suitable for porous material because the yield criterion used is a Von Mises criterion. In our case we want to take into account the local porosity due to decohesion of precipitates. So we have modified the original theory, following the same procedure used by Li and Pan [9].
The yield criterion we use is calculated with Mori Tanaka's model [10]

$$\Psi(\Sigma_{ij}) = 3a.\Sigma_m^2 + b.\Sigma_e^2 \qquad (9)$$

with $a = \frac{9 + 6c_p}{9(1-c_p)^2}$ $\quad b = \frac{9c_p}{4(1-c_p)^2}$

c_p : volume fraction of microvoids near penny-shaped crack

$$\sigma e^2 = 3a.\Sigma_m^2 + b.\Sigma_e^2 \qquad (10)$$

by taking a=0 and b=1 (Von Misès) we can find HRR solutions in all the followed equations.

$$\frac{\partial \sigma e}{\partial \sigma_{ij}} = \frac{a\Sigma m}{\Sigma e}\delta_{ij} + \frac{3bs_{ij}}{2\Sigma e} \qquad \Sigma e^2 = \frac{3}{2}s_{ij}s_{ij} \tag{11}$$

$$\delta_{ij} = 0 \text{ if } i \neq j \qquad \delta_{ij} = 1 \text{ if } i = j$$

We suppose that the stress-strain relation in the matrix can be written like :

$$\frac{\varepsilon}{\varepsilon y} = \frac{\sigma}{\sigma y} + \alpha\left(\frac{\sigma}{\sigma y}\right)^n \tag{12}$$

where n is the strain hardening exponent, α is material constant , σy and εy are the yield stress and yield strain.

Using the equations 10 and 11 we can generalize the equation 12 to a multiaxial stress state. We suppose that the hardening plasticity is isotropic and that the plastic deformation obey to the normality rule. Then we obtain the relation between the plastic stress and plastic strain :

$$\frac{\varepsilon_{ij}^p}{\varepsilon_0} = 3\alpha\left(\frac{\sigma_e}{\sigma_0}\right)^n\left(\frac{b.s_{ij}}{2\sigma_e} + \frac{a.\Sigma_m\delta_{ij}}{3\sigma_e}\right) \tag{13}$$

With the condition of plane deformation we have :

$$\frac{3bs_{11}}{2\sigma e} + \frac{a\Sigma m}{\sigma e}\delta_{ij} = 0 \tag{14}$$

We solve the equation 14 and we determine :

$$\Sigma m = \frac{3b(\Sigma_{22} + \Sigma_{33})}{6b + 2a} \tag{15}$$

And solving the equation 14 and 15 we can write :

$$\frac{\varepsilon_{22}^{p}}{\varepsilon y}=\frac{3\alpha}{2\sigma e}\left(\frac{\sigma e}{\sigma y}\right)^{n}\left[\frac{\left(3b^{2}+4ab\right)\Sigma_{22}+\left(2ab-3b^{2}\right)\Sigma_{33}}{6b+2a}\right] \tag{16a}$$

$$\frac{\varepsilon_{33}^{p}}{\varepsilon y}=\frac{3\alpha}{2\sigma e}\left(\frac{\sigma e}{\sigma y}\right)^{n}\left[\frac{\left(3b^{2}+4ab\right)\Sigma_{33}+\left(2ab-3b^{2}\right)\Sigma_{22}}{6b+2a}\right] \tag{16b}$$

$$\frac{\varepsilon_{23}^{p}}{\varepsilon y}=\frac{3\alpha}{2\sigma e}\left(\frac{\sigma e}{\sigma y}\right)^{n}\left(b\sigma_{23}\right) \tag{16c}$$

Using the same method we calculate $\sigma e=\left(3a\Sigma m^{2}+b\Sigma e^{2}\right)^{\frac{1}{2}}$

$$\frac{\Sigma e}{\sqrt{3}}=\left\{\frac{(3b+2a)^{2}-6ab}{(6b+2a)^{2}}\left(\Sigma_{22}^{2}+\Sigma_{33}^{2}\right)+\frac{6a^{2}-2(3b+a)^{2}}{(6b+2a)^{2}}\Sigma_{22}\Sigma_{33}+\Sigma_{23}^{2}\right\}^{\frac{1}{2}} \tag{17}$$

$$\frac{\sigma e}{\sqrt{3}}=\left\{\frac{3ab^{2}+b(3b+2a)^{2}}{(6b+2a)^{2}}\left(\Sigma_{22}^{2}+\Sigma_{33}^{2}\right)+\frac{24ab^{2}-2b(3b+a)^{2}}{(6b+2a)^{2}}\Sigma_{22}\Sigma_{33}+b\Sigma_{23}^{2}\right\}^{\frac{1}{2}} \tag{18}$$

We calculate the crack tip singularity field like Hutchinson, Rice and Rosengren [6]

With reference to polar coordinates, r and θ , centered at the crack tip, the asymptotic crack-tip stress, strain and displacement fields are :

$$\sigma_{ij}=\sigma y\left[\frac{J}{\alpha\varepsilon y\sigma y I(n,a,b)r}\right]^{\frac{1}{n+1}}\tilde{\sigma}_{ij}(\theta,a,b) \tag{19a}$$

$$\varepsilon_{ij}=\alpha\varepsilon y\left[\frac{J}{\alpha\varepsilon y\sigma y I(n,a,b)r}\right]^{\frac{n}{n+1}}\tilde{\varepsilon}_{ij}(\theta,a,b) \tag{19b}$$

$$u_{i}=\alpha\varepsilon y r\left[\frac{J}{\alpha\varepsilon y\sigma y I(n,a,b)r}\right]^{\frac{n}{n+1}}\tilde{u}_{i}(\theta,a,b) \tag{19c}$$

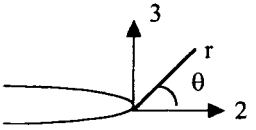

In is a dimensionless constant

$$I = \int_{-\pi}^{\pi}\left[\frac{n}{n+1}\sigma e^{n+1}\cos\theta - \left[\sin\theta\left(\tilde{\sigma}_{rr}\left(\tilde{u}_\theta - \tilde{u}_r^{\bullet}\right) - \tilde{\sigma}_{r\theta}\left(\tilde{u}_r + \tilde{u}_\theta^{\bullet}\right)\right) + \frac{\cos\theta}{n+1}\left(\tilde{\sigma}_{rr}\tilde{u}_r + \tilde{\sigma}_{r\theta}\tilde{u}_\theta\right)\right]\right]d\theta \qquad (20)$$

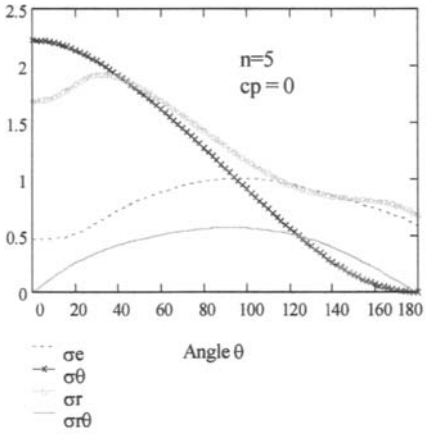

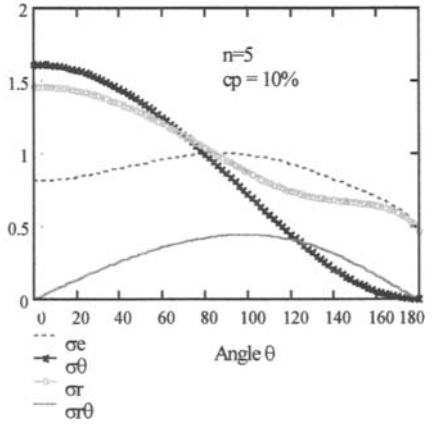

Fig 5 : *The θ-variations of the normalized stresses for n=5*

The θ–variations of the dimensionless functions $\tilde{\sigma}_{ij}$, $\tilde{\varepsilon}_{ij}$ and $\tilde{u}_i$ depend on n. These variations are normalized by setting the maximum value of the θ-variation of the effective stress $\tilde{\sigma}_e = \left[\left(\frac{3}{2}\right)\tilde{s}_{ij}\tilde{s}_{ij}\right]^{1/2}$ to unity

The θ-variations of the stresses are represented in figure 5. A comparison of the stress plots shows that for a fixed n, a large fraction of voids results in a small $\sigma_{\theta\theta}$, a small σ_{rr}. The generalized effective stress is found to peak between 90 and 100 deg for all the cases.
We find the same tendency as Li and Pan, but the advantage of our method is to be directly dependent of the volume fraction of voids c_p.

Thus the HRR modified singularity in conjunction with the value of J completely specifies the near crack tip fields.
J represents the amplitude of the singular fields. We calculate J using MTanaka's model [11]:

The energy release rate of a penny-shaped crack can be defined as

$$J = \frac{1}{2\pi r}\left|\frac{\partial P}{\partial r}\right| \qquad (21)$$

$$P = P_0 + E_{int} = P_0 + \frac{1}{2}\sigma\varepsilon^* V_c$$

P is the total potential energy
P_0 is the total potential energy without any inhomogeneity and Eint is the interaction energy between the applied stress and the inhomogeneity

V_c is the volume of the penny-shaped crack and ε* is the eigenstrain in the crack.

$$\varepsilon_c^* = \left(L_0(I - S_c)\right)^{-1}\Sigma \qquad (22)$$

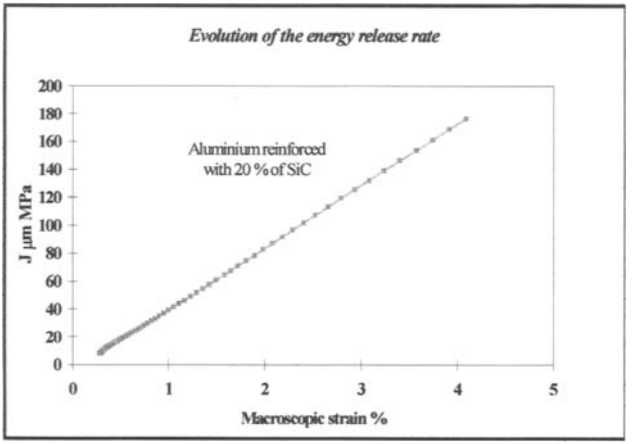

Fig 6 : *Energy release rate*

3.2 Growth of micro-voids :

With the yield criterion (eq 9) we can calculate the growth of cavities in a porous material :

$$\mathrm{Ln}\left(\frac{R}{R_0}\right) = \varepsilon_e \frac{9}{4\left(3+2c_p\right)} \frac{\Sigma_m}{\Sigma_e} \tag{23}$$

R_0 : initial radius of precipitate

$\frac{\Sigma_m}{\Sigma_e}$: triaxiality rate near the crack

c_p : volume fraction of cavities

The volume fraction of microvoids is a function of the strain field near the crack :

$$\partial c_p = (1-c_p)\, \partial \varepsilon_{kk} \tag{24}$$

3.3 Failure criterion :

The macroscopic failure begins by the failure of the matrix between to broken particles. This failure will be easier if the distance between these particles is short (this is the case for a composite reinforced by a high fraction of particles). Thus our criterion has to depend on the growth of cavities and of the volume fraction of particles.
Our criterion is that macroscopic failure is governed by a critical growth of cavities at half of the distance d between two broken particles

$$2d_f = R \cdot \left(\sqrt{\frac{2\pi}{3f}} - \sqrt{\frac{8}{3}}\right) \tag{25}$$

f : volume fraction of particles
2R : diameter of particles

This critical distance depends on the volume fraction of particles

We don't have experimentally values of the critical growth which provides the failure . However we can compare composites reinforced with different fraction of particles.
If we know the macroscopic strain failure for a composite reinforced with 15% of particles, we can calculate the critical growth of cavities at the distance $d_{15\%}$ For the other composites the failure will provide when this critical growth will be obtained at the distance d_f.

The results are represented in figure 7.

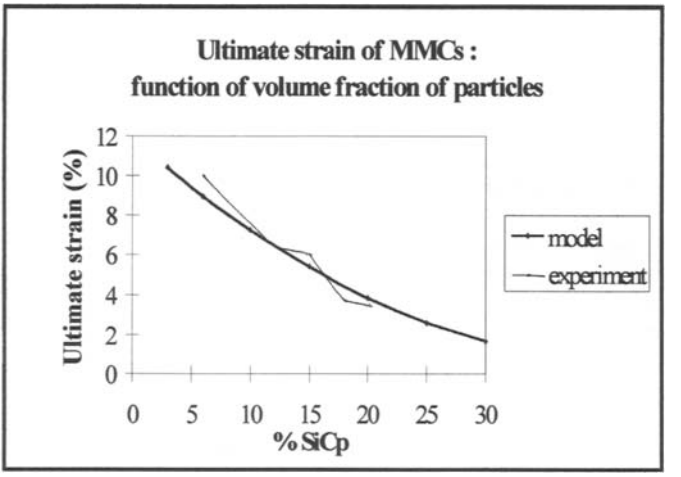

Fig 7 : *Evolution of the failure strain of the composite as a function of the particles volume fraction*

CONCLUSION :

The use of a micromechanical model to predict the failure provides good results. It takes into account the microstructure of the material, the mechanical properties of the constituents and so it can be easily extended to other composites. The advantage of the model is to be key tool for the development and optimization of composites materials.
In this study we suppose that we have an homogeneous repartition of particles which can be a restriction for the use of the model. So we have recently develop a model providing the effect of a particle distribution on deformation behavior of particulate metal matrix composite [10].

REFERENCES :

1. Mori T , Tanaka K
Average stress in matrix and average elastic energy of materials with misfitting inclusions
Acta Metall, vol 21, 1973, pp571-574

2. Tandon G.P., Weng G.J.
A theory of particle reinforced plasticity
Journal of Applied Mechanics , March 1988, vol 55 / 126-135

3. Qiu Y.P.,Weng G.J.
A Theory of plasticity for porous materials and particle-reinforced composites
Journal of Applied Mechanics, June 1992, vol59 /261-268

4. Hu Gengkai
A method of plasticity for general aligned spheroidal void or fiber reinforced composites
International Journal of Plasticity, vol 12, n°4, pp 439-449 1996

5. Mochida T, Taya M, Lloyd D.J
Fracture of particles in a particle/metal matrix composite under plastic straining and its effect on the Young's modulus of the composite
Mat Tansactions, JIM, vol32, n°10 (1991), pp 931-942

6. Bourgeois N, Derrien K, Baptiste D
Observation and modeling of damage evolution in particulate reinforced MMCs
Proceedings of ICCM-10, Whistler, B.C, Canada, August 1995

7. Derrien K
Caractérisation Expérimentale et Etude Théorique de l'Evolution de l'Endommagement dans des Composites Al/SiCp
AMAC/MECAMAT 30/31 mai 1995,Micromécanique et mécanismes de l'endommagement

8. Hutchinson J.W.
Singular behaviour at the end of a tensile crack in a hardening material
J.Mech Phys Solids, 1968, vol 16, pp 13-31

9. Li F.Z, Pan J
Plane strain crack tip fields for pressure sensitive dilatant materials
Journal of applied mechanics, vol57, march1990 pp40-49

10.Derrien K
"Approche micromecanique de la rupture d'un composite matrice metallique"
Thèse E.N.S.A.M 1997

11.Mura Toshio
Micromechanics of defects in solids
second revised edition, Martinus Nijhoff Publishers 1988

Damage Mechanics in Engineering Materials
G.Z. Voyiadjis, J.-W.W. Ju and J.-L. Chaboche (Editors)
1998 Elsevier Science B.V.

Effect of Microstructural Architecture on Flow/Damage Surfaces for Metal Matrix Composites

Cliff J. Lissenden[a] and Steven M. Arnold[b]

[a]Department of Engineering Science and Mechanics, Penn State University
227 Hammond Building, University Park, PA 16802 USA

[b]Life Prediction Branch, NASA Lewis Research Center
MS 49-7, Cleveland, OH 44135

ABSTRACT

Flow/damage surfaces are defined using a thermodynamics basis in terms of stress, inelastic strain rate, and internal variables. The most meaningful definition for viscoplasticity, surfaces of constant dissipation rate, is investigated for a unidirectional silicon carbide/titanium composite system using two micromechanics approaches; finite element analysis of a unit cell and the generalized method of cells. Damage, in terms of fiber/matrix debonding, is accounted for when a tensile interfacial traction is present. Three types of periodic microstructural architectures are considered; rectangular packing, hexagonal packing, and square diagonal packing. The microstructural architecture is observed to influence the shape and location of flow/damage surfaces and becomes more important as the fiber volume fraction increases.

1. INTRODUCTION

The advent of man-made fiber-reinforced composite materials some forty years ago enabled the design of more efficient structures and greatly expanded the domain of engineered materials. Recent developments in the processing of unidirectional metal matrix composites (MMCs) provide new opportunities for engineers and materials scientists to tailor microstructural architecture for specific applications. For example, placing individual fibers in photo-etched grooves in foils of matrix material results in a very uniform microstructure. Since the grooves hold the fiber in place during consolidation, we can engineer the microstructure by simply specifying the foil thickness and groove pattern. The question that we attempt to answer herein is 'how does microstructure effect the overall inelastic material response in the presence of multiaxial stress states?' Furthermore, for silicon carbide/titanium (SiC/Ti) composites the bond between the constituents is weak and this damage mode, when active, can greatly affect the overall material response. This affect is large or small depending on the interfacial tractions, which are dictated largely by the applied loading.

We consider the influence of microstructural architecture effects using micromechanics, by employing both a finite element analysis (FEA) approach and the generalized method of cells (GMC) approach developed by Paley and Aboudi (1992) (and further extended by Aboudi, 1995). Practical implications on experimental programs and continuum modeling are addressed. Since the material response is viscoplastic, we consider surfaces geometrically analogous to yield surfaces and include the effects of damage in their definition. In order to demonstrate how fiber/matrix debonding influences overall inelasticity we sometimes show results for the more fictitious strong bond case. We pay particular attention to definitions which indicate the onset of inelasticity, in order to stay within a consistent thermodynamical framework. This research merges and builds upon two recent publications; one dealing with microstructural architectures subjected to uniaxial loadings (Arnold et al, 1996a) and the other with macroscale flow/damage surfaces (Lissenden and Arnold, 1997a) given a fixed architecture.

1.1 Uniaxial Response

The effect of microstructural architecture on the uniaxial response of MMCs to axial (parallel to fiber direction) and transverse (normal to fiber direction) loading is well documented. There is very little effect for axial loading, but a significant effect for transverse loading, particularly in the inelastic regime. Arnold et al (1996a) provide the starting point for the current study as well as an extensive literature review on the subject. In this sequel we consider aligned continuous silicon carbide reinforcement of a titanium matrix. For a model SiC/Ti system we chose the SCS-6 fiber and TIMETAL-21S matrix system having 35% fiber volume content. The constituent response for uniaxial tensile loading is shown in Fig. 1. The fiber response is taken to be linear elastic and temperature independent, while the matrix response is elastic-viscoplastic and temperature dependent.

SiC/Ti stress-strain response is complex, even for uniaxial loading, because it exhibits a distinct direction-dependence. Tensile and compressive stress-strain responses to axial and transverse loading at room temperature (23°C) are shown in Fig. 2. Very little overall inelasticity is evident in the axial response as it is fiber-dominated and thermal residual stresses cause the proportional limit to be smaller when subjected to tensile loading than when a compressive loading is applied (see Fig. 2a). For transverse loading the proportional limit is also smaller for tensile loading than for compressive loading (Fig. 2b), but the cause is fiber/matrix debonding (for experimental results see, for example, Majumdar and Newaz, 1992). The transverse response is dominated by the matrix behavior as well as the weak interface. Not only are tensile and compressive responses different for both

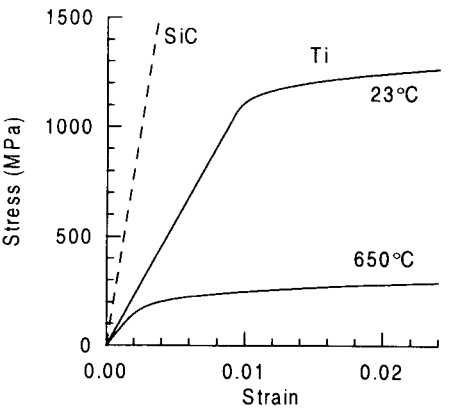

Figure 1: Predicted constituent response for SiC fiber and Ti matrix

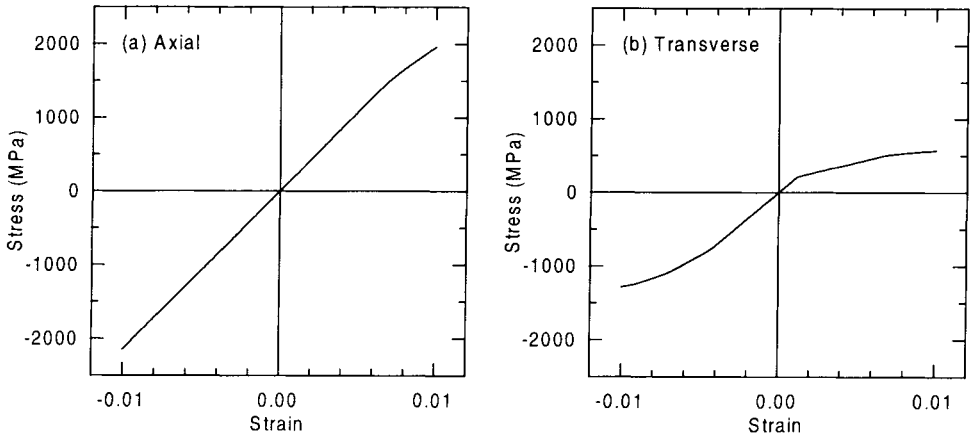

Figure 2: Response of SiC/Ti to (a) axial and (b) transverse loading

axial and transverse loadings, but of course the axial response is different than the transverse response.

1.2 Multiaxial Response

SiC/Ti is a candidate material for components in advanced aeropropulsion systems. The stress state in many of these components; such as rings, shafts, and impellers; is multiaxial -- prompting the question, 'Can we infer the multiaxial material response from the laboratory-measured uniaxial response?' If this were possible, then the additional complexity associated with multiaxial experimentation could be avoided. Otherwise, multiaxial experiments are necessary.

Consider the construction of a surface of constant deviation from proportionality (SCDFP) from uniaxial test data. A SCDFP is defined in a similar fashion to a yield surface; by an offset strain. However, for a SCDFP the offset is defined in the presence of stress, and thus includes inelasticity and damage. Figure 3 shows the four points associated with uniaxial loading in the axial-transverse stress plane as well as the complete SCDFP. It does not seem possible to construct the complete SCDFP from uniaxial data with no *a priori* knowledge of the overall multiaxial response, due to the irregular geometric shape of the SCDFP.

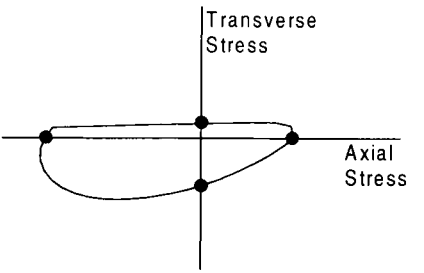

Figure 3: Surface of constant deviation from proportionality and the associated points for uniaxial loading

2. INELASTIC FLOW

Our subject is the inelastic response of metal matrix composites for applications involving elevated temperature environments. Hence, the viscoplasticity of anisotropic composite materials susceptible to internal damage must be addressed. From the viewpoint of structural analysts investigating complex components, a macroscale continuum model is preferred due to

its numerical efficiency relative to the alternative, micromechanics analysis. However, such a continuum model is not currently available; nor are the exploratory, characterization, and validation experiments required to develop such a model. Thus, in the present study we will use a theoretical framework appropriate for continuum modeling to guide us and employ two micromechanics models to numerically perform the required experiments so as to understand the theoretical and experimental implications and/or assumptions necessary in either approach (continuum or micromechanics).

2.1 Theoretical Framework

The theoretical considerations used in this paper are based on an energy balance. The primary variables are the Cauchy stress tensor, σ_{ij}, the internal stress tensor, α_{ij}, and temperature, T. Other internal state variables could also be defined and used. The current values of these variables can be used to define the Gibbs thermodynamic potential, $G = G(\sigma_{ij}, \alpha_{ij}, T)$. Conjugate to these variables are the total strain tensor, ε_{ij}, the internal strain tensor, $\mathcal{A}_{ij}$, and the entropy, S,

$$\varepsilon_{ij} = -\frac{\partial G}{\partial \sigma_{ij}} \qquad \mathcal{A}_{ij} = -\frac{\partial G}{\partial \alpha_{ij}} \qquad S = -\frac{\partial G}{\partial T}. \tag{1}$$

Our basis is that the total work performed on the system must be equal to the sum of the stored energy and the energy dissipated, where the stored energy includes an elastic component as well as an inelastic component associated with the internal state. Thus, the dissipation potential, $\Omega = \Omega(\sigma_{ij}, \alpha_{ij}, T)$, can be defined to be $\sigma_{ij}\dot{\varepsilon}^I_{ij} - \alpha_{ij}\dot{\mathcal{A}}_{ij}$.

The associated flow law and evolution equations are given by normality,

$$\dot{\varepsilon}^I_{ij} = \frac{\partial \Omega}{\partial \sigma_{ij}} \qquad \dot{\mathcal{A}}_{ij} = -\frac{\partial \Omega}{\partial \alpha_{ij}} \qquad \dot{\alpha}_{ij} = Q^{-1}_{ijkl}\dot{\mathcal{A}}_{kl}, \quad \text{where} \quad Q_{ijkl} = -\frac{\partial^2 G}{\partial \alpha_{ij}\partial \alpha_{kl}} \tag{2}$$

and Q_{ijkl} is called the internal compliance operator. Thus, once the functional dependencies of the Gibbs and dissipation potentials have been determined, all of the variables are known by simple differentiation. Let us now assume that the dissipation potential can be written in terms of two scalar functions, $\Omega = \Omega(F,G)$, where F depends on the deviatoric effective stress, Σ_{ij}, and G depends only on the internal stress (Robinson and Ellis, 1986). The deviatoric effective stress is the difference between the deviatoric Cauchy stress and the deviatoric internal stress. Now the flow law can be written, $\dot{\varepsilon}^I_{ij} = \frac{\partial \Omega}{\partial F}\frac{\partial F}{\partial \sigma_{ij}}$. Thus, the direction of the inelastic strain rate vector is normal to surfaces having F=constant. However, if it is true that the normality condition is not satisfied in MMCs, as indicated by Nigam et al (1994) for boron/aluminum, then it becomes necessary to develop a nonassociated flow law and evolution equations. We will return to this issue after discussing various surface definitions.

2.2 Surface Definitions

The concept of a yield surface is well known in rate-independent plasticity, even if no one definition of yielding has been universally adopted. The most common definitions employed

are the proportional limit, a small (usually 5 to 20×10^{-6}) offset strain, a back-extrapolation, and a large (usually 0.2%) offset strain. For rate-dependent plasticity (viscoplasticity), the concept of a strict yield surface breaks down as stress states outside the yield surface are assessable (since no consistency condition applies). Thus the need for geometrically analogous, thermodynamically based, flow surface definitions. Two different rate-dependent definitions have been proposed;

1) surfaces of constant dissipation rate (SCDRs), defined by $\sigma_{ij}\dot{\varepsilon}^I_{ij} - \alpha_{ij}\dot{\lambda}_{ij}$ and

2) surfaces of constant inelastic strain rate (SCISRs), defined by $\sqrt{\dot{\varepsilon}^I_{ij}\dot{\varepsilon}^I_{ij}}$.

Lissenden and Arnold (1997a) demonstrated, using micromechanics, that the direction of the overall inelastic strain rate vector can differ significantly from the outward normal of a SCISR. Whereas for the stress planes considered, the direction of the overall inelastic strain rate vector was reasonably close to the outward normal of the SCDRs considered. On the other hand, SCISRs may be more amenable to experimental methods than are SCDRs because stress quantities are not included in the definition.

Consider, for example, an **isotropic** monolithic metal. The effect of hydrostatic stress on the flow of most metals is quite small and usually neglected. Flow behavior can then written in terms of the deviatoric stress invariants $J_2 = \frac{1}{2}\Sigma_{ij}\Sigma_{ij}$ and $J_3 = \frac{1}{3}\Sigma_{ij}\Sigma_{jk}\Sigma_{ki}$ by taking

$$F = \frac{\left(J_2^3 + cJ_3^2\right)^{1/3}}{k^2} - 1 \tag{3}$$

where c is an experimentally determined constant and k is the yield stress (Drucker, 1949). If the metal is near the virgin state, i.e. $\alpha_{ij} \approx 0$, SCDRs and SCISRs are described by

$$\sigma_{ij}\dot{\varepsilon}^I_{ij} = 2k^2(F+1)\frac{\partial\Omega}{\partial F} \tag{4}$$

$$\sqrt{\dot{\varepsilon}^I_{ij}\dot{\varepsilon}^I_{ij}} = \frac{\sqrt{2}}{k^3(F+1)}\left\{\left[(F+1) + \frac{cJ_3^2}{k^6(F+1)^2}\left(1 - \frac{8}{27}c\right)\right]J_2^2 + \frac{2c^2J_3^2}{k^6(F+1)^2}J_4\right\}^{1/2}\frac{\partial\Omega}{\partial F} \tag{5}$$

respectively. Clearly, SCDRs are proportional to surfaces of constant F in general SCISRs are not. However, if the effect of J_3 is negligible, i.e. c=0, then SCISRs are also proportional to surfaces of constant F. A similar argument has been made for selecting SCDR's over those of SCISR's in the case of anisotropic J_2 materials as well. Also, Lissenden and Arnold (1997a) extrapolated these results to rate-independent plasticity by considering $\Sigma_{ij}\varepsilon^I_{ij}$ and $\sqrt{\frac{2}{3}\varepsilon^I_{ij}\varepsilon^I_{ij}}$, where the latter is the usual equivalent inelastic strain definition, and found results analogous to those for SCDRs and SCISRs.

One major difference exists between the above definitions and common flow surface definitions, and that is that the overall inelastic strain ε^I_{ij}, and its rate, include the effect of

fiber-matrix debonding in that we define the inelastic strain to be the strain that deviated from proportionality. Hence, the acronym SCDFP, indicating a surface of constant deviation from proportionality. A SCDFP is a yield surface if and only if there is no debonding.

2.3 Factors Influencing Flow

Many factors influence inelastic flow in metallic materials. Certainly, temperature and loading rate as well as the past loading history can be important in many metals. Additionally, microstructural architecture, degree of anisotropy, fiber-matrix bond strength, and damage influence flow in composites. Other factors, such as the stress plane, definition, and target value influence how flow is represented. Lissenden and Arnold (1997a,b) illustrated the effects of many of these factors. The current paper focuses on the influence of microstructural architecture and fiber-matrix bond strength. We consider repeating microstructures, specifically ones having rectangular, hexagonal, and square diagonal fiber packing arrays as shown in Fig. 4. The rectangular array has an aspect ratio, $R = a/b$. For the special case of a square array, R=1. Additionally, we consider strong and weak fiber-matrix bonding. Our definition of strong is that there is no discontinuity in the displacement field at the interface, likewise weak means that the interface can transmit a finite traction before debonding causes the fiber and matrix to separate.

3. MICROMECHANICS

Biaxial experiments on unidirectional continuous-fiber reinforced SiC/Ti (35% fiber by volume, unless noted otherwise) in the axial-transverse (σ_{11}-σ_{22}) and transverse-transverse (σ_{33}-σ_{22}) stress planes were simulated numerically using micromechanics. Initial overall (macroscopic) flow/damage surfaces were mapped out by probing at different angles in the various stress planes. After each probe the material state was returned to its virgin state.

3.1 Finite Element Analysis

The commercial FEA program ABAQUS (HKS, 1995) was used to determine overall stresses and strains in the repeating unit cells of interest, shown in Fig. 5a. Generalized plane strain triangular elements were used. Only SCDRs for strongly bonded SiC/Ti were considered using FEA. Overall inelastic strain components were calculated as the difference between the total strain components, found by volumetric averaging, and the elastic strain, found from the overall stress (volumetric average) and elastic properties. While no mesh convergence studies were performed, the discretization of the square array has been shown to give good overall results (Lissenden and Herakovich, 1995).

3.2 Generalized Method of Cells

The generalized method of cells (GMC) (Paley and Aboudi, 1992; Aboudi, 1995) is an approximate analytical micromechanics model that extends the original method of cells (Aboudi, 1991) to an arbitrary number of subcells, permitting the study of different microstructures. The reader is referred to Aboudi (1995) for the detailed equations of GMC. The method employs standard micromechanics relations. Elastic and inelastic/thermal strain concentration tensors, A_{ijkl} and D_{ijkl}, respectively, are determined for each subcell and the effective elastic stiffness tensor, B^*_{ijkl}, defined from them. GMC has been implemented into

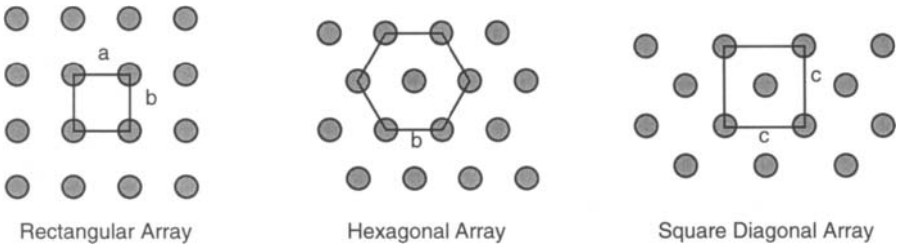

Figure 4: Repeating Microstructures

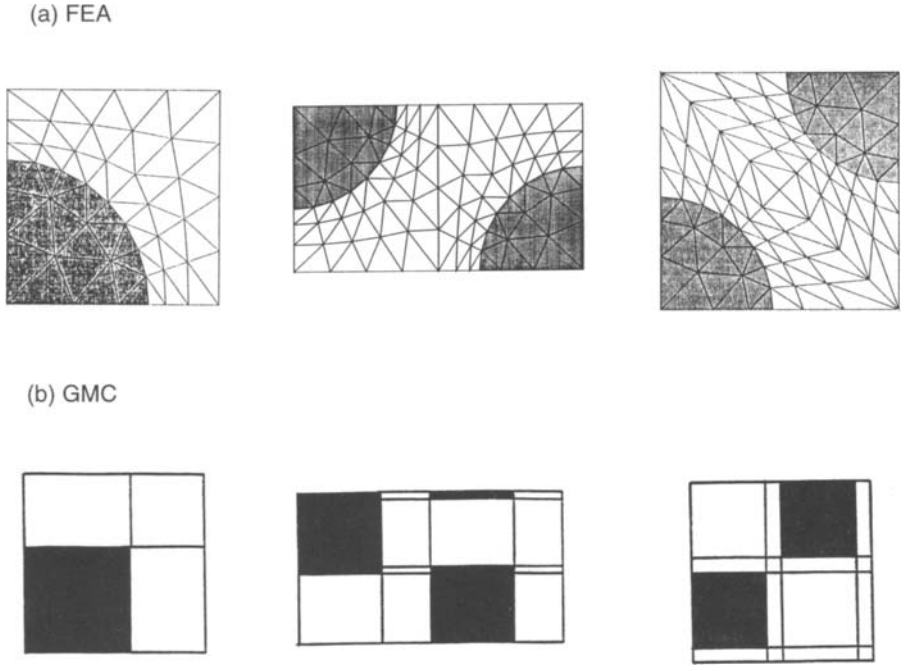

Figure 5: Square, hexagonal, and square diagonal discretizations for (a) FEA and (b) GMC

the micromechanics analysis code (MAC) which has many user friendly features and significant flexibility (Wilt and Arnold, 1996). GMC discretizations for rectangular, hexagonal, and square diagonal arrays are shown in Fig. 5b.

3.3 Constituent Models

As mentioned previously, the fiber response is assumed to be linear elastic and temperature independent. The elastic-viscoplastic behavior of the matrix is represented using a generalized viscoplastic potential structure (GVIPS) model (Arnold et al, 1996b,c). This model is a fully associative, multiaxial, nonisothermal, nonlinear kinematic hardening viscoplastic model for use with initially isotropic metallic materials. A unique aspect of this model is the inclusion of nonlinear hardening through the use of a compliance operator Q_{ijkl} in the evolution law for the back stress. This nonlinear tensorial operator is significant in that it allows both the flow and evolutionary laws to be fully associative and greatly influences the multiaxial response under nonproportional loading paths.

Weak bonding between the fiber and matrix is modeled by assuming that a jump in the displacement field may occur under certain conditions, while the traction vector remains continuous. In this model debonding initiates when the normal traction exceeds a critical value or when the tangential traction exceeds a critical value, with no interaction between the two. Once debonding has initiated, the interfacial displacement rate is made proportional to the stress rate. In the results for SiC/Ti with a weak bond the critical traction value has been taken to be 103 MPa and the ratio of interfacial displacement rate to stress rate after debonding has been taken to be 0.271 mm/MPa.

4. RESULTS

Flow/damage surfaces are mapped out in a specific stress plane by probing the surface in a number of directions from the origin. A point on the surface is found when the prescribed target value of the appropriate definition (SCDFP, SCDR, or SCISR) is surpassed. The material state is then returned to the virgin condition and the next probe initiated. The equivalent loading rate for all FEA probes was 2 MPa/sec, whereas GMC probes were actually conducted under strain control at a rate equivalent to the 2 MPa/sec in the elastic region.

FEA-determined SCDRs in the axial-transverse and transverse-transverse stress planes for target values of 1, 5, and 10 kPa/sec are shown in Fig. 6. These surfaces are for a strongly bonded SiC/Ti at room temperature and include thermal residual stresses. Both square (i.e. rectangular packing with R=1) and square diagonal fiber architectures are shown. Square and square diagonal architectures were considered because in previous work (FEA work by Brockenbrough et al, 1991; GMC work by Arnold et al, 1996a) these two architectures resulted in extremes in the overall uniaxial stress-strain response, where square packing was the stiffest and square diagonal packing was the most compliant. The observation that axial stress-strain response is unaffected by microstructure (Brockenbrough et al, 1991) is corroborated by Fig. 6. Additionally, Fig. 6 shows that SCDRs with different target values are not in general concentric. We hypothesize that this is related to the redistribution of stresses and strains as inelastic flow occurs and further analysis is under way.

The effect of modifying the aspect ratio (R=0.5, 1.0, and 2.0) associated with the rectangular fiber packing, on the 5 kPa/sec SCDRs is shown in Fig. 7 for room temperature and 650°C in the axial-transverse and transverse-transverse stress planes. These surfaces were determined using FEA and are for strongly bonded SiC/Ti. While aspect ratios of 0.5 and 2.0 are more extreme than those commonly fabricated, they illustrate that aspect ratio can have a significant effect on the shape and location of SCDRs.

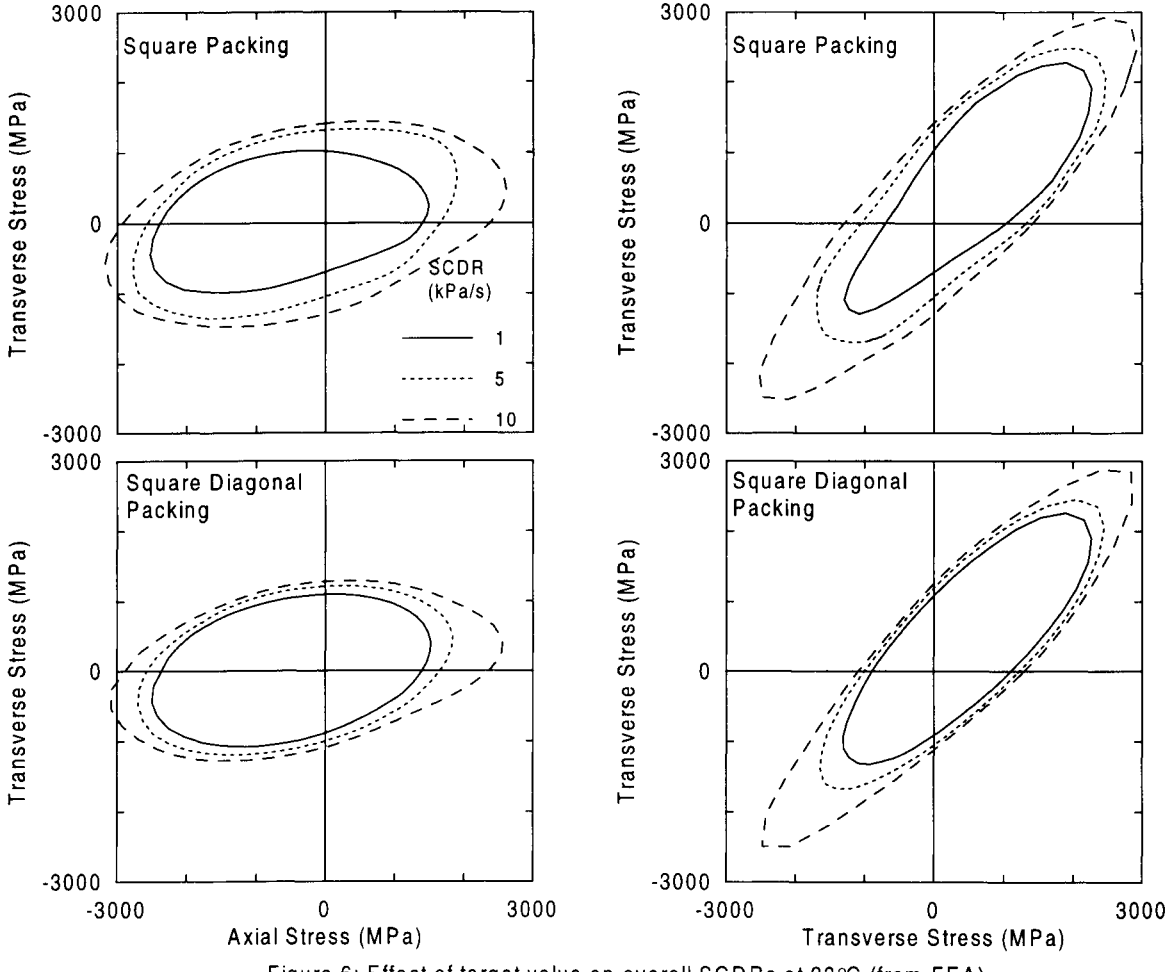

Figure 6: Effect of target value on overall SCDRs at 23°C (from FEA)

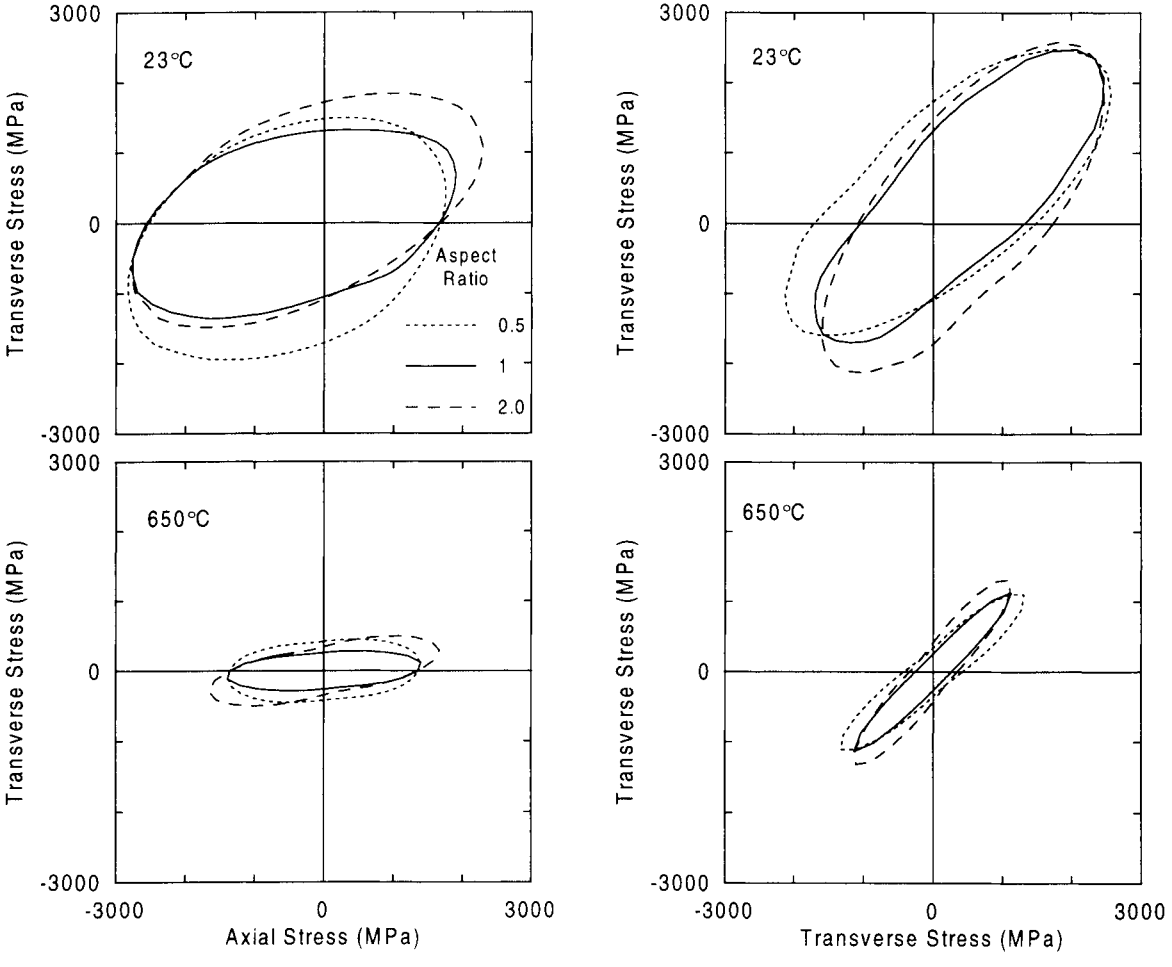

Figure 7: Effect of aspect ratio of rectangular packing on 5 kPa/s SCDRs (from FEA)

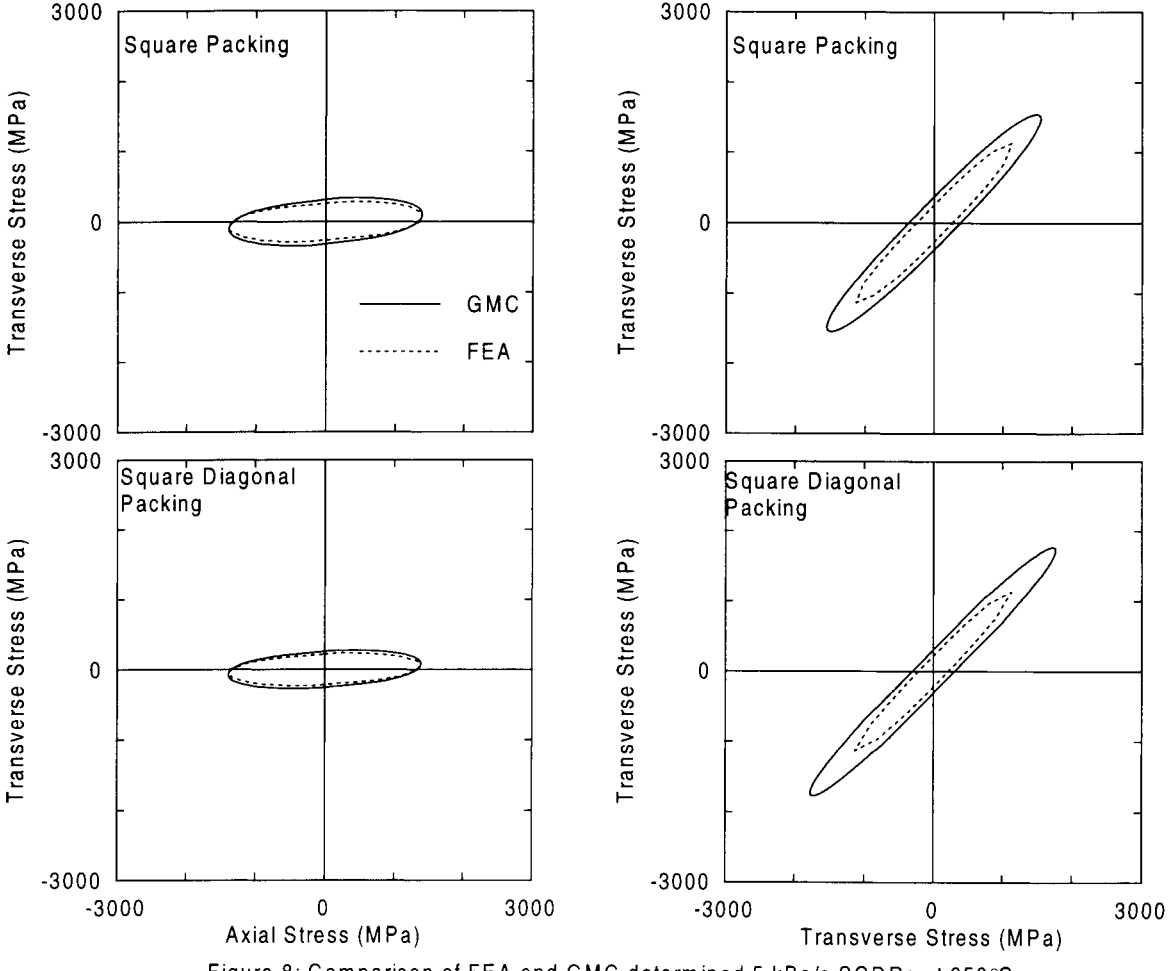

Figure 8: Comparison of FEA and GMC determined 5 kPa/s SCDRs at 650°C

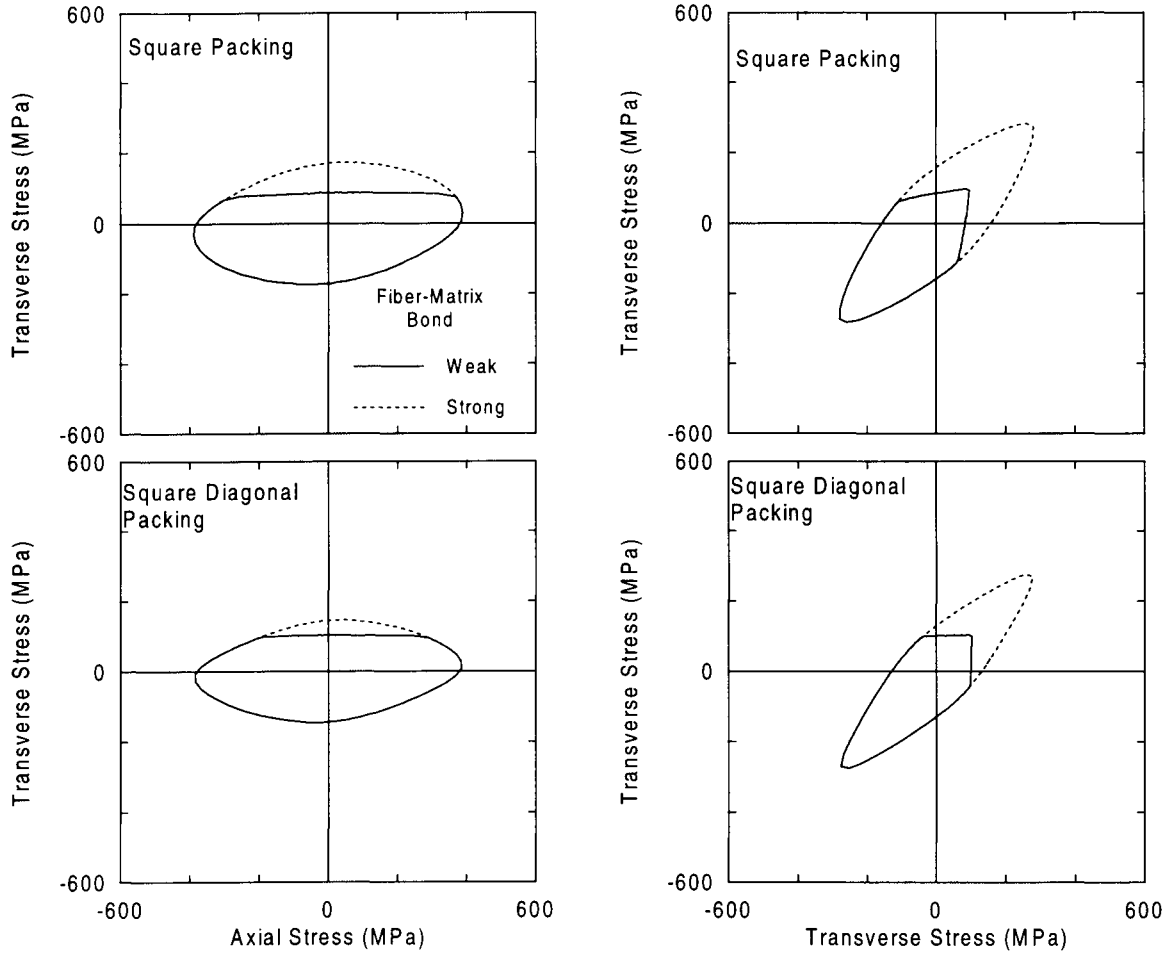

Figure 9: Effect of debonding on 206μ SCDFPs at 650°C (from GMC)

One application for the kind of information that flow surfaces provide is the design of components subjected to loads resulting in deterministic multiaxial stress states. The microstructure can then be engineered to best resist the loading. For example, a ring mounted on a shaft in a jet engine will rotate in service. Thus, the radial and circumferential stress components will be tensile. Suppose the ring is to be fabricated from a hoop-wound, strongly bonded SiC/Ti, and that the goal is to delay the onset of inelastic flow as long as possible. According to the first quadrant of the axial-transverse stress plane in Fig. 7, the largest possible aspect ratio should be used. The large aspect ratio provides a long ligament of matrix material between fibers for the transverse stress to flow through, while a small aspect ratio is associated with a short ligament of matrix between fibers and more localized flow.

In figure 8, FEA and GMC predicted 5 kPa/sec SCDRs at 650°C are compared for square and square diagonal packings with a strong fiber-matrix bond. In the axial-transverse plane the SCDRs predicted by FEA and GMC are in good agreement. However, in the transverse-transverse plane SCDRs predicted by GMC are larger than those predicted by FEA. For equi-biaxial tension the disparity is 35% for square packing and 55% for square diagonal packing. For uniaxial transverse tension the difference between FEA and GMC is 40-45%. This disparity is in contrast to the excellent agreement between yield surfaces defined by *local* yielding (Mises stress) that Pindera and Aboudi (1988) reported for the method of cells (square packing) and FEA. In Fig. 8 overall SCDRs are determined based on *overall* inelastic strain rates and stresses, as might be done in an experiment. The disparity is troubling and the subject of current study. However, it appears that the GMC results are qualitatively representative of the material response and can be used at least as a quick, inexpensive, guide for materials scientists and engineers designing microstructures.

Consider now, the more realistic case of a weak fiber-matrix bond. SCDFPs for SiC/Ti at 650°C having square and square diagonal packings are shown in Fig. 9 for strong and weak bonds. The primary effect of a weak bond is to significantly reduce the tensile stress at which deviation from proportional response begins. Since compressive interfacial tractions are not detrimental to the integrity of the interface, flow surfaces and flow/damage surfaces are the same for compressive loading (unless debonding due to Poisson expansion occurs, see Lissenden and Arnold (1997a)). Additionally, axial loading is not observed to cause debonding. The effect of debonding is slightly different for square and square diagonal packings. One of these differences is misleading. The uniaxial transverse tensile stress leading to a 206μ SCDFP is 104 MPa for square diagonal packing and 87 MPa for square packing, possibly leading one to believe that square diagonal packing would be preferred. However, the square diagonal packing exhibits no hardening while the square packing does (Fig. 10). Therefore, the square packing may be desirable even though it has a lower stress for the given SCDFP.

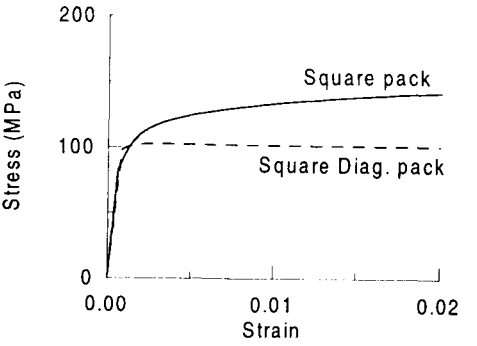

Figure 10: Uniaxial transverse tensile response

Brockenbrough et al (1991) and Arnold et al (1996a) demonstrated that as the fiber volume fraction increases, the effect of microstructural architecture increases for uniaxial loadings. Figure 11 shows 1 kPa/sec SCDRs in the axial-transverse stress plane at 650°C for square, hexagonal, and square diagonal packings and fiber volume fractions of 0.35 and 0.50. The primary effect of increasing the fiber volume fraction is to enlarge the SCDR. Additionally, larger differences in the SCDRs for the three microstructures are observed for the higher fiber volume fraction, especially in quadrant III where both stress components are compressive. Figure 11 also indicates that the effect of debonding on SCDRs is not as sharp as it is on SCDFPs (Fig. 10), at least for the target values plotted, which were chosen to be equivalent definitions for transverse loading at room temperature (these target values are not equivalent at 650°C).

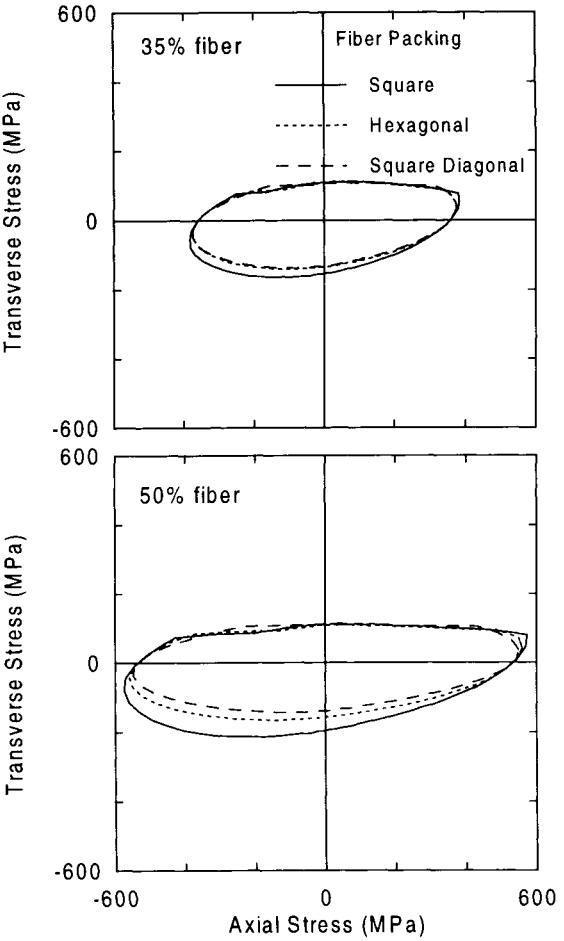

Figure 11: Effect of fiber volume fraction on 1 kPa/s SCDRs at 650°C (from GMC)

5. DISCUSSION

Multiaxial stress states are encountered in the analysis and design of most structural components due to complex loadings and geometries as well as stress concentrations. The response of MMCs to multiaxial stress states can not be inferred from uniaxial test data. It is necessary to conduct multiaxial tests to guide and later validate theoretical models. To implement the thermodynamically based framework discussed in Section 2 we need to determine the functional form the Gibbs and dissipation potentials. Experimentally determined SCDRs in various stress planes will provide excellent guidance for this task.

We have used micromechanics to generate overall flow/damage surfaces for unidirectional MMCs having different microstructures. Except for the special case of uniaxial loading in the direction of the fibers, microstructure influences the shape and location of the flow/damage surface. The magnitude of the effect that microstructure has on flow/damage surfaces depends on fiber volume fraction, definition of flow, and target value among other things. This adds yet another level of complexity to the continuum approach to modeling multiaxial inelastic

response of MMCs. Thus, in contrast to flow in isotropic materials where the dissipation potential can be written in terms of stress invariants, internal state invariants, and temperature; we must also consider directionality, microstructure, and debonding. This constitutes a most difficult task.

A weak fiber/matrix bond significantly influences the shape of the flow/damage surface. A dramatic flattening of the surface is observed for transverse tensile loading. Although not considered in this work, debonding also occurs under shear loading.

In conclusion, flow/damage surfaces need to be determined experimentally for a range of target values as well as different microstructures. These results will provide validation for micromechanics models and guidance for continuum models.

6. ACKNOWLEDGMENTS

We would like to thank Saiganesh Iyer for conducting the finite element analyses and Dr. T.E. Wilt for his assistance in extending MAC/GMC for flow surface probings. The first author gratefully acknowledges the support of the NASA Lewis Research Center, grant NCC3-481.

REFERENCES

Aboudi, J. (1992), Mechanics of Composite Materials: a unified micromechanical approach, Elsevier, Amsterdam.

Aboudi, J. (1995), "Micromechanical analysis of thermo-inelastic multiphase short-fiber composites," *Composites Eng.* Vol. 5, pp. 839-850.

Arnold, S.M., M-J. Pindera, and T.E. Wilt (1996a), "Influence of fiber architecture on the inelastic response of metal matrix composites," *Int. J. Plasticity*, Vol. 12, pp. 507-545.

Arnold, S.M., A.F. Saleeb, and M.G. Castelli (1996b), "A fully associative, nonisothermal, nonlinear kinematic, unified viscoplastic model for titanium based matrices," Thermomechanical Fatigue Behavior of Materials: Second Volume, ASTM-STP 1263, M.J. Verrilli and M.G. Castelli (eds.), American Society for Testing and Materials, Philadelphia, pp. 146-173.

Arnold, S.M., A.F. Saleeb, and M.G. Castelli (1996c), "A fully associative, nonlinear kinematic, unified viscoplastic model for titanium based matrices," Life Prediction Methodology for Titanium Matrix Composites, ASTM-STP 1253, W.S. Johnson, J.M. Larsen, and B.N. Cox (eds.), American Society for Testing and Materials, Philadelphia, pp. 231-256.

Brockenbrough, J.R., S. Suresh, and H.A. Wienecke (1991), "Deformation of metal-matrix composites with continuous fibers: geometrical effects of fiber distribution and shape," *Acta Metall. Mater.*, Vol. 39, pp. 735-752.

Drucker, D.C. (1949), "Relation of experiments to mathematical theories of plasticity," *J. Appl. Mech.*, Vol. 16, pp. A349-57.

HKS (1995), "ABAQUS/Standard User's Manual Version 5.5," Hibbitt, Karlsson, and Sorensen, Inc., Pawtucket.

Lissenden, C.J. and S.M. Arnold (1997a), "Theoretical and experimental considerations in representing macroscale flow/damage surfaces for metal matrix composites" *Int. J. Plasticity*, in press.

Lissenden, C.J. and S.M. Arnold (1997b), "Factors influencing inelastic flow under multiaxial stress states: a perspective of their importance to composites," *HITEMP Review 1997 Advanced High Temperature Engine Materials Technology Program, NASA CP-10192*, NASA Lewis Research Center, Cleveland, Paper No. 38.

Lissenden, C.J. and C.T. Herakovich (1995), "Numerical modelling of damage development and viscoplasticity in metal matrix composites," *Comput. Methods Appl. Mech. Engng.*, Vol. 126, pp. 289-303.

Majumdar, B.S. and G.M. Newaz (1992), "Inelastic deformation of metal matrix composites: plasticity and damage mechanisms" *Phil. Mag. A*, Vol. 66, pp. 187-212.

Nigam, H., G.J. Dvorak, and Y.A. Bahei-El-Din (1994), "An experimental investigation of elastic-plastic behavior of a fibrous boron-aluminum composite: I. matrix-dominated mode" *Int. J. Plasticity*, Vol. 10, pp. 23-48.

Paley, M. and J. Aboudi (1992), "Micromechanical analysis of composites by the generalized cells model," *Mech. Mater.*, Vol. 14, pp. 127-139.

Pindera, M-J. and J. Aboudi (1988), "Micromechanical analysis of yielding of metal matrix composites," *Int. J. Plasticity*, Vol. 4, pp. 195-214.

Robinson, D.N. and J.R. Ellis (1986), "A multiaxial theory of viscoplasticity for isotropic materials," *Proc. Turbine Engine Hot Section Technology, NASA CP-2444*, NASA Lewis Research Center, Cleveland, pp. 283-292.

Wilt, T.E. and S.M. Arnold (1996), "Micromechanics analysis code (MAC) User Guide: version 2.0," NASA TM-107290, NASA Lewis Research Center, Cleveland.

Damage Mechanics in Engineering Materials
G.Z. Voyiadjis, J.-W.W. Ju and J.-L. Chaboche (Editors)
© 1998 Elsevier Science B.V. All rights reserved.

Calibration and validation of an anisotropic elasto-plastic damage model for sheet metal forming

A.M. Habraken, J.F. Charles, S. Cescotto*

*MSM Department, University of Liège
Quai Banning, 6, 4000 Liège, Belgium

The anisotropic elasto-plastic damage model developed by Y.Y. Zhu [1] is summarised, then its calibration method is presented, and applied on two steel sheets : one is adapted for deep drawing and the other one is a high-tensile steel. The first results from the simulations of Nakazyma tests are discussed, then the conclusions define the potentials of such model as well as its limitation and the intended further work is described.

1. INTRODUCTION

In industry, simulations of sheet metal forming operations by means of FEM code are becoming a necessity during product and process development. However, still a lot of researches has to be done before results of such simulations become sufficiently accurate and predict correctly location and moment of failure events.

The anisotropic behaviour of sheet is well known, for instance a circular cup drawned from a circular piece of metal sheet using axisymmetric tools often presents an ondulating rim called earing. The origin of such a behaviour is the crystallographic nature of the plastic metal deformation. The use of anisotropic elasto-plastic models allow the description of such phenomena, current cases of 4 ears can be accurately predicted by a classical Hill model [2], but more singular cases of 6 ears request an accurate yield locus shape based for instance on texture measurements and polycrystal plasticity as the model developed by P. Van Houtte [3].

An accurate initial yield locus is not sufficient to model sheet metal forming of complex shapes because in such cases strain paths are not proportional. So the work hardening rate needs a particular attention, if one wants to model the Bauschinger effect and the cross effect. The physics based work-hardening model proposed by Teodosiu [4] is an interesting alternative to the conventional phenomenological models.

Concerning the failure prediction, previous studies [5] from our department have demonstrated the interest of an approach based on the continuous damage mechanics compared to an uncoupled approach based on various fracture criteria.

The uncoupled method based on post processing induces very low extra computation costs, however, it is difficult to find one criterion able to predict all failure types as many different mechanisms exist such as internal or external necking, large shear deformation, nucleation, growth and coalescence of voids and so on. From our experience, the fully coupled approach based on the continuum damage theory is more attractive as it is able to characterise micro-crack initiation and growth in ductile materials for different loading paths such as shear, tensile or compression state ... This previous work [5] was dedicated to isotropic elasto-plastic damage model and has been validated by experiments on bulk aluminium.

The damage models and their softening behaviour lead however to numerical problems as mesh dependency which can be reduced by means of viscoplastic, dynamic or thermal regularisation. Another solution to prevent mesh dependency is the non local approach [6].

Damage models such as Gurson's one [7] or its recent improvement proposed by Gologanu [8] need precise data to describe nucleation growth and coalescence of voids accurately. Such information is difficult to get from macroscopic tests and must rely on microscopic measurements of voids [9] which consists in a very long investigation. The models proposed by Lemaître and Chaboche [10] have perhaps shorter roots in microscopics physics but have the advantage of being calibrated by macroscopic tests, this is the major reason of our choice of such a type of model. Their success for isotropic materials are numerous [11], the model presented here is one trial to extend such a model to anisotropic cases.

2. Y.Y. ZHU'S ANISOTROPIC ELASTOPLASTIC DAMAGE MODEL

A short literature review of anisotropic elastoplastic damage models can be found in [12]. In fact, Zhu's model is a modified version from previous constitutive laws proposed by Cordebois and Sidoroff [13, 14], its main features are the following ones :

(1) Three major anisotropies are taken into account, including : anisotropic elasticity, anisotropic plasticity and anisotropic damage;
(2) The generalized damage effect tensor $\underline{M}$ proposed by Chow and Wang [15] is used;
(3) A new damage characteristic tensor $\underline{J}$ based on the hypothesis of damage energy equivalence is proposed;
(4) An effective computational integration algorithm with two step split operators is proposed;
(5) As large displacements and strains happen, the definition of local axes fitted on material principal axes is necessary, the local reference system proposed by Munhoven [16] is used;
(6) Hill yield locus is adapted to describe plastic behaviour, however the plastic tensor $\underline{H}$ is not assumed constant during hardening, a plastic energy equivalence rule is adopted.

2.1. The anisotropic damage

One basic hypothesis in most isotropic and anisotropic models of continuum damage mechanics is that, neglecting the details of microscopic damage growth, damage can be viewed as a macroscopic state variable which reflects the average microscopic damage growth and modifies the stress in the sense of "effective stress". This basic assumption of effective stress can be stated this way : there exists a "damage effect tensor" $\underline{M}\ (\underline{D})$ applied to the stress tensor $\underline{\sigma}$ which defines the effective stress tensor $\underline{\bar{\sigma}}$ [10], that is :

$$\underline{\bar{\sigma}} = \underline{M}(\underline{D})\underline{\sigma} \tag{1}$$

where the damage effect tensor $\underline{M}\ (\underline{D})$ is a second-order or fourth-order tensor depending on the damage tensor $\underline{D}$. Note that four fundamental variables of continuum damage mechanics have been introduced in the foregoing hypothesis, i.e. the damage tensor $\underline{D}$, the damage effect tensor $\underline{M}\ (\underline{D})$, the effective stress tensor $\underline{\bar{\sigma}}$ and effective strain tensor $\underline{\bar{\varepsilon}}$.

Anisotropic damage may be characterised by a symmetric second-order tensor $\underline{D}$, because of its mathematical simplicity. There is no uniquely defined mathematical formulation of $\underline{M}\ (\underline{D})$, Zhu's choice is the one proposed by Chow and Wang [15] which has the advantages of a possible reduction to a one scalar variable for isotropic damage and of having simple expression outside the stress tensor principle directions.

In the principal co-ordinate system of damage, which in our formulation is assumed to be the material principal system where Hill yield locus is expressed, we have :

$$[\bar{\sigma}_{11}\bar{\sigma}_{22}\bar{\sigma}_{33}\bar{\sigma}_{23}\bar{\sigma}_{31}\bar{\sigma}_{12}]^T = \underline{M}[\sigma_{11}\sigma_{22}\sigma_{33}\sigma_{23}\sigma_{31}\sigma_{12}]^T \tag{2}$$

with the fourth rank symmetric tensor :

$$\underline{M} = diag\left[\frac{1}{1-D_1}, \frac{1}{1-D_2}, \frac{1}{1-D_3}, \frac{1}{\sqrt{(1-D_2)(1-D_3)}}, \frac{1}{\sqrt{(1-D_3)(1-D_1)}}, \frac{1}{\sqrt{(1-D_1)(1-D_2)}}\right] \tag{3}$$

Instead of the conventional postulate of strain or stress equivalence, an hypothesis of energy equivalence is used. It states that the complementary elastic energy for a damaged material has the same form as that of a fictitious undamaged material except that the stress is replaced by the effective stress in the energy formulation. Mathematically,

$$W_e(\underline{\sigma}, \underline{D}) = W_e(\underline{\bar{\sigma}}, \underline{D}) \text{ or } \frac{1}{2}\underline{\bar{\sigma}}^T \underline{C}_e^{-1}\underline{\bar{\sigma}} = \frac{1}{2}\underline{\sigma}^T \underline{\bar{C}}_e^{-1}\underline{\sigma} \tag{4}$$

where $\underline{C}_e$ and $\underline{\bar{C}}_e$ are the virgin and the damage elastic material stiffness tensors respectively. By recalling (1), it can be easily proved that :

$$\underline{\bar{C}}_e^{-1} = \underline{M}(\underline{D})\underline{C}_e^{-1}\underline{M}(\underline{D}) \tag{5}$$

and according to the hypothesis of energy equivalence the effective elastic strain vector is :

$$\underline{\bar{\varepsilon}}_e = \underline{M}^{-1}\underline{\varepsilon}_e \tag{6}$$

where :

$$\underline{M}^{-1} = diag$$
$$\left[1-D_1, 1-D_2, 1-D_3, \sqrt{(1-D_2)(1-D_3)}, \sqrt{(1-D_3)(1-D_1)}, \sqrt{(1-D_1)(1-D_2)}\right] \quad (7)$$

2.2 General thermodynamic analysis

2.2.1 State variables

The internal variables to be used in the thermodynamic analysis are listed, together with their associated thermodynamic forces, in Table 1. The general structure of the constitutive equations is furnished by the well-established thermodynamic theory of irreversible processes with such state variables. Hereafter, isothermal condition is assumed.

Table 1

State variables	Associated thermodynamic forces
Elastic strain $\underline{\varepsilon}_e$	Cauchy stress $\underline{\sigma}$
Accumulated plastic strain α	Plastic hardening threshold R
Damage variable $\underline{D} = (D_1\ D_2\ D_3)$	Damage energy release rate $\underline{Y} = (Y_1\ Y_2\ Y_3)$
Overall damage β	Damage strengthening threshold B

2.2.2 Thermodynamic potential

As it has been indicated in Lemaître [10], uncoupled plasticity and elasticity are assumed such that the elastic properties depend only on damage variables and not on the dislocation density represented by α. For practical purposes, another hypothesis is introduced : energies involved in plastic flow and damage processes, dissipated by heat or stored in the material, are independent. Consequently, in the present model, the Helmholtz free energy takes the following form [17] :

$$\rho\psi(\underline{\varepsilon}_e, \underline{D}, \alpha, \beta) = W_e(\underline{\varepsilon}_e, \underline{D}) + \psi_p(\alpha) + \psi_d(\beta) \quad (8)$$

where $W_e(\varepsilon_e, D)$ is the elastic strain energy, $\psi_p(\alpha)$ the free energy due to plastic hardening and $\psi_d(\beta)$ the free energy due to damage hardening. The complementary energy is obtained from the Legendre transformation of the free energy with respect to strain, i.e.

$$\rho\Pi(\underline{\sigma}, \underline{D}, \alpha, \beta) = \underline{\sigma} : \underline{\varepsilon}_e - \rho\psi(\underline{\varepsilon}_e, \underline{D}, \alpha, \beta) = W_e(\underline{\sigma}, \underline{D}) - \psi_p(\alpha) - \psi_d(\beta) \quad (9)$$

According to the energy equivalence hypothesis, the elastic strain energy $W_e(\underline{\varepsilon}_e, \underline{D})$ and the complementary elastic energy $W_e(\underline{\sigma}, \underline{D})$ can be evaluated and following the rules of thermodynamics of irreversible processes, the associated thermodynamic forces are given by :

$$\underline{\sigma} = \frac{\rho \partial \psi}{\partial \underline{\varepsilon}_e} = \underline{M}^{-1} \underline{C}_e \underline{M}^{-1} \underline{\varepsilon}_e$$

$$R = \rho \frac{\partial \psi}{\partial \alpha} = \frac{\partial \psi_p(\alpha)}{\partial \alpha} \qquad (10a,b,c,d,)$$

$$B = \rho \frac{\partial \psi}{\partial \beta} = \frac{\partial \psi_d(\beta)}{\partial \beta}$$

$$\underline{Y} = \rho \frac{\partial \psi}{\partial \underline{D}} = -\rho \frac{\partial \Pi}{\partial \underline{D}} = -\frac{\partial W_e(\underline{\sigma}, \underline{D})}{\partial \underline{D}} = -\underline{\sigma}^T \underline{M} \underline{C}_e^{-1} \frac{\partial \underline{M}}{\partial \underline{D}} \underline{\sigma}$$

The negative of $\underline{Y}$ can be considered as the elastic strain energy rate associated with a unit damage increment as it is easy to show that :

$$-\underline{Y} = \frac{1}{2} \frac{dW_e}{d\underline{D}} \Big]_{\text{at constant } \underline{\sigma}} \qquad (11)$$

$\underline{Y}$ is often given the name of "damage energy release rate" [10].

2.2.3 The dissipation power

According to the second law of thermodynamics, the total dissipation power with convexity and normality properties is :

$$\Phi = \underline{\sigma} \dot{\underline{\varepsilon}}_p - R\dot{\alpha} - \underline{Y} \dot{\underline{D}} - B\dot{\beta} \geq 0 \qquad (12)$$

Within the hypothesis of independence of energy dissipations between plastic flow and damage processes, eq. (12) can be separated into two parts such that :

$$\underline{\sigma} \dot{\underline{\varepsilon}}_p - R\dot{\alpha} \geq 0 \text{ and } -\underline{Y} \dot{\underline{D}} - B\dot{\beta} \geq 0 \qquad (13)$$

Equation (13) shows the existence of a plastic dissipative potential and a damage dissipative potential, i.e.

$$F_p(\underline{\sigma}, \underline{D}, R) = 0 \text{ and } F_d(\underline{Y}, \underline{B}) = 0 \qquad (14)$$

in which the former represents the plastic yield criterion; the latter is the damage evolution criterion. In case the criteria $F_p = 0$ and $F_d = 0$ are satisfied, the actual values of $\underline{\sigma}, R, \underline{Y}, B$ will make the dissipation power of eq. (12) a stationary value.

If we introduce Lagrange multipliers $\dot{\lambda}_p$ and $\dot{\lambda}_d$, eq. (12) can be written :

$$\Phi = \underline{\sigma} \dot{\underline{\varepsilon}}_p - R\dot{\alpha} - \underline{Y} \dot{\underline{D}} - B\dot{\beta} - \dot{\lambda}_p F_p - \dot{\lambda}_d F_d \qquad (15)$$

Thus we have :

$$\frac{\partial \Phi}{\partial \underline{\sigma}} = 0 \Rightarrow \dot{\underline{\varepsilon}}_p = \dot{\lambda}_p \frac{\partial F_p}{\partial \underline{\sigma}} \qquad \frac{\partial \Phi}{\partial \underline{Y}} = 0 \Rightarrow \dot{\underline{D}} = -\dot{\lambda}_d \frac{\partial F_d}{\partial \underline{Y}}$$

$$\frac{\partial \Phi}{\partial R} = 0 \Rightarrow \dot{\alpha} = \dot{\lambda}_p \frac{\partial F_p}{\partial R} \qquad \frac{\partial \Phi}{\partial B} = 0 \Rightarrow \dot{\beta} = -\dot{\lambda}_d \frac{\partial F_d}{\partial B} \qquad (16)$$

2.3 Fully coupled anisotropic elastoplastic damage model

2.3.1 Anisotropic elasticity and damage

When a material is damaged, the constitutive relation is :

$$\underline{\sigma} = \overline{\underline{C}}_e \underline{\varepsilon}_e \text{ or } \underline{\varepsilon}_e = \overline{\underline{C}}_e^{-1} \underline{\sigma} \qquad (17)$$

The classical Hook's elastic tensor for orthotropic materials combined with equation (5) yields to the following expression :

$$\begin{Bmatrix} \varepsilon_{11} \\ \varepsilon_{22} \\ \varepsilon_{33} \\ \varepsilon_{23} \\ \varepsilon_{31} \\ \varepsilon_{21} \end{Bmatrix} = \begin{bmatrix} \frac{1}{E_1(1-D_1)^2} & \frac{-\nu_{12}}{(1-D_1)(1-D_2)E_1} & \frac{-\nu_{13}}{(1-D_1)(1-D_3)E_1} & 0 & 0 & 0 \\ \frac{-\nu_{21}}{(1-D_1)(1-D_2)E_2} & \frac{1}{E_2(1-D_2)^2} & \frac{-\nu_{23}}{(1-D_3)(1-D_2)E_2} & 0 & 0 & 0 \\ \frac{-\nu_{31}}{(1-D_1)(1-D_3)E_3} & \frac{-\nu_{32}}{(1-D_2)(1-D_3)E_3} & \frac{1}{E_3(1-D_3)^2} & 0 & 0 & 0 \\ 0 & 0 & 0 & \frac{1}{2G_{23}(1-D_2)(1-D_3)} & 0 & 0 \\ 0 & 0 & 0 & 0 & \frac{1}{2G_{31}(1-D_1)(1-D_3)} & 0 \\ 0 & 0 & 0 & 0 & 0 & \frac{1}{2G_{12}(1-D_1)(1-D_2)} \end{bmatrix} \begin{Bmatrix} \sigma_{11} \\ \sigma_{22} \\ \sigma_{33} \\ \sigma_{23} \\ \sigma_{31} \\ \sigma_{12} \end{Bmatrix} \quad (18)$$

In order to guarantee the positive definiteness of $\underline{\overline{C}}_e$, the following conditions should be satisfied :

$$\begin{aligned} &0 < \Delta_c \leq 1 \text{ with } \Delta_c = 1 - \nu_{21}\nu_{12} - \nu_{31}\nu_{13} - \nu_{32}\nu_{23} - \nu_{12}\nu_{23}\nu_{31} - \nu_{21}\nu_{13}\nu_{32} \\ &0 < 1 - \nu_{ij}\nu_{ji} \leq 1 \text{ (no sum on i, j)}, \; 0 \leq D_i < 1 \\ &G_{23} > 0, \quad G_{31} > 0, \quad G_{12} > 0, \quad E_1 > 0, \quad E_2 > 0, \quad E_3 > 0 \end{aligned} \quad (19)$$

Orthotropic symmetry assumes also the following equalities expressed in the initial state ($D_1 = D_2 = D_3 = 0$) :

$$\frac{\nu_{12}}{E_1} = \frac{\nu_{21}}{E_2}, \frac{\nu_{31}}{E_3} = \frac{\nu_{13}}{E_1}, \frac{\nu_{32}}{E_3} = \frac{\nu_{23}}{E_2} \quad (20)$$

2.3.2 Anisotropic plastic yield surface

In the damage characterisation of materials undergoing large plastic strains, Hill's yield criterion in stress space is expressed in the following form :

$$F_p(\underline{\sigma}, \underline{D}, R) = F_p(\underline{\sigma}, R) = \overline{\sigma}_F - R_o - R(\alpha) = 0 \quad (21)$$

where R_o is the initial strain hardening threshold.

The effective equivalent stress $\overline{\sigma}_F$ is :

$$\overline{\sigma}_F = \left\{ \frac{1}{2} \underline{\sigma}^T \underline{\overline{H}} \underline{\sigma} \right\}^{1/2} = \left\{ \frac{1}{2} \underline{\sigma}^T \underline{\overline{H}} \underline{\sigma} \right\}^{1/2} \quad (22)$$

The effective plastic characteristic tensor $\underline{\overline{H}}$ is given by :

$$\underline{\overline{H}} = \underline{M}(\underline{D}) \underline{H} \underline{M}(\underline{D}) \quad (23)$$

The positive definite tensor $\underline{H}$ for orthotropic materials is represented by a 6x6 matrix in the material principal co-ordinate system [2] :

$$\underline{H} = \begin{bmatrix} G+H & -H & -G & 0 & 0 & 0 \\ -H & H+F & -F & 0 & 0 & 0 \\ -G & -F & F+G & 0 & 0 & 0 \\ 0 & 0 & 0 & N & 0 & 0 \\ 0 & 0 & 0 & 0 & L & 0 \\ 0 & 0 & 0 & 0 & 0 & M \end{bmatrix} \tag{24}$$

where F, G, H, L, M, N are parameters characterising the current state of plastic anisotropy. For a strain-hardening material, the uniaxial yield stress varies with increasing plastic strain, and therefore the anisotropic parameters should also vary, since they are functions of the current yield stress [17]. For sheet metal forming, this can be easily experimentally checked by measuring the well-known Lankford coefficient r, ratio of transversal and thickness strain rate during a tensile test. This ratio depends on the angle between the tensile and the rolling direction, this fact is directly connected to F G H L M N parameters, expression of the anisotropic property of the sheet. However, the Lankford coefficient is not constant during each tensile test, it depends on plastic strain, this yields to the conclusion that $\underline{H}$ tensor must vary. As this increases the model complexity, a lot of Hill models neglect this fact and use a constant $\underline{H}$ tensor.

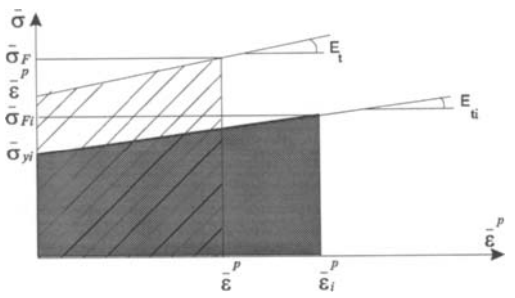

Figure 1. Equating plastic work

$\bar{\sigma}_y$ = initial effective equivalent plastic stress

$\bar{\sigma}_{yi}$ = initial effective plastic stress in direction i

$\bar{\sigma}_F$ = effective equivalent stress corresponding to α

$\bar{\sigma}_{Fi}$ = effective stress in direction i leading to the same plastic work as $\bar{\sigma}_F$

E_t = slope of effective equivalent stress plastic strain curve

E_{ti} = slope of effective stress plastic strain curve in direction i

In Zhu's model, the $\underline{H}$ tensor evolution is based on the plastic work equivalence in each direction. The simple case of a linear work hardening material is described by figure 1 where for shortness indice eq is dropped.

$$W_P = \frac{1}{2E_{ti}}(\bar{\sigma}_{Fi}^2 - \bar{\sigma}_{yi}^2) = \frac{1}{2E_t}(\bar{\sigma}_F^2 - \bar{\sigma}_Y^2) = \text{plastic work} \tag{25}$$

In this case, equating plastic work leads to following ratios :

$$a_i = \left(\frac{\bar{\sigma}_F}{\bar{\sigma}_{Fi}}\right)^2 = \frac{\bar{\sigma}_F^2}{(E_{ti}/E_t)(\bar{\sigma}_F^2 - \bar{\sigma}_y^2) + \bar{\sigma}_{yi}^2} \tag{26}$$

with i = 1, 2, 3, 23, 31, 12.

The relation between a_i and classical anisotropic parameters are listed hereafter :

$$\begin{cases} G+H=2a_1 & -H=-a_1-a_2+a_3 & N=2a_{23} \\ H+F=2a_2 & -G=-a_1+a_2-a_3 & L=2a_{31} \\ F+G=2a_3 & -F=a_1-a_2-a_3 & M=2a_{12} \end{cases} \tag{27}$$

Obviously, if direction 1 is taken as reference direction $a_1=1$. This hardening approach induces changes in yield shape and yield size.

The plastic constitutive equations incorporating material damage may be derived by taking the yield criterion (21) as a potential function. By assuming an associated flow rule, the plastic strain is characterised as follows :

$$\begin{cases} \dot{\underline{\varepsilon}}_p = \dot{\lambda}_p \dfrac{\partial F_p}{\partial \underline{\sigma}} = \dfrac{\underline{\underline{M}}\,\underline{\underline{H}}\,\underline{\underline{M}}\underline{\sigma}}{2\bar{\sigma}_F}\dot{\lambda}_p \\ (\text{plastic flow rule}) \end{cases} \tag{28}$$

$$\begin{cases} \dot{R} = \dot{\lambda}_p \dfrac{dR}{d\alpha} \\ (\text{isotropic hardening rule}) \end{cases} \tag{29}$$

$$\begin{cases} F_p \le 0, \dot{\lambda}_p \ge 0, \dot{\lambda}_p F_p = 0 \\ (\text{plastic loading / unloading rule}) \end{cases} \tag{30}$$

2.3.3 Damage evolution law and damage surface

In a similar way to the arguments leading to plastic dissipative potential, one can assume that there exists a surface $F_d=0$, which separates the damaging domain from the undamaging domain. A damage criterion in a quadratic homogeneous function of the damage energy release rate $\underline{Y}$ was proposed [13, 14] :

$$F_d = Y_{eq} - B_o - B(\beta) = 0 \tag{31}$$

where the equivalent damage energy release rate Y_{eq} is defined by :

$$Y_{eq} = \left[\frac{1}{2}\underline{Y}^T \underline{\underline{J}}\,\underline{Y}\right]^{1/2} \tag{32}$$

in which $\underline{\underline{J}}$ is the damage characteristic tensor.

The determination of a suitable damage characteristic tensor $\underline{\underline{J}}$, which is simple enough to be applied and yet describes accurately the non-linear nature of damage growth, may well be the most important aspect in the present formulation of anisotropic damage evolution law.

Normally, $\underline{\underline{J}}$ should be a fourth order tensor as $\underline{\underline{H}}$. However, since we work on the principal co-ordinate system of damage, it can be treated like a second order tensor. The damage characteristic tensor $\underline{\underline{J}}$ proposed by Zhu is an extension of the formulation due to Lu [18], it is based on the damage energy equivalence.

$$\underline{\underline{J}} = 2\begin{bmatrix} J_1 & \sqrt{J_1 J_2} & \sqrt{J_1 J_3} \\ \sqrt{J_1 J_2} & J_2 & \sqrt{J_2 J_3} \\ \sqrt{J_1 J_3} & \sqrt{J_2 J_3} & J_3 \end{bmatrix} \tag{33}$$

In the case of damage hardening materials, the equivalent damage energy released rate Y_{eq} increases with the total damage growth, and hence, the anisotropic parameters (J_1, J_2, J_3) in the above equation should also vary. Their evolution follows the same principle then for $\underline{\underline{H}}$ tensor component except that plastic work is here replaced by damage work. For the case of linear damage hardening, and the choice of component Y_1 as reference direction, J_2 and J_3 are computed by relations (34) and $J_1 = 1$.

$$J_i = \frac{Y_1^2}{(D_{ti}/D_{t1})(Y_1^2 - Y_{01}^2) + Y_{oi}^2} \tag{34}$$

with i = 2 or 3.

Figure 2 recalls Y_1, Y_i, Y_{01}, Y_{oi}, D_{t1}, D_{ti} significances.

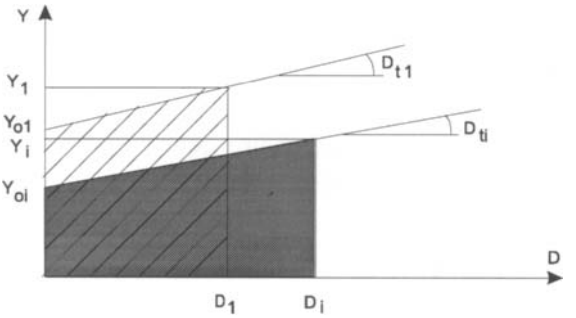

Figure 2. Equating damage work.

In much the same way as the definition of plastic flow, the evolution law of anisotropic damage is characterised below :

$$\begin{cases} \dot{\underline{\underline{D}}} = -\dot{\lambda}_d \dfrac{\partial F_d}{\partial \underline{\underline{Y}}} = -\dfrac{J\underline{\underline{Y}}}{2Y_{eq}}\dot{\lambda}_d = \underline{\underline{Y}}^* \dot{\lambda}_d \\ \text{with } Y^* = -\dfrac{JY}{2Y_{eq}} \\ \text{(damage evolution rule)} \end{cases} \tag{35}$$

$$\begin{cases} \dot{\beta} = -\dot{\lambda}_d \dfrac{\partial F_d}{\partial B} = \dot{\lambda}_d \\ \dot{B} = \dfrac{dB}{d\beta}\dot{\beta} = \dfrac{dB}{d\beta}\dot{\lambda}_d \\ \text{(damage hardening rule)} \end{cases} \tag{36}$$

$$\begin{cases} F_d \le 0,\ \dot{\lambda}_d \ge 0, \dot{\lambda}_d F_d = 0 \\ \text{(damage loading / unloading rule)} \end{cases} \tag{37}$$

2.4 Final constitutive relations

The complete set of equations is available in [1, 12], here we just recall the algebraic way to reach it and the final form of the result.

According to elastic constitutive relations and to the effective strain tensor definition (6),we have :

$$\overline{\sigma} = \underline{C}_e \underline{M}^{-1} \underline{\varepsilon}_e \tag{38}$$

Using the additive decomposition of strain rate in an elastic and plastic part as well as the time derivative of the inverse of the damage effect tensor and the damage rate equation (35), the objective rate form of equation (38) is obtained :

$$\overset{\wedge}{\overline{\sigma}} = \underline{C}_e \underline{M}^{-1} \dot{\underline{\varepsilon}} - \underline{C}^* \dot{\lambda}_p - \underline{D}^* \dot{\lambda}_d \tag{39}$$

where $\underline{C}^*$ and $\underline{D}^*$ are explicitly defined in [1] and ^ subscript means objective rate. Finally the objective rate of the stress tensor is easily computed as :

$$\hat{\underline{\sigma}} = \underline{M}^{-1} \overset{\wedge}{\overline{\underline{\sigma}}} - \underline{M}^{-1} \dot{\underline{M}} \underline{\sigma} \tag{40}$$

Concerning damage evolution, starting from the damage energy released rate $\underline{Y}$ in (10d), its time derivative is computed :

$$\dot{\underline{Y}} = \underline{J}^* \dot{\underline{\varepsilon}} + \underline{H}^* \dot{\lambda}_p + \underline{T}^* \dot{\lambda}_d \tag{41}$$

where $\underline{J}^*$, $\underline{H}^*$ and $\underline{T}^*$ are explicitly defined in [1].

The final set of equations is composed by equations (28, 29, 30, 35, 36, 37, 40, 41) and the return mapping algorithms proposed by Simo [19] is applied.

3. CALIBRATION METHOD OF Y.Y. ZHU'S ANISOTROPIC ELASTOPLASTIC DAMAGEMODEL

As implemented in the non-linear finite element code LAGAMINE from Department MSM, Y.Y. Zhu's model need following data :

- the effective stress strain curves $\overline{\sigma\varepsilon}$ in each tensile and shear direction (11, 22, 33, 23, 31, 12) in the materials reference frame ;
- the initial damage energy release rate versus associated damage component Y_i D_i in each materials principal direction 1, 2, 3 ;
- the initial materials reference frame position is expressed according to global axis used for finite element mesh.

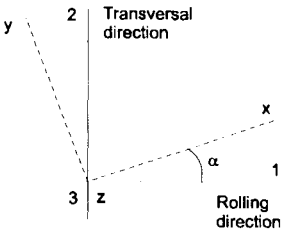

Figure 3. Definition of reference axis

Let us consider a sheet, where rolling direction is assumed to be 1 direction, three different set of experiments will provide the necessary values :

- normalized tensile tests in direction 11, 22 and in direction $\alpha = 45°$ (figure 3 defines this direction) with accurate measurements in the field of small strains for anisotropic elastic parameters ;
- normalized tensile tests performed in multiple directions α with accurate measurements in the field of large strains for anisotropic plastic parameters ;
- for damage evolution law, non classical tensile tests with numerous loading and unloading cycles in directions 11 and 22, with sample shape adapted to localize striction position for damage parameters.

The detailed procedure is described hereafter.

3.1 Calibration of the initial anisotropic elastic properties

Tensile test in direction $\alpha = 0$, 45 and 90° are performed with accurate measures of longitudinal ε_x, transversal ε_y and thickness ε_z strain. Figure 3 defines local axis during tensile experiment (x, y, z) and material reference frame (1, 2, 3). Recalling classical rotation equations , local stress and strain component (σ_x, σ_y, σ_{xy}, ε_x, ε_y, ε_{xy}) are directly related to stress and strain components in material axis (σ_{11}, σ_{22}, σ_{12}, ε_{11}, ε_{22}, ε_{23}).

$$\begin{Bmatrix} \xi_{11} \\ \xi_{22} \\ \xi_{12} \end{Bmatrix} = \begin{bmatrix} \cos^2\alpha & \sin^2\alpha & -2\cos\alpha\sin\alpha \\ \sin^2\alpha & \cos^2\alpha & 2\cos\alpha\sin\alpha \\ \cos\alpha\sin\alpha & -\cos\alpha\sin\alpha & \cos^2\alpha - \sin^2\alpha \end{bmatrix} \begin{Bmatrix} \xi_X \\ \xi_Y \\ \xi_{XY} \end{Bmatrix} \tag{42}$$

where ξ can be replaced by σ or ε.

So equation (18) written in material reference axis describes the stress-strain relation in the initial elastic field when damage has not yet occurred (D_1, D_2, D_3 = 0), we find :

- for tensile test $\alpha = 0°$: $E_1 = \dfrac{\sigma_x}{\varepsilon_x} \quad \nu_{12} = \dfrac{-E_1\varepsilon_{yy}}{\sigma_x} \quad \nu_{13} = \dfrac{-E_1\varepsilon_{zz}}{\sigma_x}$ (43)

- for tensile test $\alpha = 90°$: $E_2 = \dfrac{\sigma_x}{\varepsilon_{xx}} \quad \nu_{21} = \dfrac{-E_2\varepsilon_{yy}}{\sigma_x} \quad \nu_{23} = \dfrac{-E_2\varepsilon_{zz}}{\sigma_x}$ (44)

- for tensile test $\alpha = 45°$:

$$\varepsilon_{11} = \frac{\sigma_{11}}{E_1} - \nu_{12}\frac{\sigma_{22}}{E_1} = \frac{\varepsilon_{xx} + \varepsilon_{yy}}{2}$$

$$\varepsilon_{22} = \frac{\sigma_{22}}{E_2} - \nu_{21}\frac{\sigma_{11}}{E_2} = \frac{\varepsilon_{xx} + \varepsilon_{yy}}{2} \tag{45}$$

$$\sigma_{11} = \sigma_{22} = \sigma_{12} = \frac{\sigma_{xx}}{2}$$

which yields to :

$$\frac{1}{G_{12}} = \frac{4\varepsilon_{xx}}{\sigma_x} - \frac{1-\nu_{12}}{E_1} - \frac{1-\nu_{21}}{E_2} \tag{46}$$

So we still miss E_3, G_{23} and G_{31}, and the following assumptions are done :

$$G_{12} = G_{31} = G_{23}$$
$$E_3 = \frac{E_1 + E_2}{2} \tag{47}$$

3.2 Calibration of a classical Hill matrix for plastic behaviour

As it will be described in section 3.4, this intermediate step is necessary in order to reach the needed $(\overline{\sigma\varepsilon})_i$ curves. So forgetting, the frame of damage approach, we must fit the classical Hill parameters from tensile experiments. We have chosen the method proposed by Noat [20] because his final plastic parameters take into account in a nice weighted way both stress and strain measurements. However, we have adapted this method to our plastic work equivalence assumption in each direction.

The classical Hill model can be retrieved from (22, 23, 24) equations where no damage is assumed. This leads to following expression :

$$F(\sigma_{22} - \sigma_{33})^2 + G(\sigma_{11} - \sigma_{33})^2 + H(\sigma_{11} - \sigma_{22})^2 + 2N\sigma_{12}^2 + 2L\sigma_{23}^2 + 2M\sigma_{31}^2 = 2\sigma_F^2 \tag{48}$$

Using axis transformation relation (42) and Hill's formula (48), we can express the plastic stress for one tensile test in an α direction by :

$$\sigma_H^2(\alpha) = \frac{2\sigma_F}{(H+G) + (F-G)\sin^4(\alpha) + (2N-2H-G)\sin^2(\alpha)\cos^2(\alpha)} \tag{49}$$

The Lankford coefficient already defined in section 2.3.2 can be expressed thanks to the normalized rule applied on Hill criterium. This gives the final result :

$$\Gamma_H(\alpha) = \frac{H - (F+G+4H-2N)\sin^2(\alpha)\cos^2(\alpha)}{F\sin^2(\alpha) + G\cos^2(\alpha)} \tag{50}$$

In relations (49) and (50), H index means : value deduced from Hill plasticity, and in the following functional ϕ, exp. index significates value deduced from experiments :

$$\phi = \sum_{i=1,j} (1-\eta) \left[\frac{\sigma_H(\alpha_i) - \sigma_{exp}(\alpha_i)}{\sigma_{F_{exp}}} \right]^2 + \eta \left[r_{exp}(\alpha_i) \right]^2 \tag{51}$$

where j gives the total number of different directions α_i explored by experiments, η is a weighting factor defining the weight of stress and strain measurement and $\sigma_{F\,exp}$ is the stress measurement average.

We determine the set of parameters F, G, H, N minimising the functional ϕ by a classical least square method for different material states. From the general Hill formula (48) and the knowledge of plastic work level, the necessary multi-linear stress strain curves $(\sigma_{11}\,\varepsilon_{11})$, $(\sigma_{22}\,\varepsilon_{22})$, $(\sigma_{33}\,\varepsilon_{33})$, $(\sigma_{12}\,\varepsilon_{12})$ can be produced. As no information on $(\sigma_{13}\,\varepsilon_{13})$ and $(\sigma_{23},\,\varepsilon_{23})$ curves are available, they are assumed to be equal to $(\sigma_{12}\varepsilon_{12})$ curve.

3.3 Calibration of the damage model

The sample shape is modified from the one used in preceding sections 3.1 and 3.2. Our goal is to localize the striction phenomena where our longitudinal and

thickness extensometers are settled. The shape defined on figure 4 has been chosen among others for the quite good homogeneity property of the stress and strain fields in the reduced section [21].

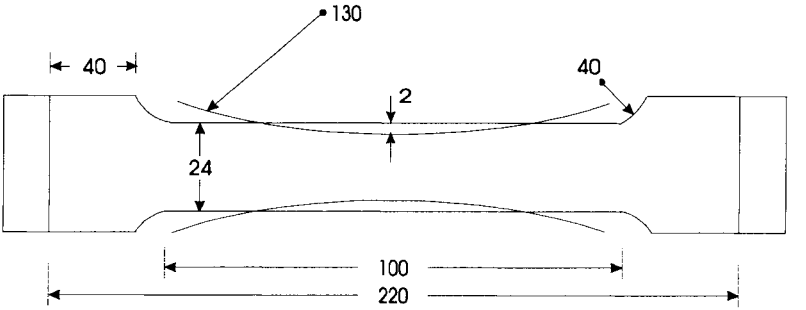

Figure 4. Shape description of the samples used for damage measures.

The needed curves are the damage energy released rate-damage ones : Y_iD_i. From equation (10d) applied on a tensile test in a direction i, we get :

$$Y_i = \frac{\sigma_{ii}^2}{E_i(1-D_i)^3} \tag{52}$$

Thanks to the loading-unloading cycles, the evolution of the effective Young modulus $\overline{E}_i(\varepsilon_{ii})$ is measured. This curve associated with equation (18) gives the damage component evolution $D_i(\varepsilon_{ii})$:

$$D_i(\varepsilon_{ii}) = 1 - \sqrt{\frac{\overline{E}_i(\varepsilon_{ii})}{E_i}} \tag{53}$$

where E_i is the initial value of the Young modulus.

So as $\sigma_{ii}(\varepsilon_{ii})$ is known by measurement and $D_i(\varepsilon_{ii})$ is defined by equation (53) using equation (52), we can produce Y_i D_i curves easily for i equal 1 and 2. In our model, a bilinear model is fitted on these experimental points (fig. 5).

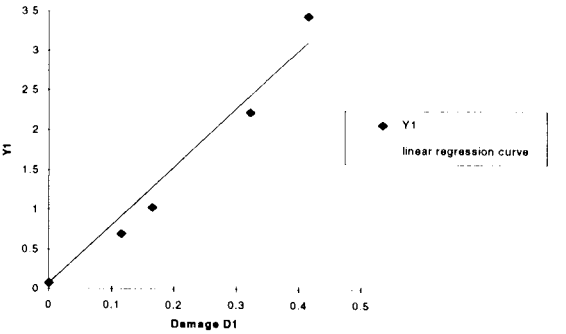

Figure 5. Bilinear description of the damage energy released rate (N/mm^2) for a classical deep drawing steel.

Concerning the thickness direction, such a direct approach cannot be applied as it is not possible to perform cyclic tensile test in this direction. However the Y_{03}

value is directly deduced from equation (52) where D_3 equal zero. For D_{t3} value, we take advantage of the thickness measurement during the performed tensile tests, a direct algebraic transformation of equation (18) gives :

$$D_3(\varepsilon_{ii}) = 1 + \frac{\nu_{3i}\sigma_{ii}}{(1 - D_i(\varepsilon_{ii}))E_3\varepsilon_{33}} \tag{54}$$

Knowing the damage work associated to ε_{ii} and the assumption of damage work equivalence in each direction, D_{t3} is obtained.

3.4 Computations of $(\bar{\sigma},\bar{\varepsilon})_i$ curves

Thanks to the previous experiment analysis, we dispose of :

- $(\sigma_{ii}\varepsilon_{ii})$ multi-linear curves for i = 11, 22, 33, 13, 32, 12 (see section 3.2) ;
- $D_{ii}(\varepsilon_{ii})$ curves are measured from equation (52) for i = 11 and 22.

So, using relation (2), $(\bar{\sigma}_{ii}\bar{\varepsilon}_{ii})$ curves are easily obtained for directions 11 and 22. To apply the same approach to other directions, we miss $D_{ii}(\varepsilon_{ii})$ curves. However, the curve Y_3 (D_3) has been computed thanks to the damage work equivalence principle. So using relation (52) with the σ_{33} stress produced by the Hill model, we can reach $D_{33}(\varepsilon_{33})$ curve and the final $(\bar{\sigma}_{33}\bar{\varepsilon}_{33})$ behaviour.

Concerning shear curve, using the (σ_{12} ε_{12}) Hill curve we integrate in a decoupled way damage evolution and then apply relation (2). Equality of shear curves is again assumed.

4. CALIBRATION OF TWO DIFFERENT STEEL SHEETS

The above procedure has been applied on one high tensile steel sheet (code 1) and on a classical deep drawing steel sheet (code 2) The table 2 gives the final set of parameters for a fitting using tensile test in large strains in 7 directions (α = 0, 15, 30, 45, 60, 75, 90) and the weighting coefficient of η equal to 0,5.

Table 2
The material parameters

Elastic parameters								
	E_1	E_2	E_3	G_{12}	μ_{12}	μ_{13}	μ_{23}	
1	210000	203500	207000	83000	0.28	0.32	0.30	
2	157000	158000	157700	53600	0.36	0.34	0.34	
Initial flow stress ($\sigma = \bar{\sigma}$ here)					Linear effective hardening assumption			
	$\bar{\sigma}_{y1}$ (N/mm²)	$\bar{\sigma}_{y2}$ (N/mm²)	$\bar{\sigma}_{y3}$ (N/mm²)	$\bar{\sigma}_{y12}$ (N/mm²)	$\bar{E}_{t1}$ (N/mm²)	$\bar{E}_{t2}$ (N/mm²)	$\bar{E}_{t3}$ (N/mm²)	$\bar{E}_{t12}$ (N/mm²)
1	266	277	284	161	5338	6026	6076	459
2	108	104	110	65	5262	5167	3029	650
Damage curve parameters								
	Y_{10} (N/mm²)	Y_{20} (N/mm²)	Y_{30} (N/mm²)	D_{t1} (N/mm²)	D_{t2} (N/mm²)	D_{t3} (N/mm²)		
1	0.34	0.38	0.39	14.65	13.45	14.05		
2	0.075	0.068	0.077	20.55	20.55	3.53		

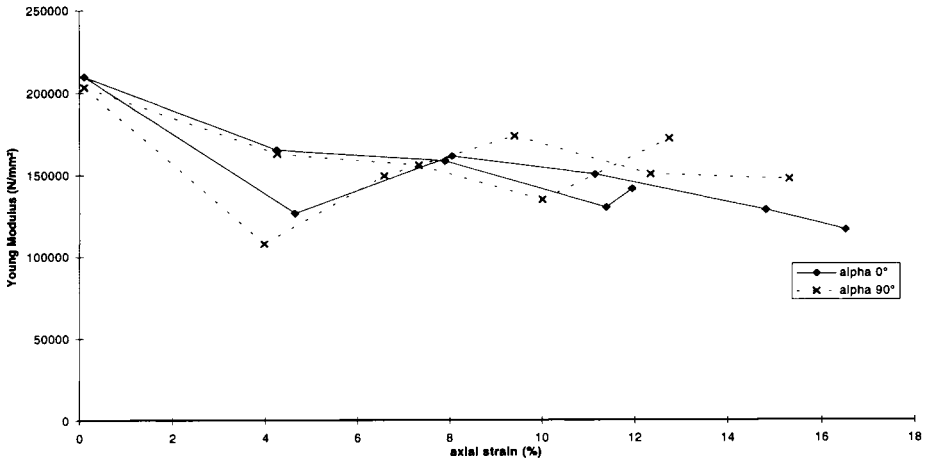

(a) high-tensile steel

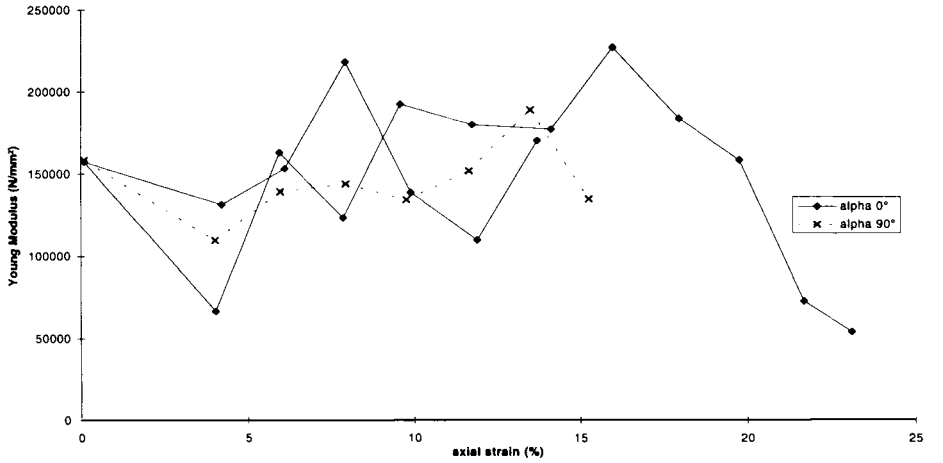

(b) deep drawing steel

Figure 6. Evolution of Young modulus with axial strain.

For high tensile steel sheet, the experiment results have defined decreasing Young modulus (figure 6a), so the model application seems quite right. However for deep drawing steel sheet, this decreasing character (figure 6b) is not observed and damage curve parameters are quite inaccurate. The first rough analysis of the experiments has produced a set of parameters using the linear hardening assumption.

5. VALIDATION EXPERIMENTS AND SIMULATIONS

Reference [1] has already presented experiments and simulations such as hemispherical punch stretching or deep drawing by cylindrical and square punches.

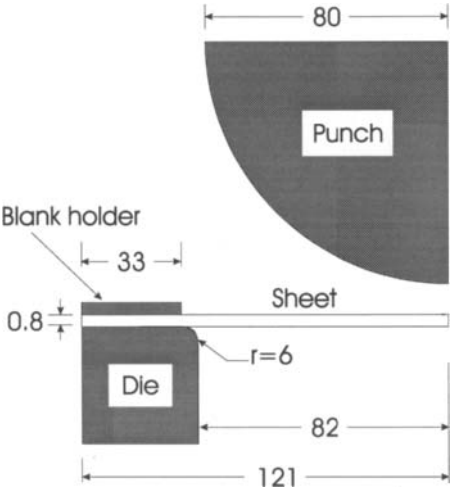

Figure 7. Biaxial Nakazyma test conditions

As one of our present goals is the prediction of forming limit diagrams, we have simulated the Nakazyma test producing the biaxial tensile condition. This test can be described by following features :

- initial rectangular blank of 0.8 mm thick;
- spherical punch with a radius of 80 mm;
- Coulomb friction coefficient of 0,05;
- blankholder shape and die shape are defined on figure 7.

The blank is fixed horizontally on a circle of 242 mm diameter, so only this zone is meshed. Vertical displacement is prevented by contact with die and blankholder which are both totally fixed.

The simulations are computed with the non linear finite element code LAGAMINE developed by the department MSM of Liège University. The volume finite element discretization consists in one layer of 705 8-node mixed elements. The tools are modelled by one spherical segment for the punch and two sets of respectively 20 and 140 triangles for the blankholder and die. The contact problem is treated by 1410 surface contact elements based on a penalty approach [22] with the penalty coefficient of 500 Mpa/mm^3. The simulation is driven by the vertical punch displacement and is stopped for a punch depth of 32 mm. By symmetry only one quarter of the experiment is simulated. Figure 8 presents the equivalent strain at the punch depth of 30 mm, the material dependence is clearly illustrated. The steel for deep drawing application shows a large repartition of the strain when the high-tensile steel has a strained zone more localized and of higher strain level.

The equivalent damage variable is very interesting, again a different behaviour can be checked for each steel (figure 9). The rupture localization predicted by the higher value of damage are in good concordance with the experimental crack observation.

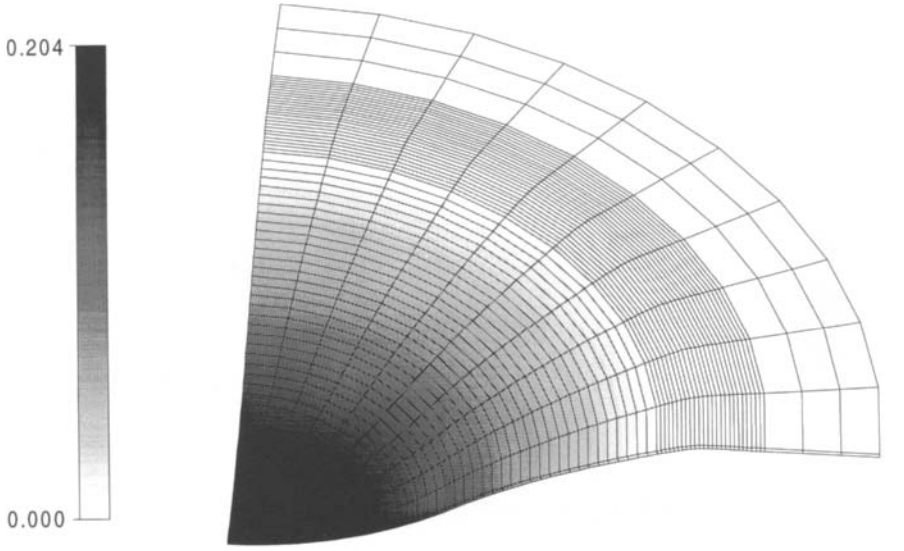

a) high tensile steel

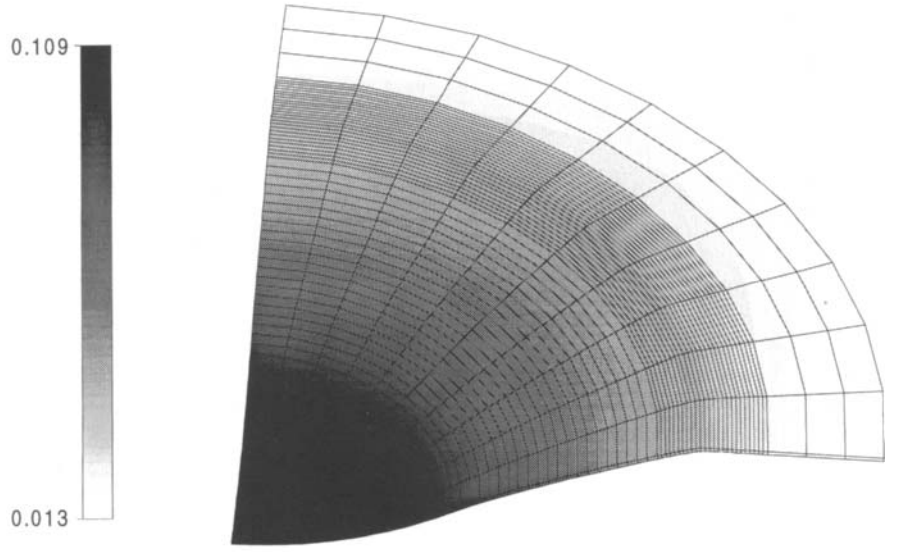

b) deep drawing steel

Figure 8. Equivalent strain computed for a punch depth of 30 mm.

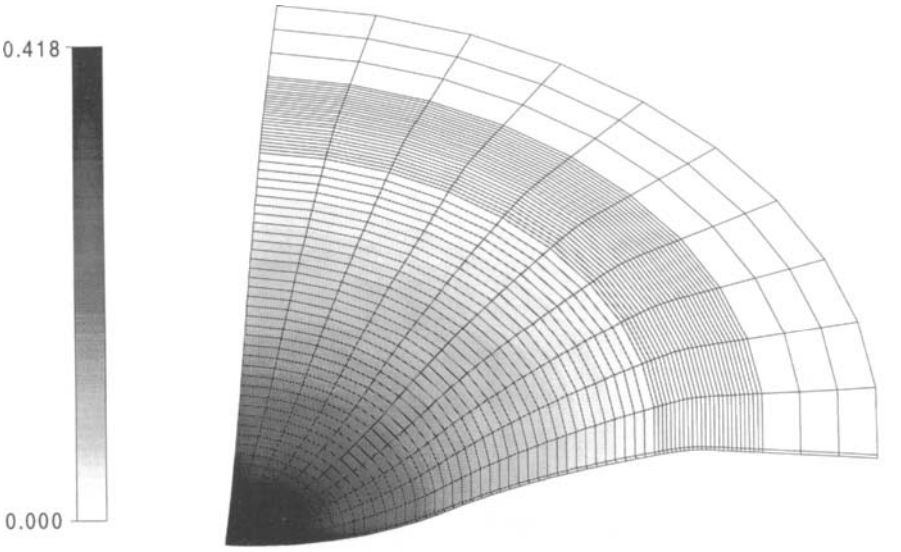

a) high tensile steel

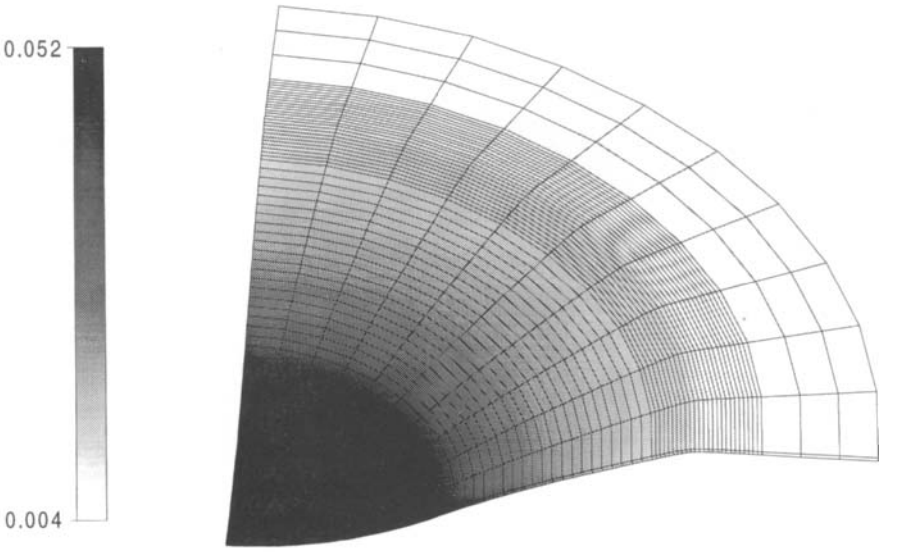

b) deep drawing steel

Figure 9. Equivalent damage variable computed for a punch depth of 30 mm.

7. CONCLUSION

An energy-based anisotropic elastoplastic damage model at finite strain has been presented in this paper to characterize progressive damage and crack growth. Throughout the discussion, the concept of energy plays a very important role not only in deriving the damage effect tensor $\underline{\underline{M}}$ ($\underline{\underline{D}}$), the damage characteristic tensor $\underline{J}$ and the effective plastic characteristic tensor $\underline{\underline{H}}$ but also in establishing the plastic evolution law and the damage evolution law.

Even if the presented model - experiment comparisons are already quite encouraging, the lack of decreasing values of Young modulus for deep drawing steel sets a problem to the basic damage theory assumptions. We think that a strong texture effect could explain this experimental observation. We are looking for an increase of Young modulus due to texture evolution compensated by a decrease of Young modulus due to damage. Our measurements should be under this assumption, the result of an unstable equilibrium between these two tendencies. This must of course be checked and it will be our main goal in our further investigation. However, validation procedure is still in progress as we intend to simulate 4 other geometries of Nakazyma tests associated to other typical points of Forming Limit Diagram.

Acknowledgements

The authors would like to acknowledge the National Fund for Scientific Research (Belgium), the Region Wallonne and the steel research center RDCS for their support.

REFERENCES

1. Y.Y. Zhu, S. Cescotto, A Fully Coupled Elasto-Visco-Plastic Damage Theory for Anisotropic Materials. Int. J. Solids and Structures, 1995, vol. 32, n° 11, 1607-1641.
2. R. Hill, A Theory of the Yielding and Plastic Flow of Anisotropic Materials. Proc. Royal Soc. London, 1948, vol. A193, 281-297
3. A. Van Bael, S. Munhoven, J. Winters, A.M. Habraken and P. Van Houtte, An Anisotropic Yield Locus Based on Texture Prediction Implemented in a Finite Element Code. General Workshop COST 512, MMSP'96 Davos, Modelling in Materials Science and Processing. Edited by M. Rappaz and M. Kadro, European Commission, Directorate General XII Science, Research Development, 1048 Brussels, 254-259.
4. C. Teodosiu, Y.Y. Zhu, Evolution of the Intergranular Microstructure at Moderate and Large Strains : Modelling and Computational Significance in "Simulation of Materials Processing : Th. Meth. and Applications", Proc. Numiform'95, ed. S. Shen, P.R. Dawson, Balkema, Rotterdam, 1995, 173.
5. Y.Y. Zhu, S. Cescotto, A.M. Habraken, Chapter "Modelling of Fracture Initiation in Metalforming Processes", in "Materials Processing Defects", ed. S.K. Ghosh, M. Predeleanu, Elsevier Science, 1995, 155-170.

6. X.K. Li, S. Cescotto "Finite Element Method for Gradient Plasticity at Large Strains", Int. J. Num. Meth. In Eng., 1996, 39, 619-633.
7. A.L. Gurson, Continuum Theory of Ductile Rupture by Void Nucleation and Growth, Part I "Yield Criteria and Flow Rules for Porous Ductile Media", ASME Journal of Engineering Materials and Technology, 1977, vol. 99, 2-15.
8. M. Gologanu, J-B Leblond, Numerical and Theoretical Study of Coalescence of Cavities in Periodically Voided Solids, Computational Material Modeling, ASME, 1994, AD-Vol. 42/PVP-vol. 294.
9. J. Carmeliet, Higher Order Damage Models for Localisation Phenomena in Quasi-Brittle Materials : Models and Experiments, Louvain-la-Neuve, 25/3/1995, Presentation on FNRS meeting.
10. J. Lemaître, J.L. Chaboche, Mécanique des matériaux solides, Dunod, 1985.
11. G. Amar, J. Dufailly, Identification and Validation of Viscoplastic and Damage Constitutive Equations, European Journal of Mechanics, A/Solids, 1993, vol. 12, n° 2, 197-218.
12. Y. Zhu, Contribution to the Local Approach of Fracture in Solid Dynamics, Thèse de doctorat en sciences appliquées, Université de Liège, 1993.
13. J.P. Cordebois, F. Sidoroff, Damage Induced Elastic Anisotropy, Euromech 115, Villard de Lans, France, 1979.
14. J.P. Cordebois, Critères d'instabilité plastique et endommagement ductile en grandes déformations, applications à l'emboutissage, PHD, Paris, 1983.
15. C.L. Chow, J. Wang, An Anisotropic Theory of Elasticity for Continuum Damage Mechanics, Int. J. Fract., 1987, 33, 3-16,.
16. S. Munhoven, A.M. Habraken, J. Winters, R. Schouwenaars, P. Van Houtte, Application of an anisotropic Yield Locus Based on Texture to a Deep Drawing Simulation, Numiform'95, Simulation of Materials Processing: Theory, Methods and Applications, Ed. Shen & Dawson, Balkema, (18-21 June 1995), 767-772.
17. S. Valliappan, P. Boonlaulohr, I.K. Lee, Non-Linear Analysis for Anisotropic Materials, Int. J. Num. Meth. In Eng., 1976, 10, 597-606.
18. T.J. Lu, C.L. Chow, On Constitutive Equations of Inelastic Solids with Anisotropic Damage, J. Theory Appl. Fract. Mech., 1990, 14, 187-218.
19. J.C. Simo and M. Ortiz, A Unified Approach to Finite Deformation Elastoplastic Analysis Based on the Use of Hyperelastic Constitutive Equations, Comp. Meth. Appl. Mech. Eng., 49, 221-245.
20. P. Noat, P. Montmitonnet, Y. Chastel, R. Shahani, Anisotropic 3-D Modelling of Hot Rolling and Plane Strain Compression of Al Alloys, Simulation of Materials Processing, 1995, 959-964.
21. R. Estevez, A.M. Habraken, Calibration Method of an Anisotropic Elastoplastic Model Coupled with Damage, Nuphymat'96, Workshop on Numerical and Physical Study of Material Forming Processes, Final Meeting, CEMEF, Sophia-Antipolis, Final Report.
22. A.M. Habraken, J.P. Radu et R. Charlier, Numerical Approach of Contact with Friction Between Two Bodies in Large Deformations, Proc. Of the Contact Mechanics, Int. Symposium, Lausanne, 7-9 octobre 1992.

Damage Mechanics in Engineering Materials
G.Z. Voyiadjis, J.-W.W. Ju and J.-L. Chaboche (Editors)
© 1998 Elsevier Science B.V. All rights reserved.

Modeling of Oxidation and its Effect on the Crack Growth Resistance of Titanium Alloys

Dimitris C. Lagoudas, Pavlin Entchev [1] and Robertus Triharjanto

Center for Mechanics of Composites
Department of Aerospace Engineering
Texas A&M University, College Station, TX 77843-3141

Metals (superalloys) and Metal Matrix Composites (MMC) are being used for elevated temperature applications such as leading edge components in hypersonic aircraft or turbine blades, which undergo highly variable mechanical loads in corrosive environments. Even though protective coatings are used to prevent oxidation, surface wear and microcracks may lead to oxygen penetration into the metallic substrate and subsequent chemical reaction, transforming the metal into a brittle oxide, with detrimental consequences for the integrity and life of the structure. The oxidation of the metal matrix is modeled in the present work by modifying the Fickian diffusion problem in order to simulate the chemical reaction (phase change) in the metal. Two different variants of a fixed grid finite element method for numerical simulation of oxidation are used. The first approach is based on reformulating the governing equation in both the oxide and matrix, resulting in a single, non-linear equation for the whole domain. The second approach tracks the oxidation front and splits the domain into metal and oxide subdomains. In both approaches, the accuracy of the numerical method is measured by comparing the numerical results with the exact solution for specific cases. Coupled with the mechanical analysis, the model is used to estimate the effect of the oxide layer on the energy release rate.

1 Introduction

Metal matrix composites have been proposed for elevated temperature advanced applications, due to their strength and ability to retain their mechanical integrity at relatively high temperatures. Most of the systems that have recently been investigated are the different

[1] On leave from Inst. of Math., Bulgarian Academy of Science. Currently Graduate Student at Texas A&M University

SiC/Ti MMCs. Enviromental effects, such as oxidation, have been shown experimentally to contribute significantly to damage development in SiC/Ti systems at elevated temperatures [1–7]. In these studies, the oxidation is shown to degrade the composite due to the development of a brittle surface oxide layer (TiO_2 on the titanium matrix at elevated temperatures. Fatigue tests on the SCS-6/β21S MMC system [6] show that the life of the unoxidized specimen is greater than the oxidized specimen. Specifically, at 650°C, the fatigue life in an oxidizing environment (air) was found to be only 25% of the fatigue life in an inert gas (argon) environment. However, another study [8] has shown that oxidation during fatigue crack growth improves the material performance by reducing the fatigue crack growth rate.

Figure1 shows an SEM photograph of an oxidized pre-cracked titanium cpecimen. The experiment was performed at Materials and Structures Laboratory at Texas A&M University. As shown on Figure1, an oxide scale of a titanium, approximately equal to $5\mu m$, has been formed after oxidation at 700°C for $24hrs$. Motivated by this and other similar experimental observations, the current research focuses on the modeling of the propagation of surface oxidation fronts and the analysis of the pre-oxidized cracked speciments under applied mechanical load. For the purposes of the numerical implementation, the oxidized crack surfaces are assumed to have a planar geometry.

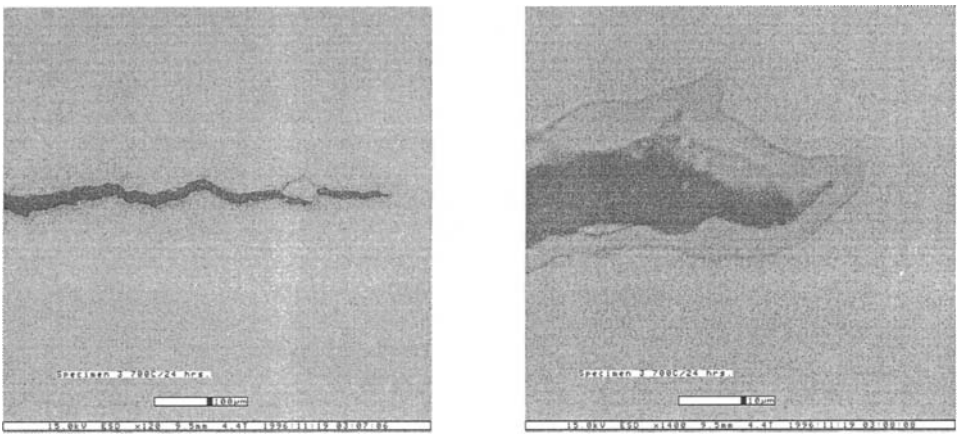

Fig. 1. Oxidized crack in Ti specimen at 700°C for $24hr$

The modeling of oxidation in titanium and the tracking of the oxidation front involves development of numerical techniques, similar to the ones used for phase change problems. Such methods can be generally divided into two groups. The first group consists of algorithms with explicit capturing of the unknown phase change interface [9–13]. The second group includes methods without explicit interface tracking, which are based on smearing the free boundary [14]. The current research investigates both of the approaches in modeling oxidation. The first approach tracks the oxidation front and splits the domain into metal and oxide subdomains. The second approach is based on reformulating the governing PDE in both the

oxide and matrix, resulting in a single non-linear PDE for the whole domain. Both methods are implemented in a fixed grid FEM.

The problem of crack propagation in an oxidized Ti-15-3 specimen is also considered. The present numerical simulation investigates the effect of the stiffness increase [2] and the oxide volumetric expansion [7,2] on the energy release rate.

2 Two-dimensional Fickian diffusion model of oxidation with a moving interface

Let $\Omega \subset R^2$ be a fixed domain with $\partial\Omega$ as its boundary. Ω is partitioned by the interface curve $\tau(t)$ with parameterization $\mathbf{r}(s,t)$, $s_1(t) \leq s \leq s_2(t)$ into two subdomains Ω_1 and Ω_2, respectively, such that $\Omega = \Omega_1 \cup \Omega_2$, $\tau = \Omega_1 \cap \Omega_2$, and $\partial\Omega = \partial\Omega_1 \cup \partial\Omega_2$ (Fig. 2). Assuming

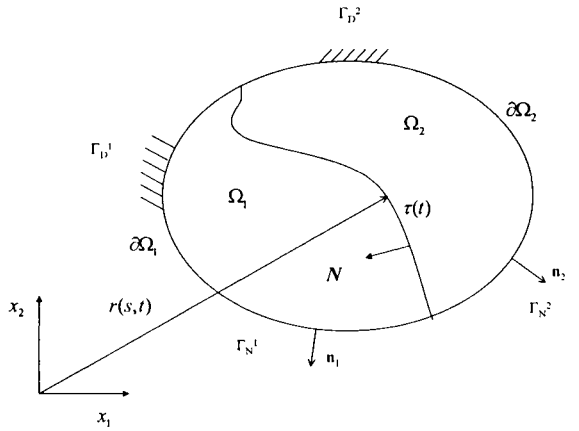

Fig. 2. Two-dimensional domain with interface $\tau(t)$ separating two different phases, which occupy Ω_1 and Ω_2, respectively

that Fickian diffusion is valid, the total mass concentration of oxygen in Ω_1 and Ω_2 satisfies the following equations [15] :

$$\frac{\partial c_1(\mathbf{x},t)}{\partial t} = \nabla \cdot (D_1 \nabla c_1(\mathbf{x},t)), \quad \mathbf{x} \in \Omega_1, \tag{1}$$

$$\frac{\partial c_2(\mathbf{x},t)}{\partial t} = \nabla \cdot (D_2 \nabla c_2(\mathbf{x},t)), \quad \mathbf{x} \in \Omega_2. \tag{2}$$

Here $c_1(\mathbf{x},t)$ and $c_2(\mathbf{x},t)$ are the total mass concentrations of oxygen in Ω_1 and Ω_2, respectively, and D_1 and D_2 are the diffusivities of the two phases (i.e., oxide scale and titanium matrix) that occupy Ω_1 and Ω_2 , respectively.

The initial conditions are

$$c_1(\mathbf{x},0) = f_1 \quad \mathbf{x} \in \Omega_1(t), \tag{3}$$

$$c_2(\mathbf{x},0) = f_2 \quad \mathbf{x} \in \Omega_2(t) \text{ and} \tag{4}$$

$$\mathbf{r}(s,0) = \mathbf{r}_0(s). \tag{5}$$

The boundary conditions on $\partial\Omega$ are

$$c_1(\mathbf{x},t) = \hat{c}_1(\mathbf{x},t) \text{ on } \Gamma_D^1 \text{ and } -D_1\nabla c_1 \cdot \mathbf{n}_1 = \hat{m}_1^n(\mathbf{x},t) \text{ on } \Gamma_N^1, \tag{6}$$

$$c_2(\mathbf{x},t) = \hat{c}_2(\mathbf{x},t) \text{ on } \Gamma_D^2 \text{ and } -D_2\nabla c_2 \cdot \mathbf{n}_2 = \hat{m}_2^n(\mathbf{x},t) \text{ on } \Gamma_N^2, \tag{7}$$

where $\hat{c}_1(\mathbf{x},t)$, $\hat{c}_2(\mathbf{x},t)$ are prescribed oxygen concentrations. $\hat{m}_1^n(\mathbf{x},t)$, and $\hat{m}_2^n(\mathbf{x},t)$ are normal components of oxygen mass fluxes through the external boundaries of Ω_1 and Ω_2 for $t > 0$, with outward unit normal vectors $\mathbf{n}_1$ and $\mathbf{n}_2$ and

$$\partial\Omega_1 = \Gamma_D^1 \cup \Gamma_N^1, \quad \partial\Omega_2 = \Gamma_D^2 \cup \Gamma_N^2. \tag{8}$$

The interface $\tau(t)$ that partitions Ω into two regions is a phase boundary that separates the oxidized part from the metallic part, where oxidation has not taken place. Assuming that the chemical reaction occurs on a short time scale compared with the diffusion process, when the concentration of oxygen reaches a critical value c_{cr}, oxidation instantaneously takes place and the interface moves, always satisfying the critical concentration requirement. The appropriate interface conditions, expressing conservation of total oxygen mass across the interface and initiation of the oxidation process whenever a critical oxygen concentration is reached, are given by

$$-D_1(\nabla c_1) \cdot \mathbf{N} = -D_2(\nabla c_2) \cdot \mathbf{N} + [c]V, \tag{9}$$

$$c_1(r,t) = c_{cr} \quad , \quad c_2(r,t) = c_{cr} - [c], \tag{10}$$

where $\mathbf{N}$ is the unit normal vector on $\tau(t)$ pointed outward Ω_2, V is the normal velocity of the oxidation interface, namely, $V = \frac{d\mathbf{r}}{dt} \cdot \mathbf{N}$ and $[c]$ is the jump discontinuity of the oxygen concentration at the interface.

3 Numerical Simulation of Oxidation Process

3.1 Discrete Interface Method

As mentioned in the introduction, the discrete interface method is a variant of front tracking techniques, whereby the location of the moving interface is found by solving the oxygen diffusion equations in adjacent to the interface domains and by connecting the solution through appropriate interface conditions. The discrete interface formulation starts by multiplying the governing equations (1),(2) in two phases with the test function φ and integrating over the region Ω, i.e.,

$$\int_{\Omega_1} D_1 \nabla^2 c_1 \varphi dA + \int_{\Omega_2} D_2 \nabla^2 c_2 \varphi dA = \int_{\Omega} \varphi \left(\frac{\partial c_1}{\partial t} + \frac{\partial c_2}{\partial t} \right) dA. \tag{11}$$

Performing integration by parts and considering the interface condition (9), the above equation yields

$$\sum_{\alpha=1}^{2} \int_{\Omega_\alpha} \left(D_\alpha \nabla\varphi \cdot \nabla c_\alpha - \varphi \frac{\partial c_\alpha}{\partial t} \right) dA = \sum_{\alpha=1}^{2} \int_{\partial\Omega_\alpha - \tau} \varphi D_\alpha \nabla c_\alpha \cdot \mathbf{N} ds + \int_{\tau} \varphi [c] V ds. \tag{12}$$

Applying Galerkin method (i.e. use similar shape function for the concentration and the test function), equation (12) can be rewritten as

$$\sum_{\alpha=1}^{2} \int_{\Omega_\alpha} \left(D_\alpha \nabla\varphi \cdot \nabla c_\alpha - \varphi \frac{\partial c_\alpha}{\partial t} \right) dA = \int_{\tau} \varphi [c] V ds, \tag{13}$$

and

$$c(\mathbf{x}) = \sum_{i=1}^{N} c_i \varphi_i,$$

where $\{\varphi\}$ are the shape functions. c_i are the nodal concentration values. Using linear interpolation in time, which is a standard procedure for the time dependent finite element problem [16], the concentration at any time point can be expressed as

$$\{c_\alpha\} = (1-\theta)\{c_\alpha^n\} + \theta\{c_\alpha^{n+1}\}, \quad 0 \le \theta \le 1, \quad \alpha = 1, 2. \tag{14}$$

Using (14) and finite difference approximation for the time derivative, the equation (13) can be rewritten as

$$\sum_{\alpha=1}^{2} \left[-\frac{\mathbf{M}_\alpha^{n+1}}{\Delta t} + \theta \mathbf{K}_\alpha^{n+1} \right] \mathbf{c}_\alpha^{n+1} = \sum_{\alpha=1}^{2} \left[-\frac{\mathbf{M}_\alpha^{n}}{\Delta t} + \theta \mathbf{K}_\alpha^{n} \right] \mathbf{c}_\alpha^{n} + \mathbf{F}^n, \tag{15}$$

where

$$K_{\alpha_{ij}} = \int_{\Omega_\alpha} D_\alpha \nabla\varphi_i \cdot \nabla\varphi_j dA \tag{16}$$

$$M_{\alpha_{ij}} = \int_{\Omega_\alpha} \varphi_i \cdot \varphi_j dA \tag{17}$$

$$F_i = \int_{\tau} [c]\varphi_i V ds = \frac{1}{\Delta t} \int_{\Omega_m} [c]\varphi_i dA \tag{18}$$

and Ω_m is the area swept by the interface during its propagation in time Δt.

An iterative approach is needed in solving eq.(15) since it has 2 interdependent variables. The solution strategy starts with guessing the interface location for the next time increment so that $\mathbf{M}_\alpha^{n+1}$ and $\mathbf{K}_\alpha^{n+1}$ can be evaluated. After solving the linear system, the interface location is calculated by interpolating the nodal concentration $\mathbf{c}_\alpha^{n+1}$. The iterative process is ended when the difference between the interface location used to calculate $\mathbf{M}_\alpha^{n+1}$ and $\mathbf{K}_\alpha^{n+1}$, and the interface location obtained by interpolating $\mathbf{c}_\alpha^{n+1}$, is smaller than a prescribed error limit.

3.2 Interface Smearing Method

To avoid dealing with the jump discontinuity, the following change of variables is introduced:

$$\overline{c_2}(\mathbf{x}, t) = c_2(\mathbf{x}, t) + [c]. \tag{19}$$

The single diffusivity coefficient D is introduced by the following equality:

$$D(c) = \begin{cases} D_1, & if \quad c > c_{cr}, \\ D_2, & if \quad c < c_{cr}. \end{cases} \tag{20}$$

By including condition (9) in the governing equations (1) and (2), we obtain

$$\{1 + [c]\,\delta(c - c_{cr})\}\,\frac{\partial c}{\partial t} = \nabla \cdot (D(c)\,\nabla c), \tag{21}$$

where

$$c = \begin{cases} c_1, & if \quad c > c_{cr}, \\ \overline{c_2}, & if \quad c < c_{cr}. \end{cases}$$

Equation (21) combines the governing equations (1) and (2), as well as the interface condition (9). The equivalence of the above two systems of equations is considered in detail

in [14]. To avoid dealing with the Dirac function, the smoothed function $\tilde{\delta}(c - c_{cr}, \Delta)$ is introduced (Δ is the length of a semi-interval in which $\delta(c - c_{cr}, \Delta) \neq 0$). The coefficient $\tilde{G}(c)$ is introduced by the following equality:

$$\tilde{G}(c) = 1 + [c]\,\tilde{\delta}(c - c_{cr}, \Delta). \tag{22}$$

In the interval $(c_{cr} - \Delta, c_{cr} + \Delta)$, the coefficient $D(c)$ is approximated by a linear function, i.e.,

$$\tilde{D}(c) = \begin{cases} D_1, & \text{if} \quad c > c_{22}, \\ \dfrac{D_1 - D_2}{2\Delta} c + \dfrac{D_2 c_{22} - D_1 c_{11}}{2\Delta}, & \text{if} \quad c_{11} \leq c \leq c_{22}, \\ D_2, & \text{if} \quad c < c_{11}, \end{cases} \tag{23}$$

where

$$c_{11} = c_{cr} - \Delta, \quad c_{22} = c_{cr} + \Delta.$$

By combining equations (21), (22) and (23), the following equation is obtained:

$$\tilde{G}(c)\frac{\partial c}{\partial t} = \nabla \cdot \left(\tilde{D}(c)\nabla c\right). \tag{24}$$

As a result of the above problem reformulation, instead of solving equations (1), (2) and (9), we have to solve a single non-linear PDE (24).

Multipying (24) by the test function φ and integrating over the domain Ω for a fixed time t, we have:

$$\int_{\Omega} \tilde{G}(c)\frac{\partial c}{\partial t}\varphi dA = \int_{\Omega} \nabla \cdot \left(\tilde{D}(c)\nabla c\right)\varphi dA. \tag{25}$$

By applying Green's formula, the right hand side term in the above equation becomes

$$\int_{\Omega} \tilde{G}(c)\frac{\partial c}{\partial t} \cdot \varphi dA + \int_{\Omega} \tilde{D}\nabla c \cdot \nabla\varphi dA - \int_{\partial\Omega} \tilde{D}\frac{\partial c}{\partial n}\varphi ds = 0. \tag{26}$$

Assuming

$$\frac{\partial c}{\partial n} = 0 \quad \text{on} \quad \Gamma_N$$

and following the standard Galerkin procedure, the weak formulation of the problem for fixed t becomes

$$\int_{\Omega} \tilde{G}(c)\frac{\partial c}{\partial t} \cdot \varphi dA + \int_{\Omega} \tilde{D}\nabla c \cdot \nabla\varphi dA = 0, \quad t > 0, \tag{27}$$

where φ is in the space of piecewise linear functions. Using the standard FEM approach, the oxygen concentration is given by

$$c(\mathbf{x}, t) = \sum_{i=1}^{N} c_i(t)\varphi_i(\mathbf{x}), \tag{28}$$

where $c_i(t)$ are the nodal values of oxygen concentration. Substituting (28) into (27) and enforcing eq. (27) for all test functions φ_j, we have:

$$\mathbf{M}\frac{d\mathbf{c}}{dt} + \mathbf{K}\mathbf{c} = 0, \tag{29}$$

where $\mathbf{K}$ and $\mathbf{M}$ are corresponding "stiffnes" and "mass" matrices with entries

$$M_{ij} = \int_{\Omega} \tilde{G}\varphi_j\varphi_i dA, \tag{30}$$

$$K_{ij} = \int_{\Omega} \tilde{D}\nabla\varphi_j \cdot \nabla\varphi_i dA. \tag{31}$$

Using the backward Euler method for the time derivative in the semi-discrete problem (29) we obtain

$$\mathbf{M}\frac{\mathbf{c}^n - \mathbf{c}^{n-1}}{\Delta t} + \mathbf{K}\mathbf{c}^n = 0, \tag{32}$$

where $\mathbf{c}^n$ and $\mathbf{c}^{n-1}$ are the evaluations of $\mathbf{c}$ at n^{th} and $(n-1)^{th}$ time steps, and Δt is the time increment. For given $\mathbf{c}^{n-1}$, eq. (32) results in the following system of equations for the unknown $\mathbf{c}^n$:

$$\left(\frac{\mathbf{M}}{\Delta t} + \mathbf{K}\right)\mathbf{c}^n = \frac{\mathbf{M}}{\Delta t}\mathbf{c}^{n-1}. \tag{33}$$

Note, that matrices $\mathbf{M}$ and $\mathbf{K}$ include the non-linear coefficients $\tilde{G}(\mathbf{c})$ and $\tilde{D}(\mathbf{c})$. Therefore, an iterative process is used in solving (33). The iterative process uses the value of $\mathbf{c}$ from the previous iteration and terminates when the maximum difference between two successive iterative solutions is less than a desired tolerance in the domain.

3.3 Numerical results

To validate the above described numerical algorithm for 2D problems, the following model problem has been solved. We consider a square domain $\Omega = \{(x_1, x_2) : 0 \leq x_1 \leq 100\mu m, 0 \leq$

$x_2 \leq 100\mu m\}$, with the following boundary and initial conditions:

$$c(\mathbf{x}, t) = c_0, \quad \mathbf{x} \in \Gamma_D \quad \text{and} \quad \frac{\partial c}{\partial n} = 0, \quad \mathbf{x} \in \Gamma_N, \tag{34}$$

$$c(\mathbf{x}, 0) = 0, \tag{35}$$

where $\Gamma_D = \{(x_1, x_2) : x_1 = 0, 0 \leq x_2 \leq 100\mu m\}$ and $\Gamma_N = \partial\Omega \setminus \Gamma_D$.

The above formulated 2D problem is equivalent to the 1D problem in x_1 direction, since the resulting concentration is independant on x_2. As it was mentioned in [17], there is an analytical solution for the 1D case, therefore we can use it for comparison purposes. The oxide layer thickness vs. time computed by the two different finite element methods discussed earlier, as well as the analytical solution and SEM photograph of oxidized Ti-15-3 specimen, are plotted in Fig.3. The following parameters, corresponding to Ti-15-3 oxidized at 700°C [15], have been used: $D_1 = 3.02{\cdot}10^{-3}\mu m^2/sec$, $D_2 = 1.431{\cdot}10^{-3}\mu m^2/sec$, $c_{cr} = 0.65{\cdot}c_0$ and $[c] = 0.5{\cdot}c_0$. As it can be seen from Fig.3, both approaches are in agreement with the analytical solu-

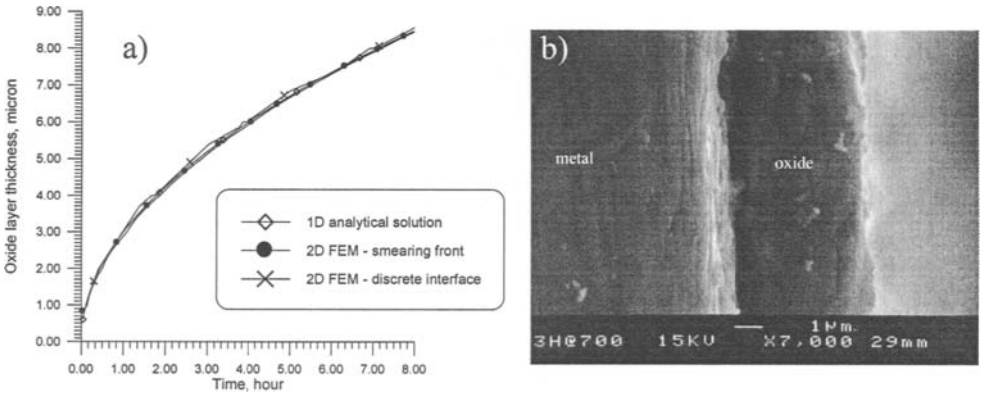

Fig. 3. Oxide layer growth in Ti-15-3: a) Modeling results; b) SEM photograph of the oxide layer on Ti-15-3 formed at 700°C for $3hrs$ [15]

tion and with experimental data. The above level of accuracy has been observed for time increment $\Delta t = 10sec$ and mesh of triangular elements with element size $1\mu m$.

The above described numerical approaches in sections 3.1 and 3.2 have also been compared with the analytical solution of a problem with a geometry similar to the one that will be later investigated for the mechanical problem, i.e., the oxide layer growth from the surface of a semi-infinite crack (see Fig.4). For comparison purposes we take $D_1 = D_2 = D$ and $[c] = 0$, since for this case the problem has an analytical solution (see Appendix A). A finite square domain with dimensions $100\mu m \times 100\mu m$ has been used for computations and the oxidation time was such that the oxide growth was not affected by the presence of the finite external boundaries. The crack length a has been assumed to be equal to $30\mu m$ for the numerical calculations. Results that compare the analytical solution and the two FEM solutions are

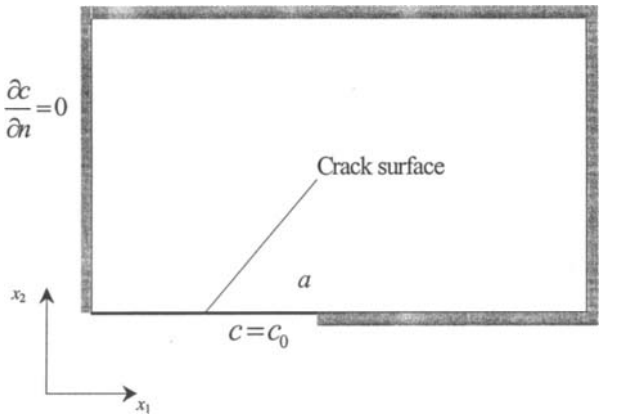

Fig. 4. Schematic of the geometry for the oxidation from a crack surface

shown in Fig.5 and Fig.6. Oxygen concentration profiles perpendicular to the crack surface along x_2 axis (for $x_1 = 0$) are plotted in Fig.5 and profiles ahead of the crack tip (for $x_2 = 0$, $x_1 \geq a$) are plotted in Fig.6. The numerical results obtained with both approaches are in agreement with the analytical solution.

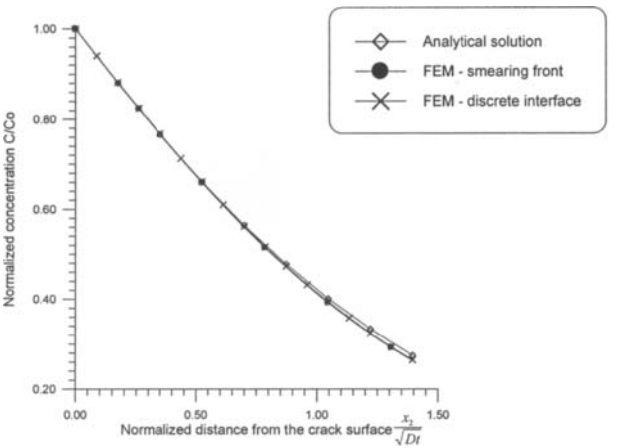

Fig. 5. Oxygen concentration profiles along x_2 perpendicular to the crack surface ($x_1 = 0$) for test case shown in Fig.4

Having gained experience in terms of discretization in space and time from the above example problem, the problem of oxide layer propagation from the surfaces of a crack in Ti-15-3 specimen has been considered under realistic conditions for different diffusion coefficients, D_1 and D_2, and a non-zero concentration jump. The material parameters, corresponding to

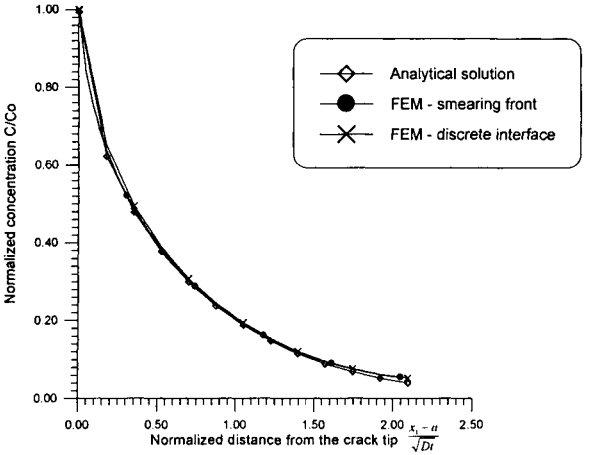

Fig. 6. Oxygen oncentration profiles ahead of the crack tip

the Ti-15-3 at 700°C [15] have been used for the numerical solution of this problem. For the purposes of the analysis, a pre-cracked square Ti-15-3 specimen $15\mu m \times 15\mu m$ with a crack length $8\mu m$ has been considered. The location of the oxidation front at times $0.25hr$, $0.5hr$ and $1hr$ is plotted in Fig.7. Direct comparison with experimental results for oxidation of pre-cracked specimen is very difficult, since the surface crack appears to be non-planar at a length scale comparable with oxide scale thickness, as seen in Fig.1.

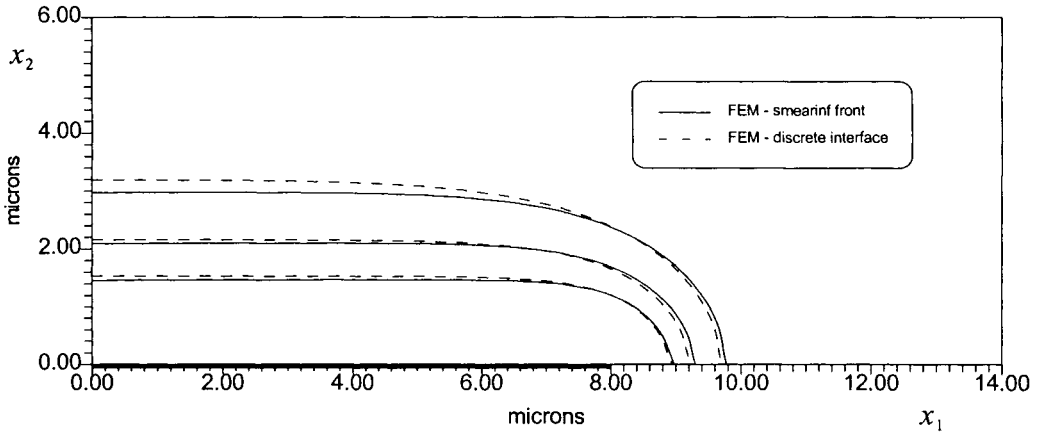

Fig. 7. Simulation of the location of oxidation front in an oxidized Ti-15-3 specimen at 700°C

4 Crack Growth Resistance of a Pre-Oxidized, Pre-Cracked Ti-15-3 Specimen under Mechanical Load.

To investigate the effect of crack surface oxidation on crack growth resistance, a mechanical model simulating pre-oxidized, pre-cracked Ti-15-3 specimen is considered. The geometry and boundary conditions for the mechanical problem are shown in Fig.8. A plate with an edge crack under uniaxial monotonic static loading perpendicular to the crack direction (Mode I) is considered. The particular problem is chosen since its analytical solution has been established and its geometry is similar to that of a compact tension specimen.

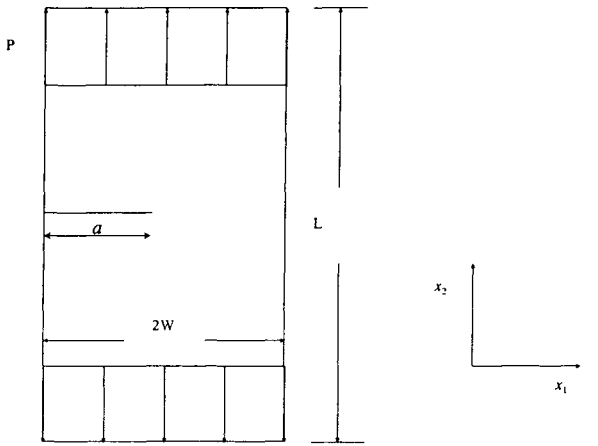

Fig. 8. Boundary value problem for the mechanically loaded oxidized specimen

Three cases are modeled corresponding to the boundary conditions shown in Fig.8. The first case assumes material properties for homogeneous linear elastic material, corresponding to Ti-15-3 (room temperature) and is introduced as a reference solution. The second case considers the mechanical analysis of a preoxidized specimen, tested at room temperature. The third case is similar to the second with additional accounting of the volumetric expansion caused by oxidation.

4.1 Finite Element Implementation

Due to the symmetry in the applied loading and geometry, only half of the domain is modeled. The schematic of the mesh configuration is described in Fig.9, while the actual mesh includes 157 8-node quadrilateral elements. The "spider web" mesh is used since it is known to be accurate in modeling fracture mechanics problem [18,19]. The 8-node quadrilateral element is chosen in order to model the stress and strain singularity at the crack tip. The quarter point method, which captures a square root singularityes in the stress, derived by Henshell

and Shaw [18] and Barsoum [19] is used here. The simulation is performed by means of the commercial finite element software **ABAQUS**.

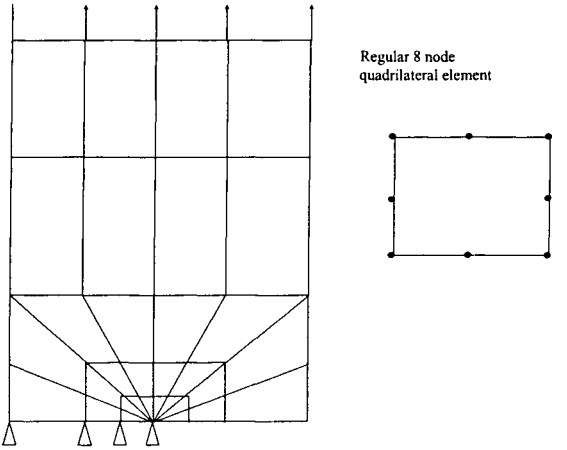

Fig. 9. The quarter point finite element mesh

In the linear elastic case and the case for homogeneous material, the energy release rate $\mathcal{G}$ is equal to the value of J-integral [20,21]. To calculate the energy release rate in FEM, the contour integral method is used. The contour integral method starts with the formulation of J-integral [22], which for the two-dimensional case, can be expressed as

$$J_\Gamma = \int_\Gamma \left(W dx_2 - T_j \frac{\partial u_j}{\partial x_1} ds \right) \tag{36}$$

where Γ is any open curve enclosing the crack tip and W is the elastic strain energy.

The finite element formulation of the J-integral as given by [23] is

$$J_\Gamma = \sum_A \sum_{p=1}^{m} \left\{ \left(W \delta_{1i} - \sigma_{ij} \frac{\partial u_j}{\partial x_1} \right) \frac{\partial q}{\partial x_i} \det \left| \frac{\partial x_k}{\partial \xi_k} \right| \right\}_p w_p, \tag{37}$$

$$\frac{\partial q}{\partial x_i} = \sum_{k=1}^{2} \frac{\varphi_p}{\partial \xi_k} \frac{\partial \xi_k}{\partial x_i} Q_p \tag{38}$$

where m designates the number of Gauss integration points for each element; w_p is the weight for the p^{th} integration point; ξ_k indicates the local coordinates of the elements; q is a smooth function which has a value of unity on Γ and zero at the crack tip, i.e. Q_p has value 1 whenever the node is located on Γ and 0 whenever the node is located at the crack tip. $\sum_A$ indicates that the summation is performed over the elements in area A enclosed by Γ

and the crack surfaces, and the quantity in brackets in eq.(37) is evaluated at the p^{th} Gauss point of each element.

The numerical results for the first case show that the numerical method has very good accuracy. Table 1 shows the comparison of J-integral values calculated using the exact solution versus the numerical method. The finite element model simulates a $20mm \times 60mm$ Ti-15-3 specimen with $1MPa$ tensile load. The material properties for the Ti-15-3 specimen are taken from [24] and are tabulated in Table 2.

	exact	numerical
J-integral, $MPa{\cdot}m$	2.056	2.028

Table 1
Comparison of the stress intensity factor on homogeneous case

	Ti-15-3	TiO_2
Young modulus, GPa	110	182
Poisson ratio	0.33	0.33

Table 2
Material properties of Ti-15-3 and TiO_2

The second case simulates the mechanical response of a pre-oxidized specimen with a center crack and an oxide layer formed along the crack surfaces. The geometry of the oxide layer is simulated by utilizing results obtained by the oxidation model presented in section 3.3, similar to ones shown in Fig.7.

The presence of the oxide, which has different elastic constants than the metal, introdusec a modification in the formulation of the J-integral, which is now path dependent [25]. To briefly show this, assume that Γ^* is a closed path, i.e. $\Gamma^* = \Gamma_1 + \Gamma_2$+surface crack connecting the curves, with Γ_1 being in the metal phase, while Γ_2 inside the oxide layer, as shown in Fig.10. By evaluating the J-integral on Γ^*, the divergence theorem can be applied so that

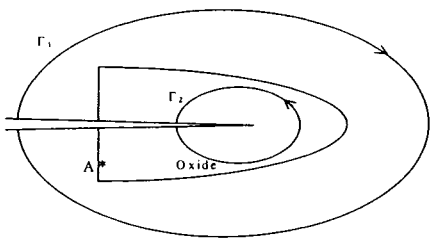

Fig. 10. Schematic representation of an oxidated cracked specimen with partial oxidation of the crack surfaces

eq.(36) can be rewritten as

$$J_{\Gamma^*} = \int_{\Gamma^*} \left(W dx_2 - T_j \frac{\partial u_j}{\partial x_1} ds \right) = \int_{A^*} \left[\frac{\partial W}{\partial x_1} - \frac{\partial}{\partial x_j} \left(\sigma_{ij} \frac{\partial u_j}{\partial x_1} \right) \right] dA. \tag{39}$$

When the material contains an inhomogeneity in area A^*, $W = W(x_i, \varepsilon_{ij})$. Therefore, the first term on the right hand side of eqn.(39) can be expressed as

$$W(x_i, \varepsilon_{ij})_{,1} = \left[\frac{\partial W}{\partial x_i} \frac{\partial x_i}{\partial \varepsilon_{ij}} + \frac{\partial W}{\partial \varepsilon_{ij}} \right] \varepsilon_{ij,1} = W_{,i} \frac{\partial x_i}{\partial \varepsilon_{ij}} \varepsilon_{ij,1} + \sigma_{ij} u_{i,j1}. \tag{40}$$

Substituting eqn.(40) into (39) yields

$$J_{\Gamma^*} = J_{\Gamma_1} - J_{\Gamma_2} = \int_{A^*} W_{,i} \frac{\partial x_i}{\partial \varepsilon_{ij}} \varepsilon_{ij,1} dA, \tag{41}$$

which concludes that the J-integral in heterogeneous material is path dependent. From the above equation it can be concluded that, if the oxide layer geometry is simulated as described in Fig.7, the J-integral would be different for different paths. To simplify the numerical implementation, only the oxide layer surrounding the crack tip is considered, as schematically shown in Fig.10. By considering only part of the oxide scale, the J-integral needs to be calculated only on two different paths (inside and outside the oxide layer). The oxide layer is described by elements with different elastic stiffness than the rest of the material. The work of Wallace [26] on Ti-β21S concludes that the oxide layer has higher stiffness than its metal phase. By simulating Wallace's oxidation experiment, we can estimate Young's modulus of the TiO_2 compound, which is also tabulated in Table 2.

Fig.11 shows the J-integral measured on the domain inside and outside the oxide layer for the second case. It can be seen from the picture that as the oxide layer grows, the J-integral decreases. This is consistent with the theoretical prediction described in equation (B.4), i.e. as the overall stiffness increases, the J-integral decreases. The result also reconfirms that the J-integral is path dependent in heterogeneous materials and is consistent with the analytical evaluation in [25]. However, since the difference between the elastic constants of the oxide and metal is small, the difference in the values of the J-integral calculated inside and outside of the oxide layer is small.

Fig.12 shows contour plots of σ_{22} values for the oxidized and unoxidized specimens close to the crack tip. The thickness of the oxide layer is $0.4mm$ for this case and metal-oxide interface is shown by a white line in Fig.12b. The result for the oxidized specimen shows that there is a jump in σ_{22} due to the difference in the elastic stiffness of the metal and the oxide.

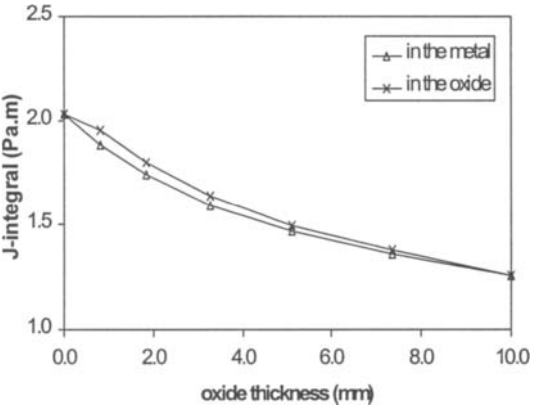

Fig. 11. J-integral for the oxidized Ti-15-3 specimen

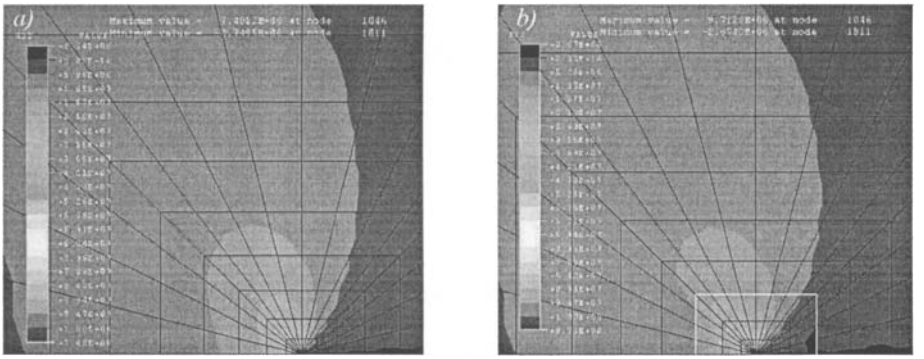

Fig. 12. Contour plot of σ_{22} for: a) unoxidized Ti-15-3 specimen; b) oxidized Ti-15-3 specimen (the domain corresponds to the shaded area in Fig.9)

5 Conclusions

Two implementations of fixed grid finite element method, for solving oxidation in Ti-15-3 have been derived from two different concepts (i.e. the interface smearing method and discrete interface method). Both approaches have been tested on problems which have analytical solution and have shown very good accuracy. Validated numerical models have been used to simulate the oxide propagating from the crack surface in Ti-15-3 specimen.

The mechanical responses of the fractured specimen have been succesfully modeled using the quarter point method. For the pre-oxidized specimen, the model predicts that the energy release rate will decrease as the oxide layer grows. The decrease is due to the oxide scale which has higher Young's modulus than the unoxidized metal phase.

The presented results can be considered as preliminary in nature and represent initial stages of thorough investigation on the behavior of metal matrix composites (MMC) at high operating temperatures. Future research will use the current oxidation and mechanical models to simulate the thermomechanical response of MMC under oxidizing environments undergoing monotonic and cyclic loading.

Acknowledgments — The authors wish to express appreciation for the support provided by the Air Force Office of Scientific Research under grant No. F49620-94-1-0341. The authors also acknowledge P.K.Imbrie and David Miller for the pictures of the oxidized specimens.

References

[1] D.H. Allen, M.R. Eggleston, and L.D. Hurtardo. Recent research on damage development in SiC/Ti continuous fiber metal matrix composites. In E.A. Armanios, editor, *Fracture of Composites*, Key Engineering Material. Trans Tech Publications. To appear.

[2] L.A. Wittig and D.H. Allen. Modeling the effect of oxidation on damage on SiC/Ti-15-3 metal matrix composites. *J. of Engr. Matls. and Tech.*, 116:421–427, 1994.

[3] B.A. Lerch, T.P. Gabb, and R.A. Mackay. Heat treatment study of the SiC/Ti-15-3 composite system. Technical Report TP-2970, NASA, 1990.

[4] P. Bartolotta and M.J. Verrilli. Thermomechanical fatigue behaviour of SiC/Ti-24Al-11Nb in air and argon environments. Technical Report TM-105723, NASA, 1992.

[5] W.C. Revelos, J.W. Jones, and E.J. Dolley. Thermal fatigue of SiC/Ti-15Mo-2.7Nb-3Al-0.2Si composite. *Metallurgical and Materials Transaction*, 26A:1167–1181, 1995.

[6] J.M. Foulk. A model for predicting the damage and oxidation dependent life of SCS-6/TI-β21S[0] metal matrix composite. Master's thesis, Texas A&M University, College Station, TX., 1997.

[7] D.C. Lagoudas, S. Xu, D. Miller, and D.H. Allen. Damage in oxidized titanium metal matrix composites. In *Proceeding of the ASME Aerospace and Material Divisions, 1996 ASME International Mechanical Engineering Congress and Exposition*, volume 73, pages 225–237, 1996.

[8] J. Ferreira, E. Aghion, and N. Comins. High temperature fatigue crack growth behavior of Timetal-21S in an oxidizing environment, 1997. Mechanical Engineering Department, University of Natal, Durban, 4001, South Africa.

[9] J. Douglas and G.M. Gallie. On numerical integration of a parabolic differential equations subject to a moving boundary. *Duke Math. J.*, 22(4):557–572, 1995.

[10] F.P. Vasil'ev and A.B. Uspenskii. Finite-difference solution of the two–phase Stefan problem. *USSR Comput. Math. & Math. Phys.*, 3(5), 1963.

[11] J.C. Chen and Y.C. Huang. Thermocapillary flows of surface melting due to a moving heat flux. *Int. J. Heat Mass Transfer*, 33:1165–1175, 1990.

[12] M.G. Worster. Solidification of an alloy from a cooled boundary. *J. Fluid Mech.*, 167:481–501, 1986.

[13] V.K. Manolov, O.P. Iliev, and I.V. Bizhev. Numerical simulation of nitrogen diffusion in a solid chromium particle. *Journal of Theoretical and Applied Mechanics*, 24, 1993.

[14] A.A. Samarskii and B.D. Moiseenko. An economic continuous calculation scheme for the Stefan multidimensional problem. *USSR Comput. Math. & Math. Phys.*, 5(5):43–58, 1965.

[15] D.C. Lagoudas, X. Ma, D.A. Miller, and D.H. Allen. Modeling of oxidation in metal matrix composites. *Int. J. Engng Sci.*, 33(15):2327–2343, 1995.

[16] J.N. Reddy. *An Introduction to the Finite Element Method.* McGraw-Hill Inc., 1993.

[17] P.B. Entchev. Algorithms for solving phase change free boundary problems : a review. Technical report, Bulgarian Academy of Sciences, 1995. Unpublished.

[18] R.D. Henshell and K.G. Shaw. Crack tip finite element are unnecessary. *Int. J. for Numerical Methods in Engng.*, 9:495–509, 1975.

[19] R.S. Barsoum. On the use of isoparametric finite element in linear fracture mechanics. *Int. J. for Numerical Methods in Engng.*, 10:25–37, 1976.

[20] K. Hellan. *Introduction to Fracture mechanics.* McGraw-Hill Inc., 1984.

[21] T.L. Anderson. *Fracture Mechanics : Fundamentals and Applications.* CRC Press Inc., 1995.

[22] J.R. Rice. A path independent integral and the approximate analysis of strain concentration by notches and cracks. *Journal of Applied Mechanics*, 35:379–386, 1968.

[23] C.F. Shih, B. Moran, and T. Nakamura. Energy release rate along 3D crack front in thermally stressed body. *International Journal of Fracture*, 30:79–102, 1986.

[24] J.C. Fanning. Ti-15-3 property data. In *Beta Titanium Alloys in the 1990's, Proceeding of Harold Margolin Symposium on Microstructure/Property Relationship of Titanium Alloys*, pages 411–438, Denver, Colorado, 1993. The Minerals, Metals and Matertials Society.

[25] P.S. Steif. A semi-infinite crack problem partially penetrating a circular inclusion. *Journal of Applied Mechanics*, 54:87–92, 1987.

[26] T.A. Wallace, R.K. Bird, and K.E. Wiedemann. The effect of oxidation on the mechanical properties of beta-21s. In *Beta Titanium Alloys in the 1990's, Proceeding of Harold Margolin Symposium on Microstructure/Property Relationship of Titanium Alloys*, pages 85–94, Denver, Colorado, 1993. The Minerals, Metals and Matertials Society.

Appendices

A Oxidation Analytical Solution

An exact analytical solution has been established to check the validity of numerical calculations. Due to the limitation in finding the closed form solution for the general 2D case, the

test case does not consider the concentration jump and different diffusion coefficients in the two phases. The boundary value problem consists of diffusion from the surfaces of a crack at $\theta = 0$ and a circular domain of radius r_0 (in the comparison with the numerical simulation $r_0 = 100\mu m$) where zero flux conditions are prescribed (see Fig. A.1).

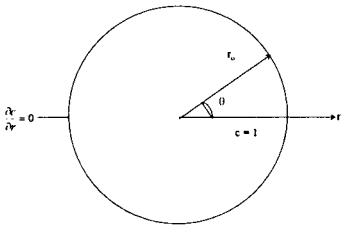

Fig. A.1. Geometry and boundary conditions for the boundary value problem solved in closed form

Taking into account these assumptions, the governing equations become the same as the single-phase diffusion problem, i.e.,

$$D\nabla^2 c = \frac{\partial c}{\partial t}. \tag{A.1}$$

The boundary conditions are then

$$c(r, 0, t) = 1, \quad \frac{\partial c}{\partial r}(r_0, \theta, t) = 0, \tag{A.2}$$

which describe the concentration on the surface of the crack and the flux at the perimeter of the domain. The initial condition is

$$c(r, \theta, 0) = 0. \tag{A.3}$$

To create homogeneous boundary conditions, the substitution $\hat{c} = c - 1$ has been made so that the boundary and initial conditions become

$$\hat{c}(r, 0, t) = 0, \quad \frac{\partial \hat{c}}{\partial r}(r_0, \theta, t) = 0, \quad \hat{c}(r, \theta, 0) = -1. \tag{A.4}$$

Applying separation of variables we have

$$\hat{c} = R(r)\Theta(\theta)T(t), \tag{A.5}$$

which eventually leads to the final form of the solution given by the following expression:

$$c(r,\theta,t) = \sum_{m=0}^{\infty}\sum_{s=1}^{\infty}\left[B_{ms}\sqrt{\frac{2}{\pi}\frac{r}{r_0}}j'_{m+1/2,s}j_m(\frac{r}{r_0}j'_{m+1/2,s})\times \right. \\ \left. \sin\left((m+1/2)\theta\right)\mathrm{e}^{-(j'_{m+1/2,s})^2\frac{Dt}{r_0^2}}\right]+1, \tag{A.6}$$

where

$$B_{ms} = -\frac{\sum_{k=0}^{\infty}\frac{(m+2k+3/2)}{(\frac{m}{2}+k+5/4)(\frac{m}{2}+k+1/4)}J_{m+2k+3/2}(j'_{m+1/2,s})}{j_m^2(j'_{m+1/2,s})\left[(j'_{m+1/2,s})^2-(m+1/2)^2\right]}, \tag{A.7}$$

and $j'_{m+1/2,s}$ is the s^{th} zero of the derivative of Bessel function $J_{m+1/2}$. Note that this solution corresponds to a singular mass flux at the crack tip. It can be shown that

$$\frac{\partial c}{\partial r} \sim r^{-1/2} \quad \text{for} \quad r \to 0. \tag{A.8}$$

B The fracture mechanics exact solution

The analytical solution for the problem described in Fig. 8 is solved in [20]. The stresses in x_2 and x_1 direction ahead of the crack tip are

$$\sigma_{x_2} = \sigma_{x_1} = \frac{K_I}{\sqrt{2\pi d}}, \tag{B.1}$$

$$K_I = \sigma_\infty\sqrt{\pi a}\left(1.12 - 0.23\frac{a}{W} + 10.6\frac{a^2}{W^2} - 21.7\frac{a^3}{W^3} + 30.4\frac{a^4}{W^4}\right), \tag{B.2}$$

where d is the distance in x_1 direction from the crack tip, outward from the crack, K_I is the stress intensity factor for the Mode I crack problem [20], and σ_∞ is the far field stress.

The displacement in x_2 direction is

$$\pm u_{x_2} = \pm\frac{4(1-\nu)(1+\nu)}{E}K_I\sqrt{\frac{-d_1}{2\pi}}, \tag{B.3}$$

where d_1 is the distance in x_1 direction from the crack tip, inward to the crack. The J-integral or the energy release rate for plain strain problem is

$$\mathcal{G} = J = \frac{K_I^2}{E}(1-\nu^2). \tag{B.4}$$

Damage Mechanics in Engineering Materials
G.Z. Voyiadjis, J.-W.W. Ju and J.-L. Chaboche (Editors)
© 1998 Elsevier Science B.V. All rights reserved.

A first step toward functionally graded plasticity in porous materials

K. Ding and G.J. Weng

Department of Mechanical and Aerospace Engineering, Rutgers University,
New Brunswick, NJ 08903, U.S.A.

Abstract

With an eye toward functionally graded plasticity in porous material, a homogenization scheme is developed to determine the overall elastoplastic behavior of a porous material with an interfacial ductile zone. The development involves four key steps: i) a linear comparison composite, ii) the secant moduli of the ductile phases, iii) an energy approach, and iv) a field-fluctuation method. With the aid of a 3-phase spherically concentric solid, the developed theory can be readily used to calculate the overall elastoplastic behavior of the porous material regardless whether the interfacial ductile layer is softer or stiffer than the matrix. To assess its accuracy, an exact local analysis is also carried out under pure dilatation, and comparison between the two indicates a close agreement. The theory is then applied to examine the influence of the ductile interfacial zone on the overall elastoplastic strength. The results show that its volume concentration and its relative stiffness to the ductile matrix can both have a very significant effect on the overall elastoplastic behavior of the porous material.

1. INTRODUCTION

A functionally graded material represents a new class of engineering materials whose properties may vary with position. To provide an optimal behavior such a variation has to be designed intelligently. Within the context of a porous material containing spherical voids, such a change may emanate from the void surface. A linear variation of the matrix property is schematically shown in Fig.1(a). The objective then is to find the precise distribution of the matrix property so that it can render the best possible overall elastoplastic strength. In this initial study, we shall not address such a continuous variation; instead a simpler microgeometry involving a step function as depicted in Fig.1(b) will be considered. A step-function provides two distinctively different elastoplastic regions such that one may be stiffer than the other. The theory developed then can serve as a basis for the future study with an arbitrarily varying matrix property. In this light the theory will represent a first step toward a full functionally graded plasticity in porous materials.

When voids with two such distinctive outer layers exist, the system can be represented by the 3-phase concentric sphere model as sketched in Fig.1(b). where the voids are re-

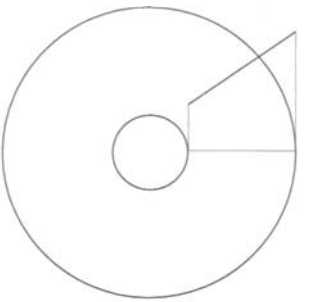

(a) Ductile matrix with a continously varying property

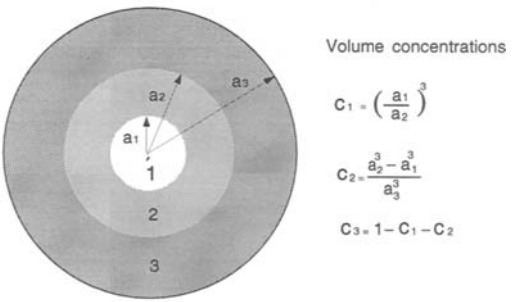

(b) Ductile porous material with a ductile interfacial zone

Figure 1: The geometrical representation of the model

ferred to as phase 1, the interfacial zone as phase 2, and the original material as phase 3. Both phase 2 and phase 3 are elastoplastic, each having its own yield stress and work-hardening characteristics. To address this nonlinear problem, an energy approach originally proposed by Qiu and Weng (1992) for a porous material (without an interphase) and particle-reinforced composite will be extended to this 3-phase problem. As will become evident later, such an extension requires the evaluation of the homogenized effective stress of both ductile phases. The original direct energy equivalence method sug-

gested there was not sufficient for this purpose, and a field-fluctuation method recently developed by Hu (1996) will be introduced here. It turns out that this method is versatile enough to provide the effective stress for a multiphase concentric sphere configuration, and can become potentially useful for the study of a functionally-graded porous material where the property changes continuously. The energy approach will also make use of a linear comparison composite in conjunction with the secant moduli of the ductile phases, an idea previously suggested by Tandon and Weng (1988) and Weng (1990) for the study of particle-reinforced plasticity and the plasticity of dual-phase metals, respectively.

2. CONSTITUTIVE EQUATIONS OF THE DUCTILE PHASES

To pave the way for the use of the secant moduli in the linear comparison composite, we first establish the dependence of these moduli on the effective stress. The effective stress and strain relation of a ductile phase in general can be represented by the modified Ludwik equation, as

$$\sigma_e^{(r)} = \sigma_y^{(r)} + h_r \cdot (\epsilon_e^{p(r)})^{n_r} \ , \ r = 2, 3 \tag{1}$$

where $\sigma_y^{(r)}$, h_r and n_r are the tensile yield stress, strength coefficient and work-hardening exponent, in turn, of the r-th phase. In terms of its deviatoric stress $\sigma_{ij}^{\prime(r)}$ and plastic strain $\epsilon_{ij}^{p(r)}$, the effective stress and plastic strain are defined as

$$\sigma_e^{(r)} = \left[\frac{3}{2}\sigma_{ij}^{\prime(r)}\sigma_{ij}^{\prime(r)}\right]^{\frac{1}{2}} \ , \ \epsilon_e^{p(r)} = \left[\frac{2}{3}\epsilon_{ij}^{p(r)}\epsilon_{ij}^{p(r)}\right]^{\frac{1}{2}} \ . \tag{2}$$

It follows that the secant Young's modulus of the r-th phase is given by

$$E_r^s = \left[\frac{1}{E_r} + \frac{\epsilon_e^{p(r)}}{\sigma_y^{(r)} + h_r \cdot (\epsilon_e^{p(r)})^{n_r}}\right]^{-1} \ , \tag{3}$$

in terms of its elastic Young's modulus, E_r. The secant shear modulus and the secant Poisson's ratio also follow from the isotropic relations and plastic incompressibility, as

$$\mu_r^s = \frac{E_r^s}{2(1+\nu_r^s)} \ , \ \nu_r^s = \frac{1}{2} - \left(\frac{1}{2} - \nu_r\right)\frac{E_r^s}{E_r} \ , \tag{4}$$

where ν_r is the elastic Poisson's ratio.

3. THE EFFECTIVE ELASTIC PROPERTIES OF THE LINEAR COMPARISON COMPOSITE

In the composite sphere model depicted in Fig.1(b), the volume concentration of the *r-th* phase is denoted by c_r, and its outer radius by a_r. It follows that

$$c_1 = (a_1/a_3)^3, \quad c_2 = (a_2^3 - a_1^3)/a_3^3, \quad c_3 = 1 - (c_1 + c_2). \tag{5}$$

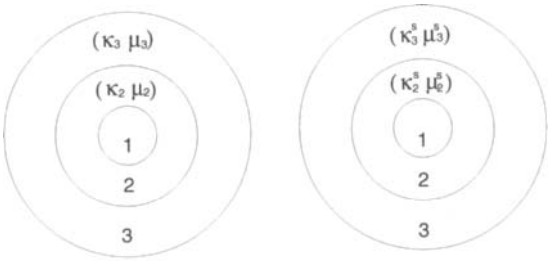

(a) Elastic comparison composite (b) Porous materials with 2 ductile phases

Figure 2: Elastic comparison composite

The concept of a linear comparison composite is shown in Fig.2, where the elastic bulk and shear moduli (κ_r and μ_r) in Fig.2(a) are set equal to the secant moduli (κ_r^s and μ_r^s) in Fig.2(b) of the original nonlinear composite at every stage of deformation. In such a model the exact effective bulk modulus has been derived by Qiu and Weng (1991), and we shall extend Christensen and Lo's (1979) generalized self-consistent scheme to find the effective shear modulus. Direct application of Qiu and Weng's results to the porous material yields

$$\begin{aligned}\kappa_s &= \kappa_3 + (3\kappa_3 + 4\mu_3^s)[-c_1\kappa_3(3\kappa_2 + 4\mu_2^s) \\ &\quad + 4c_2\mu_2^s(\kappa_2 - \kappa_3)]/\{4\mu_2^s[(3\kappa_2 + 4\mu_3^s) + 3(c_1 + c_2) \\ &\quad \cdot (\kappa_3 - \kappa_2)] + 3c_1\kappa_2[4(\mu_3^s - \mu_2^s)/(c_1 + c_2) + (3\kappa_3 + 4\mu_2^s)]\} \qquad (6)\end{aligned}$$

for the effective bulk modulus, where the subscript s reflects the secant state of the ductile phase at a given stage of deformation. Following Christensen and Lo's procedure, analysis of the 3-phase model in the generalized self-consistent scheme leads to a matrix as shown in the Appendix. When its determinant is set equal to zero, it provides a second-order algebraic equation for the effective shear modulus μ_s. The secant Young's modulus then follows as

$$E_s = \frac{9\kappa_s\mu_s}{(3\kappa_s + \mu_s)}. \qquad (7)$$

This pair of moduli provides the effective moduli tensor L_s and compliances tensor M_s

$$L_s = (3\kappa_s, 2\mu_s), \qquad M_s = (1/3\kappa_s, 1/2\mu_s), \qquad (8)$$

where the subscript s again signifies the "secant" state of the constituent phases. These results will be used as the effective secant moduli of the nonlinear composite. As both effective moduli involve the yet-unknown secant shear moduli of phase 2 and 3, these individual moduli must be determined first at a given level of the applied stress.

4. THE FIELD-FLUCTUATION METHOD

To evaluate the effective stress of the interphase and the matrix, the field-fluctuation method recently developed by Hu (1996) will be extended to this 3-phase solid. The original method based on the energy equivalence between the golbal system and the local constituent phases as suggested by Qiu and Weng (1992) provides only one equation, but now we have two unknowns, and therefore it is not sufficient. Hu's field fluctuation method also starts out from Qiu and Weng's energy equivalence, but instead of proceeding to evaluate the effective stress from this equation, he seeked for the variation of the energy due to the variation of the shear modulus of the ductile phase whose effective stress is of interest. According to Qiu and Weng' energy approach, the homogenized effective stress of a heterogeneously deformed ductile phase is defined based on the distortional energy equivalence, as

$$\frac{1}{6\mu_r^s}\sigma_e^{2(r)} = \frac{1}{V_r}\int_{V_r}\frac{1}{4\mu_r^s}\sigma_{ij}^{'(r)}(x)\sigma_{ij}^{'(r)}(x)\,dV, \tag{9}$$

which is equivalent to

$$\begin{aligned}\sigma_e^{2(r)} &= \frac{1}{V_r}\int_{V_r}\left(\sigma_e^{(r)}(x)\right)^2 dV = \frac{1}{V_r}\int_{V_r}\frac{3}{2}\sigma_{ij}^{'(r)}(x)\sigma_{ij}^{'(r)}(x)\,dV \\ &= \frac{3}{2}\bar{\sigma}_{ij}^{'(r)}\bar{\sigma}_{ij}^{'(r)} + \frac{1}{V_r}\int_{V_r}\frac{3}{2}\sigma_{ij}^{'pt(r)}(x)\sigma_{ij}^{'pt(r)}(x)\,dV,\end{aligned} \tag{10}$$

where V_r represents the volume of the *r-th* phase and superscripts *pt* refer to the "perturbed" field over the mean of the considered phase. In symbolic notation, it can be rewritten as

$$\sigma_e^{2(r)} = < \sigma_e^{2(r)}(x) > = \frac{3}{2} < \boldsymbol{\sigma}_r'\boldsymbol{\sigma}_r' >, \tag{11}$$

where the angle brackets represent the volume average of the said quantity over the *r-th* phase, and a bold-faced Greek letter signifies a second-order tensor.

Then starting out with the energy equivalence of the total elastic energy U_s between the homogenized overall system with an effective compliances tensor M_s and the individual phases with a compliances tensor M_r^s for the *r-th* phase

$$2U_s = \bar{\boldsymbol{\sigma}}M_s\bar{\boldsymbol{\sigma}} = \Sigma < \boldsymbol{\sigma}_r M_r^s \boldsymbol{\sigma}_r >, \tag{12}$$

one may proceed to seek for the variation of this energy when the shear modulus of the *r-th* phase changes from μ_r^s to $\mu_r^s+\delta\mu_r^s$. Under the same external stress $\bar{\boldsymbol{\sigma}}$ the local stress will also chenge from $\boldsymbol{\sigma}_r(x)$ to $\boldsymbol{\sigma}_r(x)+\delta\boldsymbol{\sigma}_r(x)$, but due to the vanishing perturbed outer traction the additional stress field will not contribute to the overall energy. It follows that such a variation will result in

$$c_r < \boldsymbol{\sigma}_r'\boldsymbol{\sigma}_r' > \delta\left(\frac{1}{2\mu_r^s}\right) = \bar{\boldsymbol{\sigma}}\delta M_s\bar{\boldsymbol{\sigma}}, \tag{13}$$

and this leads to the homogenized effective stress for the r-th phase

$$\sigma_e^{2(r)} = \bar{\sigma}\left(\frac{-3\mu_r^{s^2}}{c_r}\frac{\delta M_s}{\delta \mu_r^s}\right)\bar{\sigma}. \tag{14}$$

When applied for both phases r=2 and 3, it provides the needed effective stress for both the ductile interfacial zone and the outer matrix. Once these effective stresses are found, the corresponding secant moduli of the r-th phase will follow from the constitutive equations, and the effective secant moduli of the nonlinear system can then be determined from κ_s and μ_s of the comparison composite. This process may be continued by increasing the level of the applied stress $\bar{\sigma}$ until the entire stress-strain curve of the porous material is obtained.

5. AN EXACT SOLUTION UNDER HYDROSTATIC LOADING

To provide an assessment for the accuracy of the developed homogenization theory, an exact solution will be derived here under a pure hydrostatic loading with a linearly strain-hardening phases (n=1 for both phases).

5.1. Elastic field

Before the onset of plastic deformation, the field in the 3-phase porous material is elastic. The displacement field in both phase 2 and 3 for the geometry shown in Fig.1(b) are

$$u_r^{(i)} = B_1^{(i)} r + B_2^{(i)}\frac{a_2^3}{r^2}, \quad i = 2,3 \tag{15}$$

in a spherical coordinate, whereas the stress in the voids simply vanishes. The displacement fields result in the strain components

$$\epsilon_{rr}^{(i)} = B_1^{(i)} - B_2^{(i)}\frac{a_2^3}{r^3}, \quad \epsilon_{\theta\theta}^{(i)} = \epsilon_{\phi\phi}^{(i)} = B_1^{(i)} + B_2^{(i)}\frac{a_2^3}{r^3}, \quad i = 2,3 \tag{16}$$

and stress fields

$$\sigma_{rr}^{(i)} = 3\kappa_i B_1^{(i)} - 4\mu_i B_2^{(i)}\frac{a_2^3}{r^3}, \quad \sigma_{\theta\theta}^{(i)} = \sigma_{\phi\phi}^{(i)} = 3\kappa_i B_1^{(i)} + 2\mu_i B_2^{(i)}\frac{a_2^3}{r^3}, \quad i = 2,3. \tag{17}$$

The constants $B_1^{(i)}$ and $B_2^{(i)}$ can be determined from the continuity conditions and the boundary condition.

5.2. Subsequent plastic deformation

Once plastic deformation occurs in any layer, there are two possible subsequent trends under increased hydrostatic tension.

1. Plastic deformation increases in the yielded phase while the other layer remains elastic.

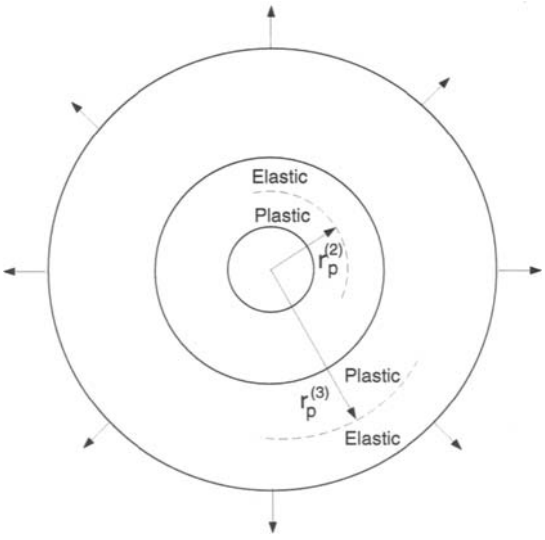

Figure 3: Partial yielding model

2. The other layer also starts to yield; in both phases the inner region is plastic and the outer one is elastic.

A schematic diagram for such a partial yielding is depicted in Fig.3, where $r_p^{(i)}$ represents the outer radius of the plastic region of the i-th layer ($i = 2, 3$). In any case under an increased loading the layer with partial yielding will proceed to become full yielding. We use e to denote that the whole region is elastic, pp partial plastic, fp fully plastic. Unlike in an ordinary 2-phase material, there are now many possible routes of plastic deformation; these routes are listed in Fig.4. Within $r_p^{(i)} < r < a_i$, the material is in the elastic state

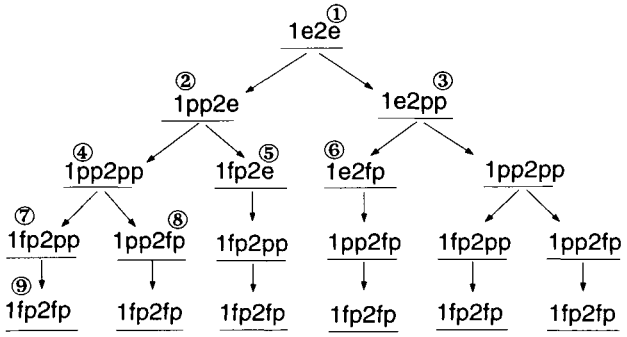

Figure 4: The routes of plastic deformation

and the results are given above . Within $a_{i-1} < r < r_p^{(i)}$, the material is in the plastic

state. To render the many possiblilities to a more manageable condition the plastic field will now be analyzed assuming both phases to be incompressible and the outer traction is tensile. Now with $\nu^{(i)} = 1/2$, one has

$$\sigma_{\theta\theta}^{(i)} > \sigma_{rr}^{(i)}, \quad \epsilon_{rr}^{(i)p} < 0, \quad \sigma_{\theta\theta}^{(i)} - \sigma_{rr}^{(i)} = \sigma_y^{(i)} - h_i \epsilon_{rr}^{(i)p}. \tag{18}$$

The analysis can be carried out in a fashion as in Qiu and Weng (1992) for a two-phase solid. After some lengthy algebra, one arrives at

$$\epsilon_{rr}^{(i)p} = \frac{D^{(i)}}{r^3} + \frac{\sigma_y^{(i)}}{h_i + E_i}, \tag{19}$$

and

$$\sigma_{rr}^{(i)} = \frac{2\sigma_y^{(i)} E_i}{h_i + E_i} \log r + \frac{2}{3} D^{(i)} h_i \frac{1}{r^3} + C^{(i)}, \tag{20}$$

and

$$u_r^{(i)} = -\frac{h_i + E_i}{2E_i} \frac{D^{(i)}}{r^2}. \tag{21}$$

Equations (19), (20) and (21) are valid expressions for radial plastic strain, radial stress and radial displacement in the plastic region in i-th layer. For the case pp, we have

$$\epsilon_{rr}^{(i)p}|_{r=r_p^{(i)}} = 0. \tag{22}$$

Substituting Equation (19) into (22), we can get $D^{(i)}$ in the case pp as

$$D^{(i)} = -\frac{\sigma_y^{(i)}}{h^{(i)} + E^{(i)}} (r_p^{(i)})^3. \tag{23}$$

So the radial plastic strain, stress and displacement for the case pp can be rewritten as

$$\begin{aligned}
\epsilon_{rr}^{(i)p} &= \frac{\sigma_y^{(i)}}{h_i + E_i} [1 - \left(\frac{r_p^{(i)}}{r}\right)^3], \\
\sigma_{rr}^{(i)} &= \frac{2\sigma_y^{(i)} E_i}{h_i + E_i} \log r - \frac{2\sigma_y^{(i)} h_i}{3(h_i + E_i)} \left(\frac{r_p^{(i)}}{r}\right)^3 + C^{(i)}, \\
u_r^{(i)} &= \frac{\sigma_y^{(i)}}{2E_i} \left(\frac{(r_p^{(i)})^3}{r^2}\right).
\end{aligned} \tag{24}$$

The continuity conditions on radial displacement and radial stress at the interfaces between the different phases and the regions with different deformation states, in addition to the prescribed traction at the boundary, lead to an equation system for each case shown in Fig.4 with which one can obtain the unknown coefficients $B^{(i)}$ and $C^{(i)}$. Among all the possible cases, there are nine distinct ones as depicted in Fig.4. The elastoplastic relationship which resembles the overall elastic bulk modulus can be obtained through the fact that $\overline{\sigma}_{kk}$ is related to the prescribed traction at the boundary through $\overline{\sigma}_{kk} = 3\overline{\sigma}_b$ and

$$\overline{\epsilon}_{kk} = c_1 \overline{\epsilon}_{kk}^{(1)} = 3c_1 \frac{\sigma_y^{(2)}}{2E_2} \left(\frac{r_p^{(2)}}{a_1}\right)^3 \tag{25}$$

due to the elastic and plastic incompressibility assumption for the two ductile layers.

6. RESULTS AND DISCUSSIONS

Now that both the energy approach and the exact solution under pure dilatation have been established, we shall first compare the results of both approaches for the hydrosatic loading. Then the energy approach will be used to examine the influence of the ductile intefacial zone on the overall behavior of the porous material.

6.1. Comparison between the exact solution and the energy approach

The comparison will be made with a bilinear stress-strain curve for both ductile phases. The tangent modulus in the plastic range E_i^p for the i-th phase is now related to the Young's modulus and work-hardening modulus as

$$\frac{1}{E_i^p} = \frac{1}{E_i} + \frac{1}{h_i}. \tag{26}$$

We first choose the following parameters in the comparison:

$$c_1 = 0.3,\ c_2 = 0.35,\ c_3 = 0.35,$$
$$E_3 = 68.3\text{GPa},\ \sigma_y^{(3)} = 250\text{MPa}, \tag{27}$$

which correspond to the Young's modulus and yield stress of a 6061-T6 alumnium alloy (Arsenault, 1984; Nieh and Chellman, 1984).

We shall first consider both phases to be ideally plastic without work-hardening.

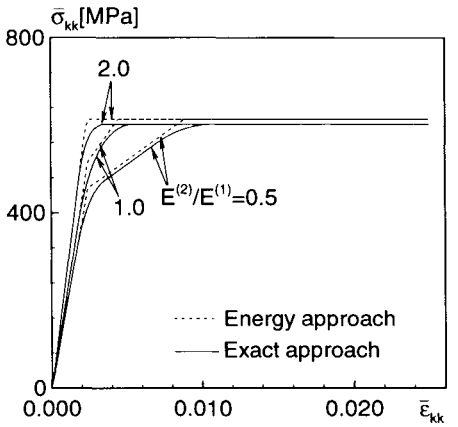

Figure 5: The overall elastoplastic relationship under hydrostatic loading with different ratios of the Young's moduli

In Fig.5, the yield stress of the intefacial layer is taken to be equal to that of the outer layer, but its Young's modulus varies by being double, equal or half of that of the

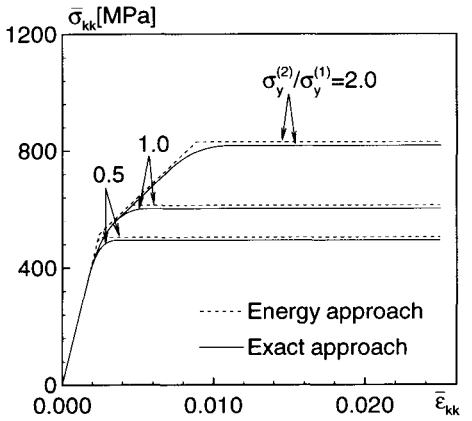

Figure 6: The elastoplastic relationship under hydrostatic loading with different ratios of $\sigma_y^{(i)}$

outer matrix. From this figure two observations can be made: First, both the energy approach and the exact solution provide very close results under dilatational loading, but the energy approach gives slightly harder response than the exact solution. The difference is due to the fact that the energy approach uses the average of the distortional energy of each layer to assess the extent of plastic deformation and therefore one gets to know the plasticity later than by the exact approach which allows one to inspect plasticity locally. Secondly, there are two major stages of the overall elastoplastic deformation contributed by these two ductile phases. In addition there is a smooth transition in the exact analysis reflecting the local plastic flow, a phenomenon absent in the homogenization scheme. Fig.6 shows the relationship with different ratios of yield stress while maintaining the same Young's modulus. Finally to examine the influence of strain hardening we keep the Young's modulus and yeild stress of both phases to be identical, but take the tangent modulus of the matrix to be $1/10th$ of its elastic Young's modulus as

$$E_3^p = 1/10E_3 \;=\; 6.83\text{GPa}. \tag{28}$$

The results are plotted in Fig.7 with different ratios of $E_p^{(2)}$. Good agreement is again evident. These three comparisons indicate that, no matter which material constant is being varied, the results of the homogenization scheme is very close to that of the exact solution.

Now it is interesting to see how the volume concentration of the interfacial zone affects the overall elastoplastic behavior of the porous material. The results with a softer interphase are shown in Fig.8 at three levels of volume concentrations: c_2=0, 0.1, 0.2 and 0.3, with an ideally plastic matrix in Fig.8(a) and a linearly work-hardening one in Fig.8(b). In these calculations, the property of the interphase is taken to be $1/10th$ of the matrix as

$$E_2 = E_3/10, \quad \sigma_y^{(2)} = \sigma_y^{(3)}/10, \quad E_2^p = E_3^p/10, \tag{29}$$

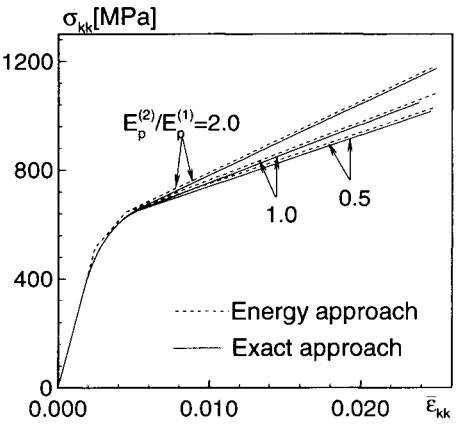

Figure 7: The elastoplastic relationship under hydrostatic loading with different ratios of $E_p^{(i)}$

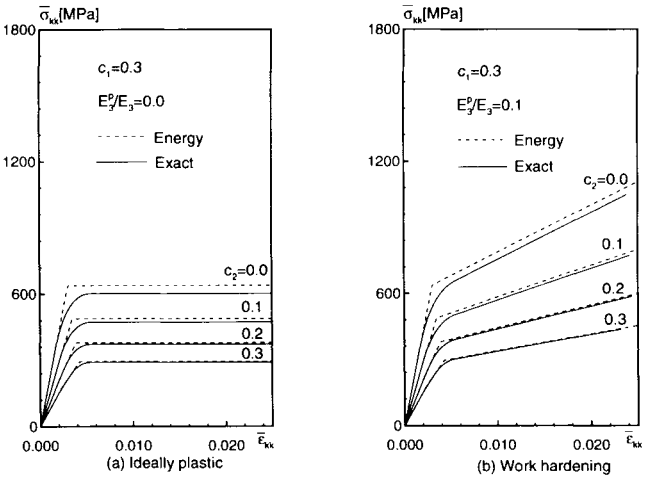

Figure 8: The influence of a soft interphase volume concentration on the overall behavior of the porous material

Comparison between the energy approach and the exact solutions are again satisfactory, both indicating the weakening effect of the degraded interfacial zone as its volume concentration increases. On the other hand the results with a harder interphase are seen in Fig.9; these have been calculated with the properties

$$E_2 = 1.1E_3, \quad \sigma_y^{(2)} = 3\sigma_y^{(3)}, \quad E_2^p = 1.1E_3^p. \tag{30}$$

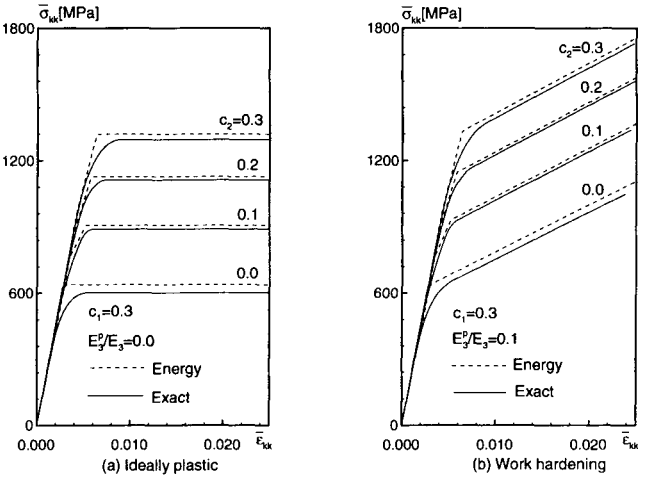

Figure 9: The influence of a hard interphase volume concentration on the overall behavior of the porous material

Both figures again display a close agreement between the two approaches, and they further indicate the strengthening effect of this interfacial region on the overall property of the system.

6.2 Tensile and shear behavior

Now that the homogenization scheme has been shown to provide estimates which are consistent with the exact solutions under dilatational loading, it can be applied to examine the influence of its volume concentration on the overall response of the porous materials under other loading conditions. For this, we shall use the 6061-T6 alumnium as the matrix, whose Young's modulus and yield stress have already been given in Eq. (27). This material further has the strength coefficient and work-hardening exponent (Qiu and Weng, 1992)

$$h_3 = 173\ MPa, \quad n_3 = 0.455. \tag{31}$$

We shall examine the tensile behavior first, and then followed by the shear one. In each case the interfacial ductile zone will be taken to be softer and then harder than the outer layer.

The tensile behavior of the porous material with a soft interfacial zone is shown in Fig.10(a), with a property only $1/10th$ of the original matrix as indicated there. Its Poisson ratio and work-hardening exponent n are kept to be the same as those of the matrix. As its volume concentration increases from 0 to 0.3, the overall behavior is seen to continue to weaken. Here the condition c_2=0 also corresponds to the ordinary porous

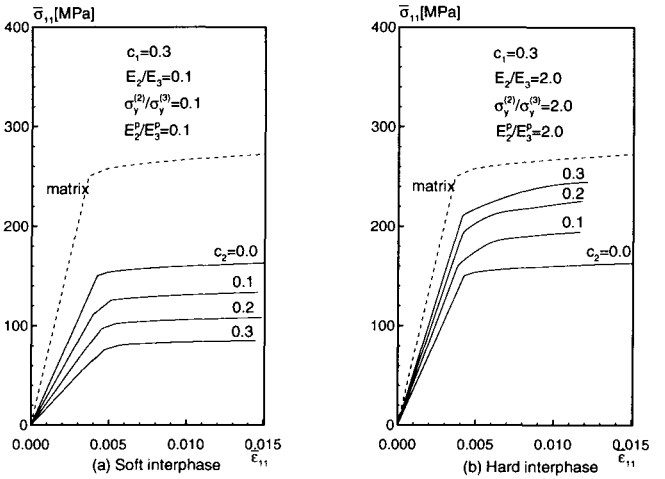

Figure 10: Tensile behavior of the porous material with a ductile interfacial zone

material without such an interfacial zone and, in all cases, the overall elastoplastic strength of the porous materials is substantially softer than that of the pure matrix itself, which is also indicated as a dotted line there. The condition with a hard interfacial zone is shown in Fig.10(b), where the interphase is taken to be twice as stiff as the matrix. As its volume concentration increases, the overall strenth of the porous material also increases. But even at c_2=0.3, the response is still not as stiff as the original matrix itself. Finally the volume-concentration dependence of the shear behavior is depicted in Fig.11(a) and (b) with a weak and a strong interfacial zone, respectively. The volume concentration of the ductile interphase again displays a significant influence on the overall elastoplastic behavior of the porous material.

7. CONCLUDING REMARKS

Based on an energy approach and a field-fluctuation method, a homogenization scheme has been developed to determine the overall stress-strain relations of a porous material containing two ductile layers. This theory is applicable to both conditions whether the interfacial zone is softer or harder than the matrix, and it can be used at finite concentrations of the constituent phases. The step-function variation of the matrix property is the simplest kind of the matrix property variation and, thus, the theory established represents a first step toward a full functionally graded plasticity in porous materials. The theory has proven to be accurate in light of an exact local analysis under hydrostatic loading, and its applications to tension and shear also reflect the strong dependence of the overall elastoplastic strength on the ductile interfacial zone.

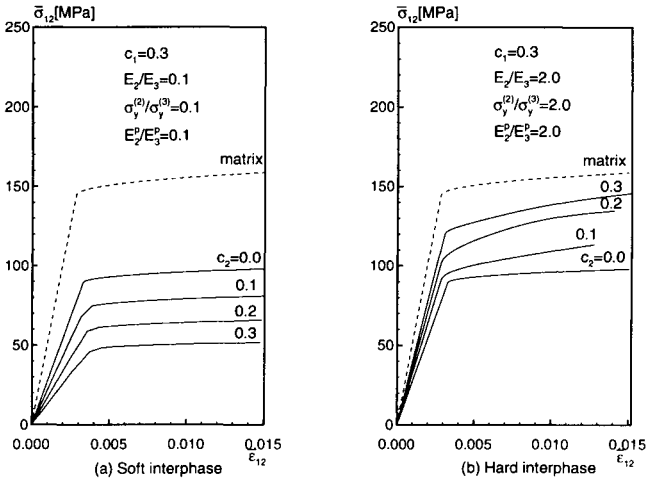

Figure 11: Shear behavior of the porous material with a ductile interfacial zone

REFERENCES

Arsenault, R.J., 1984, The strengthening of aluminum alloy 6061 by fiber and platelet silicon carbide, *Mater. Sci. Engng.*, **64**, 171-181.

Nieh, T.G. and Chellman, D.J., 1984, Modulus measurements in discontinuous reinforced aluminum composites, *Scripta Metall.*, **8**, 925-928.

Christensen, R.M. and Lo, K.H. 1979, Solutions for effective shear properties in three phase sphere and cylinder models, *J. Mech. Phys. Solids* **27**, 315-330.

Hu, G., 1996, A method of plasticity for general aligned spherical void or fiber-reinforced composites, *Int. J. Plasticity* **12**, 439-449.

Qiu, Y. P. and Weng, G. J., 1991, Elastic moduli of thickly coated particle and fiber-reinforced composites, *J. Appl. Mech.*, **58**, 388-398.

Qiu, Y. P. and Weng, G. J., 1992, A theory of plasticity for porous materials and particle-reinforced composites, *J. Appl. Mech.*, **59**, 261-268.

Tandon, G. P. and Weng, G. J., 1988, A theory of particle-reinforced plasticity, *J. Appl. Mech.*, **55**, 126-135.

Weng, G. J., 1990, The overall elastoplastic stress-strain relations of dual-phase metals, *J. Mech. Phys. Solids* **38**, 419-441.

APPENDIX: Components of the Matrix for the Effective Shear Modulus in the Generalized Self-Consistent Scheme

$$
\begin{bmatrix}
-\frac{2\mu_2}{\mu_3} & -\left[\frac{21\lambda_2}{\mu_3}-\frac{36\nu_2}{1-2\nu_2}\frac{\mu_2}{\mu_3}\right]c_1^{\frac{2}{3}} & \frac{24\mu_2}{\mu_3}\left(\frac{1}{c_1}\right)^{\frac{5}{3}} & \left[\frac{6\lambda_2}{\mu_3}+\frac{4(5-4\nu_2)}{1-2\nu_2}\frac{\mu_2}{\mu_3}\right]\left(\frac{1}{c_1}\right) & 0 & 0 & 0 & 0 & 0 & 0 \\
-\frac{\mu_2}{\mu_3} & \frac{(7+2\nu_2)\mu_2}{(1-2\nu_2)\mu_3}c_1^{\frac{2}{3}} & -\frac{8\mu_2}{\mu_3}\left(\frac{1}{c_1}\right)^{\frac{5}{3}} & -\frac{2(1+\nu_2)\mu_2}{(1-2\nu_2)\mu_3}\left(\frac{1}{c_1}\right) & 0 & 0 & 0 & 0 & 0 & 0 \\
1 & -\frac{6\nu_2}{1-2\nu_2}(c_1+c_2)^{\frac{2}{3}} & 3\left(\frac{1}{c_1+c_2}\right)^{\frac{5}{3}} & \frac{5-4\nu_2}{1-2\nu_2}\frac{1}{c_1+c_2} & -1 & \frac{6\nu_3}{1-2\nu_3}(c_1+c_2)^{\frac{2}{3}} & -3\left(\frac{1}{c_1+c_2}\right)^{\frac{5}{3}} & -\frac{5-4\nu_3}{1-2\nu_3}\frac{1}{c_1+c_2} & 0 & 0 \\
1 & -\frac{7-4\nu_2}{1-2\nu_2}(c_1+c_2)^{\frac{2}{3}} & -2\left(\frac{1}{c_1+c_2}\right)^{\frac{5}{3}} & \frac{2}{c_1+c_2} & -1 & \frac{7-4\nu_3}{1-2\nu_3}(c_1+c_2)^{\frac{2}{3}} & 2\left(\frac{1}{c_1+c_2}\right)^{\frac{5}{3}} & -\frac{2}{c_1+c_2} & 0 & 0 \\
\frac{2\mu_2}{\mu_3} & \left[\frac{21\lambda_2}{\mu_3}-\frac{36\nu_2}{1-2\nu_2}\frac{\mu_2}{\mu_3}\right](c_1+c_2)^{\frac{2}{3}} & -\frac{24\mu_2}{\mu_3}\left(\frac{1}{c_1+c_2}\right)^{\frac{5}{3}} & -\left[\frac{6\lambda_2}{\mu_3}+\frac{4(5-4\nu_2)}{1-2\nu_2}\frac{\mu_2}{\mu_3}\right]\frac{1}{c_1+c_2} & -2 & -\left[\frac{21\lambda_3}{\mu_3}-\frac{36\nu_3}{1-2\nu_3}\frac{\mu_2}{\mu_3}\right](c_1+c_2)^{\frac{2}{3}} & 24\left(\frac{1}{c_1+c_2}\right)^{\frac{5}{3}} & \left[\frac{6\lambda_3}{\mu_3}+\frac{4(5-4\nu_3)}{1-2\nu_3}\right]\frac{1}{c_1+c_2} & 0 & 0 \\
\frac{\mu_2}{\mu_3} & -\frac{7+2\nu_2}{1-2\nu_2}\frac{\mu_2}{\mu_3}(c_1+c_2)^{\frac{2}{3}} & \frac{8\mu_2}{\mu_3}\left(\frac{1}{c_1+c_2}\right)^{\frac{5}{3}} & \frac{2(1+\nu_2)}{1-2\nu_2}\frac{\mu_2}{\mu_3}\frac{1}{c_1+c_2} & -1 & \frac{7+2\nu_3}{1-2\nu_3}(c_1+c_2)^{\frac{2}{3}} & -8\left(\frac{1}{c_1+c_2}\right)^{\frac{5}{3}} & -\frac{2(1+\nu_3)}{1-2\nu_3}\frac{1}{c_1+c_2} & 0 & 0 \\
0 & 0 & 0 & 0 & 1 & -\frac{6\nu_3}{1-2\nu_3} & 3 & \frac{5-4\nu_3}{1-2\nu_3} & -3 & 1 \\
0 & 0 & 0 & 0 & 1 & -\frac{7-4\nu_3}{1-2\nu_3} & -2 & 2 & 2 & 1 \\
0 & 0 & 0 & 0 & 2 & \frac{21\lambda_3-36\nu_3}{(1-2\nu_3)} & -24 & -\frac{6\lambda_3}{\mu_3}+\frac{4(5-4\nu_3)}{1-2\nu_3} & \frac{24\mu}{\mu_3} & \frac{2\mu}{\mu_3} \\
0 & 0 & 0 & 0 & 1 & -\frac{7+2\nu_3}{1-2\nu_3} & 8 & \frac{2(1+\nu_3)}{1-2\nu_3} & -\frac{8\mu}{\mu_3} & \frac{\mu}{\mu_3}
\end{bmatrix}
$$

This Page Intentionally Left Blank

PART V

COMPUTATIONAL DAMAGE MODELS

This Page Intentionally Left Blank

Damage Mechanics in Engineering Materials
G.Z. Voyiadjis, J.-W.W. Ju and J.-L. Chaboche (Editors)
© 1998 Elsevier Science B.V. All rights reserved.

Modeling of Delamination Using a Layerwise Element with Enhanced Strains

C. M. Dakshina Moorthy and J. N. Reddy

Department of Mechanical Engineering, Texas A&M University, College Station, Texas 77843-3123, USA

A layerwise finite element with enhanced strains is developed for the analysis of laminates with special emphasis on the study of delamination characteristics. An interface model using the penalty function method is developed to calculate strain energy release rates. Since the interface model provides the facility for the closure of delamination by a small amount, strain energy release rates were evaluated by actual crack closure and by virtual crack closure methods for a comparative study. A double cantilever plate problem is used to illustrate the accuracy of the computational approaches developed herein.

1. INTRODUCTION

1.1 Background

In the analysis of composite laminates, when the primary concern is the global response, one may choose to model the laminate with layers of different mechanical properties as a single layer with equivalent mechanical characteristics. Two widely used examples of equivalent single layer (ESL) theories are the classical and first order shear deformation theories [1]. These theories are appealingly simple and economic in analysis and provide reasonably accurate solution for global response characteristics such as overall deflections, critical buckling loads, fundamental vibration frequencies and associated mode shapes.

When the emphasis of the analysis shifts from global response to the study of initiation of damage or delamination between layers, accurate determination of interlaminar stresses and strains gain more importance. For damage such as matrix cracks, intra-lamina stresses are important, and for delamination and adhesive joint separation, interlaminar stresses are important. Hence, in studying laminates with delamination, it is necessary to model the laminate using a refined theory both in terms of 3D-kinematics and constitutive relations compared to ESL theories. Basic frame work for this is provided

by the generalized layerwise plate theory (GLPT) of Reddy [1,2]. In GLPT, enhancement in kinematics over an ESL theory is made by allowing for more than one kinematic layer through the thickness. The analyst has the choice to selectively refine the kinematics through the thickness of the laminate as desired. The layerwise theory is a 3D theory in the sense that it uses full 3D constitutive relations compared to the plane stress-reduced constitutive relations used in ESL theories. Even though, the layerwise theory provides the facility for using a refined kinematics, it should be used sparingly because the refinement through the thickness increases the problem size tremendously.

1.2 Delamination Studies

In the study of delamination in laminates, the strain energy release rate has gained importance as a criterion for delamination growth. The growth of delamination is predicted by comparing the (working) strain energy release rate G near the delamination tip to its critical (allowable) value G_c. The critical strain energy release rate G_c is a quantity that is evaluated by conducting experiments. In general, G_c depends on the mode ratio, material and relative ply orientation of the lamina surrounding the delamination.

Several methods are described in the literature for evaluating the strain energy release rates. In one method it is evaluated as the rate of change of total potential energy of the system with crack extension and it is determined by evaluating total potential energy at two different crack lengths [3,4]. Another method is based on the evaluation of compliance at two different crack lengths [5,6]. These methods provide direct means of evaluating strain energy release rates and require analysis of the problem at two separate configurations differing by a small value of crack closure length. In direct contrast to these methods where the crack closure is real, another method is used where the closure of the crack is kept virtual (*i.e.*, imagined). The advantage here is that it requires only one analysis instead of two. This is achieved by approximating the load required to close the crack from the results of a single analysis. Further this method integrates well with the standard finite element method. Due to the virtual nature of the crack closure, this method is called *virtual crack closure method* (VCCM). This method has been applied successfully to 2D problems using low order elements [7] and found to be accurate even with coarse meshes near the crack tip. The method has further been extended for 3D elements [8] and found to be effective in 3D problems [9].

In the study of delaminations in composite laminates, much research has been done and a general overview is given by O'Brien [10]. Analytical investigations of the subject, in contrast to numerical studies, usually consider simple plane geometries and homogeneous, isotropic or orthotropic plates. Laminated plates with embedded delamination under the action of inplane loads have been studied for delamination buckling and the consequential growth of delamination. This type of delamination growth, called instability related delamination, has been studied for laminated plates with through width delamination [11]. This analysis has been extended to laminated plates with

elliptical embedded delamination geometries and the distribution of strain energy release rates along the delamination front has been studied [9,12]. Additional references on analytical and semi-analytical studies on delamination buckling in flat composites can be found in the review article [13].

1.3 Present Study

The objective of the present study is to develop an interface model for the recovery of accurate interlaminar stresses and study delamination characteristics in composite laminates. A layerwise finite element model with enhanced strains is developed for the purpose. The layerwise finite element model provides the framework for refinement of displacement variation through the thickness if and when it is needed. The through the thickness refinement is accompanied by refinement in the plane of the laminate, and thus proves to be expensive. On the other hand, coarse mesh through the thickness leads to the possibility of thickness locking if the Poisson effect through the thickness is not correctly represented. The enhanced strain method with enhancement field provided for transverse normal strain component is used here to overcome the thickness locking.

For the recovery of interlaminar stresses and for the study of delaminations in laminates an interface model is developed. This involves the selection of an interface in the laminate a-priori and modeling it as an adhesive contact zone between portions of the laminate separated by this interface. The adhesive contact between portion of the laminate at its interface is enforced by penalty function method [14] and the contact load that satisfies the equilibrium at the interface is used in evaluating the interlaminar stresses. Use of this interface model in the study of delamination characteristics have the advantage that it provides the framework for extending or closing the bonded portion of the laminate by a small amount as is required by the *crack closure method* (CCM). Strain energy release rate by this interface model has been evaluated using crack closure method and by virtual crack closure method (VCCM) for comparative study. This interface model is studied for its accuracy by comparing the results with reference solutions in the literature.

2. ENHANCED ASSUMED STRAIN ELEMENT

2.1 Basic Idea

Enhanced strain method [15] is an approach that is found to be effective in improving the performance of finite elements against locking. This is achieved by enhancing the strain with an incompatible field that is chosen to satisfy any constraint. The enhanced strain method is discussed here in the context of a small displacement theory and the rectangular Cartesian coordinates for the sake of simplicity and clarity in bringing out the essentials of the method. The application of this method for geometrically nonlinear problems is straightforward.

Let the total strain field ε_{ij} be the sum of the incompatible field $\tilde{\varepsilon}_{ij}$ and the compatible strain field ε_{ij}^D

$$\varepsilon_{ij} = \varepsilon_{ij}^D + \tilde{\varepsilon}_{ij} \tag{2.1}$$

where the compatible strain field ε_{ij}^D is related to the displacement components u_i by the usual strain-displacement relations

$$\varepsilon_{ij}^D = \frac{1}{2}(u_{i,j} + u_{j,i}) \tag{2.2}$$

Mathematically, the incompatible strain components $\tilde{\varepsilon}_{ij}$ should be identically zero everywhere. Therefore, the work done by the actual stresses in moving through the incompatible strains is zero. However, a computational scheme does not account for the zero work done unless it is explicity included in the formulation. That is, we must include the conditions

$$\tilde{\varepsilon}_{ij} = 0, \quad i,j = 1,2,3 \tag{2.3}$$

as constraints in the finite element development.

2.2 Variational Basis

The total potential energy functional used for the development of the displacement finite element model that includes the constraint (2.3) is derived using the Lagrange multiplier method. The Lagrange multipliers associated with the constraints (2.3) turn out to be $-\sigma_{ij}$. The functional is given by

$$\tilde{\Pi}(u_i, \tilde{\varepsilon}_{ij}, \sigma_{ij}) = \int_V \left(U_0(\varepsilon_{ij}) - f_i^B u_i\right)\, dv - \int_S f_i^s u_i\, ds - \int_V \tilde{\varepsilon}_{ij}\sigma_{ij}\, dv \tag{2.4}$$

The finite element based on the statement $\delta\tilde{\Pi} = 0$ requires independent approximation of the three fields: $u_i, \tilde{\varepsilon}_{ij}$, and σ_{ij}. In the the enhanced strain element, however, the independent stress field is eliminated by selecting the independent stress field to be orthogonal to the enhancement strain field

$$\int_V \tilde{\varepsilon}_{ij}\sigma_{ij}\, dv = 0 \tag{2.5}$$

Of course, the statement in (2.5) is a weak form of $\tilde{\varepsilon}_{ij} = 0$, which is responsible for locking. Now the variational statement for the enhanced strain finite element model can be stated as

$$\delta\hat{\Pi} = 0 \ \text{ subjected to the condition (2.5)} \tag{2.6}$$

where

$$\hat{\Pi}(u_i, \tilde{\varepsilon}_{ij}) = \int_V \left(U_0(\varepsilon_{ij}) - f_i^B u_i\right)\, dv - \int_S f_i^s u_i\, ds \tag{2.7}$$

The statement $\delta\hat{\Pi} = 0$ gives

$$\int_V \left(\delta\varepsilon_{ij}^D + \delta\tilde{\varepsilon}_{ij}\right) \frac{\partial U_0}{\partial \varepsilon_{ij}}\, dv - \int_V f_i^B \delta u_i\, dv - \int_S f_i^s \delta u_i\, ds = 0 \tag{2.8}$$

Thus, the two independent fields for the enhanced strain formulation are the displacements u_i and the enhanced assumed strains $\tilde{\epsilon}_{ij}$. By choosing the stress field to satisfy (2.6) the stresses are eliminated from the variational expression.

2.3 The Choice of Enhancement Field

Deteriorated coarse mesh performance of a layerwise element with low order (*i.e*, linear) interpolation of the thickness variation is what we wish to remedy. In this case, it is the inability of the element to model the nearly zero transverse normal strain situation that causes the problem. By the proper choice of the enhancement field it is possible to design low order elements that have improved coarse mesh performance. This is done by identifying the constraint ($\varepsilon_{33} = 0$) in strain field whose deficiency causes the deteriorated performance of the element and introducing it into the element formulation through the incompatible enhancement field, as explained in the previous section.

Identifying the enhancement field is a straightforward procedure for the case of a regular shaped element, compared to that of a distorted element. Distortion in the element geometry makes it difficult to identify the deficiency in the function field. Hence, for a general element, the procedure needs to be modified to include a mapping of a general element to an isoparametric domain. This makes it possible to work in the isoparametric domain which is regular shaped compared to a physical domain. Details on the mapping between the physical and isoparametric domains are discussed in [16].

3. FINITE ELEMENT MODEL

3.1 Layerwise Displacement Field

Equations of motion represented in (2.9) for an enhanced strain method involve two independently assumed fields, namely, the displacements and enhanced strains. In the present study, the displacements are assumed from a layerwise field suitable for the analysis of a layered media [1,2]. In order to develop a layerwise theory for a geometrically non-linear analysis it is required to model the strain distribution through the thickness in a kinematically correct manner. That is, the kinematic condition that exists at the interface between the lamina should be such that the transverse strains are piecewise continuous through the laminate thickness. The geometry of the laminate at configuration Ω_t, for example, is represented as

$${}^t x_i = \sum_{I=1}^{N} \Phi_I(\zeta^I)\ {}^t x_i^I(\xi, \eta) \tag{3.1}$$

where ${}^{t}x_i$ represents the material coordinate in a stationary Cartesian coordinate frame for a material point at (ξ, η, ζ^I) of the laminate in the configuration at Ω_t. Similar expressions hold at $t = 0$ and $t = t + \Delta t$. One dimensional linear Lagrange shape functions Φ_I are used in (3.1) for representing the variation of geometry in the thickness direction.

From the geometry of the laminate, defined at different configurations, the corresponding displacements can be expressed as

$$
\begin{aligned}
{}^{t}u_i &= {}^{t}x_i - {}^{0}x_i = \sum_{I=1}^{N} \Phi_I(\zeta^I)\, {}^{t}u_i^I(\xi, \eta) \\
{}^{t+\Delta t}u_i &= {}^{t+\Delta t}x_i - {}^{0}x_i = \sum_{I=1}^{N} \Phi_I(\zeta^I)\, {}^{t+\Delta t}u_i^I(\xi, \eta) \\
u_i &= {}^{t+\Delta t}u_i - {}^{t}u_i = \sum_{I=1}^{N} \Phi_I(\zeta^I)\, u_i^I(\xi, \eta) \quad (i = 1, 2, 3)
\end{aligned} \tag{3.2}
$$

The quantities ${}^{t}u_i^I$ and ${}^{t+\Delta t}u_i^I$ have the meaning of total displacements at the interface I between the kinematic layers for the configuration Ω_t and $\Omega_{t+\Delta t}$, respectively; u_i^I represent the incremental displacement for the same interface I. These inplane displacements are approximated using interpolation functions of 2D elements.

3.2 Element Equations

The linearized incremental equation of motion for an enhanced strain method can be written as (see Moorthy [16])

$$
\begin{aligned}
\int_{{}_tV} \left(\delta_t \varepsilon_{ij}^D + \delta_t \tilde{\varepsilon}_{ij}\right) {}_tC_{ijkl} \left({}_t\varepsilon_{kl}^D + {}_t\tilde{\varepsilon}_{kl}\right)\, dv + \int_{{}_tV}^{t} \tau_{ij}^c \delta_t \eta_{ij}\, dv \\
= {}^{t+\Delta t}R - \left[\int_{{}_tV} {}^{t}\tau_{ij}^c\, \delta_t \varepsilon_{ij}\, dv\right]_{(k-1)}
\end{aligned} \tag{3.3}
$$

where

$${}^{t+\Delta t}R = \int_{t+\Delta t_V}^{t+\Delta t} f_i^B \delta u_i\, dv + \int_{t+\Delta t_S}^{t+\Delta t} f_i^s\, \delta u_i\, ds \tag{3.4}$$

is the residual, ${}_t\varepsilon_{ij}^D = (1/2)({}_tu_{i,j} + {}_tu_{j,i})$ represent the compatible linear strains, ${}_t\tilde{\varepsilon}_{ij}$ represent the incompatible enhancement strain, ${}_t\eta_{ij} = (1/2)({}_tu_{m,i}\ {}_tu_{m,j})$ represent the non-linear part of Green-Lagrange strains, ${}^{t}\tau_{ij}^c$ are the Cartesian components of (Cauchy) stresses in Ω_t evaluated through the constitutive relations, and ${}_tC_{ijkl}$ represent the incremental material property matrix. During the equilibrium iterations (in reducing the residual error), the second term on the right hand side of (3.3), which represents the internal force vector, is updated in each iteration. That is, for the kth iteration the term is evaluated with the quantities known from the $(k-1)$th iteration. The the Cauchy stresses ${}^{t+\Delta t}\tau_{ij}$ are to be recovered in such a manner that it is orthogonal to the enhancement field ${}_{t+\Delta t}\tilde{\varepsilon}_{ij}$:

$$\int_{t+\Delta t_V} {}^{t+\Delta t}\tau_{ij}\ {}_{t+\Delta t}\tilde{\varepsilon}_{ij}\, dv = 0 \tag{3.5}$$

The element matrices are obtained when the displacement and enhancement fields are substituted into the incremental equations of motion (3.3). We obtain

$$[{}_tK]\{\Delta d\} + [{}_tP]^T\{\Delta\alpha\} = \{{}^{t+\Delta t}R^e\} - \{{}^tR^I\}_{(k-1)} \tag{3.6}$$

$$[{}_tP]\ \{\Delta d\} + [{}_tQ]\{\Delta\alpha\} = -\{{}^th^I\}_{(k-1)} \tag{3.7}$$

where

$$[{}_tK] = [{}_tK_L] + [{}_tK_N] \tag{3.8a}$$

$$\begin{aligned}
[{}_tK_L] &= \int_{{}_tV} [{}_tB_L]^T[{}_tC]\ [{}_tB_L]\ dv\ ,\ [{}_tK_N] = \int_{{}_tV} [{}_tB_N]^T[{}^t\bar{\tau}^c]\ [{}_tB_N]\ dv \\
[{}_tP] &= \int_{{}_tV} [{}_t\tilde{E}]^T\ [{}_tC]\ [{}_tB_L]\ dv\ ,\quad [{}_tQ] = \int_{{}_tV} [{}_t\tilde{E}]^T\ [{}_tC]\ [{}_t\tilde{E}]\ dv \\
\{{}^tR^I\}_{(k-1)} &= \left[\int_{{}_tV}[{}_tB_L]^T\{{}^t\tau^c\}\ dv\right]_{(k-1)}\ ,\quad \{{}^th^I\}_{(k-1)} = \left[\int_{{}_tV}[{}_t\tilde{E}]^T\{{}^t\tau^c\}\ dv\right]_{(k-1)}
\end{aligned} \tag{3.8b}$$

The terms $\{{}^tR^I\}_{(k-1)}$ and $\{{}^th^I\}_{(k-1)}$ are the internal force vector and the conjugate vector corresponding to the strain parameters, respectively. They are evaluated at the most recently known configuration. The subscript $(k-1)$ is used to indicate that the quantity is evaluated with solution from the previous iteration. For additional details, the reader may consult Reference 31.

In using the displacement field (3.2), which is C^0 continuous across the element boundary, the strain field will be discontinuous across the element layers. Consistent with the displacement field, the enhanced strains are not made continuous across the element layer boundary. The discontinuous enhancement field eliminates the coupling of unknown strain parameters from one element layer to another. This has the consequence that strain parameters can be eliminated within the element layer without increasing the number of unknowns in the global set of equations from that in a pure displacement method. Thus from equation (3.7) we have

$$\{\Delta\alpha\} = -[{}_tQ]^{-1}\ \left[\{{}^th^I\}_{(k-1)} + [{}_tP]\{\Delta d\}\right] \tag{3.9}$$

The strain parameters can be eliminated from (3.6)by using (3.9). Thus the element equations take the form

$$[{}_t\hat{K}]\{\Delta d\} = \{F\} \tag{3.10a}$$

$$\begin{aligned}
[{}_t\hat{K}] &= [{}_tK] - [{}_tP]^T[{}_tQ]^{-1}[{}_tP] \\
\{F\} &= \{{}^{t+\Delta t}R^e\} - \{{}^tR^I\}_{(k-1)} + [{}_tP]^T[{}_tQ]^{-1}\{{}^th^I\}_{(k-1)}
\end{aligned} \tag{3.10b}$$

The incremental solution for the displacements is obtained after solving the assembled set of equations from the element equations (3.10). From the displacement solution the incremental solution in the enhancement strain parameters are post computed from (3.9).

4. MODELING OF INTERLAYER DELAMINATION

4.1 Introduction

In a laminate with many layers, delamination is a major failure mechanism. It is characterized by the separation or debonding between layers and may be represented as an interlaminar crack. For the prediction of the onset of delamination and its growth, stress based criteria and strain energy release rate based criteria have been used. The stress and strain energy release rate evaluation in a region near the delamination tip is complicated by the triaxial nature of the stress and strain fields. Among the stresses at the delamination tip, the evaluation of interlaminar stresses is more important from the delamination point of view.

While the evaluation of stresses from constitutive relations is more consistent with the general formulation, the stresses recovered from the equilibrium equations are more accurate. Hence, in the present study the laminate is modeled in such a manner that it will facilitate a direct recovery of interlaminar stresses from equilibrium conditions. It is achieved by modeling the laminate as two sublaminates on either side of the delaminated interface. The total laminate is analyzed by bringing the two sublaminates together by enforcing a no-slip adhesive contact condition. Interlaminar stresses are later recovered from the contact loads that satisfy force equilibrium at the interface. There is one other advantage in modeling the interlaminar boundary in this manner compared to that evaluated from constitutive relations in a finite element analysis. Irrespective of the size of the element near the interface, the Gauss point locations where stresses are evaluated are not on the interface. In modeling the interface contact in the present approach, it is assumed that the nodes on the two faces of the delamination are in contact prior to delamination and the no-slip adhesive contact condition is enforced by the penalty function method.

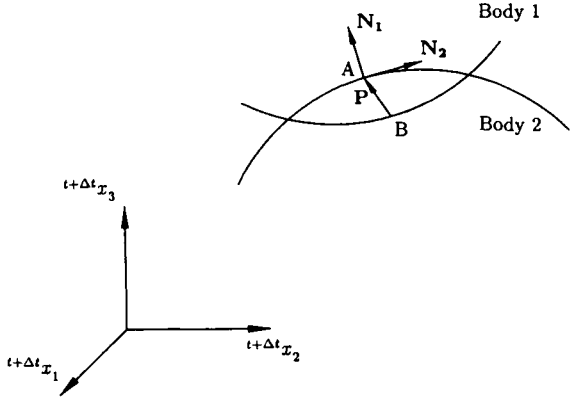

Figure 4.1: Contact between two bodies.

4.2 Penalty Formulation of Contact

Consider two bodies, hitting body 1 and target body 2 in contact (see Figure 4.1), and suppose that point B on body 1 and point A on body 2 were originally in contact. Further assume that during the motion they were separated by a small amount of penetration ${}^{t+\Delta t}\mathbf{P}$ (superscript $t+\Delta t$ is omitted inFigure 4.1 for clarity)

$$ {}^{t+\Delta t}\mathbf{P} = {}^{t+\Delta t}\mathbf{x}^2 - {}^{t+\Delta t}\mathbf{x}^1 \tag{4.1} $$

where ${}^{t+\Delta t}\mathbf{x}^2$ represents the position vector of contact point in body 2 (point A) and ${}^{t+\Delta t}\mathbf{x}^1$ is the position vector of contact point in body 1 (point B).

The components of penetration (displacement) at contact point can be expressed in the normal and tangential directions to the interface as

$$ {}^{t+\Delta t}P_I = \left({}^{t+\Delta t}x_i^2 - {}^{t+\Delta t}x_i^1\right) {}^{t+\Delta t}N_{Ii} \quad (I, i = 1, 2, 3) \tag{4.2} $$

where ${}^{t+\Delta t}N_{Ii}$ denote the ith component of the vector ${}^{t+\Delta t}\mathbf{N}_I$ represented in the global Cartesian coordinates. Now assuming that the configuration change from Ω_t to $\Omega_{t+\Delta t}$ is small such that ${}^{t+\Delta t}N_{Ii} \approx {}^{t}N_{Ii}$ and we have

$$ {}^{t+\Delta t}P_I = {}^{t}P_I + \Delta P_I \tag{4.3a} $$

$$ {}^{t}P_I = ({}^{t}x_i^2 - {}^{t}x_i^1)\,{}^{t}N_{Ii}\,, \quad \Delta P_I = (u_i^2 - u_i^1)\,{}^{t+\Delta t}N_{Ii} \tag{4.3b} $$

The finite element approximation of incremental penetration equation (4.3) is obtained by approximating the displacements u_i^2 of the body 2 at the contact point using elements on the target surface. For details, see [16].

During the motion of the bodies 1 and 2 in contact, there may be regions on the surface of the two bodies that need to be in adhesive contact. For a laminate with an embedded delamination, this region is the bonded portion of the laminate at the interface where the delamination is present. In order to enforce this adhesive contact condition on this portion of the surface, a zero penetration condition is imposed using the penalty function method. In the penalty function method, the constraint condition

$$ {}^{t+\Delta t}P_I = 0 \quad (I = 1, 2, 3) \tag{4.4} $$

is included in the finite element formulation by minimizing the modified functional

$$ \Pi_m = \tilde{\Pi} + \Pi_p \tag{4.5} $$

where $\tilde{\Pi}$ represents total energy associated with the assemblage of finite elements with enhanced strains

$$ \frac{\partial \tilde{\Pi}}{\partial \{\Delta U\}} = [\tilde{K}]\{\Delta U\} - \{\tilde{F}\} \tag{4.6} $$

and Π_p represents the penalty functional associated with the constraint (4.4)

$$\Pi_p = \frac{1}{2} \sum_{n=1}^{L_t} \alpha_n \left({}^{t+\Delta t}P_I^n \; {}^{t+\Delta t}P_I^n \right) \tag{4.7}$$

where L_t represents the total number of hitting nodes where no slip adhesive contact condition is enforced.

After obtaining the incremental solution u_i during motion from configuration Ω_t to $\Omega_{t+\Delta t}$, components of penetration along normal tangential coordinate for any contact point can be post computed from (4.2) as

$${}^{t+\Delta t}P_I = \left({}^{t+\Delta t}x_i^2 - \; {}^{t+\Delta t}x_i^1 \right) \; {}^{t+\Delta t}N_{Ii} \tag{4.8}$$

where ${}^{t+\Delta t}x_i = \; {}^{t}x_i + u_i$. Further, the contact loads at contact node n are evaluated from the penetration displacement and penalty parameter α_n as follows

$${}^{t+\Delta t}q_I^n = -\alpha_n \; {}^{t+\Delta t}P_I^n \tag{4.9}$$

The load ${}^{t+\Delta t}q_I^n$ at contact node n represents the reaction forces between the hitting node and target surface.

4.3 Strain Energy Release Rates

Even though linear elastic fracture mechanics (LEFM) is not applicable in general to laminated composites with through the thickness cracks, it has generally been accepted that delamination can be characterized by LEFM with critical strain energy release rate as a growth criterion. Three basic modes of delamination, Modes I, II and III represent the opening, sliding and twisting shear modes, respectively. In general three modes can exists in isolation or in combinations. The associated strain energy release rates G_I, G_{II} and G_{III} can be evaluated for a delamination problem for each of the three modes of delaminations. They represent the total energy that is released from the body for a small crack extension Δa during the corresponding mode of delamination. Three different methods of evaluating the strain energy release rates are discussed in the setting of finite element method. They are the virtual crack closure method (VCCM), crack closure method (CCM), and the potential energy change method (PECM). For details see [16].

5. NUMERICAL RESULTS

5.1 Problem Description

In order to illustrate the application of the finite element model developed and the strain energy release rate procedures, a double cantilever problem is chosen as an example. The geometry of the double cantilever is shown in Figure 5.1. A splitting load of magnitude P is applied at the tip of the double cantilever to produce an opening mode near the crack tip.

5.2 Analytical Solution

If the specimen is assumed to experience small displacements so that linear approximations can be used and the length a and the thickness h of one cantilever are such that a/h value is large and the shear deformation effects can be neglected, then the tip deflection can be obtained as (see Reddy [1])

$$\delta = \frac{Pa^3}{3D^b} \tag{5.1}$$

where D^b denotes the effective bending stiffness, which depends on the boundary condition at the edges $y = 0$ and $y = B$. When the cantilever is small in the width direction, it can be approximated as a beam and when it is long in the width direction it is a plate strip in cylindrical bending. The beam bending is a plane stress problem whereas the cylindrical bending is a plane strain problem. The effective bending stiffness D^b for the cantilever depends on whether it is modeled as a plane stress or plane strain problem.

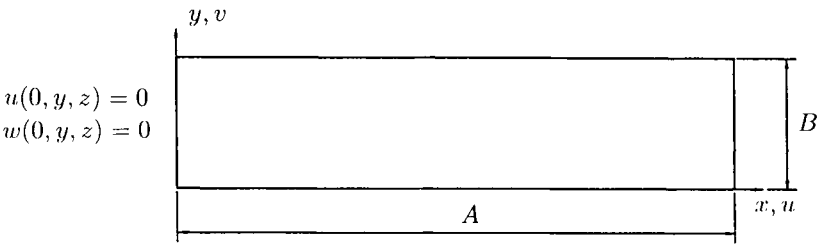

Plane strain: $v(x, 0, z) = v(x, B, z) = 0$ Plane stress: $v(0, 0, 0) = 0$

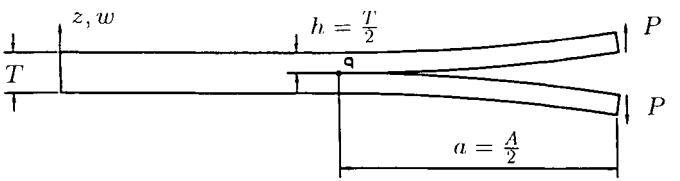

Figure 5.1: Geometry, loading and boundary conditions of the double cantilever.

The double cantilever geometry considered here is symmetric about the plane $z = T/2$ so that the mode II strain energy release rate $G_{II} = 0$. Assuming further that the dissipation of energy takes place only at the crack tip during the crack extension, total strain energy release rate G is equal to the opening mode strain energy energy rate G_I

$$G = G_I = -\frac{d\Pi}{da}$$

where Π represents the total potential energy of the body per unit width of the laminate and a is the delamination length. This can be represented graphically in the load-deflection curve, where δ_2 and δ_1 represent the tip deflections of the double cantilever at two different delamination lengths a and $a + \Delta a$ (see Figure 5.2). Then for a double cantilever, total strain energy release rate can be obtained as

$$G = G_I = 2 \times \frac{[\frac{1}{2}P\delta_2 + P(\delta_1 - \delta_2) - \frac{1}{2}P\delta_1]}{B\Delta a}|_{\Delta a \to 0} = \frac{P(\delta_1 - \delta_2)}{B\Delta a}|_{\Delta a \to 0} \tag{5.2}$$

Using the load deflection relation from (5.1)

$$\delta_1 = \frac{P(a + \Delta a)^3}{3D^b} \quad , \quad \delta_2 = \frac{Pa^3}{3D^b} \tag{5.3}$$

the strain energy release rate becomes

$$G_I = \frac{P^2a^2}{BD^b} = \frac{9D^b\delta^2}{Ba^4} \tag{5.4}$$

where δ is the tip deflection.

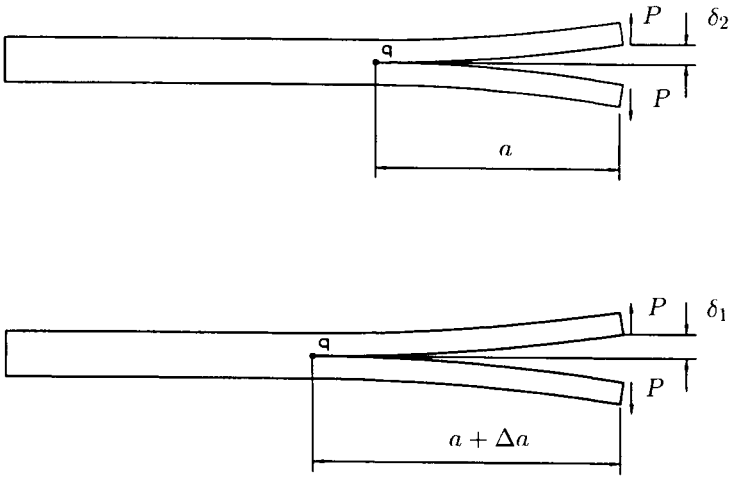

Figure 5.2: Double cantilever configurations at two different delamination lengths a and Δa.

5.3 Specially Orthtropic Double Cantilever

The geometry, loading and boundary conditions for this problem (see [11]) are the same as those shown in Figure 5.1. The dimensions of the double cantilever are: $a/h = 50$, $T = 0.04''$, $h = T/2 = 0.02''$, $A = 2''$, $a = A/2 = 1''$,

and $B = 1''$. The plane stress condition is assumed, and a splitting load of magnitude P is applied at the tip of the double cantilever for an opening mode near the delamination tip q. The material properties of the lamina used are

$$E_1 = 20 \times 10^6 \text{ psi}, \quad E_2 = E_3 = 2 \times 10^6 \text{ psi}, \quad G_{23} = G_{31} = G_{12} = 0.85 \times 10^6 \text{ psi}$$

$$\nu_{23} = \nu_{13} = \nu_{12} = 0.21$$

The lamina orientation is such that fiber direction is along the length of the double cantilever. The finite element used in the plane of the double cantilever is shown in Figure 5.3. An inplane mesh of 14×1 is used in the analysis and the sequence of lengths (in) of elements used in the analysis are: $0.32, 0.32, 0.32, 0.02, 0.01, 0.005, 0.005$ and repeated symmetrically. Linear Lagrange 1D elements are used in the thickness direction, as shown in Figure 5.4.

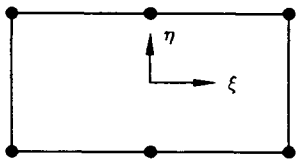

Figure 5.3: The 2D element used for inplane discretization.

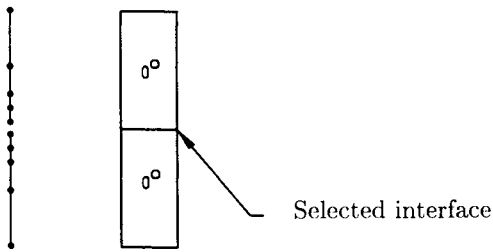

Figure 5.4: Nonuniform mesh used through the thickness.

The strain energy release rate at the crack tip is calculated by three different approaches. Even though these methods evaluate the strain energy release rate based on a small delamination closure, the VCCM requires an analysis only at one delamination length, because of the virtual nature of the crack closure considered. In the other two approaches (CCM and PECM) the delamination closure (Δa) is real and hence two different analyses are required for the evaluation of the strain energy release rate. Irrespective of whether the delamination closure (Δa) is virtual or real, all the above methods require it

to be small for an accurate determination of the strain energy release rate. In the context of the finite element method, this delamination closure is dictated by the size of the elements adjacent to the delamination tip. In this study, the delamination closure length considered is $0.005''$.

The analytical solution for the strain energy release rate can be obtained from (5.1). For the plane stress problem the effective bending stiffness is $D^b = E_1 I_{yy}$. Where, I_{yy} represents the moment of inertia of the section of the cantilever about the $y-$axis. The strain energy release rate G_I obtained from different methods are compared with the analytical solution in Figure 5.5. It can be seen that, all the three methods yield the strain energy release rate G_I very close to the analytical solution. This is despite the fact that the present analysis uses a higher-order element which has been reported [7] to be inaccurate in the evaluation of strain energy release rate.

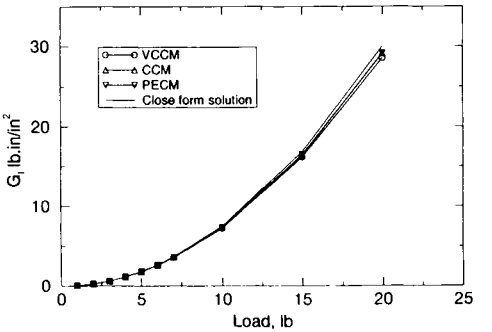

Figure 5.5: Comparison of the strain energy release rates.

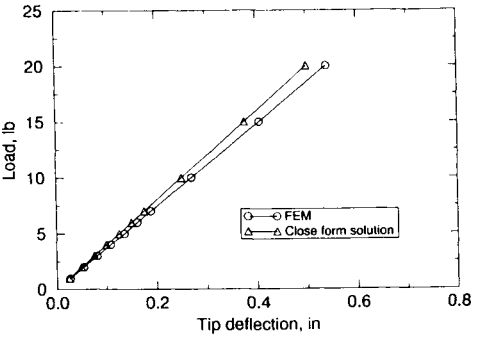

Figure 5.6: Load-deflection curves for double cantilever.

Figure 5.6 shows a comparison of the load-deflection curves obtained using FEM and the analytical solutions. It can be noted that the FEM with contact enforcement by penalty function method predicts a more compliant

response compared to that from the analytical solution. This is attributed to the assumption of clamped endcondition made in obtaining the analytical solution. The clamped endcondition is only an approximation to the actual boundary condition at the ends of the double cantilever segments (*i.e.*, near the delamination tip).

Figures 5.7 and 5.8 show the effect of penalty parameter on the tip deflection and strain energy release rate G_I for an applied load of 1 *lb*. It is noted that value of the penalty parameter greater than 10^6 has little effect on the tip deflection as well as on the strain energy release rates.

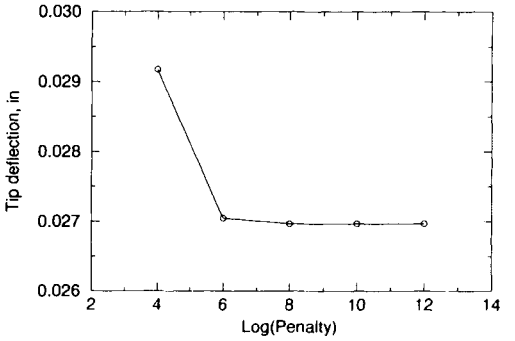

Figure 5.7: Effect of the penalty parameter on tip deflection.

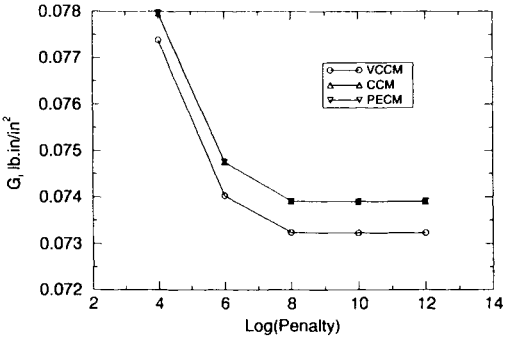

Figure 5.8: Effect of the penalty parameter on the strain energy release rate.

5.4 Cross-Ply $(0/90)_s$ Double Cantilever

In this section a cross-ply double cantilever problem is considered in plane strain state. The geometry of the cantilever is shown in Figure 5.1. It has an overall length of $A = 6''$, width $B = 1''$, and thickness is T. The total double cantilever is a composite laminate $(0/90)_s$, and the individual plies have the

following material properties in principal material directions

$$E_1 = 25 \times 10^6 \text{psi}, \quad E_2 = E_3 = 1 \times 10^6 \text{psi}, \quad G_{23} = 0.2 \times 10^6 \text{psi}$$

$$G_{12} = G_{13} = 0.5 \times 10^6 \text{psi}, \quad \nu_{12} = \nu_{23} = \nu_{13} = 0.25$$

Each of these material plies considered are of equal thickness h_k.

The laminate is assumed to have an embedded delamination in the midplane of the cantilever extending to a length of $a = 3''$ from its free end making it a double cantilever. A splitting load of magnitude $P = 1\ lb$ is applied at the tip of the cantilever. The displacements (u, v, w) along the (x, y, z) directions are constrained as follows:

$$u(0, y, z) = 0\ , \quad v(x, 0, z) = 0\ , \quad w(0, y, z) = 0\ , \quad v(x, B, z) = 0$$

A 2D mesh of 6-node elements (see Figure 5.9) is used in conjunction with a 1D mesh (Figure 5.10) of 2-node linear elements through the thickness direction. The 6-node elements used in the inplane mesh has a quadratic variation along the $x-$direction for capturing bending deflection of the laminate and has linear variation along the $y-$direction.

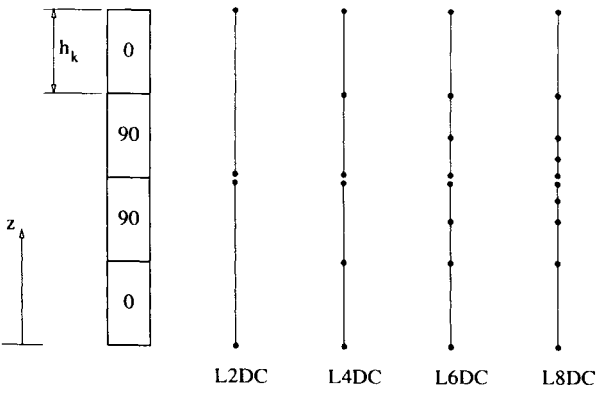

Size of sequence of elements from bottom of laminate

L2DC: $(2.0, 2.0)\ h_k$

L4DC: $(1.0, 1.0, 1.0, 1.0)\ h_k$

L6DC: $(1.0, 0.5, 0.5, 0.5, 0.5, 1.0)\ h_k$

L8DC: $(1.0, 0.5, 0.25, 0.25, 0.25, 0.25, 0.5, 1.0)\ h_k$

Figure 5.9: Mesh used through the thickness of cross-ply double cantilever.

The strain energy release rate at the crack tip is calculated by the three different approaches. In order to study the sensitivity of different approaches

to the length of delamination closures considered, strain energy release rates are evaluated using different meshes that produce different amounts of delamination closure lengths. The different inplane meshes considered are given below.

Mesh DC0:

Number of elements (along x, y): 8×1

Length of elements: $0.75''$ (8 elements)

Delamination closure length $\Delta a = 0.75''$

Mesh DC1:

Number of elements (along x, y): 10×1

Length of elements: $0.75''$ (3 elements), $0.375''$ (4 elements), $0.75''$ (3 elements)

Delamination closure length $\Delta a = 0.375''$

Mesh DC2:

Number of elements (along x, y): 12×1

Length of elements: $0.75''$ (3 elements), $0.375''$, $0.1875''$ (4 elements), $0.375''$, $0.75''$ (3 elements)

Delamination closure length $\Delta a = 0.1875''$

Mesh DC3:

Number of elements (along x, y): 14×1

Length of elements: $0.75''$ (3 elements), $0.375''$, $0.1875''$, $0.09375''$ (4 elements), $0.1875''$, $0.375''$, $0.75''$ (3 elements)

Delamination closure length $\Delta a = 0.1875''$

The strain energy release rates evaluated from different methods are plotted against $\Delta a/a$ in Figures 5.10 and 5.11 for a/h values of 2 and 100, respectively, where h is the thickness of the sublaminate. A mesh with 2 linear elements (L2DC in Figure 5.9) through the whole thickness of the laminate is considered in this study. It can be seen that all the three methods converge approximately to the same value of G_I as Δa approaches zero. Further, it is noted that VCCM is less sensitive to $\Delta a/a$ indicating that it produces more accurate value of G_I compared to CCM and PECM for larger values of $\Delta a/a$ values. Sensitivity curves from CCM and PECM are very close to each other for small values of a/h upto 50 and differ slightly for the case of $a/h = 100$. Figures 5.12 and 5.13are the log-log plots showing the variation of G_I with respect to a/h for large and small values of delamination closure lengths ($\Delta a/a = 0.25$ and 0.03125). It is noted that the curves obtained from all three methods (VCCM,CCM and PECM) are very close to each other for $\Delta a/a = 0.125$ and smaller.

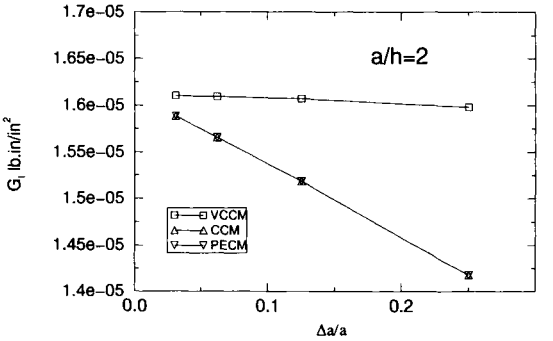

Figure 5.10: Sensitivity of G_I to the ratio $\Delta a/a$ for $a/h = 2$.

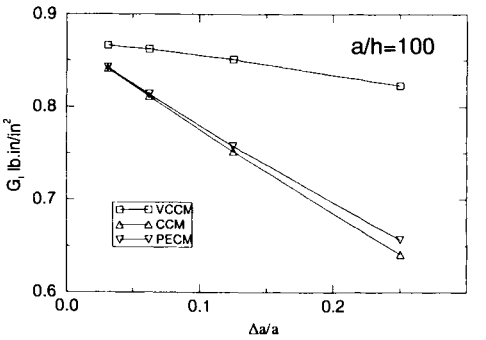

Figure 5.11: Sensitivity of G_I to the ratio $\Delta a/a$ for a/h=100.

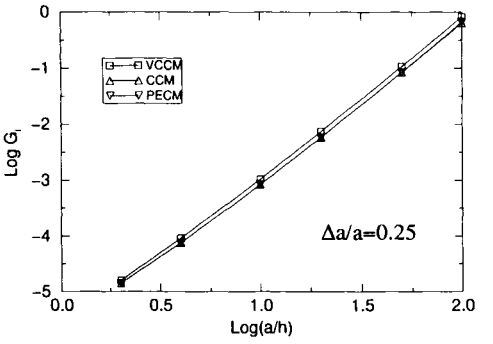

Figure 5.12: Variation of G_I with a/h for $\Delta a/a = 0.25$.

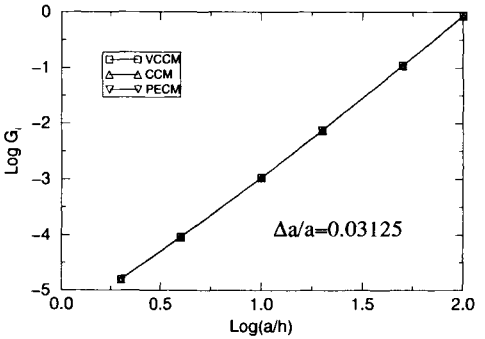

Figure 5.13: Variation of G_I with a/h for $\Delta a/a = 0.03125$.

In order to study the effect of mesh refinement through the thickness on G_I, four different thickness meshes (L2DC, L4DC, L6DC and L8DC) are considered. The number of elements used in each of these meshes and size of the elements are shown in Figure 5.9. The 2D mesh used here is DC3. The strain energy rate G_I obtained from each of these meshes is given in Table 5.1 for VCCM. It is noted that the change in the G_I values with thickness refinement is very small for large a/h values.

Table 5.1: G_I $(lb.in/in^2)$ values for different thickness meshes from VCCM.

Meshes	$a/h = 2$	$a/h = 4$	$a/h = 10$	$a/h = 20$	$a/h = 50$	$a/h = 100$
L2DC	1.610E-5	9.239E-5	1.069E-3	7.643E-3	1.112E-1	8.662E-1
L4DC	1.633E-5	9.389E-5	1.076E-3	7.671E-3	1.113E-1	8.667E-1
L6DC	1.652E-5	9.509E-5	1.082E-3	7.690E-3	1.114E-1	8.669E-1
L8DC	1.659E-5	9.550E-5	1.080E-3	7.695E-3	1.114E-1	8.669E-1

To ascertain the accuracy of the evaluated strain energy release rates, the G_I computed from different numerical methods are compared with the analytical solution. The analytical solution given in (5.1) is valid for thin laminates where shear deformation effects can be neglected. The effective bending stiffness D^b for the cross-ply laminate is given by

$$D^b = \frac{D_{11}A_{11} - B_{11}^2}{A_{11}} \tag{5.12}$$

where

$$(A_{11}, B_{11}, D_{11}) = \int_T Q_{11}(1, z, z^2)\, dz \ , \quad Q_{11} = \frac{E_1}{1 - \nu_{12}\nu_{21}} \tag{5.13}$$

The integration indicated in (5.13) is over the thickness of each cantilever. Table 5.2 gives a comparison between G_I from three alternate numerical methods to that from the analytical solution for $a/h = 50$ and 100. The meshes used in the analysis are DC3 for inplane refinement and L2DC for thickness refinement. It can be seen that G_I from VCCM, CCM and PECM are close to the analytical solution for thin laminates.

Table 5.2: Comparison of G_I $(lb.in/in^2)$ from alternate methods.

a/h	VCCM	CCM	PECM	Analytical
50	0.1112	0.1079	0.1079	0.1063
100	0.8662	0.8417	0.8424	0.8503

6. SUMMARY AND CONCLUSIONS

A layerwise finite element is developed for the geometrically nonlinear analysis of laminated composites using higher order functions for the inplane approximation and a linear function for the thickness approximation. All problems considered in the study are bending dominated and hence, require use of higher order functions in the inplane direction for capturing accurate bending response. Linear functions are used in modeling the thickness direction of the laminate because it is extremely expensive to provide refinement through the thickness. The thickness locking effects associated with the use of low order functions through the thickness are overcome by the use of enhanced strain method with enhancement field defined for the transverse normal strains.

The layerwise finite element developed herein is used in the analysis of laminates, with a chosen interface modeled with emphasis on the study of delaminations. In a laminate with an embedded delamination, the interface is modeled as a contact zone between the laminate halves separated by the interface. This is achieved by considering the total laminate as two independent sublaminates separated by the interface, but analyzed as a single laminate by enforcing a no-slip adhesive contact condition at the interface.

The interface model developed herein is used to analyze double cantilever problems. Strain energy release rates computed using the present model are found to be in good agreement with the approximate analytical solutions for the case with specified load. However, the comparison was not as good for cases with a specified displacements at the tip of the double cantilever. This is due to the fact that the analytical solution is based on the assumption of a clamped end condition for the segments of the double cantilever.

REFERENCES

1. J. N. Reddy, *Mechanics of Laminated Composite Plates: Theory and Analysis,* CRC Press, Boca Raton, FL (1997).
2. D. H. Robbins, Jr. and J. N. Reddy, "Modeling of Thick Composites Using a Layerwise Laminate Theory," *International Journal for Numerical Methods In Engineering,* **36**, 655–677 (1993).
3. V. B. Watwood, "The finite element method for prediction of crack behavior," *Nuclear Engineering and Design,* **11**, 323–332 (1969).
4. G. P. Anderson, V. L. Ruggles, and G. S. Stibor, "Use of finite element computer programs in fracture mechanics," *International Journal of Fracture,* **7**, 63–76 (1971).
5. D. F. Mowbray, "A note of finite element method in linear fracture mechanics," *Engineering Fracture Mechanics,* **2**, 173 (1970).
6. S. A. Salpekar and I. S. Raju and T. K. O'Brien, "Strain energy release rate analysis of the end-notched flexure specimen using finite element method," *J. Composite Technology and Research,* **10**, 133–139 (1988).
7. E. F. Rybicki and M. F. Kanninen, "A finite element calculation of stress intensity factors by a modified crack closure integral," *Engineering Fracture Mechanics,* **9**, 931–938 (1977).
8. K. N. Shivakumar and P. W. Tan and J. C. Newman, "A virtual crack-closure technique for calculating stress intensity factors for cracked three dimensional bodies," *International Journal of Fracture,* **36**, R43–R50 (1988).
9. J. D. Whitcomb, "Three dimensional analysis of a post buckled embedded delaminations," *Journal of Composite Materials,* **23**, 862–889 (1989).
10. T. K. O'Brien, "Interlaminar fracture of composites," *Journal of the Aeronautical Society of India,* **37**, 61–70 (1985).
11. J. D. Whitcomb, "Finite element analysis of instability related delamination growth," *Journal of Composite Materials,* **15**, 403–426 (1981).
12. J. D. Whitcomb and K. N. Shivakumar, "Strain energy release rate analysis of plates with post buckled delaminations," *Journal of Composite Materials,* **23**, 714–734 (1989).
13. A. C. Garg, "Delamination - A damage mode in composite structure," *Engineering Fracture Mechanics,* **29**, 557–584 (1988).
14. J. N. Reddy, *Applied Functional Analysis and Variational Methods in Engineering,* McGraw-Hill, 1986; reprinted by Krieger, Melbourne, FL, 1990.
15. J. C. Simo and M. S. Rifai, "A class of mixed assumed strain methods and the method of incompatible modes," *International Journal for Numerical Methods in Engineering,* **29**, 1595–1638 (1990).
16. C. M. Dakshina Moorthy, *Modeling of Laminates Using a Layerwise Finite Element with Enhanced Strains for Interlaminar Stress Recovery and Delamination Characteristics,* Ph.D. Dissertation, Department of Mechanical Engineering, Texas A&M University, College Station, Texas, May 1997.

This Page Intentionally Left Blank

Damage Mechanics in Engineering Materials
G.Z. Voyiadjis, J.-W.W. Ju and J.-L. Chaboche (Editors)
© 1998 Elsevier Science B.V. All rights reserved.

A Computational Damage Mechanics Approach for Laminates: Identification and Comparison with Experimental Results

P. Ladevèze[a], O. Allix[a] , L. Gornet[a], D. Lévêque[a] and L. Perret[b]

[a] Laboratoire de Mécanique et Technologie, E.N.S. de Cachan/C.N.R.S./ Université Paris 6, 61, avenue du Président Wilson, 94235 Cachan Cedex - France.

[b] Centre National d'Études Spatiales (CNES) / Toulouse, 18, Av. Édouard Belin - 31055 Toulouse Cedex - France.

The present study concerns finite element predictions of carbon-fiber/epoxy-resin composite coupon delamination tests up to fracture. For these predictions, a previously-defined damage mesomodel of composite laminates is used and implemented in a tridimensional F.E. code. This F.E. software includes the interlaminar interfacial deterioration as well as the main inner layer damage mechanisms. This code is able to predict at any time and at any point the "intensities" of the different damage mechanisms up to fracture. However herein, attention is being focused on the identification and comparison of F.E. predictions with M55J/M18 carbon/epoxy experimental results obtained from the AEROSPATIALE company.

1. INTRODUCTION

An initial step, which has been achieved in other studies, is to define what we call a laminate mesomodel. At the mesoscale, characterized by the thickness of the ply, the laminated structure is described as a stacking sequence of homogeneous layers throughout the thickness and interlaminar interfaces. The main damage mechanisms are described as: fiber breaking, matrix micro-cracking and adjacent layers debonding [1-3]. The single-layer model includes both damage and inelasticity. The interlaminar interface is defined as a two-dimensional mechanical model which ensures traction and displacement transfer from on ply to another. Its mechanical behavior depends on the angle between the fibers of two adjacent layers.

It is well-known that fracture simulation using a continuum damage model leads to severe theoretical and numerical difficulties. A second step which has also been achieved, is to overcome these difficulties. For laminates and, more generally, for composites, we propose the concept of the mesomodel: the state of damage is uniform within each meso-constituent. For laminates, it is uniform throughout the thickness of each single layer; as a complement, continuum damage models with delay effects are introduced.

Two models have to be identified: the single layer model and the interface model [4-7,9-11,13,16]. The appropriate tests used consist of: tension, bending, delamination. Each composite specimen, which contains several layers and interfaces, is computed in order to derive the material quantities intrinsic to the single layer or to the interlaminar interface [9-11]. The proposed procedure is rather simple and has been applied to various materials. Various comparisons with experimental results have been performed to show the possibilities and the limits of our proposed computational damage mechanics approach for laminates. A Finite Element code, devoted to stiff stress gradients, has been developed. It's an extended version of the F.E. code Castem 2000 (C.E.A.) [8]. Several tests of delamination propagation (DCB, MMF, ENF and CLS) or of initiation (edge delamination or holed plate specimens) are considered herein.

We will pay special attention to the basic aspects of the finite element simulations of interlaminar and intralaminar damages. The finite element predictions of classical Fracture Mechanics coupon tests are analyzed. In particular, the value of using a Damage Mechanics approach for initiation prediction as well as for the interpretation of standard Fracture Mechanics tests, in connection with experiments [11], is discussed.

2. MESOMODELING CONCEPT

Let us recall that delamination often appears as an interaction between fiber-breaking, transverse micro-cracking and the debonding of adjacent layers itself. For laminates, three different scales may easily be defined: the micro scale of the individual fiber, the meso scale associated with the thickness of the elementary ply, and the macro scale which is the structural one. Due to the small thickness of the elementary ply and to the kinematics of the deterioration inside the ply, it is both possible and worthwhile to derive a material model at the mesoscale. The one proposed in [5] is defined by two meso-constituents, a single layer and an interface (Figure 1). The interface is a mechanical surface connecting two adjacent layers and depends on the relative orientation of their fibers.

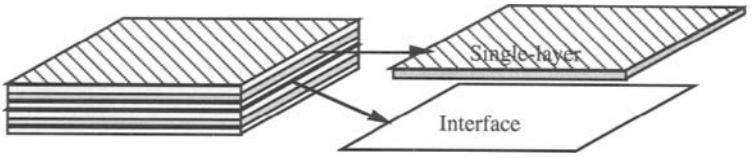

Figure 1. Laminate modeling

A mesomodel is then defined by adding another property: a uniform damage state is prescribed throughout the thickness of the elementary ply. This point plays a major role when one tries to simulate a crack with a damage model. Let us recall that in order to be able to perform a complete analysis of the delamination process in all cases, damage models with delay effects are introduced for the in-plane direction. One limitation of the proposed mesomodel is that it is able to describe only two types of macrocracks. The first type is a delamination crack within the interface, and the second type is the crack is orthogonal to the laminate with each cracked layer being completely cracked in its thickness. Let us also note that the (0°, 0°) interface appears to be something artificial if the material is well made. Normally, such an interface need not be introduced. However, such an "artificial" interface can be introduced for describing an initial crack in a thick layer.

Let us recall that the single-layer model and its identification, including damage such as fiber-breaking and transverse micro-cracking as well as inelastic effects, were previously developed in [4-5]. In section 3, the single-layer model is detailed.

3. SINGLE-LAYER MODELING

The carbon-fiber/epoxy-resin material under consideration in this study has only one reinforced direction. In what follows, subscripts 1, 2 and 3 designate the fiber direction, the transverse direction inside the layer and the normal direction, respectively. An energy is proposed here to predict the damage in a laminated structure [9]. The damaged material strain energy, by splitting the energy into a "tension" energy and a "compression" energy, is written in the case of the plane stress assumption. With the transverse rigidity in compression being supposed equal to E_2^0, one then obtains the following energy for the damaged-layer material:

$$E_D^{cp} = \frac{1}{2(1-d_F)}\left[\frac{\langle\sigma_{11}\rangle_+^2}{E_1^o} + \frac{\phi(\langle-\sigma_{11}\rangle_+)}{E_1^o} - \left(\frac{\nu_{21}^o}{E_2^o} + \frac{\nu_{12}^o}{E_1^o}\right)\sigma_{11}\sigma_{22}\right]$$

$$+ \frac{1}{2}\left[\frac{\langle\sigma_{22}\rangle_+^2}{(1-d')E_2^o} + \frac{\langle-\sigma_{22}\rangle_+^2}{E_2^o} + \frac{\sigma_{12}^2}{(1-d)G_{12}^o}\right]$$

where ϕ is a material function, that takes into accout the non-linear response in compression. d_F, d and d' are three scalar internal variables which remain constant within the thickness. They define the damage of the single layer. The forces associated with the mechanical dissipation are:

$$Y_d = \frac{\partial}{\partial d}\langle\langle E_D^e\rangle\rangle \Big|_{\sigma:cst} = \frac{\langle\langle \sigma_{12}^2\rangle\rangle}{2\,G_{12}^o(1-d)^2}$$

$$Y_{d'} = \frac{\partial}{\partial d'}\langle\langle E_D^e\rangle\rangle \Big|_{\sigma:cst} = \frac{\langle\langle \langle\sigma_{22}\rangle_+^2\rangle\rangle}{2\,E_2^o(1-d')^2}$$

$$Y_F = \frac{\partial}{\partial d_F}\langle\langle E_D^e\rangle\rangle \Big|_{\sigma:cst}$$

$$= \frac{1}{2(1-d_F)^2}\langle\langle \frac{\langle\sigma_{11}\rangle_+^2}{2\,E_1^o} + \frac{\langle-\sigma_{11}\rangle_+^2}{2\,E_1^c} - \left(\frac{\nu_{21}^o}{E_2^o} + \frac{\nu_{12}^o}{E_1^o}\right)\sigma_{11}\sigma_{22}\rangle\rangle$$

where $\langle X\rangle_+$ is the positive part of X and $\langle\langle\ \rangle\rangle$ denotes the mean value within the thickness. For static loadings, the damage evolution law can be formally written:

$$d\,|_t = A_d\,(Y_d\,|_\tau,\ Y_{d'}\,|_\tau,\ \tau \le t)\ ;\ \ d'\,|_t = A_{d'}\,(Yd\,|_\tau,\ Yd'\,|_\tau,\ \tau \le t)$$

where the operators A_d and $A_{d'}$ are material characteristics. The operator A_d is drawn for instance in Figure 2. d_F corresponds to a brittle fracture mechanism. More details, in particular for the modeling of inelastic strains, can be found in [4,7,9].

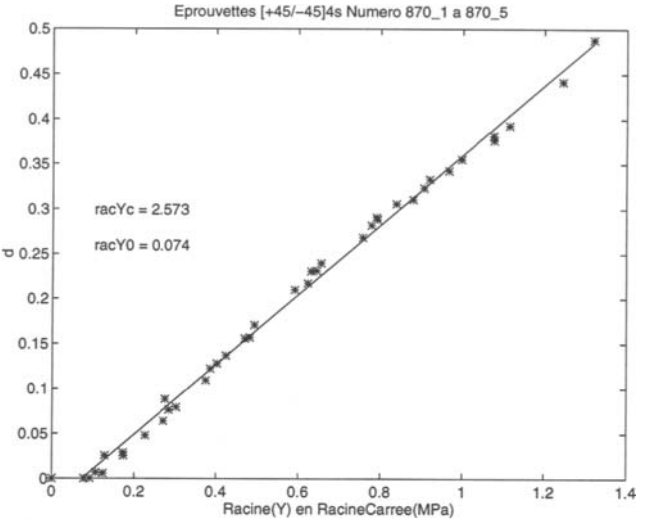

Figure 2. Shear damage evolution of the elementary ply for the M55J/M18 material.

4. INTERLAMINAR INTERFACE MODELING

4.1. Damage kinematics of the interface

The interlaminar connection is thus modeled as a two-dimensional entity which ensures stress and displacement transfers from one ply to another. The diagram leading to the definition of the interface is classical for isotropic bi-materials. The interlaminar connection can be interpreted as a ply of matrix whose thickness (denoted by e) is small compared to the in-plane dimension. Therefore, the wavelength of the displacement in the normal direction N3 is on the order of magnitude of the thickness, while the wavelength of the displacement fields in the plane is on the order of the in-plane directions.

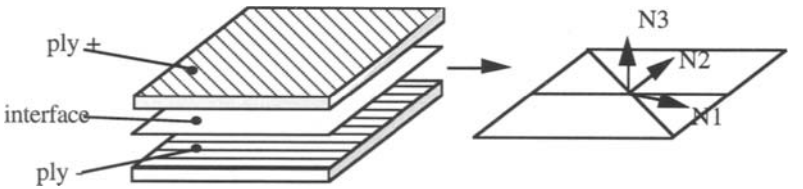

Figure 3. "Orthotropic" directions of the interface.

$$[U] = U^{+} - U^{-} = [U]_1 \underline{N}_1 + [U]_2 \underline{N}_2 + [W] \underline{N}_3 \qquad (1)$$

is the difference in displacements between the upper and lower surfaces of Ω. Thus, at the first order, the strain energy of Ω is:

$$E_d = \frac{1}{2}\int_{\Omega} \mathrm{Tr}[\, K\varepsilon_0\, \varepsilon_0\,]\, d\Omega \approx \frac{1}{2} e \int_{\Gamma} \frac{[U]^T}{e} H \frac{[U]}{e}\, d\Gamma \qquad (2)$$

where Γ is the area of the mid-plane interface, and H is a (3,3) symmetric matrix. Let us denote the bisectors of the fiber directions by $(\underline{N}_1, \underline{N}_2)$. They are necessarily "orthotropic" directions of the interface, since a $[\theta_1,\theta_2]$ interface is equivalent to a $[\theta_2,\theta_1]$ interface (Figure 3). The ideas and framework which govern the interface damage model are similar to those used for deriving the layer damage model [5],[9]. Like in the layer model, the effect of the deterioration of the interlaminar connection on its mechanical behavior is taken into account by means of internal damage variables. The different behavior in "tension" and in "compression" are distinguished by splitting the strain energy into "tension-energy " and "compression-energy". More precisely, we use the following expression, as proposed in [10], of the energy per unit area. Thus, in the $(\underline{N}_1, \underline{N}_2, \underline{N}_3)$ axes, the elastic strain energy of the interface may be written as follows in stress form:

$$E_d = \frac{1}{2}\int_{\Gamma} \left[\frac{<-\sigma_{33}>_+^2}{k_o^3} + \frac{<\sigma_{33}>_+^2}{k_o^3(1-d_3)} + \frac{\sigma_{13}^2}{k_o^1(1-d_1)} + \frac{\sigma_{23}^2}{k_o^2(1-d_2)} \right] d\Gamma \qquad (3)$$

Three internal damage indicators, associated with the three Fracture Mechanics modes, are thereby introduced.

4.2. Interfacial damage evolution laws

These evolution laws must satisfy the Clausius-Duheim inequality. Classically, the damage forces, associated with the dissipated energy ω, are introduced as follows:

$$Y_{d3} = \frac{1}{2}\frac{<\sigma_{33}>_+^2}{k^0(1-d)^2} \; ; \; Y_{d1} = \frac{1}{2}\frac{\sigma_{31}^2}{k_1^0(1-d_1)^2} \; ; \; Y_{d2} = \frac{1}{2}\frac{\sigma_{32}^2}{k_2^0(1-d_2)^2} \qquad (4)$$

with: $\omega = Y_{d3}\,\dot{d}_3 + Y_{d1}\dot{d}_1 + Y_d\,\dot{d}_2 \quad (\omega \geq 0)$

The damage evolution laws used in this study are based on the assumption that the evolution of the different damage indicators is strongly coupled and driven by a unique equivalent damage force. The following model, developed in [13], considers that the damage evolution is governed by means of an equivalent damage force of the following form:

$$\underline{Y}(t) = \sup_{\tau \le t} \left[\left(Y_{d3}^{\alpha} + (\gamma_1 Y_{d1})^{\alpha} + (\gamma_2 Y_{d2})^{\alpha} \right)^{1/\alpha}_{\tau} \right] \tag{5}$$

where γ_1, γ_2 and α are material parameters. In terms of delamination modes, the first term is associated with the first opening mode, and the two others are associated with the second and third modes. Compared to other damage evolution laws, used for example in [5-7], an enhanced coupling model, associated with the parameter α, is proposed. The effect herein is to be able to describe Fracture Mechanics failure loci which are quite general. A damage evolution law is then defined by the choice of a material function W, such that:

$d_3 = d_1 = d_2 = W(\underline{Y})$ if $d < 1$; $d_3 = d_1 = d_2 = 1$ otherwise

A simple case, used for application purposes, is:

$$W(\underline{Y}) = \left[\frac{n}{n+1} \frac{\langle \underline{Y} - Y_o \rangle_+}{Y_c - Y_o} \right]^n \tag{6}$$

where a critical value Y_c and a threshold value Y_o are introduced. High values of n correspond to a brittle interface.

To summarize, the damage evolution law is defined by means of six intrinsic material parameters Y_c, Y_o, γ_1, γ_2, α and n. The threshold Y_o is introduced here in order to expand the possibility of describing both the initiation of a delamination crack and its propagation. As regards the initiation of a delamination crack, the significant parameters are Y_o, n and α. It will be shown hereafter that Y_c, γ_1, γ_2 and α are related to the critical damage forces.

4.3. Identification method for interface propagation parameters

A simple way to identify the propagation parameters is to compare the mechanical dissipation yielded by the two approaches of Damage Mechanics and Linear Elastic Fracture Mechanics. This was performed in [13], and only the results will be presented below. In the case of pure-mode situations, when the critical energy release rate reaches its stabilized value at the propagation denoted by G_c^p, we obtain:

$$G_{cI}^{p} = Y_c \; ; \quad G_{cII}^{p} = \frac{Y_c}{\gamma_1} \; ; \quad G_{cIII}^{p} = \frac{Y_c}{\gamma_2} \tag{8}$$

For a mixed-mode loading situation, a standard LEFM model [14] is simply derived:

$$\left(\frac{G_I}{G_{cI}^{p}}\right)^{\alpha} + \left(\frac{G_{II}}{G_{cII}^{p}}\right)^{\alpha} + \left(\frac{G_{III}}{G_{cIII}^{p}}\right)^{\alpha} = 1 \tag{9}$$

4.4. Extension with delay effects

In order to obtain, in all cases, a consistent model for the description of rupture, a variant of the previous damage model that introduces delay effects [8-13,15,16] is applied. In quasi-static problems, the use of such damage evolution laws implicitly introduces a length scale into the governing equations of the problem and thus avoids the pathological mesh sensitivity for composite structures.

5. FRACTURE MECHANICS TESTS

5.1. Introduction

The aim of this section is to present the classical Fracture Mechanics tests which have been chosen to identify the interface damage model. In a second step, these examples will be predicted with the help of our F.E. code and then compared with experimental results. The tests conducted in this work are the pure-mode I DCB (Double-Cantilever Beam) Test [17], the pure-mode II ENF (End-Notched Flexure) test [18], and two mixed-mode tests: the MMF (Mixed-Mode Flexure) test and the CLS (Cracked-Lap Shear) test [19] (Figure 4). These tests were conducted on an INSTRON testing machine at ambient temperature, and the displacement rate loading was set at 2 mm min^{-1} in the DCB and CLS tests and at 1 mm min^{-1} in the ENF and MMF tests. The F.E. predictions were conducted on HP 735 machines.

The D.C.B test is probably encountered the most often in the literature. In this mode I test, the links between Linear Elastic Fracture Mechanics and Damage allow identifying the Y_c damage model parameter. The E.N.F test is used to obtain the critical energy release rate in mode II. Using both mode I and mode II experimental results, the links between Linear Elastic Fracture Mechanics and Damage allow identifying the γ_1 damage model parameter. The hypothesis ($\gamma_1 = \gamma_2$) is made without any further experimental information on mode III. In the M.M.F test, a mixed-mode critical energy release rate is obtained. In this mixed-mode test,

mode I is dominant. The evolution of the damageable area is refined. Each specimen tested is a $[(+\theta/-\theta)_{4s}/(-\theta/+\theta)_{4s}]$ laminate with $\theta = 0°$, 22.5° or 45°, according to the three kinds of $\pm\theta$ interlaminar interfaces investigated. The stacking sequence is equilibrated and symmetric in each arm of the beam in order to suppress any bending/twisting-membrane coupling effect. Such tests are usually analyzed by means of Linear Elastic Fracture Mechanics (LEFM). Nevertheless, in the case of carbon-epoxy laminates, the main assumptions of LEFM are not always satisfied even in the simple case of a D.C.B. specimen. This is true, in particular, in the case of: non-unidirectional stacking sequences and R-curve-like phenomena. In the former case, inner layer damage mechanisms may be activated; they lead to an apparent energy release rate different from the local interfacial one. In this case, a damage analysis of the layers and interfaces should be performed [11].

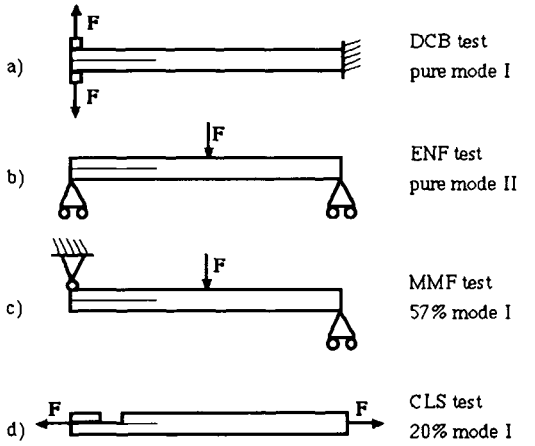

Figure 4. Standard Fracture Mechanics tests.

5.2. Identification of the damageable interface propagation parameters

From the corrected critical energy release rates at propagation (Figure 5) [11] and from the relationships existing between Fracture Mechanics and Damage Mechanics (8), we deduce the values of the critical energies Y_c and the coupling coefficient γ_1. Without any further information on mode III interlaminar fracture, let us recall that we can choose $\gamma_2 = \gamma_1$, which is justified at least for a ±45° interface. The identification results are reported in Table 1. For each kind of interface, the parameter α, which governs the shape of the failure locus in the

mixed-mode (9), is identified in the normalized mode I/mode II plane (Figure 6). It is observed that α is always greater than 1, and we can choose the same parameter α for the two $\pm\theta$ interfaces ($\theta \neq 0°$).

Table 1. Interface model parameters.

Interface	Y_c (N mm^{-1})	γ_1	α
0°/0°	0.113 ± 0.007	0.37 ± 0.15	1.59
±22.5°	0.167 ± 0.013	0.36 ± 0.17	1.12
±45°	0.192 ± 0.014	0.44 ± 0.16	1.19

With the $\pm\theta$ interfaces, the dissipative phenomena inside the layers are not insignificant in particular for the case ($\theta = \pm 45°$), and thus a critical damage force may not be entirely attributed to the delamination process. In fact, by introducing the dissipation inside the layer it is possible to clearly identify the intrinsic damage interface parameters [11]. Let us note that the interface parameters seem to be independent of θ for all $\pm\theta$ interfaces with $\theta \neq 0°$. Let us also note that the (0°/0°) interface appears to be something artificial. However, such an "artificial" interface can be introduced, for example, to describe an initial crack in a thick layer.

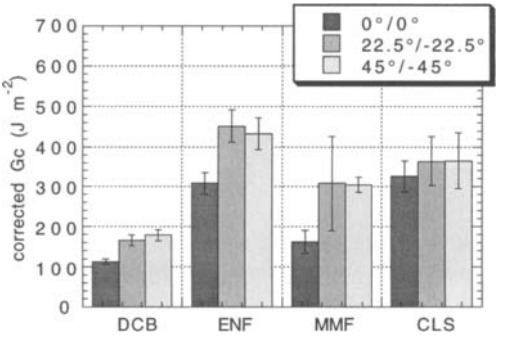

Figure 5. Critical energy release rates at propagation.

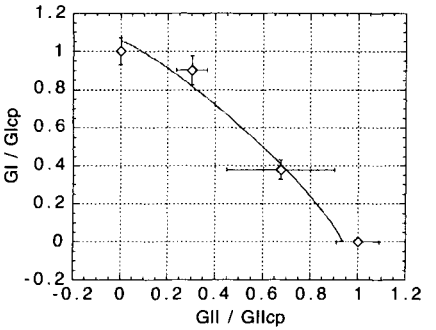

Figure 6. Identification of α for the $\pm 45°$ interface.

5.3. Simulation of classical Fracture Mechanics tests

Tridimensional F.E. predictions are conducted, with the shape of the delaminaton front also being predicted. The tests of crack propagation in interlaminar fracture specimens are usually conducted on beam specimens with an initiated crack at the studied interface. Our specimens are 300 mm long and 20 mm wide. The mean thickness of a single ply is on the order of 0.1 mm, and one element in the thickness is chosen for the prediction. An anti-adhesive film 40 mm long and 25 μm thick is inserted at the mid-plane in order to initiate cracking. From a computational point of view, an interface of zero stiffness rigidity is used, in combination with unilateral contact conditions, in order to model the initial crack (anti-adhesive film) in the F.E. predictions.

The evolution of the damaged area is then refined for all test predictions. Experimental results and finite element predicted values exhibit good correlation (Figures 7-10). In particular, the lengths of the debonding area are found to be close.

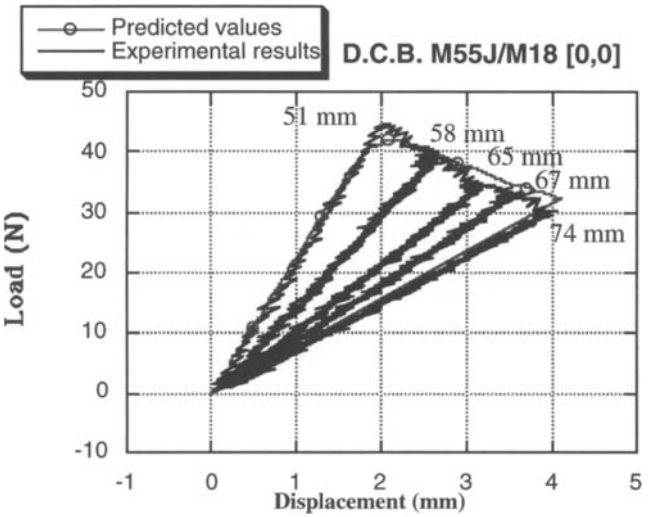

Figure 7. Prediction of a D.C.B. test. Comparison between experimental results and predicted values. The initial crack closure is a= 50 mm. The evolution of the crack length at the end of the test is 23mm.

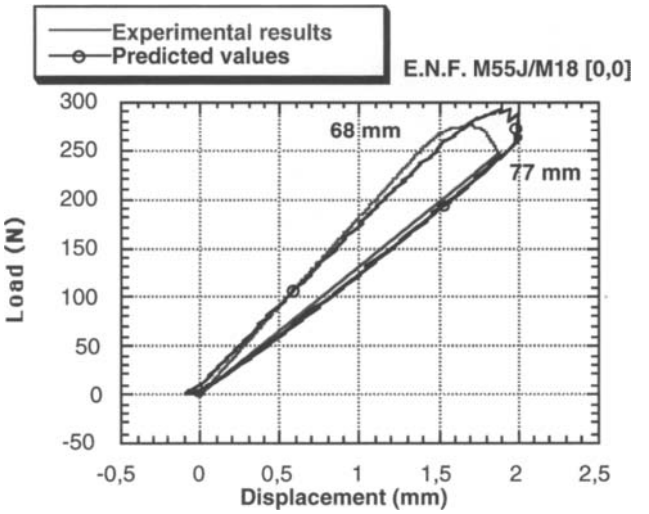

Figure 8. Prediction of an E.N.F. test. Comparison between experimental results and predicted values. The initial crack closure is a=68mm. The evolution of the crack length at the end of the test is 77mm.

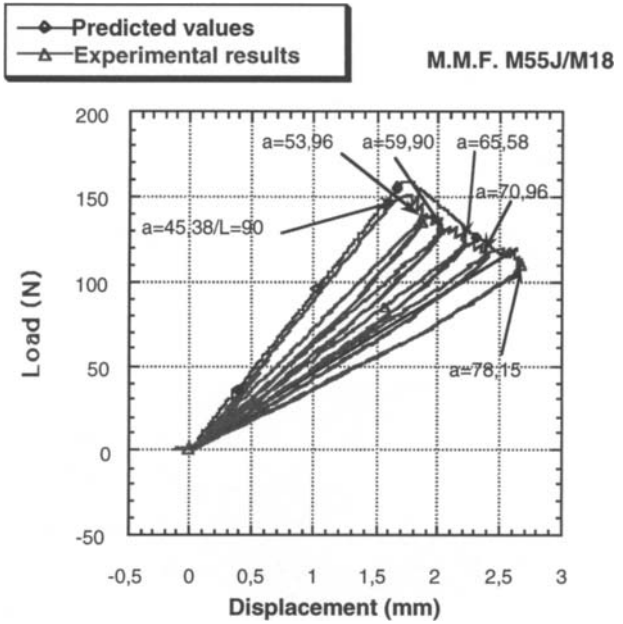

Figure 9. Prediction of an M.M.F. test. Comparison between experimental results and predicted values. The initial crack closure is a=45mm, the crack length at the end of the test is 32.77mm.

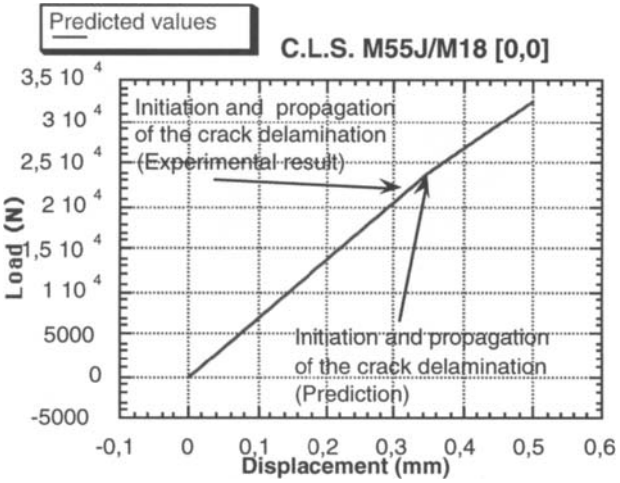

Figure 10. C.L.S. test: comparison of the initiation of the delamination crack between experimental results and predicted values.

After each Fracture Mechanics test, the experimental delamination shape of the test specimen is highlighted by an X-ray photograph. For the unidirectional M55J/M18 material, the X-ray shape is shown in Figure 11 for the D.C.B., E.N.F., M.M.F. and C.L.S. tests. The delamination front is not straight in the width direction of the test specimens. Near the edge, there is curvature of the delamination front in all tests. In the case of the C.L.S. test, this shape is not symmetric. The computed shape of the delamination area is shown for the D.C.B. test in Figure 12. It should be noted that the curvature of the delamination front is greater for tests conducted with the M55J/M18 material with θ angle values other than 0 degrees.

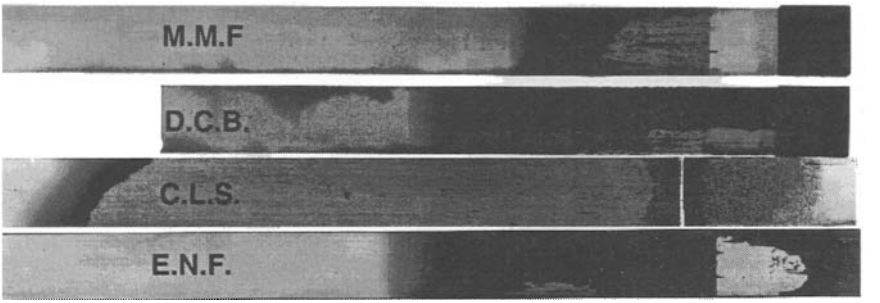

Figure 11. X-ray delamination shape photograph in the unidirectional material case.

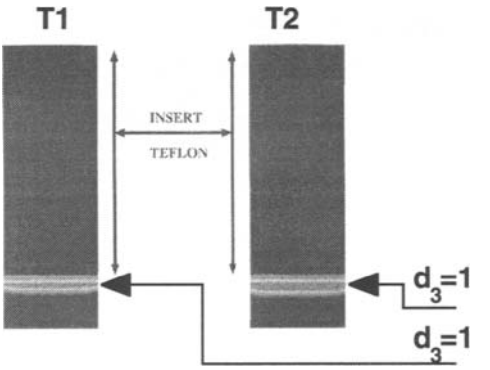

Figure 12. Prediction of the delamination front in the D.C.B. test.

6. INITIATION PREDICTION

The study of the initiation of a delamination crack is often investigated by means of Edge Delamination Tension specimens [20]. In this case, Fracture Mechanics is not well adapted. In addition, delamination, especially at its onset, appears to result from an intricate interaction between inner layer damage mechanisms and the deterioration of the interlaminar interface itself [3]. Under such conditions, it seems adequate to use the previously-defined mesomodel for the layer and the interface.

In order to emphasize the value of the Damage Mechanics of Interface in the prediction of initiation, let us consider the case where damage phenomena are located in both layers and interfaces. An EDT specimen under tension was simulated. In such a case the numerical problem is set in a strip perpendicular to the edge. This type of problem has been studied in a similar way in [6, 21]. The simulations are compared with experimental results in the case of a $[0_3,\pm45_2,90]_s$ M55J/M18 material specimen. Delamination occurs at the mid-plane interface. The values of the longitudinal strain at the onset of delamination are compared. This example shows the necessity of including all the damage mechanisms into the delamination analysis even for quite simple specimens. The edge is straight and the problem to solve can be set up as a generalized plain strain problem in a strip perpendicular to the edge. In the previous test, the delamination starts on the 0°/0° interface and after this initiation point, the load can still increase, with the maximum value of the applied tension load being around three times the initiation load. Without taking the inner layer mechanisms into account in our Finite Element Analysis, the initiation and maximum load coincide. Introducing the inner damage mechanisms (namely, the transverse and shear microcracking), the delamination propagation then becomes stable under increasing tension up to the fiber rupture of the 0° plies [22]. Figure 13 depicts the state of damage before the final failure of the specimen. The comparison between the predicted values and the experimental results is quite encouraging, and the location of the onset of delamination was correctly predicted (Figure 14).

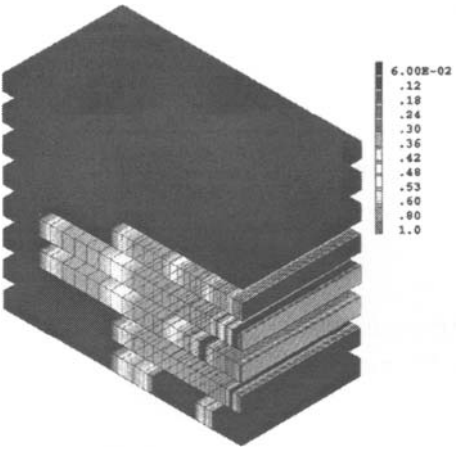

Figure 13. The laminate is a M55J/M18 $[0_3, \pm 45_2, 90]_{sym}$ stacking sequence. The F.E. damage prediction of the quarter-section represents shear failure in the ±45° layers.

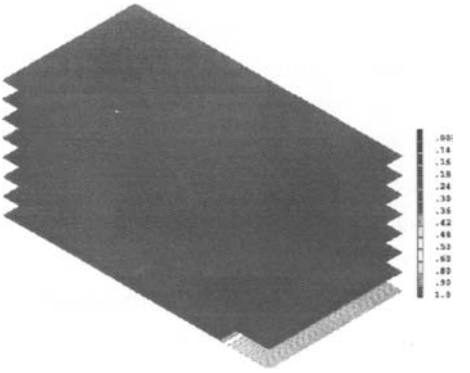

Figure 14. A crack first appears in the central interface (quarter of interface).

7. HOLED PLATE IN TENSION

Let us consider the structural computation example defined in Figure 15. It is a holed plate $[+ 22.5°, -22.5°]_s$ subjected to tension. The loading history is shown in Figure 16. At any point and at any time, the code is able to yield the "intensity" of the various damage mechanisms up until the ultimate fracture. The main damage mechanism herein is delamination, i.e. the deterioration of the (22.5°/-22.5°) interface. Figure 17 shows the value of

the damage variable "d_3" at times T_1 and T_2. The increase in the delaminated area is very significant. The layer's damage mechanisms are weakly excited (Figure 18).

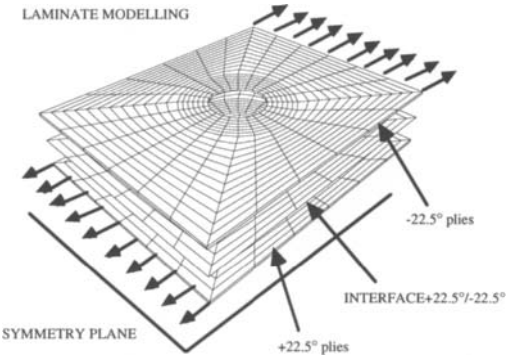

Figure 15. A structural computation example.

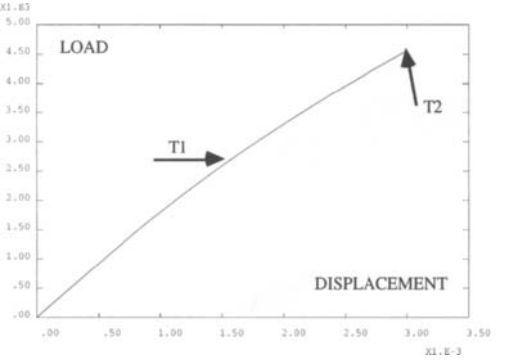

Figure 16. Loading history.

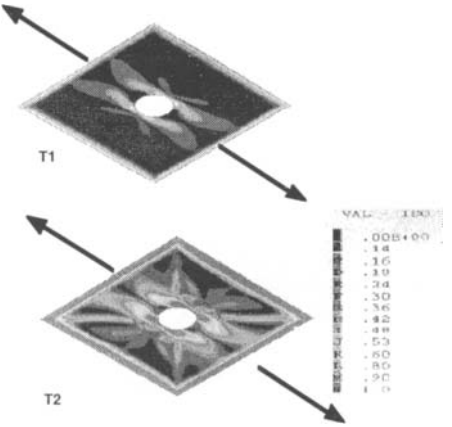

Figure 17. Damage variable d_3 of the (22.5°/-22.5°) interface at times T_1 and T_2.

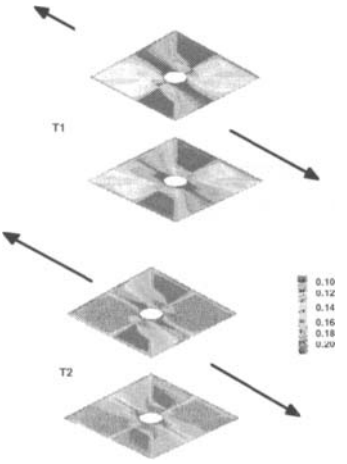

Figure 18. Damage variable d of the layers at times T_1 and T_2.

CONCLUSIONS

A mesomodel of laminate structure has been built and identified for various composites. Resistance to delamination can be characterized by a few material parameters. Comparisons with experimental results proved to be very satisfactory.

However, calculations performed with such a mesomodel lead to very large computational times. A present challenge is to develop a more effective computational strategy and, in particular, to use parallel computers.

REFERENCES

1. A.L. Highsmith, and K.L.Reifsnider, Stiffness reduction mechanism in composite material, In: ASTM-STP 775, Damage in Composite Materials, A.S.T.M., pp.103-117, 1982.
2. R. Talreja, Transverse cracking and stiffness reduction in composite laminates, Journal of Composite Materials, vol.19, pp. 355-375, 1985.
3. Whithney, J.M. Experimental characterization of delamination fracture. In: Interlaminar response of composite materials, Comp.Mat. Series, 5, Pagano, N. J. Ed, 111-239, 1989.
4. P. Ladevèze, Sur la Mécanique de l'Endommagement des composites. In: Comptes rendus des JNC 5, C. Bathias & D. Menkès Eds, Pluralis Publication, Paris, pp. 667-683, 1986.
5. P. Ladevèze, Towards a Fracture Theory, Proceedings of the Third International Conference on Computational Plasticity Part II, D.R.J. Owen, E. Onate, E. Hinton Ed, Pineridge Press, Cambridge U.K., 1992, pp. 1369-1400.
6. Daudeville L.and P. Ladevèze, A Damage Mechanics Tool for Laminate Delamination", Journal of Composite Structures n° 25, 1993, pp. 547-555.
7. P. Ladevèze, A damage computational method for composite structures, J. Computer and Structure, 44 (1/2), pp. 79-87, 1992.
8. Verpeaux P., Charras T. et Millard A. Castem 2000: Une approche moderne du calcul de structures, JM Fouet, P Ladeveze, R Ohayon, 2, 1988, pp. 261-227.
9. P. Ladevèze and E. Le Dantec, Damage modeling of the elementary ply for laminated composites, Composite Science and Technology, 43-3, pp.257-267, 1992.

10. O. Allix, O. and P. Ladevèze, Interlaminar interface modelling for the prediction of laminate delamination, Composite Structures, 22, pp. 235-242, 1992.
11. Allix O., Ladevèze P., Lévêque D., Perret L. (1997) "Identification and validation of an interface damage model for delamination prediction" Computational Plasticity, Eds Owen D.R.J., Oñate E. & Hinton E., Barcelone, pp. 1139-1147.
12. Beer, G., 1985, An isoparametric joint/interface element for finite element analysis, Int.J. for numer. methods eng., 21 , pp. 585-600.
13. O. Allix, A. Corigliano and P. Ladevèze, Damage analysis of interlaminar Fracture specimens, Composite Sructures. 31, 1995, pp. 61-74.
14. Bathias, C. 1995. Une revue des méthodes de caractérisation du délaminage des matériaux composites. Journée AMAC/CSMA *"Délaminage: bilan et perspectives"*, O. Allix & M.L. Benzeggagh Eds, Cachan, may 1995.
15. Albertsen, H., J. Ivens, P. Peters, M. Wevers & I. Verpoest, 1995, Interlaminar fracture toughness of CFRP influenced by fibre surface treatment: Part 1: Experimental results, Comp. Sc. and Tech. 54, pp. 133-145.
16. Ladevèze, P., 1995, A damage computational approach for composites: Basic aspects and micromechanical relations, Computational Mechanics, 17, pp. 142-150, 1995.
17. De Charentenay, F.-X., J.M. Harry, Y.J. Prel, & M.L Benzeggagh, 1984. Characterizing the Effect of Delamination Defect by Mode I Delamination Test. Effect of Defects in Composite Materials, ASTM STP 836, pp. 84-103.
18. Davis P., 1990. Measurement of GIc and GIIc in Carbon/Epoxy Composites, Comp. Sci. & Technol., 39 , pp. 193-205.
19. Russell, A.J. & K.N. Street 1985. Moisture and Temperature Effects on the Mixed-Mode Delamination Fracture of Unidirectional Graphite/Epoxy, Delamination and Debonding of Materials, ASTM STP 876, W.S. Johnson, Eds., Philadelphia, pp. 349-370.
20. T. K. O'Brien, Characterisation of Delamination Onset and Growth in a Composite Laminate. In: Damage in Composite Materials, Reifsnider K.L. Eds., ASTM-STP 775, 140-167, 1982.
21. J. C. Schellekens and R. De Borst, A non-linear finite element approach for the analysis of mode I-free edge delamination in composites, Int. Journal Solids Structures, Vol. 30-9, 1239-53, 1993.
22. Gornet, L., 1996. Simulation des endommagements et de la rupture dans les composites stratifiés, Thesis, Université Pierre et Marie Curie Paris 6/LMT/ENS-Cachan, ISBN 2-11-088-9705.

PART VI

DAMAGE IN POLYMERS AND ELASTOMERS

This Page Intentionally Left Blank

Damage Mechanics in Engineering Materials
G.Z. Voyiadjis, J.-W.W. Ju and J.-L. Chaboche (Editors)
© 1998 Elsevier Science B.V. All rights reserved.

Damaged hyperelastic solid with an induced volume variation. Effect of loading paths

K. Saanouni[a], F. Sidoroff[b] and F. Andrieux[c]

[a]GSM/LASMIS - Université de Technologie de Troyes (UTT), B.P. 2060, 10010 Troyes Cedex, France, e-mail: khemais.saanouni@univ-troyes.fr

[b]LTDS, UMR 5513 du CNRS, Ecole Centrale de Lyon ECL, B.P. 163, 69131 Ecully Cedex, France, e-mail: sidoroff@mecasolb.ec-lyon.fr

[c]LG2mS, UPRESA 6066 du CNRS, Université de Technologie de Compiègne (UTC), B.P. 529, 60205 Compiègne Cedex, France

ABSTRACT

Rubber like materials (hyperelastic or visco-hyperelastic solids) are characterised by large elastic deformations and are usually assumed incompressible. It is however frequently observed that a significant volume change is associated to the damage process, resulting in the so-called damaged induced compressibility. The purpose of this paper is to analyse some implications of this unusual coupling between damage and volume changes in otherwise incompressible materials. Attention will be focused on isotropic hyperelastic behaviour and rate-independent isotropic damage description (one scalar damage variable D).
The constitutive framework, based on a novel constraint condition will be briefly established. Three different models will be presented namely (i) a constrained model developed within the GSM framework (Generalised Standard Materials), (ii) a modified non GSM constrained model with simplified evolution law for damage, (iii) an unconstrained, nearly compressible model ,including the constraint as a limiting case.
Special emphasis will be laid on two specific aspects of these models: (i) coupling of the elastic law with the damage evolution through the Lagrange multiplier q associated to the constraint and which occurs in both the stress tensor and the damage thermodynamic force Y, (ii) An essential difference between stress and strain control which will then be discussed in more detail for the studied models.

1. INTRODUCTION

Elastomers are those rubberlike materials often used in confining industrial environments characterised by: large elastic deformations, non linear-rate dependence, continuous damage mechanisms, ageing, induced volume variation, Mullins effect, rigidification effect at high elongations, etc... A complete review on these physical properties are given in the pioneering reference book by Treloar [1].

1. Modelling as accurately as possible these phenomena is a very important task for the numerical computations of the elastomeric structure components. In the literature the rubber like materials are often treated as incompressible or very nearly so, as can be found in the important work of Ogden summarised in his book [2] and the references given there. The non linear rate dependence is often modelled using the basic hereditary integral formulation [3, 4] or less frequently using the framework of the thermodynamic of irreversible processes with internal state variables and intermediate configuration as proposed first by Sidoroff [5, 6, 7] and used by many others [8-11].

For many black filled elastomeric materials it is observed [12, 13] that the deformation process is often associated with damage growth which in turn induces an important volume variation. This means that the material behaves as incompressible in the beginning of the deformation process and volume changes appears as the damaging deformation increase. This has been modelled first by Ogden [2] in the case of very small volume changes associated with the deformation of rubber-like solids without any reference to the damage process.
Recently the authors [11, 14, 15] proposed a fully three-dimensional finite-strain visco-hyperelastic model accounting for the following important features :

- large hyperelastic deformations,
- rigidification at high extensions i.e. the slope of the force-extension curve begins to rise at high elongations,
- Mullins softening effect,
- isotropic continuum damage,
- non-linear rate effects (viscous effects),
- volume variation induced by the damage growth.

In this work, we limit ourselves to the modelling of the damaged hyperelastic behaviour of elastomeric solids with an induced volume changes. The framework of the thermodynamics of irreversible processes with state variables [16, 17] is used using an Eulerean description. For the sake of simplicity, attention is focused on the isothermal and fully isotropic case with the left Cauchy Green dilatation tensor B_{ij} associated to the Cauchy stress tensor T_{ij} taken as external variables. Isotropic damage is represented by a simple scalar internal variable D in the Chaboche's sense [18] associated to the generalised thermodynamic force Y. The volume variation is supposed to be exclusively due to the damage initiation and growth.
A new non classical constraint condition is proposed to describe the induced compressibility. Three different models are presented namely (i) an internally constrained model (IC Model) within the Generalised Standard Materials (GSM) framework [19], (ii) a modified non GSM constrained model with non associative damage flow, (iii) an unconstrained, weakly or nearly incompressible model (NI Model), which include the IC model as a limiting case.
Special emphasis will be laid on two specific aspects of these models : (i) coupling of the elastic law with the damage evolution through the Lagrange multiplier q associated to the constraint and which occurs in both the stress tensor and the damage thermodynamic force Y, (ii) an essential difference between stress and strain control which will then be discussed in more detail for the 3 mentioned models. In particular it will be shown that a strain-controlled loading path is highly singular and that some amount of stress-control is necessary for a reason-able material description. This will be discussed by establishing the consistency condition and differential constitutive equation under similar loading paths differing only by the control variables.

2. BASIC KINEMATICS AND THERMODYNAMIC BACKGROUND

2.1. Kinematic background

We first introduce some thermodynamic definitions and kinematic results that will be used throughout the paper. Writing the current position of a material point as x_i and the reference position of the same point as X_j, the deformation gradient is :

$$F_{ij} = \frac{\partial x_i}{\partial X_j} \tag{1}$$

then J, the volume change at the point x_i, can be written using the balance of mass as :

$$J = \det F_{ij} = \frac{\rho^0}{\rho} > 0$$

where $\rho^0(x,t)$ and $\rho(x,t)$ are the densities of the material in the initial (point X_j) and current (point x_i) configurations respectively.
Furthermore, the symmetric left Cauchy-Green tensor B_{ij} as a convenient Eulerean strain measure is used :

$$B_{ij} = F_{ik} F_{jk} \quad with \; J = \det F_{ij} = (\det B_{ij})^{1/2} \tag{2}$$

Now, our interest is concerned with hyperelastic materials being initially incompressible i.e. $J(X,t=0)=1$, which motivates splitting the deformation gradient F_{ij} and consequently B_{ij} into a volumic (dilatational) and isochoric (distortional) parts :

$$F_{ij} = (J^{1/3}\delta_{ik})\overline{F}_{kj} \; and \; B_{ij} = (J^{-2/3}\delta_{ik})\overline{B}_{kj} \tag{3}$$

giving $\overline{J} = \det \overline{F}_{ij} = (\det \overline{B}_{ij})^{1/2} = 1$ which ensures the volume preserving of the distortional deformation process.

2.2. Thermodynamic foundation of the models

Following Sidoroff [5-7] the decomposition (3) transforms the state variables (B_{ij}, T_{ij}) to the dilatational state variables (J, T_{ij}^s) and the distortional state variables $(\overline{B}_{ij}, \overline{T}_{ij})$ where T_{ij}^s is the spherical part of the Cauchy stress tensor and $\overline{T}_{ij}$ its classical deviatoric part. The free energy in the initial (undeformed) configuration is taken as a state potential. This is taken as a frame indifferent function of the main arguments $J, \overline{B}_{ij}$ and D in the strain space namely $\rho_0\psi(J,\overline{B}_{ij},D) = W(J,\overline{B}_{ij},D)$. By using the Clausius-Duhem inequality representing the second law of thermodynamics in the current (isothermal) configuration we have :

$$T_{ij}D_{ij} - \rho\dot{\Psi} \geq 0 \qquad or \qquad \tau_{ij}D_{ij} - \dot{W} \geq 0 \tag{4}$$

where use has been mode of the very useful Kirchhoff stress tensor $\tau_{ij} = J\,T_{ij}$. Following the GSM theory in the case of rate independent flow, a damage criterion, indifferently in stain or in stress spaces, is introduced by supposing that at any time of loading history the damage surface is given by :

$$f(Y;D) \leq 0 \tag{5}$$

An unloading, neutral loading or loading from a damage state shall be added to the criterion (5) according to the standard time independent flow theory. Note that in some situations the GSM frame appears as very restrictive. In that case a flow potential is introduced in the same space, namely $F(Y;D)$ so that the consistency condition still given by $\dot{f}(Y;D)=0$ while the evolution equation is obtained from the potential $F(Y;D)$ by using the generalised normality rule. This defined the so-called non associative flow theory.

3. THE INTERNALLY CONSTRAINED MODEL (MODEL IC)

This model is based on a non-classical constraint condition which impose some internal constraint in both the deformation and the damage. This can be made using the straight forward general treatment of the internally constrained material as can be found in Truesdell and Noll [20].
The state potential is taken as purely distortional with damage effect :

$$W(B_{ij}, D) = (1-D)W_0(\overline{B}_{ij}) \tag{6}$$

Using (6) the basic inequality writes :

$$\left[\tau_{ij} - 2(1-D)dev\left(\overline{B}_{ik}\frac{\partial W_0(\overline{B}_{ij})}{\partial \overline{B}_{kj}}\right)\right]D_{ij} + W_0(\overline{B}_{ij})\dot{D} \geq 0 \tag{7}$$

The motion of the body is now required to satisfy the following internal constraint :

$$J - g(D) = 0 \text{ or equivalent ly } \det F_{ij} - g(D) = 0 \tag{8}$$

where $g(D)$ is a differentiable, positive and increasing scalar function of the damage variable D with $g(D=0) = 1$ for the model NI. Note that when $D=0$ (8) reduced to the classical incompressibility condition presented in [20].
The time derivative of (8) gives :

$$JD_{ij}\delta_{ij} - \frac{\partial g(D)}{\partial D}\dot{D} = 0 \tag{9}$$

By combining (7) and (9) and using the Lagrange multiplier q one can write :

$$\left[\tau_{ij} - qJ\delta_{ij} - 2(1-D)dev\left(\overline{B}_{ik}\frac{\partial W_0(\overline{B}_{ij})}{\partial \overline{B}_{kj}}\right)\right]D_{ij} + \left(q\frac{\partial g(D)}{\partial D} + W_0(\overline{B}_{ij})\right)\dot{D} \geq 0 \tag{10}$$

which lead to the following state laws :

$$\tau_{ij} = \tau^{s}_{ij} + \tau^{D}_{ij} \quad \tau^{s}_{ij} = qJ\delta_{ij}$$
$$\tau^{D}_{ij} = 2(1-D)\mathrm{dev}\left(B_{ik} \frac{\partial W_0(B_{ij})}{\partial B_{kj}} \right) \tag{11}$$

$$Y = Y^{s} + Y^{D} \quad Y^{s} = q \frac{\partial g}{\partial D}$$
$$Y^{D} = W_0(B_{ij}) \tag{12}$$

and $$\dot{Y D} \geq 0 \tag{13}$$

Note that both the generalised thermodynamic forces τ_{ij} and Y are determined by the motion only within an arbitrary hydrostatic pressure proportional to q. These represent a reaction forces produced by the constraint (8) imposed on both : the deformation and the damage. Moreover when there is no damage ($D=0$) the state relations (11, 12) becomes those of a classical incompressible hyperelastic body defined by the free energy W_0.
Now to derive the damage evolution law for the model IC, two different cases should be examined :

MODEL IC1
In this case the GSM frame is used with the damage criterion, given by :

$$f(Y;D) = Y - Q(D) \tag{14}$$

with $Q(D)$ being a differentiable positive and increasing function of D, representing the size of the damage surface in the Y space. Following the standard normality argument the damage evolution (complementary law) is given by :

$$\dot{D} = \frac{\partial D}{\partial t} = \dot{\delta} \frac{\partial f}{\partial Y} \tag{15}$$

where $\dot{\delta}$ is the damage « multiplier » given by the consistency condition $\dot{f} = 0$:

$$\frac{\partial f}{\partial Y}\left(\frac{\partial Y}{\partial B_{ij}} \dot{B}_{ij} + \frac{\partial Y}{\partial q} \dot{q} + \frac{\partial Y}{\partial D} \frac{\partial f}{\partial Y} \dot{\delta} \right) + \frac{\partial f}{\partial D} \frac{\partial f}{\partial Y} \dot{\delta} = 0 \tag{16}$$

It is clear that this equation introduces an unusual coupling between the damage multiplier $\dot{\delta}$ and the time derivative $\dot{q}$ of the Lagrange multiplier q which is undetermined at this stage. Hence to use this model one should determine the explicit expression of q for each loading path by using some specific conditions depending on the type of the applied loading path. In fact two cases can be observed :

The first one correspond to those loading paths where the stress state is controlled and the strain is left enough freedom to satisfy the internal constraint (eq. 8). In those cases the multiplier q is completely determined by given condition imposed on some stress components and lead to q function of D and $\overline{B}_{ij}$ (i.e. $q(D,\overline{B}_{ij})$). By using (16) and after some calculations, one can obtain :

$$\dot{D} = \begin{cases} \dfrac{1}{H}\left[\zeta_{ij} D_{ij}\right] & \text{if } f = 0 \text{ and } \zeta_{ij} D_{ij} > 0 \\ 0 & \text{elsewhere} \end{cases} \tag{17}$$

$$\zeta_{ij} = 2dev\left[\overline{B}_{ik}\frac{\partial W_0(\overline{B}_{ij})}{\partial \overline{B}_{kj}} + \frac{\partial g}{\partial D}\overline{B}_{ik}\frac{\partial q}{\partial \overline{B}_{kj}}\right] \tag{18}$$

$$H = \frac{\partial Q}{\partial D} - \frac{\partial g}{\partial D}\frac{\partial q}{\partial D} - \frac{\partial^2 g}{\partial D^2} q > 0 \tag{19}$$

The main basic difficulty in this case comes from the definition of the stress control at finite strain which is not an easy task in the general case.
The second case correspond to the loading path where the strain (or the transformation gradient F_{ij}) is controlled. In general this case is highly singular in the sense that the damage evolution is completely controlled by the internal constraint i.e. by the kinematics of the motion (eq. 8) and no longer by the flow condition (eq. 14). The Lagrange multiplier is then determined by the loading condition $f(Y;D) = 0$ using both (14) and (11, 12).

$$q(D,\overline{B}_{ij}) = \frac{Q(D) - W_0(\overline{B}_{ij})}{\dfrac{\partial g(D)}{\partial D}} \tag{20}$$

MODEL IC2

To avoid these problems related to the coupling between the multipliers $\dot{\delta}$ and q, an approximate thermodynamic approach is used, namely the non associative flow theory. This leads to using two functionals :

- The damage criterion depending only on the deviatoric part Y^D of Y. This means that we suppose that the damage mechanism is associated with maximum distortional energy as in Simo [8].
  Hence the damage criterion writes :

$$f(Y^D;D) = Y^D - Q(D) \tag{21}$$

- The damage potential taken similar to eq. (14) and depends on the overall Y:

$$F(Y,D) = Y - Q(D) \tag{22}$$

so that

$$\dot{D} = \dot{\delta}\frac{\partial F}{\partial Y} = \dot{\delta} \tag{23}$$

and $\dot{D}$ is equal zero elsewhere. The consistency condition is now simplified because only Y^D is used in the damage criterion and we get :

$$\dot{\delta} = \begin{cases} \dfrac{1}{H}\zeta_{ij}D_{ij} & \text{if } f = 0 \text{ and } \zeta_{ij}D_{ij} > 0 \\ 0 & \textit{elsewhere} \end{cases} \tag{24}$$

$$\zeta_{ij} = 2dev\left(\overline{B}_{ik}\frac{\partial Y}{\partial B_{kj}}\right) \tag{25}$$

$$H = \frac{\partial Q}{\partial D} > 0 \tag{26}$$

This thermodynamically approximated model is very helpful when there is no special condition to determine explicitly the constraint multiplier q. Hence it is particularly suitable for implementation in some general purpose finite element code.

4. THE NEARLY INCOMPRESSIBLE MODEL (MODEL NI)

In this model the state potential with damage effect is taken under the following form :

$$W(J, \overline{B}_{ij}, D) = K\varphi(\tilde{J}) + (1-D)W_0(\overline{B}_{ij}) \tag{27}$$

The term $\varphi(\tilde{J})$ is the spherical part of the potential (volumetric behaviour) with :

$$\tilde{J} = \frac{J}{g(D)} \tag{28}$$

and $g(D)$ is the same function used in (8). K is the compressibility modulus. The term $W_0(\overline{B}_{ij})$ represents the distortional part of the potential (for the undamaged material) affected by the reduction factor (1-D) due to damage effect [8, 18, 21].

Using eq. (27) and (28), the basic thermodynamic inequality (4) becomes :

$$\left[\tau_{ij} - K\tilde{J}\frac{\partial\varphi(\tilde{J})}{\partial\tilde{J}}\delta_{ij} - 2(1-D)dev\left(\overline{B}_{ik}\frac{\partial W_0(\overline{B}_{ij})}{\partial\overline{B}_{kj}}\right)\right]D_{ij} + \left(W_0(\overline{B}_{ij}) + K\frac{J}{g(D)}\frac{\partial g(D)}{\partial D}\frac{\partial\varphi(\tilde{J})}{\partial\tilde{J}}\right)\dot{D} \geq 0 \tag{29}$$

which lead to the following thermodynamic forces (τ_{ij}, Y) associated to B_{ij} and D called the state laws :

$$\tau_{ij} = \tau_{ij}^{S} + \tau_{ij}^{D} \qquad \tau_{ij}^{s} = K\tilde{J}\frac{\partial\varphi(\tilde{J})}{\partial\tilde{J}}\delta_{ij}$$

$$\tau_{ij}^{D} = 2(1-D)dev\left(\overline{B}_{ik}\frac{\partial W_0(\overline{B}_{ij})}{\partial\overline{B}_{kj}}\right) \tag{30}$$

$$Y = Y^{s} + Y^{D} \qquad Y^{s} = K\tilde{J}\frac{g'}{g(D)}\frac{\partial\varphi(\tilde{J})}{\partial\tilde{J}} \tag{31}$$

$$Y^{D} = W_0(\overline{B}_{ij})$$

and :

$$\dot{Y}\dot{D} \geq 0 \tag{32}$$

Where g' denotes the derivative of g with respect to D i.e. $g' = \frac{\partial g}{\partial D}$, we note that both T_{ij} and Y are decomposed into two parts respectively related to the spherical and the distorsional behavior. The damage evolution equation is than obtained within the GSM framework using the same criterion (14) giving the relation (15) where the damage multiplier is now given by :

$$\dot{\delta} = \begin{cases} \frac{1}{H}\zeta_{ij}D_{ij} & \text{if } f = 0 \text{ and } \zeta_{ij}D_{ij} > 0 \\ 0 & \text{otherwise} \end{cases} \tag{33}$$

where H>0 is the tangent « damage » modulus defined by :

$$H = Q'(D) + K\tilde{J}\left[\tilde{J}\left(\frac{g'(D)}{g(D)}\right)^2\frac{\partial^2\varphi(\tilde{J})}{\partial\tilde{J}^2} + \frac{\partial\varphi(\tilde{J})}{\partial\tilde{J}}\left(2\left(\frac{g'(D)}{g(D)}\right)^2 - \frac{g''(D)}{g(D)}\right)\right] \tag{34}$$

and the second order tensor ζ_{ij} is given by :

$$\zeta_{ij} = 2dev\left(\overline{B}_{ik}\frac{\partial W_0(\overline{B}_{ij})}{\partial\overline{B}_{kj}}\right) + K\tilde{J}\frac{g'(D)}{g(D)}\left(\frac{\partial\varphi(\tilde{J})}{\partial\tilde{J}} + \tilde{J}\frac{\partial^2\varphi(\tilde{J})}{\partial\tilde{J}^2}\right)\delta_{ij} \tag{35}$$

To completely determine the model NC, it remains to specify the functions $W_0(\overline{B}_{ij})$, $\varphi(\tilde{J})$, $g(D)$ *and* $Q(D)$. Such a determination should be made on the basis of phenomenological approach based on available experimental data base and will be discussed in 5.

The comparison of (11/12) and (30/31) shows that the difference between the model IC and the model NI is concerned only with the spherical parts : τ^s_{ij} of τ_{ij} and Y^s of Y.

5. APPLICATION AND DISCUSSION

5.1. General considerations

To completely determine the proposed models it remains to specify the state potentials W_0 and φ and the functions g and Q. This should be made on the basis of available experimental data. Here for definiteness, the state potential is chosen as a Money-Rivlin form and for the other functions we shall adopt a very simple forms ($\overline{I}_1$ and $\overline{I}_2$ being the first and second elementary invariants of $\overline{B}_{ij}$) :

$$
\begin{aligned}
W_0 &= \frac{G}{2}\left[\left(\frac{1}{2}+\beta\right)(I_1-3)+\left(\frac{1}{2}-\beta\right)(I_2-3)\right] \\
\varphi &= \frac{1}{2}(J-1)^2 \\
g(D) &= 1+\gamma D \\
Q(D) &= Q_0{}^n D + D_0
\end{aligned}
\tag{36}
$$

where G, β, γ, Q_0, D_0 and n are five material constants under isothermal condition for the three models. G and β characterise the distortional hyperelastic behaviour, γ represents the maximum amount (when $D=1$) of the volume variation and Q_0, D_0 and n characterise the size and the non linear evolution of the damage surface.

Now the missing link between the model NI and the model IC are discussed. First it is easy to show that the model NI transforms on the model IC when compressibility modulus K goes to the infinity. In fact when $K \to \infty$ the effective volume variation $\tilde{J} \to 1$ and (30a) and (31a) of the model NI becomes :

$$
\tau^s_{ij} = q\delta_{ij} \text{ and } Y_s = q\frac{\partial g}{\partial D} \tag{37}
$$

which are identical to τ^s_{ij} and Y_s of the model IC given by (11a) and (12a). Naturally, $KJ\dfrac{\partial \varphi}{\partial J} = q$ is an arbitrary hydrostatic pressure to be determined by given conditions on some components of stress tensor.

Now from (36b), the quantity $\tilde{J}\dfrac{\partial\varphi}{\partial\tilde{J}}$ can be approximated by $\tilde{J}-1$ for the small variations of $\tilde{J}$. Accordingly the eq. (34) and (35) of the model NI becomes :

$$H=\frac{\partial Q}{\partial D}+K\left(\frac{1}{g}\frac{\partial g}{\partial D}\right)^2\tilde{J}\left(3\tilde{J}-2\right)$$
$$\zeta_{ij}=2dev\left(\overline{B}_{ij}\frac{\partial W_0}{\partial\overline{B}_{ij}}\right)+K\frac{1}{g}\frac{\partial g}{\partial D}(2\tilde{J}-1)\partial_{ij} \tag{38}$$

and when $K\rightarrow+\infty$ then $\tilde{J}\rightarrow 1$ and one can easily shown that the ratio $\dfrac{\zeta_{ij}D_{ij}}{H}$ transforms to the following relation :

$$\dot{D}\approx\frac{J}{\dfrac{\partial g}{\partial D}}D_{ij}\delta_{ij} \tag{39}$$

which is fully consistent with the time derivative (eq. 9) of the internal constraint (eq. 8).
These results give the proof that the model NI is fully compatible with the model IC when K approaches the infinity. In what follows this can be shown numerically for different simple loading paths under both stress and strain controlled conditions.

5.2. Stress controlled path. The uniaxial tension case

The simplest stress controlled loading path is the uniaxial tension which is defined by :

$$F_{ij}=\begin{bmatrix}\lambda & 0 & 0\\ 0 & \dfrac{J}{\lambda} & 0\\ 0 & 0 & \dfrac{J}{\lambda}\end{bmatrix}\qquad\text{and}\qquad\tau_{ij}=\begin{bmatrix}\tau_{11} & 0 & 0\\ 0 & 0 & 0\\ 0 & 0 & 0\end{bmatrix} \tag{40}$$

The tensor $\overline{B}_{ij}$ is then given by :

$$B_{ij}=\begin{bmatrix}\lambda^{2\,2} & 0 & 0\\ 0 & \dfrac{1}{\lambda} & 0\\ 0 & 0 & \dfrac{1}{\lambda}\end{bmatrix}\qquad\text{with}\quad\lambda=J^{-1/3}\lambda \tag{41}$$

The Eulerean deformation rate tensor is given by :

$$D_{ij} = \begin{bmatrix} \dfrac{\dot{\lambda}}{\lambda} & 0 & 0 \\ 0 & \dfrac{1}{2}\left(\dfrac{\dot{J}}{J} - \dfrac{\dot{\lambda}}{\lambda}\right) & 0 \\ 0 & 0 & \dfrac{1}{2}\left(\dfrac{\dot{J}}{J} - \dfrac{\dot{\lambda}}{\lambda}\right) \end{bmatrix} \tag{42}$$

so the deviatoric parts of $\overline{B}_{ij}$ and its inverse are :

$$\overline{B}_{ij}^{D} = \frac{1}{3}\left(\overline{\lambda}^2 - \frac{1}{\overline{\lambda}}\right) \begin{bmatrix} 2 & 0 & 0 \\ 0 & -1 & 0 \\ 0 & 0 & -1 \end{bmatrix} \tag{43a}$$

$$\left(\overline{B}_{ij}^{-1}\right)^{D} = \frac{1}{3}\left(\overline{\lambda} - \frac{1}{\overline{\lambda}^2}\right) \begin{bmatrix} -2 & 0 & 0 \\ 0 & 1 & 0 \\ 0 & 0 & 1 \end{bmatrix} \tag{43b}$$

Now the state and evolution equations of the models NI and IC will be written in this particular uniaxial stress controlled path, using the constitutive functionals given by (36).
For the model IC, the state laws (11, 12) writes :

$$\tau_{ij} = qJ\delta_{ij} + G(1-D)\left[\left(\frac{1}{2}+\beta\right)\overline{B}_{ij}^{D} - \left(\frac{1}{2}-\beta\right)\left(\overline{B}_{ij}^{-1}\right)^{D}\right] \tag{44}$$

$$Y = qg' + G\left[\left(\frac{1}{2}+\beta\right)(\overline{I}_1 - 3) + \left(\frac{1}{2}-\beta\right)(\overline{I}_2 - 3)\right] \tag{45}$$

The first component of the stress tensor is given by :

$$\tau_{11} = qJ + \frac{2}{3}(1-D)\tau(\overline{\lambda}) \tag{46}$$

where :

$$\tau(\overline{\lambda}) = G\left[\left(\frac{1}{2}+\beta\right)\left(\overline{\lambda}^2 - \frac{1}{\overline{\lambda}}\right) + \left(\frac{1}{2}-\beta\right)\left(\overline{\lambda} - \frac{1}{\overline{\lambda}^2}\right)\right] \tag{47}$$

The multiplier q is determined by the condition $\tau_{22} = 0$ to get :

$$q = \frac{1}{3}(1-D)\frac{\tau(\bar{\lambda})}{J} \tag{48}$$

For the damage evolution equation in the case of the first flow condition (eq. 14), the consistency condition writes :

$$\dot{f} = \frac{\tau_{ij}D_{ij}}{1-D} + \frac{\partial m(D)}{\partial D}\tau(\bar{\lambda})\dot{D} + m(D)\frac{\partial \tau(\bar{\lambda})}{\partial \bar{\lambda}}\dot{\bar{\lambda}} - \frac{\partial Q}{\partial D}\dot{D} = 0 \tag{49}$$

where :

$$m(D) = \frac{1}{3}(1-D)\frac{g'(D)}{g(D)} \tag{50}$$

which allows the determination of the damage evolution in the case of the associative model (i.e. model IC1) :

$$\dot{D} = \frac{1}{H}\left\langle \zeta \dot{\bar{\lambda}} \right\rangle \tag{51}$$

with :

$$\begin{cases} \zeta = \dfrac{\tau(\bar{\lambda})}{\bar{\lambda}} + m(D)\dfrac{\partial \bar{\tau}}{\partial \bar{\lambda}} \\ H = \dfrac{\partial Q}{\partial D} - \dfrac{\partial m}{\partial D}\tau(\bar{\lambda}) > 0 \end{cases} \tag{52}$$

For the non associative model (i.e. model IC2) defined by the criteria (21) and (22), it is very easy to show that the equation (52) reduces to :

$$\begin{cases} \zeta = \dfrac{\tau(\bar{\lambda})}{\bar{\lambda}} \\ H = \dfrac{\partial Q}{\partial D} \end{cases} \tag{53}$$

This indicates that the thermodynamic approximation taken in (21) leads to neglecting the second terms of the RHS of the equation (52), which comes from the spherical part Y^s of the force Y. The lose of these terms has a small influence on $\dot{D}$ so that (53) represents a good approximation of (52) as shown numerically in [11].

As a conclusion, the main equations of the model IC in the case of uniaxial stress controlled path are :

$$
\begin{aligned}
&\tau_{11} = (1-D)\tau(\lambda) \qquad \text{or} \qquad \sigma = \frac{\tau_{11}}{J} \qquad \text{or} \qquad \Pi = \frac{\tau_{11}}{\lambda} \\
&\lambda = J^{-1/3}\lambda \\
&\tau(\lambda) = G\left[\left(\frac{1}{2}+\beta\right)\left(\lambda^2 - \frac{1}{\lambda}\right)+\left(\frac{1}{2}-\beta\right)\left(\lambda - \frac{1}{\lambda^2}\right)\right] \\
&J = g(D) = 1+\gamma D \\
&\dot{D} = \frac{1}{H}\left\langle \zeta(\lambda)\dot{\lambda} \right\rangle \\
&\zeta(\lambda) = \frac{\tau(\lambda)}{\lambda} + m(D)\frac{\partial \tau(\lambda)}{\partial \lambda} \quad \text{and} \quad H = \frac{\partial Q}{\partial D} - \frac{\partial m}{\partial D}\tau(\lambda) \quad \text{for the associative model} \\
&\zeta(\lambda) = \frac{\tau(\lambda)}{\lambda} \quad \text{and} \quad H = \frac{\partial Q}{\partial D} \quad \text{for the non associative model}
\end{aligned}
\tag{54}
$$

where σ is the first component of the Cauchy stress tensor T_{ij} and Π is the first component of the first Piola-Kirchhoff stress tensor.

The model NI is now examined. The main difference with the model IC comes from the spherical parts Y^s and τ^s_{ij} which writes :

$$\tau^s_{ij} = K\tilde{J}\left(\tilde{J}-1\right)\delta_{ij} = q\delta_{ij} \tag{55}$$

$$Y^s = K\tilde{J}\left(\tilde{J}-1\right)\frac{g'}{g} = \frac{g'}{g}\tau^s_{11} \tag{56}$$

The deviatoric parts τ^s_{ij} and Y^D being unchanged compared to the model IC. As discussed in §5.1., the use of the quantity $q = K\tilde{J}\left(\tilde{J}-1\right)$ as a Lagrange multiplier allows to apply the same treatment as for the model IC. Particularly q is determined by the condition $\tau_{22} = 0$:

$$q = \frac{1}{3}(1-D)\tau(\bar{\lambda}) \tag{57}$$

which gives after assuming a small variation of $\tilde{J}$:

$$\tilde{J} = 1 + \frac{(1-D)}{3K}\tau(\bar{\lambda}) \tag{58}$$

The consistency condition is similar to the model IC with the same definition of the function *m(D)*. Hence to main equations of the model NI in this uniaxial stress case are :

$$
\begin{aligned}
&\tau_{11} = (1-D)\tau(\lambda) \quad \text{or} \quad \sigma = \frac{\tau_{11}}{J} \quad \text{or} \quad \Pi = \frac{\tau_{11}}{\lambda} \\
&\lambda = J^{-1/3}\lambda \\
&\tau(\lambda) = G\left[\left(\frac{1}{2}+\beta\right)\left(\lambda^2 - \frac{1}{\lambda}\right)+\left(\frac{1}{2}-\beta\right)\left(\lambda - \frac{1}{\lambda^2}\right)\right] \\
&J = g(D)\mathfrak{J} \qquad \text{with} \quad \mathfrak{J} = 1 + \frac{(1-D)}{3K}\tau(\lambda) \\
&\dot{D} = \frac{1}{H}\left\langle \zeta_{(\lambda)}\dot{\lambda} \right\rangle \\
&\zeta(\lambda) = \frac{\tau(\lambda)}{\lambda} + m(D)\frac{\partial \tau}{\partial \lambda} \\
&H = \frac{\partial Q}{\partial D} - \frac{\partial m}{\partial D}\tau(\lambda)
\end{aligned}
\tag{59}
$$

The only one difference between the models NI and IC comes from the equation governing the volume variation *J*.

The figures 1.a and 1.b show the comparison of the model NI with the compressibility modulus $K=1$, *10* and 100 MPa, and the model IC using the following material constants : G = 1MPa, $Q_0 = 2.5$, $D_0 = 10^{-4}$, $\beta = 0$, $n = 2$. These figures represent the variation of the first Kirschhoff stress τ *and* the damage D versus the elongation λ. It is clear that for K sufficiently high (here K=100), the model NI gives exactly the same results as the model IC. However when K is very low (here K=1 MPa) the results of the model NI are quite different from those given by the model IC as shown theoretically in §5.1. The figure 2 shows the variation of J and the function $g(D)$ versus λ for the three values of K. One can notice that for the low value of K the gap between g and J is very high. However when K grows the function $g(D)$ goes to J indicating that the model NI becomes indentical to the model IC.

Finally one can conclude that for this stress controlled loading path the proposed internally constrained model (model IC) gives results fully compatible with the nearly incompressible model when the compressibility modulus goes to the infinity.

5.3. Strain controlled path

The typical simplest strain controlled loading path is the simple shear. However to avoid some kinematic difficulties resulting from the rotation tensor a simple strain controlled loading path similar to the uniaxial tension is introduced. This path called the isochoric extension is defined by :

$$F_{ij} = \begin{bmatrix} \lambda & 0 & 0 \\ 0 & \frac{1}{\sqrt{\lambda}} & 0 \\ 0 & 0 & \frac{1}{\sqrt{\lambda}} \end{bmatrix} \quad J = \det F_{ij} = 1 \text{ and } \quad \tau_{ij} = \begin{bmatrix} \tau_{11} & 0 & 0 \\ 0 & \tau_{22} & 0 \\ 0 & 0 & \tau_{22} \end{bmatrix} \tag{60}$$

The other characteristic variables are :

$$B_{ij} = B_{ij} = \begin{bmatrix} \lambda^2 & 0 & 0 \\ 0 & \frac{1}{\lambda} & 0 \\ 0 & 0 & \frac{1}{\lambda} \end{bmatrix}, \quad D_{ij} = \frac{1}{2}\frac{\dot{\lambda}}{\lambda}\begin{bmatrix} 2 & 0 & 0 \\ 0 & -1 & 0 \\ 0 & 0 & -1 \end{bmatrix}$$

$$B_{ij}{}^{D} = \frac{1}{3}\left(\lambda^2 - \frac{1}{\lambda}\right)\begin{bmatrix} 2 & 0 & 0 \\ 0 & -1 & 0 \\ 0 & 0 & -1 \end{bmatrix}, \quad \left(B_{ij}^{-1}\right)^{D} = \frac{1}{3}\left(\lambda - \frac{1}{\lambda^2}\right)\begin{bmatrix} -2 & 0 & 0 \\ 0 & 1 & 0 \\ 0 & 0 & 1 \end{bmatrix} \tag{61}$$

For the model IC the use of equations (11, 12) gives the non zero components of the stress tensor :

$$\begin{cases} \tau_{11} = q + \frac{2}{3}(1-D)\tau(\lambda) \\ \tau_{22} = q - \frac{1}{3}(1-D)\tau(\lambda) \end{cases} \tag{62}$$

and the damage force :

$$Y = qg' + Y^D = qg' + W_0\left(\overline{B}_{ij}\right) \tag{63}$$

where Y^D being given by the second term of the RHS of (45), while $\tau(\lambda)$ is given by (47) where $\overline{\lambda}$ is replaced by λ.

This model leaves undetermined the constraint multiplier q. But the isochory of the motion transforms the constraint given by (8) to :

$$1 - g(D) = 0 \ \forall \ D \tag{64}$$

This means that the damage evolution is so that $g(D)=1$ which indicates that $D=0$. Hence the model IC excludes the damage evolution for this isochoric loading path. The multiplier q can be determined using the loading conditions $f=0$ (see eq. 14).

$$qg'+W_0(\overline{B}_{ij})-Q_0=0 \tag{65a}$$

which gives :

$$q=-\frac{1}{g'}\left[W_0(\overline{B}_{ij})-Q_0\right]\leq 0 \tag{65b}$$

where $Q_0=Q(D=0)$ is a constant representing the initial radius of the damage surface in the strain space. Finally the equations of the model IC in this case are :

$$\begin{aligned}
&\tau_{11}=-\frac{1}{g'}\left[W_0(\overline{B}_{ij})-Q_0\right]+\frac{2}{3}(1-D)\tau[\lambda]\\
&\tau_{22}=-\frac{1}{g'}\left[W_0(\overline{B}_{ij})-Q_0\right]+\frac{1}{3}(1-D)\tau[\lambda]\\
&D=0 \qquad \text{and} \qquad J=1
\end{aligned} \tag{66}$$

Note in this case the presence of an increasing compressive terms in both τ_{11} and τ_{22}. These compressive stresses insure the isochory of the motion and make the damage growth impossible. For the model NI and using the small variation of $\tilde{J}$, the non zero components of stress as well as the damage growth obtained from the consistency condition are :

$$\begin{cases}
\tau_{11}=K(\tilde{J}-1)+\frac{2}{3}(1-D)\tau(\lambda)\\
\tau_{22}=K(\tilde{J}-1)+\frac{1}{3}(1-D)\tau(\lambda)
\end{cases} \tag{67}$$

$$Y=K(\tilde{J}-1)\frac{g'}{g}+W_0(B_{ij}) \tag{68}$$

$$\dot{D}=\frac{1}{H}\left\langle\frac{\tau(\lambda)}{\lambda}\dot{\lambda}\right\rangle \tag{69}$$

$$H=\frac{\partial Q}{\partial D}-K\left[g''\left(\frac{1}{g}-1\right)-\left(\frac{g'}{g}\right)^2\right] \tag{70}$$

It is clear from (69) and (67) that if $K\rightarrow+\infty$ then $\dot{D}\rightarrow 0$ which makes the damage growth impossible as for the model IC. Hence this gives the proof that also the model NI behaves like the model IC when K increases.

The figures 3a, 3b, 3c and 3d illustrate this result using the same material constants as in §5.2. The figures 3a and 3b show the behaviour of the stress components τ_{11} and τ_{22} for the model IC and the model NI with K=1, 10 and 100 MPa. One can observe that for the low values of K

damage grows inducing the volume variation, while for the high values of K (here K=100 MPa) the damage evolution is zero and consequently J is equal 1. This result is fully compatible with the model IC which gives directly D=0 and J=1. This is clearly shown in figures 3c and 3d where the damage still equal to zero when K=100 giving a constant value of $\tilde{J} = 1$.

6. CONCLUSION

A new constraint has been introduced to account for the volume change resulting from damage in an otherwise incompressible material. This constraint introduces some unusual coupling effect between the hydrostatic pressure and the thermodynamic force associated to damage, these two variables being coupled through the Lagrange multiplier associated to the constaint condition. In order to clarify this coupling another weakly compressible model has been introduced and shown to give the constrained model as a limiting case.

Investigation of two special cases: uniaxial tension and isochoric traction has then shown the essential differences between imposed strain and stress control. It follows from these examples that strain control appears as a singular case with damage controlled by the kinematics and apparition of a high hydrostatic stress. Total or partial stress control therefore is a more realistic approximation for practical situations.

This however rises a problem for the implementation in a finite elements method where the incremental constitutive equation is required under full strain control; The approximate IC2 model may provide an appropriate and efficient framework.

REFERENCES

1. TRELOAR L.R.G. The physics of rubber elasticity, *Clarendon Press Oxford*, 1975.

2. OGDEN R.W. Non linear elastic deformations, *Ellis Hoorwood*, London, 1984

3. CHRISTENSEN R.M. Theory of viscoelasticity, *Academic Press*, 1971

4. LOCKETT F.J. Non linear viscoelastic solids, *Academic Press*, 1972

5. SIDOROFF F. Variables internes en viscoélasticité : I. Variables internes scalaires et tensorielles, *Journal de Mécanique*, vol.14, n°4, 1975, p.545-566

6. SIDOROFF F. Variables internes en viscoélasticité : II. Milieux avec configuration intermédiaire, *Journal de Mécanique*, vol.14, n°4, 1975, p.679-713

7. SIDOROFF F. Variables internes en viscoélasticité : III. Milieux avec plusieurs configurations intermédiaires, *Journal de Mécanique*, vol.14, n°4, 1975, p.679-713

8. SIMO J.C. On a fully three-dimensional finite-stain viscoelastic damage model :formulation and computational aspects, *Computer methods in applied mech. and eng.*, 60, 1987, p.153-173

9. ALAOUI-SOULIMANI A. Une méthode énergétique de modélisation de la viscoélasticité non linéaire en grandes déformations, Thesis, *ENPC*, Paris, 1993

10. CARPENTIER-GABRIELI Modélisation théorique et numérique des élastomères, Thesis, *Univ. Aix-Marseille II*, 1995

11. ANDRIEUX F. Sur les milieux visco-hyperélastiques endommageables, Thesis, *UTC*, D895, Compiègne, 1996

12. FARRIS R.J. The influence of vacuole formation on the response and failure of filled elastomers, *Trans. Soc. Rheo.*, 12, 2, 1968, p.315-334

13. HEUILLET P. Caractérisation de l'endommagement des propergols solides composites, Thesis, *UTC*, D460, Compiègne, 1992

14. ANDRIEUX F. et SAANOUNI K. Modélisation du comportement visco-hyperélastique endommageable, *Génie Mécanique des Caoutchoucs et des Elastomères*, Ed. C. Gisel et A. Coupard, Apollor, 1997, p. 283

15. ANDRIEUX F., SAANOUNI K. and SIDOROFF F. On hyperelastic solids with damage induced compressibility, *CRAS Série II*, tome 324, n°5, Paris, 1997, p.281-288

16. GERMAIN P. Cours de mécanique des milieux continus, *Masson*, Paris, 1973

17. LEMAITRE J. et CHABOCHE J.L. Mécanique des matériaux solides, *Ed. Dunod*, Paris, 1985

18. CHABOCHE J.L. Description thermodynamique et phénoménologique de la viscoplasticité cyclique avec endommagement, Thesis, *Univ. Paris III*, 1978

19. HALPHEN B. et NGUYEN Q.S. Sur les matériaux standards généralisés, *Journal de mécanique*, vol.14, n°1, 1975

20. TRUESDELL C.A. and NOLL W. Handbuch der Physics, *Springer-Verlag*, Berlin, 1965

21. SAANOUNI K., FORSTER C. and BENHATIRA F. On the anelastic flow with damage, *Int. Journ. Of Damage Mechanics*, Vol.3, 1994, p.140-169

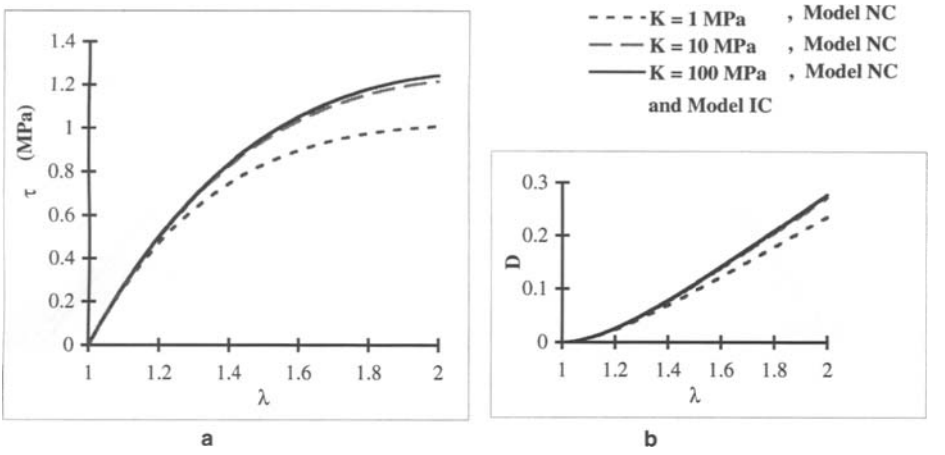

Figure 1: Variation of (a) Stress, (b) Damage versus the elongation for uniaxial tension under stress control

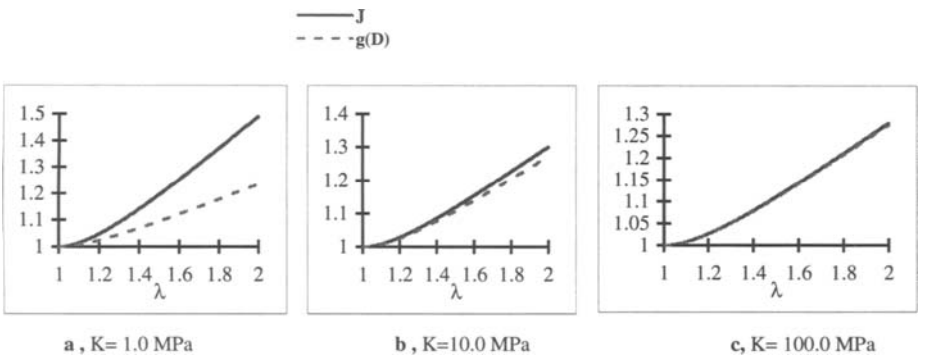

Figure 2: Variation of J and g(d) versus the elongation for uniaxial tension under stress control

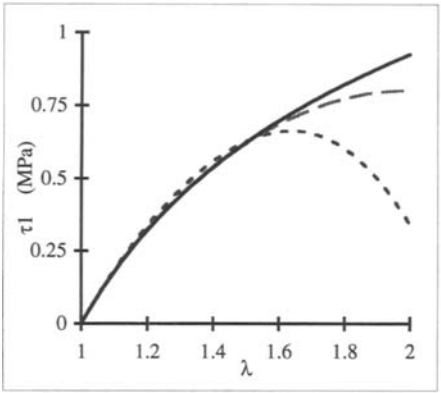

a

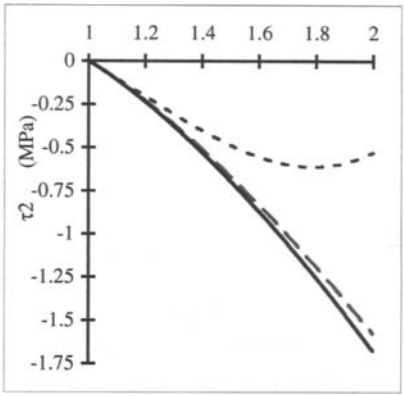

b

- - - - K = 1 MPa , Model NC
— — K = 10 MPa , Model NC
——— K = 100 MPa , Model NC
and Model IC

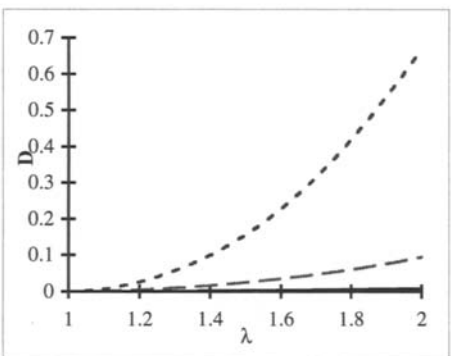

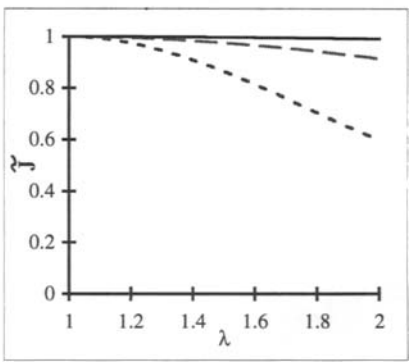

Figure 3: Variation of (a) first component of stress, (b) second component of stress, (c) damage, (d) effective volume variation versus the elongation for the isochoric extention under strain control

Damage Mechanics in Engineering Materials
G.Z. Voyiadjis, J.-W.W. Ju and J.-L. Chaboche (Editors)
© 1998 Elsevier Science B.V. All rights reserved.

A Micromechanics Approach to Predict Strength & Stiffness of Polymer Matrix Composites

A.G. Caliskan[a], S.W. Case[b] & K.L. Reifsnider[b]

[a]*Materials Science Department, Scientific Research Laboratories, Ford Motor Company, P.O. Box 2053, MD 3182, Dearborn, MI 48121*

[b]*Materials Response Group, Dept. of Engineering Science & Mechanics, Virginia Polytechnic Institute & State University, Blacksburg, VA 24061-0219*

1. ABSTRACT

The strength of unidirectional polymer matrix composites has been predicted using Pagano's axisymmetric damage model (ADM) in conjunction with Batdorf's statistical strength model. In order to utilize the axisymmetric model, hexagonally arranged fibers were converted to fiber rings. Then, the stress concentration and ineffective lengths at fibers adjacent to broken fibers could be calculated using ADM. These, quantities plus the Weibull parameters of carbon fibers were used to predict the tensile strength. Through the stress analysis, it was also shown that for large ratios of E_f/E_m there is local load sharing due to fiber breakage. The advantage of the analysis is that one can incorporate other geometric damage modes, such as interfacial debonding or matrix cracks, to investigate their effect on strength. The results of the analysis showed good comparison to experimental results for carbon fiber based systems. Finally, some stiffness predictions on fragmented and short fiber composites will be presented.

2. INTRODUCTION

Unlike homogeneous brittle materials, fiber reinforced composites contain a population of observable pre-existing defects which do not lead to final failure. Instead, an accumulation of matrix fracture or fiber fractures develop as the material is loaded. Fracture mechanics-based analysis may account for the strength of a single fiber, but it is inadequate for an unidirectional fiber composite where the behavior of the system is dominated by an accumulation and interaction of defects. As a result, any study of the strength of composites must emphasize the statistical process of damage development.

Because the damage growth process is controlled by microscopic parameters and properties, one needs to analyze these materials at this level. Traditionally, microscopic variations in these materials have been homogenized and much of the vital information, such as fiber/matrix bonding, has not been taken into account. It is for this reason that a micromechanics based approach must be used to account for the inhomogeneity of these materials. Micromechanics models can take into account details regarding fiber/matrix interface and allow one to analyze stress variations due to local effects around constituent materials.

The driving force for micromechanical strength evolution in PMC's is the stress concentration resulting from a broken fiber. In this review, various models of this phenomenon based on shear lag, elasticity, and variational analysis will be presented.

One of the first attempts to determine local stresses in and around fibers was presented by Cox [1]. He assumed that a rectangular array of aligned isotropic fibers existed in a matrix material which constituted a composite mat. The load transfer which occurs between the matrix and the fiber ends was derived to be exponentially decaying as a function of the axial coordinate. This formulation was a forerunner for the more popular classical solution describing stress redistribution which occurs near a broken fiber (i.e. the shear lag model) in a continuous composite system. This analysis provided the axial stiffness values and longitudinal contraction in the composite mat due to a uniaxial load. The results were compared to experimental values for the mechanical properties of such composites.

Rosen [2] was one of the first to investigate the stress redistribution which occurs in the vicinity of a fractured fiber of a unidirectional continuous fiber composites. By making the classical assumption of PMC's (i.e. the matrix essentially does not support axial load) the shear lag solution was formulated. This analysis suggested that the stresses decay exponentially at the fiber end as a function of the axial direction. These equations also provided a theoretical prediction for the size of the region where there is a stress rise (i.e. ineffective length). This portion of the fiber does not support any substantial load over this region.

Hedgepeth and Van Dyke [3] calculated the stress concentrations on neighboring fibers due to single and multiple fiber fractures. Their analysis used an influence function approach along with shear lag assumptions. Results were presented for both three-dimensional square and hexagonal arrays where specified numbers of fibers were broken. In addition, the stress concentration factor in the element adjacent to a broken fiber in a two dimensional array where the shear stress in the matrix adjacent to the broken fiber is restricted by a limit stress, was calculated. However, due to the shear lag assumptions, the model does not include the stiffness of the matrix. As a result, the applicability of such an analysis is limited.

In this study, Batdorf's [4] statistical strength model, which is a simplified version of an analysis developed by Harlow and Phoenix [5], will be used to predict strength of unidirectional composites. Through many approximations and simplifications the analysis was simplified to a point where the strength of a 3-D composite could be predicted. The analysis uses stress concentrations and ineffective lengths due to multiple fiber fractures to estimate stresses at which instability occurs, i.e. catastrophic failure. To study the effects of the simplifications on the predicted strength, a comparison was made to the exact solution developed by Harlow and Phoenix. It was shown that the simplifications and approximations resulted in differences on the order of only a few percent.

To calculate stress concentrations and ineffective lengths Pagano's Axisymmetric Damage model (ADM) is used [6]. The ADM is based on Reissner's variational theorem [7] and is constructed in conjunction with an equilibrium stress field in which r-dependence is assumed (i.e. σ_{zz} and $\sigma_{\theta\theta}$ are assumed to vary linearly in the radial direction). The problem is formulated in general to solve a variety of problems dealing with thermoelastic response of a concentric cylindrical body. The strength of the model is

that it is formulated in general to deal with not only fiber breakage, but any number of damage modes. In addition, axial and transverse loads can be applied, simultaneously. The only limit of the analysis is ones' ability to represent a problem by an axisymmetric concentric cylinders. Furthermore, both stress and displacement conditions are satisfied by the use of Reissner's theorem; thus a full stress and displacement field can be calculated. Furthermore, various damage modes can be included either separately or simultaneously in the representative volume element. As a result, stress states in the material due to damage growth and interaction can be examined. Finally, the ADM model will be used to predict stiffness. Two scenarios consisting of a composite with fragmented and short fibers will be studied.

3. MICROMECHANICAL MODELING

Due to the internal anisotropy of composites, one must model the mechanical behavior of these materials by considering microlevel geometry. The difficulty in analyzing the internal geometry comes from the fact that in real materials there is no well defined, periodic repeating "unit cell". That is to say, in a given composite volume, fiber spacing and orientation is not the same from point to point. Therefore, it is very difficult to define what is called a *representative volume element* (RVE), to reflect the composite as a whole. As a result, many researchers consider average values of fiber spacing and orientation.

The problem, however, arises when one decides to add various type of damage into the RVE. Numerous researchers have observed a whole family of damage modes which control macroscopic behavior [8-10]. Many times, these damage modes occur concurrently or in series. The following figure depicts some of the observed and suspected damage modes which could occur in fibrous composites.

Experimentally, it is very difficult to determine which damage mode(s) controls macroscopic behavior. Due to scale at which these processes occur, one cannot in any practical way determine initiation or growth of damage in situ during loading. Often, experimentalist can only obtain such information by post-mortem study of the fracture surface of a failed material. However, this type of information does not say much about the evolution or initiation of damage, which is most vital for micromechanical modeling.

Even if one knows the damage modes present in a given composite, there still lies the question of how to model these damage modes under the RVE scheme. Assuming one has carefully determined the damage modes in a given material experimentally, the task now lies in determining the stress states at the fiber-matrix level. Experimentally, there have been attempts at obtaining such information through the use of model composites [11]. Model composites are basically a scaled up version of a composite consisting of oversized fibers arranged in a controlled manner. At this level, one can obtain information regarding local strains and observe the evolution of damage in and around constituent materials. However, it is still unclear as to how to apply the data obtained by these studies to real composites since stiffness and certainly strength change as a function of volume. Furthermore, the effects due to geometric scaling are still unclear.

3.1 Batdorf's Statistical Strength Model

A strength model based on the statistical nature of fiber failure was developed by S.B. Batdorf [4]. Unlike previous models that base strength on chain-of-bundles model, Batdorf's model investigates the problem on the basis of formation and growth of individual fiber fracture. The model uses the well known *weakest link theory* developed by Weibull [12], which was originally used to study the strength variations in metals. The basic assumption of the model by Batdorf is that the fibers in the composite are unidirectional and the matrix is much less stiff than the fibers. As a result, the matrix does not appreciably contribute directly to the strength of the composite, but does however act to transfer stress from one fiber to another. Such is the case in carbon fiber composites, where in most cases the ratio of fiber to matrix stiffness is on the order of 100.

As a result of the loading in the fiber direction, we develop multiple single fiber breaks in the array of fibers that make up the composite. The fact that we are using a statistical theory we assume no particular fiber arrangement. In addition, fiber breaks occur in a random fashion throughout the composite. Once these breaks occur, naturally the unbroken fibers in the composite must carry the additional load not carried by the broken fibers. The resultant stress not only redistributes itself radially away from the cracked fiber, but also perpendicular to the crack plane on the neighboring fibers. The distribution of stress on the neighboring fibers has two major components of interest in this study. First, the magnitude of the stress concentration, which is at its maximum in the crack plane. The other component is the length of decay of stress to its' far field value. This value is most often referred to as the *ineffective length* or *stress transfer length.*

In this model, we first consider our composite to have an array of N fibers of length L. The fibers are all aligned in one direction, and the composite as a whole is loaded in the direction parallel to the fibers. As mentioned previously, this model assumes that there is a progression of fiber failures. That is to say, as we load the composite we form single fiber breaks (singlets) randomly in the array of fibers. These single fiber breaks cause an overstress in the neighboring fibers. As a result, a neighboring fiber fails and thus a doublet is formed. As we further increase the load doublets become triplets and in general "i-plets" are formed. Since we are interested in the progression of fiber breaks, we must know the number of fibers and the stress distribution on these fibers surrounding the fiber break. For a singlet, the number of neighboring fibers is denoted n_1, each of which is subject to an overstress described by a stress concentration factor c_1 (relative to the applied stress) at the plane of the fiber break. The overstressed region extends over a distance δ_1, but diminishes with distance from the fiber break. A doublet has n_2 neighbors that are overstressed by c_2, with the overstress extending over a distance δ_2. The subscript i will designate the above quantities for an i-plet. For multiplets of order 2 or higher, the stress concentration factor will not be the same for all neighboring fibers. But for the sake of simplicity this difference will be ignored in this study.

Since the failure of fibers is a statistical event, we assume the failure of the fibers to conform to the Weibull 2-parameter representation. That is to say, when a stress σ is applied uniformly over a length l, the cumulative probability of failure P_f is given by

$$P_f(\sigma) = 1 - e^{-lk\sigma^m} \qquad \text{,where } k = \left(\frac{1}{\sigma_o}\right)^m \tag{1}$$

where σ_o is the characteristic strength of a fiber of length l, and m is the Weibull modulus of the fiber. In Batdorf's analysis P_f is taken to be

$$P_f \approx kl\sigma^m \tag{2}$$

if P_f is assumed to be $<<1$. In the present analysis, the full form shown in equation (1) is used to predict strength. If there are N fibers with length L, the number of singlets formed in the composite is simply

$$Q_1 = NP_f \tag{3}$$

A singlet becomes a doublet when one of the neighboring fibers in its surrounding breaks due to the stress concentration. If we assume the stress varies linearly from the overstress to the far field stress, we obtain for the failure probability of such an overstress segment to be

$$P_f^{(2)} = 1 - e^{-k\lambda_1(c_1\sigma)^m} \tag{4}$$

where

$$\lambda_1 = \delta_1 \frac{c_1^{m+1} - 1}{c_1^m(c_1 - 1)(m+1)} \tag{5}$$

is the effective length of the overstress region. As a result the probability that a given singlet becomes a doublet is

$$P_{1\to 2} = n_1(1 - e^{k\lambda_1(c_1\sigma)^m}) \tag{6}$$

The number of doublets formed is given by multiplying the number of singlets by the probability of failure of a singlet becoming a doublet, i.e.

$$Q_2 = Q_1 P_{1\to 2} \tag{7}$$

In general for the number of i-plets formed we have

$$Q_{i+1} = Q_i n_i(1 - e^{k\lambda_i(c_i\sigma)^m}) \qquad \text{where } i = 1,2,3,\ldots N \tag{8}$$

If one plots this equation for $i = 1,2,3...N$, where i is the multiplet number, the following graph is produced in Figure (1). This graph is a hypothetical plot of the Q functions. The x-axis represents the applied stress and the y-axis represents the number of i-plets formed. As one goes along the x-axis the stress increases. Once σ_1 is reached, singlets are formed in the array of fibers. Further increase in stress results in more singlet formation until σ_2, at which point some of the singlets become doublets, etc. These Q-plots form a failure envelop for the material under consideration. As the multiplicity of the fiber fractures increases, the failure envelop collapses on to the x-axis. The point where this envelop crosses the x-axis is the stress at which the composite fails.

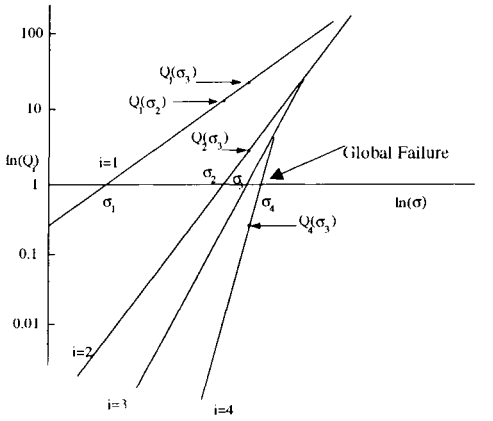

Figure 1 Schematic of Q-plots for interpretation of ultimate strength (Batdorf [4]).

3.2 Pagano's Axisymmetric Damage Model

In order to utilize the model described above, we must calculate the stress concentration and ineffective lengths at fibers adjacent to broken fibers. To do this we use Pagano's axisymmetric damage model [6]. Initially, this model was developed to study the various damage modes that occur as a result of loading a 0° unidirectional brittle matrix composites (BMC). In BMC's, it has been shown that initially matrix cracks form and grow until the matrix is fully cracked and fibers bridge the crack face. Thereafter, the cracks either grow into the fibers or deflect to form interfacial debonding on the fiber surface. Due to the circular geometry of the fibers, the unit cell considered is axisymmetric. The model can approximate stress fields and energy release rates of bodies in the form of concentric cylinders and subject to various idealized internal cracks and boundary conditions (see Figure 2).

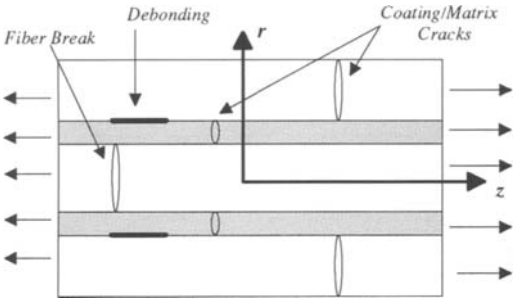

Figure 2 Damage modes in brittle matrix composites

The approach utilized is Reissner's Variational Theorem [7], which has been used to study stress fields in flat laminates [13], and in involute bodies of revolution [14]. It has been shown that such a model produces an accurate description of the stress field ahead of the stress riser, and it can also incorporate multiple sublayers to improve solution accuracy.

The model is generated by subdividing the body into regions containing a core and a number of shells (see Figure 3) and satisfying the Reissner variational equation with an assumed stress field in each region.

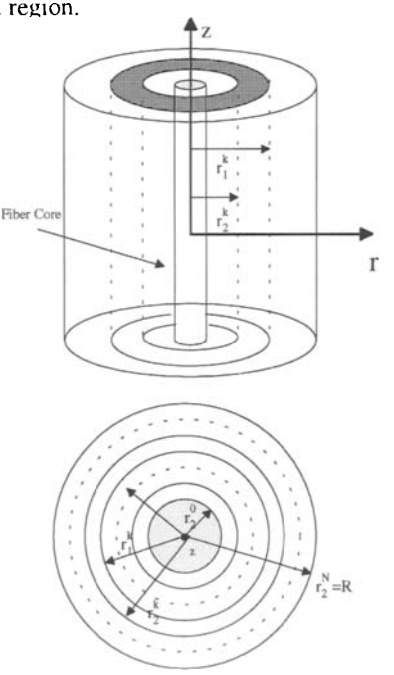

Figure 3 Axisymmetric element showing a typical layer.

Reissner has shown that the governing equations of linear elasticity can be obtained provided the variational operator δ is applied both stresses and displacements.

$$\delta J = 0 \tag{9}$$

where

$$J = \int_V F dV - \int_{S'} \tilde{T}_i \xi_i dS \tag{10}$$

and

$$F = \frac{1}{2}\sigma_{ij}(\xi_{i,j} + \xi_{j,i}) - W \tag{11}$$

in terms of the Cartesian coordinates $x_i (i = 1,2,3)$, where W is complimentary energy density, V is the volume element, S is the entire surface, $\tilde{T}_i$ are the prescribed tractions, ξ_i are the displacement components, and S' is the portion of the boundary on which one or more traction components are prescribed.

The stress field is assumed such that σ_θ and σ_z are linear in r within each region, while the forms of σ_r and τ_{rz} are chosen to satisfy the axisymmetric equilibrium equations of linear elasticity. Letting σ_1, σ_2, σ_3, and σ_5 represent σ_z, σ_θ, σ_r, and τ_{rz}, respectively, we arrive at the relations in the region $r_1 \le r \le r_2$

$$\sigma_i = p_{iJ} f_J^{(i)} \qquad (i = 1,2,3,5; J = 1,2,..5) \tag{12}$$

where $f_J^{(i)}$ are known shape functions of r defined such that

$$p_{i\alpha}(z) = \sigma_i(r_\alpha, z) \qquad (i = 1,2,3,5; \alpha = 1,2) \tag{13}$$

The remaining dependent variables follow directly from the mathematics, they include the weighted displacements

$$(\bar{u}, \hat{u}, \breve{u}, \tilde{u}) = \int_{r_1}^{r_2} u(1, r, r^2, r^3) dr \tag{14}$$

where u is the radial displacement component, and

$$(\hat{w}, \breve{w}) = \int_{r_1}^{r_2} w(r, r^2) dr \tag{15}$$

where w is the axial displacement. For a body composed of a core region plus N shells, the formulation leads to the solution of $18N + 16$ algebraic and ordinary differential equations in z. Proper end boundary conditions on the planes $z = const.$ for each region for which $r_1 \neq 0$ consists of specifying one member of each of the products

$$p_{53}\bar{u}, \left\{\frac{r_2^2 p_{51} - r_1^2 p_{52}}{r_1 r_2 (r_2 - r_1)} - \frac{(r_1^2 + r_1 r_2 + r_2^2) p_{53}}{r_1^2 r_2^2}\right\}\breve{u},$$

$$\left\{\frac{r_1 p_{52} - r_2 p_{51}}{r_1 r_2 (r_2 - r_1)} + \frac{(r_1 + r_2) p_{53}}{r_1^2 r_2^2}\right\}\bar{u} \tag{16}$$

For the core region $r_1 = 0$ these become

$$\left(\frac{p_{52}}{r_2} - r_2 p_{53}\right)\breve{u}, p_{53}\hat{u} \tag{17}$$

while for all regions, one member of each of the products

$$\left\{\frac{r_2 p_{11} - r_1 p_{12}}{r_2 - r_1}\right\}\hat{w}, \left\{\frac{p_{12} - p_{11}}{r_2 - r_1}\right\}\bar{w} \tag{18}$$

must be prescribed on planes $z = const.$. On planes $r = const.$, the appropriate prescribed functions consist of one member of each of the following products

$$p_{31}u_1, p_{51}w_1 \tag{19}$$

on surfaces $r = r_1 \neq 0$ and

$$p_{32}u_2, p_{52}w_2 \tag{20}$$

on surfaces $r = r_2$. Furthermore, continuity conditions can be written for the surfaces $r = const.$ and planes $z = const.$ which are the internal to the body (see ref. 6). The number of regions in the r direction can be increased in order to improve solution accuracy. Since the field equations within each region reduce to a system of algebraic and ordinary differential equations with constant coefficients, the general form of the solution for any of the dependent variables $P(z)$ is expressed by

$$P(z) = \sum_i A_i e^{\lambda_i z} + P_p(z) \tag{21}$$

within each region, where A_i are constants, λ_i are eigenvalues of a determinant and $P_p(z)$ is a particular solution, which in this case is a polynomial.

4. STRENGTH PREDICTIONS

In predicting strength, the specific system considered is a unidirectionally reinforced composite with continuous fibers. The fibers are also assumed to be arranged in a hexagonal pattern. This type of arrangement can be seen locally in cross-sections perpendicular to the fiber direction. This is especially true for high fiber volume fractions. In addition, hexagonal arrangement lends itself for ease in numerical studies where relative distances between fiber can be calculated using simple geometric analysis. As mentioned before, the crack growth mechanism in PMC's is generally in the form of fiber breaks which initiate at various locations in the material until clusters of fiber breaks form and coalesce until finally the material fails. In our analysis, we must determine the stress concentration as well as the ineffective lengths around singlets and multiplets. For singlets, the issue determining relative distance from the broken core fiber to neighboring fibers is nonexistent since all the adjacent fibers are he same distance away. But for doublets, for example, the distance to neighboring fibers varies, thus the extent of stress redistribution is not uniform around the break.

In order to overcome this problem the hexagonal array of fibers is transformed into concentric rings of fibers and matrix (See Fig. 4). This type of arrangement was first used by Hedgepeth and Van Dyke [3] and later by Case [15] to study stress concentrations in fiberous systems. The concentric, axisymmetric arrangement, or concentric cylinder model (CCM) consists of a single fiber at the center surrounded by annular rings of fiber consisting of 6, 12, 18... fibers radially outward from the center.

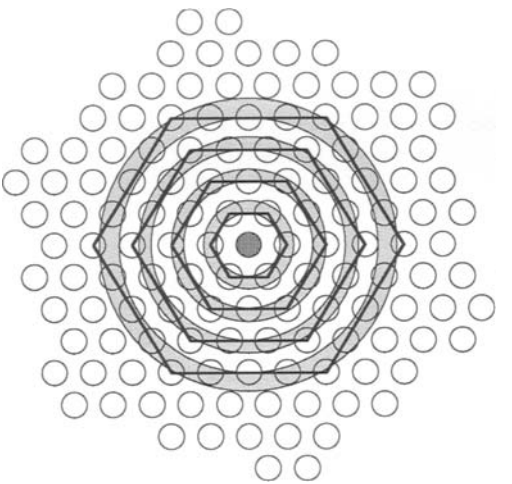

Figure 4 Schematic of hexagonal array converted to fiber rings.

As a result, the stress concentration caused by the broken fiber core will be equally distributed on the rings surrounding it. To simulate the progression of fiber breaks, we break the first fiber ring surrounding the broken fiber since it experiences the highest stresses. Then, the next ring surrounding the 7 broken fibers is broken. As a result, the progression of fiber

breaks occurs in the form of broken rings rather than individual fiber breaks. Nevertheless, as will be shown, this approximation mimics damage growth in PMC's and results in good strength predictions.

In order to utilize Pagano's axisymmetric damage model, we need to define an axisymmetric element consisting of fiber and matrix rings. The following axisymmetric element in Figure 5 shows the arrangement of the fiber and matrix rings. The dimensions are chosen so as to preserve, as well as possible, the fiber volume fraction of the composite, which is 60% for the element shown.

Due to the approximation of the hexagonal array, as we put more fiber rings the fiber volume fraction is not perfectly preserved, but decreases by about 5%. In addition to the fiber rings, we have a composite ring surrounding all the inner rings. That is to say, at a far distance from the point of damage initiation, we have the properties of the undamaged composite. The elastic properties of the graphite fibers are $E_{11} = 301$ GPa $E_{22} = 20$ GPa , $G_{12} = 20$ GPa, $\nu_{12} = 0.20$, $\nu_{23} = 0.25$.

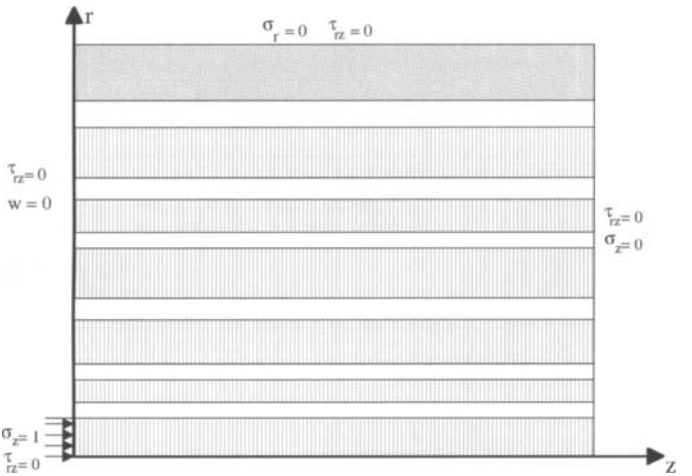

Figure 5 Axisymmetric element showing boundary conditions.

To simulate a fiber fracture, we apply a unit pressure at one of the boundaries of the fiber regions to simulate an opening crack. We can see in Figure (5) the various boundary conditions used in the study. To simulate a broken ring, we apply a pressure to the ring as done to the fiber core. Note, however, that a broken ring in actuality is the failure of a number of fibers rather than just one. From this arrangement, we calculate the axial stresses at both the surface and center of the rings surrounding the broken fiber(s).

In Figure 6, we see the calculated stress distribution using Pagano's axisymmetric damage model. As once can see, at the plane of the fiber break, we have a stress concentration which at some distance $\delta/2$, the ineffective length, dies down to the far field or applied stress. If we go on further, i.e. break the next ring of fibers, we form a total of 7 fiber breaks. In Figure 7 we see the stress distribution on the ring adjacent to the 7 broken fibers and the second most adjacent ring. As expected, both the stress concentration and the ineffective length increases at both the center and the surface of the fiber ring. In addition, one can see that at the second

neighboring ring there is very little stress concentration, and the stresses do not vary much in the axial direction. This shows the localized stress redistribution that occurs as a result of fiber fracture in PMC's. If we break yet another ring, we again see and increase in stress concentration and ineffective length. In addition, the greater number of broken fibers result in the stress distribution in the radial direction to be not as localized. This is a consistent trend seen in fracture mechanics of isotropic materials where the stress ahead of a large crack dies off slower than a small crack.

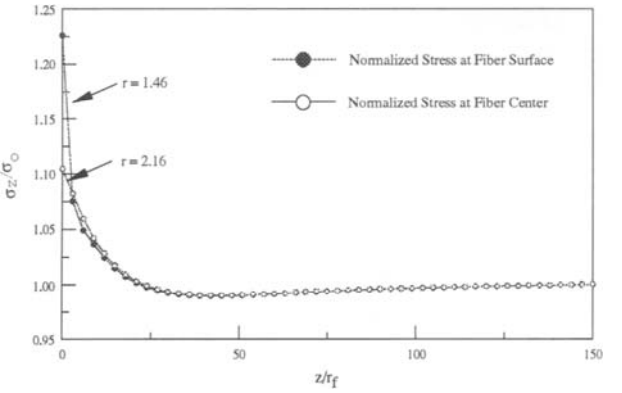

Figure 6 Stress distribution due to one fiber break at neighboring fiber ring (E_m= 0.75 GPa).

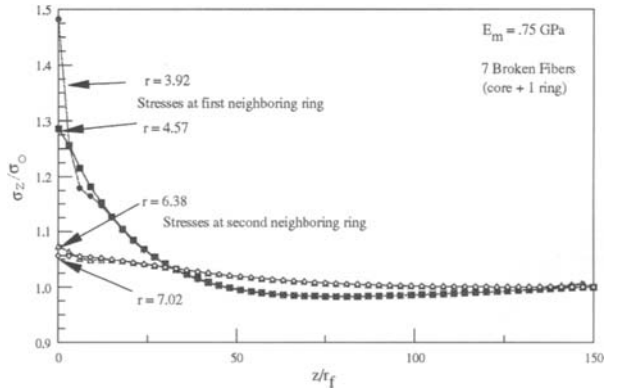

Figure 7 Stress distribution due to one fiber break plus one ring (7 fibers) at first and second neighboring fiber rings (E_m= 0.75 GPa).

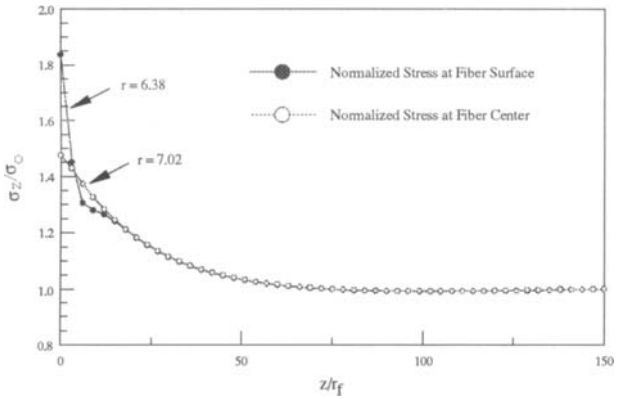

Figure 8 Stress distribution due to one fiber break plus two rings (19 fibers) at neighboring fiber ring (E_m= 0.75 GPa).

In order to predict the strength of brittle materials, a characterization of the strength distribution must be made. The most widely used and accepted methods is by using Weibull analysis [12]. In the Weibull analysis, usually two quantities are used to characterize the material's statistical strength. The first is the Weibull Modulus, m, which gives the spread in the distribution of strength around a mean. For brittle materials, m is less that 10, which suggest a large spread in strength, compared to a metal for which m is close to 20. The second parameter is characteristic strength, σ_o, which is the strength of the material for a given gauge length. For our system, σ_o and m were determined form strength versus gauge length data for AS4 carbon fibers obtained from Wimolkiatisak and Bell [16]. Then the two parameters were determined by a procedure outline by Masson and Bourgain [17]. The results of the analysis for AS4 fibers result in m = 10.649 and σ_o = 760.878 ksi for a 1 mm. gauge length.

In order to utilize Batdorf's analysis, the stress concentrations and the ineffective lengths for all values of i in this range must be known. As a result. curves were fitted to the data generated, thus stress concentrations and ineffective lengths for all multiplicties from 1 to 17 breaks were calculated (see Figures 9 and 10). The ineffective lengths were determined to be the length at which the stress crosses the far-field value (i.e. $\sigma_z/\sigma_\infty = 1$).

In Figure (11), the results of the analysis is compared to experimental tensile strengths of carbon fiber based PMC's. It should be noted that the experimental values are an average of a number of tests on specimens of same dimensions (3" X 0.5" X 0.04"). The dimensions of the specimens corresponds to the total number of fibers to be 193,358 for a fiber radius of 3.57 μm and v_f = 0.6, assuming a hexagonal arrangement. As can be seen, the results show good correlation with experimental results. In the analysis, the critical i-plet was at most 7, thus one might expect limited fiber damage prior to final failure. Since the fibers are annular rings, it is not apparent which value, i.e center or surface, is most representative of the "real" system. But,

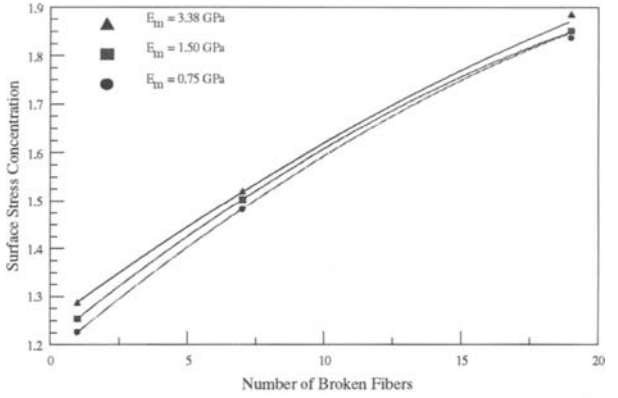

Figure 9 Surface stress concentration on adjacent fibers as a function of broken fibers and matrix stiffness for a carbon fiber polymer matrix composite

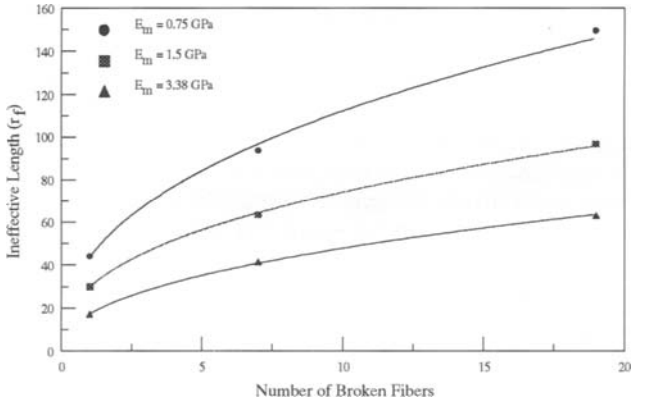

Figure 10 Ineffective length as a function of broken fibers and matrix stiffness for a carbon fiber polymer matrix composite.

it is safe to assume that the strength is somewhere within the range predicted, and the lower prediction is definitely a lower bound on the strength.

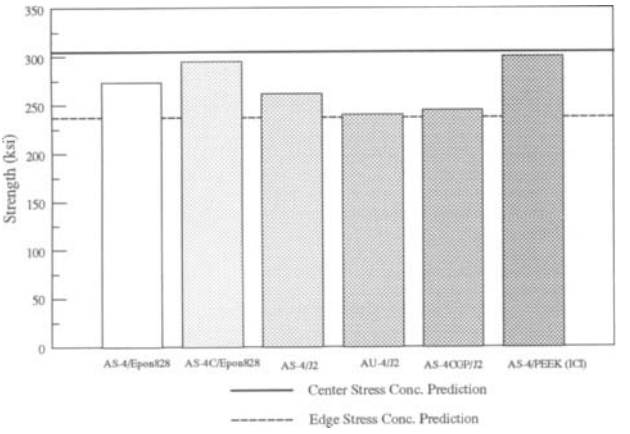

Figure 11 Strength predictions at both surface and center values compared to tensile strengths of carbon fiber polymer matrix composites.

5. STIFFNESS PREDICTIONS

One of the reasons for studying stiffness is to aid in predicting stiffness degradation due to service conditions. That is to say, in time the materials used in the structure will experience some damage due to cyclic loading and unloading. Of course, other environmental effects also degrade material properties, but these will not be modeled in this study. In PMC's, the cause of stiffness change is mainly due to fiber breakage and fragmentation, i.e. multiple fracture of a single fiber. As a result of smaller fiber fragments, the ability of the fibers to carry load diminishes, thus the stiffness of the composite decreases. As will be shown later, depending on the fiber/matrix properties and fiber arrangement, fiber fragmentation can have dramatic effects on overall stiffness.

In this section the overall stiffness of a fragmented continuous fiber composite as well as the stiffness of a short-fiber composite will be studied. To calculate the effective stiffness of the composite, we need to measure the stresses and strains in both the fiber and the matrix. To calculate these microlevel quantities, Pagano's axisymmetric damage model is used. Next, the volume average stresses and strains are determined by the following

$$< \sigma_z^{(i)} >= \frac{1}{V^{(i)}} \int_{V^{(i)}} \sigma_z^{(i)} dV \,, \quad < \varepsilon_z^{(i)} >= \frac{1}{V^{(i)}} \int_{V^{(i)}} \varepsilon_z^{(i)} dV \tag{22}$$

where i = f,m denoting fiber and matrix, respectively. Then the composite stress and strain are calculated according to rule of mixtures

$$< \sigma_z >_c = f < \sigma_z^f > + (1-f) < \sigma_z^m >$$
$$< \varepsilon_z >_c = f < \varepsilon_z^f > + (1-f) < \varepsilon_z^m > \quad (23)$$

As a result, the effective stiffness is given simply by

$$E_{eff} = \frac{< \sigma_z >_c}{< \varepsilon_z >_c} \quad (24)$$

For the following analysis, the properties were chosen to be that of AS4 carbon fibers (E_{11} = 235 GPa, $E_{22} = E_{33}$ = 20 GPa, ν_{12} = 0.20, and ν_{23} = 0.25), and the matrix E = 2.9 GPa and ν = 0.35.

5.1 Stiffness of Fragmented Fiber Composite

The advantage of using micromechanical stresses are that now one can place into the model various damage modes and recalculate the effective stiffness. The importance of such an analysis is that it enables one to predict stiffness degradation as a function of damage mode and progression. Using stiffness change as a damage parameter provides an easy way to ascertain damage accumulation in a structure. The process can also be reversed so stiffness can be determined if the amount of damage in a structure is known. As a result, stiffness of materials during service can be monitored. As mentioned previously, damage development in PMC's is mainly due to fiber breakage and fiber fragmentation. Fiber fragmentation results in damage growth throughout the material without any signs of gross failure. However, as reported by many researchers [18], the effects of microcracking on stiffness is quite significant. In the fiber fragmentation process, the degree to which fragmentation occurs is controlled mainly by interfacial properties and the fiber's statistical strength characteristics. Similarly, in PMC's fiber microcracking reaches a saturation point up to a point where matrix failure initiates and gross failure occurs. However, it has been reported that fiber crack saturation is not achieved for perfectly bonded PMC's [19]. As a result, such composites show very low toughness compared to the neat resin. This imperfect bonding has been show to be controlling property that gives CMC's improved toughness over traditional ceramics. In this study, bonding is assumed to be perfect.

In Figure (12 a), the axisymmetric element used in the analysis is shown. To simulate a fiber break, the stresses on the fiber surface are set to be zero. To load the element, far from the crack plane a unit displacement is applied. By varying the height or the z-dimension of the element, we can analyze different fragmentation lengths. As before, fiber and matrix stresses are computed and averaged over their respective volumes. In Figure (12 b), both the effects of fiber fragmentation and fiber volume fraction are presented. It is hoped that such an analysis will prove to be useful in predicting stiffness of a composite once damage modes are known. Such a curve can be generated for other damage modes such as interfacial debonding, matrix cracking, thermal effects or any combination of these phenomenon.

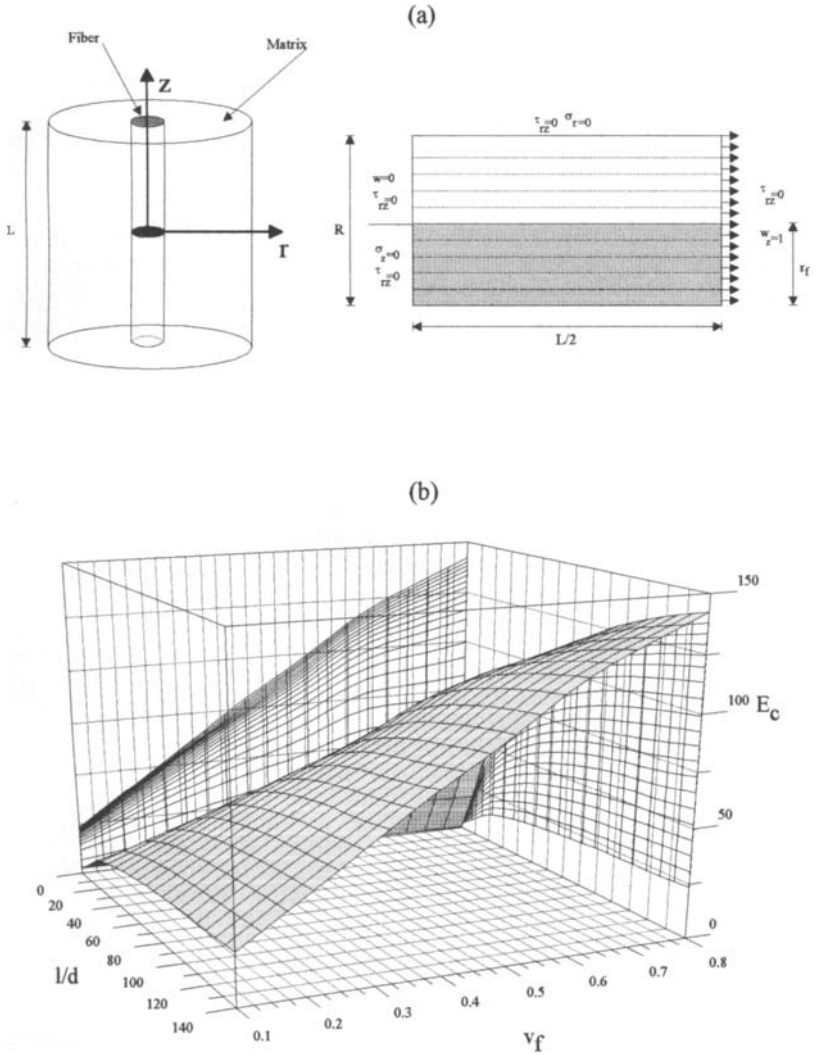

Figure 12 (a) Schematic of axisymmetric model for continuous fiber composite with fiber fracture and (b) Variation of effective modulus as a function of fiber fragmentation length and fiber volume fraction..

5.2 Short-Fiber Composites

One of the least understood areas of composite materials technology is the behavior of short fiber composites. It is, however, ironic that by volume short fiber composites are produced by greater amounts than continuous fiber systems. Of the many short fiber systems, fiber glass reinforced resins have been utilized by many different industries, including

commercial and civilian applications such as automobiles and aircraft. The main reason for this is due to the ease in manufacturing and lower material cost. In many cases, the effective properties of such systems are treated as isotropic materials. That is to say, for random short fiber materials, it is assumed that directional variation in properties do not exist. However due to manufacturing techniques fibers can assume certain orientations. In this study, the effective modulus of a short fiber composite which is unidirectionally oriented will be calculated. In Figure (13), the axisymmetric element used in the analysis is shown. The dimensions of the fiber and the surrounding matrix are chosen such that the aspect ratio of the fibers are 50. The properties of the fiber are that of steel (E = 190 GPa, $\nu = 0.3$) and the matrix is an epoxy (E = 2.5 GPa, $\nu = 0.35$). The dimensions of the fiber are varied so as to achieve different fiber volume fractions. In the limit as the dimensions of the fiber reach the outer dimensions, $v_f = 1$, and as the fiber dimension diminishes we have $v_f = 0$, as expected.

In Figure (14), the results of the analysis is shown. In addition, the results are compared to Carman's [20] results and experimental results generated by Berthelot [21] for a steel/epoxy short fiber system. Both the present and Carman's result overpredict the experimental values. This is due to the fact that during manufacturing of the specimens, there was a distribution of fiber orientations from ±10°. Another reason for the overprediction is due to the assumption of perfect bonding that both models incorporate. Nevertheless, the results show good agreement with experimental results and follow the expected trend.

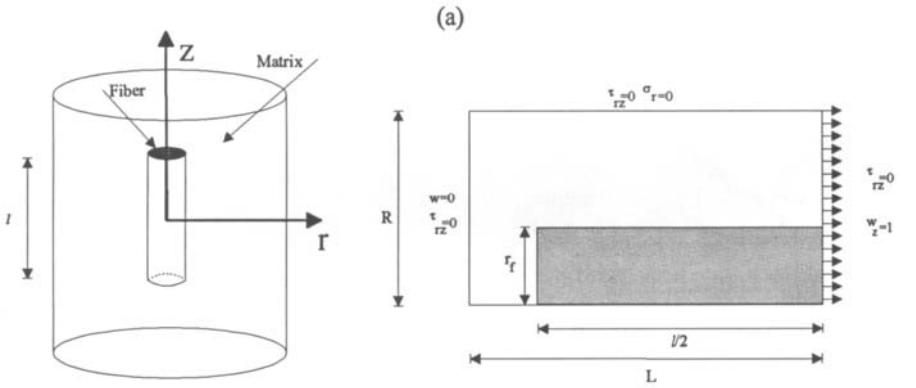

Figure 13 Schematic of axisymmetric model for short fiber composite with aspect ratio of 50.

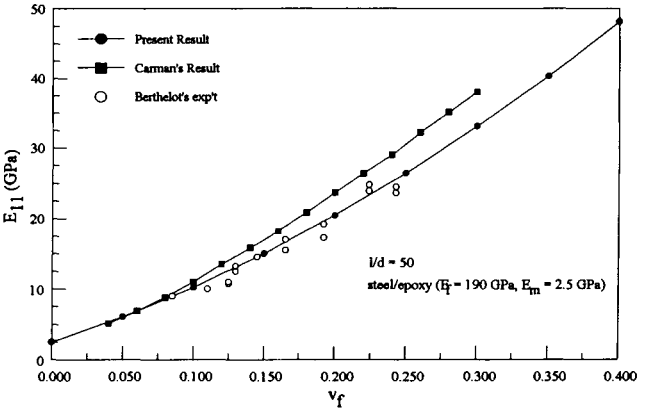

Figure 14 Results of stiffness calculations and experiments for a short-fiber composite.

6. CONCLUSIONS & FURTHER WORK

- A representative volume of a continuous fiber composite with fibers arranged in a hexagonal pattern was constructed to study the effects of fiber fracture on load sharing by neighboring fibers. The stress distribution in the fibers adjacent to the fiber breaks were calculated.
- From the stress distributions, the stress concentration and the ineffective lengths were used in conjunction with the fiber's Weibull parameters to predict the strength of the composite as a whole. This was achieved through a statistical strength model developed by Harlow and Phoenix [5] and later refined by Batdorf [4].
- The results of the strength predictions were compared to experimental results of tensile strength of carbon fiber composites.
- Using Pagano's model, the stiffness of a continuous fiber composite was determined from calculated microstresses and strains. The stresses and strains were volume averaged over each constituent and the effective modulus was determined for a fragmented fiber composite and a short-fiber composite.
- The advantage of using Pagano's model is that we can calculate the change in stress fields due to any type of damage. As a further study, the effects of different damage modes, such as debonding and matrix cracks, on stiffness and strength can be studied.

REFERENCES

1. Cox, H.L. "The Elasticity and Strength of Paper and Other Fiberous Materials," *Brit. J. Appl. Phys.*, v.3 (1952), pp. 72-79.
2. Rosen, B.W. "Fiber Composite Materials," *Am. Soc. of Metals*, Chap. 3 , (1964) pp. 37 -75.

3. Hedgepeth, J.M. and Van Dyke, P.V. "Local Stress Concentrations in Imperfect Filementary Composite Materials," *J. Comp. Mat.*, v.1 (1967), pp.294 - 309.
4. Batdorf, S.B. "Unidirectionally Reinforced Composites -I," *J. Rein. Plastics and Comp.*, v. 1 (1982), pp. 153 - 164.
5. Harlow, D.G. and Phoenix, S.L. "The Chain-of-Bundles Probability Model for the Strength of Fiberous Materials I: Analysis and Conjectures," *J. Comp. Mat.*, v.12 (1978), pp. 195 - 214.
6. Pagano, N.J. "Axisymmetric Micromechanical Stress Fields in Composites," *Proc. 1991 IUTAM Symp. on Local Mechanics Concepts for Composite Materials*, Springer-Verlag, (1991), pp.1 - 26.
7. Reissner, E. "On a Variational Theorem in Elasticity," *J. Math. Phys.*, v. 29 (1950), pp. 90-95.
8. Cho, C., Holmes, J.W., and Barber, J.R. "Distribution of Matrix Cracks in a Uniaxial Ceramic Composite," *J. Am. Ceram. Soc.*, v. 75 (1992), pp.316-324.
9. Marshall, D.B. and Cox, B.N. "The Mechanics of Matrix Cracking in Brittle-Matrix Composites," *Acta Metall.*, v. 33, (1985), pp 2013-2021.
10. Marshall, D.B. and Evans, A.G. " Failure Mechanisms in Ceramic-Fiber/Ceramic-Matrix Composites," *J. Am. Ceram. Soc.*, v. 68 (1985), pp.225-231.
11. Case, S.W., Carman, G.P., Lesko, J.J., Fajardo, A.B., and Reifsnider, K.L. "Fiber Fracture in Unidirectional Composites," *J. Comp. Mat.*, v. 29 (1995), pp. 208 - 228.
12. Weibull, W "A Statistical Distribution Function of Wide Applicability," *J. Appl. Mech.*, v. 18 (1953), pp. 293 - 297.
13. Pagano, N.J. "Stress Fields in Composite Laminates," *Int. J. Solids Structures*, v. 14 (1978), pp. 521 - 532.
14. Pagano, N.J. "Axisymmetric Stress Fields in Involute Bodies of Revolution," *J. Spacecraft and Rockets*, v. 23 (1986), pp. 231 - 245.
15. Case, S.W. *Mechanics of Fiber-Controlled Behavior in Polymeric Composite Materials*. Ph.D. Dissertation, Virginia Tech, (1996).
16. Wimolkiatisak, A.S. and Bell, J.P. "Interfacial Shear Strength and Failure Modes in Interphase-Modified Graphite-Epoxy Composites," *Polymer Composites*, v. 10 (1989), pp. 162 - 172.
17. Masson, J.J. and Bourgain, E. "Some Guidelines for a Consistent Use of the Weibull Statistics with Ceramic Fibers," *Int. J. Fract.*, v. 55 (1993), pp. 303 - 319.
18. Highsmith, A.L. and Reifsnider, K.L. "Stiffness-Reduction Mechanisms in Composite Laminates," In Damage in Composite Materials, *ASTM STP 775*, ASTM, Philadelphia, PA. (1982), pp. 103-117.
19. Feillard, P., Desarmot, G. and Favre, J.P. " A Critical Assessment of Fragmentation Tests with Glass/Epoxy Systems," *Comp. Sci. and Tech.*, v. 49 (1993), pp. 109 - 119.
20. Carman, G.P. *Micromechanics of Finite Length Fibers in Composite Materials*. Ph.D. Dissertation, Virginia Tech, (1991).
21. Berthelot, J.M. "Effect of Fiber Misalignment on the Elastic Properties of Oriented Discontinuous Fiber Composites," *Fibre Sci. and Tech.*, v. 17 (1982), pp. 25 - 39.

AUTHOR INDEX

This Page Intentionally Left Blank

AUTHOR INDEX